frontiers | Research Topics

Joint inversion and imaging in geophysics

Edited by
Jianzhong Zhang, Jiefu Chen, Wanyin Wang,
Qizhen Du and Jian Sun

Published in
Frontiers in Earth Science

ISSN 1664-8714
ISBN 978-2-8325-3362-8
DOI 10.3389/978-2-8325-3362-8

About Frontiers

Frontiers is more than just an open access publisher of scholarly articles: it is a pioneering approach to the world of academia, radically improving the way scholarly research is managed. The grand vision of Frontiers is a world where all people have an equal opportunity to seek, share and generate knowledge. Frontiers provides immediate and permanent online open access to all its publications, but this alone is not enough to realize our grand goals.

Frontiers journal series

The Frontiers journal series is a multi-tier and interdisciplinary set of open-access, online journals, promising a paradigm shift from the current review, selection and dissemination processes in academic publishing. All Frontiers journals are driven by researchers for researchers; therefore, they constitute a service to the scholarly community. At the same time, the *Frontiers journal series* operates on a revolutionary invention, the tiered publishing system, initially addressing specific communities of scholars, and gradually climbing up to broader public understanding, thus serving the interests of the lay society, too.

Dedication to quality

Each Frontiers article is a landmark of the highest quality, thanks to genuinely collaborative interactions between authors and review editors, who include some of the world's best academicians. Research must be certified by peers before entering a stream of knowledge that may eventually reach the public - and shape society; therefore, Frontiers only applies the most rigorous and unbiased reviews. Frontiers revolutionizes research publishing by freely delivering the most outstanding research, evaluated with no bias from both the academic and social point of view. By applying the most advanced information technologies, Frontiers is catapulting scholarly publishing into a new generation.

What are Frontiers Research Topics?

Frontiers Research Topics are very popular trademarks of the *Frontiers journals series*: they are collections of at least ten articles, all centered on a particular subject. With their unique mix of varied contributions from Original Research to Review Articles, Frontiers Research Topics unify the most influential researchers, the latest key findings and historical advances in a hot research area.

Find out more on how to host your own Frontiers Research Topic or contribute to one as an author by contacting the Frontiers editorial office: frontiersin.org/about/contact

Joint inversion and imaging in geophysics

Topic editors

Jianzhong Zhang — Ocean University of China, China
Jiefu Chen — University of Houston, United States
Wanyin Wang — Chang'an University, China
Qizhen Du — China University of Petroleum, Huadong, China
Jian Sun — Ocean University of China, China

Citation

Zhang, J., Chen, J., Wang, W., Du, Q., Sun, J., eds. (2023). *Joint inversion and imaging in geophysics*. Lausanne: Frontiers Media SA.
doi: 10.3389/978-2-8325-3362-8

Table of contents

frontiers | Frontiers in Earth Science

ORIGINAL RESEARCH
published: 25 July 2022
doi: 10.3389/feart.2022.951033

Rupture Characteristics Analysis of the 2020 *M*w 7.4 Oaxaca, Mexico Earthquake Using Teleseismic, High-Rate GPS, and InSAR Data

Guisen Wen[1], *Xingxing Li*[1]*, *Yingwen Zhao*[1], *Caijun Xu*[1] *and Guangyu Xu*[2]

[1]School of Geodesy and Geomatics, Wuhan University, Wuhan, China, [2]Faculty of Geomatics, East China University of Technology, Nanchang, China

The June 23 2020 Oaxaca *M*w 7.4 interplate thrust earthquake struck the state of Oaxaca in Mexico, generating strong shaking and a long-lived tsunami. This earthquake is well recorded by the teleseismic, high-rate Global Positioning System (GPS) and Interferometric Synthetic Aperture Radar (InSAR) data, which provides an opportunity to understand the rupture characteristics of the Mexican subduction zone. Here, an integrated inversion strategy involving centroid moment tensor inversion and kinematic finite-fault inversion is used to study the rupture history of the 2020 Oaxaca earthquake. The fault geometry and source duration time derived from the centroid moment tensor solution are used as prior information in linear kinematic finite-fault joint inversion. The rupture initial point and relative weight of each dataset are determined to estimate a well-constrained rupture model. The finite-fault model shows the rupture expanded bilaterally around the hypocenter, the peak slip is 3.5 m, the main slip was located at a depth of 15–30 km, the whole rupture lasted about 20 s, and a 95% moment rate was released at 15 s. The half-duration of the finite-fault inversion is consistent with the centroid moment tensor inversion results (half-duration 9 s), which shows the good resolution of the temporal information. The total scalar moment was 1.5×10^{20} Nm, equivalent to a moment magnitude of *M*w 7.4. The integrated inversion strategy used in this study is useful since the prior information can be derived and used to constrain the rupture process. Both the centroid moment tensor and finite-fault inversion mainly rely on identical temporal information provided by teleseismic *P* waveforms. The 2020 Oaxaca earthquake was mainly the interaction between Cocos and the North American plate, and the slow slip events may be the key factor affecting the seismogenic zone width in the Oaxaca region.

Keywords: moment tensor, finite-fault model, joint inversion, prior information, integrated inversion strategy

OPEN ACCESS

Edited by:
Jian Sun,
Ocean University of China, China

Reviewed by:
Yanchuan Li,
China Earthquake Administration, China
Lei Zhao,
Central South University, China

***Correspondence:**
Xingxing Li
xxli@sgg.whu.edu.cn

Specialty section:
This article was submitted to Solid Earth Geophysics, a section of the journal Frontiers in Earth Science

Received: *23 May 2022*
Accepted: *23 June 2022*
Published: *25 July 2022*

Citation:
Wen G, Li X, Zhao Y, Xu C and Xu G (2022) Rupture Characteristics Analysis of the 2020 Mw 7.4 Oaxaca, Mexico Earthquake Using Teleseismic, High-Rate GPS, and InSAR Data. Front. Earth Sci. 10:951033. doi: 10.3389/feart.2022.951033

1 INTRODUCTION

The June 23 2020 *M*w 7.4 Oaxaca, Mexico Earthquake nucleated at the southern Mexican subduction zone of the Cocos plate which is beneath the North American plate at 15:29:04 UTC. The relative convergence rate at the Oaxaca state is ~70 mm/yr (**Figure 1**; DeMets et al., 2010) and the interseismic coupling has been inferred to be high (at least 50%) (Rousset et al., 2017). The subduction zones have accounted for most major and great earthquakes in the world because of the

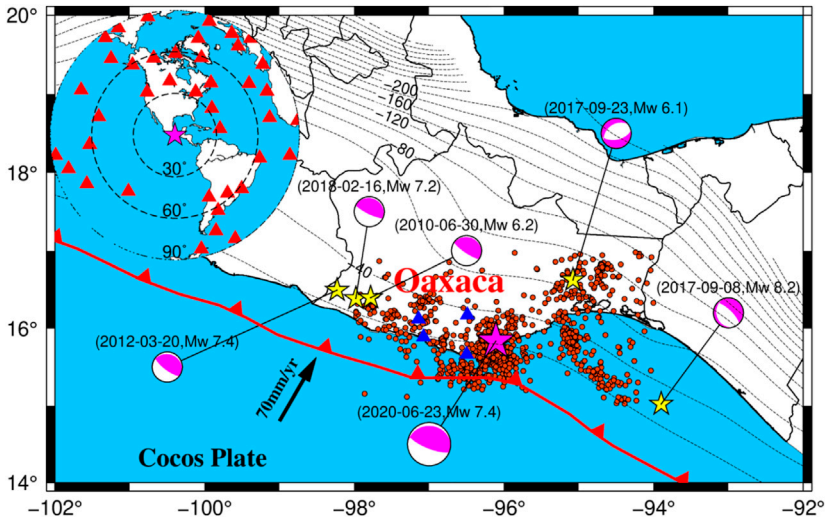

FIGURE 1 | Map of the epicentral region of the 2020 Oaxaca earthquake in the Mexican subduction zone; the yellow and magenta stars denote the epicentral locations of historical earthquakes which Mw >6 since 2012 from the USGS earthquake catalogs and 2020 Oaxaca earthquake, respectively. The magenta beach balls denote the focal mechanism of each earthquake event. The dashed black contours denote slab surface depths from the slab 2.0 model (Hayes et al., 2018) with a contour interval of 20 km. The blue and red triangles (upper-left insets) denote the 4 high-rate GPS stations and 40 teleseismic stations with an epicenter distance of 30°–90°. The red circles denote the Mw ≥3.5 aftershocks a month after the 2020 Oaxaca earthquake.

lithospheric plates sinking into the viscous fluid-like mantle (Ruff, 1996; Wen et al., 2021). In the Mexican subduction zone, most of the large Mexican earthquakes were *M*w 7–8 and this area has a short seismic average recurrence of 30–50 yr (Singh et al., 1981, 1983). Recently, the Mexican subduction zone experienced a series of large earthquakes, for example, the 2012 *M*w 7.4, 2017 *M*w 8.2, and 2018 *M*w 7.2 earthquakes (**Figure 1**), indicating the strong seismicity in this region. The Oaxaca earthquake caused large surface deformation and was well recorded by the geodetic observations, involving Global Positioning System (GPS) measurements and Interferometric Synthetic Aperture Radar (InSAR) images, and global teleseismic stations which were well distributed with a good azimuth coverage and takeoff angle. This earthquake provides an opportunity to study the slip behavior to better understand the dynamic mechanism and potential seismic risk in the Mexican subduction zone.

This earthquake caused at least 10 fatalities and damage to 2,000 homes (Tracy et al., 2020), due to the devastating shaking and landslides. Generally, the U.S. Geological Survey (USGS), Global Centroid Moment Tensor (GCMT) group, and GEOFOrschungsNetz (GEOFON) provide fast moment solutions to analyze the preliminary earthquake using different wave phases (e.g., teleseismic body wave, surface wave, or very long-period W phase (100–1,000 s) (Duputel et al., 2012)). The regional institution Servicio Sismológico Nacional (SSN) also provides the epicenter location and moment tensor solution of the 2020 Oaxaca earthquake. The hypocenter (15.803° N, 96.134° W, and 22.6 km depth) reported by SSN is located about ~16 km southwest of the hypocenter from the USGS (15.886° N, 96.008° W, and 20 km), which is closer to the coast. The moment tensor solutions reported from SSN, USGS, GCMT, and GEOFON show that this earthquake was a thrust event with a low dip angle (**Table 1**). However, moment tensor solutions are not enough to describe all source characteristics and assess the seismic hazards.

The spatiotemporal information of an earthquake from finite-fault inversion has been used to analyze seismic source processes and characteristics (Olson and Apsel, 1982; Hartzell and Heaton, 1983). For the 2020 Oaxaca earthquake, the rupture models from finite-fault inversion have been investigated (Melgar et al., 2020; Guo et al., 2021; Wen et al., 2021). The finite-fault model from existing studies shows that the main slip was located at depths of 15–30 km, while the fault geometry and hypocenter location are different in their research. Melgar et al. (2020) used an average strike of 278° and an average dip of 21° according to the hypocentral region to inverse the rupture process. Guo et al. (2021) used a grid search method to determine the strike and dip angle, and finally, a strike and dip of 272° and 23°, respectively, are used. Wen et al. (2021) used a rectangular fault dislocation model in elastic half-space (Okada, 1985) to estimate the fault geometry from static GPS and InSAR observations, and the derived strike, dip, and rake angles are 264.6°, 28.8°, and 58.6°, respectively. To some extent, near-field geodetic data could not constrain the fault geometry well since they are located on one side of the epicenter for megathrust earthquakes, and lack temporal information. Therefore, the centroid moment tensor inversion, including fault geometry and source duration time should be used to constrain the linear kinematic finite-fault inversion. In addition, seismic data, geodetic data, and/or tsunamis buoy data are involved in their finite-fault joint inversion, and the finite-fault model from existing studies shows that the main slip was located at depths of 15–30 km, even though the fault geometry and hypocenter location are different in their research. However, the relative weight of each dataset, which

TABLE 1 | Comparisons of the earthquake parameter of the 2020 Oaxaca Earthquake with different studies.

	Longitude (°)	Latitude (°)	Depth (km)	Strike (°)	Dip (°)	Rake (°)	*M*w
USGS	–96.008	15.886	20	271	17	70	7.37
GCMT	–96.06	16.04	21.5	270	16	62	7.40
SSN	–96.120	15.784	22.6	266.8	17.2	60.5	7.40
GEOFON	–95.73	16.17	25	270	21	61	7.41
Melgar et al. (2020)	–96.120	15.784	22.6	278	21		7.40
Guo et al. (2021)	–96.22	15.87	20	272	23		7.40
Wen et al. (2021)	–96.01	15.70	28.9	264.6	28.8	58.6	7.40
This study	–96.10	15.70	18	276 ± 2.5	24 ± 0.6	67 ± 2.1	7.40

is a critical challenge in joint inversion, has not been well studied. The resolution of the finite-fault joint inversion result should be further discussed during this earthquake.

In this study, we use an integrated strategy involving centroid moment tensor solution and finite-fault inversion to study the 2020 *M*w 7.4 Oaxaca earthquake. We use the vertical-component teleseismic *P* waves to invert the centroid moment tensor and extract the fault geometry parameter (i.e. strike, dip, and rake). The standard deviation of the fault parameter is calculated using the jackknife re-sampling method. Compared with the existing studies, we performed the linear kinematic joint inversion (Zhang et al., 2012) combining the teleseismic *P* waves, high-rate GPS waveforms, static GPS offsets, and InSAR data. The rupture initial point and the relative weight of each dataset are determined by using the grid search in this study to obtain a well-constrained rupture model. To assess the rupture model obtained from this event, we performed the resolution test and stability test to verify the efficiency of the joint inversion method. Finally, we discuss the rupture characteristics of this event through our finite-fault model.

2 DATA PROCESSING

2.1 Teleseismic Data Processing

In this study, the broadband teleseismic records were downloaded from the Incorporated Research Institutions for Seismology (IRIS) website. We only selected the *P* waves on the vertical components and the stations with an epicentral distance of 30°–90°. We reselected the stations with an azimuth interval of 5° to provide a good homogeneous azimuthal coverage of the stations on the epicenter and only retained records with high signal-to-noise ratios. Finally, 40 *P* waveforms were selected (inset in **Figure 1**) to invert the moment tensor and finite-fault model. The raw data were resampled to 1 Hz and translated into displacements after removing the instrument response. To satisfy the point source approximation, we used a third-order Butterworth bandpass filter of 0.01–0.05 Hz on the teleseismic *P* waves in centroid moment tensor inversion, and applied a bandpass filter of 0.01–0.2 Hz in finite-fault inversion. It is noted that we use identical teleseismic waveforms that mainly provide temporal information of the earthquake in moment tensor inversion and finite-fault inversion; this data consistency contributes to avoiding possible biases in prior information due to different observed data handling strategies.

2.2 GPS Data Processing

We collect four high-rate GPS data (1 Hz sampling rate at station OXPE and 5 Hz sampling rate at stations OXUM, TNNP, and TNSJ) from the University NAVSTAR Consortium (UNAVCO) where the minimum and maximum epicentral distances are about 45 km (OXUM) and 113 km (TNNP), respectively. The raw observed data are processed using the precise point positioning algorithm with ambiguity resolution (PPP-AR) using UPD products (Li et al., 2013; Li et al., 2021). The precise orbits and clocks with 30 s from the Center for Orbit Determination in Europe are used for the PPP method. Finally, we obtained the displacement position time series and rotated to local north, east, and up coordinates (Bock et al., 2011; Li et al., 2014). The displacement time series are resampled to 1 Hz and we obtain the static offset after the displacement sequence converges. The maximum offset of the OXUM station which is closest to the epicenter is about 14 cm in horizontal and 3.8 cm in vertical components. We applied a bandpass filter of 0.02–0.2 Hz to the high-rate GPS displacement waveforms in finite-fault inversion.

2.3 InSAR Data Processing

We collected InSAR data from the European Space Agency (ESA) Copernicus Sentinel-1A. Two ascending (T005A and T107A) and one descending (T070D) orbits were selected to cover the whole area affected by the event. The pre-event images of T005A, T107A, and T070D were collected on 12, 19, and 22 June 2020, respectively, and the post-event scenes are from 24, 25, and 28 June 2020, respectively. We used an open-source Jet Propulsion Laboratory (JPL) InSAR Scientific Computing Environment (ISCE) version 2 software (Rosen et al., 2012) to process the SAR images from the single look complex products. The precise orbit data were used to reduce potential orbit errors. We use a Shuttle Radar Topography Mission (SRTM) digital elevation model with a spatial resolution of about 30 m (Farr et al., 2007) to remove the topographic contribution of the interferograms. A stick, high-precision co-registration is performed on the Sentinel-1 data to meet the co-registration accuracy of at least 0.001 pixels. A power spectrum filter method (Goldstein and Werner, 1998) is used to smooth the interferograms. The interferograms are then unwrapped using the Snaphu method (Chen and Zebker, 2000) and geocoded into the World Geodetic System 84 coordinate system. The line-of-sight (los) displacement images are shown in **Supplementary Figure S1**. Finally, 99, 186, and 172 data points were retrieved from the T005A, T107A, and T070D tracks, respectively, using

the quadtree sampling algorithm (Jónsson et al., 2002) to downsample the InSAR observations.

3 METHODS

Earthquake rupture processes inverted from finite-fault inversion are critical to understanding source physics and assessing hazards. Finite-fault inversion often pre-assumes a fault plane, and this fault plane can be solved by seismic or geodetic data. Teleseismic *P* waves are useful because of their well homogeneous azimuthal coverage, while geodetic data are located on one side of the epicenter for megathrust earthquakes. In addition, teleseismic *P* waves show a good convergence with the depth since the takeoff angles for teleseismic stations are quite small and the ray path is straight down from the source (Wei et al., 2013). The centroid moment rate function (or source duration time) and fault mechanism derived from the moment tensor solution provide prior information to the kinematic finite-fault inversion. Finite-fault joint inversion is widely used to imagine the earthquake processes since it is complementary to different observed data and different resolutions (i.e., spatial and temporal resolution) (Ji et al., 2002; Yue and Lay, 2013; Yi et al., 2017). The prior assumptions (e.g., maximum duration of the rupture history) should be given to constrain the inversion results. Therefore, an integrated inversion strategy involving the centroid moment tensor and finite-fault joint inversion is used in this study to analyze the 2020 Oaxaca earthquake source characteristics. We use teleseismic *P* waves to invert the centroid moment tensor and extract the strike, dip, and rake of the nodal planes and the duration of the earthquake rupture history to finite-fault joint inversion.

3.1 Centroid Moment Tensor Inversion

The earthquake event can be treated as a point source if the epicenter distance was large enough. The form of observation, coefficient matrix, and unknown parameter can be expressed as

$$U_n(k,t) = G'_{np,q}(k,t) \cdot M_{pq} \tag{1}$$

where $G'_{np,q}(k,t)$ is the convolution of $G_{np,q}(k,t) * S(t)$, $G_{np,q}(k,t)$and $S(t)$ denote the Green's function and normalized source time function, respectively, M_{pq} denotes the moment tensor, and $*$ is the convolution operator. The source time function and moment tensor are unknown parameters that need to be solved, and the source time function can be treated as an isosceles triangle in point source approximation that the half-duration needs to be determined.

For a preliminary location (i.e. hypocenter from the earthquake research institutions), we can obtain a moment tensor solution after determining the optimum source time function (or half-duration time). To better explain the observed data, we attempt to find a centroid location that is better than the preliminary location estimate. The procedure is consistent with the W phase source inversion (Duputel et al., 2012); we set up a 3D grid search (latitude-longitude-depth), where each grid node is used as a potential centroid location and a moment tensor inversion is made. The normalized misfit ($\sigma = \frac{\sum (ob-syn)^2}{\sum ob^2}$) is used as an objective function to choose the optimal centroid location. The dimension of the grid is [-1° 1°] in horizontal with an interval of 0.1°, centered on the SSN location (longitude −96.1°, latitude 15.8°), and 2–50 km with an interval of 4 km. The difference between our procedure and W phase inversion is that we determine the half-duration at each grid node rather than fix the source time function. To test the stability of this result, the jackknife re-sampling method is used to calculate the standard deviation of the inversion results.

3.2 Finite-Fault Joint Inversion

Our finite-fault joint inversion method is based on the study by Zhang et al. (2012). This method is a linear combination with the seismic and geodetic data performed at the time domain which is convenient to realize. In addition, this method only set a maximum rupture velocity and duration time to constrain the rupture area, indicating that each subfault is allowed to rupture complex. We use vertical-component teleseismic *P* waveforms, three components of high-rate GPS displacement waveforms, static GPS offset, and InSAR data to invert the rupture process. The joint inversion equation can be expressed as

$$\begin{bmatrix} \lambda_1 \boldsymbol{U}_1 \\ \lambda_2 \boldsymbol{U}_2 \\ \lambda_3 \boldsymbol{U}_3 \\ \boldsymbol{0} \\ \boldsymbol{0} \\ \boldsymbol{0} \end{bmatrix} = \begin{bmatrix} \lambda_1 \begin{bmatrix} \boldsymbol{G_x} & \boldsymbol{G_y} \end{bmatrix} \\ \lambda_2 \begin{bmatrix} \boldsymbol{K_x} & \boldsymbol{K_y} \end{bmatrix} \\ \lambda_3 \begin{bmatrix} \boldsymbol{Q_x} & \boldsymbol{Q_y} \end{bmatrix} \\ \lambda_I \begin{bmatrix} \boldsymbol{D} & \boldsymbol{0} \\ \boldsymbol{0} & \boldsymbol{D} \end{bmatrix} \\ \lambda_{II} \begin{bmatrix} \boldsymbol{T} & \boldsymbol{0} \\ \boldsymbol{0} & \boldsymbol{T} \end{bmatrix} \\ \lambda_{III} \begin{bmatrix} \boldsymbol{Z} & \boldsymbol{0} \\ \boldsymbol{0} & \boldsymbol{Z} \end{bmatrix} \end{bmatrix} \begin{bmatrix} \boldsymbol{m_x} \\ \boldsymbol{m_y} \end{bmatrix} \tag{2}$$

where $\mathbf{m}_x$ and $\mathbf{m}_y$ are the time histories of slip rate amplitudes and slip angles of all subfaults on the fault plane, $\lambda_1, \lambda_2, \lambda_3$ are the relative weights of waveforms data, static GPS offsets data, and InSAR data, $\boldsymbol{U}_1, \boldsymbol{U}_2, \boldsymbol{U}_3$ are the observation data of waveform, static GPS displacement, and InSAR, respectively, $\boldsymbol{G}, \boldsymbol{K}, \boldsymbol{Q}$ are the Green's function of waveforms data, static GPS offsets, and InSAR data, $\boldsymbol{D}$ and $\boldsymbol{T}$ are spatial and temporal smoothness matrixes, which are constructed with Laplace's equations (Horikawa 2001; Yagi et al., 2004; Zhang et al., 2012), $\boldsymbol{Z}$ is the matrix for minimization scalar moment constraints (Hartzell and Iida 1990), and $\lambda_I, \lambda_{II}, \lambda_{III}$ are the corresponding weights of the constraints. Green's functions of teleseismic and high-rate GPS waveform were calculated by using the code "QSSP" of Wang et al. (2017) to construct the database based on the Crust 1.0 crustal velocity model (Laske et al., 2013). The static Green's functions (i.e. static GPS offset and InSAR) were calculated using the Okada model (1985).

4 INVERSION AND RESULTS

4.1 Centroid Moment Tensor Solution

Figure 2A shows the locations obtained from our centroid moment tensor solution and others reported from existing

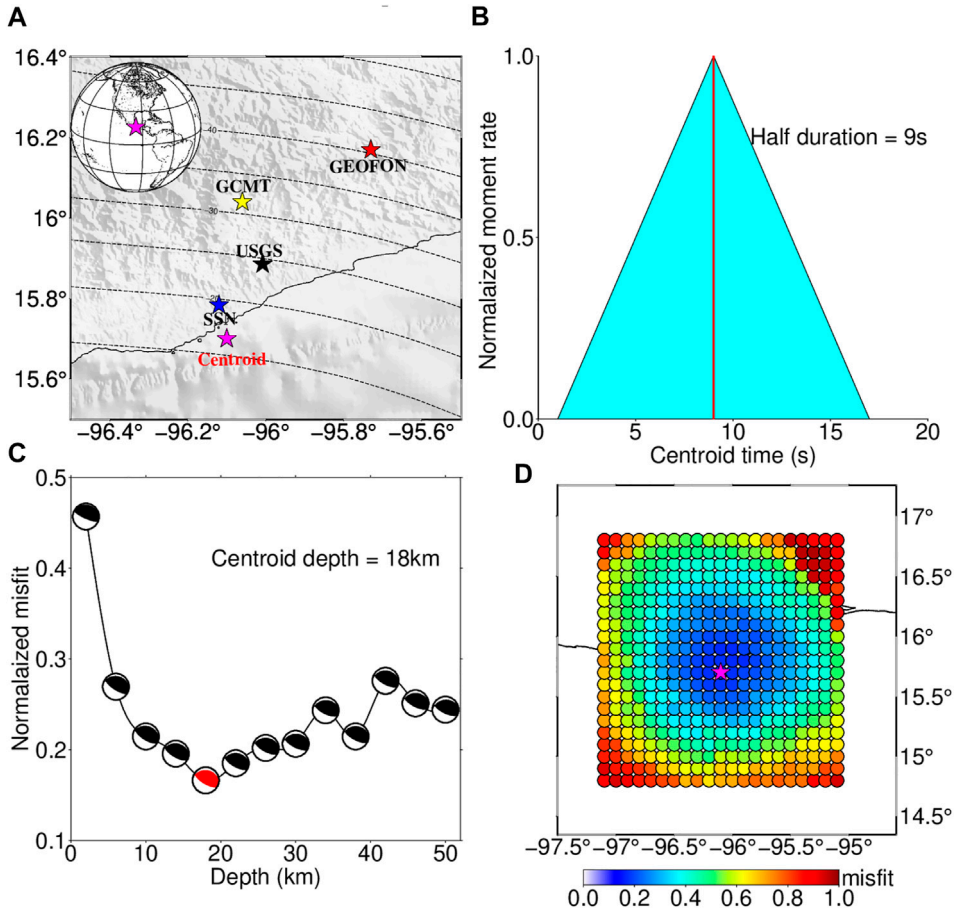

FIGURE 2 | Map of the epicentral region of the 2020 Oaxaca earthquake and centroid moment tensor solution. **(A)** Map view of the epicentral locations, black, yellow, red, blue, and magenta stars show the epicenters from the USGS, GCMT, GEOFON, SSN, and this study, respectively. **(B)** Searched normalized moment rate function. **(C)** Map view of the normalized misfit between the observed and synthetic data with different centroid depths; the black beach ball denotes the focal mechanism with the depth and the red beach ball denotes the optimal focal mechanism when the centroid depth is selected at 18 km. **(D)** Normalized residual with the different centroid epicentral locations used in our study areas.

research institutions (i.e. USGS, GCMT, SSN, and GEOFON). The centroid location obtained in this study is longitude −96.1° and latitude 15.7°, which is about 9.5 km to the south of the SSN location (**Figure 2A**). The centroid depth is 18 km (**Figure 2C**) and is close to the depth contour of 20 km corresponding to the Slab 2.0 model (Hayes et al., 2018) of the megathrust. The fault geometry parameters extracted from the moment tensor solution are listed in **Table 1**. The final fault mechanism obtained from the centroid moment tensor solution is 276° strike, 24° dip, and 67° rake, which is consistent with the 2020 Oaxaca earthquake region with the northwest direction and low dip angle. The standard deviations of strike, dip, and rake angles calculated from the jackknife re-sample method are 2.5°, 0.6°, and 2.1°, respectively (**Supplementary Figure S2**). These results are acceptable compared with the existing studies. **Figure 2B** shows the normalized moment rate function, indicating that the whole duration time is 18 s. The half duration which reaches the peak moment rate is 9 s and slightly small than the USGS (13.1 s) and GCMT moment tensor solution (11.9 s). **Figure 2C** shows the optimal depth we obtained and its fault mechanism with each depth from the moment tensor solution. **Figure 2D** shows the normalized misfit between the observed and synthetic data at each grid node, and the minimum misfit is 0.1663. In addition, the comparison between the observed and synthetic data shows a good fit (**Figure 3**), and most correlation coefficients are larger than 0.8. The average correlation coefficient between the observed and synthetic waves is 0.9, which means that the centroid moment tensor solution can explain the observed data well.

4.2 Finite-Fault Source Model

The fault mechanism of the strike and dip obtained from our centroid moment tensor solution is used in finite-fault inversion, and the slip angles are estimated in the inversion. The fault plane used is 85 km long and 110 km wide, and is discretized into 374 subfaults where each has dimensions of 5 km × 5 km. This fault plane is large enough to cover the rupture area according to the existing studies. We used the epicenter location reported by

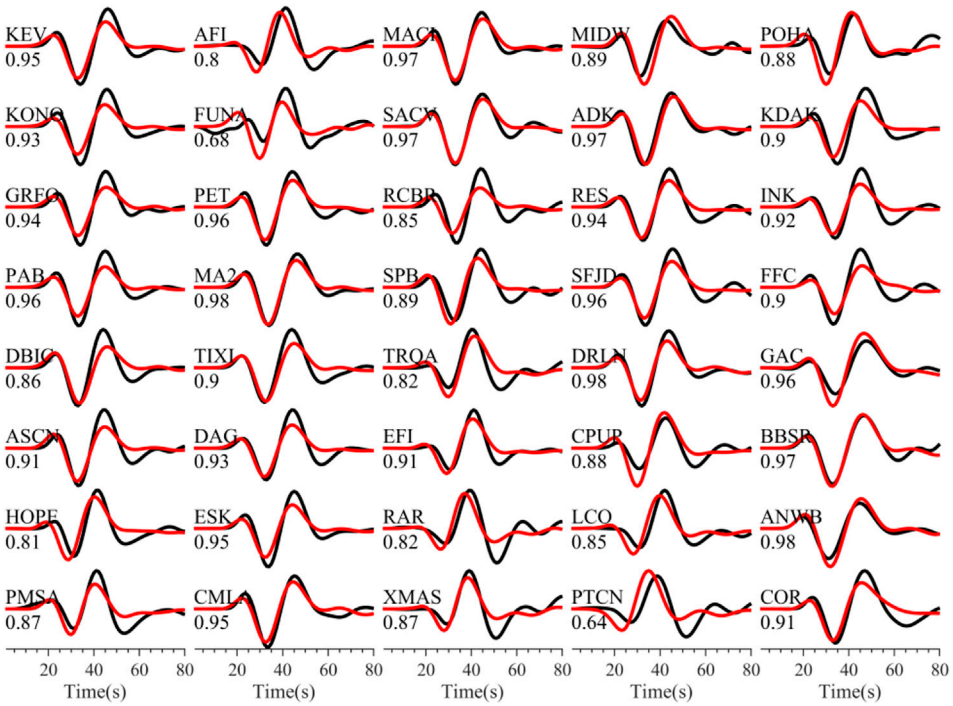

FIGURE 3 | Comparisons of the 40 observed (black) and synthetic (red) teleseismic *P* waves data. The letters above the waves denote the station name of teleseismic and the digit under the waveforms denotes the correlation coefficient between the observed and synthetic waves.

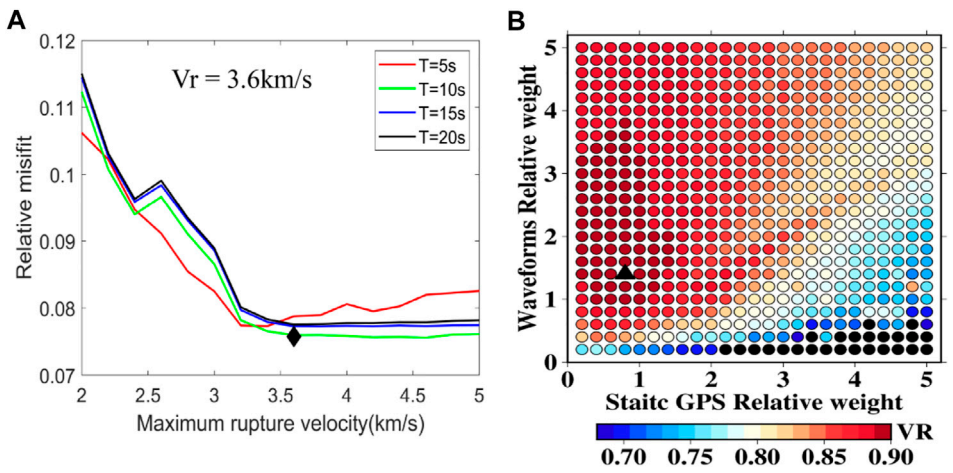

FIGURE 4 | (A) Normalized misfit plotted against different maximum rupture velocities for maximum rupture durations of 5 s (red), 10 s (green), 15 s (blue), and 20 s (black). The black diamond marks the maximum rupture velocity of 3.6 km/s and a maximum rupture duration of 10 s for each subfault used in this study. **(B)** Total VR distribution with different relative weights of static GPS and waveform data. The black triangle marks the relative weight. The static GPS and waveform are 0.8 and 1.4, respectively, used in this study.

SSN as a rupture initiation point of the earthquake first. A total rupture duration of 25 s is assumed, that is, the rupture window of each subfault lies in 0–25 s. It is to be noted that the maximum duration of the finite-fault inversion should be close to or larger than the centroid moment rate duration to capture the rupture history. Therefore, the centroid moment tensor inversion is necessary to provide prior information on fault geometry and source duration time. To stabilize the inversion, a maximum rupture velocity and maximum duration are generally used to limit the subfault rupture window. The cost is the possible loss of actual source information which lies outside of the time window. In principle, we prefer a narrow time that generates a small

enough misfit, and a balance should be made between the window width and the normalized misfit. We tested different values of maximum rupture velocity and duration and found 3.6 km/s and 10 s to be suitable (**Figure 4A**).

In this study, the variance reduction (VR) (Kim and Dreger, 2008; Zhang et al., 2012; Melgar et al., 2017) for each type of data and the total are used as an objective function to evaluate the inversion results and the differences of synthetics. The variance reduction is calculated as (Xu et al., 2022)

$$\begin{cases} VR_i = \left(1 - \dfrac{\sum_n \left(u^{obs}(n) - u^{syn}(n)\right)^2}{\sum_n \left(u^{obs}(n)\right)^2}\right) \\ VR_{Total} = \left(1 - \dfrac{\sum_{i=1}^{3}\sum_n \left(\lambda_i u_i^{obs}(n) - \lambda_i u_i^{syn}(n)\right)^2}{\sum_{i=1}^{3}\sum_n \left(\lambda_i u_i^{obs}(n)\right)^2}\right) \end{cases} \quad (3)$$

where superscript "obs" and "syn" represent observed and synthetic data points in the inversion, respectively, n denotes the points of data, and the subscript i and variable λ_i stand for three types (waveforms, static GPS displacement, and InSAR) data and the relative weights between them shown in **Eq. 2**, respectively. The weights of smoothness are determined using the trial-and-error method to ensure that the observed data can be well fitted, and the source time function and slip pattern change smoothly. We tested different combinations of the smoothness, finally, the weights of spatial and temporal smoothness are set to 1 and the scalar moment minimization constraint is set to 4 so that the model changes smoothly (**Supplementary Figure S3**). In addition, the relative weighting of each dataset which displayed their importance and contribution to the inversion is a challenge for joint inversions. In this study, each type of dataset was normalized by dividing by its vector $L^2 - norm$ (i.e. $ob_{inv} = \frac{ob_{ori}}{\sqrt{\sum (ob_{ori})^2}}$; here, ob_{inv} is the normalized data used in the inversion and ob_{ori} is the original data), and the relative weights of each dataset are determined using the grid search method. The relative weight of InSAR data is set to 1 first, and the relative weights of waveform data (teleseismic waves and high-rate GPS waves) and static GPS offset are searched to vary from 0.1–5 to obtain an optimal total variance reduction (Kim and Dreger, 2008; Zhang et al., 2012; Melgar et al., 2017). **Figure 4B** shows the distribution of total variance reduction with the different relative weights of waveforms and static GPS displacement data. It is noted that we can improve the data fitting in which the variance reduction of each dataset will be increased when we increase the relative weight, but there is no specific reason to justify the increase in the relative weight (Kim and Dreger, 2008). Finally, the relative weight of static GPS, waveforms, and InSAR data are chosen to be 0.8, 1.4, and 1 (**Figure 4B**), respectively, in which the total VR is 90% and the moment magnitude is *M*w 7.4. It is considered that the hypocenter is the point of initiation of the rupture (Chu et al., 2011; Yang et al., 2019), while the centroid is the point of mean moment release (Melgar et al., 2012). The optimal hypocenter location is determined by the grid search method under the assumption that the center of each subfault is a potential

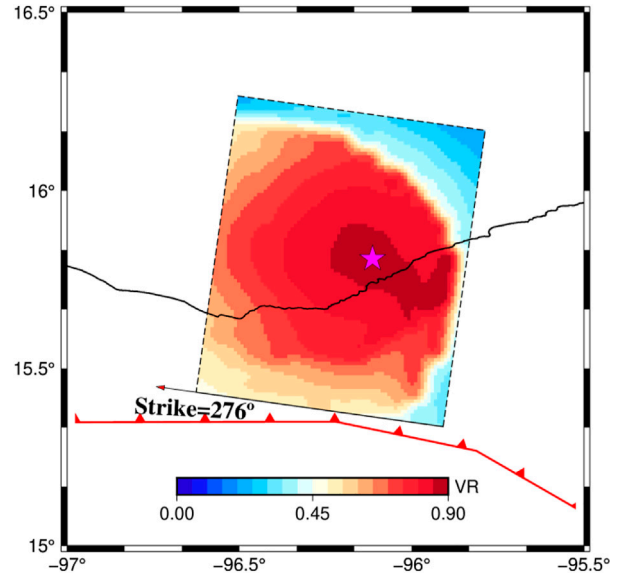

FIGURE 5 | Total VR with the model parameters in joint inversion at each grid on the fault plane; the magenta star denotes the hypocenter location corresponding to the maximum VR.

hypocenter. **Figure 5** shows the variation reduction of each subfault and the inversion result can be accepted when the initiation point is close to the SSN results or our centroid location (total VR large than 85%), the optimal hypocenter is 15.835° N, 96.108° W. To some extent, the rupture initiation points mainly influence the waves' inversion since we use a given rupture velocity and rupture duration time to constrain the rupture area, while the static inversion uses near-field data (i.e. static GPS or InSAR data) and does not consider the temporal information and have good resolution on spatial information. Therefore, the total VR is decreased when the potential epicenter location is far away from the real hypocenter. It is complementary to join the seismic and geodetic data in finite-fault inversion to constrain the spatiotemporal information on the fault plane (Ji et al., 2002; Yue and Lay, 2013; Yi et al., 2017).

The slip distribution, source time function (STF), subfault source time functions, and slip angle obtained from our joint inversion results are shown in **Figure 6**. The total seismic scalar moment is about 1.5×10^{20} Nm, equivalent to a moment magnitude of *M*w 7.4, consistent with the results reported from GCMT and GFZ. The peak slip of 3.5 m is mostly confined to the major slip area around the hypocenter, the peak slip is slightly smaller than the USGS solution (~8 m) and those shown by Melgar et al. (2020) and Wen et al. (2021) (~5 m); it is mainly because the rupture area shows a greater elliptical asperity around the epicenter. The main slip of this model is well constrained between 15 and 30 km, and is consistent with the existing studies (Melgar et al., 2020; Guo et al., 2021; Wen et al., 2021; Yan et al., 2022). The slip angle of our model shows that the 2020 *M*w 7.4 Oaxaca earthquake was a thrust slip with a minor right slip event (**Figure 6B**). In our preferred model, the slip angle is

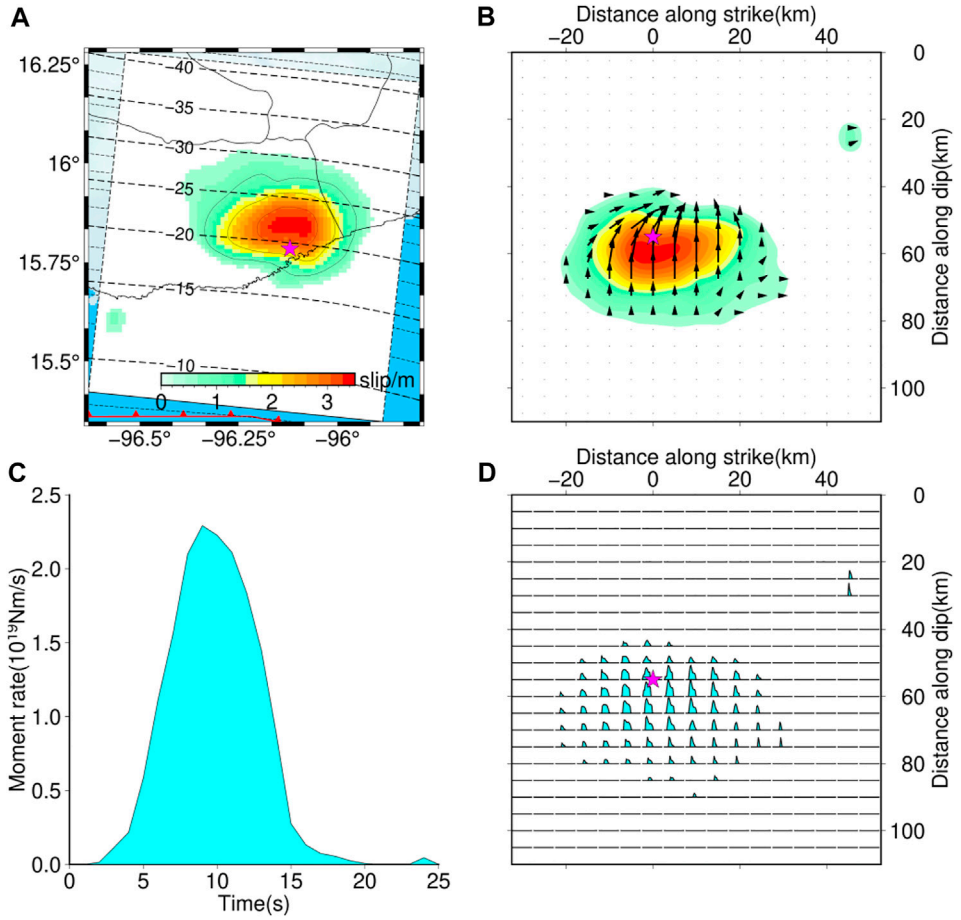

FIGURE 6 | Finite-fault results of the 2020 Oaxaca earthquake from joint inversion. **(A)** Surface projections of fault slip distribution; the magenta stars denote the epicentral location. **(B)** Slip distribution on the fault plane, the black arrow denotes the slip direction of each subfault. **(C)** Source time function (STF) of this earthquake. **(D)** Subfault source time functions of each subfault on the fault plane.

decreased from the deep to shallow depth, and the slip angle we obtained is close to 90° below the epicenter and close to 67° above the epicenter. The whole rupture process lasted for about 20 s (**Figure 6C**), and the source time function and subfault source time functions (**Figure 6D**) show that the rupture process of this earthquake is simple with a single asperity. The moment rate reached a peak value of 2.37 × 10^{19} Nm/s at 9 s, the half-duration of the finite-fault inversion is consistent with the centroid moment tensor inversion results (half duration 9 s), indicating the consistency of the centroid moment tensor and finite-fault inversion.

Figure 7 shows the fitting of the teleseismic data and high-rate GPS data. The average correlation coefficient between the observed and synthetic waveform of teleseismic data is greater than 0.82. In addition, the InSAR data show a good fitting that the average residual is 0.01 m (**Figure 8**). The VR of the waveforms (teleseismic and high-rate GPS), static GPS, and InSAR data are 84.0, 98.2, and 95%, respectively, indicating that the model can explain the observed data well. **Figures 9A,B** show the fitting of the static GPS displacement in horizontal and vertical components, and the OXUM station shows a good consistency of the observed and synthetic data because of the high signal-to-noise ratio of the observed data. In addition, to better verify the robustness of the slip model, we make forward predictions using the observations not included in the joint inversion. The coastal uplift observation data 2 days after the events were collected from the study by Ramírez-Herrera et al. (2020). The observed data show that the maximum coastal uplift is about 0.53 m near the epicenter, and this observed data fit well with the 0.55 m of the uplift reported by tide gauge data at Huatulco (Melgar et al., 2020). We calculated the synthetic coastal uplift using our preferred rupture model and compared it with the observed data (Ramírez-Herrera et al., 2020), and the VR is 89.7% and the result is shown in **Figure 9C**, indicating a well-fitting with the observed data.

To better understand the rupture process of the 2020 *M*w 7.4 Oaxaca earthquake, we present the snapshot form of the slip rate distributions of this rupture model in **Figure 10**. The result shows that the rupture expanded bilaterally around the hypocenter, and that the rupture initiated at 4 s around the hypocenter and propagated outward. The source time functions show that the moment rate increased and decreased rapidly, at 9 s, the moment rate reached a peak value of 2.32 × 10^{19} Nm/s, corresponding to the peak slip of 1.6 m. The average

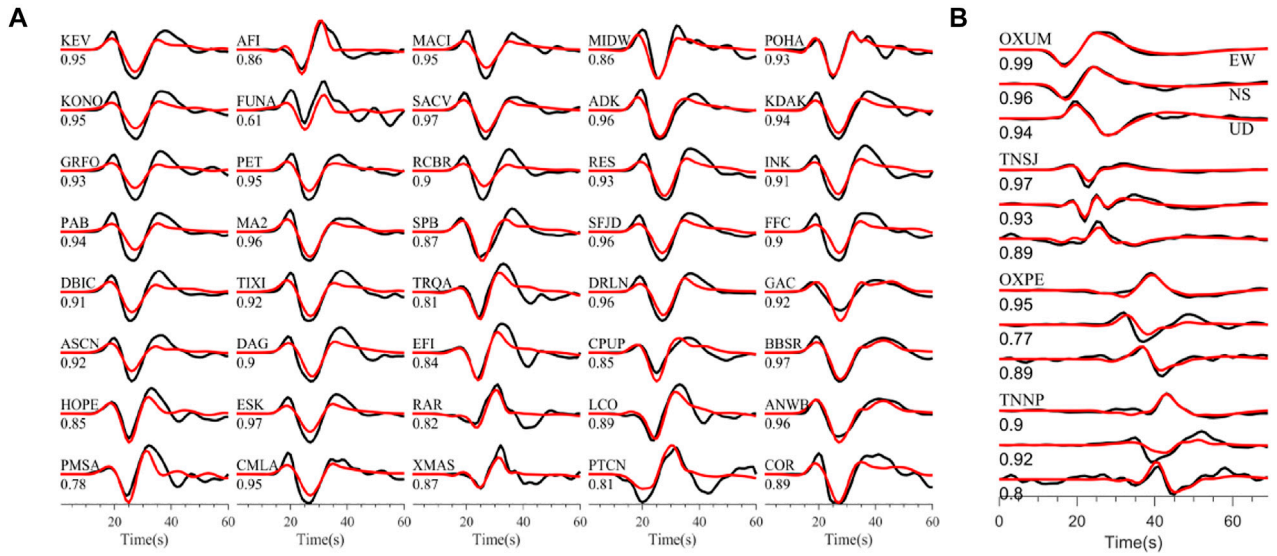

FIGURE 7 | Comparisons of the observed (black) and synthetic (red) waves. **(A)** Denotes the 40 teleseismic *P* waves' data. **(B)** Denotes the four high-rate GPS waves. The letters above the waves denote the station names and the digit under the waves denotes the correlation coefficient between the observed and synthetic waves.

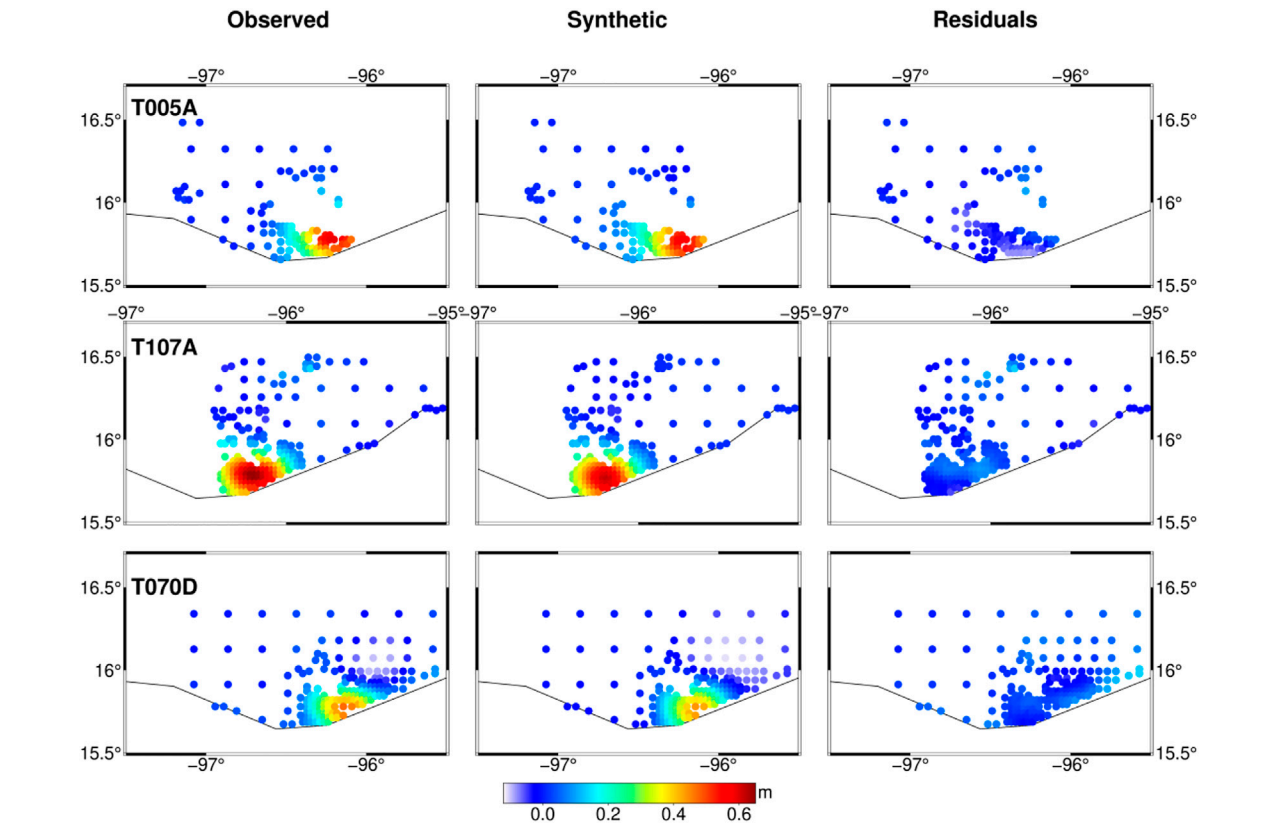

FIGURE 8 | InSAR observed (left panel), synthetic (middle panel), and associated residuals (right panel). The first and second row denotes the T005A and T107A images, respectively, and the third denotes the T070D image.

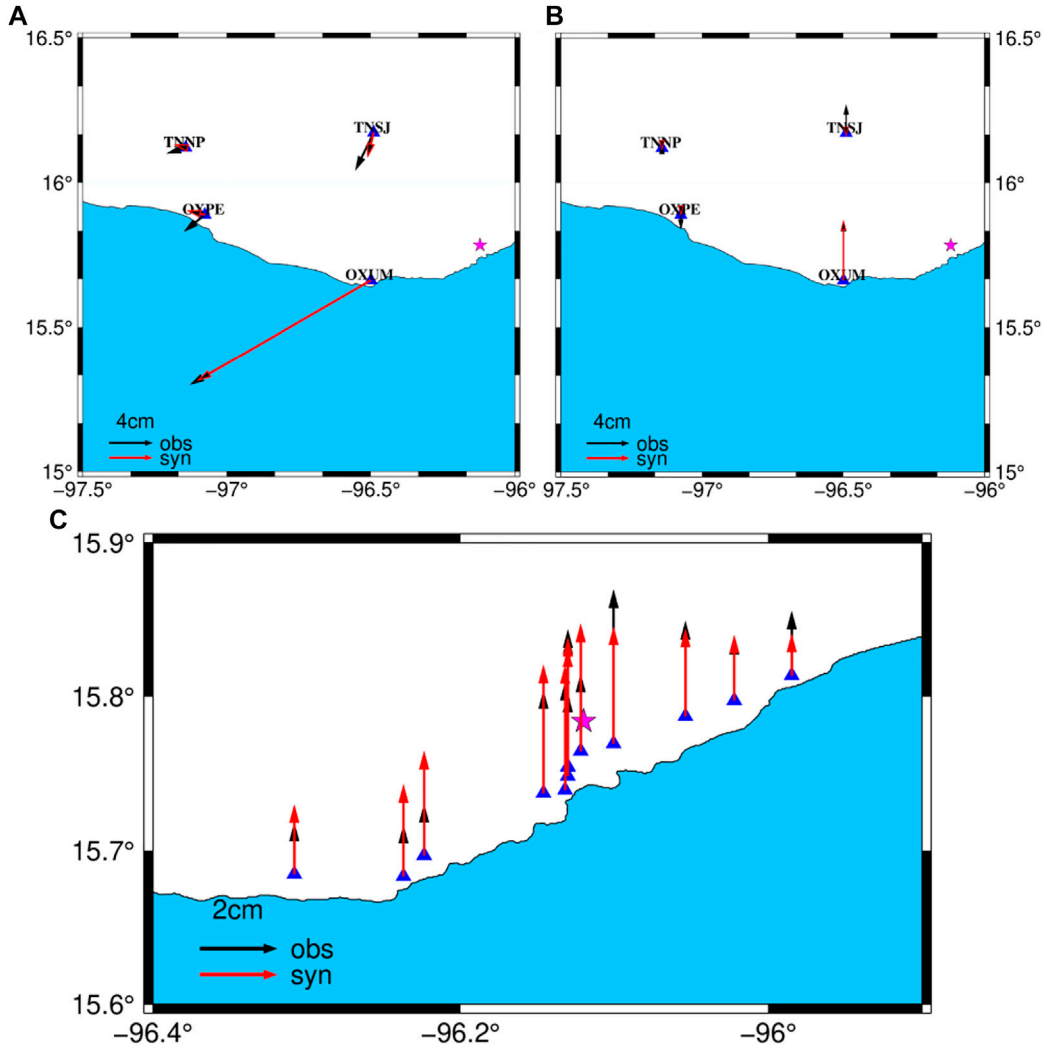

FIGURE 9 | (A) Comparison between the observed horizontal (black) and synthetic horizontal (red) static GPS data. **(B)** Comparison between the observed vertical (black) components and synthetic vertical (red) static GPS data. **(C)** Comparison between the observed (black) and synthetic (red) coastal uplift data from the study by Ramírez-Herrera et al. (2020).

rupture velocity calculated is about 3 km/s, consistent with the existing studies (Melgar et al., 2020; Guo et al., 2021; Wen et al., 2021). In the first 4 s, the rupture initiated gradually, and at 4–8 s, the moment released rapidly and the magnitude reached *M*w 7.17 at 9 s. At 8–14 s, the moment rate propagates below the epicenter, and most moment rates are released at 14 s. The source time function shows a symmetrical energy release pattern and the slip distribution model shows that this earthquake was a simple event with a single asperity.

5 DISCUSSION

5.1 Stability of the Joint Rupture Model

In this study, we also tested different datasets to examine the coseismic slip model of the 2020 Oaxaca earthquake. The geodetic (static GPS and InSAR) inversion result (**Supplementary Figure S3B**) shows a slightly narrow rupture area than the waveforms' (teleseismic and high-rate GPS) result (**Supplementary Figure S3A**). This is mainly because the geodetic data are located on one side of the epicenter of the megathrust earthquake, resulting in a low resolution on the shallow and deep portions. Compared with the geodetic data, global teleseismic data show a good azimuthal coverage, while the teleseismic data only constrain the relative position of fault slips compared with the hypocenter. Therefore, it is complementary to join the seismic and geodetic data in finite fault inversion to constrain the spatiotemporal history.

For joint inversion, the critical challenge is to determine the relative weights between different datasets. In this study, the VR which is influenced by the relative weight of each dataset is defined as a function to evaluate the inversion model. We examine the rupture model with different weights through the trial-and-error

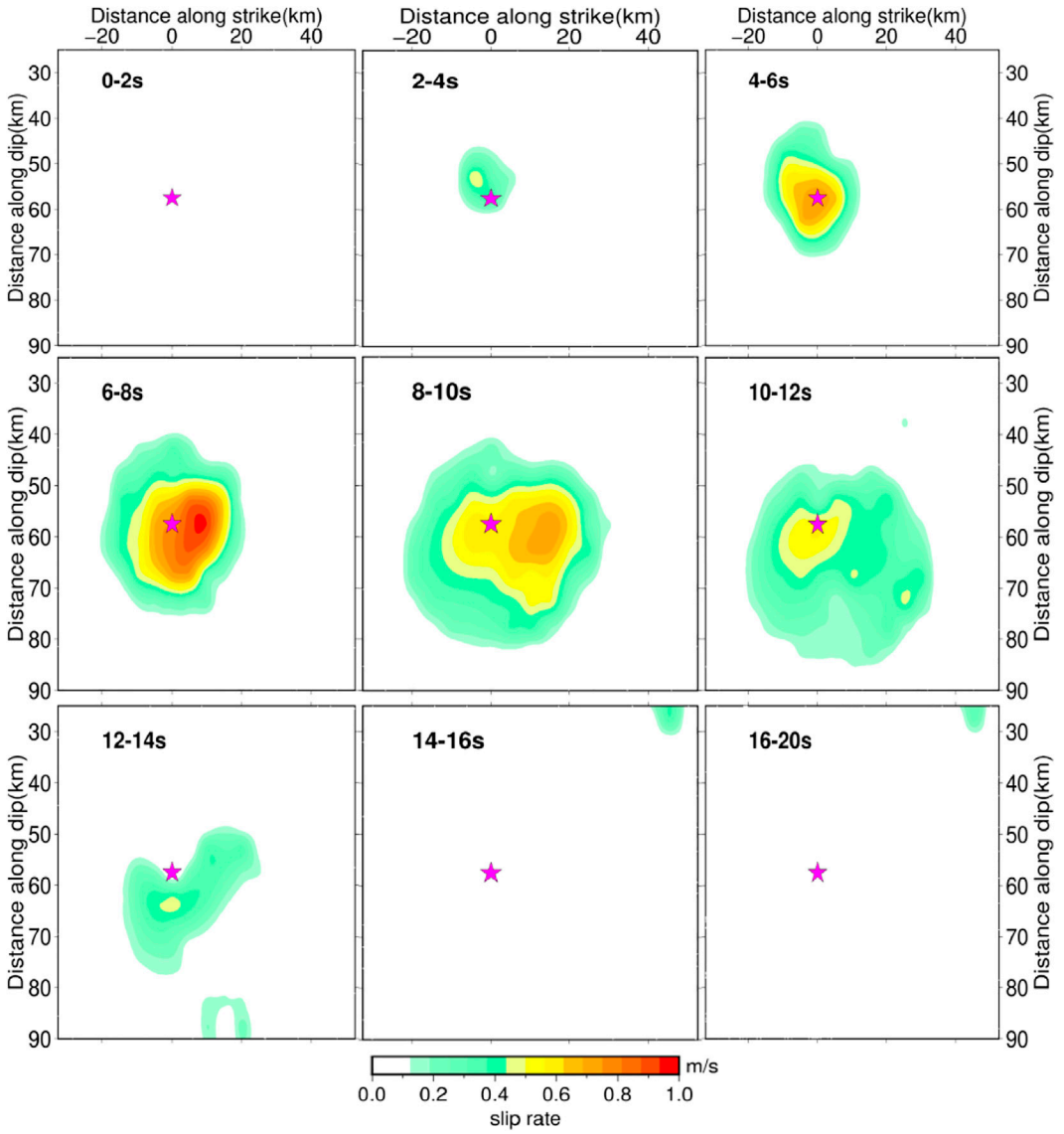

FIGURE 10 | Snapshots of the slip rate for the 2020 Oaxaca earthquake with a time interval of 2 s, most of the moment was released at 14 s. The magenta star denotes the epicenter.

method, and the rupture model changes smoothly with different smoothness weights (**Supplementary Figures S4A–D**), relative weights (**Supplementary Figures S4E–H**), and maximum rupture velocity (**Supplementary Figures S4I–L**). It is noted that the rupture area is slightly small than the others and close to the result from geodetic inversion (**Supplementary Figure S3B**) when the relative weights of waveform, static GPS, and InSAR data are 0.2, 1, and 1, respectively. This is mainly because the relative weight of each dataset is inappropriate and the weight of the waveform data is small, leading to the result being close to the result from geodetic inversion. In our preferred rupture model, the relative weight of waveforms data, static GPS, and InSAR data are 1.4, 0.8, and 1, respectively. These weights were chosen by considering that **(1)** the waveform (teleseismic and high-rate GPS) and static deformation (static GPS and InSAR) are weighted equally since they are normalized by dividing by its vector L^2 – *norm* and (2) the grid search result (**Figure 4B**) shows that the maximum VR is obtained with these relative weights. The comparison of the rupture model with different weights shows that the results obtained in this study are credible since the main rupture feature are consistent with existed studies and observed data are fitting well.

5.2 Finite-Fault Model With Different Fault Geometry

The fault mechanism obtained from existing institutions and studies shows a slight difference from each other. We test the stability of

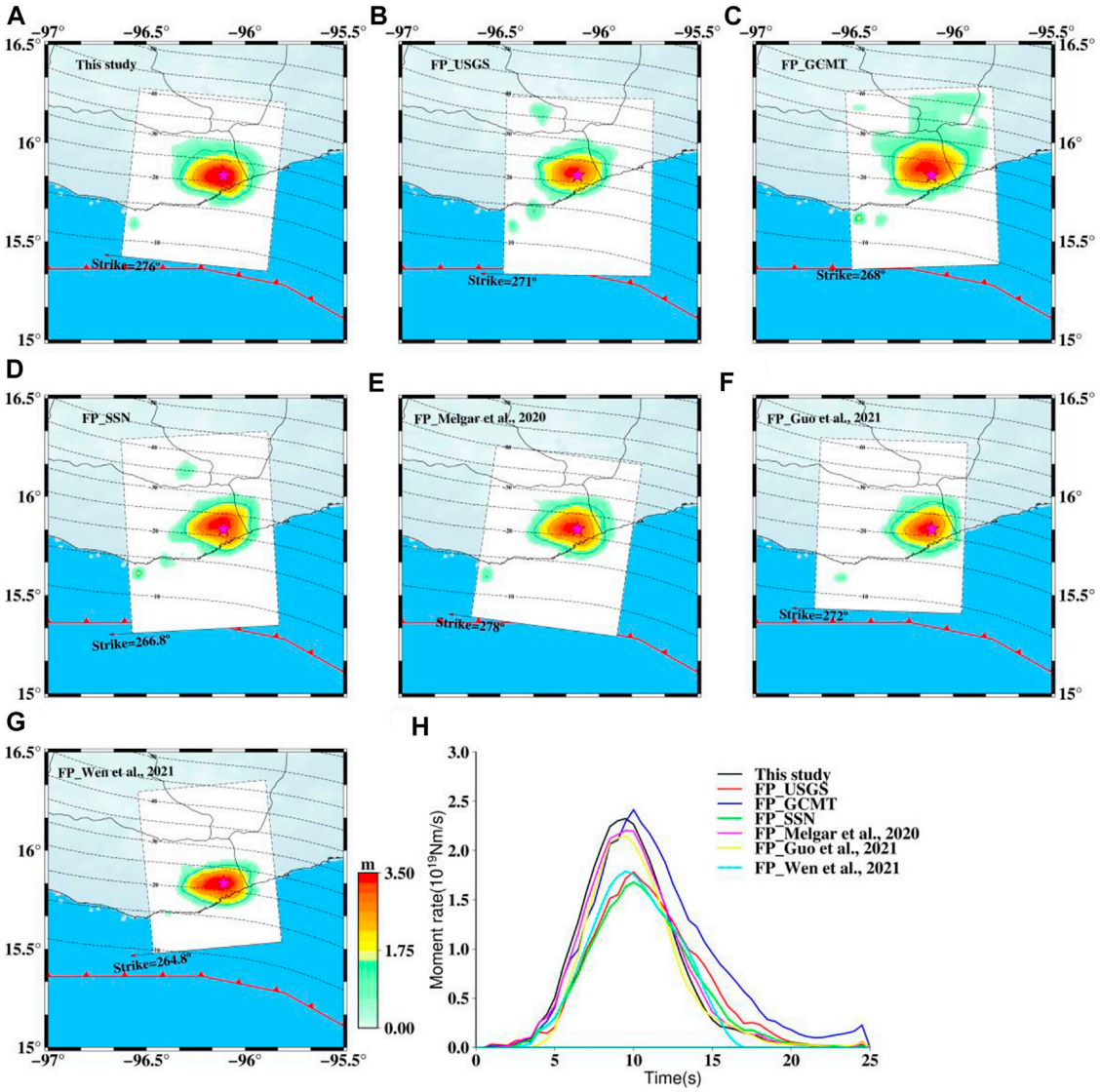

FIGURE 11 | Surface projections of the slip distribution and source time functions. **(A-G)** denote the surface projections of the slip distribution used different fault plane [i.e. fault geometry from this study, USGS (FP_USGS), GCMT (FP_GCMT), SSN (FP_SSN)], Melgar et al. (2020) (FP_Melgar et al., 2020), Guo et al. (2021) (FP_Guo et al., 2021), and Wen et al. (2021) (FP_Wen et al., 2021), respectively. The magenta star denotes the epicentral location. **(H)** Source time functions derived from the results of **(A-G)**.

inversion with different fault geometry listed in **Table 1**. **Figure 11** shows the different slip distribution models and source time functions. The results show that the main slip is constrained at depths of 15–30 km, the whole rupture process lasted about 20 s, and the main characteristics of these rupture models are consistent with each other. The InSAR data that have dense coverage over the main slip result in a well constrain resolution on spatial information even if the strike and dip are varied from each other. It is mainly because the finite-fault inversion tends to put ruptures to the locations closest to their real positions after determining the hypocenter locations. The source time functions also show a good consistency with each other, indicating the efficiency of joining the seismic and geodetic data in finite-fault inversion to constrain the spatiotemporal information on the fault plane.

5.3 Resolution Test

Resolution tests can tell us how well the slip distribution can be recovered through the given observation data and constraining equations (Kim and Dreger, 2008). For a megathrust earthquake event, the shallow slip and deep slip are important to assess the tsunami generation and seismic hazard. To test the resolution of our preferred model, we use the same fault plane, datasets, Green's functions, and constraint equations as previously to simulate synthetic data when we consider the fault plane has double, three, and six slip asperities, respectively (**Figure 12**). The input model of each slip patch contains 5 × 5 (25 km × 25 km) subfaults, and the subfaults have the same slip value and slip angle of 67°. The average rupture velocity is 3 km/s, and the maximum duration

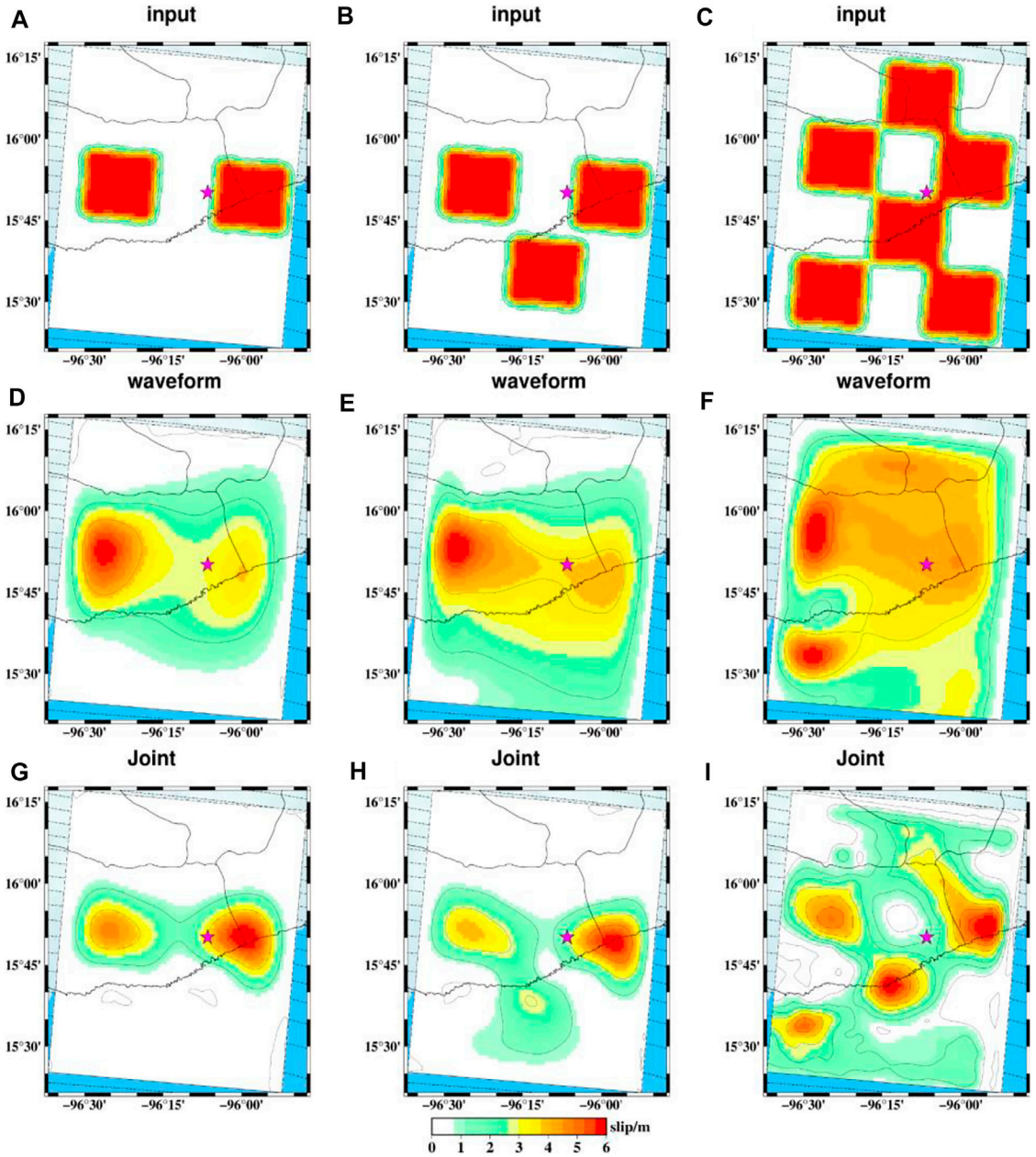

FIGURE 12 | Checkboard test of the inversion resolution with different slip patches and different datasets combination. **(A–C)** denote the input model we simulated. **(D–F)** denote the inversion results used waveform data. **(G–I)** denote the inversion results used joint data.

time of the source time function is 12 s for each subfault. Then, we add 5% Gaussian noise to these synthetic waveforms. It is noted that the residuals of static GPS and InSAR from our preferred result are added to the synthetic static GPS and InSAR data. In a synthetic inversion, we use a rupture velocity of 3.2 km/s which is slightly larger than the previous value and a maximum duration time of 20 s for each subfault, and the rake angle of the subfaults is allowed to vary between 22° and 112°. To some extent, teleseismic data can improve the deficiency of near-field data (i.e. GPS or InSAR) when these data are located on one side of the epicenter of a megathrust earthquake. We used waveform data (teleseismic *P* waves and high-rate GPS displacement data) and joined all data to invert the slip distribution model.

The inversion results show that the joint inversion can retrieve the slip distribution well (**Figures 12G–I**), and the dense near-field InSAR data can improve the spatial resolution of the slip distribution. **Figures 12D–F** show that the inversion results have poor resolution overall except for the slip near the hypocenter since the teleseismic data have weak resolution in spatial

information and the near-field high-rate GPS stations are sparse. The slip patches around the epicenter can be well retrieved because of the density of InSAR data covering the fault plane (**Figures 12G–I**). **Figure 12I** shows weak resolution of the slip distribution in deep depth, and the InSAR data have diminishing resolution with depth, consistent with the results shown by Melgar et al. (2017). The shallow slip distribution close to the trench can be retrieved and the resolution is decreased when they are far from the coast. The checkboard test shows that the joint inversion can well resolve the slip distribution and achieve an ideal resolution near the trench.

5.4 Comparison With the Existing Rupture Model

Several authors have analyzed the source characteristics of the 2020 Oaxaca earthquake using different datasets (e.g. Melgar et al., 2020; Guo et al., 2021; Wen et al., 2021; Yan et al., 2022). Usually, the results estimated from finite-fault inversion vary a lot because of the intrinsic resolution provided by each dataset and different inversion strategies. In the fault geometry, one of the factors that influences the rupture model has been tested in this study, showing slight differences and that the main characteristics are consistent. In the existing studies, seismic data, geodetic data, and tsunamis buoy data are involved in the investigation of the finite-fault model. Yan et al. (2022) summarized the rupture model from the existing studies. Melgar et al. (2020) derived a slip model constrained within 15–30 km in depth with a high energy-to-moment ratio using InSAR data, high-rate real-time Global Navigation Satellite Systems (hr-GNSS) time series, and one Deep-ocean assessment and tsunamis buoy waveform. A narrow rupture model (17–24 km) is obtained from Guo et al. (2021) using joint inversion of the teleseismic waveforms and GNSS static offsets. Wen et al. (2021) developed a slip model (20–30 km) with a higher cumulative seismic moment of 1.7×10^{20} Nm using teleseismic waveforms, hr-GPS time series, static GPS offset, and InSAR data. In addition, Yan et al. (2022) obtained a rupture model (20–30 km) with a higher rupture speed and slip magnitude using teleseismic, strong-motion, hr-GPS, static GPS, and InSAR data. Our preferred model shows that the main slip is concentrated at a depth of 15–30 km and the average rupture velocity is 3 km/s. The inversion results are consistent with each other even though the fault geometry and inversion datasets are different. The main difference between our preferred model and the published models is the inversion strategy. A linear combination inversion method is used in this study, whereas the others' is the nonlinear inversion method (Guo et al., 2021; Wen et al., 2021; Yan et al., 2022). In addition, we considered the relative weight of each dataset in linear joint inversion and obtained a well-constrained rupture model through the grid search method. The coastal uplift data which were not involved in joint inversion were used to verify the robustness of the slip model, and the VR is 89.7% between the normalized observed and synthetic data, indicating that the rupture model obtained in this study explains the observed data well.

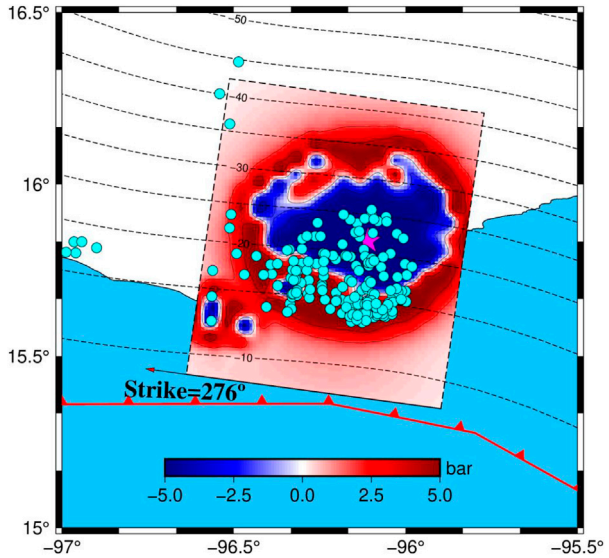

FIGURE 13 | Coulomb failure stress change on the fault plane; the cyan circle denotes the aftershock distribution a month after earthquake origin time, which the depth small than 20 km. The magenta star denotes the epicenter.

5.5 Rupture Characteristics

The 2020 Oaxaca earthquake was mainly because of the interaction between the Cocos plate and the North American plate. The main slip in our inversion result is located at depths of 15–30 km, consistent with the existing studies (15–30 km (Melgar et al., 2020), 17–24 km (Guo et al., 2021), and 20–30 km (Wen et al., 2021)). A slight difference shows the non-unique inversion results with large earthquakes (Lay et al., 2010). However, the main rupture characteristics of this earthquake shows that the rupture located upon 30 km contour are consistent with each other. Deep slow slip events are observed in the Oaxaca region and represent transient behaviors where the fault releases accumulated stress (Graham et al., 2016; Almeida et al., 2018; Cruz-Atienza et al., 2021). These slow slip events may release most down-dip shear stress, limiting the rupture area and hindering the coseismic down-dip rupture within this earthquake.

The up-dip region is fully creeping (Byrne et al., 1988; Hyndman et al., 1997; Chlieh et al., 2007; Hubbard et al., 2015) and is mostly velocity strengthening with stable-sliding (Hyndman et al., 1997; Almeida et al., 2018) than the seismogenic zone. The creeping released the most stress and little stress, which would accumulate that nucleated small earthquake events in the shallowest part over the period between large earthquakes. Additionally, few slow slip events have been found on the shallow part of this fault (Cruz-Atienza et al., 2021; Plata-Martinez et al., 2021); this may be one of the reasons for the absence of the slip in the up-dip zone (Correa-Mora et al., 2009; Graham et al., 2014, 2016; Obara and Kato, 2016; Maury et al., 2018; Cruz-Atienza et al., 2021). We calculated Coulomb failure stress change (Toda et al., 2005) using our rupture model, and the friction coefficient is set to 0.6 because previous studies have shown that thrust faults have high friction coefficients of around

0.8 (Freed et al., 2007; Xiong et al., 2010; Guo et al., 2020). The result shows that the aftershocks located at 5–10 km are rare even if the coseismic Coulomb stress is propagated to a shallow depth (**Figure 13**). It seems that stress is released by the creeping or slow-slip events of the shallow part.

6 CONCLUSION

In this study, we use an integrated inversion strategy to study the 2020 Oaxaca *M*w 7.4 earthquake source characteristics. The centroid moment tensor inversion using teleseismic *P* waves was performed to determine the fault geometry and source duration time. The result shows that the 2020 Oaxaca earthquake was a thrust event in the northwest direction and with a low dip angle, corresponding to the strike angle of 276°, dip angle of 24°, and rake angle of 67°. Then we obtained finite-fault joint inversion based on the fault geometry from our moment tensor solution. The relative weight of each dataset is determined using the grid search method to obtain a rupture model that explains the observed data better. This inversion strategy shows good consistency in temporal information of the moment tensor and finite-fault inversion. A well-resolved model can be estimated through joint inversion even if the fault geometry is different from one another. The results from this integrated inversion strategy show good consistency with existing studies, and the stability of this method is discussed, indicating that this inversion strategy can be used to analyze other megathrust earthquake source characteristics. The 2020 Oaxaca earthquake in the Mexican subduction zone is mainly because of the interaction between the Cocos and the North American plate. The down-dip boundary is limited by deep slow slip events, and the up-dip is fully creeping so that most stress is released, resulting in a small aftershock in the shallow depth. Considering the plate tectonics and high coupling of the Mexican subduction zone, this area still has the potential for large earthquakes.

6.1 Data and Resources

All data in this article are available. The teleseismic waveforms are downloaded from the Incorporated Research Institutions for Seismology (IRIS) Data Management Center (http://ds.iris.edu/wilber3/find_event). The Global Positioning System (GPS) RENIX data were downloaded from the University NAVSTAR Consortium (UNAVCO; ftp://data-out.unavco.org). The Sentinel-1 Synthetic Aperture Radar (SAR) data were downloaded from the European Space Agency (ESA) through the Sentinel-1 Scientific Data Hub (Scihub; https://vertex.daac.asf.alaska.edu). The focal mechanisms were available from the U.S. Geological Survey (USGS; https://earthquake.usgs.gov/earthquakes/eventpage/us6000ah9t), Global Centroid Moment Tensor (Global CMT; https://www.globalcmt.org), and GEOFOrschungsNetz (GEOFON; http://geofon.gfz-potsdam.de/eqinfo/event.php?id=gfz2020mhce). Aftershock hypocenters were available from the Servicio Sismológico Nacional (SSN; http://www.ssn.unam.mx). Maps for this work were made using the Generic Mapping Tools program (https://www.generic-mapping-tools.org/).

DATA AVAILABILITY STATEMENT

The datasets presented in this study can be found in online repositories. The names of the repository/repositories and accession number(s) can be found as follows: the teleseismic waveforms are downloaded from the Incorporated Research Institutions for Seismology (IRIS) Data Management Center (http://ds.iris.edu/wilber3/find_event). The Global Positioning System (GPS) RENIX data are downloaded from the University NAVSTAR Consortium (UNAVCO; ftp://data-out.unavco.org). The Sentinel-1 Synthetic Aperture Radar (SAR) data were downloaded from the European Space Agency (ESA) through the Sentinel-1 Scientific Data Hub (Scihub; https://vertex.daac.asf.alaska.edu).

AUTHOR CONTRIBUTIONS

GW and XL proposed the idea of this manuscript, designed and performed the experiments, and wrote the paper. Data analysis was conducted by GW, YZ, and GX. CX, YZ, and GX reviewed the manuscript and provided suggestions for improvements. All authors reviewed the final submitted version of the manuscript.

FUNDING

This study is financially supported by the National Natural Science Foundation of China (Grant Nos. 41974027 and 42104008), the National Key R&D Program of China (Grant No. 2021YFC3000504), the Hubei Province Natural Science Foundation (Grant No. 2020CFA002), and the Sino-German mobility program (Grant No. M-0054).

SUPPLEMENTARY MATERIAL

The Supplementary Material for this article can be found online at: https://www.frontiersin.org/articles/10.3389/feart.2022.951033/full#supplementary-material

REFERENCES

Almeida, R., Lindsey, E. O., Bradley, K., Hubbard, J., Mallick, R., and Hill, E. M. (2018). Can the Updip Limit of Frictional Locking on Megathrusts Be Detected Geodetically? Quantifying the Effect of Stress Shadows on Near-Trench Coupling. *Geophys. Res. Lett.* 45 (10), 4754–4763. doi:10.1029/2018GL077785

Bock, Y., Melgar, D., and Crowell, B. W. (2011). Real-time Strong-Motion Broadband Displacements from Collocated GPS and Accelerometers. *Bull. Seismol. Soc. Am.* 101 (6), 2904–2925. doi:10.1785/0120110007

Byrne, D. E., Davis, D. M., and Sykes, L. R. (1988). Loci and Maximum Size of Thrust Earthquakes and the Mechanics of the Shallow Region of Subduction Zones. *Tectonics* 7 (4), 833–857. doi:10.1029/TC007i004p00833

Chen, C. W., and Zebker, H. A. (2000). Network Approaches to Two-Dimensional Phase Unwrapping: Intractability and Two New Algorithms. *J. Opt. Soc. Am. A* 17 (3), 401–414. doi:10.1364/josaa.17.000401

Chlieh, M., Avouac, J.-P., Hjorleifsdottir, V., Song, T.-R. A., Ji, C., Sieh, K., et al. (2007). Coseismic Slip and Afterslip of the Great Mw 9.15 Sumatra-Andaman Earthquake of 2004. *Bull. Seismol. Soc. Am.* 97 (1A), S152–S173. doi:10.1785/0120050631

Chu, R., Wei, S., Helmberger, D. V., Zhan, Z., Zhu, L., and Kanamori, H. (2011). Initiation of the Great Mw 9.0 Tohoku-Oki Earthquake. *Earth Planet. Sci. Lett.* 308 (3), 277–283. doi:10.1016/j.epsl.2011.06.031

Correa-Mora, F., DeMets, C., Cabral-Cano, E., Diaz-Molina, O., and Marquez-Azua, B. (2009). Transient Deformation in Southern Mexico in 2006 and 2007: Evidence for Distinct Deep-Slip Patches beneath Guerrero and Oaxaca. *Geochem. Geophys. Geosyst.* 10, a–n. doi:10.1029/2008GC002211

Cruz-Atienza, V. M., Tago, J., Villafuerte, C., Wei, M., Garza-Girón, R., Dominguez, L. A., et al. (20212021). Short-term Interaction between Silent and Devastating Earthquakes in Mexico. *Nat. Commun.* 12 (1), 1–14. doi:10.1038/s41467-021-22326-6

DeMets, C., Gordon, R. G., and Argus, D. F. (2010). Geologically Current Plate Motions. *Geophys. J. Int.* 181 (1), 1–80. doi:10.1111/j.1365-246X.2009.04491.x

Duputel, Z., Rivera, L., Kanamori, H., and Hayes, G. (2012). W Phase Source Inversion for Moderate to Large Earthquakes (1990-2010). *Geophys. J. Int.* 189 (2), 1125–1147. doi:10.1111/j.1365-246x.2012.05419.x

Farr, T. G., Rosen, P. A., Caro, E., Crippen, R., Duren, R., Hensley, S., et al. (2007). The Shuttle Radar Topography Mission. *Rev. Geophys.* 45 (2). doi:10.1029/2005rg000183

Freed, A. M., Ali, S. T., and Bürgmann, R. (2007). Evolution of Stress in Southern California for the Past 200 Years from Coseismic, Postseismic and Interseismic Stress Changes. *Geophys. J. Int.* 169, 1164–1179. doi:10.1111/j.1365-246X.2007.03391.x

Goldstein, R. M., and Werner, C. L. (1998). Radar Interferogram Filtering for Geophysical Applications. *Geophys. Res. Lett.* 25, 4035–4038. doi:10.1029/1998gl900033

Graham, S., DeMets, C., Cabral-Cano, E., Kostoglodov, V., Rousset, B., Walpersdorf, A., et al. (2016). Slow Slip History for the MEXICO Subduction Zone: 2005 through 2011. *Pure Appl. Geophys.* 173 (10), 3445–3465. doi:10.1007/s00024-015-1211-x

Graham, S. E., DeMets, C., Cabral-Cano, E., Kostoglodov, V., Walpersdorf, A., Cotte, N., et al. (2014). GPS Constraints on the 2011-2012 Oaxaca Slow Slip Event that Preceded the 2012 March 20 Ometepec Earthquake, Southern Mexico. *Geophys. J. Int.* 197 (3), 1593–1607. doi:10.1093/gji/ggu019

Guo, R., Yang, H., Zhu, Y., Zheng, Y., Xu, J., Zhang, L., et al. (2021). Narrow Rupture of the 2020 *M*w 7.4 La Crucecita, Mexico, Earthquake. *Seismol. Res. Lett.* 92 (3), 1891–1899. doi:10.1785/0220200328

Guo, R., Zheng, Y., and Xu, J. (2020). Stress Modulation of the Seismic Gap between the 2008 Ms 8.0 Wenchuan Earthquake and the 2013 Ms 7.0 Lushan Earthquake and Implications for Seismic Hazard. *Geophys. J. Int.* 221 (3), 2113–2125. doi:10.1093/gji/ggaa143

Hartzell, S. H., and Heaton, T. H. (1983). Inversion of Strong Ground Motion and Teleseismic Waveform Data for the Fault Rupture History of the 1979 Imperial Valley, California, Earthquake. *Bull. Seismol. Soc. Am.* 73 (6A), 1553–1583. doi:10.1785/BSSA07306A1553

Hartzell, S., and Iida, M. (1990). Source complexity of the 1987 Whittier Narrows, California, earthquake from the inversion of strong motion records. *Journal of Geophysical Research: Solid Earth* 95 (B8), 12475–12485. doi:10.1029/jb095ib08p12475

Hayes, G. P., Moore, G. L., Portner, D. E., Hearne, M., Flamme, H., Furtney, M., et al. (2018). Slab2, a Comprehensive Subduction Zone Geometry Model. *Science* 362 (6410), 58–61. doi:10.1126/science.aat4723

Horikawa, H. (2001). Earthquake Doublet in Kagoshima, Japan: Rupture of Asperities in a Stress Shadow. *Bull. Seismol. Soc. Am.* 91, 112–127. doi:10.1785/0119990131

Hubbard, J., Barbot, S., Hill, E. M., and Tapponnier, P. (2015). Coseismic Slip on Shallow Décollement Megathrusts: Implications for Seismic and Tsunami Hazard. *Earth-Science Rev.* 141, 45–55. doi:10.1016/j.earscirev.2014.11.003

Hyndman, R. D., Yamano, M., and Oleskevich, D. A. (19971997). The Seismogenic Zone of Subduction Thrust Faults. *Isl. Arc* 6 (3), 244–260. doi:10.1111/j.1440-1738.1997.tb00175.x

Jónsson, S., Zebker, H., Segall, P., and Amelung, F. (2002). Fault Slip Distribution of the 1999 M W 7.1 Hector Mine, California, Earthquake, Estimated from Satellite Radar and GPS Measurements. *Bull. Seismol. Soc. Am.* 92 (4), 1377–1389.

Ji, C., Wald, D. J., and Helmberger, D. V. (2002). Source Description of the 1999 Hector Mine, California, Earthquake, Part I: Wavelet Domain Inversion Theory and Resolution Analysis. *Bull. Seismol. Soc. Am.* 92 (4), 1192–1207. doi:10.1785/0120000916

Kim, A., and Dreger, D. S. (2008). Rupture Process of the 2004 Parkfield Earthquake from Near-fault Seismic Waveform and Geodetic Records. *J. Geophys. Res. Solid Earth* 113 (B7). doi:10.1029/2007jb005115

Laske, G., Masters, G., Ma, Z., and Pasyanos, M. (2013). Update on CRUST1.0—A 1-degree Global Model of Earth's Crust. *Geophys. Res. Abstr.* 15, 2658.

Lay, T., Ammon, C. J., Hutko, A. R., and Kanamori, H. (2010). Effects of Kinematic Constraints on Teleseismic Finite-Source Rupture Inversions: Great Peruvian Earthquakes of 23 June 2001 and 15 August 2007. *Bull. Seismol. Soc. Am.* 100 (3), 969–994. doi:10.1785/0120090274

Li, X., Ge, M., Zhang, X., Zhang, Y., Guo, B., Wang, R., et al. (2013). Real-time High-Rate Co-seismic Displacement from Ambiguity-Fixed Precise Point Positioning: Application to Earthquake Early Warning. *Geophys. Res. Lett.* 40 (2), 295–300. doi:10.1002/grl.50138

Li, X., Guo, B., Lu, C., Ge, M., Wickert, J., and Schuh, H. (2014). Real-time GNSS Seismology Using a Single Receiver. *Geophys. J. Int.* 198 (1), 72–89. doi:10.1093/gji/ggu113

Li, X., Han, X., Li, X., Liu, G., Feng, G., Wang, B., et al. (2021). GREAT-UPD: An Open-Source Software for Uncalibrated Phase Delay Estimation Based on Multi-GNSS and Multi-Frequency Observations. *GPS Solut.* 25 (2). doi:10.1007/s10291-020-01070-2

Maury, J., Ide, S., Cruz-Atienza, V. M., and Kostoglodov, V. (2018). Spatiotemporal Variations in Slow Earthquakes along the Mexican Subduction Zone. *J. Geophys. Res. Solid Earth* 123 (2), 1559–1575. doi:10.1002/2017JB014690

Melgar, D., Ruiz-Angulo, A., Pérez-Campos, X., Crowell, B. W., Xu, X., Cabral-Cano, E., et al. (2020). Energetic Rupture and Tsunamigenesis during the 2020 *M*w 7.4 La Crucecita, Mexico Earthquake. *Seismol. Res. Lett.* 92, 140–150. doi:10.1785/0220200272

Melgar, D., Bock, Y., and Crowell, B. W. (2012). Real-time Centroid Moment Tensor Determination for Large Earthquakes from Local and Regional Displacement Records. *Geophys J. Int.* 188 (2), 703–718. doi:10.1111/j.1365-246x.2011.05297.x

Melgar, D., Ganas, A., Geng, J., Liang, C., Fielding, E. J., and Kassaras, I. (2017). Source Characteristics of the 2015 Mw6. 5 Lefkada, Greece, Strike-slip Earthquake. *J. Geophys. Res. Solid Earth* 122 (3), 2260–2273.

Obara, K., and Kato, A. (2016). Connecting Slow Earthquakes to Huge Earthquakes. *Science* 353 (6296), 253–257. doi:10.1126/science.aaf1512

Okada, Y. (1985). Surface Deformation Due to Shear and Tensile Faults in a Half-Space. *Bull. Seismol. Soc. Am.* 75 (4), 1135–1154. doi:10.1785/BSSA0750041135

Olson, A. H., and Apsel, R. J. (1982). Finite Faults and Inverse Theory with Applications to the 1979 Imperial Valley Earthquake. *Bull. Seismol. Soc. Am.* 72 (6A), 1969–2001. doi:10.1785/BSSA07206A1969

Plata-Martinez, R., Ide, S., Shinohara, M., Garcia, E. S., Mizuno, N., Dominguez, L. A., .Taira, T., Yamashita, Y., Toh, A., Yamada, T., Real, J., Husker, A., Cruz-Atienza, V. M., and Ito, Y. (2021). Shallow Slow Earthquakes to Decipher Future Catastrophic Earthquakes in the Guerrero Seismic Gap. *Nat. Commun.* 12 (1), 3976–3978. doi:10.1038/s41467-021-24210-9

Ramírez-Herrera, M.-T., Corona, N., Cerny, J., Castillo-Aja, R., Melgar, D., Lagos, M., et al. (2020). Sand Deposits Reveal Great Earthquakes and Tsunamis at Mexican Pacific Coast. *Sci. Rep.* 10 (1), 1–10. doi:10.1038/s41598-020-68237-2

Rosen, P. A., Gurrola, E., Sacco, G. F., and Zebker, H. (2012). The InSAR scientific computing environmentEUSAR 2012; 9th European con. *ference synthetic aperture radar, VDE, 730-733.*

Rousset, B., Campillo, M., Lasserre, C., Frank, W. B., Cotte, N., Walpersdorf, A., et al. (2017). A Geodetic Matched Filter Search for Slow Slip with Application to the Mexico Subduction Zone. *J. Geophys. Res. Solid Earth* 122 (12), 498–510. doi:10.1002/2017JB014448

Ruff, L. J. (1996). Large earthquakes in subduction zones: Segment interaction and recurrence times. *Subduction: Top to bottom* 96, 91–104. doi:10.1029/GM096p0091

Singh, S. K., Astiz, L., and Havskov, J. (19811981). Seismic Gaps and Recurrence Periods of Large Earthquakes along the Mexican Subduction Zone: A Reexamination. *Bull. Seismol. Soc. Am.* 71, 827–843. doi:10.1785/bssa0710030827

Singh, S. K., Rodríguez, M., and Esteva, L. (1983). Statistics of Small Earthquakes and Frequency of Occurrence of Large Earthquakes along the Mexican Subduction Zone. *Bull. Seismol. Soc. Am.* 73, 1779–1796.

Toda, S., Stein, R. S., Richards-Dinger, K., and Bozkurt, S. (2005). Forecasting the Evolution of Seismicity in Southern California: Animations Built on Earthquake Stress Transfer. *J. Geophys. Res.* 110, B05S16. doi:10.1029/2004JB003415

Tracy, K.-C., Ian, R., David, R., Khalid, M., David, P., Wael, H., et al. (2020). *StEER—Crucecitas, Mexico* M*w 7.4 Earthquake*. DesignSafe-CI: Preliminary virtual Reconnaissance Report. doi:10.17603/ds2-k2bp-t724

Wang, R., Heimann, S., Zhang, Y., Wang, H., and Dahm, T. (2017). Complete Synthetic Seismograms Based on a Spherical Self-Gravitating Earth Model with an Atmosphere-Ocean-Mantle-Core Structure. *Geophys. J. Int.* 210 (3), 1739–1764. doi:10.1093/gji/ggx259

Wei, S., Helmberger, D., and Avouac, J.-P. (2013). Modeling the 2012 Wharton Basin Earthquakes Off-Sumatra: Complete Lithospheric Failure. *J. Geophys. Res. Solid Earth* 118 (7), 3592–3609. doi:10.1002/jgrb.50267

Wen, Y., Xiao, Z., He, P., Zang, J., Liu, Y., and Xu, C. (2021). Source Characteristics of the 2020 *M*w 7.4 Oaxaca, Mexico, Earthquake Estimated from GPS, InSAR, and Teleseismic Waveforms. *Seismol. Res. Lett.* 92 (3), 1900–1912. doi:10.1785/0220200313

Xiong, X., Shan, B., Zheng, Y., and Wang, R. (2010). Stress Transfer and its Implication for Earthquake Hazard on the Kunlun Fault, Tibet. *Tectonophysics* 482, 216–225. doi:10.1016/j.tecto.2009.07.020

Xu, Y., Zhang, Y., and Xu, L. (2022). Geometry-dependent Rupture Process of the 2015 Gorkha, Nepal, Earthquake Determined Using a Dip-Varying Inversion Approach with Teleseismic, High-Rate GPS, Static GPS and InSAR Data. *Geophys. J. Int.* 229 (2), 1408–1421. doi:10.1093/gji/ggab519

Yagi, Y., Mikumo, T., Pacheco, J., and Reyes, G. (2004). Source Rupture Process of the Tecoman, Colima, Mexico Earthquake of 22 January 2003, Determined by Joint Inversion of Teleseismic Body-Wave and Near-Source Data. *Bull. Seismol. Soc. Am.* 94, 1795–1807. doi:10.1785/012003095

Yan, Z., Xiong, X., Liu, C., and Xu, J. (2022). Integrated Analysis of the 2020 Mw 7.4 La Crucecita, Oaxaca, Mexico, Earthquake from Joint Inversion of Geodetic and Seismic Observations. *Bull. Seismol. Soc. Am.* 112 (3), 1271–1283. doi:10.1785/0120210276

Yang, H., Yao, S., He, B., and Newman, A. V. (2019). Earthquake Rupture Dependence on Hypocentral Location along the Nicoya Peninsula Subduction Megathrust. *Earth Planet. Sci. Lett.* 520, 10–17. doi:10.1016/j.epsl.2019.05.030

Yi, L., Xu, C., Zhang, X., Wen, Y., Jiang, G., Li, M., et al. (2017). Joint Inversion of GPS, InSAR and Teleseismic Data Sets for the Rupture Process of the 2015 Gorkha, Nepal, Earthquake Using a Generalized ABIC Method. *J. Asian Earth Sci.* 148, 121–130. doi:10.1016/j.jseaes.2017.08.029

Yue, H., and Lay, T. (2013). Source Rupture Models for the *M*w 9.0 2011 Tohoku Earthquake from Joint Inversions of High-Rate Geodetic and Seismic Data. *Bull. Seismol. Soc. Am.* 103, 1242–1255. doi:10.1785/0120120119

Zhang, Y., Feng, W. P., Chen, Y. T., Xu, L. S., Li, Z., and Forrest, D. (2012). The 2009 L'Aquila MW 6.3 Earthquake: a New Technique to Locate the Hypocentre in the Joint Inversion of Earthquake Rupture Process. *Geophys. J. Int.* 191 (3), 1417–1426. doi:10.1111/j.1365-246X.2012.05694.x

Conflict of Interest: The authors declare that the research was conducted in the absence of any commercial or financial relationships that could be construed as a potential conflict of interest.

Publisher's Note: All claims expressed in this article are solely those of the authors and do not necessarily represent those of their affiliated organizations, or those of the publisher, the editors, and the reviewers. Any product that may be evaluated in this article, or claim that may be made by its manufacturer, is not guaranteed or endorsed by the publisher.

frontiers | Frontiers in Earth Science

TYPE Methods
PUBLISHED 07 September 2022
DOI 10.3389/feart.2022.991093

OPEN ACCESS

EDITED BY
Lidong Dai,
Institute of Geochemistry (CAS), China

REVIEWED BY
Qiancheng Liu,
Institute of Geology and Geophysics (CAS), China
Xuebao Guo,
Tongji University, China
Kai Yang,
Southern University of Science and Technology, China

*CORRESPONDENCE
Qizhen Du,
multicomponent@163.com

SPECIALTY SECTION
This article was submitted to Solid Earth Geophysics, a section of the journal Frontiers in Earth Science

RECEIVED 11 July 2022
ACCEPTED 15 August 2022
PUBLISHED 07 September 2022

CITATION
Lv W, Du Q, Fu L-Y, Li Q, Zhang J and Zou Z (2022), A new scheme of wavefield decomposed elastic least-squares reverse time migration. *Front. Earth Sci.* 10:991093. doi: 10.3389/feart.2022.991093

A new scheme of wavefield decomposed elastic least-squares reverse time migration

Wenhao Lv[1], Qizhen Du[1,2]*, Li-Yun Fu[1,2], Qingqing Li[1], Jianlei Zhang[3] and Zhen Zou[3]

[1]Shandong Provincial Key Laboratory of Deep Oil and Gas, China University of Petroleum (East China), Qingdao, China, [2]Qingdao National Laboratory for Marine Science and Technology, Laboratory for Marine Mineral Resources, Qingdao, China, [3]R&D Center, Bureau of Geophysical Prospecting Inc., Zhuozhou, China

Elastic least-squares reverse time migration (ELSRTM) describes the reflectivity of the underground media more accurately than acoustic LSRTM in theory while suffering from the P- and S-waves crosstalk artifacts. We propose a new wavefield decomposed ELSRTM scheme to alleviate these crosstalk artifacts, which is different from conventional methods. In our new scheme, we implement the wavenumber domain elastic wavefield vector decomposition equivalently in the time-space domain to decompose source wavefield without Fourier transform, but with high precision. Then we decompose adjoint wavefield by constructing the shear component in a decoupled adjoint wave equation. Finally, based on elastic impedance parameterization, we derive the gradients with respect to elastic reflectivity in the wavefield-decomposed ELSRTM. Numerical examples show that our method is feasible even when applied to models with complex and uncorrelated P- and S-wave velocity structures.

KEYWORDS

elastic, LSRTM, crosstalk artifacts, wavefield decomposition, decoupled wave equation

1 Introduction

The work of several scholars marked the advent of reverse time migration (RTM) in the 1980s (Hemon, 1978; Baysal et al., 1983; McMechan, 1983; Whitmore, 1983). Compared with other migration methods, the reverse time migration based on the two-path wave equation has stronger amplitude preservation and higher image quality for the complex geological structure with steep dip angle and sharp velocity changes.

However, conventional RTM assumes that seismic data is obtained by regular surface sampling with a recording aperture as large as possible, which cannot be achieved in practice. Without these perfect assumptions, the conventional RTM algorithm is likely to fail even fed with accurate velocity and density models (Zhang et al., 2015).

The least square migration (LSM) (LeBras and Clayton, 1988) is a revolutionary innovation which solves imaging problems by an inversion method: match the

observed data with the numerical simulation data under the Born approximation, and update the imaging results through multiple inversion iterations (Schuster, 1993; Nemeth et al., 1999). LSM is believed to be able to image subsurface structure and reflections with higher resolution and better amplitude preservation, which is beneficial to more reliable and high-precision elastic parameter inversion and reservoir characterization. The LSM idea can be combined with a variety of imaging techniques. Scholars have introduced the idea of LSM into RTM, which is called least-squares reverse time migration (LSRTM) (Dong et al., 2012; Yao and Jakubowicz, 2012; Dai and Schuster, 2013; Zhang et al., 2013, 2015; Feng and Schuster, 2017; Liu and Peter, 2018; Yang et al., 2019).

Most studies about LSRTM have been focused on acoustic medium assumptions, the elastic characteristics of the wavefield are treated as noise rather than an additional source of information of the subsurface parameters (Sears et al., 2010). However, elastic assumptions describe the underground media more accurately than acoustic. In addition, with PP and PS reflectivity, the identification of fluid contacts, lithologies, fractures and hydrocarbon reservoirs will be clear. Therefore, it is necessary to study LSRTM based on elastic theory for land seismic data. Considering that ELSRTM suffers from crosstalk between P- and S-waves, wavefield decomposition methods are usually used to suppress crosstalk artifacts.

One of the wavefield decomposition methods is based on the Helmholtz theorem (Dellinger and Etgen, 1990; Sun and McMechan, 2001), in a homogeneous and isotropic medium, the elastic wavefield can be separated into a curl-free P wavefield and a divergence-free S wavefield. However, extra complex and computationally expensive polarity corrections are needed since the divergence and curl operators lead to phase shift and amplitude distortion (Yan and Sava, 2008; Du et al., 2012; Duan and Sava, 2015).

The second strategy for wavefield decomposition is the decoupled wave equations (Ma and Zhu, 2003; Li et al., 2007; Zhang et al., 2007; Xiao and Leaney, 2010), which decompose wavefields by solving the P- and S-wave separated wave equations. In recent years, the decoupled wave equations prevail in elastic RTM (Wang and McMechan, 2015; Du et al., 2017; Zhou et al., 2018) and ELSRTM (Gu et al., 2018; Qu et al., 2018; Zhong et al., 2021; Shi et al., 2021; Zhang and Gao ,2022; Liu et al., 2022) because it is easy to implement and does not cause phase shift and amplitude distortion of decomposed wavefields (Duan and Sava, 2015; Du et al., 2017; Gong et al., 2018). However, if migration models are not smooth enough, the decoupled wave equation methods may suffer.

The third wavefield decomposition method, which with clear physical significance and higher accuracy, is the wavefields decomposition in the wavenumber domain (Zhang and McMechan, 2010; Du et al., 2014; Zhang et al., 2020), the output decomposed P- and S-wavefields have the same amplitude, phase, and physical units as the input wavefields even in the case of inaccurate migration velocity. However, methods in the wavenumber domain suffer from expensive computation.

Shi et al. (2021), Zhong et al. (2021), Zhang & Gao (2022) and Liu et al. (2022) constructed the decoupled wave equation and applied it to both source and adjoint wavefields decomposition. It is different in this paper: we propose a compound strategy to suppress P- and S-wave cross-talk artifacts in an efficient way. Inspired by the work of Zhang and McMechan (2010) in the wavenumber domain, but avoiding taking the Fourier transform, we reconstruct the wavenumber domain decomposition operator, and transform it into time-space domain to decompose source wavefields. Then we decompose the adjoint wavefields by constructing the shear component in a decoupled adjoint wave equation. Finally, we obtain the gradients with respect to elastic reflectivity in the wavefield-decomposed ELSRTM. In addition, the gradients were updated using the conjugate gradient method.

This paper is organized as follows. First, we review the basic theory of ELSRTM including the Born approximation for the velocity-stress elastic wave equations, the virtual sources of the elastic demigration, the adjoint equations and gradients of ELSRTM. Next, we introduce an elastic wavefield vector decomposition method in the time-space domain and a decoupled adjoint wave equation. Then we obtain the gradients with respect to elastic reflectivity in the decoupled P- and S-wave frame. Finally, we use two numerical examples to demonstrate the feasibility of the proposed wavefield decomposed ELSRTM scheme.

2 Methodology

2.1 Basic theory of ELSRTM

In the 2D case, the elastic isotropic wave equation can be expressed by the first-order particle velocity and stress equation (Virieux, 1986) as

$$\begin{aligned}
\rho\frac{\partial v_x}{\partial t} &= \frac{\partial \sigma_{xx}}{\partial x} + \frac{\partial \tau_{zx}}{\partial z},\\
\rho\frac{\partial v_z}{\partial t} &= \frac{\partial \tau_{xz}}{\partial x} + \frac{\partial \sigma_{zz}}{\partial z},\\
\frac{\partial \sigma_{xx}}{\partial t} &= (\lambda+2\mu)\frac{\partial v_x}{\partial x} + \lambda\frac{\partial v_z}{\partial z},\\
\frac{\partial \sigma_{zz}}{\partial t} &= \lambda\frac{\partial v_x}{\partial x} + (\lambda+2\mu)\frac{\partial v_z}{\partial z},\\
\frac{\partial \tau_{xz}}{\partial t} &= \mu\left(\frac{\partial v_x}{\partial z} + \frac{\partial v_z}{\partial x}\right).
\end{aligned} \tag{1}$$

Where ρ stands for the density, λ and μ are the Lame constants of models, v_x and v_z represent particle velocities in the horizontal

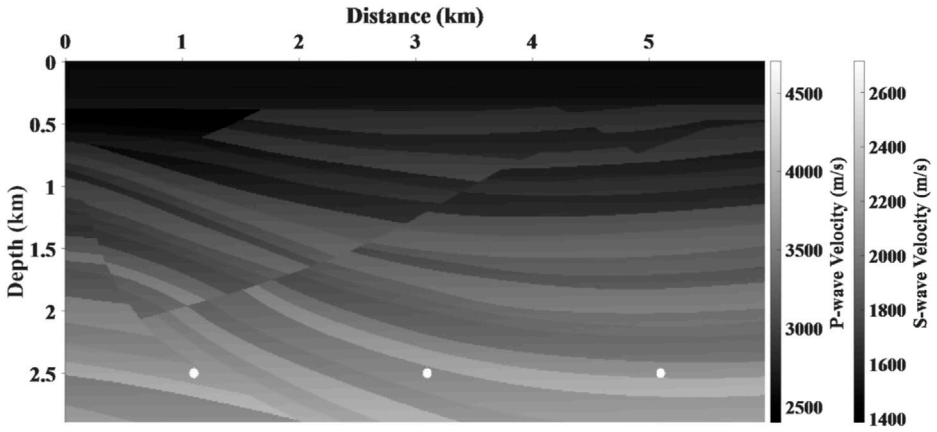

FIGURE 1
Quasi Sigsbee2A model. The structure of the P- and S-wave velocity models is identical.

and vertical respectively, σ_{xx} and σ_{zz} are the normal stresses, τ_{xz} (or τ_{zx}) is the shear stress.

According to the perturbation theory, a perturbation $\mathbf{\delta m} = [\delta\rho, \delta\lambda, \delta\mu]^T$ of the background model parameters $\mathbf{m} = [\rho, \lambda, \mu]^T$ will lead to wavefields perturbation $\mathbf{\delta u} = [\delta v_x, \delta v_z, \delta\sigma_{xx}, \delta\sigma_{zz}, \delta\tau_{xz}]^T$ with respect to the background wavefields $\mathbf{u} = [v_x, v_z, \sigma_{xx}, \sigma_{zz}, \tau_{xz}]^T$. The perturbed source wavefields which can be expressed as:

$$\begin{aligned}
&\rho\frac{\partial\delta v_x}{\partial t} - \frac{\partial\delta\sigma_{xx}}{\partial x} - \frac{\partial\delta\tau_{zx}}{\partial z} = f_x,\\
&\rho\frac{\partial\delta v_z}{\partial t} - \frac{\partial\delta\tau_{xz}}{\partial x} - \frac{\partial\delta\sigma_{zz}}{\partial z} = f_z,\\
&\frac{\partial\delta\sigma_{xx}}{\partial t} - (\lambda+2\mu)\frac{\partial\delta v_x}{\partial x} - \lambda\frac{\partial\delta v_z}{\partial z} = f_{xx},\\
&\frac{\partial\delta\sigma_{zz}}{\partial t} - \lambda\frac{\partial\delta v_x}{\partial x} - (\lambda+2\mu)\frac{\partial\delta v_z}{\partial z} = f_{zz},\\
&\frac{\partial\delta\tau_{xz}}{\partial t} - \mu\left(\frac{\partial\delta v_x}{\partial z} + \frac{\partial\delta v_z}{\partial x}\right) = f_{xz}.
\end{aligned} \tag{2}$$

Where the virtual sources are as follows:

$$\begin{aligned}
f_x &= -\delta\rho\frac{\partial v_x}{\partial t},\\
f_z &= -\delta\rho\frac{\partial v_z}{\partial t},\\
f_{xx} &= \delta\lambda\left(\frac{\partial v_x}{\partial x} + \frac{\partial v_z}{\partial z}\right) + 2\delta\mu\frac{\partial v_x}{\partial x},\\
f_{zz} &= \delta\lambda\left(\frac{\partial v_x}{\partial x} + \frac{\partial v_z}{\partial z}\right) + 2\delta\mu\frac{\partial v_z}{\partial z},\\
f_{xz} &= \delta\mu\left(\frac{\partial v_x}{\partial z} + \frac{\partial v_z}{\partial x}\right).
\end{aligned} \tag{3}$$

Equation 2 are the Born approximation for the velocity-stress elastic wave equation in the 2D case.

Using the adjoint-state method (Liu and Tromp, 2006; Plessix, 2006), the adjoint wave equations can be derived as:

$$\begin{aligned}
&\rho\frac{\partial\phi_x}{\partial t} - \lambda\frac{\partial\varphi_{zz}}{\partial x} - (\lambda+2\mu)\frac{\partial\varphi_{xx}}{\partial x} - \mu\frac{\partial\varphi_{xz}}{\partial z} = \delta V_x - \delta V_x^{obs},\\
&\rho\frac{\partial\phi_z}{\partial t} - \lambda\frac{\partial\varphi_{xx}}{\partial z} - (\lambda+2\mu)\frac{\partial\varphi_{zz}}{\partial z} - \mu\frac{\partial\varphi_{xz}}{\partial x} = \delta V_z - \delta V_z^{obs},\\
&\frac{\partial\varphi_{xx}}{\partial t} - \frac{\partial\phi_x}{\partial x} = 0,\\
&\frac{\partial\varphi_{zz}}{\partial t} - \frac{\partial\phi_z}{\partial z} = 0,\\
&\frac{\partial\varphi_{xz}}{\partial t} - \left(\frac{\partial\phi_x}{\partial z} + \frac{\partial\phi_z}{\partial x}\right) = 0.
\end{aligned} \tag{4}$$

Here, ϕ represents the adjoint wavefields of velocity, φ denotes the adjoint wavefields of stress, δV_i and δV_i^{obs}, $i \in \{x, z\}$ represent the simulated and observed seismogram received in the horizontal (x) and vertical (z) directions respectively.

And gradients are derived as:

$$\begin{aligned}
\frac{\partial J}{\partial\delta\rho} &= \int_0^T \phi_x\frac{\partial v_x}{\partial t} + \phi_z\frac{\partial v_z}{\partial t}dt,\\
\frac{\partial J}{\partial\delta\lambda} &= \int_0^T -(\varphi_{xx}+\varphi_{zz})\left(\frac{\partial v_x}{\partial x} + \frac{\partial v_z}{\partial z}\right)dt,\\
\frac{\partial J}{\partial\delta\mu} &= \int_0^T -\left(2\varphi_{xx}\frac{\partial v_x}{\partial x} + 2\varphi_{zz}\frac{\partial v_z}{\partial z} + \varphi_{xz}\left(\frac{\partial v_x}{\partial z} + \frac{\partial v_z}{\partial x}\right)\right)dt.
\end{aligned} \tag{5}$$

2.2 The elastic wavefields decomposition

2.2.1 Decomposition of source wavefields

Zhang and McMechan (2010) proposed elastic wavefield decomposition in the wavenumber domain, which has been

used to improve elastic full waveform inversion in Ren and Liu (2016). However, the two-dimensional forward and inverse Fourier transforms must be repeated in each time slice, resulting in expensive calculations. Different from Ren and Liu (2016), in our scheme, the work of Zhang and McMechan (2010) was introduced into the time-spatial domain, thereby avoiding the Fourier transforms, and was applied to ELSRTM efficiently.

The P- and S- wavefields in 2D case are decomposed in the wavenumber domain according to the following equations given by Zhang and McMechan (2010) as follows:

$$\begin{aligned}
\tilde{v}_x^p(k_x,k_z) &= K_x^2\tilde{v}_x(k_x,k_z) + K_xK_z\tilde{v}_z(k_x,k_z),\\
\tilde{v}_z^p(k_x,k_z) &= K_z^2\tilde{v}_z(k_x,k_z) + K_xK_z\tilde{v}_x(k_x,k_z),\\
\tilde{v}_x^s(k_x,k_z) &= K_z^2\tilde{v}_x(k_x,k_z) - K_xK_z\tilde{v}_z(k_x,k_z),\\
\tilde{v}_z^s(k_x,k_z) &= K_x^2\tilde{v}_z(k_x,k_z) - K_xK_z\tilde{v}_x(k_x,k_z).
\end{aligned} \tag{6}$$

where $\tilde{v}_x$ and $\tilde{v}_z$ represent particle velocities in the wavenumber domain, $K_x = k_x/k$ and $K_z = k_z/k$ are normalized wavenumbers, in which (k_x, k_z) is the wavenumber vector that defines the direction of wave propagation in 2D case, and $k = \sqrt{k_x^2 + k_z^2} = \omega/v_{pha}$, v_{pha} is the phase velocity, ω denotes angular frequency. Zhang and McMechan (2010) further described Eq. 6 in a short form as:

$$\begin{aligned}
\tilde{\mathbf{V}}^{\mathbf{P}} &= \mathbf{K}\left(\mathbf{K}\cdot\tilde{\mathbf{V}}\right),\\
\tilde{\mathbf{V}}^{\mathbf{S}} &= -\mathbf{K}\times\left(\mathbf{K}\times\tilde{\mathbf{V}}\right).
\end{aligned} \tag{7}$$

where $\tilde{\mathbf{V}} = \tilde{\mathbf{V}}^{\mathbf{P}} + \tilde{\mathbf{V}}^{\mathbf{S}}$, $\tilde{\mathbf{V}} = (\tilde{v}_x, \tilde{v}_z)$, $\tilde{\mathbf{V}}^{\mathbf{P}} = (\tilde{v}_x^p, \tilde{v}_z^p)$, $\tilde{\mathbf{V}}^{\mathbf{S}} = (\tilde{v}_x^s, \tilde{v}_z^s)$, and we noticed that the operator $\mathbf{K} = K_x\mathbf{a_x} + K_z\mathbf{a_z} = \tilde{\nabla}/ik$, where $\tilde{\nabla} = ik_x\mathbf{a_x} + ik_z\mathbf{a_z}$ denotes the nabla operator in the wavenumber domain which corresponds to $\nabla = \partial/\partial x\mathbf{a_x} +$

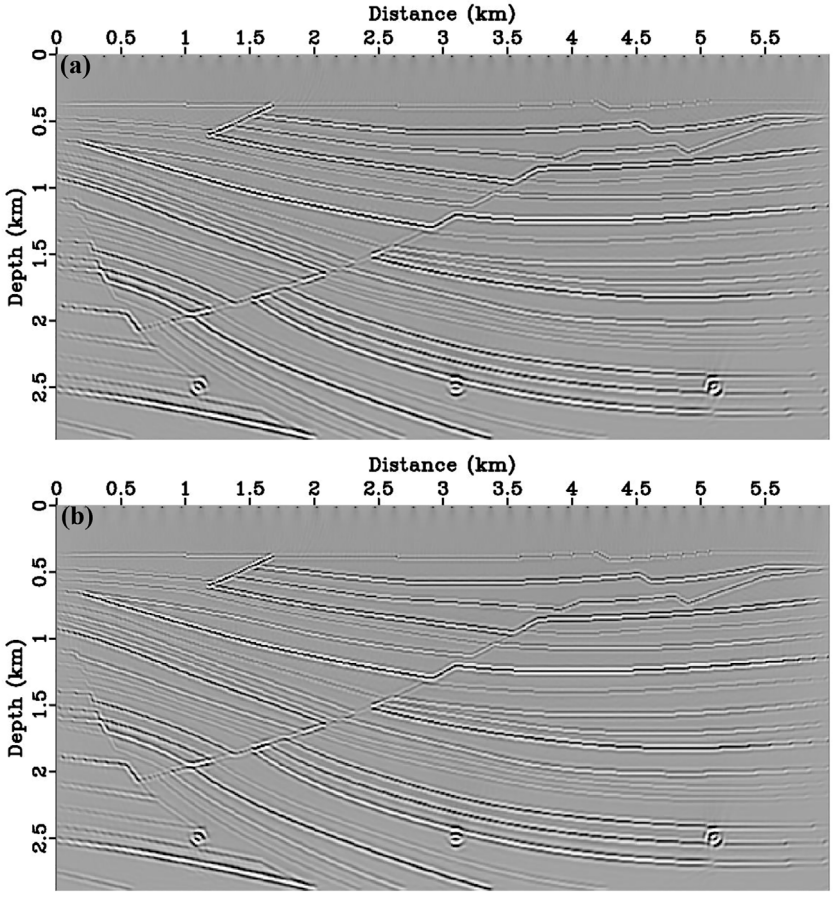

FIGURE 2
Migration results for the Quasi Sigsbee2A model. The true **(A)** PP and **(B)** PS reflectivity distribution without filtering processed.

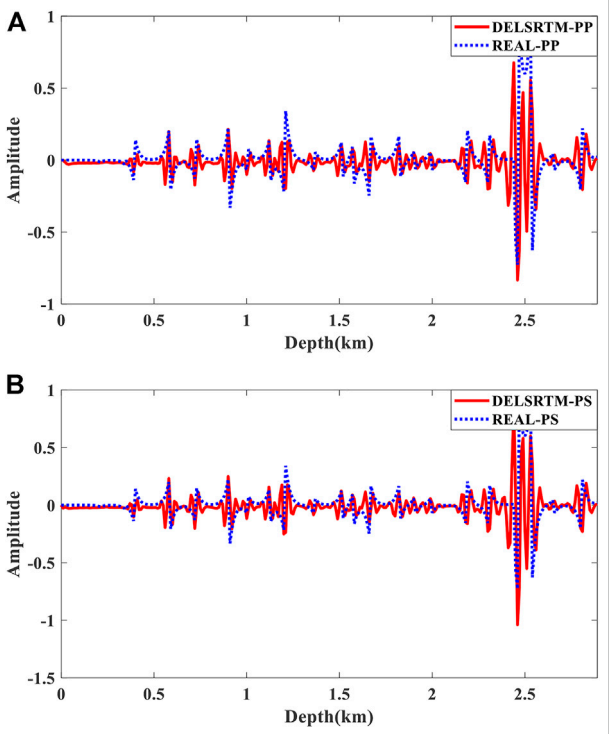

FIGURE 3
For the quasi-Sigsbee2A model, the DELSRTM image reflectivity profiles are compared with the real reflectivity in a single trace at 3090 m. **(A)** for PP comparison, **(B)** for PS comparison, the dashed blue lines and solid red lines indicate real and DELSRTM reflectivity, respectively.

$\partial/\partial z\mathbf{a_z}$ in the spatial domain ($\mathbf{a_x}$ and $\mathbf{a_z}$ are defined as unit basic vectors in the Cartesian coordinate system).

Naturally, set the intermediate results in parentheses as $\tilde{V}^P_{tmp} = \mathbf{K}\cdot\tilde{\mathbf{V}}$ and $\tilde{\mathbf{V}}^{\mathbf{S}}_{\mathbf{tmp}} = \mathbf{K}\times\tilde{\mathbf{V}}$, and note that $k = \omega/v_{pha}$, more specifically:

$$\begin{aligned}\tilde{V}^P_{tmp} &= \frac{1}{ik}\tilde{\nabla}\cdot\tilde{\mathbf{V}} = \frac{v^p_{pha}}{i\omega}\tilde{\nabla}\cdot\tilde{\mathbf{V}},\\ \tilde{\mathbf{V}}^{\mathbf{S}}_{\mathbf{tmp}} &= \frac{1}{ik}\tilde{\nabla}\cdot\tilde{\mathbf{V}} = \frac{v^s_{pha}}{i\omega}\tilde{\nabla}\times\tilde{\mathbf{V}}.\end{aligned} \tag{8}$$

Note that $i\omega$ denotes the derivative operator in the frequency domain, which corresponds to $\partial/\partial t$ in the time domain. Moreover, according to the differential property of the Fourier transform, correspondingly, in the time-space domain:

$$\begin{aligned}\frac{\partial V^p_{tmp}}{\partial t} &= v^p_{pha}\nabla\cdot\mathbf{V},\\ \frac{\partial \mathbf{V}^{\mathbf{S}}_{\mathbf{tmp}}}{\partial t} &= v^s_{pha}\nabla\times\mathbf{V}.\end{aligned} \tag{9}$$

where $\mathbf{V} = \mathbf{V^P} + \mathbf{V^S}$, $\mathbf{V} = (v_x, v_z)$, v_x and v_z represent particle velocities in the spatial domain.

In the same way as $\tilde{\mathbf{V}}^{\mathbf{P}} = \mathbf{K}\tilde{V}^P_{tmp}$ and $\tilde{\mathbf{V}}^{\mathbf{S}} = -\mathbf{K}\times\tilde{\mathbf{V}}^{\mathbf{S}}_{\mathbf{tmp}}$, the decomposed vector wavefields in the spatial domain are described as:

$$\begin{aligned}\frac{\partial \mathbf{V^P}}{\partial t} &= v^p_{pha}\nabla V^P_{tmp},\\ \frac{\partial \mathbf{V^S}}{\partial t} &= -v^s_{pha}\nabla\times\mathbf{V}^{\mathbf{S}}_{\mathbf{tmp}}.\end{aligned} \tag{10}$$

where $\mathbf{V^P} = (v^p_x, v^p_z)$, and $\mathbf{V^S} = (v^s_x, v^s_z)$.

2.2.2 Decomposition of adjoint wavefields

It is different from the decomposition of source wavefields, since the first-order particle velocity-stress equation is not self-adjoint, we reconstruct the adjoint wave equations (Eq. 4) as follows to decompose adjoint wavefields into P- and S-wave components:

$$\begin{aligned}&\rho\frac{\partial\phi_x}{\partial t} = \lambda\frac{\partial\varphi_{zz}}{\partial x} + (\lambda+2\mu)\frac{\partial\varphi_{xx}}{\partial x} + \mu\frac{\partial\varphi_{xz}}{\partial z} + f^{adj}_x,\\ &\rho\frac{\partial\phi_z}{\partial t} = \lambda\frac{\partial\varphi_{xx}}{\partial z} + (\lambda+2\mu)\frac{\partial\varphi_{zz}}{\partial z} + \mu\frac{\partial\varphi_{xz}}{\partial x} + f^{adj}_z,\\ &\rho\frac{\partial\phi^S_x}{\partial t} = \mu\left(\frac{\partial\varphi_{xz}}{\partial z} - 2\frac{\partial\varphi_{zz}}{\partial x}\right),\\ &\rho\frac{\partial\phi^S_z}{\partial t} = \mu\left(\frac{\partial\varphi_{xz}}{\partial x} - 2\frac{\partial\varphi_{xx}}{\partial z}\right),\\ &\phi^P_x = \phi_x - \phi^S_x,\\ &\phi^P_z = \phi_z - \phi^S_z,\\ &\frac{\partial\varphi_{xz}}{\partial t} = \frac{\partial\phi_x}{\partial z} + \frac{\partial\phi_z}{\partial x},\\ &\frac{\partial\varphi_{xx}}{\partial t} = \frac{\partial\phi_x}{\partial x},\\ &\frac{\partial\varphi_{zz}}{\partial t} = \frac{\partial\phi_z}{\partial z}.\end{aligned} \tag{11}$$

Where ϕ^P_x, ϕ^P_z, ϕ^S_x, ϕ^S_z are the decoupled P- and S- adjoint wavefields of particle velocity.

2.3 The gradient of wavefield decomposed ELSRTM

According to the work of Feng and Schuster (2017) and Ren et al. (2017), the reflectivity images of elastic impedances can be defined as:

$$R_p = \frac{\delta I_p}{I_p}, R_s = \frac{\delta I_s}{I_s}, R_\rho = \frac{\delta\rho}{\rho}. \tag{12}$$

where $I_p = \rho\sqrt{\lambda+2\mu}$, $I_s = \rho\sqrt{\mu}$, δI_p and δI_s are the perturbed P- and S- impedance, and the perturbed λ and μ can be express as:

$$\delta\lambda = \frac{2}{\rho}\left(I_p^2 R_p - 2I_s^2 R_s\right), \delta\mu = \frac{2}{\rho}I_s^2 R_s. \tag{13}$$

Then substitute Eq. 13 into Eq. 3, the new virtual sources of elastic demigration can be written as:

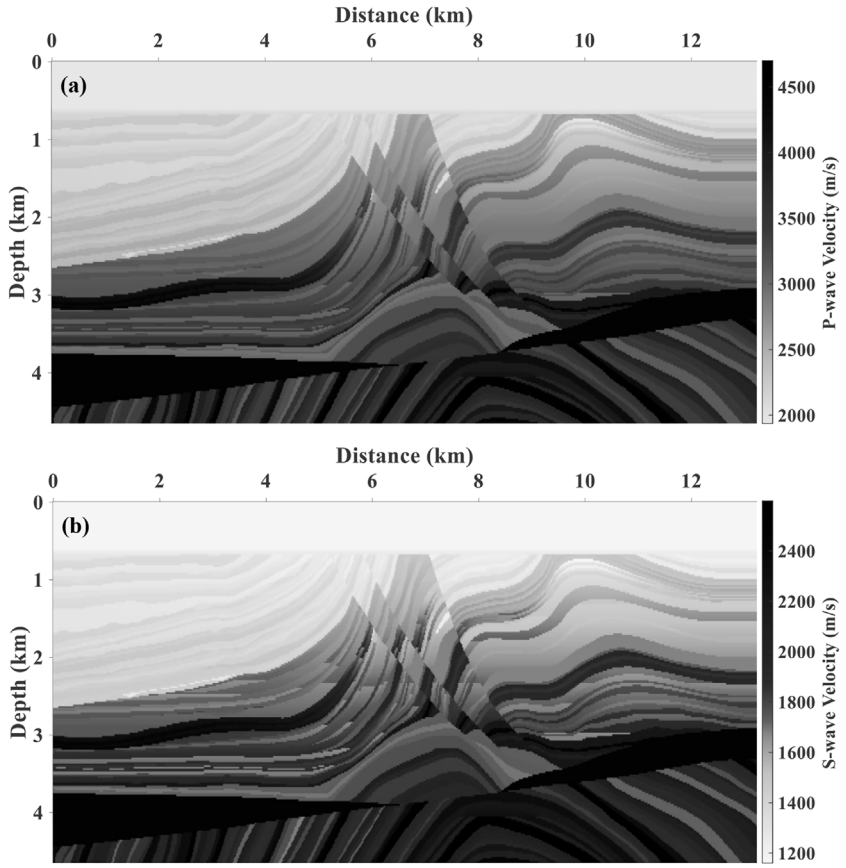

FIGURE 4
Modified marmousi2 model with uncorrelated **(A)** P- and **(B)** S-wave velocity models

$$
\begin{aligned}
f_x &= -\rho R_\rho \frac{\partial v_x}{\partial t},\\
f_z &= -\rho R_\rho \frac{\partial v_z}{\partial t},\\
f_{xx} &= \left(\frac{2I_p^2 R_p - 4I_s^2 R_s}{\rho}\right)\left(\frac{\partial v_x}{\partial x} + \frac{\partial v_z}{\partial z}\right) + \frac{4I_s^2 R_s}{\rho}\frac{\partial v_x}{\partial x},\\
f_{zz} &= \left(\frac{2I_p^2 R_p - 4I_s^2 R_s}{\rho}\right)\left(\frac{\partial v_x}{\partial x} + \frac{\partial v_z}{\partial z}\right) + \frac{4I_s^2 R_s}{\rho}\frac{\partial v_z}{\partial z},\\
f_{xz} &= \frac{2I_s^2 R_s}{\rho}\left(\frac{\partial v_x}{\partial z} + \frac{\partial v_z}{\partial x}\right).
\end{aligned}
\tag{14}
$$

Equation 15 express the gradients of elastic impedance parameterization which are related to the Lamé parameters in Eq. 5:

$$
\begin{aligned}
\frac{\partial J}{\partial R_p} &= 2v_p I_p \frac{\partial J}{\partial \delta\lambda},\\
\frac{\partial J}{\partial R_s} &= -4v_s I_s \frac{\partial J}{\partial \delta\lambda} + 2v_s I_s \frac{\partial J}{\partial \delta\mu}.
\end{aligned}
\tag{15}
$$

Then substitute Eq. 5 into Eq. 15, the new gradients based on elastic impedance parameterization are:

$$
\begin{aligned}
\frac{\partial J}{\partial R_p} &= -2v_p I_p \int_0^T (\varphi_{xx} + \varphi_{zz})\left(\frac{\partial v_x}{\partial x} + \frac{\partial v_z}{\partial z}\right)dt,\\
\frac{\partial J}{\partial R_s} &= 2v_s I_s \int_0^T \left(2\varphi_{xx}\frac{\partial v_x}{\partial x} + 2\varphi_{zz}\frac{\partial v_z}{\partial z} - \varphi_{xz}\left(\frac{\partial v_x}{\partial z} + \frac{\partial v_z}{\partial x}\right)\right)dt.
\end{aligned}
\tag{16}
$$

In P- S- decoupled elastic system, the elastic wavefields will be replaced by separated P- or S- wavefields to derive pure wave mode gradients, while the adjoint strains exist in the gradients with respect to reflectivity (Eq. 16) but not decoupled in our algorithm (Eq. 11). Ren and Liu (2015, 2016) suggested that according to the particular solutions of portion adjoint equations, the transformation from strains to particle velocities in the gradient equations can be written as:

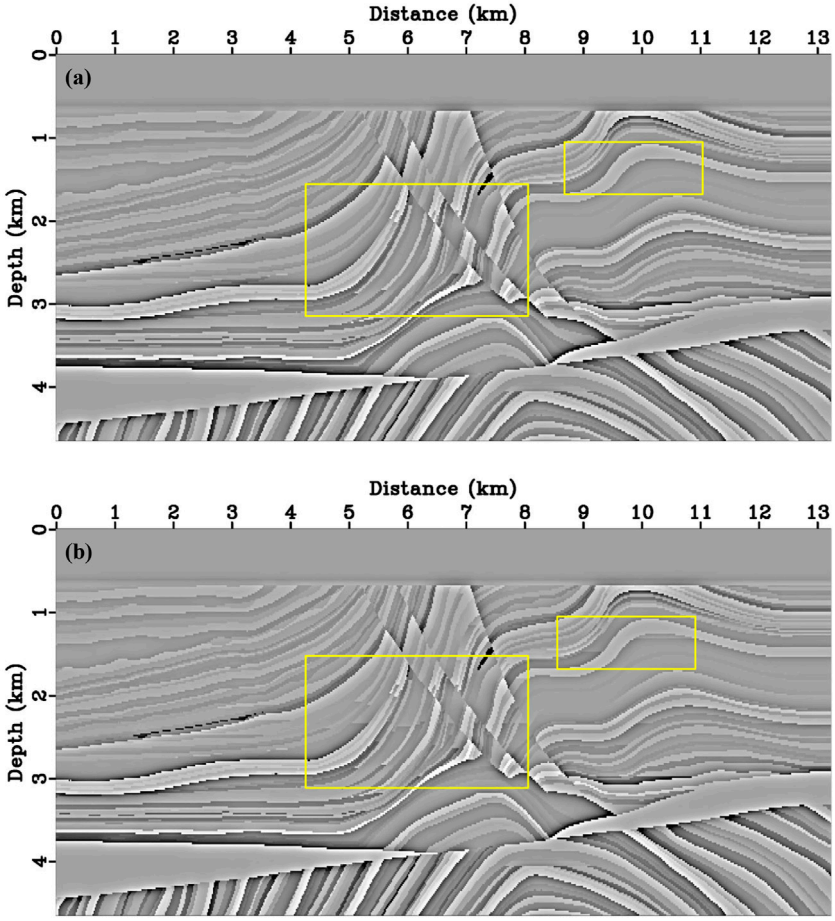

FIGURE 5
The true **(A)** PP and **(B)** PS reflectivity distribution of the Modified Marmousi2 model in our numerical test. The reflectivity distribution of uncorrelated P and S-wave velocity structures is indicated by yellow boxes.

$$
\begin{aligned}
\varphi_{xx} &= \frac{\partial \psi_x}{\partial x},\\
\varphi_{zz} &= \frac{\partial \psi_z}{\partial z},\\
\varphi_{xz} &= \frac{\partial \psi_x}{\partial z} + \frac{\partial \psi_z}{\partial x},\\
\psi_x &= \int_T^t \phi_x^P d\tau + \int_T^t \phi_x^S d\tau,\\
\psi_z &= \int_T^t \phi_z^P d\tau + \int_T^t \phi_z^S d\tau.
\end{aligned}
\tag{17}
$$

Moreover, the gradients with respect to elastic reflectivity in the wavefield decomposed ELSRTM frame can be derived as:

$$
\begin{aligned}
\frac{\partial J}{\partial R_p} &= -2v_p I_p \int_0^T \left(\frac{\partial v_x^P}{\partial x} + \frac{\partial v_z^P}{\partial z}\right)\left(\frac{\partial \psi_x^P}{\partial x} + \frac{\partial \psi_z^P}{\partial z}\right) dt,\\
\frac{\partial J}{\partial R_s} &= 2v_s I_s \int_0^T \left(\begin{array}{l} 2\dfrac{\partial v_x^P}{\partial x}\dfrac{\partial \psi_x^S}{\partial x} + 2\dfrac{\partial v_z^P}{\partial z}\dfrac{\partial \psi_z^S}{\partial z} \\ -\left(\dfrac{\partial v_x^P}{\partial z} + \dfrac{\partial v_z^P}{\partial x}\right)\left(\dfrac{\partial \psi_x^S}{\partial z} + \dfrac{\partial \psi_z^S}{\partial x}\right) \end{array} \right) dt.
\end{aligned}
\tag{18}
$$

3 Numerical examples

To verify the feasibility of the proposed wavefield decomposed ELSRTM (DELSRTM), we designed two experiments based on quasi-Sigsbee2A model and modified Marmoisi2 model, respectively. To ensure the efficiency and stability of finite difference, we made some modifications based on the original

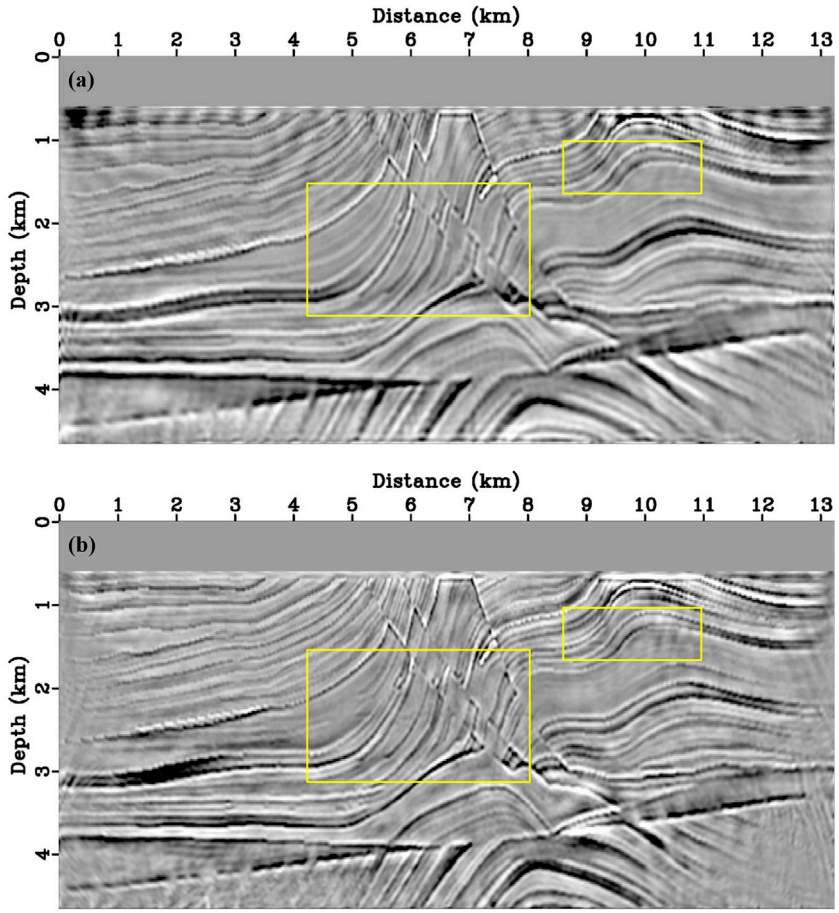

FIGURE 6
Migration results for the modified marmousi2 model. No filtering processed **(A)** PP- and **(B)** PS-image which generated from proposed DELSRTM after 40 times iteration. The images of uncorrelated P and S-wave velocity structures are indicated by yellow boxes.

velocity models. In the quasi-Sigsbee2A experiment, we investigated the accuracy of DELSRTM. In the modified Marmoisi2 experiment, we focused on suppressing crosstalk artifacts and compared the DELSRTM imaging results with true reflectivity. We define (Vtrue-Vmig)/Vmig as the true reflectivity distribution, where the subscript true and mig means true velocity model and migration velocity model, respectively.

3.1 Quasi-Sigsbee2A model

To demonstrate the accuracy of our proposed DELSRTM, we used a portion of the Sigsbee2A model structure (Figure 1) and modified the velocity to meet the stability of finite difference and cost-less calculation. The S-wave velocity is constructed by linear calculation based on the P-wave velocity. Moreover, the density is set to be a constant (1.0kg/m3). The size of this model is 290(z) by 600(x), and the spatial sampling interval is 10 m. We planned 40 sources and 600 receivers, which were 150 m apart and 10 m apart. The Ricker wavelet with a peak frequency of 30 Hz was injected into normal stress items in elastic wave equations and received 40 shots as the observed seismic data. Before imaging, we muted the direct waves and most of the diving waves to reduce the interference of low-frequency noise.

The migration results of iteration 40th for the quasi-Sigsbee2A model are shown in Figure 2. To demonstrate the accuracy of DELSRTM, the DELSRTM image reflectivity profiles are compared with the real reflectivity in a single trace (Figure 3), which located at the distance of 3090 m and cross the middle diffraction point. Compared with true PP and PS reflectivity, we found that without the help of filtering process, the PP- and PS-image generated by our DELSRTM clearly reconstructed the reflectivity distribution and all the high-speed diffraction points converged perfectly.

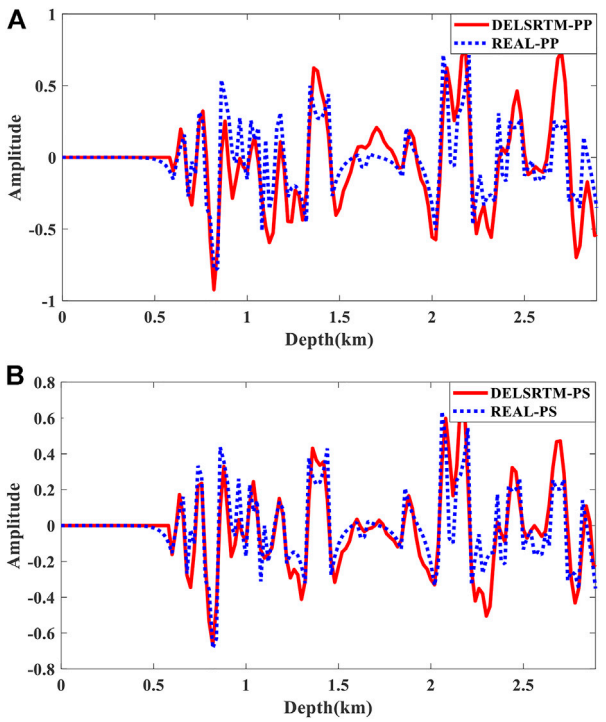

FIGURE 7
For the modified Marmousi2 model, the DELSRTM image reflectivity profiles compared with the real reflectivity in a single trace at 5340 m. **(A)** for PP comparison, **(B)** for PS comparison, the dashed blue lines and solid red lines indicate real and DELSRTM reflectivity, respectively.

3.2 Modified Marmousi2 model

To further verify the anti-crosstalk effect of the DELSRTM, we tested our algorithm using a modified marmousi2 model (Figure 4) with uncorrelated P- and S-wave velocity structures. Moreover, the density is set to be constant (1.0kg/m3). This model is discrete into a grid of 233(z) by 662(x) with a spatial sampling interval of 20 m in both directions. We deployed 30 P-wave sources and 662 receivers, which were uniformly deployed along the surface with 440 and 20 m apart. We used Ricker wavelet with a peak frequency of 40 Hz as the source signature, and the total recording time is 2s, with a sample interval of 0.5 ms. To simulate the propagation of seismic waves numerically in time domain, we used the high-order staggered grid finite-difference (FD) scheme to solve the elastic wave equation with a 5 m by 5 m discrete spatial grid size. Before imaging, we only removed the direct wave to ensure that the DELSRTM gradient is not contaminated by low wave components.

Figure 6 shows the migration results after forty iterations performed. There are a few low wave-number artifacts in the imaging results since the residual diving waves. The energy of artifacts suppressed some of the weak reflectivity imaging, however, a low-cut filtering process can also annihilate weak reflectivity imaging, which is why we chose not to do high-pass filtering. Compared with the true reflectivity distribution (Figure 5), migration results for the modified marmousi2 model (Figure 6) imaging complex structures accurately, and according to the comparison of single trace which is located at the distance of 5790 m in Figure 7, the proposed DELSRTM reflectivity imaging results are close to the real one. Besides, these yellow boxes in Figure 6 marked imaging results of where P- and S-wave velocity models are uncorrelated. There are few crosstalk artifacts in the image of the marked structures. From what has been discussed above, the P- and S-waves crosstalk artifacts are suppressed in our new DELSRTM scheme when applied to complex and uncorrelated elastic structures.

4 Conclusion

We propose a new scheme of decomposed wavefield least-squares reverse time migration, which effectively suppressed the P- and S-waves crosstalk artifacts. Since the first-order particle velocity-stress equation is not self-adjoint, we adopt a compound strategy to ensure that our algorithm is robust. In the processing of source wavefields vector decomposition, we transform the advantages of wavenumber domain-based wavefields vector decomposition method into time-space domain and improve the computational efficiency with minimal computational cost. Different from the method of source wavefields vector decomposition, in the process of adjoint-wavefield decomposition, we construct the shear component which is subtracted to separate P- and S-waves mode. The gradient of the decomposed wavefield least-squares reverse time migration was calculated using the separated P- and S-waves wavefields on both sides, and crosstalk-less gradients guarantee the accuracy of reflectivity imaging. Unlike ELSRTM, which is based on the decoupled wave equation method, our scheme produces correct results even when the P- and S-wave velocity models are uncorrelated and change dramatically. In addition, the physical significance of our new wavefield-decomposed ELSRTM scheme is clear.

Data availability statement

The raw data supporting the conclusions of this article will be made available by the authors, without undue reservation.

Author contributions

WL contributed to the conception and design of the study. QD modified the manuscript. All authors contributed to manuscript revision and read and approved the submitted version.

Funding

This research is supported by the Key Project of National Natural Science Foundation of China (41930429) and 14th 5-Year Prospective and Basic Research Program of CNPC (2021DJ3506).

Acknowledgments

We are grateful to editor LD and reviewers QL, XG, and KY for reviewing this manuscript.

Conflict of interest

Authors JZ and ZZ were employed by the R&D Center, Bureau of Geophysical Prospecting Inc.

The remaining authors declare that the research was conducted in the absence of any commercial or financial relationships that could be construed as a potential conflict of interest.

Publisher's note

References

Baysal, E., Kosloff, D., and Sherwood, J. (1983). Reverse time migration. *Geophysics* 48, 1514–1524. doi:10.1190/1.1441434

Dai, W., and Schuster, G. T. (2013). Plane-wave least-squares reverse-time migration. *Geophysics* 78 (4), S165–S177. doi:10.1190/geo2012-0377.1

Dellinger, J., and Etgen, J. (1990). Wave-field separation in two-dimensional anisotropic media. *Geophysics* 55 (7), 914–919. doi:10.1190/1.1442906

Dong, S., Cai, J., Guo, M., Suh, S., Zhang, Z., Wang, B., et al. (2012). Least- squares reverse time migration: Towards true amplitude imaging and improving the resolution. 82nd Annual International Meeting, SEG, Expanded Abstracts, Las Vegas, NV, November 2012. doi:10.1190/segam2012-1488.1

Du, Q. Z., Guo, C., Zhao, Q., Gong, X., Wang, C., and Li, X. (2017). Vector- based elastic reverse time migration based on scalar imaging condition. *Geophysics* 82, S111–S127. doi:10.1190/geo2016-0146.1

Du, Q. Z., Zhang, M. Q., Chen, X. R., Gong, X. F., and Guo, C. F. (2014). True-amplitude wavefield separation using staggered-grid interpolation in the wavenumber domain. *Appl. Geophys.* 11 (4), 437–446. doi:10.1007/s11770-014-0458-9

Du, Q. Z., Zhu, Y. T., and Ba, J. (2012). Polarity reversal correction for elastic reverse time migration. *Geophysics* 77 (2), S31–S41. doi:10.1190/geo2011-0348.1

Duan, Y., and Sava, P. (2015). Scalar imaging condition for elastic reverse time migration. *Geophysics* 80 (4), S127–S136. doi:10.1190/geo2014-0453.1

Feng, Z. C., and Schuster, G. T. (2017). Elastic least-squares reverse time migration. *Geophysics* 82, S143–S157. doi:10.1190/segam2016-13863861.1

Gong, X. F., Du, Q. Z., and Zhao, Q. (2018). SP- and SS-imaging for 3D elastic reverse time migration. *Geophysics* 83 (1), A1–A6. doi:10.1190/geo2017-0286.1

Gu, B., Li, Z., and Han, J. (2018). A wavefield-separation-based elastic least-squares reverse time migration. *Geophysics* 83 (3), S279–S297. doi:10.1190/geo2017-0131.1

Hemon, C. (1978). Equations d'onde et modeles. *Geophys. Prospect.* 26, 790–821. doi:10.1111/j.1365-2478.1978.tb01634.x

LeBras, R., and Clayton, W. (1988). An iterative inversion of back-scattered acoustic waves. *Geophysics* 53 (4), 501–508. doi:10.1190/1.1442481

Li, Z., Zhang, H., Liu, Q., and Han, W. (2007). Numeric simulation of elastic wavefield separation by staggering grid high-order finite-difference algorithm. *Oil Geophys. Prospect.* 42 (5), 510–515. doi:10.3321/j.issn:1000-7210.2007.05.006

Liu, B., Wang, J. S., Ren, Y. X., Guo, X., Chen, L., and Liu, L. B. (2022). Decoupled elastic least-squares reverse time migration and its application in tunnel geologic forward prospecting. *Geophysics* 87, EN1–EN19. doi:10.1190/geo2020-0875.1

Liu, Q., and Peter, D. (2018). One-step data-domain least-squares reverse time migration. *Geophysics* 83 (4), R361–R368. doi:10.1190/geo2017-0622.1

Liu, Q., and Tromp, J. (2006). Finite-frequency kernels based on adjoint methods. *Bull. Seismol. Soc. Am.* 96 (6), 2383–2397. doi:10.1785/0120060041

Ma, D., and Zhu, G. (2003). P- and S-wave separated elastic wave equation numerical modeling. *Oil Geophys. Prospect.* 38, 482–486. doi:10.3321/j.issn:1000-7210.2007.05.006

McMechan, G. (1983). Migration by extrapolation of time-dependent boundary values. *Geophys. Prospect.* 31, 413–420. doi:10.1111/j.1365-2478.1983.tb01060.x

Nemeth, T., Wu, C., and Schuster, G. T. (1999). Least-squares migration of incomplete reflection data. *Geophysics* 64 (1), 208–221. doi:10.1190/1.1444517

Plessix, R. -E. (2006). A review of the adjoint-state method for computing the gradient of a functional with geophysical applications. *Geophys. J. Int.* 167 (2), 495–503. doi:10.1111/j.1365-246X.2006.02978.x

Qu, Y., Li, J., Huang, J., and Li, Z. (2018). Elastic least-squares reverse time migration with velocities and density perturbation. *Geophys. J. Int.* 212 (2), 1033–1056. doi:10.1093/gji/ggx468

Ren, Z., and Liu, Y. (2015). Elastic full-waveform inversion using the second-generation wavelet and an adaptive-operator-length scheme. *Geophysics* 80 (4), R155–R173. doi:10.1190/geo2014-0516.1

Ren, Z., Liu, Y., and Sen, M. K. (2017). Least-squares reverse time migration in elastic media. *Geophys. J. Int.* 208 (2), 1103–1125. doi:10.1093/gji/ggw443

Ren, Z. M., and Liu, Y. (2016). A hierarchical elastic full-waveform inversion scheme based on wavefield separation and the multistep-length approach. *Geophysics* 81 (3), R99–R123. doi:10.1190/geo2015-0431.1

Schuster, G. T. (1993). Least-squares cross-well migration. 63rd Annual International Meeting, SEG, Expanded Abstracts, Washington, DC, September 1993, 110–113. doi:10.1190/1.1822308

Sears, T. J., Barton, P. J., and Singh, S. C. (2010). Elastic full waveform inversion of multicomponent ocean-bottom cable seismic data: Application to Alba field, U.K. North Sea. *Geophysics* 75 (6), R109–R119. doi:10.1190/1.3484097

Shi, Y., Li, S., and Zhang, W. (2021). Prestack correlative elastic least-squares reverse time migration based on wavefield decomposition. *J. Appl. Geophys.*, 194, 104447. doi.org/doi:10.1016/j.jappgeo.2021.104447

Sun, R., and McMechan, G. A. (2001). Scalar reverse-time depth migration of prestack elastic seismic data. *Geophysics* 66, 1519–1527. doi:10.1190/1.1487098

Virieux, J. (1986). P-SV wave propagation in heterogeneous media: Velocity-stress finite-difference method. *Geophysics* 51 (4), 889–901. doi:10.1190/1.1442147

Wang, W., and McMechan, G. A. (2015). Vector-based elastic reverse time migration. *Geophysics* 80 (6), S245–S258. doi:10.1190/geo2014-0620.1

Whitmore, D. (1983). Iterative depth migration by backward time propagation. SEG Technical Program Expanded Abstracts, Las Vegas, NV, September 1983 382–385. doi:10.1190/1.1893867

Xiao, X., and Leaney, W. S. (2010). Local vertical seismic profiling (VSP) elastic reverse-time migration and migration resolution: Salt-flank imaging with transmitted P-to-S waves. *Geophysics* 75 (2), S35–S49. doi:10.1190/1.3309460

Yan, J., and Sava, P. (2008). Isotropic angle-domain elastic reverse-time migration. *Geophysics* 73 (6), S229–S239. doi:10.1190/1.2981241

Yang, J. D., Zhu, H. J., McMechan, G., Zhang, H. Z., and Zhao, Y. (2019). Elastic least-squares reverse time migration in vertical transverse isotropic media. *Geophysics* 84 (6), S539–S553. doi:10.1190/geo2018-0887.1

Yao, G., and Jakubowicz, H. (2012). Least-squares reverse-time migration. SEG Technical Program Expanded Abstracts, Las Vegas, NV, November 2012, 1–5. doi:10.1190/segam2012-1425.1

Zhang, J., Tian, Z., and Wang, C. (2007). P-and S-wave separated elastic wave equation numerical modeling using 2D staggered-grid. SEG Technical Program Expanded Abstracts, San Antonio, TX, United States, September 2007, 2014–2019. doi:10.1190/1.2792904

Zhang, Q. S., and McMechan, A. G. (2010). 2D and 3D elastic wavefield vector decomposition in the wavenumber domain for VTI media. *Geophysics* 75, D13–D26. doi:10.1190/1.3431045

Zhang, W., and Gao, J. (2022). Attenuation compensation for wavefield-separation-based least-squares reverse time migration in viscoelastic media. *Geophys. Prospect.*, 70(2), 280–317. doi.org/doi:10.1111/1365-2478.13161

Zhang, W., Gao, J., Gao, Z., and Shi, Y. (2020), 2D and 3D amplitude-preserving elastic reverse time migration based on the vector-decomposed P- and S-wave records. *Geophys. Prospect.*, 68(9), 2712–2737. doi.org/doi:10.1111/1365-2478.13023

Zhang, Y., Duan, L., and Xie, Y. (2013). A stable and practical implementation of least-squares reverse time migration. SEG Technical Program Expanded Abstracts, Houston, TX, September 2013, 3716–3720. doi:10.1190/segam2013-0577.1

Zhang, Y., Duan, L., and Xie, Y. (2015). A stable and practical implementation of least-squares reverse time migration. *Geophysics* 80 (1), V23–V31. doi:10.1190/geo2013-0461.1

Zhong, Y., Gu, H. M., Liu, Y. T., and Mao, Q. H. (2021). Elastic least-squares reverse time migration based on decoupled wave equations. *Geophysics* 86 (6), S371–S386. doi:10.1190/geo2020-0805.1

Zhou, X., Chang, X., Wang, Y., and Yao, Z. (2018). Scalar PP and PS imaging of elastic RTM by wavefield decoupling method. SEG Technical Program Expanded Abstracts, Anaheim, CA, October 2018, 2417–2421. doi:10.1190/segam2018-2995359.1

frontiers | Frontiers in Earth Science

TYPE Methods
PUBLISHED 13 September 2022
DOI 10.3389/feart.2022.967771

OPEN ACCESS

EDITED BY
Jianzhong Zhang,
Ocean University of China, China

REVIEWED BY
Guoqing Ma,
Jilin University, China
Bingqiang Yuan,
Xi'an Shiyou University, China
Gengmeixia Geng,
Khalifa University, United Arab Emirates

*CORRESPONDENCE
Yabin Yang,
yyabin@mail.cgs.gov.cn

SPECIALTY SECTION
This article was submitted to Solid Earth Geophysics,
a section of the journal
Frontiers in Earth Science

RECEIVED 13 June 2022
ACCEPTED 04 August 2022
PUBLISHED 13 September 2022

CITATION
Jing L, Yang Y, Yao C, Qiu L, Chen D and Xu M (2022), Detection of geological boundaries by 3D gravity inversion for density gradients in different directions. *Front. Earth Sci.* 10:967771. doi: 10.3389/feart.2022.967771

Detection of geological boundaries by 3D gravity inversion for density gradients in different directions

Lei Jing[1,2], Yabin Yang[1,2]*, Changli Yao[3], Longjun Qiu[1,2], Deyuan Chen[1,2] and Menglong Xu[1,2]

[1]The National Center for Geological Exploration Technology, Langfang, China, [2]Institute of Geophysical and Geochemical Exploration, Chinese Academy of Geological Scineces, Langfang, China, [3]School of Geophysics and Information Technology, China University of Geosciences, Beijing, China

The spatial position and dip feature of the density boundary are significant to the study of fault and tectonic frameworks. Edge detection methods generally attach importance to the horizontal position of the boundary, but it is difficult to determine the dip feature expressly. A density gradient inversion method was proposed based on the corresponding relationship among the gravity forward field, forward kernel matrix, and model attributes. The inversion result of this method is that the density gradient value is different from the conventional gravity inversion. It can directly display the 3D distribution features integrated with 3D inversion results of the density gradient in different directions. The theoretical model means that the inversion results can not only identify the horizontal position of the boundary but also qualitatively determine the dip feature of faults. It has been widely applied to fault identification in the Songliao Basin. According to the joint inversion results, the strike feature and the dip feature can be quantitatively and qualitatively identified, respectively, making up for the shortcomings of sparse distribution and poor lateral resolution of existing seismic data.

KEYWORDS

gravity, 3D inversion, density gradient, dip recognition, joint inversion

Introduction

The gravity method is important in detecting the spatial distribution features of underground density and is also an emphasized geophysical prospecting method for regional geological research and energy mineral exploration. In addition, it plays an important role in investigating the geological and structural features of the bedrock, delineating the scope of the sedimentary basin, studying the fluctuation of the sedimentary rock layer or stratigraphic density interface, as well as the volcanic structure, crustal equilibrium, crustal, and upper mantle structure among others. There are many processing methods for boundary recognition and 3D inversion in gravity data processing and interpretation.

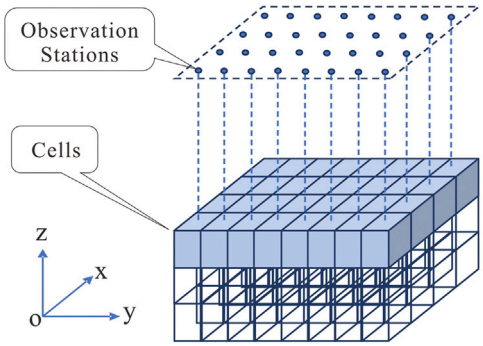

FIGURE 1
One-to-one correspondence between the model element grid and measuring point grid.

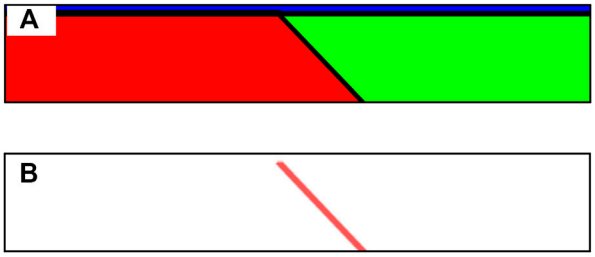

FIGURE 2
Fracture model and the horizontal gradient diagram. **(A)** Density model of fracture. **(B)** Horizontal gradient model of fracture density.

One of the important contents of gravity interpretation is to identify the spatial distribution features of geological body boundaries effectively. Gravity anomalies have a high lateral resolution, and gravity cascade belts with different scales often correspond to the boundaries of underground fault structures and geological bodies such as rock and ore bodies. The derivative operation, mathematical statistics, and multi-scale detection use gravity data to identify a geological body boundary. There are many methods based on the derivative operation, such as the vertical derivative method (VDR) (Hood and Mcclure, 1965; Hood and Teskey, 1989), a total horizontal derivative method based on x and y-direction derivatives (THDR) (Grauch and Cordell, 1987), analytical signal amplitude method based on x-, y-, and z-direction derivatives (ASM) (Nabighian, 1972; Nabighian, 1984; Li, 2006), dip angle method based on the ratio calculation of the aforementioned methods (TA) (Miller and Singh, 1994; Wang and Li, 2004), and θ diagram method (Theta Map) (Wijns et al., 2005), among others. The methods based on mathematical statistics include small domain filtering and standard deviation. Scale separation of multi-scale edge detection methods mainly includes the wavelet multi-scale decomposition (Hornby et al., 1999; Yang et al., 2015) and upward continuation transformation (Holden et al., 2000; Yan et al., 2015).

The 3D constrained gravity inversion can reduce the multi-solution of the gravity field inversion by increasing constraint conditions (Boulanger and Chouteau, 2001). When there is enough prior information, the depth and structural features of inversion results conform to the geological cognition (Camacho et al., 2000; Bosch et al., 2006). Different solutions would be obtained when different weighting factors and calculation strategies are used for constraint conditions. The main constraint methods are as follows: 1) depth constraint: it is used to cancel the natural attenuation of the kernel function with depth, eliminate the situation that the inversion density distribution does not conform to the real anomaly source due to its excessive weight near the surface, and then improve the depth resolution (Li et al., 1996, Li et al., 1998; Commer, 2011; Liu et al., 2013); 2) focus constraint: it can depict the boundary features of abnormal bodies, which is convenient for later processing and interpretation (Last et al., 1983; Portniaguine et al., 1999; Zhdanov, 2009; Wang et al., 2022); 3) physical property boundary constraint: to achieve more reasonable inversion physical property distribution, the upper and lower limit constraints of the geological physical property need to be supplemented in the process of physical property inversion, and the inversion density value is forced to be limited within a certain range (Portniaguine et al., 1999; Gao et al., 2017); 4) structural constraints: it can be used for joint constraints between different geophysical attributes, including cross gradient constraints (Gallardo and Meju, 2003; Fregoso and Gallardo, 2009; Gross, 2019) and summative gradient constraints (Molodtsov et al., 2015; Colombo and Rovetta, 2018; Liu and Zhang, 2022); 5) geostatistical constraints: regional geological characteristics and laws and geologists' understanding of geological conditions can be added to the model (Shamsipour et al., 2010; Geng et al., 2014; Geng et al., 2019a; Geng et al., 2019b).

Random access memory and computing power are essential for large-scale 3D gravity inversion in massive datasets and this could lead to overall inefficiency. Researchers have studied from different perspectives, mainly including 1) dimension reduction methods: decreasing storage space and computation by reducing dimensions, including random sub-domain inversion (Yao et al., 2007), wavelet compression (Li et al., 2010), and polynomial-based inversion (Liu et al., 2019); 2) symmetry processing method: the geometric lattice method reduces the computational complexity by translation invariance of the gravity field forward kernel matrix (Yao et al., 2002). Jing et al. (2019) further realized a fast algorithm with spatial domain calculation accuracy and frequency domain calculation speed by the fast Fourier transform.

The actual geological body boundary is distributed and the boundary features should be studied in a 3D space. The boundary

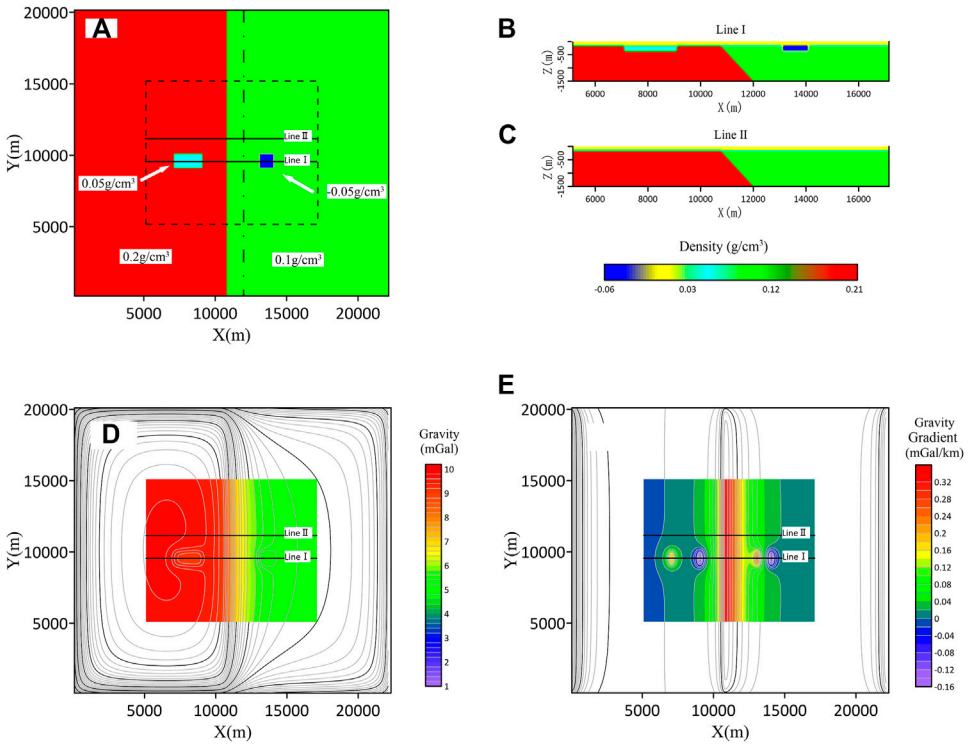

FIGURE 3
Normal fault fracture model and forward modeling field. **(A)** Model z = −200 m plane distribution map. **(B)** Model I line position profile; **(C)** Model II line position profile. **(D)** Forward gravity modeling results of the model. **(E)** Forward results of the horizontal gradient in the x-direction of gravity in the model.

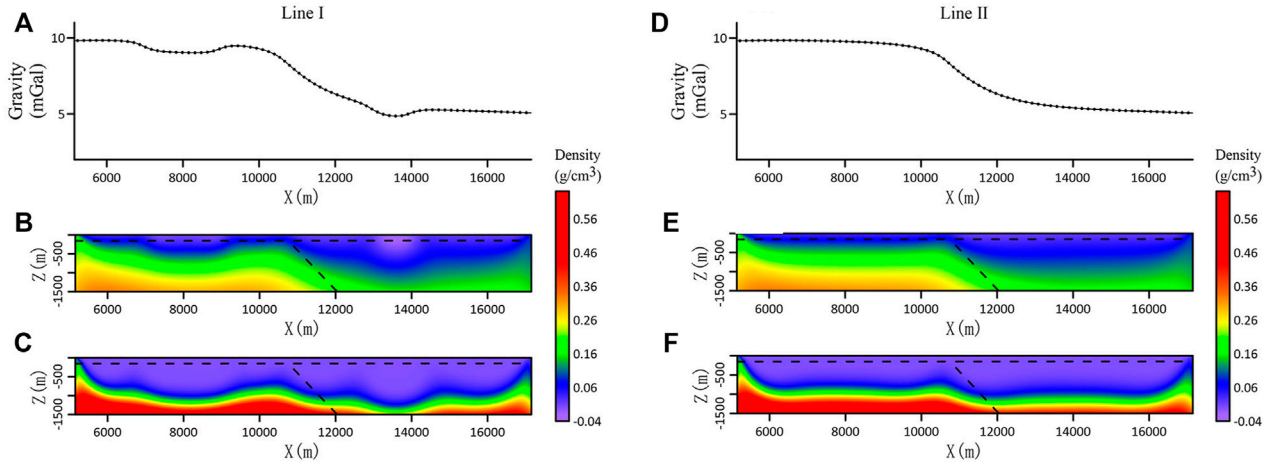

FIGURE 4
Gravity curves and inversion results profiles of line I and line II. **(A)** Gravity anomaly curve of line I. **(B)** Slice the inversion result of line I without focusing constraint. **(C)** Slicing of line I focusing inversion results. **(D)** Gravity anomaly curve of line II. **(E)** Slice the inversion result of line II without focusing constraint. **(F)** Slicing of II line focusing inversion results.

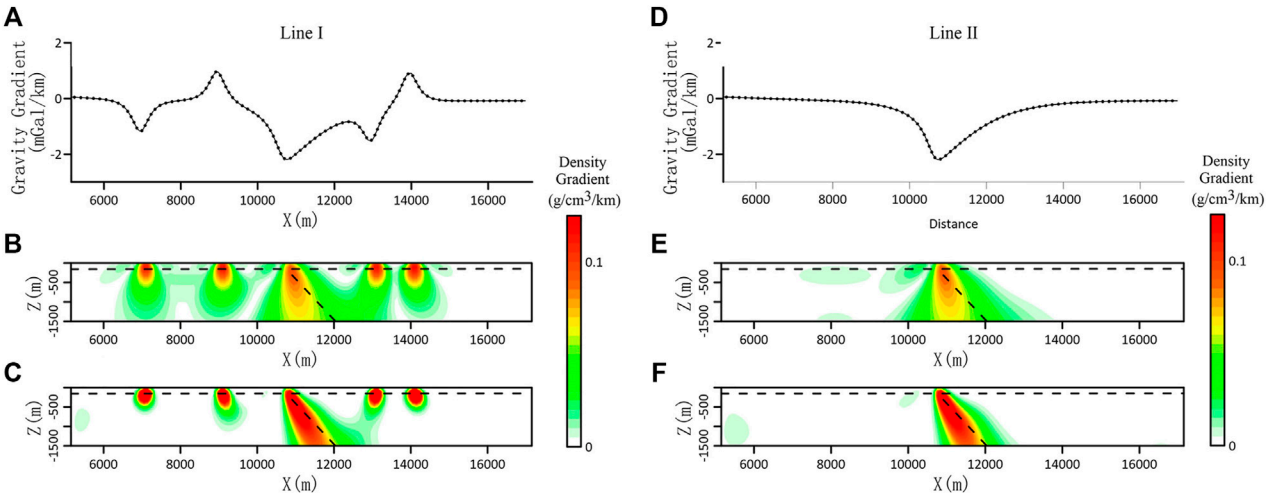

FIGURE 5
Horizontal gravity gradient curve and density gradient inversion result profile in the x-direction of line I and line II. **(A)** Horizontal gravity gradient anomaly curve of line I. **(B)** Slice the inversion result of line I without focusing constraint. **(C)** Line I focusing inversion result slice. **(D)** Horizontal gravity gradient anomaly curve of line II. **(E)** Slice the inversion result of line II without focusing constraint. **(F)** Slicing of line II focusing inversion results.

recognition methods are mainly 2D or pseudo-3D (multi-scale) methods; the processing method is used to reduce the dimension after assuming 3D geological density bodies, and the processing results often simplify the features of geological body boundaries. The 3D gravity field inversion is a 3D method in an ideal case, and its processing results can include all density features of geological bodies. A new boundary recognition method, the 3D density gradient inversion method, was proposed to improve the resolution of density boundary recognition. It directly inverts the horizontal density gradient parameter, that is, density boundary, and it has the advantage of flexible use for constraint information. The principle and technology would be explained below, and the application effect of the method would be verified using the theoretical model and measured data.

Density gradient inversion method

Relationship between the density gradient and gravity gradient

Assuming that the underground space is divided into $M\,(M = m \times n \times p)$ prism grids, where m and n are the number of grids in the x (north) direction and y (east) direction, respectively, and p represents the number of grids in the z (vertical) direction, $N\,(N = m \times n)$ measuring points are observed on the surface and correspond to the center of top surfaces of prisms one by one (Figure 1).

According to the forward theory of gravity field, gravity anomaly can be expressed as (Jing et al., 2019).

$$\mathbf{d} = \mathbf{F}^{-1}\left(\sum_{k=1}^{p} \mathbf{F}(\tilde{\mathbf{G}}_k) \cdot \mathbf{F}(\tilde{\boldsymbol{\rho}}_k)\right), (1 \le k \le p), \tag{1}$$

where $\mathbf{d}$ is the gravity anomaly of the model, $\mathbf{F}$ is the forward fast Fourier transform, $\mathbf{F}^{-1}$ is inverse fast Fourier Transform, $\tilde{\mathbf{G}}_k$ $((2m-1)\times(2n-1))$ is the prism forward kernel matrix representing the k-th layer, $\tilde{\boldsymbol{\rho}}_k$ $((2m-1)\times(2n-1))$ is the extended matrix after adding zeros to the density matrix of the k-th layer, and $''\cdot''$ represents the Hadamard product, that is, the multiplication of corresponding elements in two matrixes of the same order.

The first $m \times n$ element in matrix $\tilde{\boldsymbol{\rho}}_k$ is the density matrix element of the k-th layer in the model, and the remaining elements in matrix $\tilde{\boldsymbol{\rho}}_k$ are zero values. The first $m \times n$ element in matrix $\tilde{\mathbf{G}}_k$ is the gravity response value of the prism $\tilde{\rho}_{m,n,k}$ numbered (m,n) in the k-th density matrix at the surface measuring point (the default starting number is 1). At this time, the density of the prism $\tilde{\rho}_{m,n,k}$ is set to unit density, and the remaining elements in the matrix $\tilde{\mathbf{G}}_k$ are stored symmetrically about $\tilde{G}_{m,n,k}$.

Fourier transforms Eq. 1 and multiplies it by the conversion factor $\boldsymbol{\varphi}$ to obtain Eq. 2:

$$\mathbf{F}\left(\mathbf{d}_{\varphi}\right) = \tilde{\boldsymbol{\varphi}} \cdot \sum_{k=1}^{p} [\mathbf{F}(\tilde{\mathbf{G}}_k)] \cdot \mathbf{F}(\tilde{\boldsymbol{\rho}}_k), \tag{2}$$

where $\mathbf{d}_{\varphi}$ is the gravity conversion field obtained by the conversion factor $\boldsymbol{\varphi}$ of the gravity field, $\mathbf{F}(\tilde{\mathbf{d}}_{\varphi}) = \tilde{\boldsymbol{\varphi}} \cdot \mathbf{F}(\tilde{\mathbf{d}})$.

When the conversion factor $\boldsymbol{\varphi}$ is a horizontal gradient operator, its expression form is as follows:

$$\tilde{\boldsymbol{\varphi}}_x = i\mathbf{u}, \tag{3}$$

$$\tilde{\boldsymbol{\varphi}}_y = i\mathbf{v}, \tag{4}$$

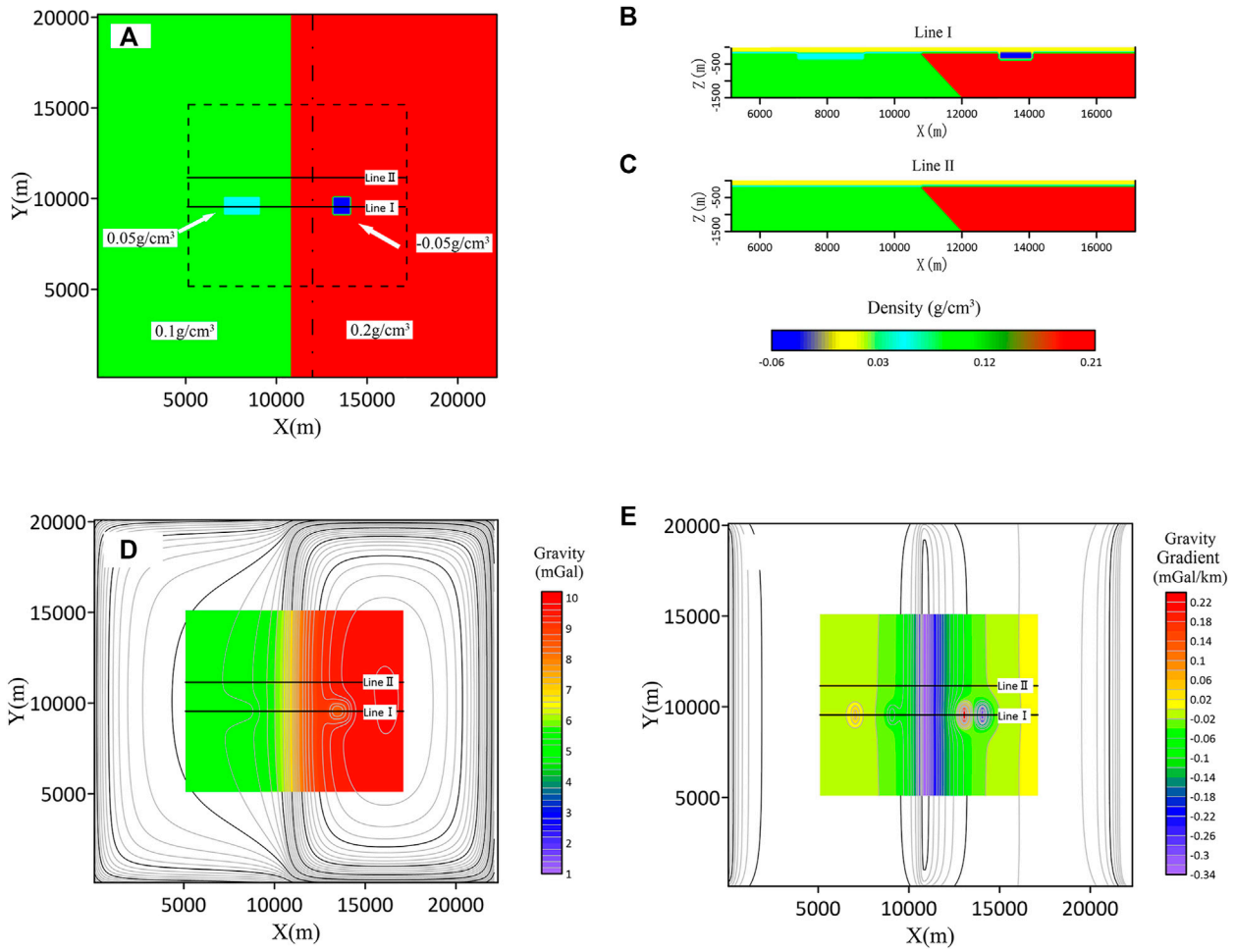

FIGURE 6
Schematic diagram of the reverse fault fracture model. **(A)** Model z = -200 m plane distribution map. **(B)** Model line I position profile, **(C)** Model line II position profile. **(D)** Forward gravity modeling results of the model. **(E)** Forward results of the horizontal gradient in the x-direction of gravity in the model.

where $\mathbf{u}$ and $\mathbf{v}$ are the wavenumbers in x and y directions, respectively, $\tilde{\boldsymbol{\varphi}}_x$ is the x-direction horizontal gradient conversion factor, and $\tilde{\boldsymbol{\varphi}}_y$ is the y-direction horizontal gradient conversion factor. Based on the physical meaning, the left term $\mathbf{F}(\mathbf{d}_{\boldsymbol{\varphi}})$ in Eq. 2 represents the horizontal gradient field of gravity in the x-direction or y-direction. When the conversion factor $\tilde{\boldsymbol{\varphi}}$ is combined with density $\tilde{\boldsymbol{\rho}}$, Eq. 2 is as follows:

$$\mathbf{F}\left(\tilde{\mathbf{d}}_{\boldsymbol{\varphi}}\right) = \sum_{k=1}^{p} \mathbf{F}(\tilde{\mathbf{G}}_k) \cdot \left[\tilde{\boldsymbol{\varphi}} \cdot \mathbf{F}(\tilde{\boldsymbol{\rho}}_k)\right] = \sum_{k=1}^{p} \mathbf{F}(\tilde{\mathbf{G}}_k) \cdot \mathbf{F}\left(\tilde{\boldsymbol{\rho}}_{\boldsymbol{\varphi}k}\right), \quad (5)$$

where $\tilde{\boldsymbol{\rho}}_{\boldsymbol{\varphi}k}$ is the conversion density distribution obtained by the conversion factor $\tilde{\boldsymbol{\varphi}}$ of density distribution $\tilde{\boldsymbol{\rho}}_k$.

Eq. 5 is the relationship between the 3D density gradient and gravity gradient, in which the kernel function is the forward kernel function of the gravity field, which is fixed, and the model parameters can change with the type of observation field.

The model parameter is no longer density, but the horizontal gradient of the density parameter. Generally, the conversion factor may also be used as various conversion filters, such as vertical gradient filters, high-order derivative filters, and combinations of various filters. Different filters can theoretically highlight the different features of the density model and this is not discussed in this study.

For the case where the conversion factor is a horizontal gradient filter, a density model of concealed fracture is set up to visually demonstrate the difference between the density model and the density horizontal gradient model (Figure 2A). The horizontal gradient transformation model of the density model is obtained by summing the horizontal derivatives of the x and y directions of the density model (Figure 2B). Comparing the two models, it can be seen that the density model of concealed fracture consists of two block models and

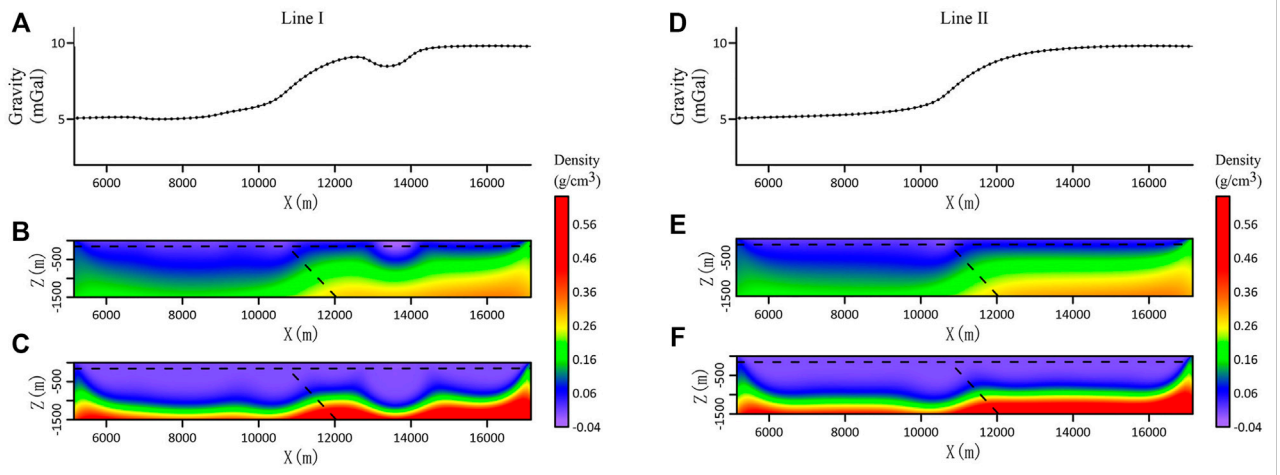

FIGURE 7
Gravity curves and inversion results profiles of lines I and II. **(A)** Gravity anomaly curve of line I. **(B)** Slice the inversion result of line I without focusing constraint. **(C)** Slicing of line I focusing inversion results. **(D)** Gravity anomaly curve of line II. **(E)** Slice the inversion result of line II without focusing constraint. **(F)** Slicing of II line focusing inversion results.

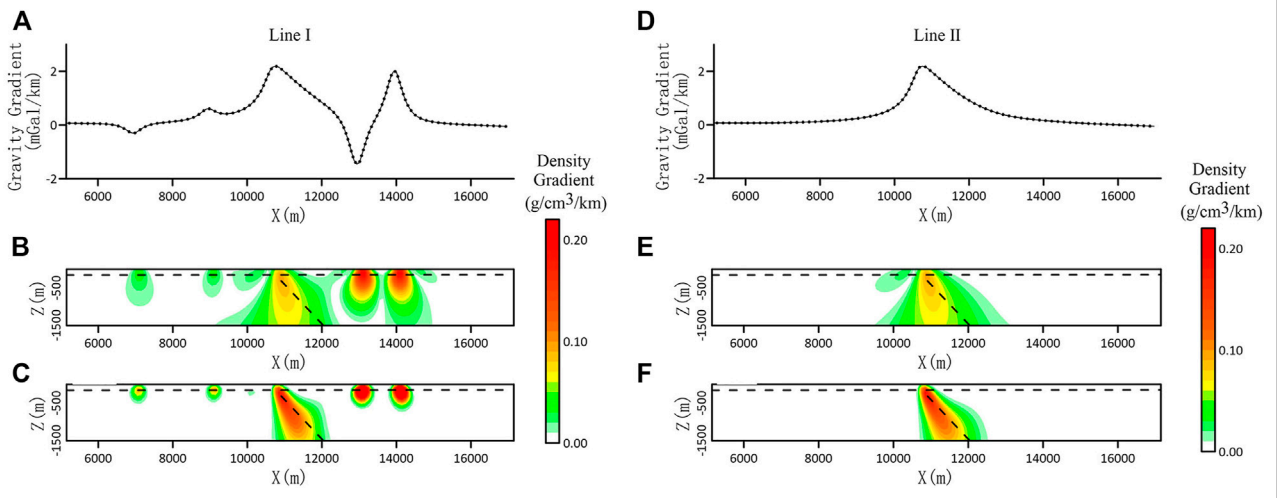

FIGURE 8
Horizontal gradient curve of gravity in the x-direction and inversion result in the profile of the density gradient on line I. **(A)** Horizontal gravity gradient anomaly curve of line I. **(B)** Slice the inversion result of line I without focusing constraint. **(C)** Slicing of line I focusing inversion results. **(D)** Horizontal gravity gradient anomaly curve of line II. **(E)** Slice the inversion result of line II without focusing constraint. **(F)** Slicing of line II focusing inversion results.

one layered model. After transformation, only one inclined plate remains in the transformed density horizontal gradient model, and the position of the inclined plate is the key feature to identify the fracture model. The horizontal gradient model of the density model can highlight the boundary features of the density model, and this is the significant theoretical foundation of the 3D density gradient inversion.

Gravity density gradient inversion

In line with the forward-thinking of Eq. 5, the objective function $\rho_{\varphi}(\alpha)$ of Tikhonov regularization is constructed (Tikhonov and Arsenin, 1977).

$$\rho_{\varphi}(\alpha) = \left\{ \left\| \mathbf{D}\left(\mathbf{d}_{\varphi} - \mathbf{G}\boldsymbol{\rho}_{\varphi}\right) \right\|_2^2 + \alpha \left\| \mathbf{W}\left(\boldsymbol{\rho}_{\varphi} - \boldsymbol{\rho}_{\varphi 0}\right) \right\|_2^2 \right\}, \quad (6)$$

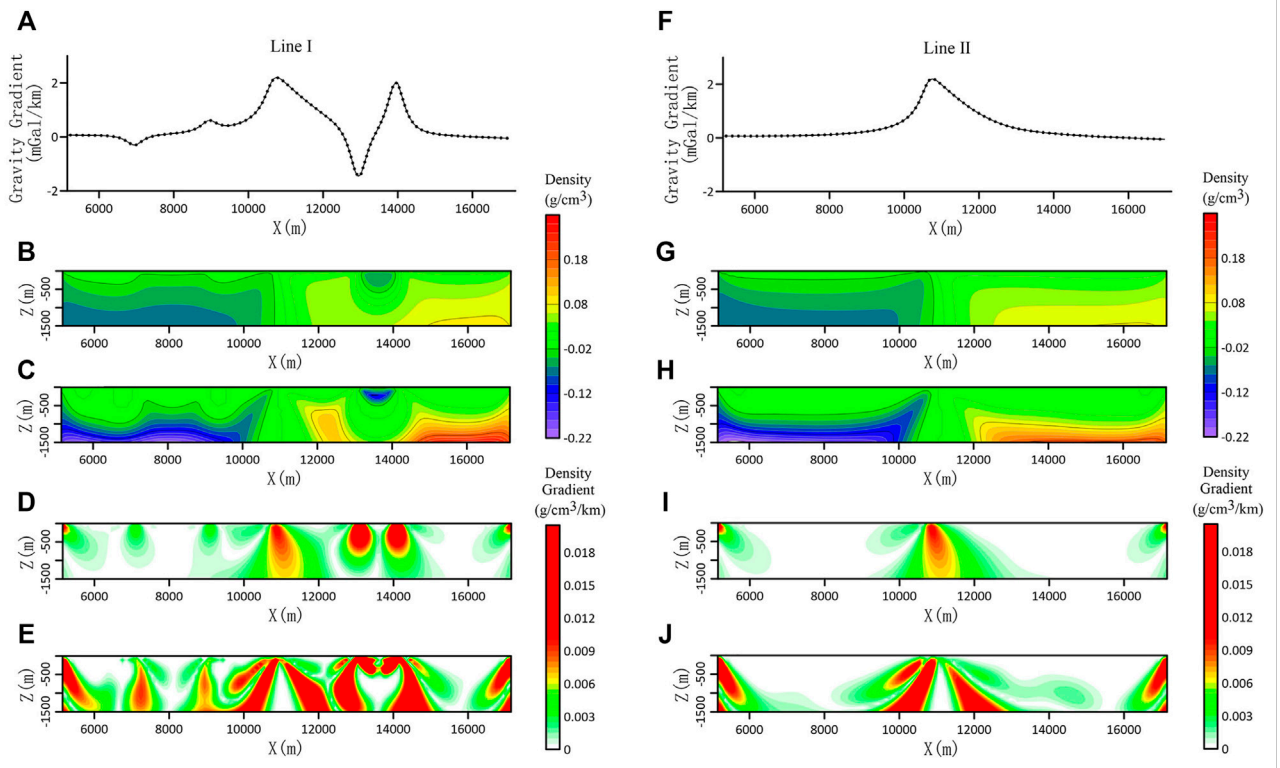

FIGURE 9
Horizontal gravity gradient curve and gradient inversion result profile in the x-direction of lines I and II. **(A)** Horizontal gradient anomaly curve of gravity in the x-direction on line I. **(B)** Slice the inversion result of line I without focusing constraint. **(C)** Slice of line I focusing inversion results. **(D) (E)** Horizontal derivative in the x-direction of Figures b and c. **(F)** Horizontal gradient anomaly curve of gravity in the x-direction on line II. **(G)** Slice the inversion result of line II without focusing constraint. **(H)** Slice of II line focusing inversion results. **(I) (J)** Horizontal derivative in the x-direction of images **(G)** and **(H)**.

where $\rho_\varphi(\alpha)$ is the expected density model and α is the regularization factor. $\|\mathbf{D}(\mathbf{d}_\varphi - \mathbf{G}\boldsymbol{\rho}_\varphi)\|_2^2$ is the objective function of the fitting difference of gravity transformation data, and the matrix $\mathbf{G}$ is the sensitivity matrix (dimension is $N \times M$), and the elements in the matrix $\mathbf{G}$ corresponds to those in the matrix $\tilde{\mathbf{G}}$ (dimension is $(2m-1) \times (2n-1) \times p$) (Yao et al., 2003). $\|\mathbf{W}(\boldsymbol{\rho}_\varphi - \boldsymbol{\rho}_{\varphi 0})\|_2^2$ is the objective function of Tikhonov regularization, $\mathbf{D}$ is the diagonal data covariance $N \times N$ matrix (dimension is $N \times N$), and the elements on the diagonal line are the estimated data noise variance. $\boldsymbol{\rho}_{\varphi 0}$ is the reference model and $\mathbf{W}$ is the model weighting matrix (dimension is $M \times M$), including the depth weighting matrix and focusing weighting matrix.

Inversion calculation is used to find the minimum solution of the objective function equation (Equation 6). The gradient at the minimum of the objective function must be 0, and the fixed-point iterative equation of the model $\boldsymbol{\rho}_\varphi$ in the model space is obtained (Li et al., 2018).

$$\boldsymbol{\rho}_\varphi = \boldsymbol{\rho}_{\varphi 0} + \left(\mathbf{G}^{\mathrm{T}}\mathbf{D}^{\mathrm{T}}\mathbf{D}\mathbf{G} + \alpha\mathbf{W}^{\mathrm{T}}\mathbf{W}\right)^{-1}\mathbf{G}^{\mathrm{T}}\mathbf{D}^{\mathrm{T}}\mathbf{D}\left(\mathbf{d}_\varphi - \mathbf{G}\boldsymbol{\rho}_{\varphi 0}\right). \quad (7)$$

The density gradient inversion results are obtained using the iterative Eq. 7 inversion calculation. Due to that, the kernel function of this inversion method remains unchanged, only the observation quantity is changed, and the inversion algorithm is consistent with the conventional inversion algorithm. Eq. 7 can also apply an optimization algorithm of 3D gravity inversion for fast inversion calculation of massive data (Jing et al., 2019). It should be noted that the setting of depth weighting function parameters in inversion calculation refers to the values in gravity gradient inversion calculation (Commer, 2011; Qin and Huang, 2016), instead of the values in gravity inversion calculation, and the reference model matrix $\boldsymbol{\rho}_{\varphi 0}$ is set to matrix zero.

Calculation process:

(1) Preparing the gravity horizontal gradient data. The gravity data are obtained by the transformation of the 3D equivalent source.
(2) Performing the inversion results of the density gradient in two horizontal gradient directions and obtaining the

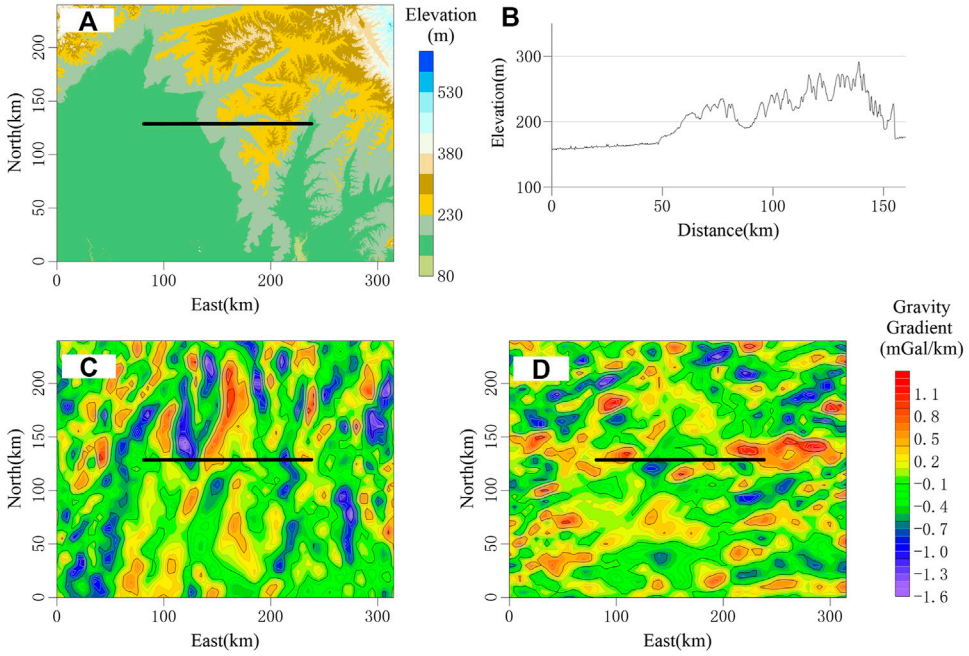

FIGURE 10
Anomaly map of horizontal gravity gradient in the study area. **(A)** Topographic map of the study area (https://lpdaac.usgs.gov/product_search/?collections=Terra+ASTER&status=Operational&view=list). **(B)** Topographic data curve at seismic line. **(C)** Horizontal gravity gradient in the east–west direction. **(D)** Horizontal gravity gradient in the north–south direction.

inversion results of focusing density gradient according to Eq. 7.

(3) Combining the inversion results of the two horizontal gradient models to obtain the final density gradient inversion result.

Model test

The fault zone is a significant geological feature, and the two models, namely, normal fault and reverse fault, are designed to check the effect of the 3D density gradient algorithm on boundary recognition of the fault zone.

Normal fault model test

The normal fault model (Figure 3A) is made up of a north–south strike fault zone (the bottom position of the fault is indicated by dotted lines) and two small anomaly bodies, which have high density in the footwall and low density in the hanging wall. Figures 3B,C show model sections corresponding to lines I and II in Figure 3A, respectively. The underground space is divided into 201 × 121 × 15 prism units of 100 m × 100 m × 100 m. The ground observation data are located in the center of the prism plane, and the data area is the position of the dashed box, totaling 101 × 121 observation data. The gravity forward field (Figure 3D) and the gravity x-direction horizontal gradient forward field (Figure 3E) of the model are taken as the basic fields.

The 3D gravity inversion and 3D density gradient inversion of the horizontal gravity gradient in the x-direction are applied in model experiments as well as further focused inversion tests. To facilitate comparison, the inversion results of the 3D density gradient in the model test are represented in absolute values.

The observation data for 3D gravity inversion have the same trend on lines I and II (Figures 4A,D). The anomaly features of gravity data are high in the west and low in the east, in which line I crosses local anomaly bodies, and there are local anomalies in the curve. For the results of unfocused inversion (Figures 4,E), it can be seen that there are longitudinal cascade zones in both sections, and the dip of cascade zones is consistent with the dip of faults (black dotted lines), and the sections of line I show local anomaly bodies to some extent. For the results of focused inversion (Figures 4C,E), it can be seen that the vertical cascade belt in the inversion slice moves down as a whole and becomes relatively gentle, and the recognition of a fault dip becomes blurred.

The experimental results show that for the normal fault model, the 3D gravity inversion results are in agreement with the fault dip feature of the theoretical model. However, the focused inversion reduces the coincidence.

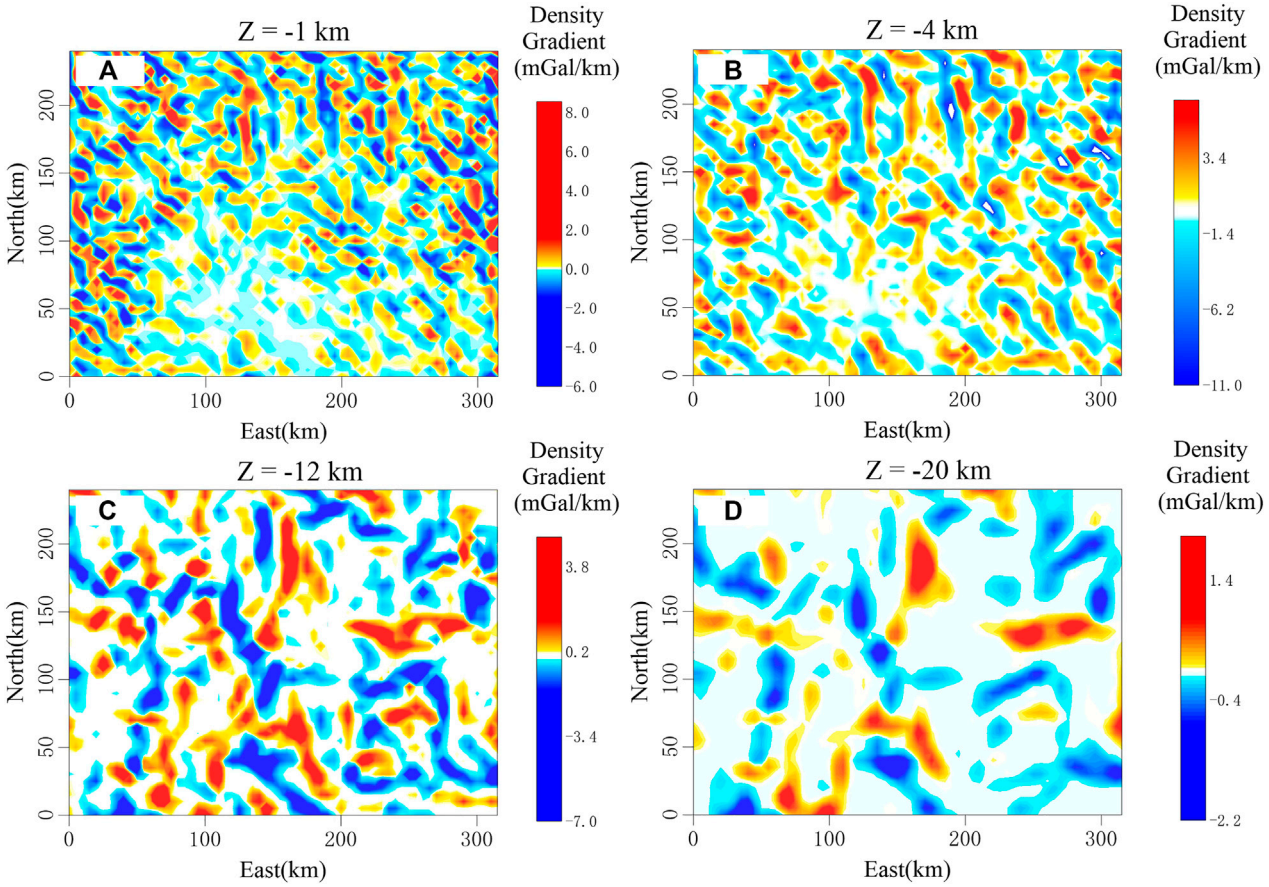

FIGURE 11
Horizontal slices of 3D focusing density gradient inversion results for different vertical depths.

The horizontal gradient data of the gravity x-direction for the density gradient inversion have differences in the features of lines I and II (Figures 5A,D). The features of line II data are simple, and its extreme value points correspond well to the fault position, so the horizontal position of a fault can be directly determined. The extreme value points of line I data correspond well to the boundary of the local anomaly body and the position of the fault. However, the amplitude of each extreme value point is close to each other. It is difficult to distinguish the fault zone or the boundary of the local anomaly body directly based on the extreme value points according to the features of the curve. From the results of unfocused inversion (Figures 5B,E), it can be seen that the horizontal position of the fault and the boundary position of the local anomaly are displayed in the section of line I. Although there is a certain indication of a fault dip, the features are not obvious. Section II shows that the horizontal position of the fault is relatively clear, but it does not show the features of the fault dip. From the results of focusing inversion (Figures 5C,F), it can be seen that the profiles of line I and line II clearly depict the fault features, which not only show the horizontal position of the fault but also the fault dip feature, and are close to the fault dip angle of the theoretical model. The boundary of the local anomaly body is clearly depicted by the section of line I.

The model test results show that for the normal fault model, it is difficult to determine the dip feature of faults clearly from 3D density gradient inversion based on the x-direction, and the focus inversion based on the x-direction can enhance the dip features of faults and accurately depict the spatial distribution features of faults, which means that the focus inversion based on the x-direction can directly determine the dip of faults.

Reverse fault model test

The reverse fault model (Figure 6) is also composed of a north–south strike fault zone and two small anomaly bodies, which have a low density in the footwall and high density in the

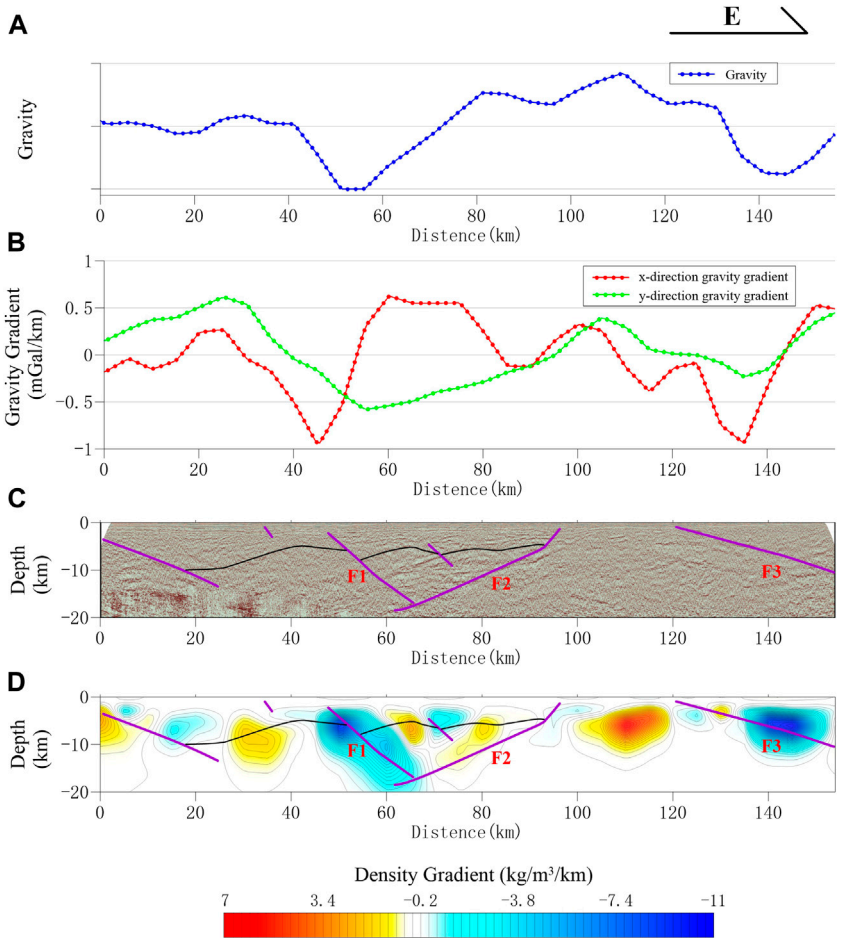

FIGURE 12
Comprehensive interpretation section. **(A)** Profile gravity anomaly curve. **(B)** Profile gravity horizontal gradient anomaly curve. **(C)** Seismic profiles and fault interpretation maps. **(D)** Inversion result slice and interpretation comparison chart.

hanging wall. Other parameters are consistent with normal fault model tests. The 3D gravity inversion and horizontal density gradient inversion in the x-direction are designed, as well as the further focused inversion tests.

The gravity inversion data have a similar trend on lines I and II (Figures 7A,D), and the anomaly features of gravity data are low in the west and high in the east, where line I crosses local anomaly bodies. In addition, there are local anomalies in the curve. From the results of unfocused inversion (Figures 7B,E), it can be seen that there are longitudinal cascade zones in both section slices, but the dip of cascade zones is opposite to that of faults (black dotted lines). The section of line I shows the local anomaly body on the east side of the fault to some extent. As for the results of focused inversions (Figures 7C,E), it can be seen that the longitudinal cascade zones in the inversion slices move down as a whole and become relatively gentle, the recognition of fault dip becomes blurred, and the dip feature also indicates reverse direction.

The experimental results show that for the reverse fault model, the 3D gravity inversion and focusing inversion cannot correctly identify the fault dip feature.

The x-direction horizontal gradient data for the density gradient inversion (Figures 8A,D) are consistent with those of the normal fault model, and the main difference is positive and negative symmetries (Figures 5A,D). For the results of unfocused inversion (Figures 8B,E), the section slices of lines I and II indicate the fracture dip to some extent, but the features are not obvious. The boundary of the local anomaly body in the eastern part of the fault can be displayed by the section of line I, but the boundary of the local anomaly body in the western part is weaker. For the results of focusing on inversion (Figures 8D,F), the sections of lines I and II show fracture features, and their dip angles are very close to those of the theoretical model. The section of line I depicts the boundary of the local anomaly body clearly, and it shows the boundary position of the local anomaly body in the east and west of the fault.

To compare with the conventional gravity inversion results, the horizontal gradient inversion calculation in the x-direction is established, and the horizontal derivative in the x-direction is obtained from the inversion density results (Figure 9). When there is no focusing constraint, it can be seen that the section slices of lines I and II (Figures 9B,G) have no indication features for the dip of the fault, and the section slices of line I have a display for the position of the local anomaly body on the east side of the fault, and weak display for that on the west. When the focus constraint is added (Figures 9C,H), the inversion results show that the cascade zone features of the section slices of lines I and II at the fault are ambiguous. The anomaly becomes wide and flat, and it is difficult to identify the transverse position of the fault. However, the position of the local anomaly on the east side of the fault is enhanced, and the local anomaly on the west side of the fault is also enhanced to a certain extent.

The horizontal derivative in the x-direction is obtained from the aforementioned inversion results. Compared with the results of gravity horizontal gradient density gradient inversion (without focusing constraint) (Figures 8B,E), the horizontal gradient results of unfocused inversion (Figures 9D,I) have a slight advantage in depicting faults and abnormal bodies. Compared with the results of gravity horizontal gradient density gradient inversion (focusing constraint) (Figures 8C,F), the horizontal gradient results from focusing constraint inversion (Figures 9E,J) are not only difficult to identify the features of faults and anomaly bodies but also show messy false anomalies. As a result, the experiments indicate that it is difficult to identify the dip features of faults by the gravity horizontal gradient inversion.

The experimental results show that for the reverse fault model, the horizontal position of the fault can be identified by 3D inversion based on the x-direction gravity gradient data, but it is difficult to accurately identify a fault dip feature. The focus inversion of the 3D density gradient based on the x-direction gravity gradient data can enhance the dip features of faults and depict the spatial distribution features of faults.

Application of measured data

The study area is located in the north-central part of the Songliao Basin in China, which is an important oil production base. The research goal was to study the fault structure in this area. This is significant to the study of sedimentation, deformation, hydrocarbon generation, and reservoir formation of basin caprocks on accurately identifying the spatial distribution features of fault structures. The gravity survey work in this study area is relatively up-to-date, and the whole area is covered by medium-scale gravity data. Moreover, the surface is mainly covered by Quaternary deposits, and the terrain is flat; therefore, the gravity anomaly caused by topographic relief can be ignored as shown in Figures 10A,B.

Figures 10C,D show the gravity horizontal gradient anomaly in the study area, calculated by the method of 3D equivalent source according to the gravity anomaly data. The structure of the study area is mainly in the north–south direction, and there is evidence that there should be fault zones from the seismic section data, which is a survey line passing through gradient zones at a large angle as shown by the black line in the figure. Figure 11 shows the inversion results of two gradient directions calculated by the method, and the inversion results of the density gradient in the study area are obtained by adding and combining. The results show that the fault development degree in this area is relatively high. The shallow results (Figure 11A) show that the NW-trending fault structure is dominant, middle-shallow results (Figure 11B) show that the NS-trending fault structure is based on the NW-trending fault structure, and middle-deep results (Figure 11C) and deep results (Figure 11D) show that the NNE and NNW-trending faults are dominant, and some EW-trending faults occur.

Comparing the interpretation results of the seismic profiles (Figure 12C), gravity anomaly curves (Figure 12A), and gravity horizontal gradient curves (Figure 12B), it can be seen that although the three faults (F1, F2, and F3) have different corresponding relations with the cascade zones or extreme value points in each curve, it is difficult to directly ascertain the dip feature of faults according to these features.

Comparing the interpretation results of the inversion section (Figure 12D) and the seismic section (Figure 12C), it can be seen that there is a good corresponding relationship between them: the dip angle of the F3 fault in the seismic section is relatively small, and its spatial position corresponds to the positive and negative anomaly areas in the deep part of the inversion result slice, so it is impossible to judge the dip feature of the fault in the inversion slice. The F2 fault corresponds to the positive anomaly area in the inversion result slice to some extent. Although there is some disposition in the spatial position, the dip features indicated by the F2 fault are similar, and they all dip westward. The position and dip feature of the F1 fault correspond well to the negative anomaly area in the inversion result slice, that is, the F1 fault can be inferred directly from the inversion slice.

The experimental results show that the inversion results of the gravity 3D density gradient can not only identify the transverse distribution features of faults but also identify the vertical features of faults, that is, the dip features of faults. The positions with clear anomaly features in the inversion results have a high degree of coincidence with the results of seismic profile interpretation, showing that this method can identify faults with high reliability. The gravity inversion results based on this method can make up for the

shortage of sparse distribution and poor lateral resolution of existing seismic data.

Conclusion

A gravity anomaly inversion method for direct inversion of the density gradient is proposed. The method has the following features:

(1) The parameter of the traditional gravity inversion model is the density attribute, and the parameter of the inversion model is the density gradient attribute. The density gradient model has a more direct correspondence with the density boundary compared with the density model.
(2) The inversion iteration equation and calculation process of this method are almost identical to the conventional gravity inversion method, and all kinds of constraint weighting functions are retained. The main difference is that gravity data are converted into gravity horizontal gradient data, so the cost of programming calculation of this method is minimal, and it is convenient to popularize and apply.
(3) The method adopts a fast algorithm, which can carry out fast inversion calculation of massive gravity data, and the inversion results are relatively stable; hence, this method is expected to become one of the basic methods of gravity processing and interpretation.
(4) The method in this study can only identify the faults with a certain scale, and the inversion results can only show the tendency of the faults. It cannot accurately or quantitatively identify the inclination of the faults.

This method has been successfully applied to fault identification in the northern-central part of the Songliao Basin. The inversion results not only show the different variation features of a fault strike at different depths but also can be directly applied to the identification of fault dip features.

Notably, this study only considers the inversion of the density gradient in two horizontal directions and can discuss the research of the vertical gradient, high-order gradient, and different gradient combinations.

Data availability statement

Requests to access these datasets should be directed to LJ. lebesgue@126.com

Author contributions

LJ: overall responsible for the method research and numerical simulation of the manuscript. YY: project management. CY: method instruction. LQ: document editing and language polishing. DC: seismic data source. MX: data arrangement.

Funding

This study is financially supported by the National Key R&D Program of China [grant numbers: 2018YFE0208300]. China Geological Survey Project [DD20221639-03; DD20221638; DD20190030]. Engineering innovation and promotion of fine detection technology in deep Geophysical and Chemical exploration.

Acknowledgments

In particular, the authors would like to thank the reviewers and the editor-in-chief for their valuable amendments and suggestions.

Conflict of interest

The authors declare that the research was conducted in the absence of any commercial or financial relationships that could be construed as a potential conflict of interest.

Publisher's note

All claims expressed in this article are solely those of the authors and do not necessarily represent those of their affiliated organizations, or those of the publisher, the editors, and the reviewers. Any product that may be evaluated in this article, or claim that may be made by its manufacturer, is not guaranteed or endorsed by the publisher.

References

Bosch, M., Meza, R., Jiménez, R., and Hönig, A. (2006). Joint gravity and magnetic inversion in 3D using Monte Carlo methods. *Geophys.* 71 (4), G153–G156. doi:10.1190/1.2209952

Boulanger, O., and Chouteau, M. (2010). Constraints in 3D gravity inversion. *Geophys. Prospect.* 49 (2), 265–280. doi:10.1046/j.1365-2478.2001.00254.x

Camacho, A. G., Montesinos, F. G., and Vieira, R. (2000). Gravity inversion by means of growing bodies[J]. *Geophys.* 318 (65), 655–664. doi:10.1190/1.1444729

Colombo, D., and Rovetta, D. (2018). Coupling strategies in multiparameter geophysical joint inversion. *Geophys. J. Int.* 215, 1171–1184. doi:10.1093/gji/ggy341

Commer, M. (2011). Three-dimensional gravity modelling and focusing inversion using rectangular meshes[J]. *Geophys. Prospect.* 59 (5), 966–979. doi:10.1111/j.1365-2478.2011.00969.x

Fregoso, E., and Gallardo, L. A. (2009). Cross-gradients joint 3d inversion with applications to gravity and magnetic data[J]. *Geophysics* 74 (4), L31–L42. doi:10.1190/1.3119263

Gallardo, L. A., and Meju, M. A. (2003). Characterization of heterogeneous near-surface materials by joint 2d inversion of dc resistivity and seismic data. *Geophys. Res. Lett.* 30, 1658. doi:10.1029/2003gl017370

Gao, X.-H., and Huang, D. N. (2017). Research on 3D focusing inversion of gravity gradient tensor data based on a conjugate gradient algorithm. *Chinese J. Geophys.* 60 (4), 1571–1583. doi:10.6038/cjg20170429

Geng, M., Huang, D., Yang, Q., and Liu, Y. (2014). 3D inversion of airborne gravity-gradiometry data using cokriging. *Geophysics* 79, G37–G47. doi:10.1190/geo2013-0393.1

Geng, M., Welford, J. K., Farquharson, C. G., and Hu, X. (2019a). Gravity modeling for crustal-scale models of rifted continental margins using a constrained 3D inversion method. *Geophysics* 84, G25–G39. doi:10.1190/geo2018-0134.1

Geng, M., Welford, J. K., Farquharson, C. G., and Peace, A. L. (2019b). 3D inversion of airborne gravity gradiometry data for the budgell harbour stock, newfoundland: A case history using a probabilistic approach. *Geophysics* 84, B269–B284. doi:10.1190/geo2018-0407.1

Grauch, V. J. S., and Cordell, L. (1987). Limitations of determining density or magnetic boundaries from the horizontal gradient of gravity or pseudogravity data. *Geophysics* 52 (1), 118. doi:10.1190/1.1442236

Gross, l. (2019). Weighted cross-gradient function for joint inversion with the application to regional 3-d gravity and magnetic anomalies. *Geophys. J. Int.* 217, 2035–2046. doi:10.1093/gji/ggz134

Holden, D. J., Archibald, N. J., Boschetti, F., and Jessell, M. W. (2000). Inferring geological structures using wavelet-based multiscale edge analysis and forward models. *Explor. Geophys.* 31 (4), 617–621. doi:10.1071/eg00617

Hood, P. J., and Teskey, D. J. (1989). Aeromagnetic gradiometer program of the geological survey of Canada. *Geophysics* 54 (8), 1012. doi:10.1190/1.1442726

Hood, P., and Mcclure, D. J. (1965). Gradient measurements in ground magnetic prospecting [J]. *Geophysics* 30 (3), 403. doi:10.1190/1.1439592

Hornby, P., Boschetti, F., and Horowitz, F. (1999). Analysis of potential field data in the wavelet domain. *Geophys. J. Int.* 137, 175–196. doi:10.1046/j.1365-246x.1999.00788.x

Jing, L., Yao, C.-L., Yang, Y.-B., Xu, M. L., Zhang, G. Z., and Ji, R. Y. (2019). Optimization algorithm for rapid 3d gravity inversion[J]. *Appl. Geophys.* 16 (4), 507–518. doi:10.1007/s11770-019-0781-2

Last, B. J., and Kubik, K. (1983). Compact gravity inversion[J]. *Geophys.* 48 (48), 713. doi:10.1190/1.1441501

Li, X. (2006). Understanding 3d analytic signal amplitude [J]. *Geophysics* 71 (2), l13–l16. doi:10.1190/1.2184367

Li, Y., and Oldenburg, D. W. (1996). 3-D inversion of magnetic data. *Geophys.* 61 (2), 394–408. doi:10.1190/1.1443968

Li, Y., and Oldenburg, D. W. (1998). 3-D inversion of gravity data. *Geophys.* , 63 (1), 109–119. doi:10.1190/1.1444302

Li, Y., Oldenburg, D. W., Wei, C., Wang, H., Sui, N., and Kirouac, G. J. (2010). Orexins in the paraventricular nucleus of the thalamus mediate anxiety-like responses in rats. *Psychopharmacology* 152 (2), 251–265. doi:10.1007/s00213-010-1948-y

Li, Z. L., Yao, C. L., and Zheng, Y.-M. (2018). Joint inversion of surface and borehole magnetic amplitude data. *Chin. J. Geophys. (in Chinese)* 61 (12), 4942–4953. doi:10.6038/cjg2018l0618

Liu, J., Zhang, J., Jiang, L., Lin, Q., and Wan, L. (2019). Polynomial-based density inversion of gravity anomalies for concealed iron-deposit exploration in North China. *Geophysics* 84 (5), b325–b334. doi:10.1190/geo2018-0740.1

Liu, J., and Zhang, J.-Z. (2022). Structure-guided gravity inversion for layered density modeling with an application in the Chezhen Depression, Bohai Bay Basin. *Geophysics* 87 (1), B45–B56. doi:10.1190/geo2021-0213.1

Liu, Y. P., Wang, Z. W., Du, X. J., Liu, Q. H., and Xu, J. S. (2013). 3D constrained inversion of gravity data based on Extrapolation Tikhonov regularization algorithm. *Chinese J. Geophys. (in Chinese)* 56 (5), 1650–1659. doi:10.6038/cjp20130522

Miller, H. G., and Singh, V. (1994). Potential field tilt—A new concept for location of potential field sources. *Journal of applied geophysics* 32 (2-3), 213. doi:10.1016/0926-9851(94)90022-1

Molodtsov, D., Colombo, D., Roslov, Y. V., Troyan, V. N., and Kashtan, B. M. (2015). Comparison of structural constraints for seismic-MT joint inversion in a subsalt imaging problem. *saint petersburg state university bulletin* 2 (3), 230–236.

Nabighian, M. N. (1972). The analytic signal of two-dimensional magnetic bodies with polygonal cross-section: Its properties and use for automated anomaly interpretation. *Geophysics* 37 (3), 507. doi:10.1190/1.1440276

Nabighian, M. N. (1984). Toward a three-dimensional automatic interpretation of potential field data via generalized Hilbert transforms: Fundamental relations. *Geophysics* 49 (6), 780. doi:10.1190/1.1441706

Portniaguine, O., and Zhdanov, M. S. (1999). Focusing geophysical inversion images. *Geophys.*, 64, 874–887. doi:10.1190/1.1444596

Qin, P.-B., and Huang, D.-N. (2016). Integrated gravity and gravity gradient data focusing inversion[J]. *Chinese journal of geophysics (in Chinese)* 59 (6), 2203–2224. doi:10.6038/cjg20160624

Shamsipour, P., Marcotte, D., Chouteau, M., and Keating, P. (2010). 3D stochastic inversion of gravity data using cokriging and cosimulation. *Geophysics* 75, I1–I10. doi:10.1190/1.3295745

Tikhonov, A. N., and Arsenin, V. V. (1977). Solutions of Ill Posed Problems. Washington DC: V. H. Winston & Sons. doi:10.1190/1.3295745

Wang, X., and Li, T.-L. (2004). Locating the boundaries of magnetic or gravity sources with Tdr and Tdr -Thdr methods[J]. *Progress in geophysics* 19 (3), 625–630.

Wang, Y. C., Liu, L.-T., and Xu, H.-Z. (2022). Integrated focusing inversion of gravity and gravity gradients with multi-scale source grids[J]. *Geomatics and information science of Wuhan university* 47 (2), 181–188. doi:10.13203/j.whugis20190263

Wijns, C., Perez, C., and Kowalczyk, P. (2005). Theta map: Edge detection in magnetic data. *Geophysics* 70 (4), L39–L43. doi:10.1190/1.1988184

Yan, J.-Y., Lv, Q.-T., Chen, M.-C., Deng, Z., Qi, G., Zhang, K., et al. (2015). Identification and extraction of geological structure information based on multi-scale edge detection of gravity and magnetic fields: An example of the tongling ore concentration area[J]. *Chinese journal of geophysics (in Chinese)* 58 (12), 4450–4464. doi:10.6038/cjg20151210

Yang, W.-C., Sun, Y.-Y., Hou, Z.-Z., and Yu, C.-Q. (2015). An multi-scale scratch analysis method for quantitative interpretation of regional gravity fields[J]. *Chinese journal of geophysics (in Chinese)* 58 (2), 520–531. doi:10.6038/cjg20150215

Yao, C.-L., Hao, T.-Y., and Guan, Z.-N. (2002). Restrictions in gravity and magnetic inversions and technical strategy of 3d properties inversion. *Geophysical and geochemical exploration* 26 (4), 253–257. doi:10.1007/s11769-002-0042-8

Yao, C.-L., Hao, T.-Y., Guan, Z.-N., and Zhang, Y.-W. (2003). High-speed computation and efficient storage in 3d gravity and magnetic inversion based on genetic algorithms[J]. *Chinese journal of geophysics (in Chinese)* 46 (2), 252–258. doi:10.1002/cjg2.351

Yao, C.-L., Zheng, Y.-M., and Zhang, Y.-W. (2007). 3-d gravity and magnetic inversion for physical properties using stochastic subspaces[J]. *Chinese journal of geophysics (in Chinese)* 50 (5), 1576–1583.

Zhdanov, M. S. (2009). New advances in regularized inversion of gravity and electromagnetic data. *Geophys. Prospect.* 57 (4), 463–478. doi:10.1111/j.1365-2478.2008.00763.x

frontiers | Frontiers in Earth Science

TYPE Original Research
PUBLISHED 26 September 2022
DOI 10.3389/feart.2022.961750

OPEN ACCESS

EDITED BY
Jianzhong Zhang,
Ocean University of China, China

REVIEWED BY
Zedong Wu,
General Company of Geophysics, United Kingdom
Peng Song,
Ocean University of China, China

*CORRESPONDENCE
Jie Xu,
3416899030@qq.com
Jianping Huang,
jphuang@upc.edu.cn

SPECIALTY SECTION
This article was submitted to Solid Earth Geophysics, a section of the journal Frontiers in Earth Science

RECEIVED 05 June 2022
ACCEPTED 25 July 2022
PUBLISHED 26 September 2022

CITATION
Yang J, Xu J, Huang J, Yu Y and Sun J (2022), The connection of velocity and impedance sensitivity kernels with scattering-angle filtering and its application in full waveform inversion. *Front. Earth Sci.* 10:961750. doi: 10.3389/feart.2022.961750

The connection of velocity and impedance sensitivity kernels with scattering-angle filtering and its application in full waveform inversion

Jidong Yang, Jie Xu*, Jianping Huang*, Youcai Yu and Jiaxing Sun

Department of Geophysics, China University of Petroleum (East China), Qingdao, China

Multi-scale strategies such as starting from the low-frequency and early-arrival part of recorded data are commonly used in full waveform inversion (FWI) to maneuver complex nonlinearity. An alternative way is to apply appropriate filtering and conditioning to the misfit gradient in the model domain. In acoustic constant-density media, we prove that velocity and impedance sensitivity kernels are equivalent to applying a high-pass and a low-pass scattering-angle filter to a conventional single-parameter velocity (CSV) kernel. The high-pass scattering-angle filter allows the velocity kernel to include low-wavenumber updates (tomography component). In contrast, the low-pass scattering-angle filter helps the impedance kernel to yield high-wavenumber updates (migration component). The velocity model can be updated using a hybrid gradient of two components combined with appropriate weights. This FWI scheme is able to overcome the potential nonlinearity and partially mitigate the cycle-skipping problem. Numerical examples for the SEG/EAGE overthrust model and the Marmousi model demonstrate that the hybrid gradient facilitates FWI to converge faster to the true model even in cases when conventional CSV-based FWI fails.

KEYWORDS

full waveform inversion, sensitivity kernels, scattering-angle filtering, hybrid gradient, migration component, tomography component

1 Introduction

Full waveform inversion (FWI) aims to estimate subsurface rock parameters by minimizing misfits between observed and synthetic data (Lailly, 1983; Tarantola, 1984; Mora, 1989; Pratt et al., 1998; Pratt, 1999; Pratt and Shipp, 1999). To date, global optimization methods are still expensive in practice due to high computational costs for forward calculations and high dimensionality of model space. Gradient-based local optimization techniques are commonly used to update model parameters (Tromp et al., 2005; Liu and Tromp, 2006; Plessix, 2006). Due to irregular acquisition, limited

offset, ambient noise and lack of low-frequency signals, the nonlinearity of FWI becomes much complicated and the gradient-based solvers are prone to be trapped in the local minima (Brossier et al., 2009; Virieux and Operto, 2009; Sears et al., 2010; Vigh et al., 2010).

Multi-scale strategy is a natural way to reduce the potential nonlinearity through data decimation and selection, which helps FWI to mitigate the cycle-skipping problems (Bunks et al., 1995; Pratt et al., 1996; Virieux and Operto, 2009). One implementation of this strategy is to gradually increase frequency bands to ensure that the phase difference between the predicted and observed data is always less than half a period (Pratt, 1999; Ravaut et al., 2004; Sirgue and Pratt, 2004; Brossier et al., 2009; Fichtner et al., 2013; Xue et al., 2016). The success of this approach requires the existence of effective low-frequency signals in the recorded data, which can be achieved by either acquiring broadband data or utilizing low-frequency enhanced techniques (Xie, 2013; Li and Demanet, 2016; Wang and Herrmann, 2016). Another implementation of multi-scale strategy is to gradually include later arrivals by designing particular windows in the time domain (Shipp and Singh, 2002; Sheng et al., 2006; Brossier et al., 2009; Boonyasiriwat et al., 2010) or introducing proper damping terms in the frequency domain (Shin et al., 2002; Brenders and Pratt, 2007; Shin and Cha, 2008). In addition, layer-stripping and offset-dependent windowing can also be combined with the above two strategies to reduce the nonlinearity and improve the success probability of FWI (Shipp and Singh, 2002; Brossier et al., 2009; Virieux and Operto, 2009).

As analyzed by Wu and Toksöz (1987) and Mora (1989), the resolved wavenumbers of velocity model are determined by scattering patterns in diffraction tomography. Such works provide insights in the model domain instead of the data domain, such as filtering and conditioning the misfit gradient, to reduce the potential nonlinearity in FWI (Albertin et al., 2013; Almomin and Biondi, 2013; Tang et al., 2013; Alkhalifah, 2016). Using the slopes of subsurface structures, Guitton et al. (2012) and Ma et al. (2012) design a directional smoothing operator for the gradients, which can help them to generate smooth velocity models and mitigate the cycle-skipping problem. Tang et al. (2013) notice that the FWI gradient includes tomography and migration components. They propose to enhance the tomography part at early stages in order to recover long-wavelength velocity perturbations. From the standpoint of wavenumber continuation, Alkhalifah (2015) design a scattering-angle filter to extract different wavenumber components and prove that even 10 Hz data can produce vertical near-zero wavenumber components in the FWI gradients. This allows him to update the velocity model from low-to high-wavenumbers by successively relaxing the scattering-angle filter (Wu and Alkhalifah, 2015; Alkhalifah, 2016; Kazei et al., 2016). Wu and Alkhalifah (2017) split the velocity model into background and perturbation components, integrate them directly in the wave equation and introduce a new cheap implementation of scattering angle enrichment, achieving the separation of the background and perturbation components efficiently (Wu and Alkhalifah, 2017).

In this study, we parameterize the acoustic wave equation with velocity and impedance and derive their sensitivity kernels using the Lagrange multiplier method. For a constant-density model, we analytically prove that the velocity and impedance kernels are equivalent to applying a high-pass and a low-pass scattering-angle filter to the conventional single-parameter velocity (CSV) kernel. The high-pass scattering-angle filter allows the velocity kernel to recover low-wavenumber perturbations (tomography component) and can be used to estimate macro velocity models. The low-pass scattering-angle filter helps the impedance kernel to update high-wavenumber perturbations (migration component) and produces high-resolution results. Similar to Tang et al. (2013), we combine these two components into a hybrid gradient (HG) to update the velocity model. By emphasizing the velocity kernel at a few early iterations and then relaxing its weights at later iterations, HG-based FWI provides us with a way to reduce FWI nonlinearity and partially mitigate the cycle-skipping problem. Numerical examples for the SEG/EAGE overthrust and the Marmousi models demonstrate that the proposed method is much more accurate than CSV-based FWI for recovering deep low-wavenumber velocity anomalies.

This paper is organized as follows. First, we derive the velocity and impedance sensitivity kernels using the Lagrange multiplier method. Next, we establish a connection between the velocity and impedance kernels with scattering-angle filtering. Then, we combine these two kernels into a hybrid gradient by properly choosing weights, and apply it to FWI to recover velocity models. Finally, two synthetic examples are used to illustrate the performance of the proposed method.

2 Theory

2.1 Velocity and impedance sensitivity kernels

Using velocity $v(\mathbf{x})$ and impedance $z(\mathbf{x})$ as model parameters, the second-order acoustic wave equation can be written as (Plessix and Li, 2013)

$$\frac{1}{v(\mathbf{x})z(\mathbf{x})}\frac{\partial^2 p(\mathbf{x},t)}{\partial t^2} - \nabla\cdot\left(\frac{v(\mathbf{x})}{z(\mathbf{x})}\nabla p(\mathbf{x},t)\right) = f(\mathbf{x}_s,t), \quad (1)$$

where $\mathbf{x}_s$ and $\mathbf{x}$ are the source and subsurface locations, $f(\mathbf{x}_s, t)$ is the source function, $p(\mathbf{x}, t)$ is the pressure wavefield, which is subject to the initial conditions: $p(\mathbf{x}, 0) = 0$ and $\partial p(\mathbf{x}, t)/\partial t=0$.

To derive the adjoint wave equation and sensitivity kernels, we use the Lagrange multiplier method. The augmented least-squares waveform function can be formulated as (Tromp et al., 2005; Liu and Tromp, 2006; Plessix, 2006)

$$J = \frac{1}{2}\sum_{\mathbf{x}_r}\int_0^T [p(\mathbf{x}_r,t) - d(\mathbf{x}_r,t)]^2 dt - \int_0^T \int_\Omega q(\mathbf{x},t)\left[\frac{1}{v(\mathbf{x})z(\mathbf{x})}\frac{\partial^2 p(\mathbf{x},t)}{\partial t^2} - \nabla\cdot\left(\frac{v(\mathbf{x})}{z(\mathbf{x})}\nabla p(\mathbf{x},t)\right)\right] d\mathbf{x}^3 dt, \tag{2}$$

where $\mathbf{x}_r$ is the receiver location, q ($\mathbf{x}$, t) is the Lagrange multiplier, [0, T] denotes the record duration, Ω is the subsurface volume of interest. Taking the variation of J in Eq. 2 and using integration by parts for the spatial derivatives of p ($\mathbf{x}$, t), we obtain

$$\begin{aligned}\delta J = &\int_0^T \int_\Omega \sum_{\mathbf{x}_r} [p(\mathbf{x}_r,t) - d(\mathbf{x}_r,t)]\delta p(\mathbf{x},t)\delta(\mathbf{x}-\mathbf{x}_r) d\mathbf{x}^3 dt \\ &- \int_0^T \int_\Omega \left\{\delta p(\mathbf{x},t)\left[\frac{1}{v(\mathbf{x})z(\mathbf{x})}\frac{\partial^2 q(\mathbf{x},t)}{\partial t^2} - \nabla\cdot\left(\frac{v(\mathbf{x})}{z(\mathbf{x})}\nabla q(\mathbf{x},t)\right)\right]\right. \\ &-\delta \ln v\left[\frac{1}{z(\mathbf{x})v(\mathbf{x})}\frac{\partial^2 p(\mathbf{x},t)}{\partial t^2}q(\mathbf{x},t) - \frac{v(\mathbf{x})}{z(\mathbf{x})}\nabla p(\mathbf{x},t)\cdot\nabla q(\mathbf{x},t)\right] \\ &\left.-\delta \ln z\left[\frac{1}{z(\mathbf{x})v(\mathbf{x})}\frac{\partial^2 p(\mathbf{x},t)}{\partial t^2}q(\mathbf{x},t) + \frac{v(\mathbf{x})}{z(\mathbf{x})}\nabla p(\mathbf{x},t)\cdot\nabla q(\mathbf{x},t)\right]\right\} d\mathbf{x}^3 dt,\end{aligned} \tag{3}$$

where $\delta(\mathbf{x})$ is the Dirac delta function, δp ($\mathbf{x}$, t) is the perturbed pressure wavefield. $\delta \ln z = \delta z(\mathbf{x})/z_0(\mathbf{x})$, $\delta \ln v = \delta v(\mathbf{x})/v_0(\mathbf{x})$, where $\delta z(\mathbf{x})$ and $z_0(\mathbf{x})$ are the perturbed and background impedances respectively, $\delta v(\mathbf{x})$ and $v_0(\mathbf{x})$ are the perturbed and background velocities. Note that in (Eq. 3), we only consider the first-order expansion for the pressure wavefield and model parameters, which is known as the Born approximation (Tarantola, 2005; Tromp et al., 2005; Plessix, 2006).

Provided the Lagrange multiplier q ($\mathbf{x}$, t) satisfies

$$\frac{1}{v(\mathbf{x})z(\mathbf{x})}\frac{\partial^2 q(\mathbf{x},t)}{\partial t^2} - \nabla\cdot\left(\frac{v(\mathbf{x})}{z(\mathbf{x})}\nabla q(\mathbf{x},t)\right) = \sum_{\mathbf{x}_r}[p(\mathbf{x}_r,t) - d(\mathbf{x}_r,t)]\delta(\mathbf{x}-\mathbf{x}_r) \tag{4}$$

and is subject to the final conditions

$$q(\mathbf{x},T) = 0, \quad \frac{\partial q(\mathbf{x},T)}{\partial t} = 0, \tag{5}$$

(Eq. 3) can be simplified to

$$\begin{aligned}\delta J = -\int_0^T \int_\Omega &\left\{\delta \ln v\left[\frac{1}{z(\mathbf{x})v(\mathbf{x})}\frac{\partial^2 p(\mathbf{x},t)}{\partial t^2}q(\mathbf{x},t) - \frac{v(\mathbf{x})}{z(\mathbf{x})}\nabla p(\mathbf{x},t)\cdot\nabla q(\mathbf{x},t)\right]\right. \\ &\left.+\delta \ln z\left[\frac{1}{z(\mathbf{x})v(\mathbf{x})}\frac{\partial^2 p(\mathbf{x},t)}{\partial t^2}q(\mathbf{x},t) + \frac{v(\mathbf{x})}{z(\mathbf{x})}\nabla p(\mathbf{x},t)\cdot\nabla q(\mathbf{x},t)\right]\right\} d\mathbf{x}^3 dt.\end{aligned} \tag{6}$$

This equation tells us that the change of the misfit δJ may be caused by the changes of the model parameters $\delta \ln z$ and $\delta \ln v$ in terms of the forward wavefield p ($\mathbf{x}$, t) and the Lagrange multiplier wavefield q ($\mathbf{x}$, t). The adjoint wavefield is defined as $p^\dagger(\mathbf{x}, t) = q(\mathbf{x}, T - t)$ and inserted into Eq. 4 to obtain the adjoint wave equation

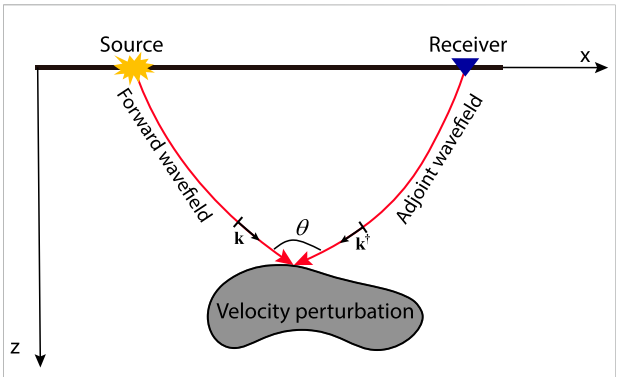

FIGURE 1
Geometry of incident and scattering waves. Red lines are the wave paths of the forward and adjoint wavefields. $\mathbf{k}$ and $\mathbf{k}^\dagger$ denote their propagation directions. (x, z) is the Cartesian coordinate system and θ is the scattering angle.

$$\frac{1}{v(\mathbf{x})z(\mathbf{x})}\frac{\partial^2 p^\dagger(\mathbf{x},t)}{\partial t^2} - \nabla\cdot\left(\frac{v(\mathbf{x})}{z(\mathbf{x})}\nabla p^\dagger(\mathbf{x},t)\right) = \sum_{\mathbf{x}_r}[p(\mathbf{x}_r,T-t) - d(\mathbf{x}_r,T-t)]\delta(\mathbf{x}-\mathbf{x}_r). \tag{7}$$

Then, the variation of the misfit function in (Eq. 6) is reduced to

$$\delta J = -\int_\Omega (\delta \ln v K_v + \delta \ln z K_z) d\mathbf{x}^3. \tag{8}$$

where the velocity (K_v) and impedance (K_z) kernels are defined as

$$\begin{aligned}K_v(\mathbf{x}) &= \int_0^T \left[\frac{1}{z(\mathbf{x})v(\mathbf{x})}\frac{\partial^2 p(\mathbf{x},t)}{\partial t^2}p^\dagger(\mathbf{x},T-t) - \frac{v(\mathbf{x})}{z(\mathbf{x})}\nabla p(\mathbf{x},t)\cdot\nabla p^\dagger(\mathbf{x},T-t)\right] dt, \\ K_z(\mathbf{x}) &= \int_0^T \left[\frac{1}{z(\mathbf{x})v(\mathbf{x})}\frac{\partial^2 p(\mathbf{x},t)}{\partial t^2}p^\dagger(\mathbf{x},T-t) + \frac{v(\mathbf{x})}{z(\mathbf{x})}\nabla p(\mathbf{x},t)\cdot\nabla p^\dagger(\mathbf{x},T-t)\right] dt.\end{aligned} \tag{9}$$

Note that the adjoint wave equation is exactly the same as the forward wave (Eq. 1), except for replacing f ($\mathbf{x}_s$, t) by time-reversed data residual (adjoint source).

For comparison, herein present the CSV kernel (the detailed derivation is given in Appendix A):

$$K_{csv}(\mathbf{x}) = 2\int_0^T \left[\frac{1}{z(\mathbf{x})v(\mathbf{x})}\frac{\partial^2 p(\mathbf{x},t)}{\partial t^2}p^\dagger(\mathbf{x},T-t)\right] dt. \tag{10}$$

(Eqs. 9, 10) show that the CSV kernel equal the summation of the velocity and impedance kernels, indicating that the updates in CSV-based FWI include both velocity and impedance information. Zhou et al. (2015) show that due to the different responses to the scattering angles, the velocity and impedance kernels produce low-wavenumber (tomography) and high-wavenumber (migration) components, respectively (Wu and Toksöz, 1987; Mora, 1989; Alkhalifah, 2015). Therefore,

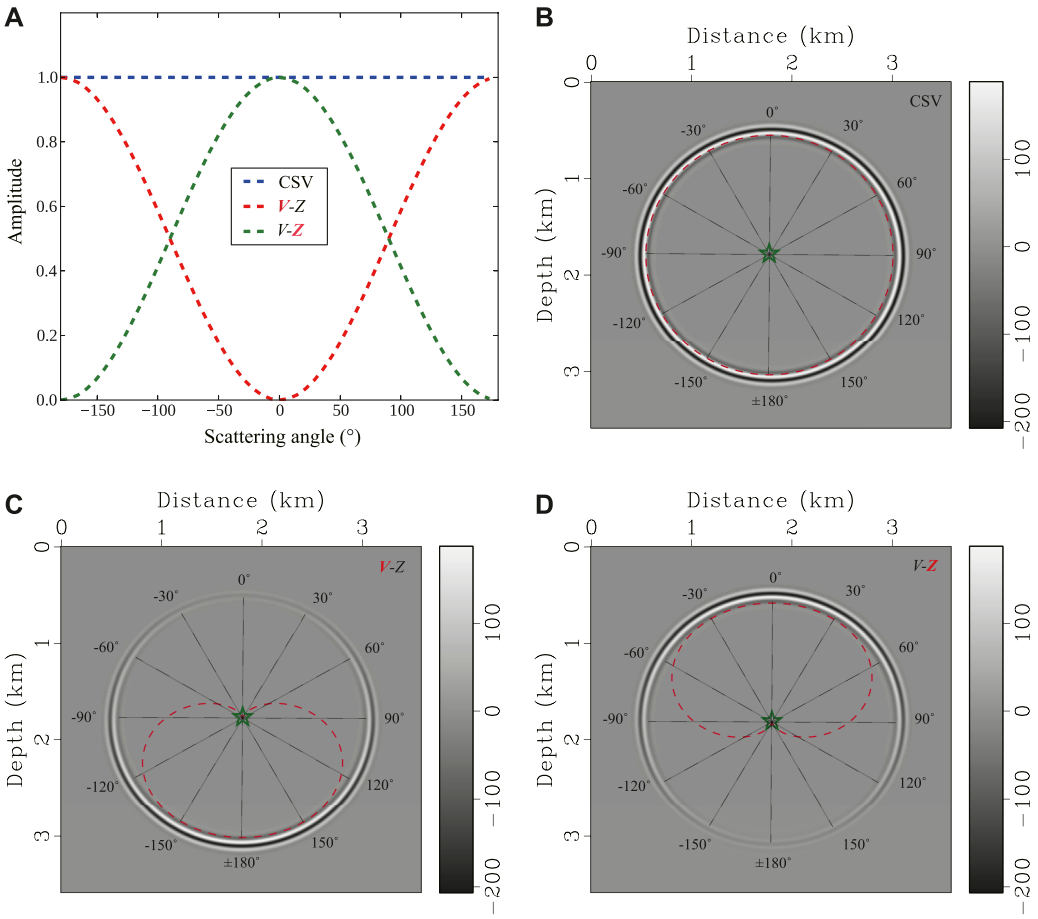

FIGURE 2
Scattering angle filters and radiation patterns for a vertically incident plane wave in a homogenous medium with v =2 km/s **(A)** Angle filters for different kernels; **(B)** CSV radiation pattern; **(C)** velocity and **(D)** impedance radiation patterns. A unit model perturbation indicated by a green star is located at x =2 km and z =2 km. Red dashed lines in **(B)**, **(C)** and **(D)** denote the amplitude variations with respect to different scattering angles.

conventional CSV-based FWI simultaneously update the macro and detail structures in velocity model building, which increases the nonlinearity and is prone to be trapped into local minima. One way to mitigate this problem in the model domain is to use the wavenumber continuation strategy that combines the two separated components with proper weights (Tang et al., 2013; Alkhalifah, 2016).

2.3 Connection between velocity and impedance kernels with scattering-angle filtering in constant-density media

Douma et al. (2010) prove that the impedance kernel in adjoint tomography is equivalent to the application of Laplacian filtering to reverse-time migration (RTM) images. Zhang and Sun (2009) notice that the application of the Laplacian filtering to RTM images is equivalent to the application of a $\cos^2\phi$ filter to angle-domain gathers, where ϕ is the reflection angle. Such conclusions confirm that the impedance-based imaging condition produces fewer low-wavenumber artifacts on RTM images (Zhu et al., 2009; Whitmore and Crawley, 2012; Pestana et al., 2014). In this section, we extend Douma et al. (2010)'s derivation to both velocity and impedance kernels and establish a connection between these kernels with scattering-angle filtering.

Considering the initial and final conditions for the forward and adjoint wavefields

$$p(\mathbf{x},0) = p^{\dagger}(\mathbf{x},T) = 0, \quad p(\mathbf{x},T) = p^{\dagger}(\mathbf{x},0) = 0, \tag{11}$$

and using integration by parts for the time derivatives, we have the following identity

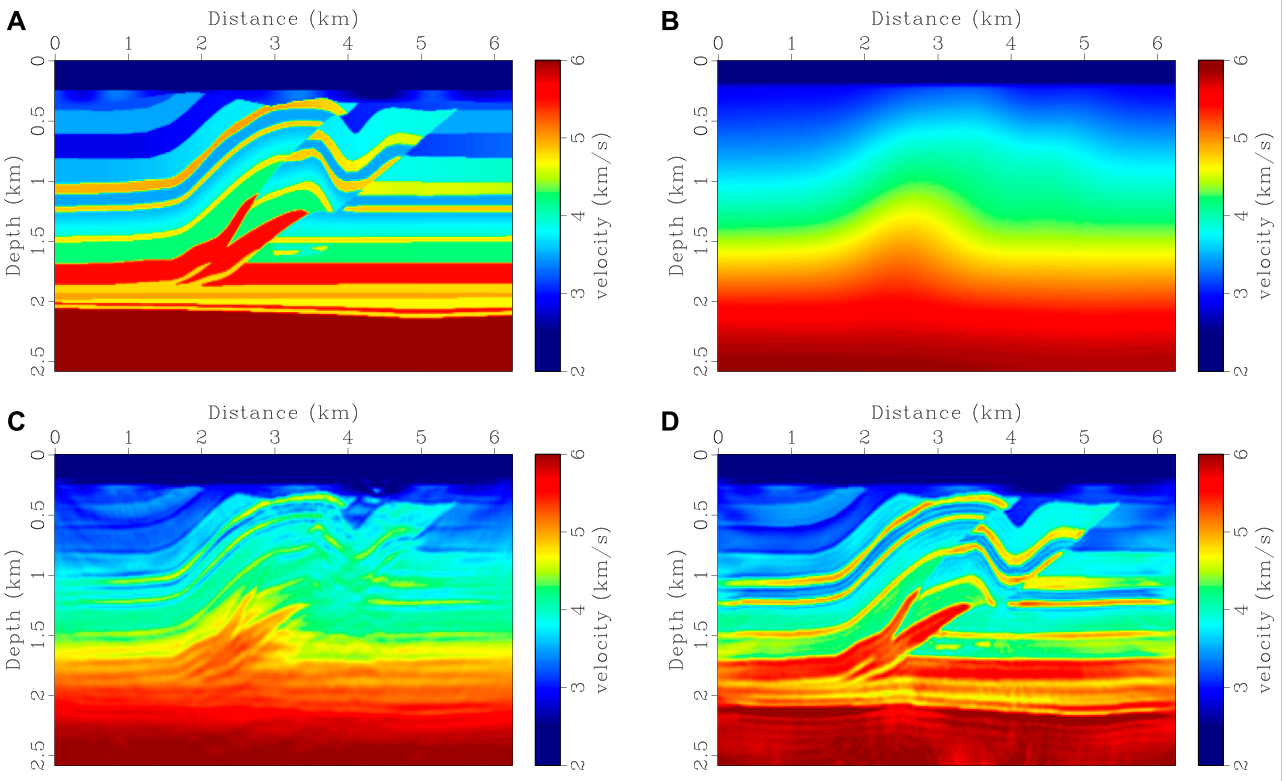

FIGURE 3
FWI experiments for SEG/EAGE overthrust model. **(A)** True velocity model, **(B)** initial velocity model, **(C)** recovered velocity model using CSV-based FWI, and **(D)** recovered velocity model using HG-based FWI. 40 iterations are performed in **(C,D)**. The lowest effective frequency used in **(C,D)** is 5 Hz.

$$\int_0^T \left[\frac{\partial^2 p(\mathbf{x},t)}{\partial t^2} p^\dagger(\mathbf{x},T-t)\right] dt = -\int_0^T \left[\frac{\partial p(\mathbf{x},t)}{\partial t}\frac{dp^\dagger(\mathbf{x},T-t)}{dt}\right] dt = \int_0^T \left[p(\mathbf{x},t)\frac{\partial^2 p^\dagger(\mathbf{x},T-t)}{\partial t^2}\right] dt. \tag{12}$$

This notation simplifies the velocity and impedance kernels in (Eq. 9) to

$$\begin{aligned} K_v(\mathbf{x}) &= \frac{1}{2}\frac{v(\mathbf{x})}{z(\mathbf{x})}\int_0^T \left[\frac{1}{v^2(\mathbf{x})}\frac{\partial^2 p(\mathbf{x},t)}{\partial t^2} p^\dagger(\mathbf{x},T-t)\right. \\ &\quad \left. -2\nabla p(\mathbf{x},t)\cdot\nabla p^\dagger(\mathbf{x},T-t) + \frac{1}{v^2(\mathbf{x})} p(\mathbf{x},t)\frac{\partial^2 p^\dagger(\mathbf{x},T-t)}{\partial^2 t}\right] dt, \\ K_z(\mathbf{x}) &= \frac{1}{2}\frac{v(\mathbf{x})}{z(\mathbf{x})}\int_0^T \left[\frac{1}{v^2(\mathbf{x})}\frac{\partial^2 p(\mathbf{x},t)}{\partial t^2} p^\dagger(\mathbf{x},T-t)\right. \\ &\quad \left. +2\nabla p(\mathbf{x},t)\cdot\nabla p^\dagger(\mathbf{x},T-t) + \frac{1}{v^2(\mathbf{x})} p(\mathbf{x},t)\frac{\partial^2 p^\dagger(\mathbf{x},T-t)}{\partial^2 t}\right] dt. \end{aligned} \tag{13}$$

In isotropic acoustic media with constant density, i.e., $z(\mathbf{x})/v(\mathbf{x}) = \rho_0$, the forward and adjoint wavefields satisfy

$$\begin{aligned} \frac{1}{v^2(\mathbf{x})}\frac{\partial^2 p(\mathbf{x},t)}{\partial t^2} - \nabla^2 p(\mathbf{x},t) &= \rho_0 f(\mathbf{x}_s), \\ \frac{1}{v^2(\mathbf{x})}\frac{\partial^2 p^\dagger(\mathbf{x},t)}{\partial t^2} - \nabla^2 p^\dagger(\mathbf{x},t) &= \rho_0 f^\dagger(\mathbf{x},t), \end{aligned} \tag{14}$$

where $f^\dagger(\mathbf{x}, t)$ is the adjoint source, that is, the right-hand side of (Eq 7). Inserting (Eq. 14) into (Eq. 13) and replacing the time-derivatives with the spatial-derivatives of $p(\mathbf{x}, t)$ and $p^\dagger(\mathbf{x}, t)$ yields

$$\begin{aligned} K_v(\mathbf{x}) &= \frac{1}{2\rho_0}\int_0^T \left[\nabla^2 p(\mathbf{x},t) p^\dagger(\mathbf{x},T-t) - 2\nabla p(\mathbf{x},t)\cdot\nabla p^\dagger(\mathbf{x},T-t)\right. \\ &\quad \left. + p(\mathbf{x},t)\nabla^2 p^\dagger(\mathbf{x},T-t)\right] dt, \\ K_z(\mathbf{x}) &= \frac{1}{2\rho_0}\int_0^T \left[\nabla^2 p(\mathbf{x},t) p^\dagger(\mathbf{x},T-t) + 2\nabla p(\mathbf{x},t)\cdot\nabla p^\dagger(\mathbf{x},T-t)\right. \\ &\quad \left. + p(\mathbf{x},t)\nabla^2 p^\dagger(\mathbf{x},T-t)\right] dt. \end{aligned} \tag{15}$$

In (Eq. 15), the terms associated with the source and the adjoint source are neglected because they vanish for far-field wavefields (Douma et al., 2010). Applying Fourier transform

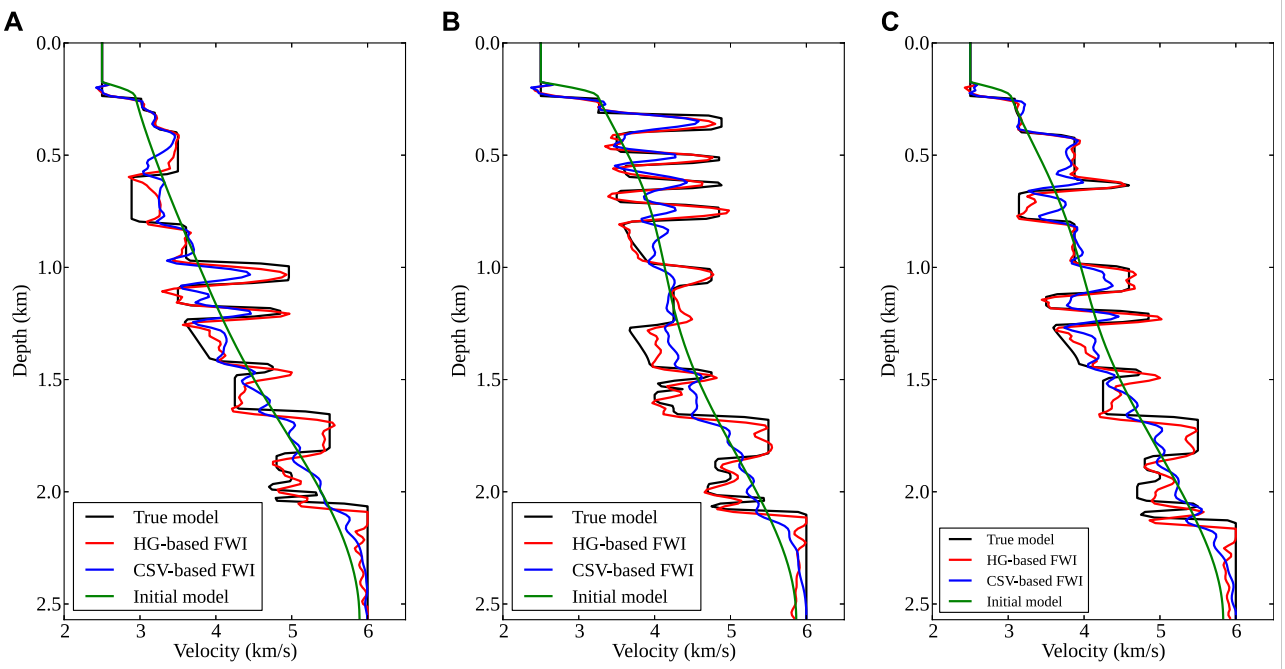

FIGURE 4
Comparisons of velocity logs for SEG/EAGE overthrust model. **(A–C)** are located at the midpoints of 1.25, 3.5, and 5.0 km, respectively. Black and green lines are from true and initial models, blue and red lines are from CSV-based FWI and HG-based FWI. HG-based FWI produces more accurate results than CSV-based method, especially at great depths with large-scale velocity anomalies.

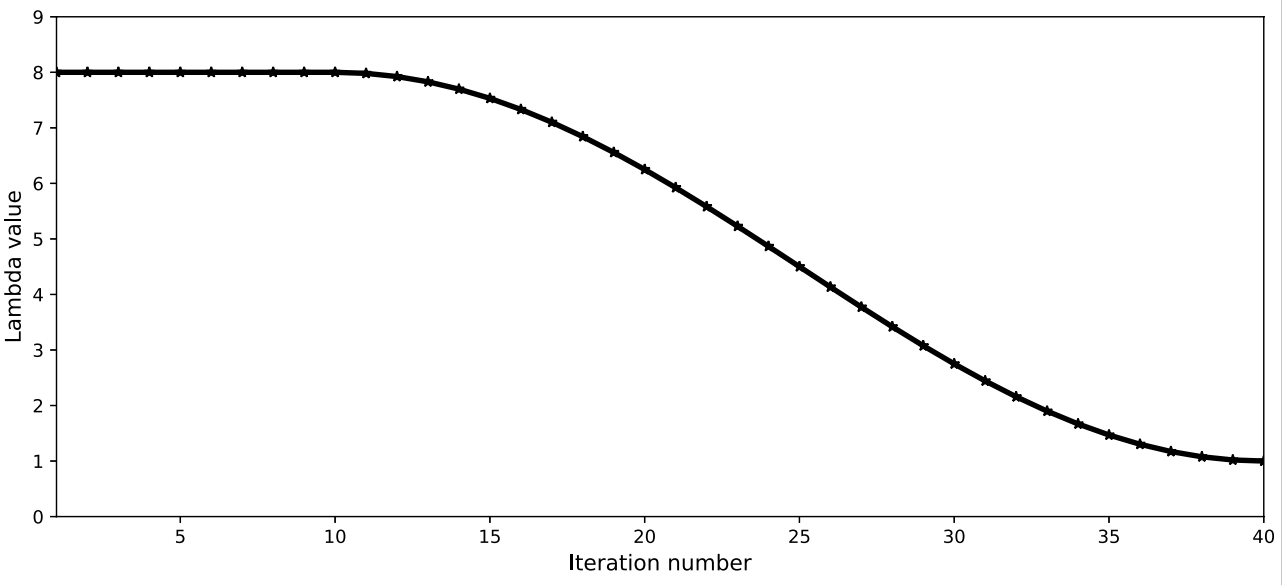

FIGURE 5
The relationship between the weight factor lambda and iterations. λ is set to 8.0 in the first 10 iterations, and then gradually reduces to 1.0 according to the change of cosine function in subsequent iterations.

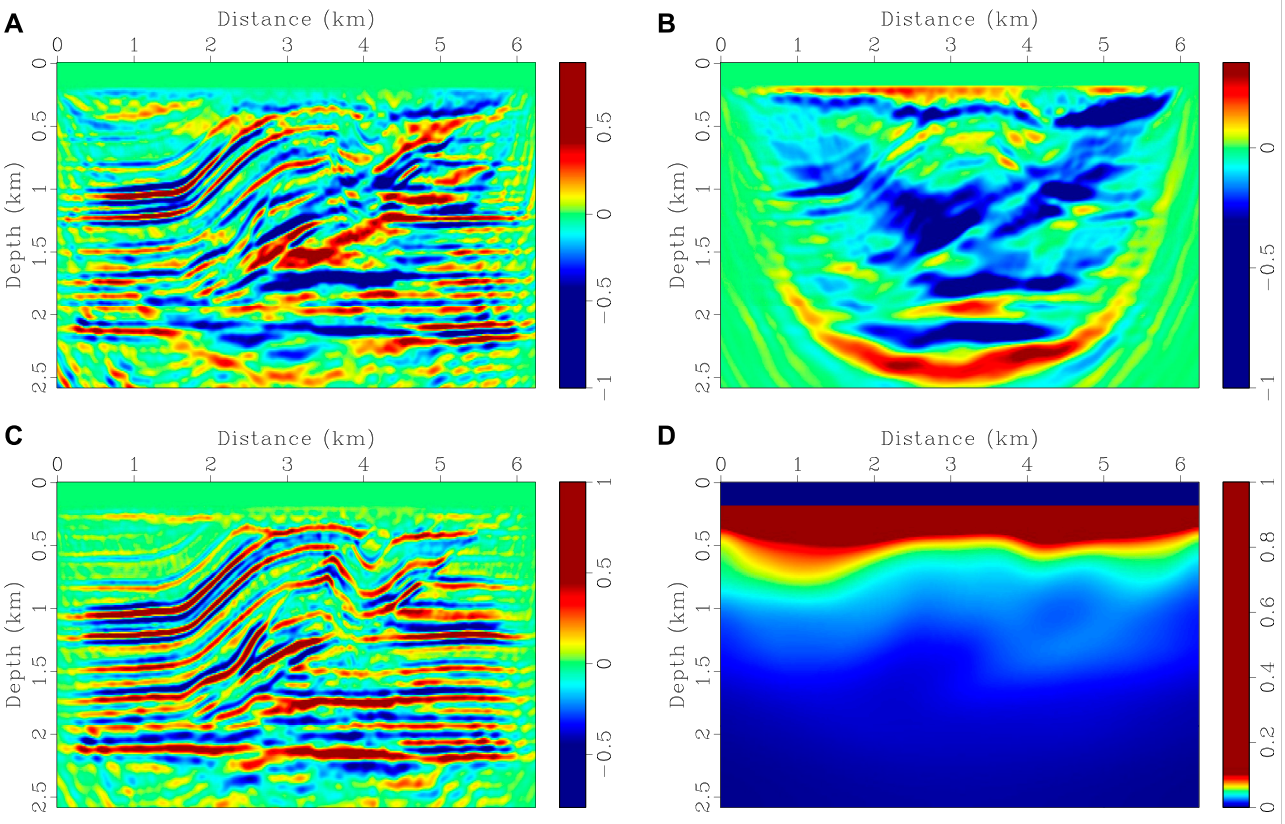

FIGURE 6
Comparison of different gradients in the first iteration for SEG/EAGE overthrust model. **(A)** CSV-based gradient, **(B)** velocity and **(C)** impedance gradients, and **(D)** phase-encoding diagonal Gauss-Newton Hessian. **(D)** Is used as a preconditioner in both CSV-based and HG-based FWI methods. The magnitude of each panel is normalized with respect to their maximum values.

to (Eq. 15) and because $|\mathbf{k}| = |\mathbf{k}^{\dagger}| = \omega/v$, the kernels have the following form:

$$K_v(\mathbf{k}) = \frac{1}{\rho_0}\sum_{\omega}|\mathbf{k}|^2\left(1-\frac{\mathbf{k}\cdot\mathbf{k}^{\dagger}}{|\mathbf{k}|^2}\right)P(\mathbf{k},\omega)P^{\dagger}(\mathbf{k},\omega),$$
$$K_z(\mathbf{k}) = \frac{1}{\rho_0}\sum_{\omega}|\mathbf{k}|^2\left(1+\frac{\mathbf{k}\cdot\mathbf{k}^{\dagger}}{|\mathbf{k}|^2}\right)P(\mathbf{k},\omega)P^{\dagger}(\mathbf{k},\omega). \quad (16)$$

where ω is the angular frequency, $p(\mathbf{k}, \omega)$ and $p^{\dagger}(\mathbf{k}, \omega)$ are the forward and adjoint Fourier-domain wavefields, $\mathbf{k}$ and $\mathbf{k}^{\dagger}$ are the forward and adjoint wavenumbers. Considering the relation $\frac{\mathbf{k}\cdot\mathbf{k}^{\dagger}}{|\mathbf{k}|^2} = \cos\theta$ and using the dispersion relation $|\mathbf{k}|^2 = \omega^2/v^2$, (Eq. 16) can be reformulated as

$$K_v(\mathbf{x}) = \frac{2}{\rho_0}\sum_{\omega}\frac{\omega^2}{v^2(\mathbf{x})}P(\mathbf{x},\omega)P^{\dagger}(\mathbf{x},\omega)\frac{(1-\cos\theta)}{2},$$
$$K_z(\mathbf{x}) = \frac{2}{\rho_0}\sum_{\omega}\frac{\omega^2}{v^2(\mathbf{x})}P(\mathbf{x},\omega)P^{\dagger}(\mathbf{x},\omega)\frac{(1+\cos\theta)}{2}. \quad (17)$$

where θ is the scattering angle (see Figure 1). Similarly, CSV kernel in (Eq. 10) can be rewritten in the frequency domain as

$$K_{csv}(\mathbf{x}) = \frac{2}{\rho_0}\sum_{\omega}\frac{\omega^2}{v^2(\mathbf{x})}P(\mathbf{x},\omega)P^{\dagger}(\mathbf{x},\omega). \quad (18)$$

(Eqs. 17, 18) show that the differences between K_v and K_z with K_{csv} are the multiplication with $(1 - \cos\theta)/2$ and $(1 + \cos\theta)/2$, which appear as band-pass filters associated with scattering angles. Note that K_z includes both velocity and density updates when density varies significantly in the subsurface. Since (Eqs. 12–17) are derived based on the assumption of constant density, K_z and K_v herein represent the velocity perturbations within different scattering-angle bands.

A simple experiment (Figure 2) is used to illustrate the effects of these two scattering-angle filters. Since the sensitivity kernels in (Eqs. 17, 18) are derived based on Born approximation, we calculate Born modeling results using CSV parameterization as well as velocity and impedance parameterization (Figures 2B–D). These results are also known as radiation patterns (Virieux and Operto, 2009; Wang et al., 2015; Zhou et al., 2015). Figure 2A shows that

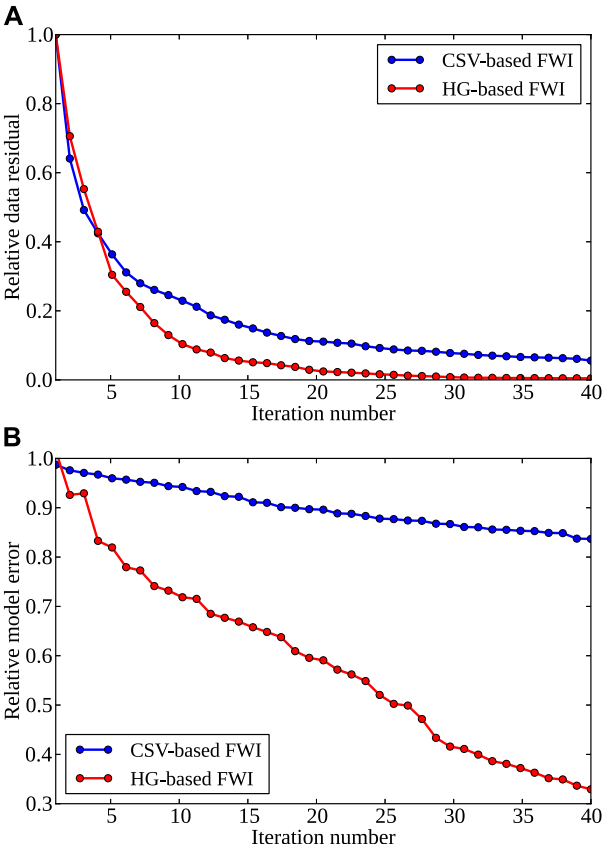

FIGURE 7
Convergence rates for SEG/EAGE overthrust model. **(A,B)** are relative data residual and model error, respectively. Blue and red lines are results from CSV-based FWI and the proposed HG-based FWI.

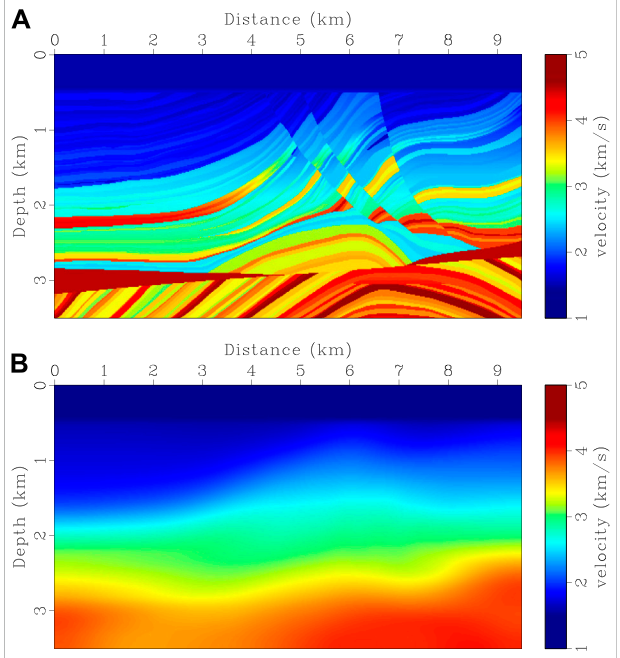

FIGURE 8
FWI experiment for Marmousi model. **(A)** True velocity model and **(B)** initial velocity model.

2.4 Full waveform inversion with a hybrid gradient

In the CSV-based FWI, the velocity model can be updated using the following gradient-based scheme:

$$\mathbf{m}^{k+1} = \mathbf{m}^{k} - \alpha \mathbf{H}^{-1}\mathbf{g}^{k} \tag{19}$$

where $\mathbf{m}^{k+1}$ and $\mathbf{m}^{k}$ are the velocity models in the next and current iterations, respectively; $\mathbf{g}^{k}$ is the misfit gradient, which can be computed by summing K_{csv} in (Eq. 10) over sources; α is the step length, which can be computed with a line-search algorithm (Potra and Shi, 1995); $\mathbf{H}^{-1}$ is the Hessian inverse and can be used to speed up convergence (Pratt et al., 1998; Shin et al., 2001; Plessix and Mulder, 2004; Tang, 2009; Métivier et al., 2013).

Using wavefield decomposition, Tang et al. (2013) and Wang et al. (2016) show that the enhancement of tomography components in the misfit gradient helps FWI to reduce nonlinearity and mitigate the cycle-skipping problem. This can also be implemented with a wavenumber continuity strategy, designing an appropriate scattering-angle filter (Wu and Alkhalifah, 2015; Alkhalifah, 2016). In the previous section, the connection between the velocity and impedance kernels is established by scattering-angle filtering

the CSV kernel has an all-pass response with respect to scattering angles, which corresponds to a homogenous radiation pattern (Figure 2B). This suggests that the CSV kernel includes both large and small scattering-angle updates (Tang et al., 2013). The velocity kernel K_v behaves like applying a high-pass filter to the CVS kernel (red line in Figure 2A), which emphasizes large-angle forward scattering contributions (Figure 2C). This indicates that the tomography component in FWI gradient is enhanced in K_v and can be used to recover large- and intermediate-scale velocity perturbations. In contrast, the impedance kernel K_z is a result of applying a low-pass scattering-angle filter to the CSV kernel (green line in Figure 2A), emphasizing the small-angle backscattering component (Figure 2D). This high-pass scattering-angle filter helps us to produce migration profiles and can be used to resolve detail structures (Luo et al., 2009; Zhu et al., 2009; Pestana et al., 2014).

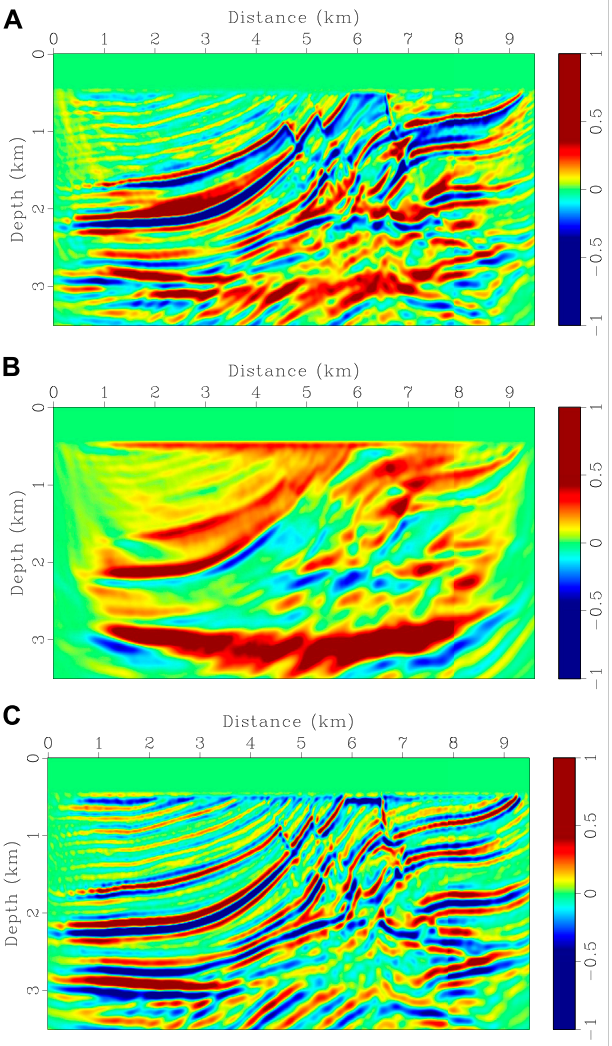

FIGURE 9
Comparisons of different gradients in the first iteration for Marmousi model. **(A)** CSV-based gradient, **(B)** velocity and **(C)** impedance gradients. The magnitude of each panel is normalized with respect to their maximum values.

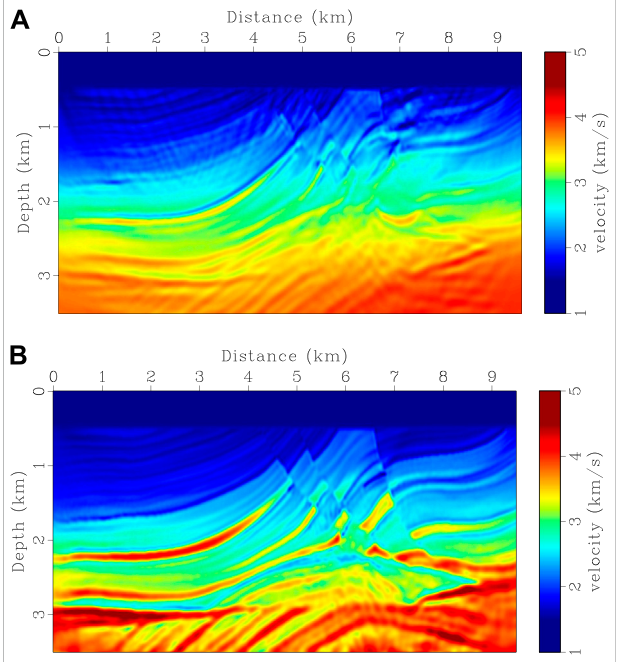

FIGURE 10
Recovered Marmousi velocity model from different FWI methods. **(A,B)** are CSV-based FWI and our method using data without frequency components below 3 Hz. 40 iterations are used in **(A,B)**.

in acoustic constant-density media. Similar to Tang et al. (2013), we combine the velocity and impedance kernels into a hybrid gradient:

$$\mathbf{g}_h = \lambda \sum_{\mathbf{x}_s} K_v(\mathbf{x}_s) + \sum_{\mathbf{x}_s} K_z(\mathbf{x}_s), \tag{20}$$

where $\mathbf{x}_s$ is the source location, $K_v(\mathbf{x}_s)$ and $K_z(\mathbf{x}_s)$ are the kernels in (Eq. 9), and λ is an adjustable scalar parameter to balance the relative weights of K_v and K_z.

Note that the large scattering-angle components in the gradient are enhanced by setting λ greater than one in (Eq. 20) at early iterations, the large scattering-angle components in the gradient are enhanced. This allows us to recover large- and intermediate-scale velocity perturbations. In subsequent iterations, reducing λ gradually to one can increase the relative weight of K_z and use more smaller scattering-angle contributions, which enables us to update detail structures. We refer to this workflow as the HG-based FWI. Since we first update large scattering-angle perturbations and then introduce smaller scatting-angle information, HG-based FWI provides us a possible way to reduce potential nonlinearity during FWI iterations.

3 Numerical examples

We present two synthetic examples to illustrate the performance of the proposed HG-based FWI scheme. The first example is the 2D SEG/EAGE overthrust model, which is modified by adding a 175 m thick water layer on the top of the model. The true velocity model is shown in Figure 3A. Initial model in Figure 3B is built by applying a 625 m × 625 m Gaussian filter to the true model. Seismograms are calculated using a staggered-grid finite-difference scheme with eighth-order accuracy in space and second-order accuracy in time. 25 shots are evenly distributed on the surface with a 250 m interval. Each shot is recorded by 250 receivers, which are uniformly deployed on the surface with a 25 m spacing. A

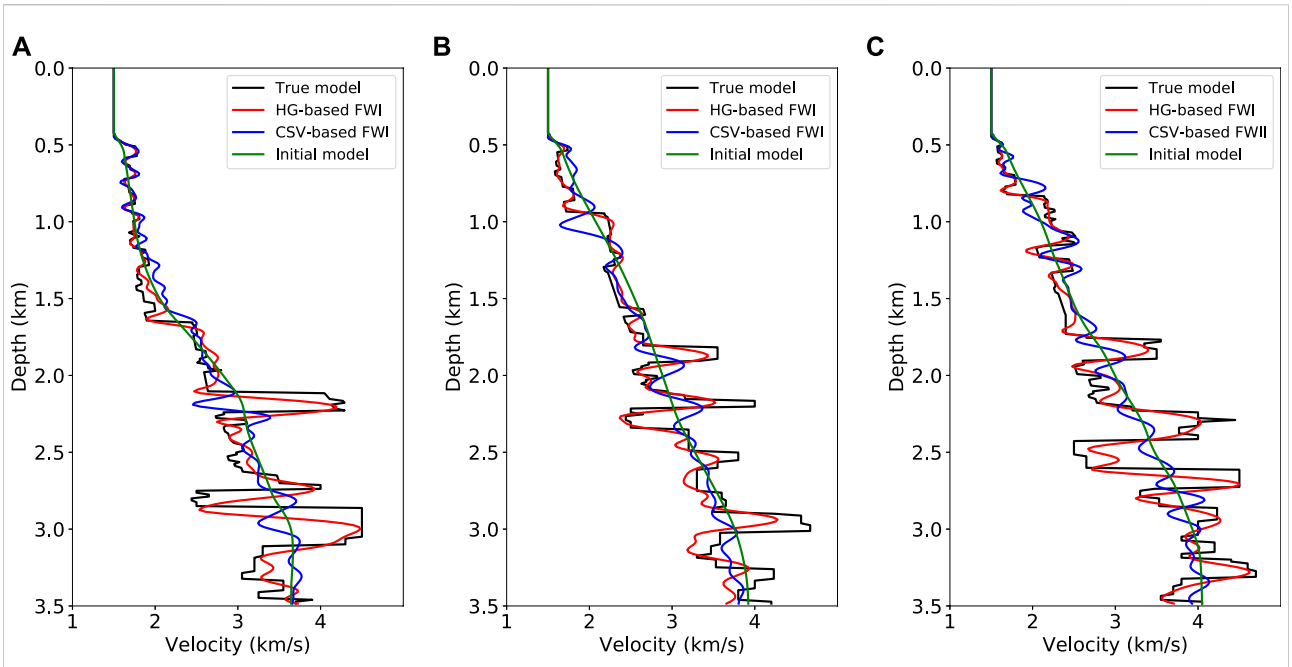

FIGURE 11
Comparisons of velocity logs for Marmousi model. **(A–C)** are located at the midpoints of 1.8, 5.0, and 8.1 km, respectively. Black and green lines are from true and initial models; blue and red lines are from CSV-based FWI and the proposed method. The proposed method is much more accurate than CSV-based FWI for recovering deep low-wavenumber velocity anomalies.

Ricker wavelet with a peak frequency of 20 Hz is used as the source function. A high-pass filter is applied to filter out low-frequency signals below 5 Hz.

Inversion results using CSV-based FWI and our method are shown in Figures 3, 4. 40 iterations are performed and a phase-encoding diagonal Hessian (Figure 6D) is used as a pre-conditioner (Tang, 2009) in both methods. In our method, λ is set to 8.0 in the first 10 iterations, and then gradually reduces to 1.0 during the following iterations as shown in Figure 5. Gradients calculated using different kernels at the first iteration are shown in Figure 6. We notice that the gradient in CSV-based FWI includes almost high-wavenumber updates, i.e., migration components (see Figure 6A). This does not mean there are no low-wavenumber components, but their magnitudes are relatively small in comparison with high-wavenumber components. As shown in Figures 6B,C, the low- and high-pass scattering-angle filters decompose the CSV kernel into a tomography component (K_v) and a migration component (K_z). This favorable scale-separation property allows HG-based FWI to update the low-wavenumber tomography component by enhancing the weight of K_v, and to resolve detail structures by gradually increasing the weight of K_z (see Figures 3D, 4).

Figure 7 shows the evolutions of data residuals and model errors for these two FWI schemes. Data residuals and model errors are defined as

$$r = \frac{\|\mathbf{d}_{obs} - \mathbf{d}_{syn}\|^2}{\|\mathbf{d}_{obs}\|^2}, \quad e = \frac{\|\mathbf{m}_{tru} - \mathbf{m}_{fwi}\|^2}{\|\mathbf{m}_{tru}\|^2}, \tag{21}$$

where $\mathbf{d}_{obs}$ and $\mathbf{d}_{syn}$ are the observed and synthetic data, $\mathbf{m}_{tru}$ and $\mathbf{m}_{fwi}$ are the true and recovered velocity models. Relative data residuals and model errors are calculated by normalizing r and e by their initial values (r_0 and e_0). Although the data residual of CSV-based FWI has been reduced by about 90%, it is stuck around 10% (blue line in Figure 7A), suggesting that it is trapped into a local minimum. This is also reflected in the corresponding model errors in Figure 7B. With a hybrid gradient, the proposed method recovers low-wavenumber components first and then gradually increases high-wavenumber components, leading to a faster convergence rate and a higher inversion accuracy in comparison with CSV-based FWI (see Figures 4, 7).

In the second example, the Marmousi model is used to test the robustness of the proposed method for complicated structures. True velocity model is shown in Figure 8A. Starting model (Figure 8B) is built by applying a 1,250 m × 1,250 m Gaussian filter to the true model. Seismograms are generated using the same finite-difference scheme as the previous example. Source function is a Ricker wavelet with a peak frequency of 8 Hz. 38 shots are distributed on the surface with a 250 m spacing. 761 receivers are deployed evenly on the model surface with a 12.5 m interval. A dataset is built by filtering frequency components below 3 Hz and is used for both CVS-based

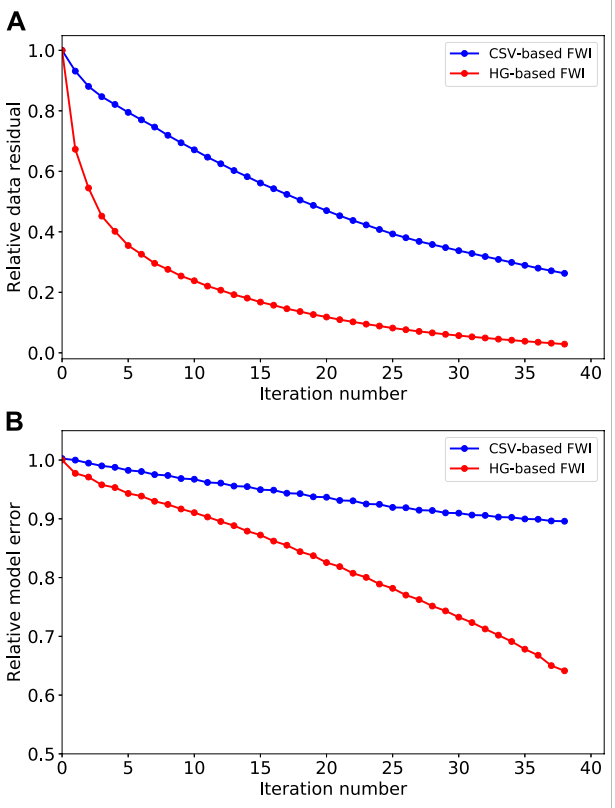

FIGURE 12
Convergence rates for Marmousi model. **(A,B)** are relative data residual and model error, respectively. Blue and red lines are results from CSV-based FWI and the proposed method.

FWI and the proposed method. The setting of λ in HG-based FWI is the same as the previous example. Inversion results are shown in Figures 10A,B. Gradients for the first iteration and velocity logs are shown in Figures 9, 11, respectively. CSV-based FWI produces accurate results at shallow depths for both low- and high-wavenumber perturbations, but fails to recover low-wavenumber velocity anomalies at greater depths (see Figures 10A, 11). This is caused by uneven subsurface scattering-angle illuminations. At shallow depths, there is sufficient illumination for both large and small scattering angles due to large offset-to-depth ratio (O/D). As depth increases, O/D decreases and the CSV-based gradient is dominated by small scattering-angle components (Figure 9A). Although large scattering-angle components in deep areas are very weak, they do exist as proved by Alkhalifah (2015). Instead of using the CSV kernel, HG-based FWI combines the K_v and K_z kernels to update velocity model (Figures 9B,C). This helps us to recover low-wavenumber perturbations at greater depths by enhancing the K_v kernel in FWI gradient. Then, high-wavenumber structures are recovered by gradually reducing the weight of the K_v kernel, producing a final high-resolution result (Figures 10B, 11).

To better quantitatively evaluate the inversion results of these two methods, we compare their convergence rates (Figure 12) and predicted seismograms using final recovered models (Figure 13). Compared with CSV-based FWI method (red line in Figure 12), the proposed method has a faster convergence rate and a higher inversion accuracy (blue line in Figure 12), which also can illustrate that the proposed method has better adaptability to complex structures.

4 Discussion

By parameterizing the acoustic wave equation using velocity and impedance, we derive their sensitivity kernels based on the Lagrange multiplier method. In a constant-density case, we prove that the velocity (K_v) and impedance (K_z) kernels are equivalent to applying a high-pass and a low-pass scattering-angle filters to the CSV (K_{csv}) kernel. K_v mainly provides low-wavenumber updates and is helpful to recover large-scale anomalies. Although impedance is defined as $z = \rho v$, K_z represents high-wavenumber velocity perturbations in constant-density media and helps us to resolve detail structures. By choosing weights properly, we can enhance K_v contribution in the hybrid gradient at early iterations and then gradually increase K_z contribution in subsequence iterations. This workflow reduces FWI nonlinearity and partially mitigate the cycle-skipping problem.

The proposed HG-based FWI scheme is similar to the tomography-enhanced FWI presented by Tang et al. (2013). But there are several key differences. First, Tang et al. (2013) use wavefield decomposition to extract the tomography and migration components from the CSV-based gradient. There is no clear relation between these two components with the scattering-angle filtering. Second, in areas with complicated structures, cross-correlations between source-side and receiver-side upgoing waves or between source-side and receiver-side downgoing waves might still produce certain migration components. Third, separating upgoing and downgoing waves requires the construction of an analytical wavefield at every time step. This can be implemented by either solving the wave equation twice (Shen and Albertin, 2015) or calculating a complex-valued wave equation (Zhang and Zhang, 2009; Pestana and Revelo, 2017), thus with a higher computational cost. Our approach only needs to modify the gradient calculation with time- and spatial-derivatives and hence no additional computational costs are required.

In our derivation from (Eqs. 12–18), the subsurface density is assumed to be constant. Therefore, our method is applicable for areas without significant density variations. When density varies greatly, we should consider the spatial derivation of $1/\rho$ in Eq. 14 and cannot obtain an analytic relation between K_v and K_z with K_{csv}. In this case, K_z includes both velocity and density perturbations (Prieux et al., 2013; Zhou et al., 2015), and thus cannot be combined with K_v to

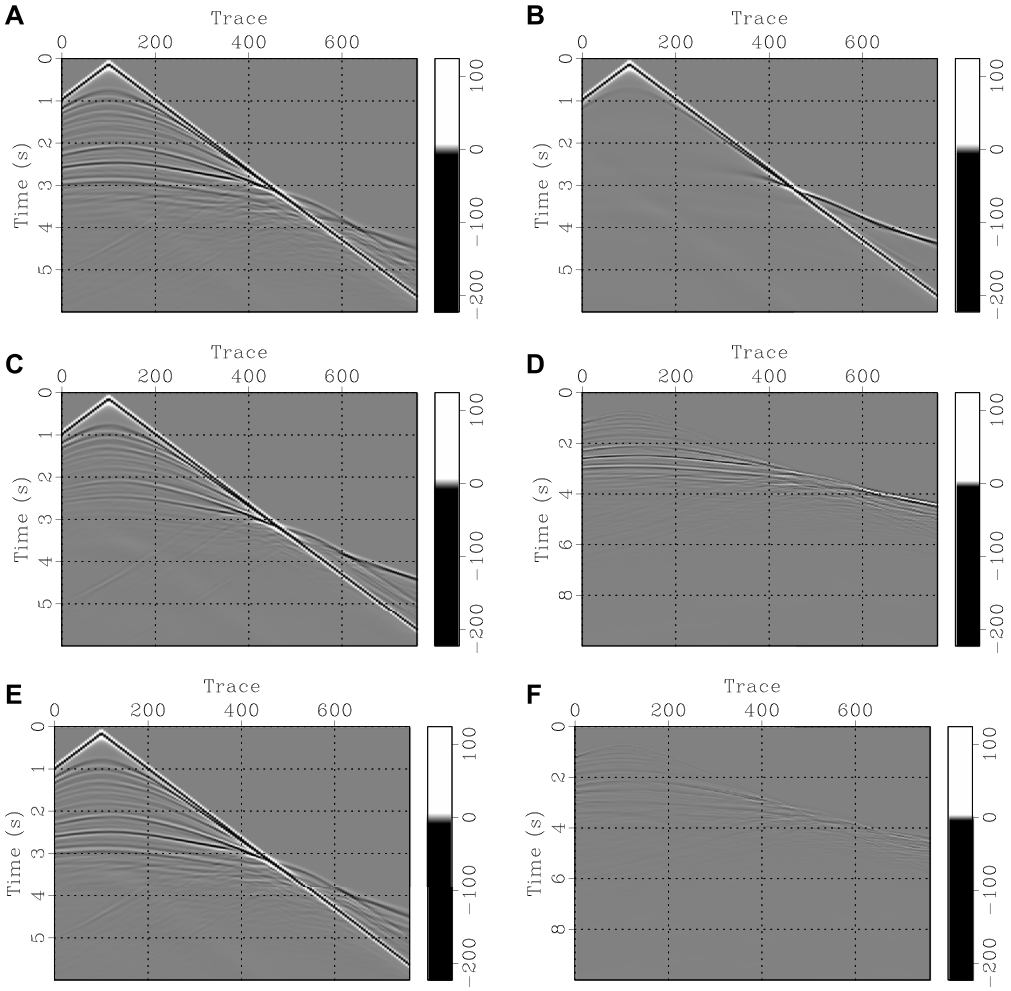

FIGURE 13
Comparisons of common-shot gathers for Marmousi model. **(A)** Observed data, **(B)** synthetic data using initial model; **(C)** synthetic data using CSV-based FWI velocity model, **(D)** difference between **(A)** with **(C)**; **(E)** synthetic data using recovered velocity model from the proposed method, **(F)** difference between **(A,E)**.

update the velocity model. How to simultaneously invert multi-parameters, such as velocity and density, velocity and impedance or impedance and density, is beyond the scope of this paper and needs further investigation.

5 Conclusion

We establish a connection between the velocity and impedance kernels with scattering angle filtering in acoustic constant-density media. This allows us to combine these two kernels into a HG-based FWI workflow to update the velocity model. By enhancing the velocity kernel contribution at early iterations, which mainly gives tomography updates, the proposed method enables us to recover large- and intermediate-scale velocity anomalies. In the subsequence iterations, gradually increasing the weight of the impedance kernel helps us to resolve small-scale structures. This workflow provides us with a way to reduce the potential nonlinearity of FWI and partially mitigate the cycle-skipping problem. Synthetic examples demonstrate that the proposed method produces an inversion result with faster convergence and higher accuracy than CSV-based FWI method.

Data availability statement

The datasets presented in this study can be found in online repositories. The names of the repository/repositories and accession number(s) can be found below: https://wiki.seg.org/wiki/SEG/EAGE_Salt_and_Overthrust_Models https://wiki.seg.org/wiki/Dictionary:Marmousi_model/zh.

Author contributions

YY: be responsible for correcting and modifying articles and checking procedures. JS: be responsible for correcting and modifying articles.

Funding

This research is supported by the startup funding (no. 20CX06069A) of Guanghua Scholar at Geophysics Department, China University of Petroleum (East China). We thank the support from the Funds of Creative Research Groups of China (no. 41821002), the National Outstanding Youth Science Foundation (no. 41922028), the National Natural Science Foundation of China (General Program) (no. 41874149), the Strategic Priority Research Program of the Chinese Academy of Sciences (no. XDA14010303), the Key Program for International Cooperation Projects of China (no. 41720104006), the National Key R&D Program of China (no. 2019YFC0605503), the Major Scientific and Technological Projects of CNPC (no. ZD 2019-183-003).

Acknowledgments

We appreciate the comments and suggestions from editor J. Zhang and two reviewers, which significantly improve the manuscript.

Conflict of interest

The authors declare that the research was conducted in the absence of any commercial or financial relationships that could be construed as a potential conflict of interest.

Publisher's note

References

Albertin, U., Shan, G., and Washbourne, J. (2013). "Gradient orthogonalization in adjoint scattering-series inversion," in SEG Technical Program Expanded Abstracts, Houston, September 22, 2013, 1058–1062. doi:10.1190/segam2013–0580.1

Alkhalifah, T. (2016). Full-model wavenumber inversion: An emphasis on the appropriate wavenumber continuation. *Geophysics* 81, R89–R98. doi:10.1190/geo2015–0537.1

Alkhalifah, T. (2015). Scattering-angle based filtering of the waveform inversion gradients. *Geophys. J. Int.* 200 (1), 363–373. doi:10.1093/gji/ggu379

Almomin, A., and Biondi, B. (2013). "Tomographic full waveform inversion (TFWI) by successive linearizations and scale separations," in SEG Technical Program Expanded Abstracts, Houston, September 22, 2013, 1048–1052. doi:10.1190/segam2013–1378.1

Boonyasiriwat, C., Schuster, G. T., Valasek, P., and Cao, W. (2010). Applications of multiscale waveform inversion to marine data using a flooding technique and dynamic early-arrival windows. *Geophysics* 75 (6), R129–R136. doi:10.1190/1.3507237

Brenders, A. J., and Pratt, R. G. (2007). Full waveform tomography for lithospheric imaging: results from a blind test in a realistic crustal model. *Geophys. J. Int.* 168 (1), 133–151. doi:10.1111/j.1365–246X.2006.03156.x

Brossier, R., Operto, S., and Virieux, J. (2009). Seismic imaging of complex onshore structures by 2D elastic frequency-domain full-waveform inversion. *Geophysics* 74, WCC105–WCC118. doi:10.1190/1.3215771

Bunks, C., Saleck, F. M., Zaleski, S., and Chavent, G. (1995). Multiscale seismic waveform inversion. *Geophysics* 60 (5), 1457–1473. doi:10.1190/1.1443880

Douma, H., Yingst, D., Vasconcelos, I., and Tromp, J. (2010). On the connection between artifact filtering in reverse-time migration and adjoint tomography. *Geophysics* 75 (6), S219–S223. doi:10.1190/1.3505124

Fichtner, A., Trampert, J., Cupillard, P., Saygin, E., Taymaz, T., Capdeville, Y., et al. (2013). Multiscale full waveform inversion. *Geophys. J. Int.* 194 (1), 534–556. doi:10.1093/gji/ggt118

Guitton, A., Ayeni, G., and Díaz, E. (2012). Constrained full-waveform inversion by model reparameterization. *Geophysics* 77, R117–R127. doi:10.1190/geo2011–0196.1

Kazei, V., Tessmer, E., and Alkhalifah, T. (2016). "Scattering angle-based filtering via extension in velocity," in SEG Technical Program Expanded Abstracts, Dallas, TX, October 21, 2016, 1157–1162. doi:10.1190/segam2016–13870908.1

Lailly, P. (1983). "The seismic inverse problem as a sequence of before stack migrations: Conference on Inverse Scattering, Theory and Application," in Expanded Abstracts (Society for Industrial and Applied Mathematics), 206–220.

Li, Y. E., and Demanet, L. (2016). Full-waveform inversion with extrapolated low-frequency data. *Geophysics* 81, R339–R348. doi:10.1190/geo2016–0038.1

Liu, Q., and Tromp, J. (2006). Finite-frequency kernels based on adjoint methods. *Bull. Seismol. Soc. Am.* 96 (6), 2383–2397. doi:10.1785/0120060041

Luo, Y., Zhu, H., Meyer, T. N., Morency, C., and Tromp, J. (2009). Seismic modeling and imaging based upon spectral-element and adjoint methods. *Lead. Edge* 28 (5), 568–574. doi:10.1190/1.3124932

Ma, Y., Hale, D., Gong, B., and Meng, Z. J. (2012). Image-guided sparse-model full waveform inversion. *Geophysics* 77 (4), R189–R198. doi:10.1190/geo2011–0395.1

Métivier, L., Brossier, R., Virieux, J., and Operto, S. (2013). Full waveform inversion and the truncated Newton method. *SIAM J. Sci. Comput.* 35 (2), B401–B437. doi:10.1137/120877854

Mora, P. (1989). Inversion = migration + tomography. *Geophysics* 54 (12), 1575–1586. doi:10.1190/1.1442625

Pestana, R. C., dos Santos, A. W. G., and Araujo, E. S. (2014). "RTM imaging condition using impedance sensitivity kernel combined with Poynting vector," in SEG Technical Program Expanded Abstracts, Denver, CO, October 26, 2014, 3763–3768. doi:10.1190/segam2014–0374.1

Pestana, R. P., and Revelo, D. (2017). "An improved method to calculate the analytical wavefield for causal imaging condition," in SEG Technical Program Expanded Abstracts, Houston, September 29, 2017, 4640–4644. doi:10.1190/segam2017–17664808.1

Plessix, R.-E. (2006). A review of the adjoint-state method for computing the gradient of a functional with geophysical applications. *Geophys. J. Int.* 167 (2), 495–503. doi:10.1111/j.1365–246X.2006.02978.x

Plessix, R.-E., and Li, Y. (2013). Waveform acoustic impedance inversion with spectral shaping. *Geophys. J. Int.* 195 (1), 301–314. doi:10.1093/gji/ggt233

Plessix, R.-E., and Mulder, W. A. (2004). Frequency-domain finite-difference amplitude-preserving migration. *Geophys. J. Int.* 157 (3), 975–987. doi:10.1111/j.1365–246X.2004.02282.x

Potra, F. A., and Shi, Y. (1995). Efficient line search algorithm for unconstrained optimization. *J. Optim. Theory Appl.* 85 (3), 677–704. doi:10.1007/BF02193062

Pratt, R. G. (1999). Seismic waveform inversion in the frequency domain, Part 1: Theory and verification in a physical scale model. *Geophysics* 64 (3), 888–901. doi:10.1190/1.1444597

Pratt, R. G., Shin, C., and Hick, G. J. (1998). Gauss-Newton and full Newton methods in frequency–space seismic waveform inversion. *Geophys. J. Int.* 133 (2), 341–362. doi:10.1046/j.1365–246X.1998.00498.x

Pratt, R. G., and Shipp, R. M. (1999). Seismic waveform inversion in the frequency domain, Part 2: Fault delineation in sediments using crosshole data. *Geophysics* 64 (3), 902–914. doi:10.1190/1.1444598

Pratt, R., Song, Z.-M., Williamson, P., and Warner, M. (1996). Two-dimensional velocity models from wide-angle seismic data by wavefield inversion. *Geophys. J. Int.* 124 (2), 323–340. doi:10.1111/j.1365-246x.1996.tb07023.x

Prieux, V., Brossier, R., Operto, S., and Virieux, J. (2013). Multiparameter full waveform inversion of multicomponent ocean-bottom-cable data from the valhall field. part 1: imaging compressional wave speed, density and attenuation. *Geophys. J. Int.* 194 (3), 1640–1664. doi:10.1093/gji/ggt177

Ravaut, C., Operto, S., Improta, L., Virieux, J., Herrero, A., and Dell'Aversana, P. (2004). Multiscale imaging of complex structures from multifold wide-aperture seismic data by frequency-domain full-waveform tomography: application to a thrust belt. *Geophys. J. Int.* 159 (3), 1032–1056. doi:10.1111/j.1365–246X.2004.02442.x

Sears, T. J., Barton, P. J., and Singh, S. C. (2010). Elastic full waveform inversion of multicomponent ocean-bottom cable seismic data: Application to Alba Field, U. K. North Sea. *U. K. North Sea Geophys.* 75, R109–R119. doi:10.1190/1.3484097

Shen, P., and Albertin, U. (2015). "Up-Down separation using hilbert transformed source for causal imaging condition," in SEG Technical Program Expanded Abstracts, New Orleans, Louisiana, October 18, 2015, 4175–4179. doi:10.1190/segam2015–5862960.1

Sheng, J., Leeds, A., Buddensiek, M., and Schuster, G. T. (2006). Early arrival waveform tomography on near-surface refraction data. *Geophysics* 71, U47–U57. doi:10.1190/1.2210969

Shin, C., and Cha, Y. H. (2008). Waveform inversion in the Laplace domain. *Geophys. J. Int.* 173 (3), 922–931. doi:10.1111/j.1365–246X.2008.03768.x

Shin, C., Jang, S., and Min, D.-J. (2001). Improved amplitude preservation for prestack depth migration by inverse scattering theory. *Geophys. Prospect.* 49 (5), 592–606. doi:10.1046/j.1365–2478.2001.00279.x

Shin, C., Min, D., Marfurt, K. J., Lim, H. Y., Yang, D., Cha, Y., et al. (2002). Traveltime and amplitude calculations using the damped wave solution. *Geophysics* 67 (5), 1637–1647. doi:10.1190/1.1512811

Shipp, R. M., and Singh, S. C. (2002). Two-dimensional full wavefield inversion of wide-aperture marine seismic streamer data. *Geophys. J. Int.* 151 (2), 325–344. doi:10.1046/j.1365–246X.2002.01645.x

Sirgue, L., and Pratt, R. G. (2004). Efficient waveform inversion and imaging: A strategy for selecting temporal frequencies. *Geophysics* 69 (1), 231–248. doi:10.1190/1.1649391

Tang, Y., Lee, S., Baumstein, A., and Hinkley, D. (2013). "Tomographically enhanced full wavefield inversion," in SEG Technical Program Expanded Abstracts, Houston, September 22, 2013, 1037–1041. doi:10.1190/segam2013–1145.1

Tang, Y. (2009). Target-oriented wave-equation least-squares migration/inversion with phase-encoded Hessian. *Geophysics* 74, WCA95–WCA107. doi:10.1190/1.3204768

Tarantola, A. (2005). *Inverse problem theory and methods for model parameter estimation*. Philadelphia, PA: SIAM.

Tarantola, A. (1984). Inversion of seismic reflection data in the acoustic approximation. *Geophysics* 49 (8), 1259–1266. doi:10.1190/1.1441754

Tromp, J., Tape, C., and Liu, Q. (2005). Seismic tomography, adjoint methods, time reversal and banana-doughnut kernels. *Geophys. J. Int.* 160 (1), 195–216. doi:10.1111/j.1365–246X.2004.02453.x

Vigh, D., Starr, B., Kapoor, J., and Li, H. (2010). "3D full waveform inversion on a Gulf of Mexico WAZ data set," in SEG Technical Program Expanded Abstracts, Denver, CO, October 17, 2010, 957–961. doi:10.1190/1.3513935

Virieux, J., and Operto, S. (2009). An overview of full-waveform inversion in exploration geophysics. *Geophysics* 74, WCC1–WCC26. doi:10.1190/1.3238367

Wang, F., Donno, D., Chauris, H., Calandra, H., and Audebert, F. (2016). Waveform inversion based on wavefield decomposition. *Geophysics* 81, R457–R470. doi:10.1190/geo2015–0340.1

Wang, H., Singh, S. C., Audebert, F., and Calandra, H. (2015). Inversion of seismic refraction and reflection data for building long-wavelength velocity models. *Geophysics* 80, R81–R93. doi:10.1190/geo2014–0174.1

Wang, R., and Herrmann, F. (2016). "Frequency down extrapolation with TV norm minimization," in SEG Technical Program Expanded Abstracts, Dallas, TX, October 21, 2016, 1380–1384. doi:10.1190/segam2016–13879674.1

Whitmore, N. D., and Crawley, S. (2012). "Applications of RTM inverse scattering imaging conditions," in SEG Technical Program Expanded Abstracts, Las Vegas, Nevada, November 4, 2012, 1–6. doi:10.1190/segam2012–0779.1

Wu, R., and Toksöz, M. N. (1987). Diffraction tomography and multisource holography applied to seismic imaging. *Geophysics* 52 (1), 11–25. doi:10.1190/1.1442237

Wu, Z., and Alkhalifah, T. (2017). Efficient scattering-angle enrichment for a nonlinear inversion of the background and perturbations components of a velocity model. *Geophys. J. Int.* 210, 1981–1992. doi:10.1093/gji/ggx283

Wu, Z., and Alkhalifah, T. (2015). "Full waveform inversion based on scattering angle enrichment with application to real dataset," in SEG Technical Program Expanded Abstracts, 1258–1262. doi:10.1190/segam2015–5922173.1

Xie, X.-B. (2013). "Recover certain low-frequency information for full waveform inversion," in SEG Technical Program Expanded Abstracts, Houston, September 22, 2013, 1053–1057. doi:10.1190/segam2013–0451.1

Xue, Z., Alger, N., and Fomel, S. (2016). "Full-waveform inversion using smoothing kernels," in SEG Technical Program Expanded Abstracts, Dallas, TX, October 21, 2016, 1358–1363. doi:10.1190/segam2016–13948739.1

Zhang, Y., and Sun, J. (2009). Practical issues in reverse time migration: true amplitude gathers, noise removal and harmonic source encoding. *First Break* 27 (1), 53–59. doi:10.3997/1365-2397.2009002

Zhang, Y., and Zhang, G. (2009). One-step extrapolation method for reverse time migration. *Geophysics* 74, A29–A33. doi:10.1190/1.3123476

Zhou, W., Brossier, R., Operto, S., and Virieux, J. (2015). Full waveform inversion of diving and reflected waves for velocity model building with impedance inversion based on scale separation. *Geophys. J. Int.* 202 (3), 1535–1554. doi:10.1093/gji/ggv228

Zhu, H., Luo, Y., Nissen-Meyer, T., Morency, C., and Tromp, J. (2009). Elastic imaging and time-lapse migration based on adjoint methods. *Geophysics* 74, WCA167–WCA177. doi:10.1190/1.3261747

Appendix

Derivation of conventional single-parameter velocity (CSV) kernel. The constant-density acoustic wave equation can be written as

$$\frac{1}{v^2(\mathbf{x})}\frac{\partial^2 p(\mathbf{x},t)}{\partial t^2}-\nabla^2 p(\mathbf{x},t)=f(t)\delta(\mathbf{x}-\mathbf{x}_s), \tag{A-1}$$

where $p(\mathbf{x}, t)$ is the pressure wavefield, $f(t)$ is the source time function, and $\mathbf{x}_s$ denotes the source location. The augmented misfit function can be constructed as

$$\begin{aligned} J=&\frac{1}{2}\sum_{\mathbf{x}_r}\int\left[d_{syn}(\mathbf{x}_r,t)-d_{obs}(\mathbf{x}_r,t)\right]^2dt\\ &-\iint q(\mathbf{x},t)\left(\frac{1}{v^2(\mathbf{x})}\frac{\partial^2 p(\mathbf{x},t)}{\partial t^2}-\nabla^2 p(\mathbf{x},t)\right)dtd\mathbf{x}^3, \end{aligned} \tag{A-2}$$

where q is the Lagrange multiplier, and $d_{syn}(\mathbf{x}_r,t)=p(\mathbf{x},t)\delta(\mathbf{x}-\mathbf{x}_r)$. Taking the variation of the augmented misfit function and neglecting the high-order terms, we obtain

$$\begin{aligned} \delta J=&\sum_{\mathbf{x}_r}\iint\left[d_{syn}(\mathbf{x}_r,t)-d_{obs}(\mathbf{x}_r,t)\right]\delta p(\mathbf{x},t)\delta(\mathbf{x}-\mathbf{x}_r)dtd\mathbf{x}^3\\ &-\iint\left\{\delta p(\mathbf{x},t)\left[\frac{1}{v^2(\mathbf{x})}\frac{\partial^2 q(\mathbf{x},t)}{\partial t^2}-\nabla^2 q(\mathbf{x},t)\right]\right.\\ &\left.-\delta\ln v\left[\frac{2}{v^2(\mathbf{x})}\frac{\partial^2 p(\mathbf{x},t)}{\partial t^2}q(\mathbf{x},t)\right]\right\}d\mathbf{x}^3dt. \end{aligned} \tag{A-3}$$

Therefore, the adjoint equation can be derived by setting $\frac{\partial J}{\partial p}=0$, which results in

$$\begin{aligned} &\frac{1}{v^2(\mathbf{x})}\frac{\partial^2 q(\mathbf{x},t)}{\partial t^2}-\nabla^2 q(\mathbf{x},t)\\ &\quad=\sum_{\mathbf{x}_r}\left[d_{syn}(\mathbf{x}_r,t)-d_{obs}(\mathbf{x}_r,t)\right]\delta(\mathbf{x}-\mathbf{x}_r). \end{aligned} \tag{A-4}$$

The CSV sensitivity kernel can be derived by setting $\frac{\partial J}{\partial \ln v}=0$, which gives

$$K_{csv}(\mathbf{x})=\frac{2}{v^2(\mathbf{x})}\int_0^T\frac{\partial^2 p(\mathbf{x},t)}{\partial t^2}q(\mathbf{x},t)dt. \tag{A-5}$$

Define the adjoint wavefield as $p^\dagger(\mathrm{x}, t)=q(\mathrm{x}, T-t)$, the adjoint wave equation can be rewritten as

$$\frac{1}{v^2(\mathbf{x})}\frac{\partial^2 p^\dagger(\mathbf{x},t)}{\partial t^2}-\nabla^2 p^\dagger(\mathbf{x},t)=\sum_{\mathbf{x}_r}\left[d_{syn}(\mathbf{x}_r,T-t)-d_{obs}(\mathbf{x}_r,T-t)\right]\delta(\mathbf{x}-\mathbf{x}_r), \tag{A-6}$$

and the sensitivity kernel is

$$K_{csv}(\mathbf{x})=\frac{2}{v^2(\mathbf{x})}\int_0^T\frac{\partial^2 p(\mathbf{x},t)}{\partial t^2}p^\dagger(\mathbf{x},T-t)dt. \tag{A-7}$$

frontiers | Frontiers in Earth Science

TYPE Original Research
PUBLISHED 06 January 2023
DOI 10.3389/feart.2022.1028399

OPEN ACCESS

EDITED BY
Jiefu Chen,
University of Houston, United States

REVIEWED BY
Qiang Guo,
China University of Mining and Technology, China
Xiaoyun Wan,
China University of Geosciences, China

*CORRESPONDENCE
Shi Chen,
chenshi@cea-igp.ac.cn

SPECIALTY SECTION
This article was submitted to Solid Earth Geophysics, a section of the journal Frontiers in Earth Science

RECEIVED 26 August 2022
ACCEPTED 12 December 2022
PUBLISHED 06 January 2023

CITATION
Li Y, Chen S, Zhang B and Li H (2023), Fast imaging for the 3D density structures by machine learning approach.
Front. Earth Sci. 10:1028399.
doi: 10.3389/feart.2022.1028399

Fast imaging for the 3D density structures by machine learning approach

Yongbo Li[1,2], Shi Chen[1,2,3]*, Bei Zhang[1,2] and Honglei Li[1,2]

[1]Institute of Geophysics, China Earthquake Administration, Beijing, China, [2]Beijing Baijiatuan Earth Science National Observation and Research Station, Beijing, China, [3]National Engineering Research Center of Offshore Oil and Gas Exploration, Beijing, China

Residual Bouguer gravity anomaly inversion can be used to imaging for local density structures or to interpret near-surface anomalous mass distribution. The reasonable prior information is the crucial recipe for obtaining a realistic geological inversion result, especially for the ill-posed geophysical inversion problem. The conventional strategies introduce the prior constraints or joint multidisciplinary information in object function as regularization, and then use some optimization algorithm to minimize the object function. This process is called model-driven approach and is usually time-consuming. In recent years, the rapid development of machine learning technology has provided new solutions for solving geophysical inversion problems. Machine learning methods can reduce the dependence on prior information in the inversion process through setting special training datasets, and the time consumption of an inversion process executed by the trained model can be shortened by several orders of magnitude, which is conducive to fast inversion for the same type of application scenarios. In this study, we were inspired by the U-net model and develops the GV-Net (Gravity voxels inversion network) model using the convolutional neural network for the inversion of residual gravity anomalies. We first discussed the effects of different loss functions on the convergence speed of model training and prediction accuracy. Then, we analyzed the robustness of our model by changing noise levels of the datasets. At last, we employed this model in a real scenario. The results have demonstrated that the GV-Net model has the ability to deal with specific inverse problems by predefined training datasets.

KEYWORDS

gravity inversion, convolutional neural network, machine learning, ore body identification, fast inversion, bouguer gravity anomaly

1 Introduction

Gravity method as one of multidisciplinary geophysics methods is sensitive to density distribution, which can be used to imaging for the density structure of the shallow Earth (Wang et al., 2014; Honglei et al., 2021). In general, different sort of gravity anomaly exist their own special geophysical meaning (Johannes and Smilde, 2009). The Bouguer gravity anomaly can be divided into regional and residual parts according to the characteristics of

the field sources. The regional Bouguer gravity anomalies are controlled by large-scale structural anomalies or deep density anomalies, such as Moho depth (Fu et al., 2014) and basement relief. The residual Bouguer gravity anomaly, also known as local gravity anomaly, correspondence to the distribution of residual mass in the shallow crust. Generally, the residual Bouguer gravity anomaly can be used in the mineral exploration or the near-surface geological structure detection (Rosid et al., 2020; Chen and Zhang, 2022).

Gravity inversion is a necessary procedure for retrieving geological information from gravity anomalies. However, similar to other geophysical inversion problems, gravity inversion problem is usually ill-posed and the result is inherent non-unique. For the same gravity anomaly, infinite mathematical solutions can be found for fitting the input anomaly within a certain tolerance. Therefore, geoscientists usually introduce certain prior information to constrain the inversion process for obtaining a reasonable outcome, such as minima structure constraint, smoothness assumption (Li and Oldenburg, 1996; Li and Oldenburg, 1998), and so on. Nevertheless, how to select the prior constraints are generally limited by researchers' experience, and improper prior constrains will inevitably introduce spurious features into the inversion results. The joint inversion with multidisciplinary geophysical data is an effective approach to reducing the non-uniqueness of inversion results (Bosch et al., 2006; Lelièvre et al., 2012; Liu et al., 2022). But this approach relies on the relationships between different physical properties, these are also empirical and not suitable for all geological conditions. Additionally, in traditional inversion strategies, the large-scale systems of linear or non-linear equations must be solved whatever using the direct or iterative method. Especially for regularized inversion method, the 'trade-off' parameter is often obtained through multiple iterations, this process is time-consuming.

Recent development of machine learning (ML) technique brings a new strategy for scientists to solve tough problems. ML term first appeared in literature can be traced to the 1950s (Turing, 1950). Nevertheless, due to the limitation of computer performance and the high requirement of mathematical ability for researchers, ML has not received much attention for a long time. In the past decade, computer performance has developed rapidly, especially with the emergence of general ML frameworks such as TensorFlow, PyTorch, MXNet, Keras, and Theano. Kinds of ML frameworks make us deploy and train the ML models simply and efficiently. At the same time, the powerful GPU continually enhances the training efficiency of complex ML model and makes it feasible to deal with high dimensionality problems with a large-scale degree of freedom. ML approach has already shown extraordinary potential and for solving the geophysical inversion problems in numerous geoscience scenarios.

ML is a sort of data-driven method, which has been widely used in geosciences, including seismology (Kong et al., 2018; Ming et al., 2019a; Ming et al., 2019b), solid Earth geoscience (Bergen et al., 2019), hydro-geophysics (Shen, 2018), geomorphometry (Valentine and Kalnins, 2016) and sea ice forecasting (Andersson et al., 2021). In this study, we introduce ML to imaging the 3D density structure in the shallow crust. For the 3D gravity inverse problem, the input data can be regarded as a single-channel image, and the output can be assumed as multi-channel images, so this problem can be

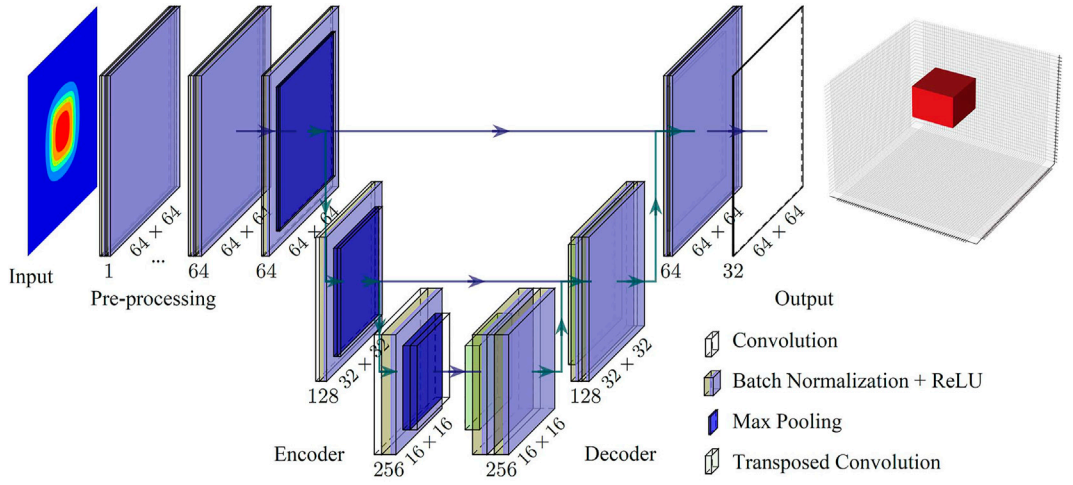

FIGURE 1
Schematic of GV-Net architecture.

TABLE 1 The algorithm of GV-Net.

```
Algorithm: Convolution Neural Network for Gravity Voxels Inversion
Input：Residual Bouguer gravity anomaly
Train：for i = 1:epochs
        Forward
            tmp = input
            Pre-processing
                for j = 1:7
                    tmp = Conv2d(tmp)
                    tmp = BatchNorm2d(tmp)
                    tmp = Relu(tmp)
                    tmp = Conv2d(tmp)
                    tmp = BatchNorm2d(tmp)
                    tmp = Relu(tmp)
            Encoder
                for k = 1:3
                    tmp = Conv2d(tmp)
                    tmp = BatchNorm2d (tmp)
                    tmp = Relu(tmp)
                    tmp = Max_pool2d (tmp)
                    tmp = Conv2d(tmp)
                    Down[i] = tmp
            Decoder
                for z = 1:3
                    tmp = ConvTranspose2d(tmp)
                    tmp = BatchNorm2d (tmp)
                    tmp = Relu(tmp)
                    tmp = Conv2d(tmp)
                    tmp = ConvTranspose2d(tmp)
                    tmp = Relu(tmp)
                    if z in [1,2]:
                        tmp = Cat(tmp, Down[4-i])
            Out：
                    Result = Conv2d(tmp)
            Backward
                    Loss = Loss_function(Result, True)
                    Loss.backward()
Predict：Predict = GV-Net(Input)
```

applied with CNN(Convolutional Neural Network), which is a typical ML method.

During the training process, the model updates the parameters according to the pre-defined loss function to fitting the mapping relationship between the observed data and the field source parameters. The well-trained ML model transforms the conventional inverse problem into a forward problem, which greatly shortens the time required for model prediction. In this study, we first proposed the GV-Net model inspired by U-Net (Ronneberger et al., 2015) for the 3D density structure imaging. Then we generated a large number of model-observation data samples by a random algorithm as training datasets artificially. Subsequently, we test the influence of two different loss functions with respect to the model training speed, model convergence characteristics, and model prediction accuracy. At last, we verified that the GV-net model is noise resistant, and we also demonstrated the practicality of the GV-net model through a real scenario.

2 Methodology

2.1 The architecture of GV-Net

In this study, we developed the GV-Net model based on CNN technology. Figure 1 illustrates the architecture of the GV-Net model, which is primarily composed of four components, namely preprocessing, encoder, decoder, and output respectively. The activation function uses the Relu function, and the pooling method is maximum pooling. The detailed procedure of the GV-Net model is illustrated in Table 1. We use PyTorch framework to construct and train the GV-Net model.

The input data of GV-Net is a single-channel image with 64 × 64 pixels, each pixel represents a gravity data point. Then, we gradually increased the number of channels to 64 through the preprocessing part, with the horizontal resolution of the data in the preprocessing part remains unchanged. The horizontal resolution of the data is then reduced to 8×8 in the encoder part by three Max-pooling processes, while the number of channels is increased to 512. In the decoder part, the number of channels of the model is reduced to 64 by three transposed convolution operations, and the resolution will be increased to 64×64. Finally, the output part generates the 32 channels, which have 64×64 data points in each channel to express the density voxel layers in the three-dimensional space implemented by a convolution layer.

2.2 Loss function

During the CNN training, the model parameters will be updated according to the variation of the loss function. Therefore, selecting a suitable loss function is critical for improving the model performance. We chose two sorts of loss functions as candidates to test the effect on the GV-Net model, including training speed, convergence characteristics, and prediction accuracy.

1) Mean squared Error (MSE) function

Mean squared error (MSE) is one of the most common loss functions used in machine learning, which has been widely adopted in regression problems (Mitra et al., 2020; Wang et al., 2020; He et al., 2021). MSE_{Loss} function can be expressed as

$$MSE_{\mathrm{Loss}(\hat{m},m)} = \frac{1}{N}\sum_{i=1}^{N}(\hat{m}_i - m_i)^2 \tag{1}$$

where m is the true model, $\hat{m}$ is the predicted model, N is number of elements in model m

2) Dice function

Milletari et al. (2016) proposed a loss function based on Dice coefficient to measure the similarity of two models. The dice coefficient can be written as

$$Dice(\hat{m}, m) = \frac{2\sum_{i=1}^{N}\hat{m}_i m_i}{\sum_{i=1}^{N}\hat{m}_i^2 + \sum_{i=1}^{N} m_i^2} \tag{2}$$

Then, the Dice function can be expressed as

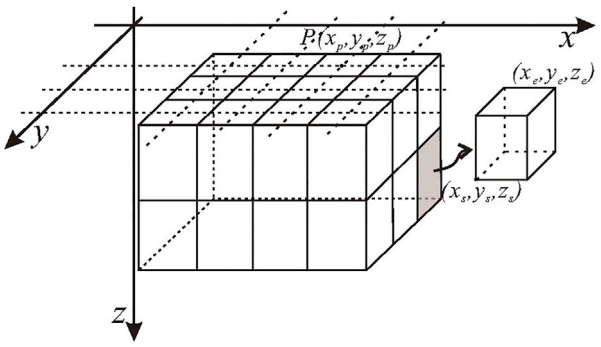

FIGURE 2
Schematic diagram for the gravity anomaly of discretized prism models.

$$Dice_{Loss(\hat{m},m)} = 1 - Dice(\hat{m}, m) \tag{3}$$

Based on Eq. 2, when the predicted model is closer to the real model, the Dice coefficient is closer to one, which makes the $Dice_{Loss}$ closer to zero. Huang et al. (2021) use this loss function to deal with sparsity inversion problems with binary density distribution and got good results.

In the following sections, we refer to the GV-Net with MSE_{Loss} function as MGV-Net and refer to the GV-Net with $Dice_{Loss}$ function as DGV-Net.

2.3 Result evaluation metrics

For evaluating the prediction accuracy of GV-Net and comparing the effect of two different loss functions, we introduce two metrics to quantitatively evaluate the predicted result from different aspects. The first metric is called model relative error ε, which can be used to evaluate the predicted density source, and this metric is expressed as follows:

$$\varepsilon = \frac{\|\hat{m} - m\|_2}{\|\hat{m}\|_2 + \|m\|_2} \tag{4}$$

This metric function is range from 0 to 1, as shows in Eq. 4, which means the more accurate the model predicts, the smaller ε is.

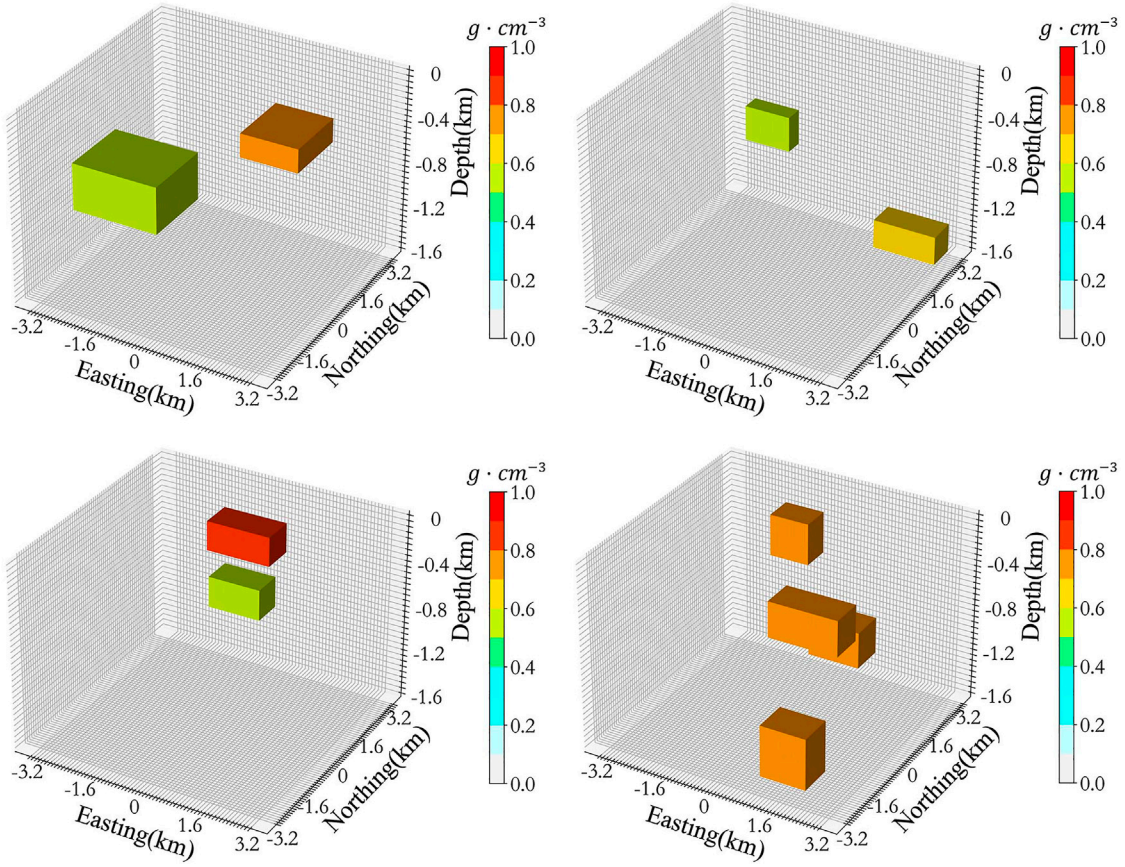

FIGURE 3
Examples of random density model.

TABLE 2 Time cost.

	Training	Predicting
DGV-Net	2h34min04s	0.0061(s)
MGV-Net	1h25min57s	0.0053(s)
*The computer configurations and hyperparameters setting :		
Hardware configurations :		
CPU: Intel(R) Xeon(R) CPU E5-2620 v4 @ 2.10GHz		
GPU: NVIDIA GeForce GTX 1080×3		
Soft environment :		
CUDA Version: 10.2		
Python Version: 3.7.13		
ML Framework: Pytorch 1.4.0		
Hyperparameters setting :		
Batch size: 128		
Epochs: 300		
Optimizer: Adma		
Activation function: Relu		

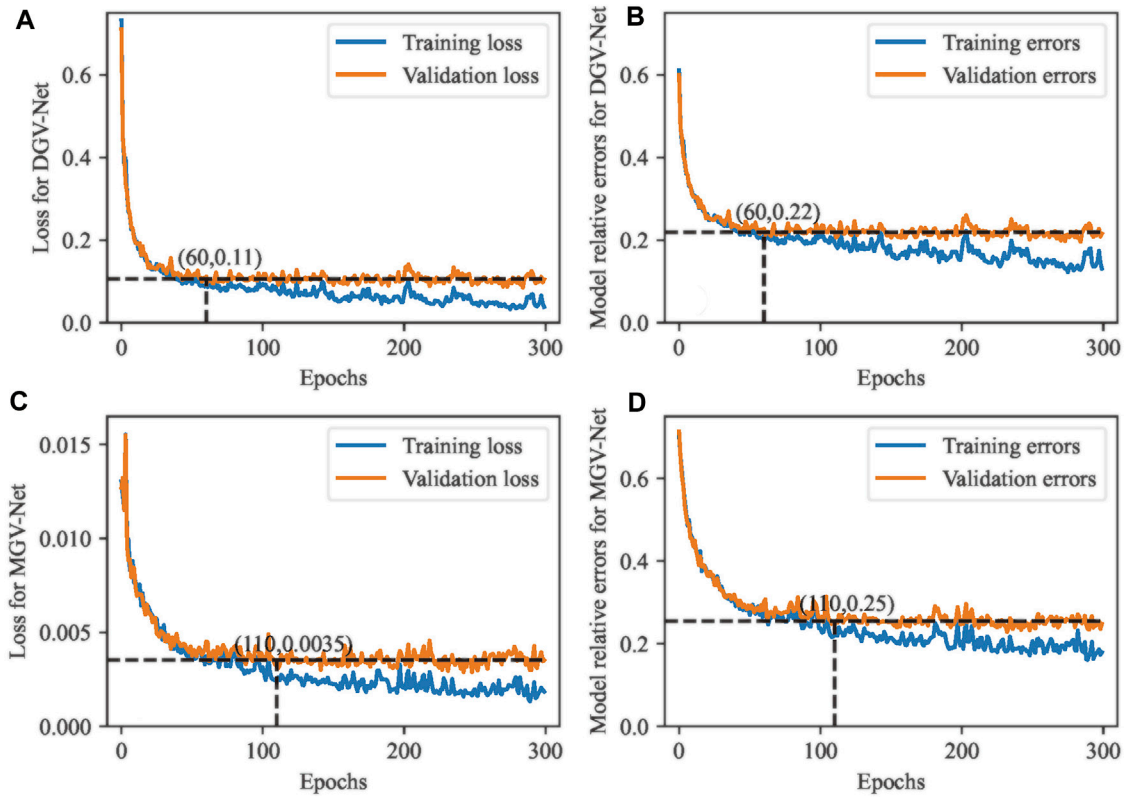

FIGURE 4
Loss curves and model relative errors for the training and validation datasets.

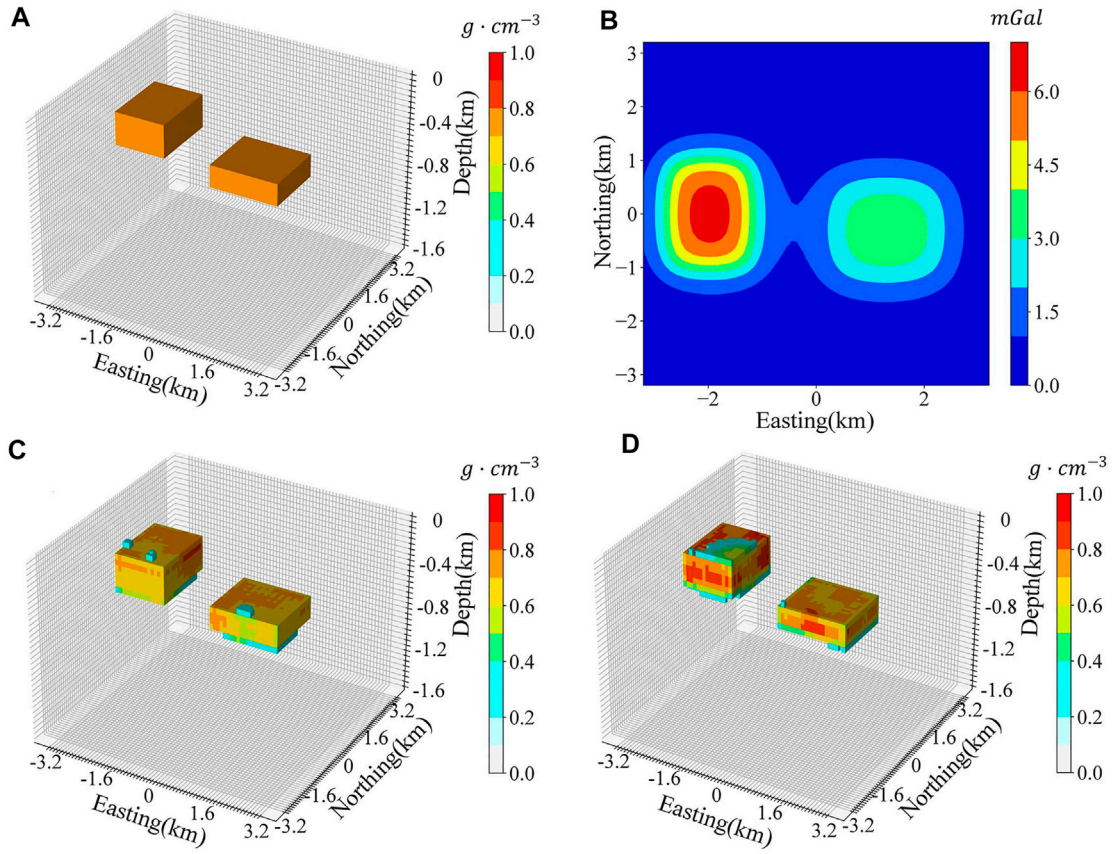

FIGURE 5
Horizontal distributed density model **(A)** The shape of the horizontal distributed density model; **(B)** Gravity anomalies that correspond to the true model; **(C)** The model recovered by DGV-Net; **(D)** The model recovered by MGV-Net.

The second metric index is to assess the gravity anomaly generated by the predicted density model. We introduce the mean squared of data misfit to express how the recovered gravity fits the true gravity anomaly in each prediction, which shows in Eq. 5.

$$\bar{\omega} = \frac{1}{N}\sum_{i=1}^{N}\left(\bar{d}_i - d_i\right)^2 \tag{5}$$

where N is the number of gravity anomaly data, d_i is the ith true gravity anomaly, $\bar{d}_i$ is the ith predicted gravity.

3 Training datasets

3.1 Voxel modeling

In geophysical research, it is necessary to modeling the research object and then parameterization the characteristics of the geophysical field source through a number of models. In gravity field inversion, we generally use a series of regular bodies to approximate the field source model for different research problems, and each regular body has a specific density. Common regular density models include sphere model, cylinder model, and rectangular prism model.

In this study, to describe the characteristics of the stochastic distribution of density contrast flexibly, we simulated the subsurface structure with regularly arranged rectangle prism cells according to a certain grid spacing, and the gravity data are measured from fixed ground observation points. The density model and the observing system illustrated in Figure 2. Borrowing the term pixel in two-dimensional images, we refer to each density prism in three-dimensional space as a voxel. The relationship between the gravity anomaly and the density voxels can be expressed as:

$$\begin{bmatrix} d_1 \\ d_2 \\ d_3 \\ \vdots \\ d_N \end{bmatrix} = \begin{bmatrix} \gamma_{1,1} & \gamma_{1,2} & \gamma_{1,3} & & \gamma_{1,M} \\ \gamma_{2,1} & \gamma_{2,2} & \gamma_{2,3} & \cdots & \gamma_{2,M} \\ \gamma_{3,1} & \gamma_{3,2} & \gamma_{3,3} & & \gamma_{3,M} \\ & \vdots & & \ddots & \vdots \\ \gamma_{N,1} & \gamma_{N,2} & \gamma_{N,3} & \cdots & \gamma_{N,M} \end{bmatrix} \begin{bmatrix} m_1 \\ m_2 \\ m_3 \\ \vdots \\ m_M \end{bmatrix} \tag{6}$$

where d_i is the gravity datum at i th observation station, m_j is the density contrast of j th prism, $\gamma_{i,j}$ is the kernel operator, N is the number of observation points, and M is the number of voxels.

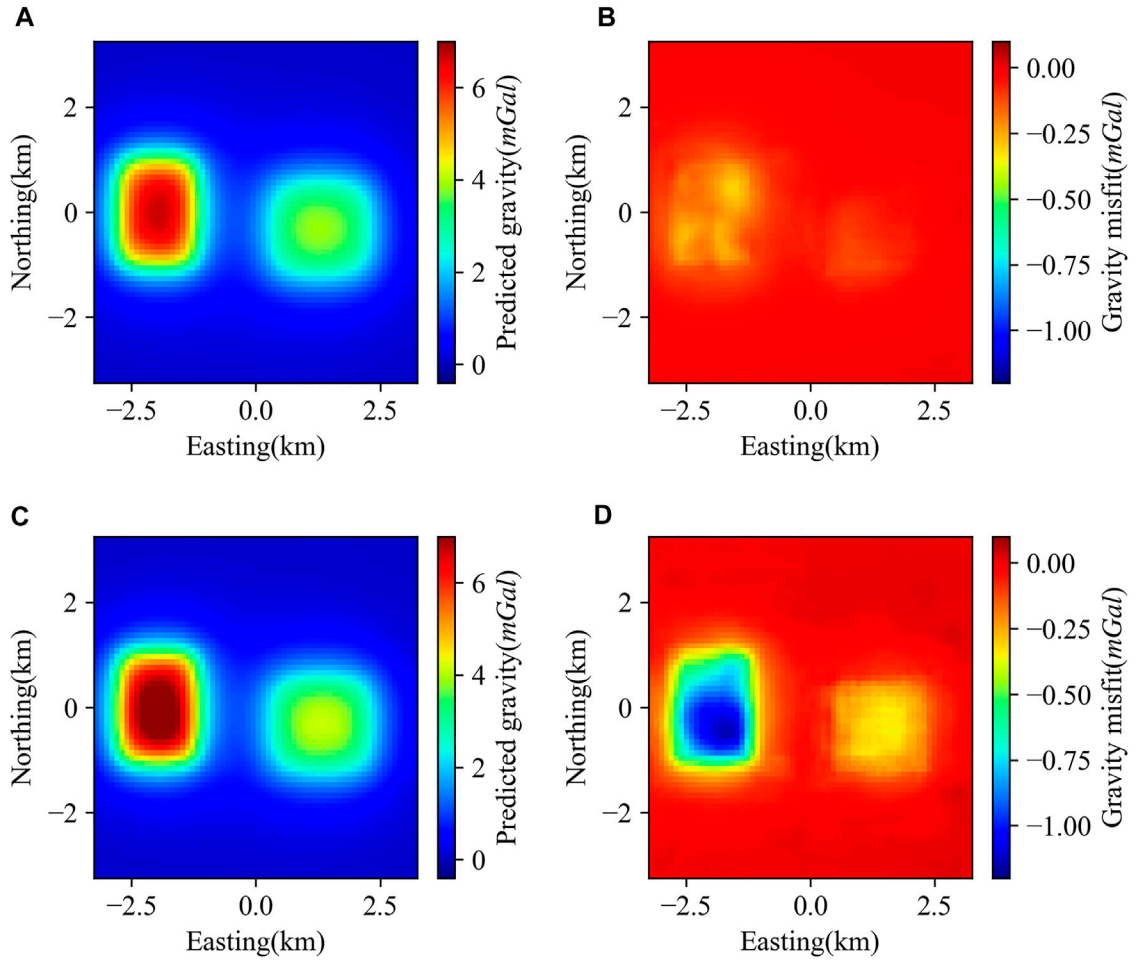

FIGURE 6
Predicted gravity anomaly and gravity misfit characteristics of horizontal distributed model **(A)** Gravity anomaly calculated by density contrast predicted by DGV-Net; **(B)** Gravity anomaly misfit produced by DGV-Net; **(C)** Gravity anomaly calculated by density contrast predicted by MGV-Net; **(D)** Gravity anomaly misfit produced by MGV-Net.

TABLE 3 The evaluating indicators of recovered horizontal distributed model.

	Model relative error (ε)	MSE of gravity ($\bar{\omega}$)
DGV-Net	.14036	.0055
MGV-Net	.14099	.063

The kernel operator is defined by the volume of the voxel, density contrast, the location of observation points, and the position of the voxel. The kernel operator $\gamma_{i,j}$ can be expressed as follows:

$$\gamma_{i,j} = G\int_{z_s}^{z_e}\int_{y_s}^{y_e}\int_{x_s}^{x_e}\frac{\Delta\rho\left(z_p - z\right)}{r^3}dxdydz \tag{7}$$

where $G = 6.67 \times 10^{-1} N \cdot m^2 \cdot kg^{-2}$ is the gravitational constant, x, y, z are coordinates of the density body in the three directions respectively, $r = \sqrt{(x_p - x)^2 + (y_p - y)^2 + (z_p - z)^2}$ represent the distance from the field source to the observed position. While the density is constant, which mean $\Delta\rho = \rho_c$, Eq. 7 becomes (Nagy et al., 2000):

$$\gamma_{i,j} = \rho_c G|||\left(x_p - x\right)\ln\left[\left(y_p - y\right) + r\right] + y\ln\left[\left(x_p - x\right) + r\right] - z\tan^{-1}\frac{\left(x_p - x\right)\left(y_p - y\right)}{\left(z_p - z\right)r}\Big|_{x_s}^{x_e}\Big|_{y_s}^{y_e}\Big|_{y_s}^{y_e} \tag{8}$$

3.2 Datasets generation

The ML model training is necessary to utilize large enough labeled datasets. Because the conventional Green's function between the gravity response and field source cannot be

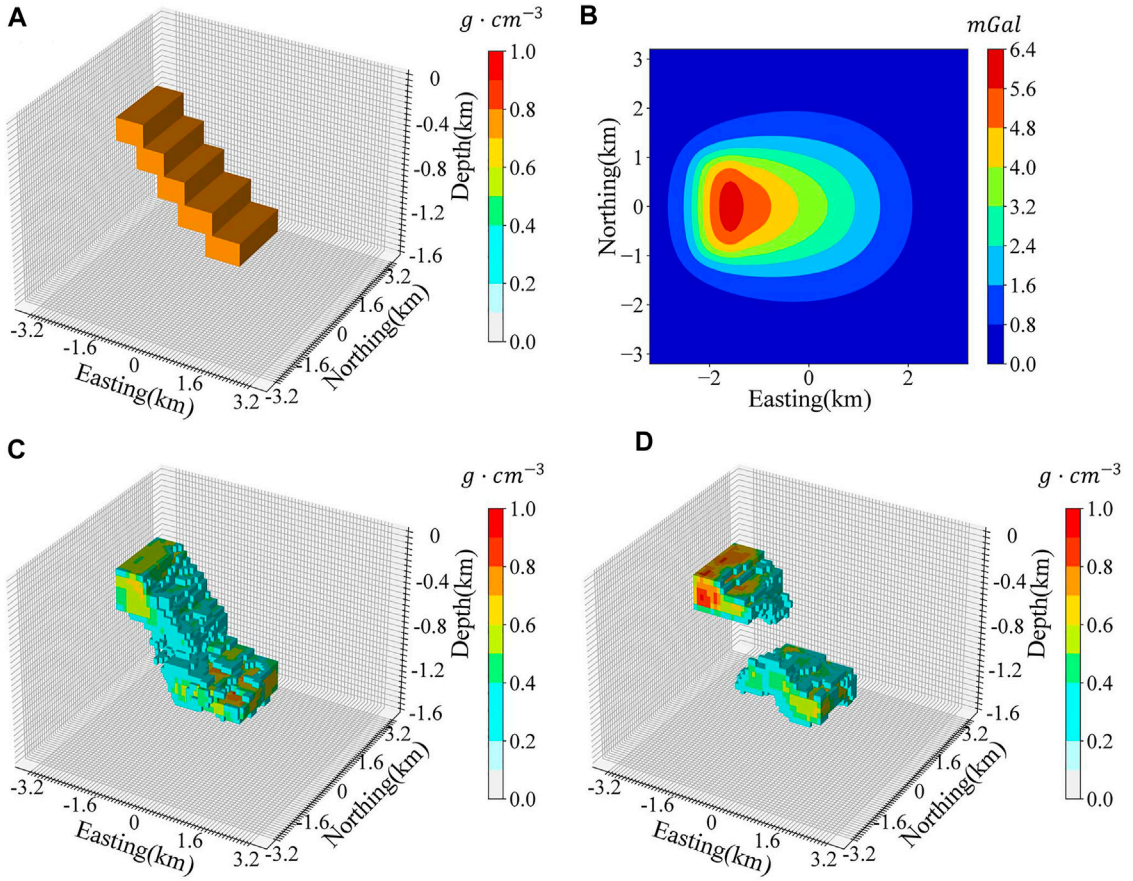

FIGURE 7
Dipping dyke density model **(A)** The shape of the dipping dyke density model; **(B)** Gravity anomalies that correspond to the true model; **(C)** The model recovered by DGV-Net; **(D)** The model recovered by MGV-Net.

TABLE 4 The evaluating indicators of recovered dipping dike model.

	Model relative error (ε)	MSE of gravity ($\bar{\omega}$)
DGV-Net	.39563	.1079
MGV-Net	.45065	.0412

directly transformed to the weight values of the designed CNN model. In the training process, an abundant training dataset needs to be used to build the mapping relationship between the input and output. The features of the training datasets directly determine the application scenarios of the model. In this study, we trained the GV-net model with plenty of voxels by the presupposed prior density assumption as the output of the GV-Net and calculated the corresponding gravity anomaly at the observed grid as the input of the GV-Net. The input gravity anomaly was the superposition of all voxel anomalies in one field source. If repeated this generation time by time, the location of a voxel in the field source model is stochastic for simulating various density distribution situations as much as possible.

Figure 3 shows four randomly generated density models. The models are composed of rectangle prisms of different scales and arrangements, so theoretically, they can approximately represent the distribution of density anomalies with different shapes. In this study, the size of each voxel is 50 m×100 m×100 m, and the density contrast of each block is .5–1.0 g/cm^3. A total of 19,200 sets of data are used for training and 2,000 sets of data were used for validation for both DGV-Net and MGV-Net.

4 Result

4.1 Model training

Figure 4 shows the loss function and model relative error of DGV-Net and MGV-Net, respectively. To reduce time costs and

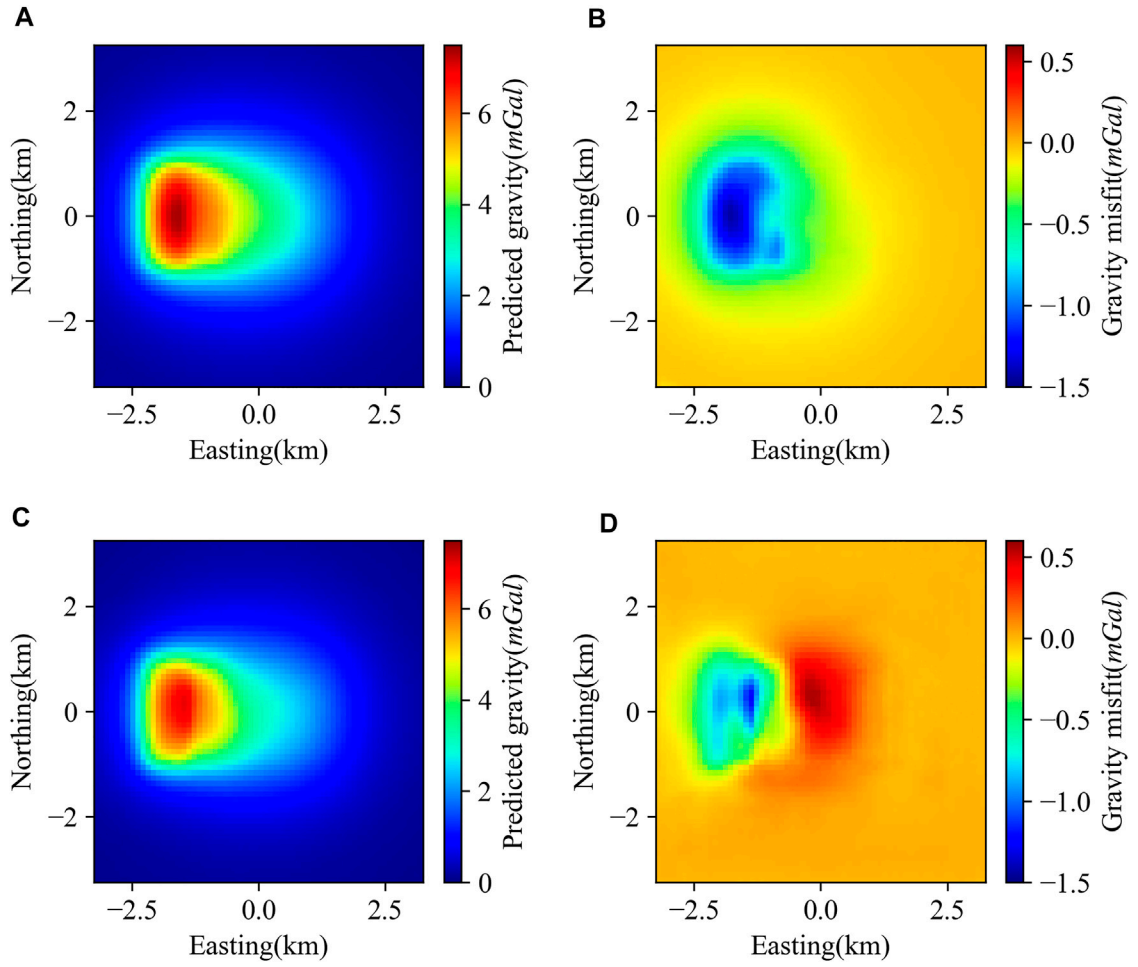

FIGURE 8
Predicted gravity anomaly and gravity misfit characteristics of dipping dyke model **(A)** Gravity anomaly calculated by density contrast predicted by DGV-Net; **(B)** Gravity anomaly misfit produced by DGV-Net; **(C)** Gravity anomaly calculated by density contrast predicted by MGV-Net; **(D)** Gravity anomaly misfit produced by MGV-Net.

ensure the stability of the loss curves and error curves, the loss value and error on curves are calculated by the prediction results of 200 random samples from relevant datasets, rather than all datasets.

During the training of DGV-Net and MGV-Net, both the loss curves and error curves decreased smoothly with the increase of epochs, but there are a few different behaviors between training datasets and validation datasets. The curves associated with validation datasets (Orange curves) tend to be stable when the epochs reach a certain value, while the curves associated with training datasets (Blue curves) are not stable until the end of epochs. These features illustrated that for a random model, which are most likely not in the training datasets, the GV-Net predicts accuracy restricted to a level because of using the finite training datasets.

Moreover, the validation loss curve of DGV-Net reaches to a steady state faster than MGV-Net, which means the Dice loss is more conducive to the convergence of the GV-Net model.

The model relative error curves in Figure 3 and Figure 3 show that the prediction accuracy of DGV-Net is better than MGV-Net. Therefore, we can estimate that DGV-Net will have better performance than MGV-Net for anomalous models that are not in the training datasets.

Table 2 shows the time required for GV-Net training process and single prediction. We can see that the training time when employing the root mean square loss function is significantly less than that using the Dice loss function. The time required for single prediction using the trained model is far less than 1s. Consequently, when the GV-Net is used for inversion problems, as long as the model is well-trained, fast

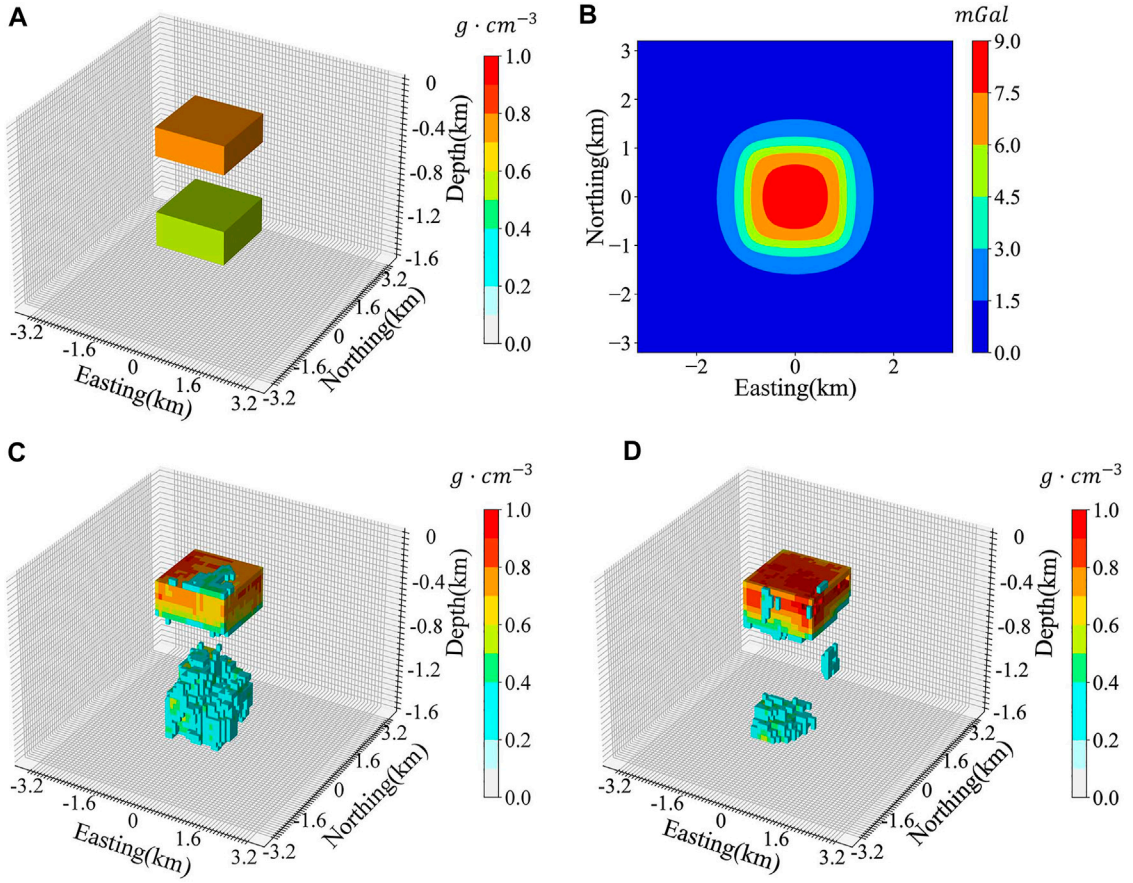

FIGURE 9
Vertical distributed model **(A)** The shape of the vertical distributed density model; **(B)** Gravity anomalies that correspond to the true model; **(C)** The model recovered by DGV-Net; **(D)** The model recovered by MGV-Net.

inversion can be executed for the same type of problems. Comparison with other research for fast inversion solutions, such as compressive inversion (Foks et al., 2014), and adaptive mesh inversion (Davis and Li, 2011). Our approach reflects sufficient efficiency.

4.2 Model validation

In order to illustrate the inversion effect of GV-Net more intuitively, we designed three typical density models to evaluate the performance of GV-Net with two different loss functions. The three models were the horizontal distributed density model, the dipping dyke density model, and the vertical distributed density model respectively. The residual density and model grid setting are consistent with the training datasets. To clearly show the shape of the retrieved model, only the voxels with a density greater than or equal to 0.3 g/cm^3 are drawn for the results in the following figures.

TABLE 5 The evaluating indicators of recovered vertical distribute density model.

	Model relative error (ε)	MSE of gravity ($\bar{\omega}$)
DGV-Net	.347	.0494
MGV-Net	.39653	.1014

1) Horizontal distributed density model

Generally, gravity is sensitive to the lateral variations of the density contrast, so we designed a model with two density blocks that are totally separate in horizontal (Figure 5A) to test the ability of GV-Net to identify lateral density variations. The gravity response of this model (Figure 5B) sharply depicts the contour of this model in the horizontal direction. The results (Figures 5C, D) demonstrated that both DGV-Net and MGV-Net can predict the outcome with reasonable accuracy for the density contrast with horizontal distribution characteristics.

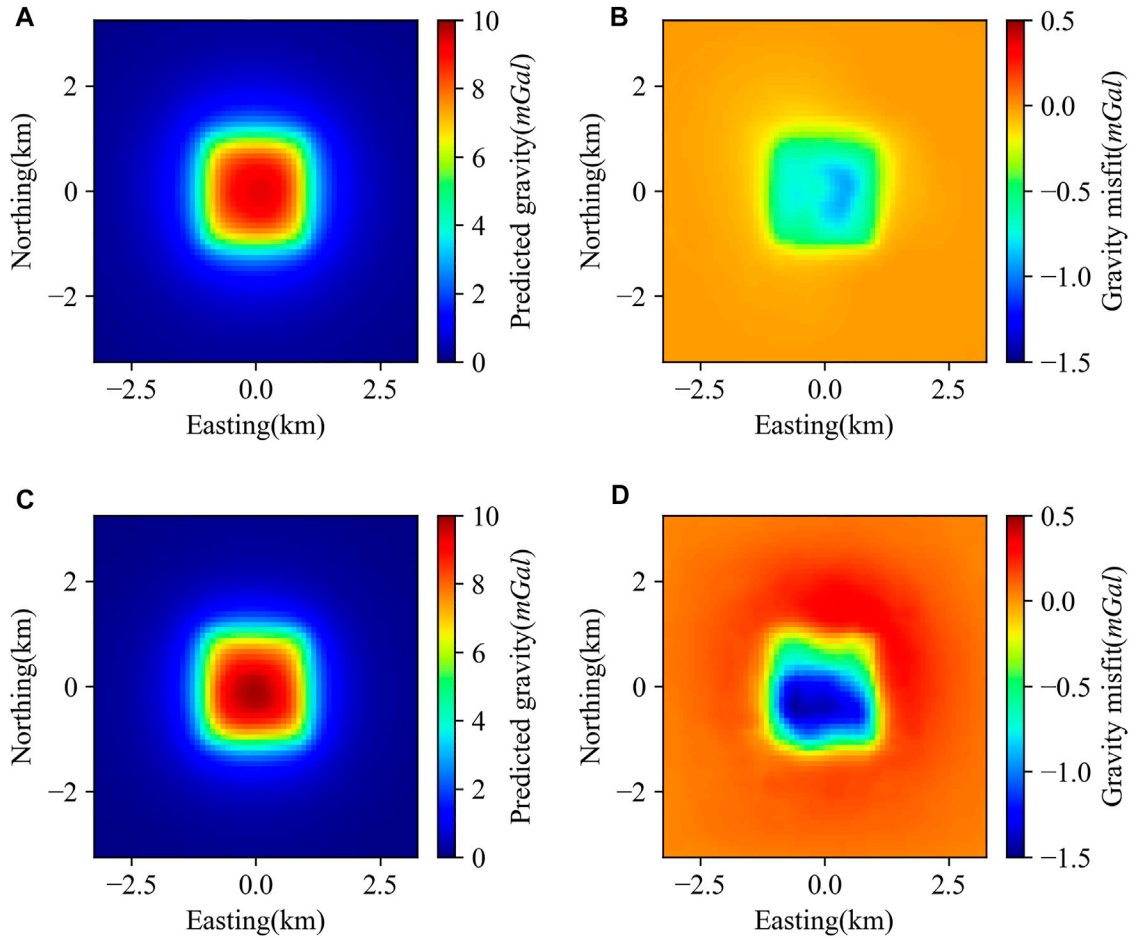

FIGURE 10
Predicted gravity anomaly and gravity residual characteristics of vertical distributed model **(A)** Gravity anomaly calculated by density contrast predicted by DGV-Net; **(B)** Gravity anomaly misfit produced by DGV-Net; **(C)** Gravity anomaly calculated by density contrast predicted by MGV-Net; **(D)** Gravity anomaly misfit produced by MGV-Net.

Figure 6 shows the forward gravity and gravity misfit from predicted density contrast. The max misfit in recovered gravity is less than 5% of the maximum of the input gravity for the DGV-Net model, and the max error in gravity recovered is reach 15% due to the left block error in MGV-Net.

Table 3 summarizes the model relative error and the mean square error of recovered gravity. From Table 3, we found that the model relative errors don't have a significant difference between DGV-Net and MGV-Net, this feature may illustrate that the two sorts of loss functions we used in this study have no distinct differences for GV-Net to predict simple density model.

2) Dipping dyke density model

The dipping dyke model is a classical 3D density model that can be used to evaluate the effectiveness of inversion methods (Zhu et al., 2020; Peng and Liu, 2021). Figure 7A illustrates a dipping dyke model and Figure 7B is the forward gravity. Figure 7C and Figure 7D are the inversion results predicted by DGV-Net and MGV-Net. Table 4 lists the relative error of the predicted models and the mean squared of gravity misfit. The prediction of DGV-Net recovered the shape of the true model mostly but exists a big bias in density value. The prediction of MGV-Net did not retrieve the true shape of the real model and the density value is also incorrect. But we found that the gravity misfit was not so bad as the density model, both models gave acceptable gravity misfit.

Figure 8 shows the predicted gravity and gravity misfit of the dipping dyke model. From Figures 8A, C, the predicted gravity anomalies are generally consistent with input gravity anomalies, but the gravity anomalies misfit have obvious non-Gaussian characteristics (Figures 8B, D).

In our training datasets, considering the generation strategy of our density model, models like dipping dyke are very rare. The GV-Net can recover this dipping dyke model proving that our method has the power to image the complicated density models even if they were not included in the training datasets.

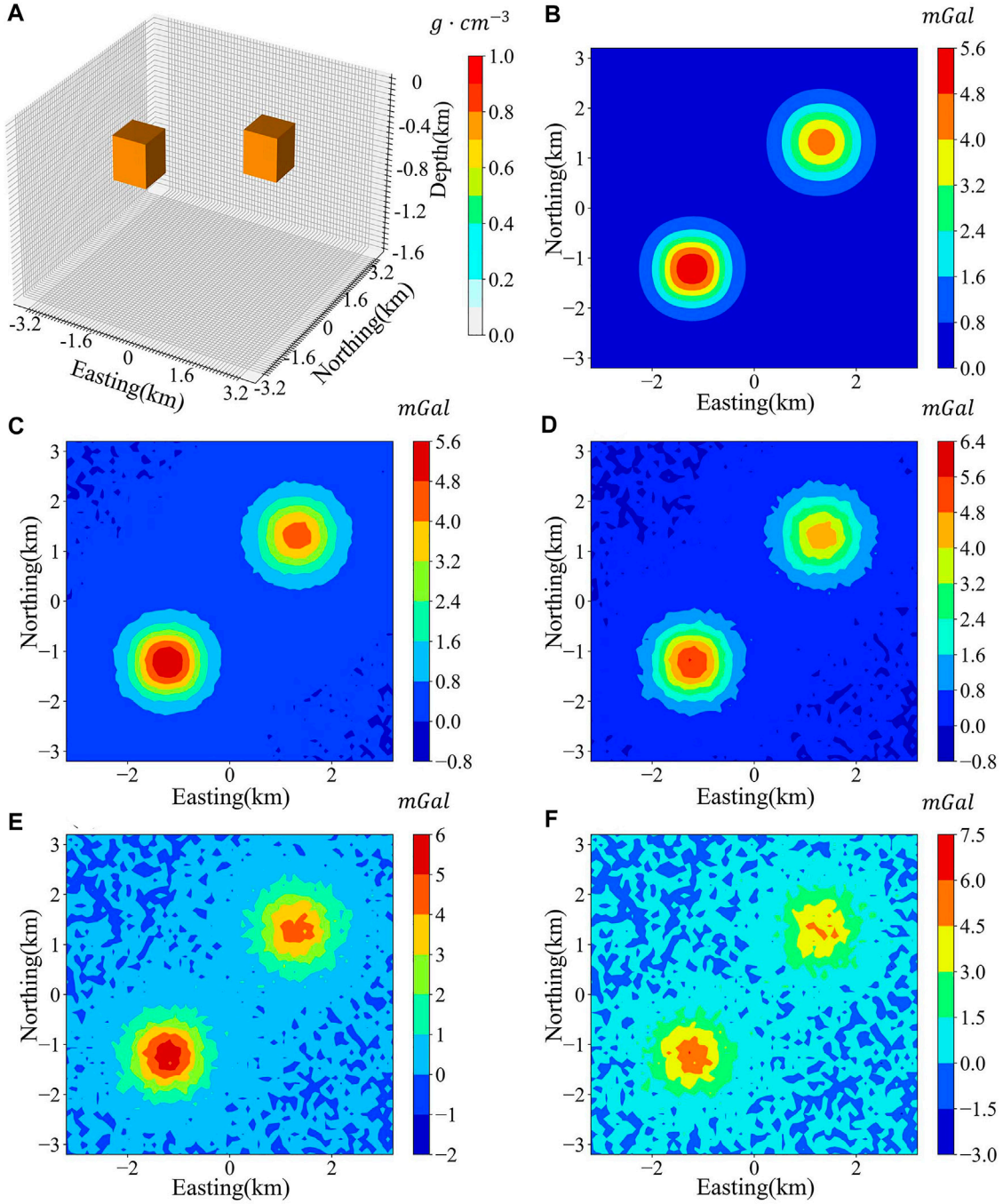

FIGURE 11
The density model and theoretical gravity with different noise levels. **(A)** The true model; **(B)** Gravity with noise-free; **(C)** Gravity with 1% Gaussian noise; **(D)** Gravity with 2% Gaussian noise; **(E)** Gravity with 5% Gaussian noise; **(F)** Gravity with 10% Gaussian noise.

3) Vertical distributed model

It is tough to revive vertical density information through gravity inversion. The conventional gravity inversion methods use the depth weighting function to control the density located in a suitable depth, but this process is depending on the researchers' experience. To verify the performance of GV-Net to separate the density distribution in the vertical direction, we design an extreme vertical density model which means the different bodies have different depths but the same

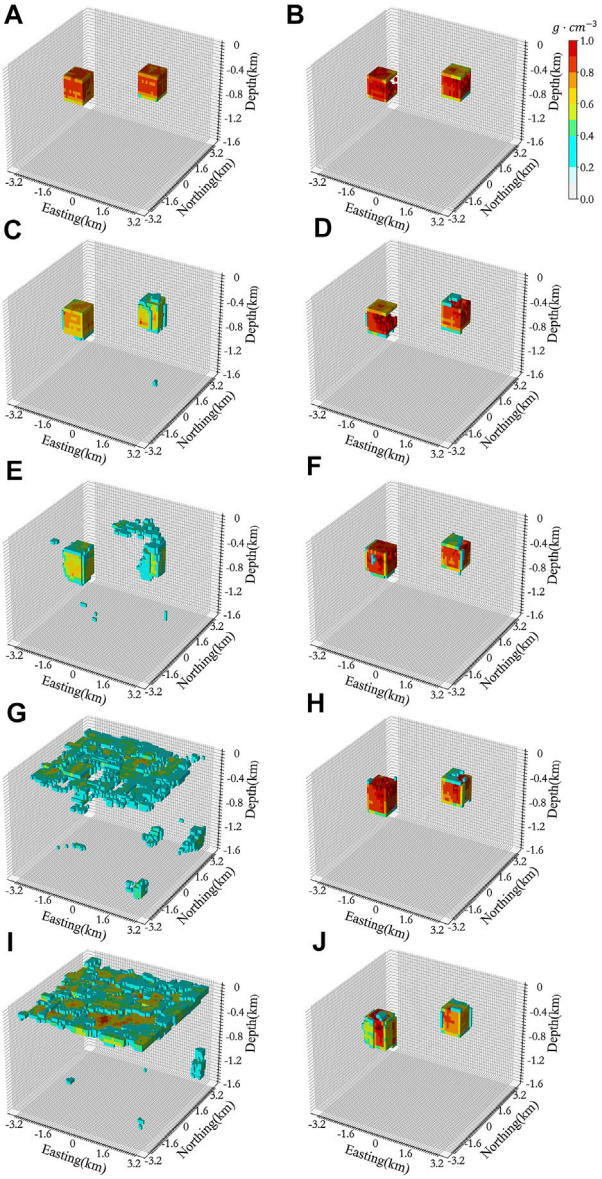

FIGURE 12
Results predicted by DGV-Net and NDGV-Net with various noise contained gravity data. Fig **(A)**, **(C)**, **(E)**, **(G)** and **(I)** are the DGV-Net inversion results when the noise levels are 0%, 1%, 2%, 5% and 10%, respectively; Fig **(B)**, **(D)**, **(F)**, **(H)** and **(J)** are the NDGV-Net inversion results when the noise levels are 0%, 1%, 2%, 5% and 10%, respectively.

horizontal position (Figure 9A). It is difficult to intuitively retrieve any vertical characteristics from the forward gravity (Figure 9B).

Table 5 summarized the model relative error and mean squared error of recovered gravity, from these two metrics, the DGV-Net has better performance in separating the density bodies in the vertical direction. Figure 9C and Figure 9D show the inversion results, the shallow body is well predicted by both DGV-Net and MGV-Net, but for the deeper body, the DGV-Net shows better results than MGV-Net.

The predicted gravity and gravity misfit of the vertical distributed model are shown in Figure 10. The gravity misfit produced by MGV-Net is obviously bigger than that obtained by DGV-Net.

TABLE 6 The relative error(ε) of recovered models under different noise contained gravity for NDGV-Net and DGV-Net.

Noise level	0%	1%	2%	5%	10%
DGV-Net	.0059	.1768	.3354	.6515	.6888
NDGV-Net	.1479	.1398	.1777	.186	.2892

4.3 Noise effect

Actual gravity data is affected by various factors, such as the observation environment, instrument features, and human operations, which inevitably contain a certain degree of noise. In most cases, these noises are stochastic. We assumed that the noise is Gaussian noise with zero mean. We found that the DGV-Net mostly outperforms the MGV-Net in the model prediction accuracy in section 4.1. Therefore, in this part, we chose DGV-Net to test the robustness to the noise of our method.

We first use the well-trained DGV-Net model in section 4.1 to deal with the noise-contained gravity. The true density model is shown in Figure 11A, and the forward gravity contaminated by 0%, 1%, 2%, 5%, and 10% Gaussian noise are shown in Figures 11B–F respectively. The results predicted by DGV-Net are shown in Figures 12A, C, E, G, I, these results illustrated that the DGV-Net model can accurately predict the density structure while the noise is less than 2%, and this model can't retrieve any useful information when the noise increases to 5%.

We reproduced the training datasets that contain different noise strengths. 0%, .1%, .2%, .3%, .4%, .5%, 1%, 1.5%, 2%, 4% and 6% Gaussian noise was randomly added in the process of generating the training datasets, the occurrence probability of 0% noise level is 3/13, and the occurrence probability of other noise levels is 1/13. For the convenience of expression, we call the DGV-Net model trained by noise-contained datasets as NDGV-Net.

The results predicted by NDGV-Net are shown in Figures 12B, D, F, H, J, the density contrast can be effectively recovered even with the noise level up to 10%. However, the NDGV-Net model can restore the contour of density volume well, but it sacrifices the accuracy in density value prediction. Table 6 shows that the relative error of the result predicted by NDGV-Net for noise-free gravity is far greater than the result predicted by DGV-Net. These features illustrated that the robustness to noise of GV-Net is mainly controlled by the training datasets. It is important to balance the robustness and prediction accuracy through

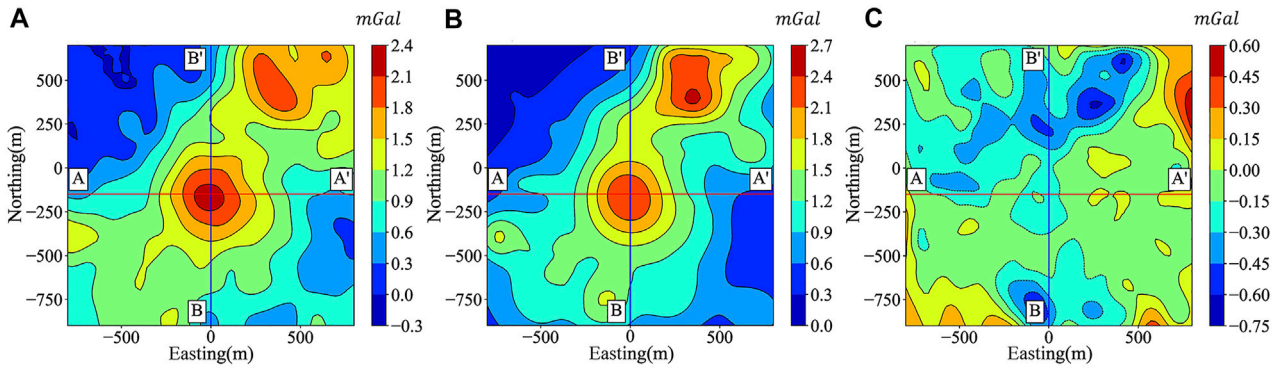

FIGURE 13
(A) Residual gravity anomaly map of the San Nicolas deposit (Huang et al., 2021); **(B)** Predicted gravity from invert density model; **(C)** Characteristics of gravity anomaly misfit.

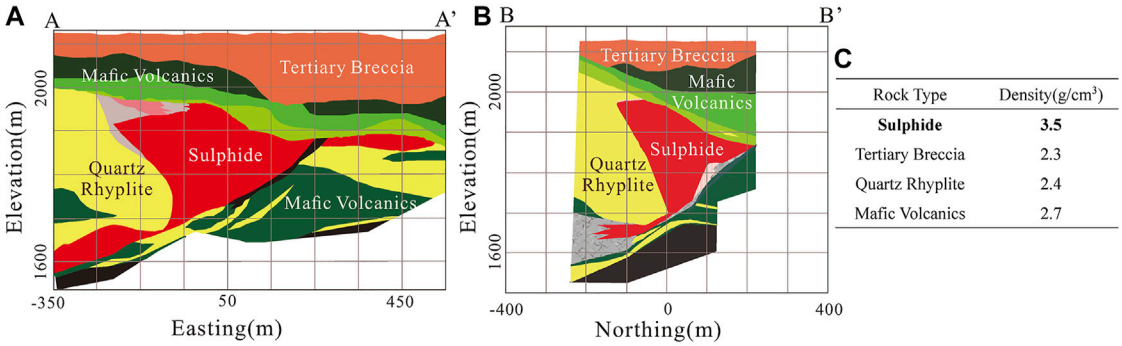

C

Rock Type	Density(g/cm³)
Sulphide	**3.5**
Tertiary Breccia	2.3
Quartz Rhyplite	2.4
Mafic Volcanics	2.7

FIGURE 14
(A) Geologic cross-section along the AA′ line; **(B)** Geologic cross-section along the BB′ line; **(C)** Density of the major rock units.

special noise setting of the training datasets for a specific inversion problem.

5 Case study

To verify the ability of the proposed method in this study to deal with real scenarios, we employed GV-Net to image the San Nicolas sulfide copper-zinc mine in Zacatecas, Mexico. The mining area has been studied in detail by different scholars using different inversion methods (Phillips et al., 2001; Lelièvre and Oldenburg, 2009; Zelin et al., 2019; Huizhen et al., 2021).

The residual Bouguer gravity anomaly is shown in Figure 13A, and the geological profiles in the location of AA′ and BB’ are shown in Figure 14, which are interpreted from logging data. On the basis of the size of the research region, orebody burial depth, and surrounding rock density characteristics, we regenerated the training datasets suitable for this mining area, and the new training datasets still divide the model into 32 × 64 × 64 three-dimensional cells, the size of a single cell is 25 m × 25 m × 25 m, and the density of the training datasets varies from .7 to 1.2 g/cm^3 on the basis of prior information from the geological profiles. Considering that the actual data may be containing noise, the same noise addition strategy is adopted in the training datasets as in the NDGV-Net training datasets.

We intercepted six two-dimensional profiles of the 3D density structure along the AA’, BB’ positions and its left and right 100 m, respectively. The corresponding cross-section results are shown in Figure 15, in order to clearly highlight the orebody position, only the voxels with a density greater than 0.6 g/cm^3 is shown in Figure 15.

Figures 13B, C are the predicted gravity anomalies and gravity misfit, respectively. We can see that the predicted gravity anomalies and true gravity anomalies have the same

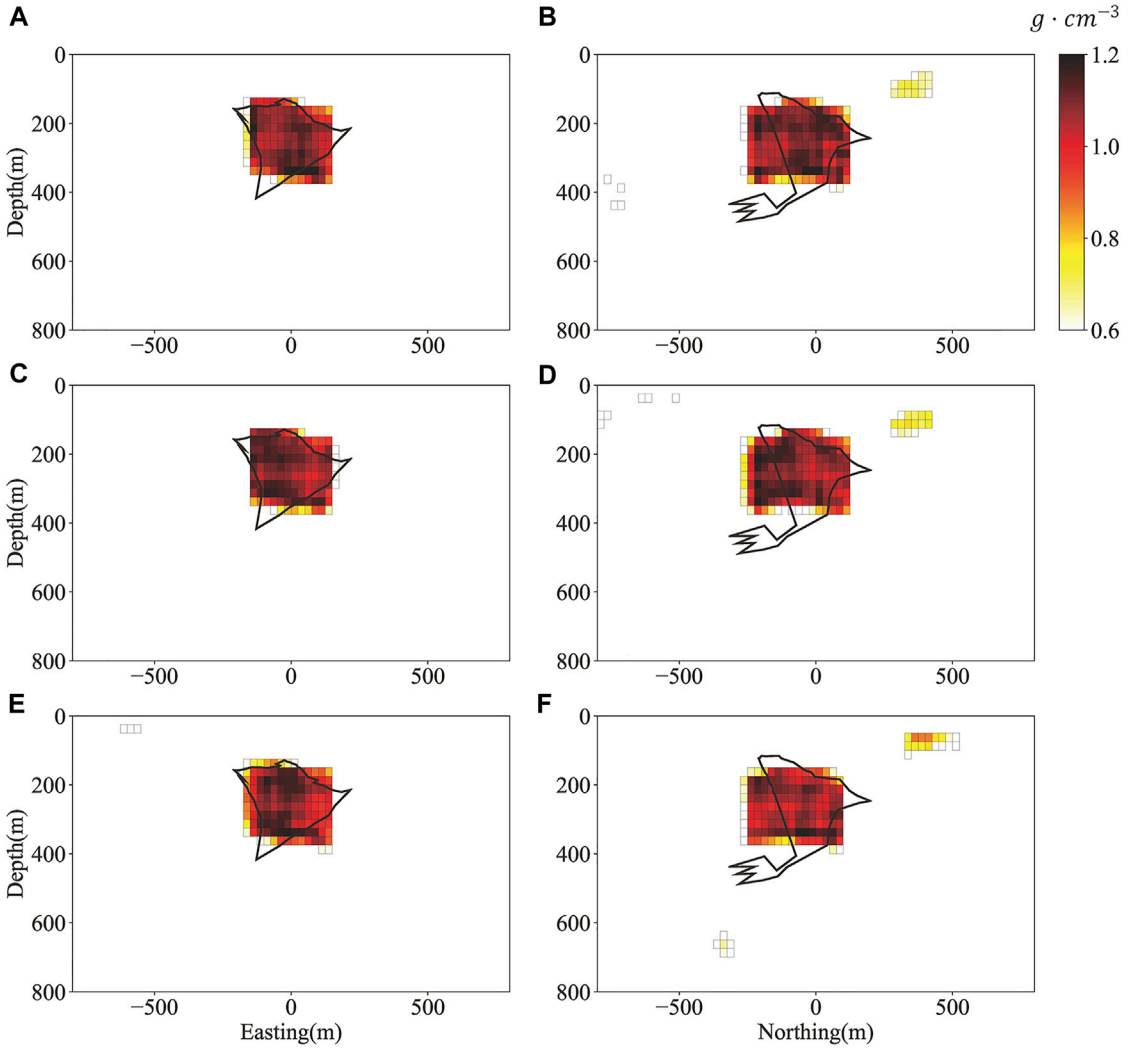

FIGURE 15
Inversion result at different cross-sections (The black lines indicate the true outline of the sulfide deposit) **(A)** Density Cross-section at AA′ line; **(B)** Density Cross-section at BB′ line; **(C)** Density Cross-section at 100 m south of AA′ line; **(D)** Density Cross-section at 100 m west of BB′ line; **(E)** Density Cross-section at 100 m north of AA′ line; **(F)** Density Cross-section at 100 m east of AA′ line.

change trend, but there is a certain large and non-normal distribution of gravity misfit characteristics.

The predicted results in Figure 15 shows that our inversion method accurately restores the orebody position. The ore body size is basically the same as the real ore, but the ore body morphology is more like a regular prism, which should be related to the characteristics of the training datasets adopted in this article. Compared to the application of traditional inversion methods in this area (Phillips et al., 2001; Zelin et al., 2019; Huizhen et al., 2021), our method obtained a desirable result through the trained ML model based on targeted training datasets and no longer rely on the subjective experience of researchers.

6 Conclusions and discussions

This study purposes a CNN model named GV-Net, which implements inversion of the residual Bouguer gravity anomaly based on the ML technique. We first analyzed the effect of different loss functions on the GV-Net model and evaluated the prediction accuracy by three typical density contrast models. Then we tested the robustness to noise of our method by the noise or noise-free training datasets. Ultimately, the practicability of the method has been demonstrated by actual mining area data. The main conclusions of this research are as follows:

1) The selection of the loss function will influence the training speed, convergence characteristics, and model prediction accuracy. In this study, the $Dice_{Loss}$ function has better performance in model prediction accuracy, and the MSE_{Loss} needs less time for the training process. Therefore, when we try to solve a practical problem, an appropriate loss function should be selected on the basis of weighing the prediction accuracy of the model against the training time cost of the model.
2) From the three synthetic tests, our GV-Net model has shown the ability to revive the shape of shallow density contrast, but it still lacks sufficient recovery for the abnormal density distribution of complex structures or abnormal bodies with obvious vertical distribution characteristics. There is no significant difference between DGV-Net and MGV-Net in predicting simple density models, but for sophisticated models, the DGV-Net has better performance in depicting the shape of density blocks. The mean squared error of gravity is acceptable for three synthetic models, but it seems independent of the relative error of the model. This feature may be caused by the absence of gravity constraint in the model training phase.
3) The robustness to noise of the GV-Net is closely related to the noise characteristics in the training datasets. While training datasets are designed by reasonable noise control, the anti-noise ability of the model is significantly improved.
4) In the GV-Net model, prior knowledge is directly included in the training dataset, rather than relying on the experience of researchers that is required by traditional inversion methods. When we predict a density anomaly body using the trained model, only the gravity anomaly is required as input, and we will obtain a reasonable result.
5) Using the GV-Net model to solve inversion problems, the training process is also time-consuming. But if a suitable AI model with good generalization ability can be achieved, the time needed to invert a density model is very small. The single prediction time of all models in this study is in milliseconds which demonstrated that our method can be used to fast imaging for specific inversion problems.
6) Using GV-Net for inversion of actual mining area data, the results are consistent with previous studies, which demonstrates the practicability of this method.

Although the method proposed in this study can better realize the fast inversion of residual Bouguer gravity anomaly, there are still some problems that need to be further solved, such as how to construct a training dataset that can represent real geologically density distribution better. In addition, in the model prediction process, the gravity data is used as the input to directly invert the three-dimensional density model, and the gravity misfit shown certain non-stochastic characteristics.

Data availability statement

The original contributions presented in the study are included in the article/supplementary material, further inquiries can be directed to the corresponding author.

Author contributions

YL, SC, BZ, and HL designed the research. BZ and YL designed the model and wrote the program code. SC contributed to building the synthetic model and interpretation the inversion result. YL and HL drew figures and tables and wrote the first draft of the manuscript. All authors revised the manuscript and approved the version to be published.

Funding

This work is jointly supported by the National Key R&D Program of China (2017YFC1500503), and the National Natural Science Foundation of China (Grant U1939205, 42004069, 42104090).

Conflict of interest

The authors declare that the research was conducted in the absence of any commercial or financial relationships that could be construed as a potential conflict of interest.

Publisher's note

All claims expressed in this article are solely those of the authors and do not necessarily represent those of their affiliated organizations, or those of the publisher, the editors and the reviewers. Any product that may be evaluated in this article, or claim that may be made by its manufacturer, is not guaranteed or endorsed by the publisher.

References

Andersson, T. R., Hosking, J. S., Perez-Ortiz, M., Paige, B., Elliott, A., Russell, C., et al. (2021). Seasonal Arctic sea ice forecasting with probabilistic deep learning. *Nat. Commun.* 12 (1), 5124. doi:10.1038/s41467-021-25257-4

Bergen, K. J., Johnson, P. A., de Hoop, M. V., and Beroza, G. C. (2019). Machine learning for data-driven discovery in solid Earth geoscience. *Science* 363 (6433), eaau0323. doi:10.1126/science.aau0323

Bosch, M., Meza, R., Jiménez, R., and Hönig, A. (2006). Joint gravity and magnetic inversion in 3D using Monte Carlo methods. *Geophysics* 71 (4), G153–G156. doi:10.1190/1.2209952

Chen, T., and Zhang, G. (2022). Mineral exploration potential estimation using 3D inversion: A comparison of three different norms. *Remote Sens.* 14 (11), 2537. doi:10.3390/rs14112537

Davis, K., and Li, Y. (2011). Fast solution of geophysical inversion using adaptive mesh, space-filling curves and wavelet compression. *Geophys. J. Int.* 185 (1), 157–166. doi:10.1111/j.1365-246X.2011.04929.x

Foks, N. L., Krahenbuhl, R., and Li, Y. (2014). Adaptive sampling of potential-field data: A direct approach to compressive inversion. *Geophysics* 79 (1), IM1–IM9. doi:10.1190/geo2013-0087.1

Fu, G., Gao, S., Freymueller, J. T., Zhang, G., Zhu, Y., and Yang, G. (2014). Bouguer gravity anomaly and isostasy at Western Sichuan Basin revealed by new gravity surveys. *J. Geophys. Res. Solid Earth* 119 (4), 3925–3938. doi:10.1002/2014jb011033

He, S., Cai, H., Liu, S., Xie, J., and Hu, X. (2021). Recovering 3D basement relief using gravity data through convolutional neural networks. *J. Geophys. Res. Solid Earth* 126 (10). doi:10.1029/2021jb022611

Honglei, L., Shi, C., Jiancang, Z., Bei, Z., and Lei, S. (2021). Gravity inversion method base on Bayesian-assimilation and its application in constructing crust density model of the Longmenshan region. *Chin. J. Geophys. Chin.* 64 (4), 1263–1252. doi:10.6038/cjg2021O0130

Huang, R., Liu, S., Qi, R., and Zhang, Y. (2021). Deep learning 3D sparse inversion of gravity data. *J. Geophys. Res. Solid Earth* 126. doi:10.1029/2021jb022476

Huizhen, Y., Jinduo, W., and Qianjun, W. (2021). Gravity inversion based on sparse representation of density model. *Chin. J. Geophys. Chin.* 64 (3), 1061–1073. doi:10.6038/cjg2021O0113

Johannes, W. J., and Smilde, P. L. (2009). *Gravity interpretation: Fundamentals and application of gravity inversion and geological interpretation[M]*. Springer.

Kong, Q., Trugman, D. T., Ross, Z. E., Bianco, M. J., Meade, B. J., and Gerstoft, P. (2018). Machine learning in seismology: Turning data into insights. *Seismol. Res. Lett.* 90 (1), 3–14. doi:10.1785/0220180259

Lelièvre, P. G., and Oldenburg, D. W. (2009). A comprehensive study of including structural orientation information in geophysical inversions. *Geophys. J. Int.* 178 (2), 623–637. doi:10.1111/j.1365-246X.2009.04188.x

Lelièvre, P. G., Farquharson, C. G., and Hurich, C. A. (2012). Joint inversion of seismic traveltimes and gravity data on unstructured grids with application to mineral exploration. *Geophysics* 77 (1), K1–K15. doi:10.1190/geo2011-0154.1

Li, Y. G., and Oldenburg, D. W. (1998). 3-D inversion of gravity data. *Geophysics* 63 (1), 109–119. doi:10.1190/1.1444302

Li, Y., and Oldenburg, D. W. (1996). 3-D inversion of magnetic data. *Geophysics* 61 (2), 394–408. doi:10.1190/1.1443968

Liu, S., Jin, S., Xuan, S., and Liu, X. (2022). 3-D data-space joint inversion of gravity and magnetic data using a correlation-analysis constraint. *Ann. Geophys.* 65. doi:10.4401/ag-8750

Milletari, F., Navab, N., and Ahmadi, S-A. (2016). "V-Net: Fully convolutional neural networks for volumetric medical image segmentation," in 2016 Fourth International Conference on 3D Vision (3DV), 565–571.

Ming, Z., Shi, C., and Yuen, D. (2019b). Waveform classification and seismic recognition by convolution neural network. *Chin. J. Geophys. Chin.* 62 (1), 374–382. doi:10.6038/cjg2019M0151

Ming, Z., Shi, C., LiHua, F., and Yuen, D. A. (2019a). Earthquake phase arrival auto-picking based on U-shaped convolutional neural network. *Chin. J. Geophys. Chin.* 62 (8), 3034–3042. doi:10.6038/cjg2019M0495

Mitra, R., Naruse, H., and Abe, T. (2020). Estimation of tsunami characteristics from deposits: Inverse modeling using a deep-learning neural network. *J. Geophys. Res. Earth Surf.* 125 (9). doi:10.1029/2020jf005583

Nagy, D., Papp, G., and Benedek, J. (2000). The gravitational potential and its derivatives for the prism. *J. Geodesy* 74 (7-8), 552–560. doi:10.1007/s001900000116

Peng, G., and Liu, Z. (2021). 3D inversion of gravity data using reformulated L -norm model regularization. *J. Appl. Geophys.* 191, 104378. doi:10.1016/j.jappgeo.2021.104378

Phillips, N., Oldenburg, D., Chen, J., Li, Y., and Routh, P. (2001). Cost effectiveness of geophysical inversions in mineral exploration: Applications at San Nicolas. *Lead. Edge* 20 (12), 1351–1360. doi:10.1190/1.1487264

Ronneberger, O., Fischer, P., and Brox, T. (2015). U-Net: Convolutional networks for biomedical image segmentation. *Lect. Notes Comput. Sci.* 9531, 234–241. doi:10.1007/978-3-319-24574-4_28

Rosid, M. S., Riska, I. A., and Jaman, A. P. (2020). 3D inversion modelling of gravity data to identify gold mineralization zones in region "X", Pongkor. *IOP Conf. Ser. Earth Environ. Sci.* 481 (1), 012049. doi:10.1088/1755-1315/481/1/012049

Shen, C. (2018). A transdisciplinary review of deep learning research and its relevance for water resources scientists. *Water Resour. Res.* 54 (11), 8558–8593. doi:10.1029/2018wr022643

Turing, A. M. (1950). I.—computing machinery and intelligence. *Mind* LIX (236), 433–460. doi:10.1093/mind/LIX.236.433

Valentine, A., and Kalnins, L. (2016). An introduction to learning algorithms and potential applications in geomorphometry and Earth surface dynamics. *Earth Surf. Dyn.* 4 (2), 445–460. doi:10.5194/esurf-4-445-2016

Wang, Q., Ma, Y., Zhao, K., and Tian, Y. (2020). A comprehensive survey of loss functions in machine learning. *Ann. Data Sci.* 9 (2), 187–212. doi:10.1007/s40745-020-00253-5

Wang, X., Fang, J., and Hsu, H. (2014). Three-dimensional density structure of the lithosphere beneath the North China Craton and the mechanisms of its destruction. *Tectonophysics* 610, 150–158. doi:10.1016/j.tecto.2013.11.002

Zelin, L., Changli, Y., and Yuanman, Z. (2019). 3D inversion of gravity data using Lp-norm sparse optimization. *Chin. J. Geophys. Chin.* 62 (10). doi:10.6038/cjg2019M0430

Zhu, W., Peng, J., Luo, S., Meng, X., Liu, J., and Zhu, C. (2020). Gravity sparse inversion using the interior-point method and a general model weighting function. *Studia Geophys. Geod.* 64 (4), 419–435. doi:10.1007/s11200-020-0831-5

frontiers | Frontiers in Earth Science

TYPE Original Research
PUBLISHED 09 January 2023
DOI 10.3389/feart.2022.1025935

OPEN ACCESS

EDITED BY
Jianzhong Zhang,
Ocean University of China, China

REVIEWED BY
Robert Hawman,
University of Georgia, United States
Derman Dondurur,
Dokuz Eylül University, Turkey

*CORRESPONDENCE
Zhengbo Li,
lizb3@sustech.edu.cn

SPECIALTY SECTION
This article was submitted to Solid Earth Geophysics,
a section of the journal
Frontiers in Earth Science

RECEIVED 23 August 2022
ACCEPTED 26 September 2022
PUBLISHED 09 January 2023

CITATION
Guo W, Li Z, Zhao S and Chen X (2023), Characterizing the shallow structure with the multimodal dispersion curves and the body wave refraction traveltimes from deep seismic sounding data.
Front. Earth Sci. 10:1025935.
doi: 10.3389/feart.2022.1025935

Characterizing the shallow structure with the multimodal dispersion curves and the body wave refraction traveltimes from deep seismic sounding data

Wenbin Guo[1,2], Zhengbo Li[3,4]*, Shuai Zhao[5] and Xiaofei Chen[3,4]

[1]School of Earth and Space Sciences, University of Science and Technology of China, Hefei, China, [2]Geophysical Exploration Center, China Earthquake Administration, Zhengzhou, China, [3]Shenzhen Key Laboratory of Deep Offshore Oil and Gas Exploration Technology, Southern University of Science and Technology, Shenzhen, China, [4]Department of Earth and Space Sciences, Southern University of Science and Technology, Shenzhen, China, [5]Beijing Earthquake Administration, Beijing, China

Deep seismic sounding (DSS) profiles are one of the most powerful tools for detecting crustal structures, and they have been deployed worldwide. Generally, the analysis of DSS data mainly focuses on body waves, while the surface waves are considered noise. We suggest that the surface waves in DSS data can be used to constrain subsurface structures. In this study, we use a DSS profile in the Piedmont and Atlantic Coastal Plain as an example to present the usage of the DSS surface wave. Multimodal dispersion curves were extracted from the DSS data with the Frequency-Bessel transform method, and were used in Monte Carlo joint inversions with body wave refraction traveltimes to constrain the shallow structures. Through the inversion, a horizontal stratum on the surface was identified in the Piedmont, and a two-layer sedimentary structure was identified in the Atlantic Coastal Plain. Comparisons with existing studies verified the accuracy of the shallow structures obtained in this study, demonstrating that the shallow velocity structure could be well constrained with the additional constraints provided by the multimodal dispersion curves. Thus, we believe that further research on the surface waves recorded in DSS surveys is warranted.

KEYWORDS

deep seismic sounding data, frequency-bessel transform method, multimodal dispersion curves, refraction, joint inversion

1 Introduction

Deep seismic sounding profiles (abbreviated as DSS, also known as active source seismic wide-angle reflection/refraction profiles) are an important tool for interpreting crustal and lithospheric structures (Chen et al., 2017). With seismic wide-angle reflections and refractions, DSS profiles can obtain deep crustal and lithospheric velocity structures with little prior information. A large number of DSS profiles have been constructed to

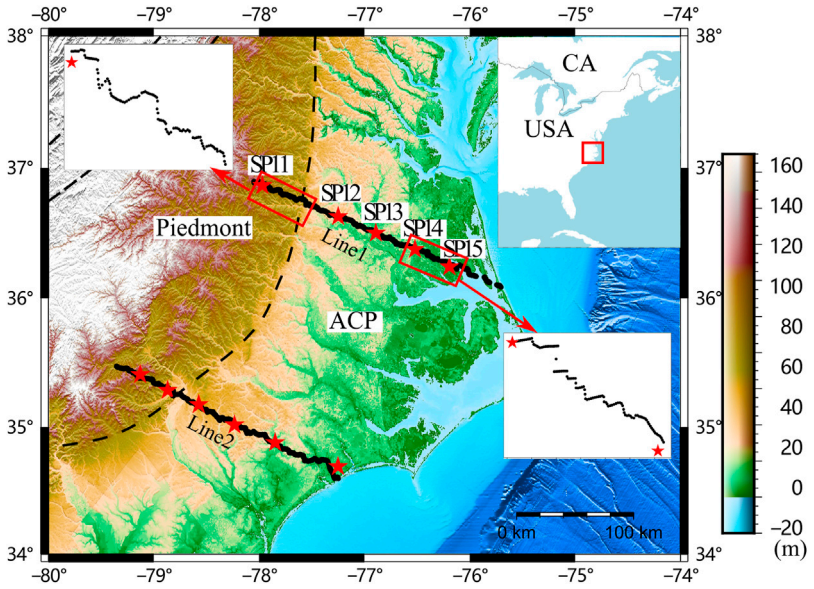

FIGURE 1
Geometry of the ENAM-CSE onshore seismic lines. The black dashed lines represent the geological terrane boundaries, and the red stars represent explosion sources. The black dots represent the seismographs. ACP denotes the Atlantic Coastal Plain. The detailed views in the figure show the crooked-line geometries.

study crustal and lithospheric structures worldwide (e.g., Kosminskaya, 1971; Pakiser & Mooney, 1989; Benz et al., 1992; Mooney et al., 1998; Li et al., 2006; Hübscher & Gohl, 2014; Duan et al., 2016; Lin et al., 2019; Marzen et al., 2019; Guo e al., 2019; Zhao & Guo et al., 2019), and their results were collected to build global crustal models (e.g., CRUST 5.1 presented by Mooney et al., 1998) and regional crustal models (e.g., HBCrust 1.0 presented by Duan et al., 2016; Lin et al., 2019). These models have been used to solve a wide range of both seismological and nonseismological problems (Mooney et al., 1998).

Generally, the P-wave phases and surface waves are clear in most DSS datasets, and they are therefore easy to identify; in contrast, the S-wave phases are relatively difficult to identify. The P-and S-wave phases from the deep crust (e. g. refractions Pn and Sn from the uppermost mantle, and the reflections PmP and SmS from Moho) are mainly used to constrain the middle-lower crust and the uppermost mantle structure, while the P-and S-wave refractions (Pg and Sg) from the basement are used to constrain the upper crustal structure. However, surface waves are always considered coherent noise. In shallow/near-surface geophysics, surface wave analysis is a powerful and widely used tool for detecting subsurface structures (e.g., Socco & Strobbia, 2004; Lu and Zhang, 2006; Park et al., 2007; Maraschini and Foti, 2010). Thus, we suggest that surface waves in DSS data could also be used to constrain shallow/near-surface structures. With the additional information from the surface wave, a finer shallow structure (approximately 0–2 km depth) can be constrained by the DSS data, and it will be helpful for the many studies, such as estimating site response (Schleicher & Pratt, 2021), earthquake ground motion simulation (Fischer et al., 1995; Frankel et al., 2009), receiver function analysis (Zheng et al., 2005; Li et al., 2017; Anggono et al., 2018) and tectonic evolution research (Lawrence & Hoffman, 1993a; Marzen et al., 2020).

In this study, we extracted multimodal dispersion curves from the onshore DSS line in the Atlantic Coastal Plain (ACP) with the Frequency-Bessel transform (F-J) method, and then we performed the joint inversion of the multimodal dispersion curves and the Pg and Sg travel times to constrain the shallow structure. A thin layer in the Piedmont and a two-layer sediment structure in the ACP were identified with the additional constraints provided by the dispersion curves, demonstrating that surface wave analysis is helpful when imaging a higher resolution shallow structure for DSS datasets.

2 Data and methods

2.1 The data

From 2014 to 2015, onshore and offshore seismic surveys were conducted by the Eastern North American Margin Community Seismic Experiment (ENAM-CSE) project, which was funded by NSF-GeoPRISMS. The profiles extended from the eastern Piedmont to the Atlantic Ocean and yielded high quality data (P- and S-body waves and surface waves from both active sources and earthquakes) (Lynner et al., 2020). The seismic line

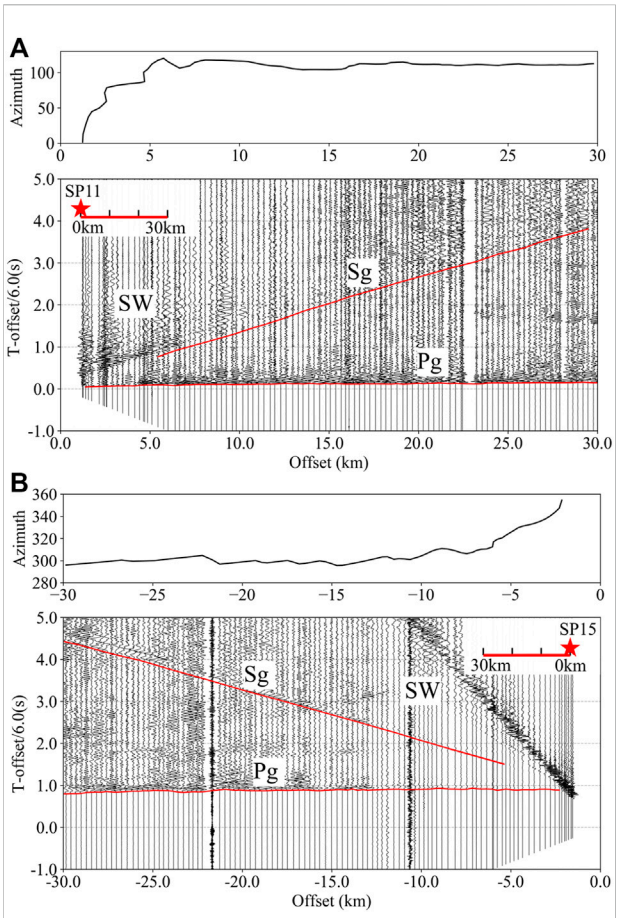

FIGURE 2
Azimuths of the source-receiver raypaths and seismic record sections plotted at a reduction velocity of 6.0 km/s. In the upper right corner of the seismic record sections, the red stars represent the sources, and the seismic record sections are recorded by the seismographs on the red line. Pg and Sg are the P- and S-wave refractions respectively, and the picked traveltimes are marked by the red lines. SW represents the surface wave. **(A)** Azimuths of the SP11 source-receiver raypaths and the corresponding seismic record section. **(B)** Azimuths of the SP15 source-receiver raypaths and the corresponding seismic record section.

used in this study is the north onshore ENAM-CSE seismic line (Line one in Figure 1). Line one is a 220 km-long seismic line located in Virginia and North Carolina, consisting of five borehole explosions (182 kg bulk emulsion in each borehole) and 708 vertical component seismographs (4.5 Hz Geospace GS11D instruments). The spacing between the western two shots (SP11 and SP12) is approximately 70 km, and the spacing between the other shots is approximately 30 km. The seismograph spacing is approximately 320 m. Both P- and S-body waves and surface waves are visible on the seismic record sections (Figure 2; Guo et al., 2019).

Although the acquisition geometry for the ENAM DSS Line one is not straight (Figure 1), the azimuths of the source-receiver raypaths (Figure 2) show that the crooked seismic line could be considered a straight line after ~10 km offset. The seismic line near the source is very crooked, indicating that it is better to treat the velocity structure as laterally homogeneous when we process the seismic data near the sources (Zelt, 1999).

2.2 The conventional DSS data processing method

The seismic record section in the DSS data (Figure 2) is the shot gather plotted with the reduction velocity (V_{red}). The y-axis of the seismic record section map is the reduced time (T_{red}) calculated by the $V_{\mathrm{red}}$and real time:

$$T_{red} = t - offset/V_{red.} \tag{1}$$

With the seismic record sections, we could identify and manually pick the traveltimes according to the characteristics of each seismic phase (Braile and Smith, 1975; Giese et al., 1976). As the first arrivals, the Pg traveltimes are very easy to pick, and then the Sg traveltimes can be picked under the guidance of picked Pg traveltimes (Musacchio et al., 1997). The uncertainties of the picked traveltimes could be evaluated by the signal-to-noise ratio (SNR) of the seismic data (Zelt and Forsyth 1994).

After picking the traveltimes from each shot gather, 1D models are constructed using the traveltimes and the corresponding amplitudes with little prior information (Braile and Smith, 1975; Giese et al., 1976). Then, an initial 2D model along the seismic line is constructed by combining the 1D models, and the preferred 2D model is obtained by the inversion of all the body wave traveltimes.

Because of the large DSS source spacing and the receiver spacing, minimum-structure models should be applied in the 1D/2D model constructions to avoid overinterpreting the data (Constable et al., 1987; Zelt, 1999). The desirability of the minimum-structure model is the principle of Occam's razor: the velocity structure should be as simple, or as smooth as possible to reduce the temptation to overinterpret the data (Constable et al., 1987; Zelt, 1999). To characterize the subsurface structure including the velocity layers with large velocity contrast (e.g., the sediment structure in this study), the minimum-structure model is usually the simplest layered models fitting the DSS data. x^2 is usually set as the misfit function for minimum-structure model inversions (Zelt & Smith, 1992; Zelt & Barton, 1998; Zelt, 1999) and is expressed as follows:

$$x^2 = \frac{1}{n}\sum_i \left[(t_i^o - t_i^s)/e_i \right] \tag{2}$$

where t_i^o represents the *ith* value of the observed body traveltimes, t_i^s represents the *ith* value of the calculated body traveltimes, and e_i is the uncertainty of the value t_i^o. n is the number of picked traveltimes. $x^2 = 0$ represents that the fitting errors are equal to 0, and$x^2 = 1$ represents that the fitting errors

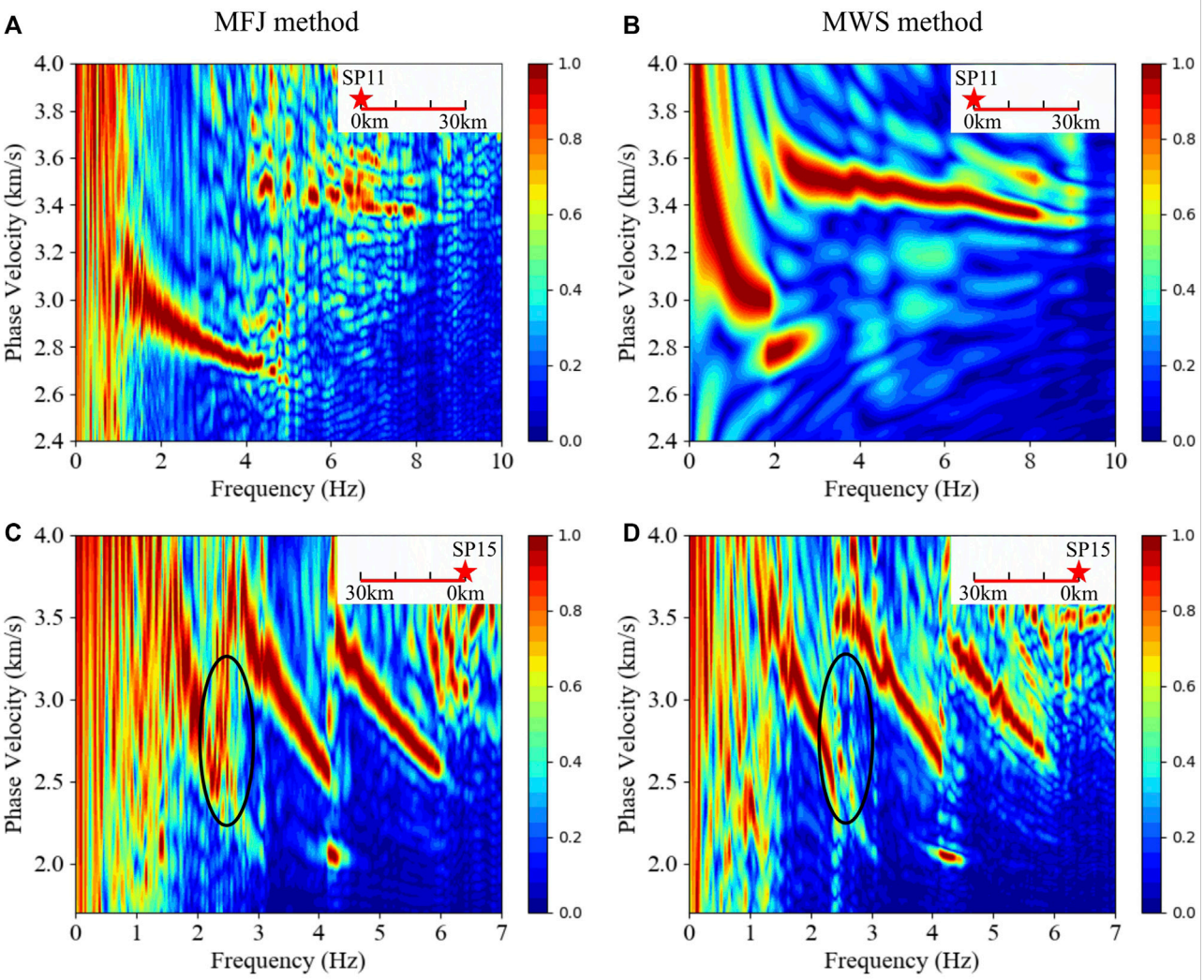

FIGURE 3
F–J spectrograms extracted from 30-km-long seismic record sections. In the upper right corner of each figure, the red star represents the source, and the F-J spectrogram is extracted from the seismic data on the red line. **(A)** and **(B)** are the spectrograms extracted from the SP11 data with the MFJ method and MWS method, respectively. **(C)** and **(D)** are the spectrograms extracted from the SP15 data with the MFJ method and MWS method, respectively.

are equal to the uncertainties of the picked data, indicating that the corresponding model has already satisfied the data (Bevington, 1969; Zelt, 1999).

2.3 Analysis methods for the surface wave

2.3.1 The F-J method for multimodal dispersion curves extraction

The F-J method is an array-based surface wave analysis method designed for extracting multimodal dispersion curves from ambient noise cross-correlation functions (Wang et al., 2019). Li & Chen (2020) extended this method to the application of earthquake records when the azimuth range is controlled within 90°, which could also be used for active source seismic records. The multimodal dispersion curves obtained by this method has been used in the imaging of many shallow/near-surface structures (Wu et al., 2019; Yang et al., 2019;Li et al., 2020) and deep structures (Wu et al., 2020; Zhan et al., 2020; Sun et al., 2021).

A simple formula is used in the F-J method to retrieve the dispersion spectrum ($I(c,\omega)$) from Green's function ($C(r,\omega)$) and is expressed as follows:

$$I(c,\omega) = \int C(r,\omega) J_0(kr) r dr, \tag{3}$$

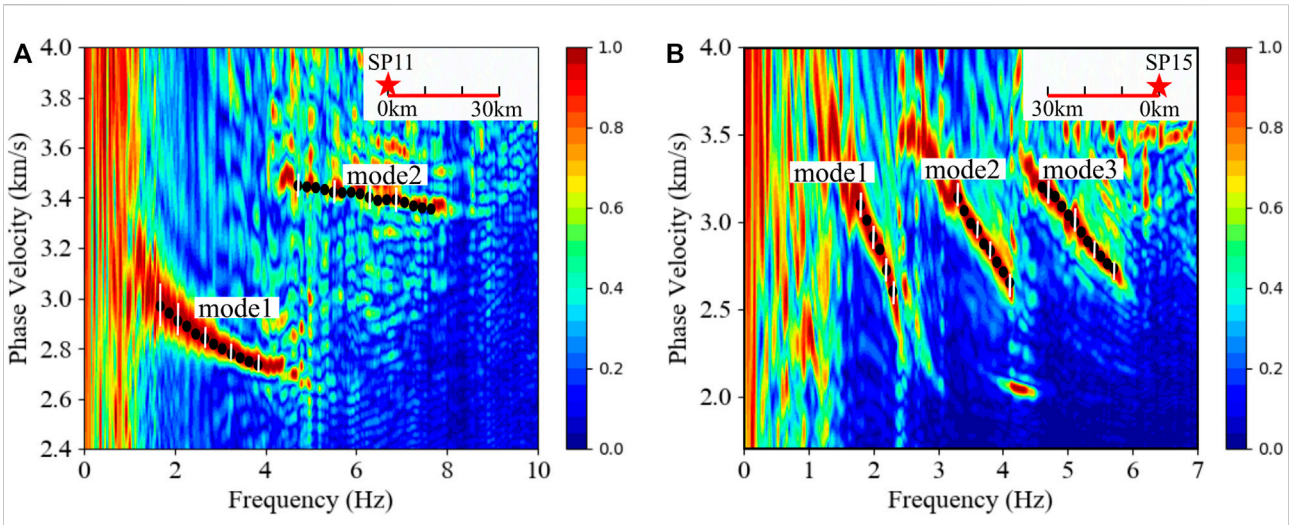

FIGURE 4
The multimodal dispersion curves picked from the F-J spectrograms. The black dots are the picked dispersion curves. The white vertical lines are the uncertainties of the picked dispersion curves. In the upper right corner of each figure, the stars represent the sources, and the F-J spectrograms are extracted from seismic data on the red lines. **(A)** The multimodal dispersion curves picked from the 0–30 km offset seismic record section of SP11. **(B)** The multimodal dispersion curves picked from the 0–30 km offset seismic record section of SP15.

where $J_0(kr)$ is the 0^{th}-order Bessel function of the first type. k represents the wavenumber, r is the distance between the receiver and the source, c denotes the velocity, and $\omega$is the frequency. The surface wave dispersion curves can be identified by the maximum of $I(c,\omega)$. For the observed seismic data, $C(r,\omega)$ is the seismic trace with offset r, so a seismic array is needed to calculate $I(c,\omega)$, and the dispersion curves identified from $I(c,\omega)$ are associated with the average structure beneath the seismic array.

Recently, the F-J method has been improved to include the multiwindow scanning (MWS) method (Li & Chen, 2020; Li et al., 2021a, b) and modified frequency-Bessel transform (MFJ) method (Li et al., 2021b; Xi et al., 2021; Zhou & Chen, 2021). In the MWS method, time windows calculated by the surface wave group velocity are applied on the seismic traces to improve the SNR of the F-J spectrum ($I(c,\omega)$), and additional modes can be resolved by the MWS method (Li & Chen, 2020). In the MFJ method, the Bessel function $J_0(kr)$ is replaced by the Hankel function, and some of the crossed artifacts in the F-J spectrum can be removed (Xi et al., 2021; Zhou & Chen, 2021). In this study, both the MWS and MFJ methods were applied to extract the dispersion curves from the DSS data.

2.3.2 The inversion scheme

Since Pg, Sg and the surface waves are visible in the ACP DSS data, we suggest that the joint inversion of body wave refraction traveltimes and dispersion curves should be performed to constrain the shallow structure. In addition, to ensure that our inversion scheme can be conveniently applied to most of the existing DSS data, the inversion scheme with surface waves should be as close as possible to the inversion scheme of conventional DSS data processing. We first use all seismic data (multimodal dispersion curves, Pg and Sg travel times) in each shot gather to construct 1D models, and then construct the 2D model by using the interpolation of these 1D models.

In this study, the Monte Carlo inversion method (Socco and Boiero, 2008; Maraschini and Foti, 2010.) was used to construct 1D models with the extracted dispersion curves and Pg and Sg traveltimes. In the Monte Carlo inversion, generous random initial models were generated to perform the model parameter space sampling, and the preferred models were selected according to the acceptance criterion from the initial models. The acceptance criterion of the Monte Carlo method for the joint inversion of Pg and Sg traveltimes and multimodal dispersion curves is as follows:

$$x_p^2 \le 1 \,\&\, x_s^2 \le 1 \,\&\, x_{dis}^2 \le 1, \tag{4}$$

where x_p^2 , x_s^2 and $x_{\mathrm{dis}}^2$are the x^2 of Pg, Sg and the multimodal dispersion curves respectively.

The x^2 of Pg and Sg are calculated by Eq. 2. The calculation of the multimodal dispersion curves x_{dis}^2 should avoid the errors caused by associating a picked dispersion curve with an incorrect mode number (Maraschini et al., 2010). To solve this problem, we calculated the errors between a picked dispersion curve and each of the calculated multimodal dispersion curves, and then the picked dispersion curve was associated with the calculated dispersion curve corresponding to minimum error. The error between the *jth* picked dispersion curve and the *kth* calculated multimodal dispersion curves is calculated as follows:

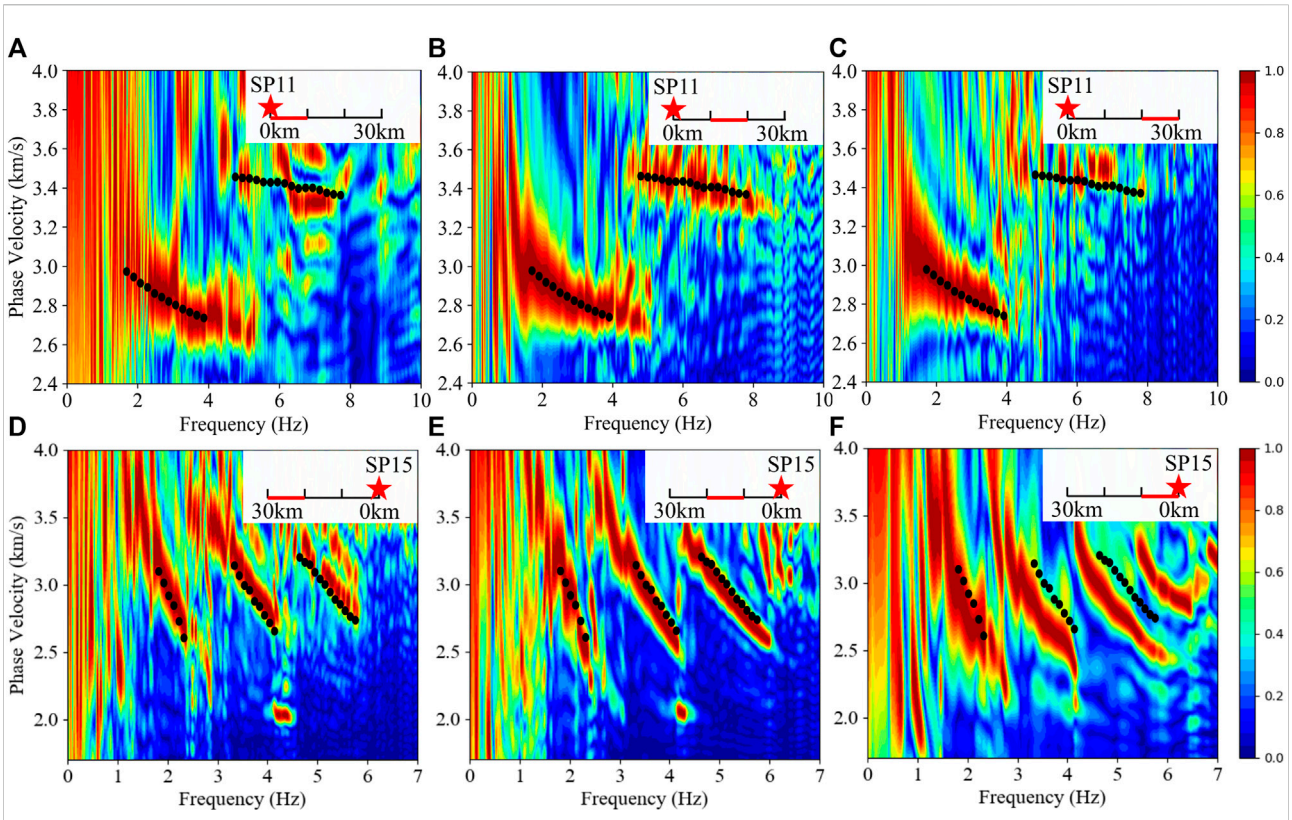

FIGURE 5
F–J spectrograms extracted from the 10-km-long seismic record sections. In the upper right corner of each figure, the stars represent the sources, and the F-J spectrograms are extracted from seismic data on the red lines. The black dots in (a)–(c) are the dispersion curves picked from the 30-km-long SP11 F-J spectrograms (Figure 4A), and the black dots in **(D–F)** are the dispersion curves picked from the 30-km-long SP15 F-J spectrograms (Figure 4B). **(A–C)** are the F-J spectrograms extracted from the 0–10 km offset, 10–20 km offset, and 20–30 km offset of SP11, respectively. **(D–F)** are the F-J spectrograms extracted from the 20–30 km offset, 10–20 km offset, and 0–10 km offset of SP15, respectively.

$$f_{jk} = \frac{1}{n_j} \sum_i \left[(V_{ij}^o - V_{ik}^s)/e_{ij} \right] \tag{5}$$

where f_{jk} denotes the error between the *jth* picked dispersion curve and the *kth* calculated dispersion curve, and n_j is the number of values in the *jth* picked dispersion curve.; V_{ij}^o and V_{ik}^s are the *ith* values in the *jth* picked modal dispersion curve and the *kth* calculated modal dispersion curve respectively, and e_{ij} is the uncertainty of the picked value V_{ij}^o.

The *jth* picked dispersion curve is associated with the calculated dispersion curve corresponding to minimum error, so the fitting error $x_j$of the *jth* picked dispersion curve is as follows:

$$x_j = \min\left(f_{j1}, f_{j2}, \ldots, f_{jk}\right). \tag{6}$$

The χ_{dis}^2 of the picked multimodal dispersion curves is the average fitting error of all picked dispersion curves, and is expressed as follows:

$$x_{dis}^2 = \frac{1}{m} \sum_j x_j, \tag{7}$$

where m is the number of picked dispersion curves.

3 Results

3.1 Multimodal dispersion curves extracted from the DSS data

To implement the F-J method on the DSS data, we should transform the seismic traces from the time domain $C(r,t)$ to the frequency domain $C(r,\omega)$ using Fourier transform. With $C(r,\omega)$ observed in different traces (rs), $I(c,\omega)$ can be numerically integrated by Eq. 3, and then, the F-J spectrogram is plotted with $I(c,\omega)$ to pick dispersion curves and corresponding uncertainties. For each shot gather, we first divided the seismic line to 30 km-long segments, which is equal to the

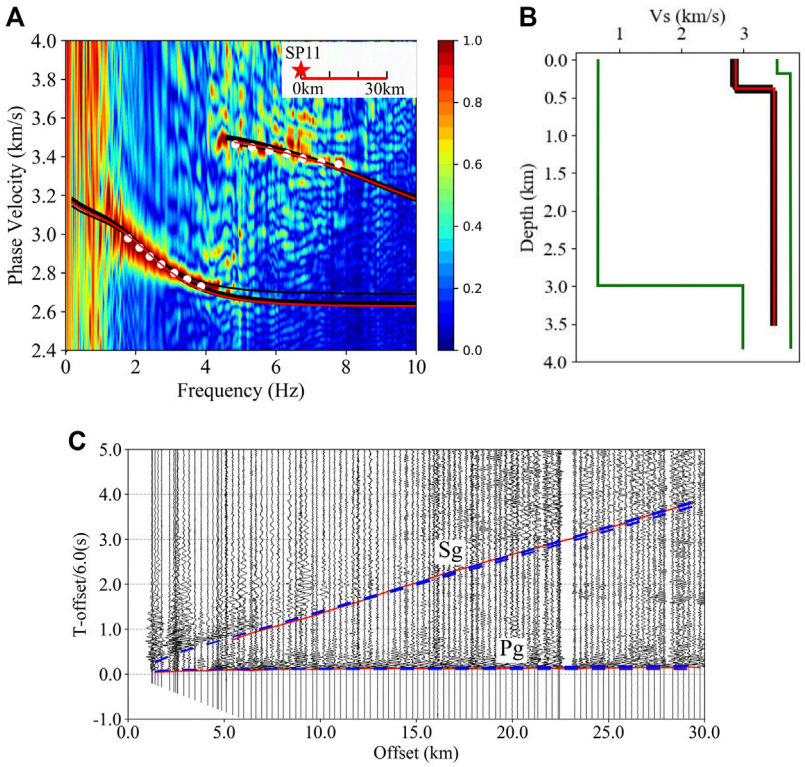

FIGURE 6
The results of the joint Monte Carlo inversion with the multimodal dispersion curves and the Pg and Sg travel times from the SP11 seismic data. **(A)** The black lines are the calculated dispersion curves of the accepted models, the red lines are the calculated dispersion curves of the best fitting model, and the white dots are the picked dispersion curves. In the upper right corner, the red star represents the source, and the F-J spectrogram is extracted from the seismic data on the red line. **(B)** The black lines are the accepted models, and the red line is the best fitting model. The green lines are the boundaries of the model parameters, and 10^6 initial two-layer models were randomly generated between the green lines. **(C)** The red lines are the picked Pg and Sg, and the blue dashed lines are the calculated Pg and Sg of the accepted models.

TABLE 1 The models fitting the SP11 seismic data.

Accepted model	Vs.1 (km/s)	Vs.2 (km/s)	T1 (km)
model 1	2.87	3.51	0.43
model 2	2.88	3.49	0.42
model 3	2.89	3.49	0.44
model 4	2.94	3.48	0.46
model 5*	2.87	3.48	0.42
model 6	2.89	3.51	0.44
model 7	2.89	3.46	0.42
model 8	2.87	3.50	0.43
model 9	2.87	3.49	0.42

*Thea best fitting model

shot source spacing, to extract the dispersion curves. Then, the multimodal dispersion curves were extracted from the shorter segments to increase the lateral resolution of the inversion result.

3.1.1 Multimodal dispersion curves extracted from the 30-km-long seismic record sections

Figure 3 shows the F-J spectrograms extracted from the 0–30 km offset seismic record section of SP11 and SP15 with the MFJ and MWS methods. Two dispersion curves are visible in the spectrograms of SP11 (Figures 3A,B). The higher modal dispersion curve is not clear in the MFJ spectrogram (Figure 3A), but it can be greatly enhanced by the MWS method (Figure 3B). Three dispersion curves are visible in all of the spectrograms of SP15 (Figures 3C,D). It is noteworthy that a vertical signal (marked by the ellipse in Figure 3C) exists in the spectrogram extracted by the MFJ method. Compared with the F-J spectrogram obtained by the original F-J method (Supplementary Figure S6A), this vertical signal is attenuated by the MWS method (Figure 3D) but enhanced by the MFJ method (Figure 3C), so it is difficult to determine whether this vertical signal is a dispersion curve or an artifact. We ignore this confusing "vertical signal" for now and will discuss whether it is a dispersion curve using the inversion results.

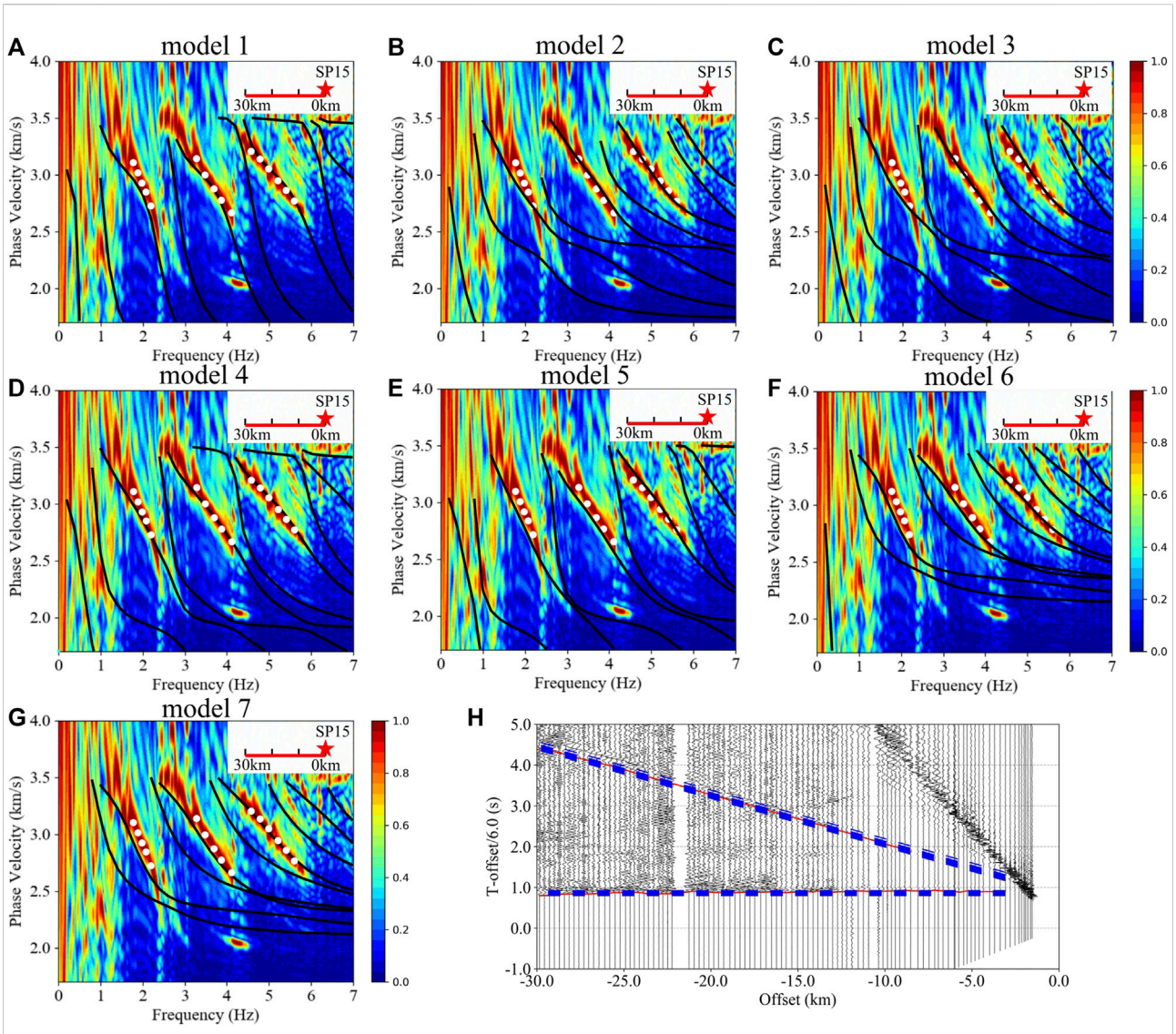

FIGURE 7
The results of the joint Monte Carlo inversion with the multimodal dispersion curves and the Pg and Sg travel times from the SP15 seismic data. In the upper right corner of **(A–G)**, the red star represents the source, and the F-J spectrogram is extracted from the seismic data on the red line. **(A–G)** are the dispersion curves of the accepted models one to seven in Table 2. **(H)** The red lines are the picked Pg and Sg, and the blue dashed lines are the calculated Pg and Sg of the accepted models in Table 2.

The dispersion curves are picked from the overtones of the F-J spectrograms, and the uncertainties of the dispersion curves are set to the widths of the red overtones in the F-J spectrograms (Figure 4). Because of the "vertical signal", it is difficult to associate the picked dispersion curves with correct mode numbers. Thus, the picked dispersion curves are named mode 1, mode 2, and mode three for convenience.

3.1.2 Multimodal dispersion curves extracted from the 10-km-long seismic record sections

We successfully extracted F-J spectrograms from the 10-km-long seismic record sections (Figure 5). For the F-J spectrograms extracted from the 10-km-long SP11 data (Figures 5A–C), the overtones are nearly located in the same place, indicating the subsurface structure within 30 km offset of SP11 is nearly laterally homogenous. For the F-J spectrograms extracted from the 10-km-long SP15 data (Figures 5D–F), the variation in the overtones suggests that the phase wave velocities gradually increase from the 0 km offset to the 30 km offset of SP15.

Overall, we applied the F-J method to the seismic data of the ENAM Line1, and multimodal dispersion curves could be successfully obtained within a 30 km offset of SP11 and between SP14 and SP15. The shortest segment that can be

TABLE 2 The models fitting the SP15 seismic data.

Accepted model	Vs.1 (km/s)	Vs.2 (km/s)	Vp1/Vs.1	Vp2/Vs.2	T1 (km)	T2 (km)
model 1	1.11	3.4	1.10	1.4	0.36	1.32
model 2	1.71	3.47	1.37	1.25	0.82	0.72
model 3	1.57	3.46	1.44	1.24	0.7	0.78
model 4*	1.42	3.42	1.31	1.53	0.59	1.32
model 5	1.16	3.46	1.68	1.39	0.50	1.46
model 6	2.09	3.4	1.10	1.49	0.98	0.40
model 7	2.11	3.32	1.10	1.60	1.00	0.46

Note: The models are three-layer models, and the S- and P-wave velocities of the third layer are 3.5 km/s and 6.0 km/s, respectively. The models including the 1.10 Vp/Vs. ratio (models 1, 6, and 7) could further be excluded by the "vertical signal" the near mode one dispersion curve.
*The best fitting model.

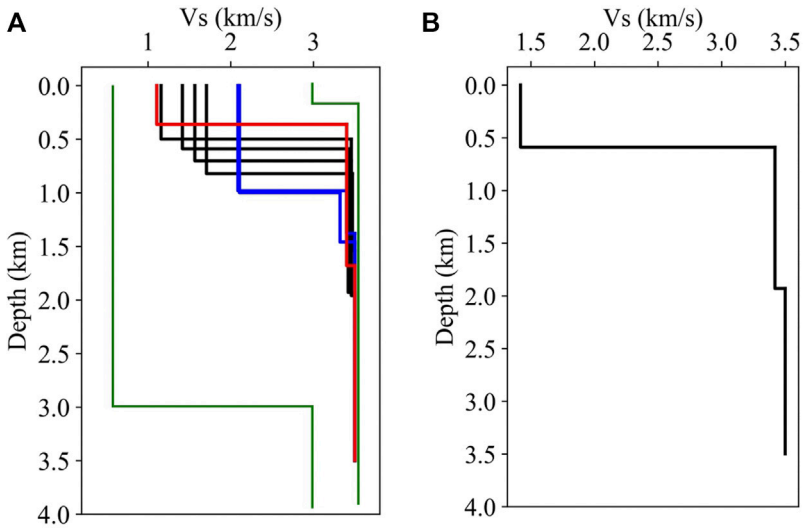

FIGURE 8
The accepted models in Table 2. **(A)** The green lines are the limits of the model parameters, and 10^6 initial three-layer models were generated between the green lines. The red line represents model one in Table 2, the blue lines represent models six and seven in Table 2, and the black lines represent the other models. **(B)** The best fitting model (model four in Table 2).

used to extract dispersion curves is approximately 10 km. However, dispersion curves cannot be obtained from the seismic data between SP12 and SP14. Guo et al. (2019) showed that the jump of refractions, the disappearance of refractions and very curved refractions are visible in the seismic record section between SP12 and SP14, suggesting a large lateral variation in the shallow structure between SP12 and SP14. Generally, in array-based surface wave analyses such as the F-J method, the obtained dispersion curves are regarded as an average effect of the structure beneath the array, so we inferred that the failure of applying the F-J method to the seismic data between SP12 and SP14 may be related to the complex shallow structure.

3.2 The inversion results

To obtain the minimum-structure 1D model, we first used two-layer models to perform the inversion. If the inversion failed, the three-layer models were used to perform the inversion instead.

3.2.1 The velocity models constrained by the 30-km-long seismic record section from SP11

Two-layer models were successfully used to perform the joint inversion of the multimodal dispersion curves and the Pg and Sg traveltimes from seismic data within a 30 km offset of SP11. The model spacing for the Monte Carlo inversion included

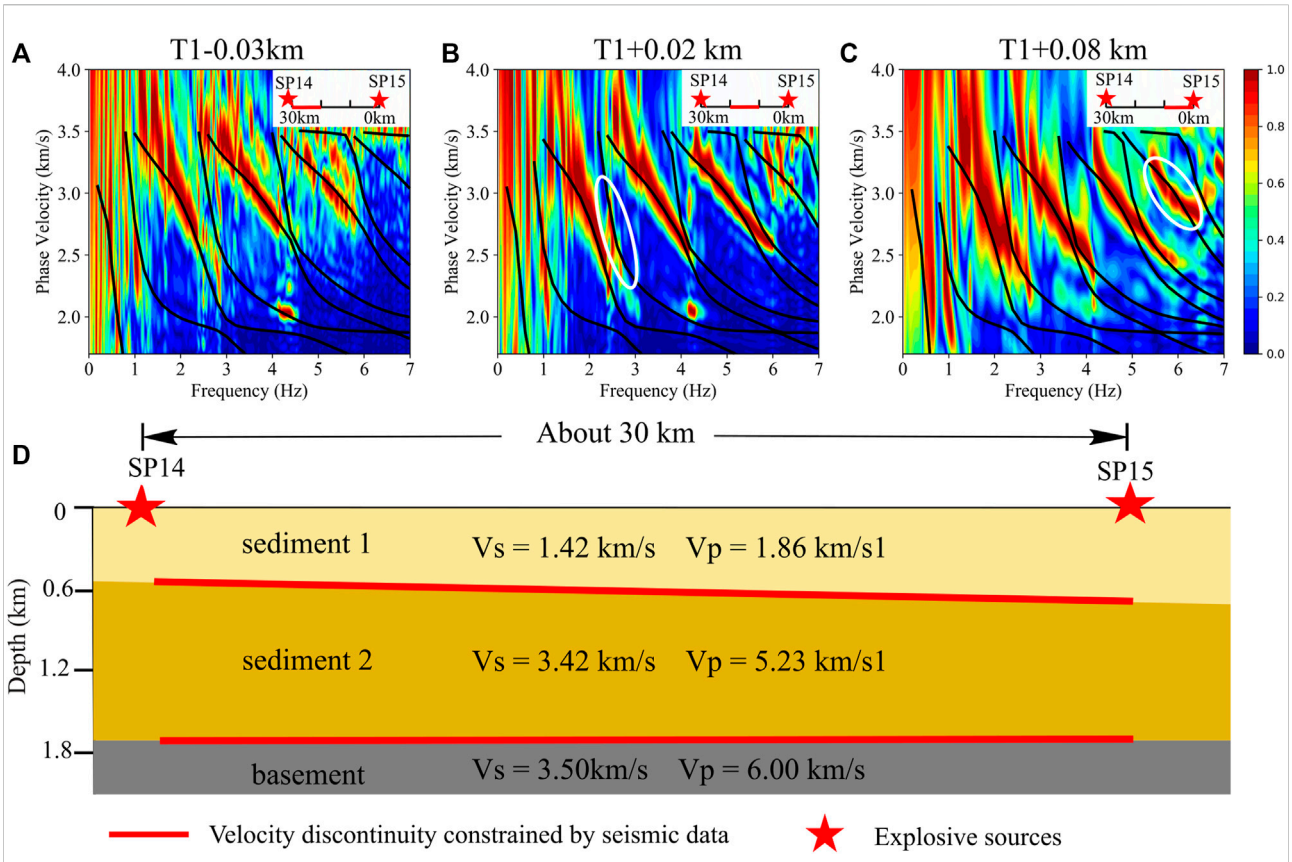

FIGURE 9
The analysis of the F-J spectrograms extracted from the 10-km-long seismic record sections. In the upper right corners of **(A–C)**, the red stars represent the source, and the F-J spectrograms are extracted from the seismic data on the red lines. In the titles of **(A–C)**, T1 represents the first layer thickness of the best fitting model (model 4) in Table 2. The F-J spectrograms in **(A)**, **(B)**, **(C)** are extracted from the 20–30 km offset, 10–20 km offset, and 0–10 km offset of SP15 seismic data respectively. The dispersion curves in each F-J spectrogram were calculated by **(A)** the model obtained by subtracting 0.03 km from the first layer thickness of model 4; **(B)** the model obtained by adding 0.02 km to the first layer thickness of model four; and **(C)** the model obtained by adding 0.08 km to the first layer thickness of model 4. **(D)** The 2D minimum-structure model constructed by combining the three 1D models of **(A–C)**.

3 parameters: Vs.1 and Vs.2 denoting the S-wave velocities of the first and second layers respectively, and T1 denoting the thickness of the first layer. The P-wave velocities were calculated by Vs.1 and Vs.2 with the empirical Vp-Vs relation (Brocher, 2005) during the inversion. The upper and lower limits of Vs.1, Vs.2 and T1 were 0.5–3.5 km/s, 3.0–3.8 km/s and 0.2–3 km (shown as the green lines in Figure 6B), respectively. A total of 10^6 two-layer models were randomly generated in the model space, and nine models (Figure 6B; Table 1) were accepted by the acceptance criterion of the joint inversion (Eq. 4). In the model space, the accepted models (Figure 6B) were concentrated in a very small range, indicating that high resolution shallow structure was constrained by the inversion.

3.2.2 The velocity models constrained by the 30-km-long seismic record section from SP15

According to a previous study on body wave arrivals (Guo et al., 2019), the average Vp/Vs. ratio of the ACP sediment may be much lower than the empirical value calculated by Brocher (2005), indicating that the Vp/Vs. ratio should be introduced as a variable in the inversion of the SP15 seismic data. A total of 10^6 two-layer models were randomly generated to perform the Monte Carlo inversion, but none of the models were accepted by the acceptance criterion (Eq. 4), so the three-layer models were used to perform the inversion.

Based on the prior information provided by the DSS body wave traveltimes analysis (Guo et al., 2019), the bottom layer (third layer) of the three-layer models was set as the basement, and the corresponding P- and S-wave velocities were 6.0 km/s and 3.5 km/s, respectively. There are six model parameters in the model space: Vs.1 and Vs.2 denoting the S-wave velocities of the first two layers, the corresponding Vp1/Vs.1 ratio and Vp2/Vs.2 ratio and thicknesses T1 and T2. The upper and lower limits of the model parameters were set as follows: 0.5–3.0 km/s for Vs.1, 0.5–3.49 km/s for Vs.2, 1.1–5.0 for both Vp1/Vs.1 and Vp2/Vs.2 and 0.two to two km for both T1 and

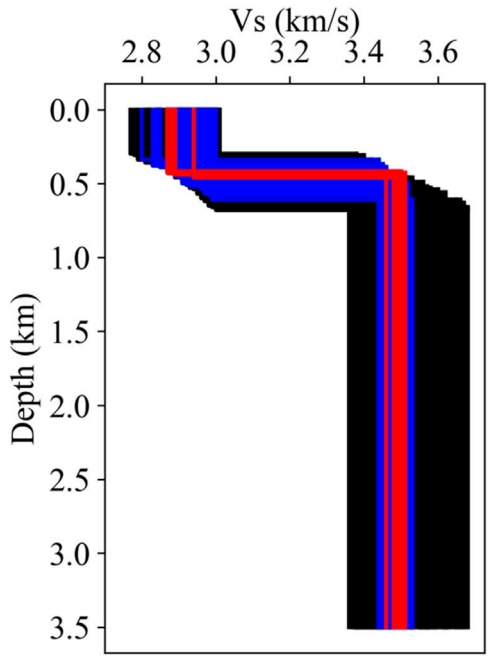

FIGURE 10
The inversion results with the subset data of the SP11 seismic data. The black lines are models obtained by the fundamental dispersion curve; blue lines are models obtained by the joint inversion of the fundamental dispersion curve and the Pg and Sg traveltimes; and red lines are models obtained by the joint inversion of the fundamental and first dispersion curves.

T2. In addition, the sum of the first two layer thicknesses was less than 3 km.

Seven models were selected from the 10^6 initial three-layer models according to the acceptance criterion (Eq. 4). The dispersion curves of the accepted models are very different from each other, so we plotted them separately in Figure 7. All of the accepted model parameters are shown in Table 2 and Figure 8, and the best fitting model is model 4 (Figure 8B).

In the analysis of the SP15 F-J spectrograms, it was not clear that the "vertical signal" near the mode one dispersion curve is a dispersion curve. The dispersion curves of accepted models two to five show that there is a dispersion curve near the "vertical signal", suggesting that this "vertical signal" is the low-resolution image of a dispersion curve. By confirming that the "vertical signal" is a dispersion curve, it is further proved that the F-J method is an effective surface wave analysis method for DSS data. In addition, the models 1, 6, and seven could be excluded from the accepted models because: these models produce dispersion curves between the picked mode one and mode two dispersion curves, but these dispersion curves are far from the "vertical signal".

3.2.3 The velocity models/2D velocity model constrained by the 10-km-long seismic record sections from SP15

The Rayleigh wave phase velocities shown in the 10 km-long F-J spectrograms of SP15 (Figures 5D–F) decrease gradually from west to the east (from 30 km offset to 0 km offset), while the sediment thickness presented by the drill hole data (Lawrence & Hoffman, 1993b) increases gradually from west to east. It seems that the variation in the Rayleigh wave phase velocities is caused by the variation of the sediment thickness (Socco & Boiero, 2008). Therefore, we changed the layer thicknesses of the best fitting model (model four in Table 2) to fit the F-J spectrograms extracted from the 10-km-long seismic record sections. We successively reduced the first layer thickness of mode four by 0.03 km, increased the first layer thickness of mode four by 0.02 km, and increased the first layer thickness of mode four by 0.08 km. Then the dispersion curves calculated from the corresponding 1D models could fit the spectrograms from the 20–30 km offset, 10–20 km offset and 0–10 km offset, respectively (Figure 9). The 2D shallow structure (Figure 9D) was then constructed by the three 1D models.

4 Discussion

4.1 The sensitivity of the seismic data

To explore the sensitivity of the multimodal dispersion curves and the Pg and Sg traveltimes, we performed Monte Carlo inversion with the subset data of the SP11 and SP15 data.

4.1.1 The sensitivity of the SP11 seismic data

In the Piedmont, the reduced Pg traveltimes (Figure 2A) are slightly larger than zero, suggesting that a thin layer should exist on the surface. However, detailed information about this layer cannot be constrained by the Pg and Sg traveltimes inversion (Guo et al., 2019), indicating that the Pg and Sg traveltimes are not sensitive to the velocity and thickness of this layer.

We performed the Monte Carlo inversion only with the fundamental dispersion curve (the picked mode 1), and the low-resolution layered structure on the surface (black lines in Figure 10) was constrained by the fundamental dispersion curve. With the joint inversion of the fundamental dispersion curve and the Pg and Sg traveltimes, the bottom layer velocity could be further constrained (blue lines in Figure 10), demonstrating that the Pg and Sg traveltimes are mainly sensitive to the velocity of the bottom layer. With the joint inversion of the fundamental and first dispersion curves, both the velocities and thickness were further constrained, and the range of the accepted models (red lines in Figure 10) is close to the range of the models accepted by the joint inversion of the multimodal dispersion curves and the

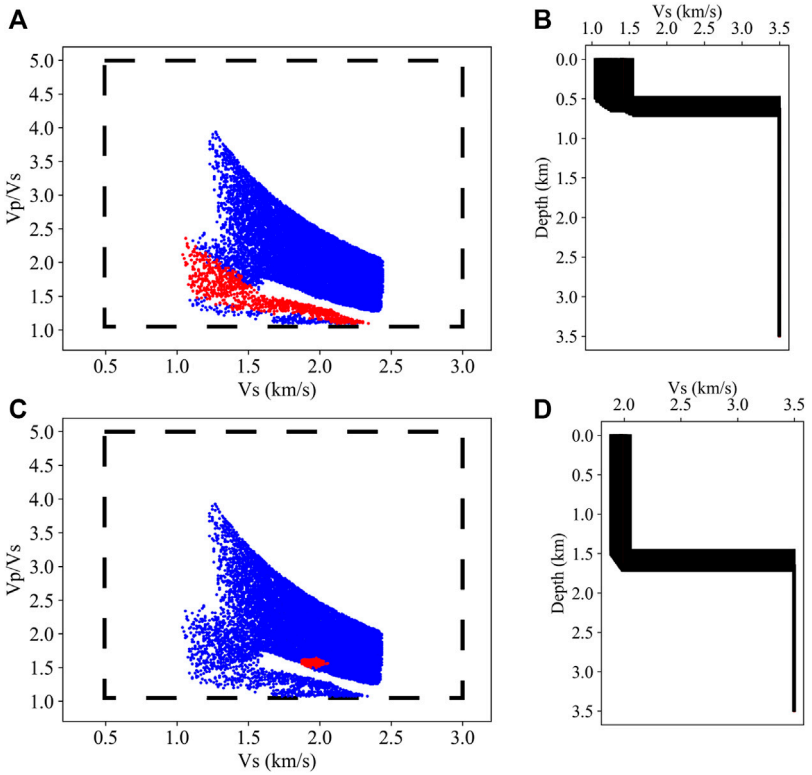

FIGURE 11
The inversion results with the subset data of the SP15 seismic data. A total of 10^6 two-layer models were randomly generated in the model space outlined by the black dashed box in **(A)** and **(C)**. The blue dots in **(A)** and **(C)** are the models accepted by multimodal dispersion curves. The red dots in **(A)** are the models accepted by the multimodal dispersion curves and the Sg traveltimes, and the red dots in **(C)** are the models accepted by the multimodal dispersion curves and Pg traveltimes. **(B)** and **(D)** present accepted models (the red dots in (a) and **(C)**) with the Vs-depth relation. The contradictory results accepted by different subset data demonstrate that it is important to use both the surface waves and the P-and S-body waves to constrain the subsurface structure.

Pg and Sg traveltimes (Figure 6). It is suggested that the multimodal dispersion curves could be sensitive to both the velocity and layer thickness and that the body wave traveltimes only play a minor role in the joint inversion of SP11 data.

4.1.2 The sensitivity of the SP15 seismic data

In the ACP, the Pg reduced times are nearly flat between the 0 km offset and 30 km offset of SP15 (Figure 2B), while there are obvious differences between the 10-km-long F-J spectrograms (Figures 5D–F), suggesting that the dispersion curves are more sensitive to lateral variation in the sediment structure than the refraction traveltimes. The variation in the first layer thickness of the 2D model does not introduce significant errors in the Pg and Sg traveltimes, confirming that the multimodal dispersion curves could be much more sensitive to the first sedimentary layer thickness than the refraction traveltimes.

We adjusted the second layer thickness of the accepted models and found that halving the thickness of the second layer did not introduce significant errors into the dispersion curves, suggesting that the dispersion curves exerted little constraint on the second layer. Because the Pg and Sg traveltimes are determined by the basement velocity and the quotient of sedimentary thickness and velocity, the Pg and Sg traveltimes also provide little constraint on the second layer.

Although both the dispersion curves and the body wave traveltimes exerted little constraint on the second layer, this layer was still constrained by the joint inversion of the dispersion curves and the Pg and Sg traveltimes, suggesting that the join inversion of body waves and surface waves is an effective way to improve the resolution of subsurface structures. We performed the joint inversions with the multimodal dispersion curves and Sg traveltimes, and the results were presented in Figures 11A,B. We also performed the joint inversions with the multimodal dispersion curves and Pg traveltimes respectively, and the results were presented in Figures 11C,D. The contradictory results accepted by different subset data (Figures 11A,B and Figures 11C,D) demonstrate that a completed seismic dataset, including the surface waves and the P-and S- body waves, is helpful to constrain the fine subsurface structure.

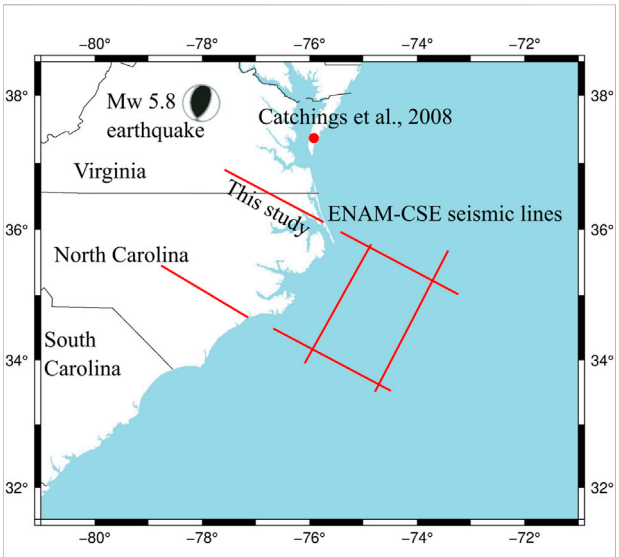

FIGURE 12
The locations of the existing studies near our study area. The red lines are the onshore and offshore seismic lines constructed by the ENAM-CSE. Red dot represents the location discussed in Catchings et al. (2008), and the focal sphere is the Mw 5.8 earthquake in Virginia.

4.2 Comparisons with the existing results

In the Piedmont, the velocities of the thin layer agree with the near-surface velocities constrained by the seismic-wave propagation of the Mw5.8 earthquake (Figure 12, Pollitz and Mooney, 2014). In the ACP, our study revealed a two-layer sediment structure, while only one sediment layer was identified by conventional DSS data processing (Guo et al., 2019). The offshore ENAM-CSE seismic lines (Figure 12) indicate that the sediment in the ocean consists of two layers (Shuck et al., 2019; Lynner et al., 2020), and the P-wave velocities in the ocean sedimentary layers are approximately consistent with the P-wave velocities in our models. Catchings et al. (2008) (Figure 12) constrained the shallow P-wave velocity structure of the ACP with a 30 km-long shallow seismic reflection/refraction survey in Delmarva Peninsula, Virginia, and the P-wave tomograph they presented is also approximately consistent with the two-layer sediment structure obtained by our study. With the results from Shuck et al. (2019), Catchings et al. (2008) and our study, we infer that the two-layer sediment structure extends from the ocean to the land.

The sedimentary Vp/Vs. ratios constrained by this study are much lower than the empirical values (Brocher, 2005), but experimental data samples have shown that extremely low sedimentary Vp/Vs. ratios are not unusual (Kassab & Weller, 2015; Zaitsev et al., 2017). Combined with the surface lithology (King& Beikman 1974; Glover & Klitgord 1995) in the ACP and the studies on low sedimentary Vp/Vs. ratios (Gregory, 1976; Christensen, 1996; Salem, 2000; Brocher, 2005; Mavko et al., 2009; Kassab & Weller, 2015), we inferred that the low Vp/Vs. ratios in this study may be associated with high quartz content (Christensen, 1996; Brocher, 2005) and/or groundwater undersaturation (Gregory, 1976; Christensen, 1996; Salem, 2000; Mavko et al., 2009; Kassab & Weller, 2015; Berg et al., 2021).

5 Conclusion

In this study, we extracted the multimodal dispersion curves from DSS data in the Piedmont and ACP with the F-J method and constrained the shallow velocity structure with the Monte Carlo inversion of the multimodal dispersion curves and the body wave refraction traveltimes. A ~0.42 km thick layer in the Piedmont and a two-layer sediment structure in the ACP are effectively constrained by the joint inversions. These subsurface structures are not identified in the conventional DSS data processing, indicating that the resolution of the shallow/near-surface structure (0–2 km depth) could be improved by extracting dispersion curves from the DSS data.

Since clear surface waves are also observed and consider noise in deep seismic reflection and shallow seismic reflection/refraction experiments, it is suggested that analysis of surface waves recorded by these seismic experiments would also be worthwhile.

Data availability statement

Publicly available datasets were analyzed in this study. This data can be found here: The data are stored in International Federation of Digital Seismograph Networks (Magnani et al., 2015, doi: 10.7914/SN/ZI_2015), Interdisciplinary Earth Data Alliance (IEDA) (Magnani et al., 2018, doi: 10.1594/ IEDA/ 500088).

Author contributions

All of the authors contributed to this manuscript. WG and ZL analyzed the surface waves and wrote the manuscript draft; WG and SZ analyzed the body waves and collected the references; and WG contributed to the inversion. XC and ZL contributed to the conception and design of the study.

Funding

This work was supported by the National Natural Science Foundation of China (Grants No. 41790465, U1901602, 42074070, and 42104048), Shenzhen Key Laboratory of Deep

Offshore Oil and Gas Exploration Technology (Grant No. ZDSYS20190902093007855), the National Key R and D Program of China (2017YFC1500204), the China Postdoctoral Science Foundation (Grant No. 2021M691406), and the China Earthquake Science Experiment Project (202107086728).

Acknowledgments

The collection of these data was coordinated by Southern Methodist University and the Woods Hole Oceanographic Institution. We are grateful to the dedicated twenty-person field crew from various universities, the USGS and two IRIS-PASSCAL technicians who participated in the field. Seismic sources were coordinated by S. Harder and others from UT-El Paso. We gratefully acknowledge the ENAM-CSE principal investigators: Harm van Avendonk, Donna Shillington, Beatrice Magnani, Dan Lizarralde, Brandon Dugan, Matt Hornback, Steven Harder, Anne Bécel, Jim Gaherty, Maureen Long, Gail Christeson, Lara Wagner, and Maggie Benoit. The Python package containing the F-J method (CC-FJpy, Li et al., 2021) can be obtained from http://dx.doi.org/10.1785/0220210042. A slim Python wrapper around the program 'surf96' from "Computer programs in seismology" by R. Herrmann (2013) (http://www.eas.slu.edu/eqc/eqccps.html) was used to calculate the layer model dispersion curves in this study (https://github.com/miili/pysurf96).

Conflict of interest

The authors declare that the research was conducted in the absence of any commercial or financial relationships that could be construed as a potential conflict of interest.

Publisher's note

All claims expressed in this article are solely those of the authors and do not necessarily represent those of their affiliated organizations, or those of the publisher, the editors and the reviewers. Any product that may be evaluated in this article, or claim that may be made by its manufacturer, is not guaranteed or endorsed by the publisher.

Supplementary material

The Supplementary Material for this article can be found online at: https://www.frontiersin.org/articles/10.3389/feart.2022.1025935/full#supplementary-material

References

Anggono, T., SyuhadaFebriani, F., Soedjatmiko, B., and Amran, A. (2018). Investigation of sediment thickness effect to the receiver function through forward modelling. *J. Phys. Conf. Ser.* 985, 012014. doi:10.1088/1742-6596/985/1/012014

Benz, H. M., Unger, J. D., Leith, W. S., Mooney, W. D., Solodilov, L., Egorkin, A. V., et al. (1992). Deep-seismic sounding in northern Eurasia. *Eos Trans. AGU.* 73 (28), 297. doi:10.1029/91EO00233

Berg, E. M., Lin, F., Schulte-Pelkum, V., Allam, A., Qiu, H., and Gkogkas, K. (2021). Shallow crustal shear velocity and vp/vs across southern California: Joint inversion of short-period Rayleigh wave ellipticity, phase velocity, and teleseismic receiver functions. *Geophys. Res. Lett.* 48 (15). doi:10.1029/2021GL092626

Bevington, P. R. (1969). *Data reduction and error analysis for the physical sciences*. New York: McGraw-Hill.

Braile, L. W., and Smith, R. B. (1975). Guide to the interpretation of crustal refraction profiles. *Geophys. J. Int.* 40 (2), 145–176. doi:10.1111/j.1365-246X.1975.tb07044.x

Brocher, T. M. (2005). Empirical relations between elastic wavespeeds and density in the earth's crust. *Bull. Seismol. Soc. Am.* 95 (6), 2081–2092. doi:10.1785/0120050077

Catchings, R. D., Powars, D. S., Gohn, G. S., Horton, J. W., Goldman, M. R., and Hole, J. A. (2008). Anatomy of the chesapeake bay impact structure revealed by seismic imaging, Delmarva Peninsula, Virginia, USA: Chesapeake bay impact structure. *J. Geophys. Res.* 113 (B8). doi:10.1029/2007JB005421

Christensen, N. I. (1996). Poisson's ratio and crustal seismology. *J. Geophys. Res.* 101 (B2), 3139–3156. doi:10.1029/95JB03446

Constable, S. C., Parker, R. L., and Constable, C. G. (1987). Occam's inversion: A practical algorithm for generating smooth models from electromagnetic sounding data. *Geophysics* 52, 289–300. doi:10.1190/1.1442303

Cunningham, E., and Lekic, V. (2020). Constraining properties of sedimentary strata using receiver functions: An example from the atlantic Coastal Plain of the southeastern United States. *Bull. Seismol. Soc. Am.* 110 (2), 519–533. doi:10.1785/0120190191

Duan, Y., Wang, F., Zhang, Lin J., Liu, Z., Liu, B., Yang, Z., et al. (2016). Three-dimensional crustal velocity structure model of the middle-eastern north China Craton (HBCrust1.0). *Sci. China Earth Sci.* 59, 1477–1488. doi:10.1007/s11430-016-5301-0

Essien, U. E., Akankpo, A. O., and Igboekwe, M. U. (2014). Poisson's ratio of surface soils and shallow sediments determined from seismic compressional and shear wave velocities. *Int. J. Geosciences* 05 (12), 1540–1546. doi:10.4236/ijg.2014.512125

Fischer, K. M., Salvati, L. A., HoughGonzalezNelsen, S. E. E. C. E., and Roth, E. G. (1995). Sediment-induced amplification in the northeastern United States: A case study in providence, Rhode Island. *Bull. Seismol. Soc. Am.* 85 (5), 1388–1397. doi:10.1785/bssa0850051388

Frankel, A. (2009). A constant stress-drop model for producing broadband synthetic seismograms: Comparison with the next generation attenuation relations. *Bull. Seismol. Soc. Am.* 99, 664–680. doi:10.1785/0120080079

Giese, P., Prodehl, C., and Stein, A. (1976). *Explosion seismology in central europe: Data and results*. Berlin/Heidelberg, Germany: Springer-Verlag.

Glover, L., and Klitgord, K. D. (1995). *E-3 southwestern Pennsylvania to baltimore canyon trough*. Boulder, United States: Geological Society of America. doi:10.1130/DNAG-COT-E-3

Gregory, A. R. (1976). Fluid saturation effects on dynamic elastic properties of sedimentary rocks. *Geophysics* 41, 895–921. doi:10.1190/1.1440671

Guo, W., Zhao, S., Wang, F., Yang, Z., Jia, S., and Liu, Z. (2019). Crustal structure of the eastern Piedmont and Atlantic coastal plain in North Carolina and Virginia, eastern North American margin. *Earth Planets Space* 71 (1), 69. doi:10.1186/s40623-019-1049-z

Herrmann, R. B. (2013). Computer programs in seismology: An evolving tool for instruction and research. *Seismol. Res. Lett.* 84, 1081–1088. doi:10.1785/0220110096

Hübscher, C., and Gohl, K. (2014). "Reflection/refraction seismology," in *Encyclopedia of marine geosciences*. Editors J. Harff, M. Meschede, S. Petersen, and J. Thiede Dordrecht: Springer Netherlands, 1–15. doi:10.1007/978-94-007-6644-0_128-1

Kassab, M. A., and Weller, A. (2015). Study on P-wave and S-wave velocity in dry and wet sandstones of Tushka region, Egypt. *Egypt. J. Petroleum* 24 (1), 1–11. doi:10.1016/j.ejpe.2015.02.001

Keskar, N. R., and Chelikowsky, J. R. (1992). Negative Poisson ratios in crystalline SiO_2 from first-principles calculations. *Nature* 358, 222–224. doi:10.1038/358222a0

King, P. B., and Beikman, H. M. (1974). Geologic map of the United States: U.S. *Geol. Surv. scale* 1 (2), 500, 000.

Kosminskaya, I. P. (1971). "Deep seismic sounding and its relation to other seismic methods," in *Deep seismic sounding of the earth's crust and upper mantle* (Boston, MA: Springer). doi:10.1007/978-1-4684-7867-9_1

Lawrence, D. P., and Hoffman, C. W. (1993b). *Geology of basement rocks beneath the North Carolina Coastal Plain*. N.C. Geol. Surv, North Carolina.

Lawrence, D. P., and Hoffman, C. W. (1993a). Interpretive geologic map of basement rocks beneath the North Carolina Coastal Plain. *N. C. Geol. Surv. Bull.* 95, 60. 1 plate.

Li, J., Song, X., Zhu, L., and Deng, Y. (2017). Joint inversion of surface wave dispersions and receiver functions with *P* velocity constraints: Application to southeastern tibet: Joint inversion and application to tibet. *J. Geophys. Res. Solid Earth* 122 (9), 7291–7310. doi:10.1002/2017JB014135

Li, J., Tang, Y., Wu, T., Zhao, J., Wu, H., Wu, W., et al. (2020). Overpressure origin and its effects on petroleum accumulation in the conglomerate oil province in Mahu Sag, Junggar Basin, NW China. *Petroleum Explor. Dev.* 47 (4), 726–739. doi:10.1016/S1876-3804(20)60088-X

Li, S., Mooney, W. D., and Fan, J. (2006). Crustal structure of mainland China from deep seismic sounding data. *Tectonophysics* 420 (1–2), 239–252. doi:10.1016/j.tecto.2006.01.026

Li, X., Chen, X., Yang, Z., Wang, B., Yang, B., Tao, G., et al. (2020). Application of high-order surface waves in shallow exploration: An example of the Suzhou river, Shanghai. *Chin. J. Geophys. (in Chinese)* 63 (1), 247–263.e1. doi:10.1016/j.ajodo.2019.08.014

Li, Z., and Chen, X. (2020). An effective method to extract overtones of surface wave from array seismic records of earthquake events. *J. Geophys. Res. Solid Earth* 125. doi:10.1029/2019JB018511

Li, Z., Shi, C., and Chen, X. (2021a). Constraints on crustal P-wave structure with leaking mode dispersion curves. *Geophysical Research Letters* 48, e2020GL091782. doi:10.1029/2020GL091782

Li, Z., Zhou, J., Wu, G., Wang, J., Zhang, G., Dong, S., et al. (2021b). CC-FJpy: A Python package for extracting overtone surface-wave dispersion from seismic ambient-noise cross correlation. *Seismological Research Letters* XX, 3179–3186.

Lin, J., Mooney, W. D., Wang, F., Duan, Y., Tian, X., Xu, T., et al. (2019). Crustal P wave velocity structure beneath the SE margin of the Tibetan Plateau from Deep Seismic Sounding results. *Tectonophysics* 755, 109–126. doi:10.1016/j.tecto.2019.01.010

Lu, L., and Zhang, B. (2006). Inversion of Rayleigh waves using a genetic algorithm in the presence of a low-velocity layer. *Acoust. Phys.* 52, 701–712. doi:10.1134/S106377100606011X

Lynner, C., Van Avendonk, J. A. H., Bécel, A., Christeson, G. L., Dugan, B., Gaherty, J. B., et al. (2020). The Eastern North American margin community seismic experiment: An amphibious active and passive-source dataset. *Seismological Research Letters* 91 (1), 533–540. doi:10.1785/0220190142

Magnani, M. B., Harder, S., and Lizarralde (2018). *Explosion seismic refraction data acquired on land in eastern North Carolina and virgina as part of the Eastern North American Margin (ENAM) community seismic experiment (CSE) (2015)*. New York, Palisades: Interdisciplinary Earth Data Alliance IEDA.

Magnani, M. B., Lizarralde, D., and Harder, S. (2015). "A community seismic experiment targeting the pre-syn, post-rift evolution of the Mid-Atlantic US: The ENAM CSE land active source experiment," in *International federation of digital seismograph Networks, Dataset/Seismic Network*.431-438 doi:10.7914/SN/ZI_2015

Maraschini, M., Ernst, F., Foti, S., and Socco, L. V. (2010). A new misfit function for multimodal inversion of surface waves. *Geophysics* 75 (4), G31–G43. doi:10.1190/1.3436539

Maraschini, M., and Foti, S. (2010). A Monte Carlo multimodal inversion of surface waves: Monte Carlo multimodal surface wave inversion. *Geophys. J. Int.* 182 (3), 1557–1566. doi:10.1111/j.1365-246X.2010.04703.x

Marzen, R. E., Shillington, D. J., Lizarralde, D., and Harder, S. H. (2019). Constraints on appalachian orogenesis and continental rifting in the southeastern United States from wide-angle seismic data. *J. Geophys. Res. Solid Earth* 124 (7), 6625–6652. doi:10.1029/2019JB017611

Marzen, R. E., Shillington, D. J., Lizarralde, D., Knapp, J. H., Heffner, D. M., Davis, J. K., et al. (2020). Limited and localized magmatism in the central atlantic magmatic province. *Nat. Commun.* 11 (1), 3397. doi:10.1038/s41467-020-17193-6

Mavko, G., Mukerji, T., and Dvorkin, J. (2009). "The rock physics handbook," in *Tools for seismic analysis in porous media*. second edition (Cambridge, U.K: Cambridge University Press).

Mooney, W. D., Laske, G., and Masters, T. G. (1998). Crust 5.1: A global crustal model at 5° × 5°. *J. Geophys. Res.*, 103, 727–747. doi:10.1029/97JB02122

Musacchio, G., Mooney, W. D., Luetgert, J. H., and Christensen, N. I. (1997). Composition of the crust in the grenville and appalachian provinces of north America inferred from V_P/V_Sratios. *J. Geophys. Res.* 102 (B7), 15225–15241. doi:10.1029/96JB03737

Pakiser, L. C., and Mooney, W. D. (1989). *Geophysical framework of the continental United States*, Vol. 172. Boulder: Geological Society of America Memoir.

Park, C. B., Miller, R. D., Xia, J., and Ivanov, J. (2007). Multichannel analysis of surface waves (MASW)—Active and passive methods. *The Leading Edge* 26 (1), 60–64. doi:10.1190/1.2431832

Pollitz, F. F., and Mooney, W. D. (2014). Regional seismic-wave propagation from the M5. 8 23 August 2011, Mineral, Virginia, earthquake. *Geological Society of America Special Papers* 509. , SPE509–06.

Pratt, T. L. (2018). Characterizing and imaging sedimentary strata using depth-converted spectral ratios: An example from the atlantic Coastal Plain of the eastern United States. *Bull. Seismol. Soc. Am.* 108 (5A), 2801–2815. doi:10.1785/0120180046

Salem, H. S. (2000). Poisson's ratio and the porosity of surface soils and shallow sediments, determined from seismic compressional and shear wave velocities. *Géotechnique* 50 (4), 461–463. doi:10.1680/geot.2000.50.4.461

Schleicher, L. S., and Pratt, T. L. (2021). Characterizing fundamental resonance peaks on flat-lying sediments using multiple spectral ratio methods: An example from the atlantic Coastal Plain, eastern United States. *Bull. Seismol. Soc. Am.* 111 (4), 1824–1848. doi:10.1785/0120210017

Shuck, B. D., Van Avendonk, H. J. A., and Bécel, A. (2019). The role of mantle melts in the transition from rifting to seafloor spreading offshore eastern North America. *Earth and Planetary Science Letters* 525, 115756. doi:10.1016/j.epsl.2019.115756

Socco, L. V., and Boiero, D. (2008). Improved Monte Carlo inversion of surface wave data. *Geophys. Prospect.* 56 (3), 357–371. doi:10.1111/j.1365-2478.2007.00678.x

Socco, L. V., and Strobbia, C. (2004). Surface-wave method for near-surface characterization: A tutorial. *Near Surface Geophysics* 2 (4), 165–185. doi:10.3997/1873-0604.2004015

Sun, N., Pan, L., Wang, W., Ye, B., Wang, B., and Chen, X. (2021). Inversion of shear wave velocity structure beneath the Binchuan airgun source area using a nested combination of multi-scale arrays. *Chinese Journal of Geophysics* 64 (11), 4012–4021. doi:10.6038/cjg2021P0064

Wang, J., Wu, G., and Chen, X. (2019). Frequency-bessel transform method for effective imaging of higher-mode Rayleigh dispersion curves from ambient seismic noise data. *J. Geophys. Res. Solid Earth* 124 (4), 3708–3723. doi:10.1029/2018JB016595

Wu, G., Pan, L., Wang, J., and Chen, X. (2020). Shear velocity inversion using multimodal dispersion curves from ambient seismic noise data of USArray transportable array. *J. Geophys. Res. Solid Earth* 125 (1), e2019JB018213. doi:10.1029/2019jb018213

Wu, H., Chen, X., and Pan, L. (2019). S-wave velocity imaging of the Kanto basin in Japan using the frequency-Bessel transformation method. *Chinese J. Geophys. (in Chinese)* 62 (9), 3400–3407. doi:10.6038/cjg2019N0205

Xi, C., Xia, J., Mi, B., Dai, T., Liu, Y., and Ning, L. (2021). Modified frequency-bessel transform method for dispersion imaging of Rayleigh waves from ambient seismic noise. *Geophysical Journal International* 225 (2), 1271–1280. doi:10.1093/gji/ggab008

Yang, Z., Chen, X ., Pan, L., Wang, J., Xu, J., and Zhang, D. (2019). Multi-channel analysis of Rayleigh waves based on the vector wavenumber tansformation method (VWTM). *Chinese J. Geophys. (in Chinese)* 62 (1), 298–305. doi:10.6038/cjg2019M0641

Zaitsev, V. Y., Radostin, A. V., Pasternak, E., and Dyskin, A. (2017). Extracting real-crack properties from non-linear elastic behaviour of rocks: Abundance of cracks with dominating normal compliance and rocks with negative Poisson ratios. *Nonlinear Process. Geophys.* 24 (3), 543–551. doi:10.5194/npg-24-543-2017

Zelt, C. A., and Barton, P. J. (1998). Three-dimensional seismic refraction tomography: A comparison of two methods applied to data from the faeroe basin. *J. Geophys. Res.* 103 (B4), 7187–7210. doi:10.1029/97JB03536

Zelt, C. A., and Forsyth, D. A. (1994). Modeling wide-angle seismic data for crustal structure: Southeastern Grenville Province. *J. Geophys. Res.* 99 (B6), 11687–11704. doi:10.1029/93JB02764

Zelt, C. A. (1999). Modelling strategies and model assessment for wide-angle seismic traveltime data. *Geophysical Journal International* 139 (1), 183–204. doi:10.1046/j.1365-246X.1999.00934.x

Zelt, C. A., and Smith, R. B. (1992). Seismic traveltime inversion for 2-D crustal velocity structure. *Geophysical Journal International* 108 (1), 16–34. doi:10.1111/j.1365-246x.1992.tb00836.x

Zhan, W., Pan, L., and Chen, X. (2020). A widespread mid-crustal low-velocity layer beneath Northeast China revealed by the multimodal inversion of Rayleigh waves from ambient seismic noise. *Journal of Asian Earth Sciences* 196, 104372. doi:10.1016/j.jseaes.2020.104372

Zhao, S., and Guo, W. (2019). Crustal structure of eastern North Carolina: Piedmont and Coastal Plain. *Bull. Seismol. Soc. Am.* 109 (6), 2288–2304. doi:10.1785/0120180281

Zhou, J., and Chen, X. (2021). Removal of crossed artifacts from multimodal dispersion curves with modified frequency–bessel method. *Bull. Seismol. Soc. Am.* 112 (1), 143–152. doi:10.1785/0120210012

frontiers | Frontiers in Earth Science

TYPE Methods
PUBLISHED 10 January 2023
DOI 10.3389/feart.2022.1085441

OPEN ACCESS

EDITED BY
Jian Sun,
Ocean University of China, China

REVIEWED BY
Bo Wang,
China University of Mining and Technology, China
Wenyong Pan,
Institute of Geology and Geophysics (CAS), China

*CORRESPONDENCE
Yuzhu Liu,
liuyuzhu@tongji.edu.cn

SPECIALTY SECTION
This article was submitted to Solid Earth Geophysics, a section of the journal Frontiers in Earth Science

RECEIVED 31 October 2022
ACCEPTED 28 December 2022
PUBLISHED 10 January 2023

CITATION
Yang T, Liu Y and Yang J (2023), Joint towed streamer and ocean-bottom-seismometer data multi-parameter full waveform inversion in acoustic-elastic coupled media.
Front. Earth Sci. 10:1085441.
doi: 10.3389/feart.2022.1085441

Joint towed streamer and ocean-bottom-seismometer data multi-parameter full waveform inversion in acoustic-elastic coupled media

Tao Yang[1], Yuzhu Liu[1,2]* and Jizhong Yang[1,2]

[1]School of Ocean and Earth Science, Tongji University, Shanghai, China, [2]State Key Laboratory of Marine Geology, Tongji University, Shanghai, China

Short-offset towed streamer data, and sparse ocean-bottom seismometer (OBS) data are not conducive to applying multi-parameter full waveform inversion (FWI) in production. It is challenging to reconstruct deep velocity in the former, and the latter suffers from severe acquisition footprints. We developed a joint acoustic-elastic coupled full waveform inversion (J-AEFWI) method, in which towed streamer data and ocean-bottom seismometer data were used jointly to build P-wave and S-wave velocity models. A new joint objective function was established using the least-squares theory, and the joint acoustic-elastic coupled full waveform inversion method on the acoustic-elastic coupled equation was derived. The method can inject the residuals of the towed streamer data and the ocean-bottom seismometer data in time backward propagating to update P-wave and S-wave velocity models. The synthetic experimental results show that joint acoustic-elastic coupled full waveform inversion obtains more accurate results than when using these two types of data alone. Compared to using the towed streamer or ocean-bottom seismometer data alone, the joint acoustic-elastic coupled full waveform inversion method leads to better illumination of the deep background velocities and suppression of acquisition footprints. The results of joint acoustic-elastic coupled full waveform inversion were slightly better than those of the cascaded full waveform inversion strategy. To further demonstrate the benefit of the proposed method, we applied it to the field data, and better results are obtained as expected.

KEYWORDS

towed streamer data, ocean-bottom-seismometer data, joint multi-parameter FWI, full waveform inversion, acoustic-elastic coupled media

1 Introduction

Since it was proposed (Lailly, 1983; Tarantola, 1984), full waveform inversion (FWI) has been successfully applied to practical seismic data to build subsurface geophysical parameters (Crase et al., 1990; Operto et al., 2013; Pan et al., 2018; Pan et al., 2020; Borisov et al., 2020; Peter et al., 2022). In recent decades, the development and application of FWI ranges from acoustic media (Gauthier et al., 1986; Ravaut et al., 2004; Plessix et al., 2010; Xukai and Robert, 2015; Yang et al., 2016) to elastic media (Sears et al., 2008; Vigh et al., 2014; Liu et al., 2021), using towed streamer acquisition (Dessa et al., 2004; Plessix et al., 2010; Shen, 2010) or ocean-bottom node/ocean-bottom seismometer (OBN/OBS) acquisition (Sears et al., 2008; Vigh et al., 2014; Peter et al., 2022).

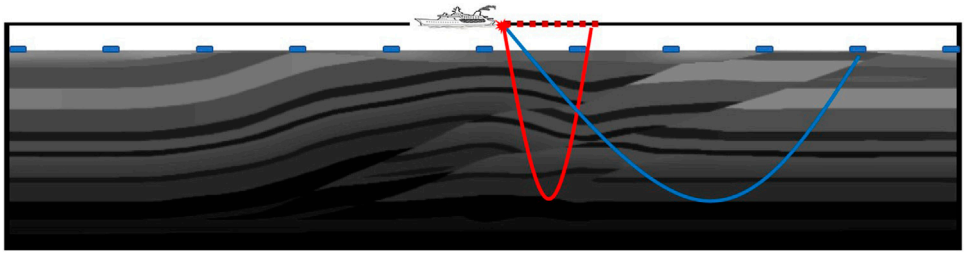

FIGURE 1
Combined towed streamer and OBS acquisition geometry. The red dots on the seawater surface indicate the towed streamer hydrophones, and the blue squares on the sea floor indicate the OBS. The solid red line indicates the wave path of the towed streamer, and the solid blue line indicates the wave path of the OBS.

When OBN/OBSs cannot be deployed on a large scale, a towed streamer is the primary marine seismic wave observation tool. The low cost and low processing effort have appealed to recent researchers and have led to successful cases of acoustic FWI (Dessa et al., 2004; Plessix et al., 2010; Shen, 2010; Agudo et al., 2018); however, several issues need to be addressed. To facilitate macro-model building, FWI relies on a wide-azimuthal acquisition to obtain sufficient transmitted waves (Bunks et al., 1995; Pratt, 1999; Virieux and Operto, 2009; Plessix, 2010). The fixed spreading and cable length limit the towed steamer observation aperture, resulting in insufficient diving waves recorded, especially in deep seawater environments. In this case, FWI tends to fall into cycle skipping without considering other methods to supplement low frequencies (Yao et al., 2019). On the other hand, the modeling equation for acoustic FWI is a simplified approximation of the elastic equation. The converted P-waves generated by the elastic parameters (e.g., S-wave velocity) cannot be simulated using the acoustic equation. When significant converted waves are present in towed streamer data, acoustic FWI tends to incorrectly project converted waves onto P-wave velocity instead of the correct S-wave velocity. Some studies have also focused on this issue, considering that the application of towed streamer data in elastic media in a more advanced approach (Li and Williamson, 2019; Thiel et al., 2019; Sun and Jin, 2020; Yang and Liu, 2020). In addition, the absence of necessary low frequencies and surge noise in streamer data is not conducive to FWI, resulting in the need for other waveform shaping methods.

The multi-parameter elastic FWI for OBN/OBS seismic data is now considered as a more advanced solution to solve some of the complex imaging problems, which usually has the advantages of low frequencies, long offsets, and full azimuthal coverage (Sears et al., 2008; Dellinger et al., 2017; Peter et al., 2022). The benefits of low frequencies need not be elaborated, while the long-offsets and full-azimuthal coverage can receive a sufficient number of diving waves. This weakens the dependence on the starting velocities for obtaining large-scale structures (Plessix et al., 2010). In addition, the abundant S-waves in the OBN/OBS data play a key role in S-wave velocity inversion, which improves the resolution of the multi-parameter inversion results. All of these can overcome the shortcomings of towed streamer acquisition, but limitations of towed streamer cannot be ignored. Its expensive cost and low quantity (hundreds or even thousands of meters apart) constrain its dense deployment in practical production. Insufficient or under-sampled data is not enough for FWI to cover subsurface structures. In general, FWI requires dense, fully sampled data for migration stacking. The under-sampled data, in turn, causes the inversion to fall into a system of underdetermined solutions, causing sharp acquisition footprints and layer discontinuities in the inversion results (Zheglova and Malcolm, 2019; Faucher et al., 2020).

Because OBN/OBS is still expensive to deploy densely, a scheme of a joint towed streamer and OBN/OBS acquisition has been successfully applied (Yang and Zhang, 2019; Yu and Sun, 2022). One of its advantages is that the towed streamer and OBN/OBS simultaneously receive seismic waves from the subsurface (Figure 1). The solid red line indicates the wave path of the towed streamer, and the solid blue line indicates the wave path of the OBS. The OBS is sparsely placed on the seafloor, which can receive P- and S-waves in x, y, and z directions, whereas the densely connected towed streamer hydrophones in seawater can only receive P-waves (containing S-P converted waves). Moreover, their wave paths intuitively showed that OBS acquisition has a larger imaging angle than towed streamer acquisition, and a larger imaging angle is more conducive to FWI macromodel building (Virieux and Operto, 2009). Currently, most FWI applications use only streamer data or OBS data, but few studies use both. We propose a joint acoustic-elastic coupled FWI (J-AEFWI) method that combines towed streamers and OBS data using the acoustic-elastic coupled equation (AECE), which can simultaneously record the pressure component, x, y, and z components in acoustic-elastic coupled media (Yu et al., 2016; Yu and Geng, 2019). The method can inject the residuals of the towed streamer data and the OBS data in time backward propagating to update P-wave and S-wave velocity models. The J-AEFWI approach complements FWI with wide-azimuthal coverage to make obtaining long-wave information easier and make S-wave velocity inversion better than FWI with towed streamer data alone. It complements FWI with dense data simultaneously to suppress the acquisition footprints more than FWI with OBS data alone. Next, the AECE is reviewed, and the J-AEFWI method is illustrated. A set of synthetic and field data inversion experiments were conducted.

2 Methodology

In acoustic-elastic coupled media, AECE was used to simulate wave propagation (Yu et al., 2016) as follows:

$$\mathbf{L}_{AE}\mathbf{U}_{AE} = \mathbf{F}_{\boldsymbol{AE}} \tag{1}$$

where $\mathbf{U}_{AE} = (v_x, v_z, P, \tau^s_{xx}, \tau^s_{xz})^T$ is the wavefield components and $\mathbf{F}_{\boldsymbol{AE}} = (0, 0, f, 0, 0)^T$ is the source vector. T indicates transposition. The operator $\mathbf{L}_{AE}$ is the AECE forward operator and satisfies the following:

$$\mathbf{L}_{AE} = \begin{pmatrix} \rho\frac{\partial}{\partial t} & 0 & \frac{\partial}{\partial x} & -\frac{\partial}{\partial x} & -\frac{\partial}{\partial z} \\ 0 & \rho\frac{\partial}{\partial t} & \frac{\partial}{\partial z} & \frac{\partial}{\partial z} & -\frac{\partial}{\partial x} \\ (\lambda+\mu)\frac{\partial}{\partial x} & (\lambda+\mu)\frac{\partial}{\partial z} & \frac{\partial}{\partial t} & 0 & 0 \\ -\mu\frac{\partial}{\partial x} & \mu\frac{\partial}{\partial z} & 0 & \frac{\partial}{\partial t} & 0 \\ -\mu\frac{\partial}{\partial z} & -\mu\frac{\partial}{\partial x} & 0 & 0 & \frac{\partial}{\partial t} \end{pmatrix} \tag{2}$$

where v_x and v_z are the particle velocity components, P is the pressure, τ^s_{xx} and τ^s_{xz} are the deviatoric stress components, ρ is the density, and λ and μ are Lamé parameters. The pressure, x, and z components are integrated into the AECE, allowing pure P-waves to be obtained directly (Yu et al., 2016).

In J-AEFWI, the joint pressure component of the towed streamer and the x and z components of the OBS objective function based on the l_2-norm can be written as

$$\min_m J(m) = \gamma^*\varphi \parallel P^{sim}_{ts} - P^{obs}_{ts} \parallel_2^2 + \alpha \parallel v^{sim}_{xo} - v^{obs}_{xo} \parallel_2^2 + \beta \parallel v^{sim}_{zo} - v^{obs}_{zo} \parallel_2^2, \tag{3}$$

where J indicates the objective function, m indicates the model parameters, superscripts *sim* and *obs* indicate the simulated and observed data, subscripts *ts*, *xo*, and *zo* indicate the pressure component of the towed streamer, and x and z components of the OBS, respectively.

We used the adjoint-state method to deduce the adjoint equation (included in Appendix A):

$$\mathbf{L}^*_{AE}\tilde{\mathbf{U}}_{AE} = \tilde{\mathbf{F}}_{AE} \tag{4}$$

where, $\tilde{\mathbf{U}}_{AE} = (\tilde{v}_x, \tilde{v}_z, \tilde{P}, \tilde{\tau}^s_{xx}, \tilde{\tau}^s_{xz})^T$ is the adjoint wavefield, $\mathbf{L}^*_{AE}$ is the adjoint operator, and

$$\tilde{\mathbf{F}}_{AE} = \left(\alpha\left(v^{sim}_{xo} - v^{obs}_{xo}\right), \beta\left(v^{sim}_{zo} - v^{obs}_{zo}\right), \gamma^*\varphi\left(P^{sim}_{ts} - P^{obs}_{ts}\right), 0, 0\right)^T \tag{5}$$

is the adjoint source function and satisfies

$$\begin{cases} \alpha = 0,\ \beta = 0,\ \gamma = 1, \text{or} \\ \alpha = 1,\ \beta = 1,\ \gamma = 0, \text{or} \\ \alpha = 1,\ \beta = 1,\ \gamma = 1. \end{cases} \tag{6}$$

Parameters α, β, and γ act as switches in the inversions. When $\alpha = 0, \beta = 0$, and $\gamma = 1$, it indicated towed streamer data alone. When $\alpha = 1$, $\beta = 1$, and $\gamma = 0$, AEFWI was indicated for OBS data alone. J-AEFWI is indicated when $\alpha = 1$, $\beta = 1$, and $\gamma = 1$. The φ is a weighting parameter used to control the contribution of different data points in the inversion. The selection strategy for parameter φ is explained in a subsequent discussion. $\mathbf{L}^*_{AE}$was given by:

$$\mathbf{L}^*_{AE} = \begin{pmatrix} \rho\frac{\partial}{\partial t} & 0 & -\frac{\partial}{\partial x}(\lambda+\mu) & \frac{\partial}{\partial x}\mu & \frac{\partial}{\partial z}\mu \\ 0 & \rho\frac{\partial}{\partial t} & -\frac{\partial}{\partial z}(\lambda+\mu) & -\frac{\partial}{\partial z}\mu & \frac{\partial}{\partial x}\mu \\ -\frac{\partial}{\partial x} & -\frac{\partial}{\partial z} & \frac{\partial}{\partial t} & 0 & 0 \\ \frac{\partial}{\partial x} & -\frac{\partial}{\partial z} & 0 & \frac{\partial}{\partial t} & 0 \\ \frac{\partial}{\partial z} & \frac{\partial}{\partial x} & 0 & 0 & \frac{\partial}{\partial t} \end{pmatrix} \tag{7}$$

The gradients of the objective function with respect to the parameters λ and μ are derived as follows:

$$\begin{cases} \frac{\partial J}{\partial \lambda} = \sum_{shot} \int dt \left(\frac{\partial v_x}{\partial x} + \frac{\partial v_z}{\partial z}\right)\tilde{P} \\ \frac{\partial J}{\partial \mu} = \sum_{shot} \int dt \left(\frac{\partial v_x}{\partial x} + \frac{\partial v_z}{\partial z}\right)\tilde{P} - \left(\frac{\partial v_x}{\partial x} - \frac{\partial v_z}{\partial z}\right)\tilde{\tau}^s_{xx} - \left(\frac{\partial v_x}{\partial z} + \frac{\partial v_z}{\partial x}\right)\tilde{\tau}^s_{xz} \end{cases} \tag{8}$$

Finally, P- and S-wave velocity gradients were obtained using the chain rule. The parameters were updated by:

$$m_{k+1} = m_k + \alpha_k g_k \tag{9}$$

where m is the model parameter, α is the updating step length, g is the conjugate update direction of the model parameters, and k is the number of iterations.

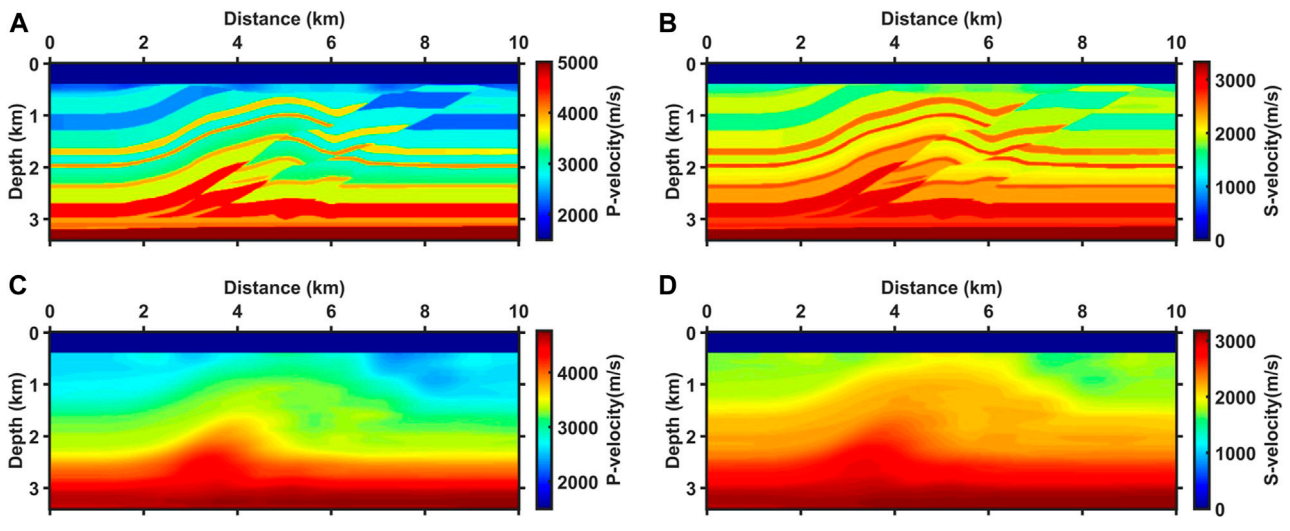

FIGURE 2
The true P-wave velocity **(A)** and S-wave velocity **(B)** models and their starting models **(C,D)**.

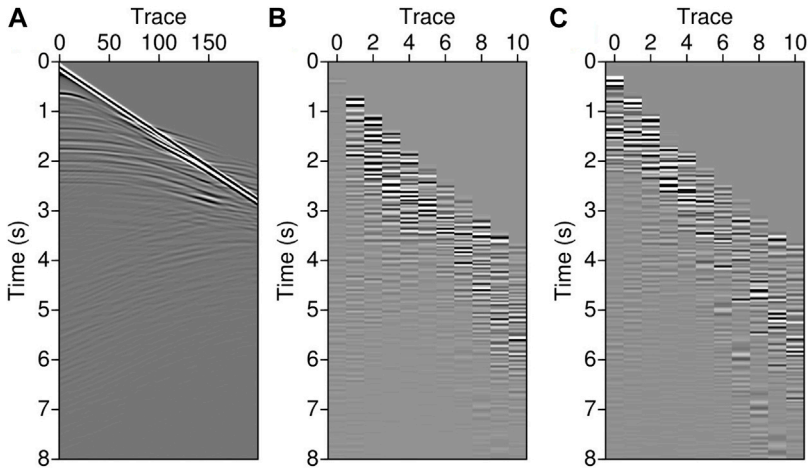

FIGURE 3
Shot gathers of the towed streamer **(A)**, OBS x **(B)**, and z **(C)** components.

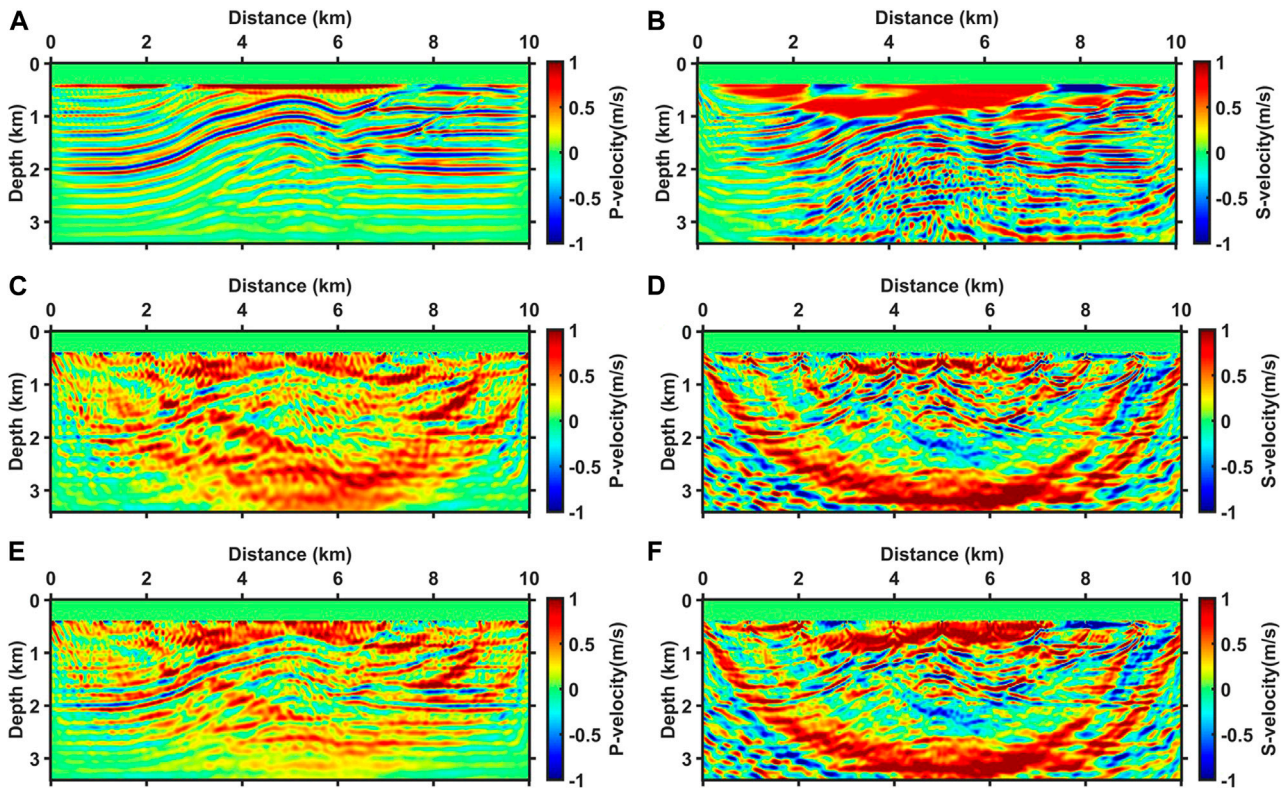

FIGURE 4
The P-wave velocity **(A,C,E)** and S-wave velocity **(B,D,F)** updating directions for the first iteration of three inversion experiments. **(A,B)** are updating directions of towed streamer data alone, **(C,D)** are updating directions of OBS data alone, and **(E,F)** are updating directions of joint towed streamer and OBS data.

3 Synthetic inversion examples

We conducted three FWI experiments for towed streamer data alone, OBS data alone, and combined towed streamer and OBS data. All experiments used Eqs 1, 4, 8, 9 to invert P- and S-wave velocities, and the difference is the selection of the weighting parameters in Eq. 6. The size of the true and starting models was 10 km × 3.5 km shown in Figure 2. The experimental acquisitions followed the towed streamer and the OBS acquisition. A total of 200 streamer hydrophones were spaced 20 m apart at the seawater surface, and 11 OBS were spaced 1,000 m apart

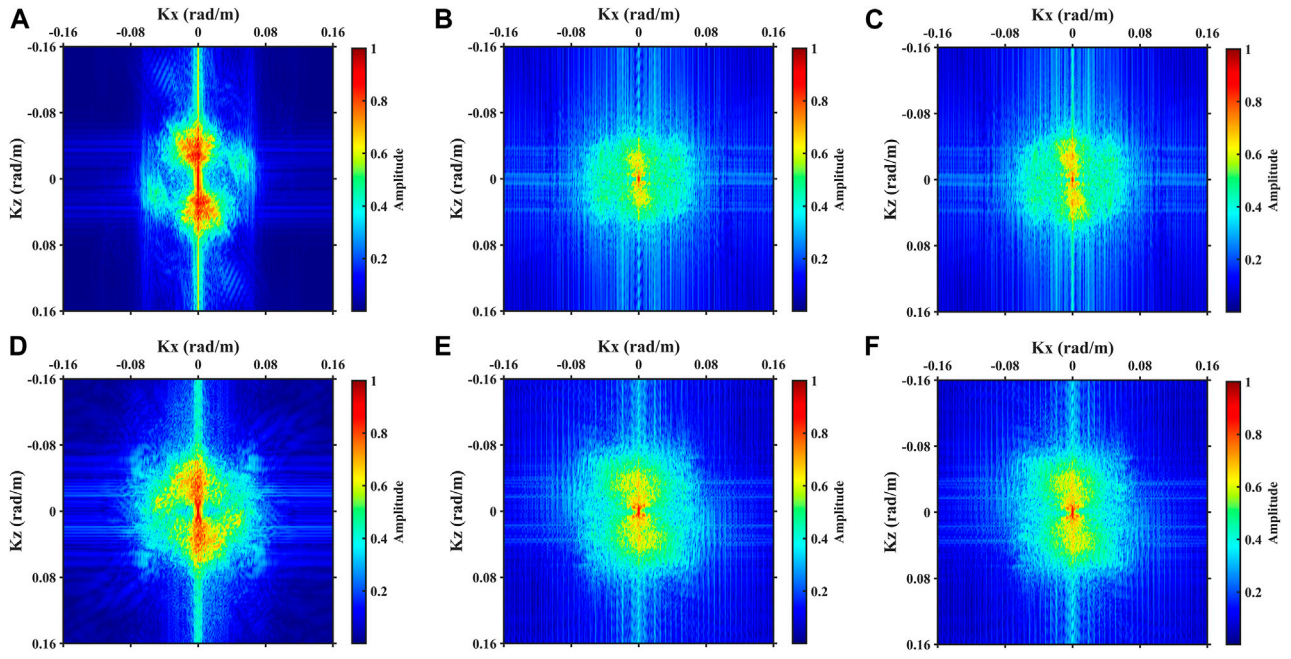

FIGURE 5
The spectrums of updating directions. **(A–C)** are the P-wave velocity updating direction of TS-FWI, OBS-FWI and J-AEFWI, respectively. **(D–F)** are the S-wave velocity updating direction of TS-FWI, OBS-FWI and J-AEFWI, respectively.

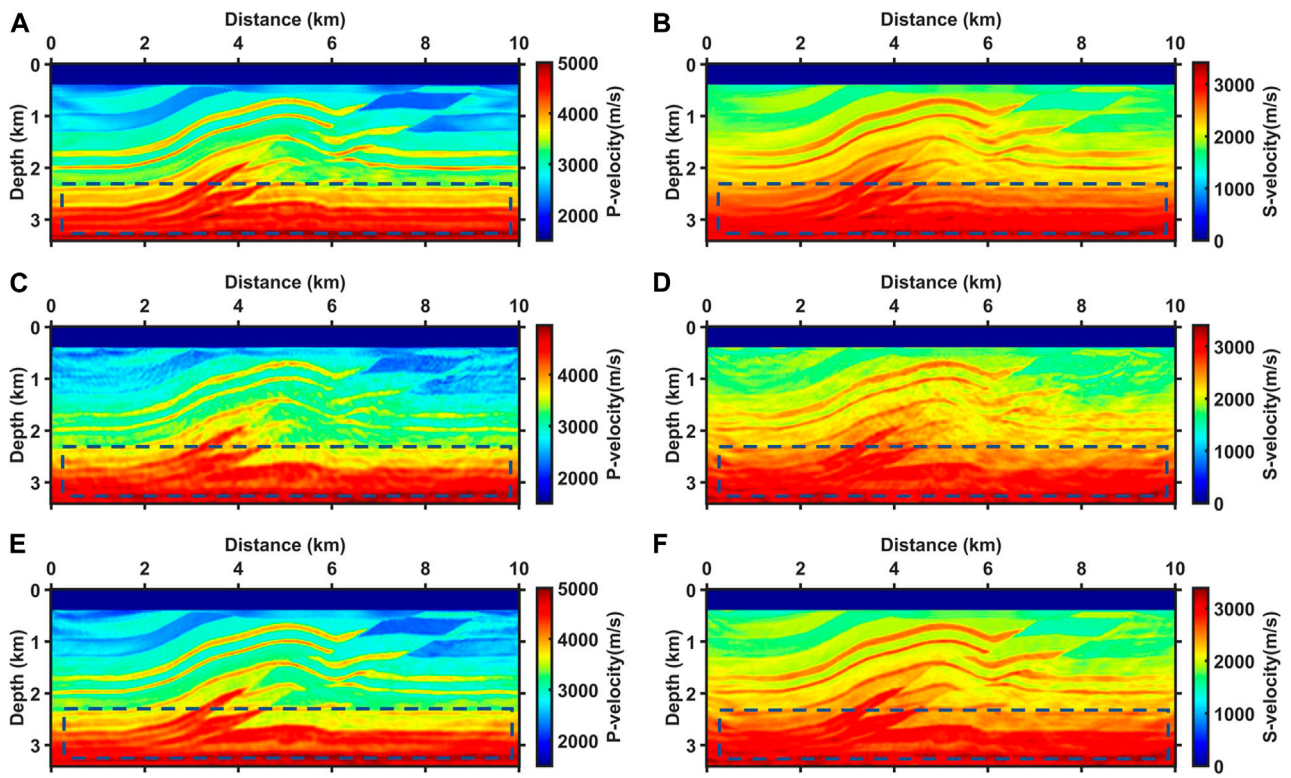

FIGURE 6
The P-wave velocity **(A,C,E)** and S-wave velocity **(B,D,F)** inversion results. **(A,B)** are results for towed streamer data alone, **(C,D)** are results for OBS data alone, **(E,F)** are results for joint towed streamer and OBS data.

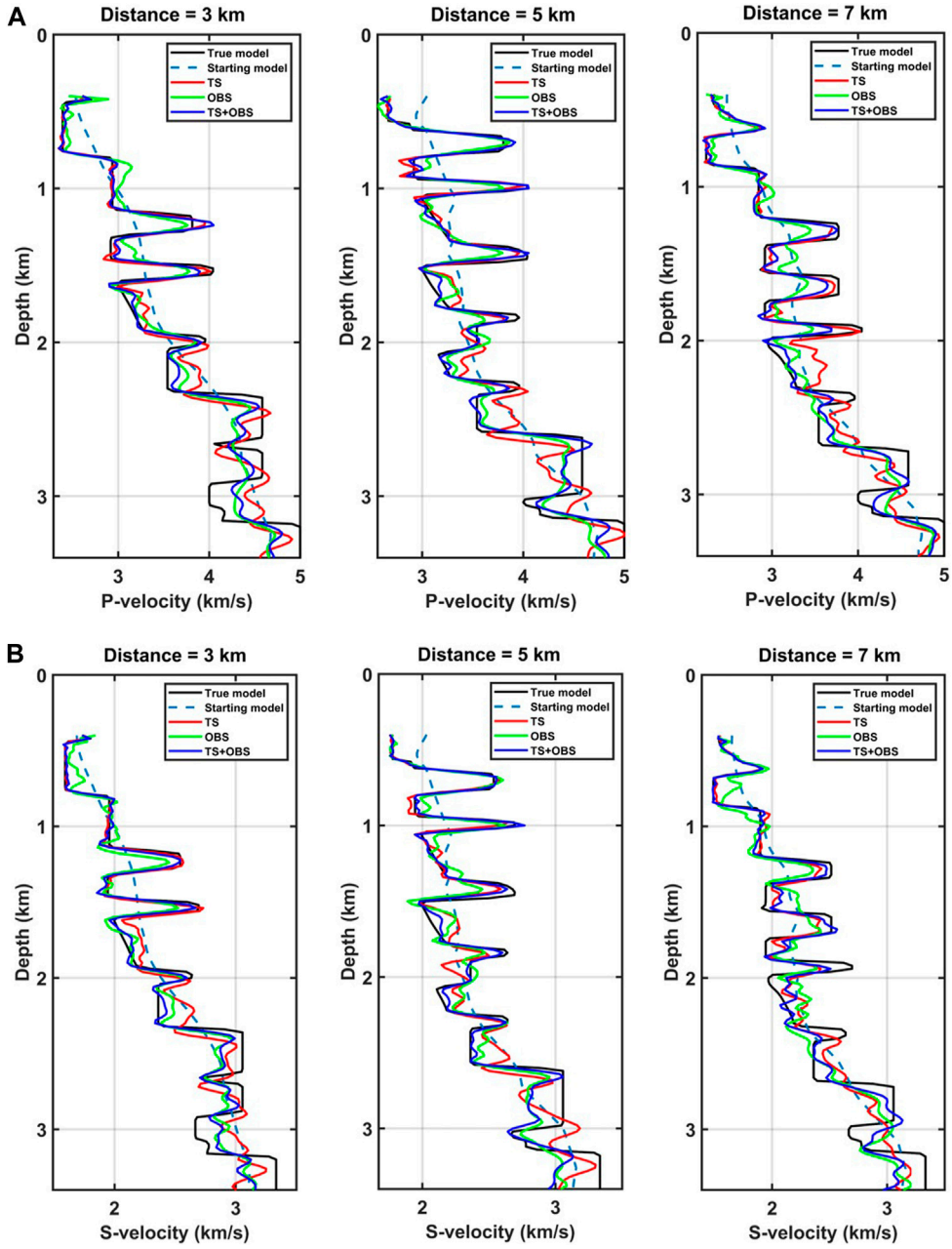

FIGURE 7
Vertical P-wave velocity **(A)** and S-wave velocity **(B)** profiles at three different locations. The solid black lines indicate the true velocities, the dashed lines indicate the starting velocities, the red lines indicate the results for towed streamer data, the green lines indicate the results for OBS data, and the blue lines indicate the J-AEFWI results.

TABLE 1 The data residuals of the final inversion results.

Method	Vx of OBS	Vz of OBS	Pressure of towed streamer
FWI for towed streamer data	23.6%	22.6%	1.3%
FWI for OBS data	16.5%	20.6%	20.2%
J-AEFWI	5.7%	5.9%	2.2%

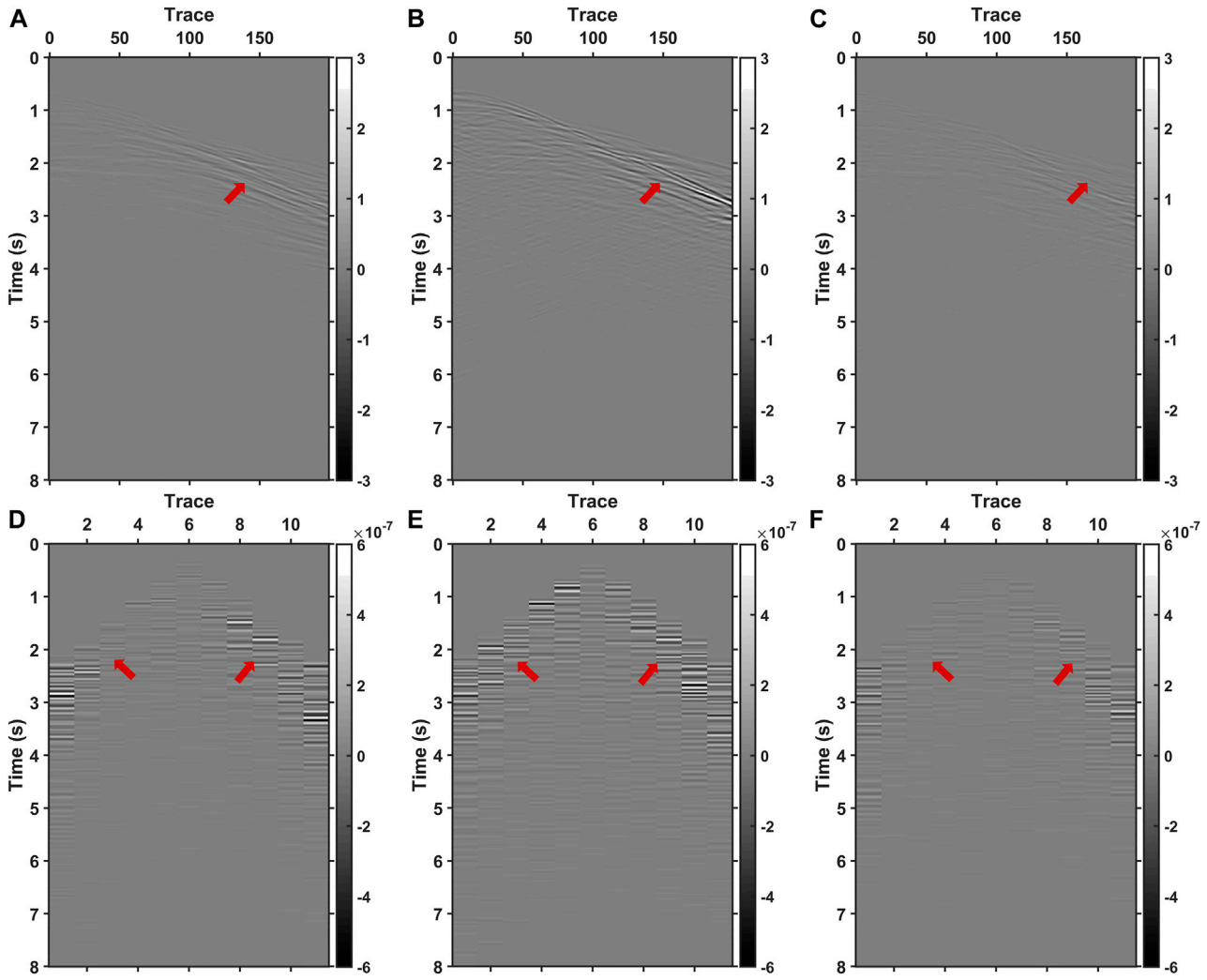

FIGURE 8
Pressure residuals of FWI results for **(A)** towed streamer data, **(B)** OBS data and **(C)** J-AEFWI. The *z*-components residuals of FWI results for **(D)** towed streamer data, **(E)** OBS data and **(F)** J-AEFWI.

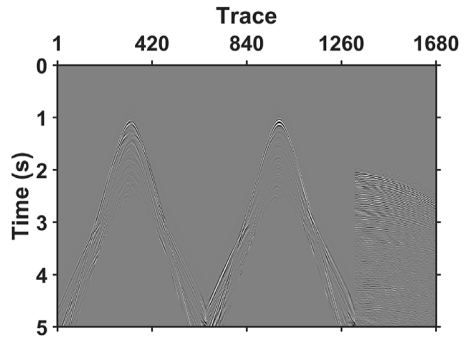

FIGURE 9
The *x*, *z*-component data of OBS and towed streamer data.

on the seafloor. Figure 3 shows the common shot gathers for both acquisitions. The towed streamer data had a clear acquisition density advantage, but only a few diving waves were recorded. In contrast, OBS data are sparse, but its long-offset data are abundant. The experiments are concerned with P-wave velocity and S-wave velocity building, and the weak parameter density is the true value that is not updated in the inversions. All three experiments were iterated 200 times to maintain consistency in the computation effort.

The characteristics of these three experiments can be observed in the updated directions for the first iteration of the inversion, as shown in Figure 4. Figures 4A, B show the P-wave velocity and S-wave velocity updating directions of the AEFWI for towed streamer data. The updating direction of the P-wave velocity has good continuity of layers (especially in shallow parts), which is attributed to the dense acquisition of the towed streamer. The weakness of (A) is that the updating direction is dominated by the high-wavenumber information mainly concentrated on the layers rather than the most desired low-wavenumber information. This is because of the slight imaging angle, which is attributed to the narrow aperture of the towed streamer acquisition. Although FWI can slowly recover models after multiple iterations, such small-angle data are unfavorable for inversion. Moreover, relying only on small-angle reflected waves, the illumination of the shallow part of the updating

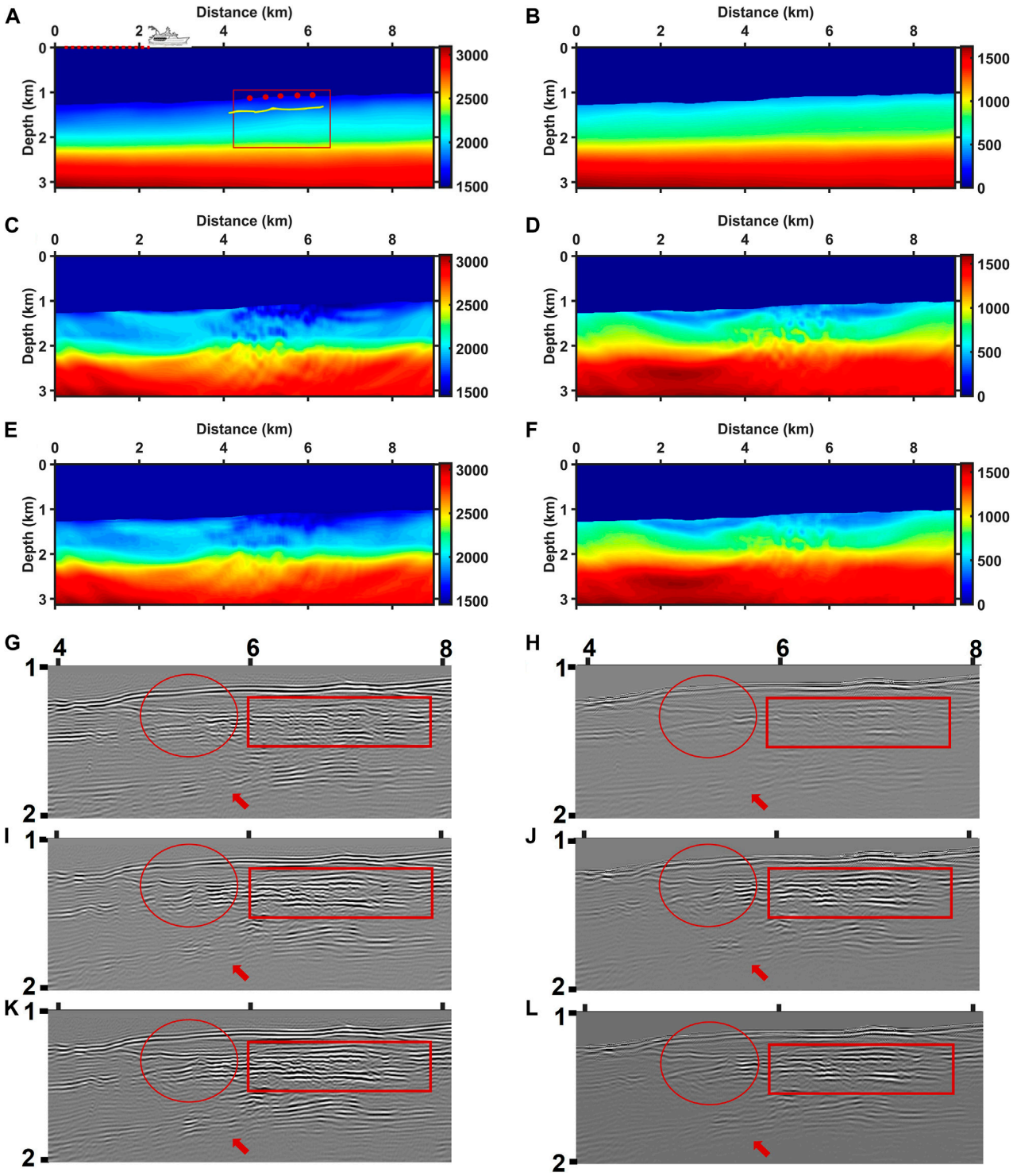

FIGURE 10
The starting P-wave **(A)** and S-wave **(B)** velocities; P-wave **(C)** and S-wave **(D)** velocities of AEFWI for OBS data; and P-wave **(E)** and S-wave **(F)** velocities of J-AEFWI. The dotted line behind the ship indicates the towed streamer, the red balls represent OBS, and the target area is in the red box. The yellow line indicates the free gas layer. The part of images of starting P-wave velocity **(G)**, starting S-wave velocity **(H)**, P-wave velocity of AEFWI for OBS data **(I)**, S-wave velocity of AEFWI for OBS data **(J)**, P-wave velocity of J-AEFWI **(K)** and S-wave velocity of J-AEFWI **(L)**, respectively. The areas indicated by arrows, rectangles and circles show improvements for J-AEFWI.

direction is excellent, whereas the illumination of the deep part is insufficient (Peter et al., 2022). In addition, without S-waves, the direction of the S-wave velocity relying only on the converted P-waves is insufficient and shows dispersion in depth.

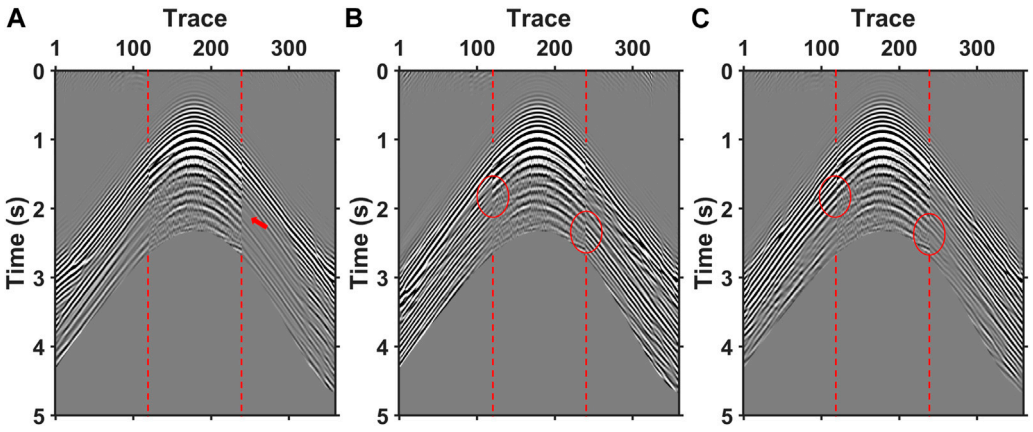

FIGURE 11
Synthetic data generated using initial models **(A)**, AEFWI results for OBS data **(B)** and J-AEFWI results, compared to the observed data. The middle of each image shows the field data and the sides show the synthetic data, which are separated by red lines. The waveforms after multiples are muted.

Figure 4C, D show P-wave and S-wave velocity updating directions of sparse OBS data AEFWI. As expected, the updating directions of the OBS data are very poor for layer continuity compared with the updating directions of the towed streamer data. The sparse data indicate that imaging stacking is insufficient, and many acquisition footprints (show arcs) appear in the direction profiles. Encouragingly, long-offset data play a significant role in determining the background velocity. The updated directions of the OBS data have more low-wavenumber information, which is crucial for recovering large-scale structures. The deep illumination of the model is much better because of wide-azimuthal acquisition (Shen et al., 2018). Virieux and Operto (2009) found that the frequency and imaging angle influence the wavenumber of the imaging. The lower the frequencies and the larger the imaging angles, the lower the wavenumber of the imaging results. If the starting model is not good enough, the low frequency and long observation aperture become keys to the success of FWI (Shipp and Singh, 2002; Ravaut et al., 2004; Operto et al., 2006; Plessix et al., 2010). In addition, positively influenced by the abundant S-waves, the updating direction of the S-wave velocity is better illuminated in the deep part (Figure 4D), making the S-wave velocity inversion more likely to succeed (Ren and Liu, 2016; Wang and Cheng, 2017).

Figures 4E, F show the P-wave and S-wave velocity updating directions of the J-AEFWI. The updating directions of J-AEFWI are shaped as a combination of the towed streamer and OBS updating directions. On the one hand, the strong acquisition footprints are faded, and the continuity of the layers was enhanced owing to the addition of the towed streamer data. On the other hand, the low-wavenumber information from the wide-azimuthal OBS data remained, and the superior illumination of the deep parts was preserved. As observed, the updated directions of J-AEFWI carry more information for P-wave and S-wave velocity buildings.

Figure 5 shows the wavenumber spectrum of the updating directions of the FWI for towed streamer data, OBS data and J-AEFWI. The low wavenumbers in the updating directions of the OBS data are dominant, whereas updating the directions of the towed streamer data contain higher wavenumbers. The updating directions of J-AEFWI contain both low and high wavenumbers.

The characteristics of the updating directions are projected in the inversion results. Figure 6 shows the results of the three inversion experiments. Figures 6A, B are P-wave and S-wave velocity results for the towed streamer data. Benefiting from dense acquisition, FWI accurately depicts the structural layers, which are almost consistent with the true velocities. However, below 2 km depth, the different background velocities are not adequately inverted and blended, which affects the identification of deeper structures (low-velocity structures indicated by the dashed boxes). In the results of the OBS data (Figures 6C, D), large-scale background velocities are adequately inverted, especially at the depth indicated by the dashed boxes, where the low-velocity structures are well illuminated and can be identified clearly. The shortcoming is that insufficient data leads to inadequate stacking, resulting in poor continuity and shallow acquisition footprints. Figures 6E, F show better inversion results for J-AEFWI. In the shallow part, the results depict the layers at high resolution, and the acquisition footprints are suppressed; in the deep part, sufficient illumination and accurate macroscopic velocities remain.

Figure 7 shows vertical velocity profiles at three different locations. Above 2 km depth, the results for towed streamer data (red lines) closely match true velocities (black lines), while the results deviate from true velocities below it. On the contrary, the results for OBS data (green lines) are slightly worse at shallow depth and slightly better at a deeper depth. The inversion results of J-AEFWI accurately fit the true velocities in both the deep and shallow parts. Overall, the results of J-AEFWI are better than those of AEFWI for towed streamer data alone or AEFWI for OBS data alone.

To further illustrate the accuracy of the inversion results, the data residuals are quantitatively shown. Figure 8 shows the final data residuals of FWI for towed streamer data, OBS data, and J-AEFWI. Where the red arrows indicate, the amplitudes of residuals are smaller for J-AEFWI. Compared to the residuals of the initial model, the data residuals of the final inversion results are shown in Table 1. Naturally, the FWI for towed streamer data uses only towed streamer data and not the OBS data, which has the

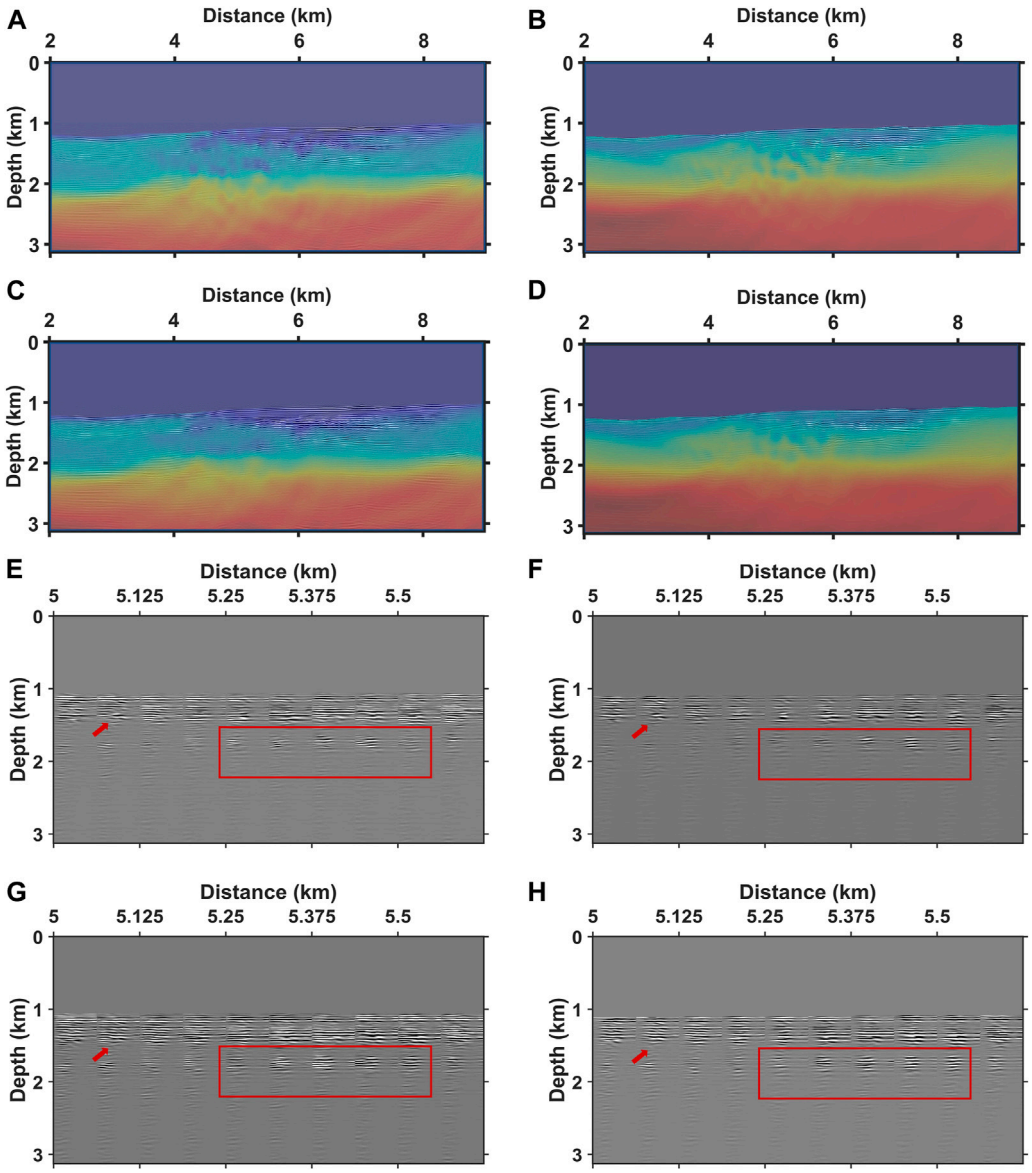

FIGURE 12
The images with corresponding velocity models overlay. P-wave velocity of AEFWI for OBS data **(A)**, S-wave velocity of AEFWI for OBS data **(B)**, P-wave velocity of J-AEFWI **(C)** and S-wave velocity of J-AEFWI **(D)**. The ADCIGs of **(E)** P-wave velocity of AEFWI for OBS data, **(F)** S-wave velocity of AEFWI for OBS data, **(G)** P-wave velocity of J-AEFWI, and **(H)** S-wave velocity of J-AEFWI. The areas indicated by arrows and rectangles show improvements for J-AEFWI.

smallest residuals for the towed streamer data and the larger residuals for the OBS data. The FWI for OBS data uses only OBS data and not the towed streamer data, which has the smallest residuals for the OBS data and the larger residuals for the towed streamer data. The J-AEFWI uses both towed streamer and OBS data, and have the smallest residuals.

4 Field data examples

We tested the J-AEFWI approach on South China Sea field data. A total of 875 shots were distributed evenly over a straight line of approximately 20 km. Considering the calculation cost, we selected only a part of the data to implement in the experiments. The collection ship carried 360 towed streamer hydrophones, and only five OBSs were arranged on the seafloor with 400 m spacing. Figure 9 shows the *x*, *z*-component of an OBS, and the towed streamer data. We know from early works that free gas layers exist in the target area (indicated by the yellow line in Figure 10A). During pre-processing, we applied a transformation from 3D to 2D geometric spreading (Crase et al., 1990), and a band-pass filter was applied to the data. A time window is applied to mute the reflected waves after multiple arrivals.

In approximately 1 km deep water, the towed streamer hardly received the diving waves, so it is unwise to implement FWI for multi-parameter building using towed streamer data alone. In this

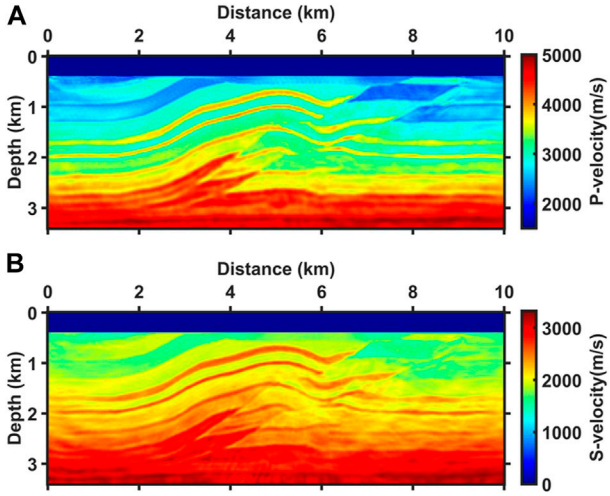

FIGURE 13
P-wave **(A)** and S-wave **(B)** velocity of cascaded AEFWI.

section, we describe the implementation of an AEFWI experiment for OBS data and a J-AEFWI experiment. The starting P-wave and S-wave models are presented in Figures 10A, B. Before the FWI, we improved the starting models using tomography techniques.

Figures 10C, D shows AEFWI results for OBS data alone. Compared with the starting models, the inversion results change on macroscopic velocities and appear to have some high wavenumber information which is beneficial to identify the layers. In particular, a well-defined low-velocity layer appears in the shallow part, which is consistent with prior information provided by the early works that free gas layers exist in the target area. Unfortunately, sparse data led to poor continuity and irregular perturbations in these layers. J-AEFWI improved these anomalies caused by insufficient data. As shown in Figures 10E, F, the irregular disturbances of the layers are suppressed, and layers are more continuous.

Conventionally, the reverse time migration (RTM) imaging technique is used to verify the accuracy of inversion results. Figures 10G–L shows the P-wave velocity (G) and S-wave velocity (H) images of the starting models, P-wave velocity (I) and S-wave velocity (J) images of AEFWI for OBS data, and P-wave velocity (K) and S-wave velocity (L) images of J-AEFWI. In the target area, both inversion experiments improved the RTM images (indicated by rectangular areas). More accurate velocities allowed the images to migrate to the correct position, as evidenced by the more continuous and clear images. In particular, the images of S-wave velocities, which were blurred for the starting models, improved significantly with the inversion results. In addition, the images of the J-AEFWI results are more converged and clearer than those of the OBS data (indicated by the circles and arrows).

Figure 11 presents a comparison between field data and synthetic data for the initial models, OBS data AEFWI results, and J-AEFWI results. The center of the red lines represents the field data, with the synthetic data on either side. The waveforms after multiples have been suppressed. In Figure 11A, the initial model's synthetic data lacks some reflection events and exhibits poor continuity (as indicated by the red arrow). In contrast, Figure 11B demonstrates that the OBS data inversion results exhibit improved continuity in the reflection events. Finally, Figure 11C shows that the synthetic data generated by the J-AEFWI method most closely aligns with the field data, as indicated by the red circles.

To verify the reliability of the inversion results, we show the P-wave and S-wave velocity images with a velocity model overlay, as shown in Figures 12A–D, where the emerging velocity layers largely coincide with the image positions. We also show the angle-domain common-image gathers (ADCIGs) to illustrate the accuracy of the inversion results. Figures 12E–H shows ADCIGs at locations in the target region. Figures 12E–F show the ADCIGs of P-wave velocity and S-wave velocity for the AEFWI of OBS data, and Figures 12G–H show the ADCIGs of P-wave velocity and S-wave velocity for the AEFWI of joint data. The ADCIGs of the two FWIs are generally similar, and a comparison shows that the ADCIGs of the J-AEFWI results are flatter and clearer at some locations than those of the OBS data (indicated by arrows and rectangles).

5 Discussion

The weighting parameter φ played a key role in the success of the J-AEFWI approach. For simplicity, the value of φ was set to balance the proportions of the two data in the objective function. In addition, before calculating the updating directions of J-AEFWI, φ can be adjusted such that the energy of the gradients of the two types of data is approximately half. In practice, the value of φ can be adjusted according to the quality of the different data. If the spacing of OBS in the field data is large, it is appropriate to increase the weighting of towed streamer data and decrease the weighting of

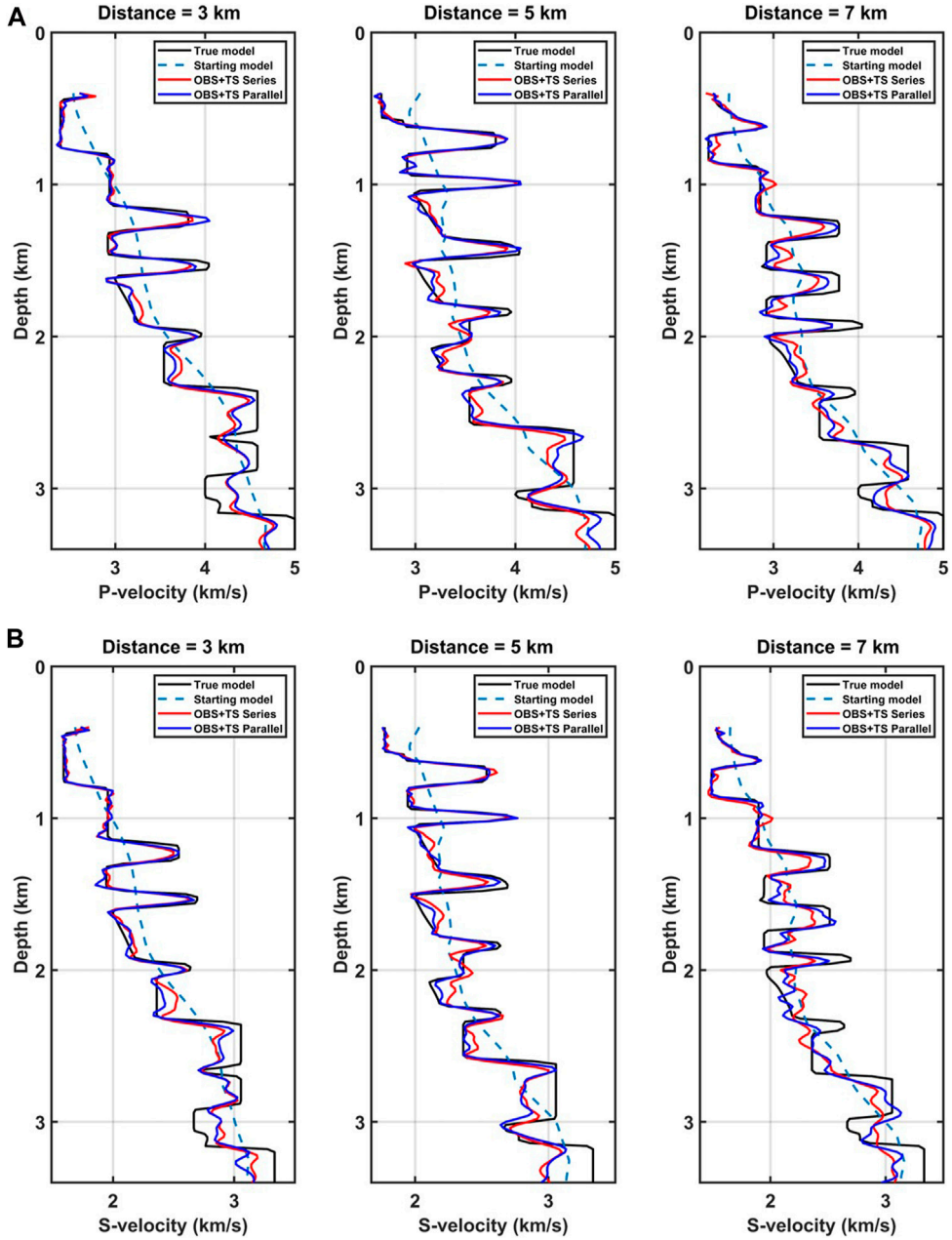

FIGURE 14
Vertical P-wave velocity **(A)** and S-wave velocity **(B)** profiles at three different locations. The solid black lines indicate the true velocities, the dashed lines indicate the starting velocities, the red lines indicate the cascaded AEFWI results, and the blue lines indicate the J-AEFWI results.

OBS data in this case. The weighting of the OBS data can be increased as the OBS interval decreases, or the weighting of the towed streamer data can be adjusted downward if the noise pollution is serious.

Next, we present a cascaded AEFWI approach that does not require determining the value of the weighting parameters. We first inverted 100 times using the OBS data, and the inversion results were then inverted 100 times using the towed streamer data, with the same inversion parameters as above for AEFWI. As shown in Figure 13, the cascaded AEFWI accurately reconstructs the velocity models. In the vertical velocity profiles (Figure 14), the inversion accuracy of the cascaded FWI was slightly worse than that of J-AEFWI. This is because cascaded FWI utilizes both data in segments, whereas J-AEFWI utilizes both data in the entire inversion process.

Figure 15 shows P-wave and S-wave velocity normalized misfits between inversion and true models. First, the decline of J-AEFWI in P-wave velocity misfit is leading in the whole process, and cascaded AEFWI takes inversion results of OBS data as the starting point, which inevitably lags behind J-AEFWI. This pattern is the same in S-wave velocity misfit, but inversion for OBS data is ahead of inversion for towed streamer data. This is because S-waves in OBS data play a significant role in S-wave velocity building.

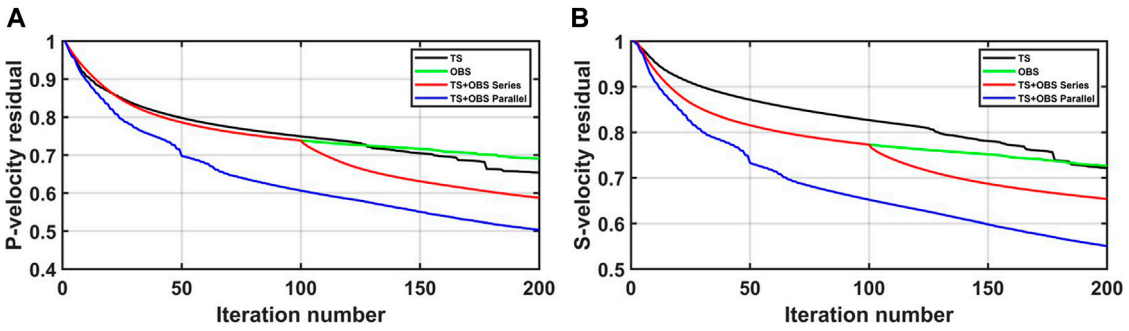

FIGURE 15
P-wave **(A)** and S-wave **(B)** velocity normalized misfits between inversion and true models. Black lines indicate AEFWI for towed streamer data; green lines indicate AEFWI for OBS data; red lines indicate cascaded AEFWI; blue lines indicate J-AEFWI.

6 Conclusion

We developed a J-AEFWI method, in which towed streamer and OBS data were used to build P-wave and S-wave velocity models based on the same acoustic-elastic coupled equations. This method combines the advantages of both types of data. On the one hand, towed streamer data with dense acquisition can accurately depict model layers and suppress acquisition footprints. On the other hand, the long-offset OBS data with rich diving waves benefit deep illumination and large-scale background velocity building. The synthetic experimental results show that J-AEFWI obtains more accurate results than when using these two types of data alone. The results of J-AEFWI were slightly better than those of the cascaded FWI strategy. This method was applied to the field data, and better results were obtained.

Data availability statement

The original contributions presented in the study are included in the article/supplementary material, further inquiries can be directed to the corresponding author.

Author contributions

TY: investigation, methodology and writing manuscript. YL and JY: checking and modifying manuscript.

Funding

We are grateful for financial support from National Natural Science Foundation of China (grant nos 41930105; 41774122; 41630964; 41874127; 42004096), the National Key R&D Program of China (grant nos 2018YFC0310100 and 2019YFC0312004), the Fundamental Research Funds for the Central Universities of China, and the Strategic Priority Research Program of the Chinese Academy of Sciences (grant no. XDA14010203).

Conflict of interest

The authors declare that the research was conducted in the absence of any commercial or financial relationships that could be construed as a potential conflict of interest.

Publisher's note

All claims expressed in this article are solely those of the authors and do not necessarily represent those of their affiliated organizations, or those of the publisher, the editors and the reviewers. Any product that may be evaluated in this article, or claim that may be made by its manufacturer, is not guaranteed or endorsed by the publisher.

References

Agudo, O. C., da Silva, N. V., Warner, M., and Morgan, J. (2018). Acoustic full-waveform inversion in an elastic world. *Geophysics* 83 (3), R257–R271. doi:10.1190/geo2017-0063.1

Borisov, D., Gao, F., Williamson, P., and Tromp, J. (2020). Application of 2D full-waveform inversion on exploration land data. *Geophysics* 85 (2), R75–R86. doi:10.1190/geo2019-0082.1

Bunks, C., Saleck, F. M., Zaleski, S., and Chavent, G. (1995). Multiscale seismic waveform inversion. *Geophysics* 60, 1457–1473. doi:10.1190/1.1443880

Crase, E., Pica, A., Noble, M., McDonald, J., and Tarantola, A. (1990). Robust elastic nonlinear waveform inversion: Application to real data. *Geophysics* 55, 527–538. doi:10.1190/1.1442864

Dessa, J. -X., Operto, S., Kodaira, S., Nakanishi, A., Pascal, J., Virieux, J., et al. (2004). Multiscale seismic imaging of the eastern Nankai trough by full waveform inversion. *Geophys. Res. Lett.* 31, L18606. doi:10.1029/2004GL020453

Dellinger, J., Brenders, A., Sandschaper, J. R., Regone, C., Etgen, J., Ahmed, S., et al. (2017). The Garden Banks model experience. *The Leading Edge* 36, 151–158. doi:10.1190/tle36020151.1

Faucher, F., Alessandrini, G., Barucq, H., de Hoop, M. V., Gaburro, R., and Sincich, E. (2020). Full reciprocity-gap waveform inversion enabling sparse-source acquisition. *Geophysics* 85 (6), R461–R476. doi:10.1190/GEO2019-0527.1

Gauthier, O., Virieux, J., and Tarantola, A. (1986). Two-dimensional nonlinear inversion of seismic waveforms: numerical results. *Geophysics* 51 (7), 1387.

Lailly, P. (1983). *The Seismic Inverse Problem as a Sequence of Before Stack Migrations: Conference on Inverse Scattering: Theory and Application*. Expanded Abstracts: SEG. New Delhi, India: SIAM, 206–220.

Lanzarone, P., Shen, X., Brenders, A., Xia, G., Dellinger, J., Ritter, G., et al. (2022). Innovative application of full-waveform inversion applied to extended wide-azimuth marine streamer seismic data in a complex salt environment. *Geophysics* 87 (3), B193–B205. doi:10.1190/geo2021-0374.1

Li, D., Gao, F., and Williamson, P. (2019). *A Deep Learning Approach for Acoustic FWI With Elastic Data: 89th Annual International Meeting*. Expanded Abstracts: SEG, New Delhi, India. 2303–2307.

Liu, Y., Huang, X., Yang, J., Liu, X., Li, B., Dong, L., et al. (2021). Multiparameter model building for the Qiuyue structure using 4C ocean-bottom seismometer data. *Geophysics* 86, B291–B301. doi:10.1190/geo2020-0537.1

Operto, S., Gholami, Y., Prieux, V., Ribodetti, A., Brossier, R., Metivier, L., et al. (2013). A guided tour of multiparameter full-waveform inversion with multicomponent data: From theory to practice. *Lead. EDGE* 32, 1040–1054. doi:10.1190/tle32091040.1

Operto, S., Virieux, J., Dessa, J. -X., and Pascal, G. (2006). Crustal seismic imaging from multifold ocean bottom seismometer data by frequency domain full waveform tomography: Application to the eastern Nankai trough. *J. Geophys. Res. SOLID EARTH* 111, B09306. doi:10.1029/2005JB003835

Pan, W., Geng, Y., and Innanen, K. A. (2018). Interparameter trade-off quantification and reduction in isotropic-elastic full-waveform inversion: Synthetic experiments and hussar land data set application. *Geophys. J. Int.* 212, 1305–1333. doi:10.1093/gji/ggy037

Pan, W., Innanen, K. A., and Wang, Y. (2020). Parameterization analysis and field validation of VTI-elastic full-waveform inversion in a walk-away vertical seismic profile configuration. *Geophysics* 85 (3), B87–B107. doi:10.1190/geo2019-0089.1

Peter, L., Xukai, S., Andrew, B., Ganyuan, X., Joe, D., Gabriel, R., et al. (2022). Innovative application of full-waveform inversion applied to extended wide-azimuth marine streamer seismic data in a complex salt environment. *Geophysics* 87, B193–B205. doi:10.1190/geo2021-0374.1

Plessix, R. E., Baeten, G., de Maag, J. W., Klaassen, M., Rujie, Z., and Zhifei, T. (2010). *Application of Acoustic Full Waveform Inversion to a Low-Frequency Large-Offset Land Data Set: 2010 Annual Meeting*. Expanded Abstracts: SEG, New Delhi, India, 930–934.

Pratt, R. G. (1999). Seismic waveform inversion in the frequency domain, Part 1: Theory and verification in a physical scale model. *Geophysics* 64, 888–901. doi:10.1190/1.1444597

Ravaut, C., Operto, S., Improta, L., Virieux, J., Herrero, A., and Dell'Aversana, P. (2004). Multiscale imaging of complex structures from multifold wide-aperture seismic data by frequency-domain full-waveform tomography: Application to a thrust belt. *Geophys. J. Int.* 159, 1032–1056. doi:10.1111/j.1365-246X.2004.02442.x

Ren, Z., and Liu, Y. (2016). A hierarchical elastic full-waveform inversion scheme based on wavefield separation and the multistep-length approach. *Geophysics* 81 (3), R99–R123. doi:10.1190/geo2015-0431.1

Sears, T. J., Singh, S. C., and Barton, P. J. (2008). Elastic full waveform inversion of multi-component OBC seismic data. *Geophys. Prospect.* 56, 843–862. doi:10.1111/j.1365-2478.2008.00692.x

Shen, X., Ahmed, I., Brenders, A., Dellinger, J., Etgen, J., and Michell, S. (2018). Full-waveform inversion: The next leap forward in subsalt imaging. *Lead. EDGE* 37, 67b1–67b6. doi:10.1190/tle37010067b1.1

Shen, X., and Clapp, R. G. (2015). Random boundary condition for memory-efficient waveform inversion gradient computation. *Geophysics* 80, R351–R359. –R359. doi:10.1190/geo2014-0542.1

Shen, X. (2010). *Near-Surface Velocity Estimation by Weighted Early-Arrival Waveform Inversion: 2010 Annual Meeting*. Expanded Abstracts: SEG, New Delhi, India.

Shipp, R. M., and Singh, S. C. (2002). Two-dimensional full wavefield inversion of wide-aperture marine seismic streamer data. *Geophys. J. Int.* 151, 325–344. doi:10.1046/j.1365-246X.2002.01645.x

Sun, M., and Jin, S. (2020). Multiparameter elastic full waveform inversion of ocean bottom seismic four-component data based on a modified acoustic-elastic coupled equation. *Remote Sens.* 12, 2816. doi:10.3390/rs12172816

Tarantola, A. (1984). Inversion of seismic reflection data in the acoustic approximation. *Geophysics* 49, 1259–1266. doi:10.1190/1.1441754

Thiel, N., Hertweck, T., and Bohlen, T. (2019). Comparison of acoustic and elastic full waveform inversion of 2D towed-streamer data in the presence of salt. *Geophys. Prospect.* 67, 1365-2478.12728–361. doi:10.1111/1365-2478.12728

Vigh, D., Jiao, K., Watts, D., and Sun, D. (2014). Elastic full-waveform inversion application using multicomponent measurements of seismic data collection. *Geophysics* 79, R63–R77. doi:10.1190/geo2013-0055.1

Virieux, J., and Operto, S. (2009). An overview of full-waveform inversion in exploration geophysics. *Geophysics* 74, WCC1–WCC26. doi:10.1190/1.3238367

Wang, T. F., and Cheng, J. B. (2017). Elastic full waveform inversion based on mode decomposition: The approach and mechanism. *Geophys. J. Int.* 209, 606–622. doi:10.1093/gji/ggx038

Yang, H., and Zhang, J. (2019). Full waveform inversion of combined towed streamer and limited OBS seismic data: A theoretical study. *Mar. Geophys. Res.* 40, 237–244. doi:10.1007/s11001-018-9363-6

Yang, J., Liu, Y., and Dong, L. (2016). Simultaneous estimation of velocity and density in acoustic multiparameter full-waveform inversion using an improved scattering-integral approach. *GEOPHYSICS* 81, R399–R415. doi:10.1190/geo2015-0707.1

Yang, T., and Liu, Y. (2020). Full waveform inversion based on the acoustic-elastic coupled equation. *2020 Annu. Conf. Exhib. OnlineEAGE* 2020, 1–5. doi:10.3997/2214-4609.202010563

Yao, G., da Silva, N. V., Warner, M., Wu, D., and Yang, C. (2019). Tackling cycle skipping in full-waveform inversion with intermediate data. *Geophysics* 84, R411–R427. doi:10.1190/geo2018-0096.1

Yu, P., and Geng, J. (2019). Acoustic-elastic coupled equations in vertical transverse isotropic media for pseudoacoustic-wave reverse time migration of ocean-bottom 4C seismic data. *Geophysics* 84, S317–S327. doi:10.1190/geo2018-0295.1

Yu, P., Geng, J., Li, X., and Wang, C. (2016). Acoustic-elastic coupled equation for ocean bottom seismic data elastic reverse time migration. *Geophysics* 81, S333–S345. doi:10.1190/geo2015-0535.1

Yu, P., and Sun, M. (2022). Acoustic-elastic coupled equations for joint elastic imaging of TS and Sparse OBN/OBS Data. *Pure Appl. Geophys.* 179, 311–324. doi:10.1007/s00024-021-02899-5

Zheglova, P., and Malcolm, A. (2019). *Vector Acoustic Full Waveform Inversion: Taking Advantage of De-Aliasing and Receiver Ghosts*, 05427. arXiv preprint arXiv. https://arxiv.org/abs/1910.05427. doi:10.48550/arXiv.1910.05427

Appendix A

We used Lagrangian multiplier method to derive the adjoint equations and gradients. The acoustic-elastic coupled equation and the objective function can be expressed as

$$\begin{cases} \rho\dfrac{\partial v_x}{\partial t} - \dfrac{\partial \tau^s_{xx}}{\partial x} + \dfrac{\partial P}{\partial x} - \dfrac{\partial \tau^s_{xz}}{\partial z} = \mathcal{O}_1 \\ \rho\dfrac{\partial v_z}{\partial t} + \dfrac{\partial \tau^s_{xx}}{\partial z} + \dfrac{\partial P}{\partial z} - \dfrac{\partial \tau^s_{xz}}{\partial x} = \mathcal{O}_2 \\ \dfrac{\partial P}{\partial t} + (\lambda+\mu)\left(\dfrac{\partial v_x}{\partial x} + \dfrac{\partial v_z}{\partial z}\right) = \mathcal{O}_3 \\ \dfrac{\partial \tau^s_{xx}}{\partial t} - \mu\left(\dfrac{\partial v_x}{\partial x} - \dfrac{\partial v_z}{\partial z}\right) = \mathcal{O}_4 \\ \dfrac{\partial \tau^s_{xz}}{\partial t} - \mu\left(\dfrac{\partial v_x}{\partial z} + \dfrac{\partial v_z}{\partial x}\right) = \mathcal{O}_5 \end{cases} \tag{A1}$$

and

$$J = \frac{1}{2}\int_0^{Xr}\int_0^t \gamma^*\varphi\left(P^{sim}_{ts} - P^{obs}_{ts}\right)^2 + \alpha\left(v^{sim}_{xo} - v^{obs}_{xo}\right)^2 + \beta\left(v^{sim}_{zo} - v^{obs}_{zo}\right)^2 dt \tag{A2}$$

Expanding the objective function using the Lagrange multiplier method yields:

$$\begin{aligned} O\left(m, \mathbf{U}, \tilde{\mathbf{U}}\right) = J &+ \int_0^t \langle \tilde{v}_x, \mathcal{O}_1\rangle_{\mathbf{x}} dt + \int_0^t \langle \tilde{v}_z, \mathcal{O}_2\rangle_{\mathbf{x}} dt + \int_0^t \langle \tilde{P}, \mathcal{O}_3\rangle_{\mathbf{x}} dt \\ &+ \int_0^t \langle \tilde{\tau}^s_{xx}, \mathcal{O}_4\rangle_{\mathbf{x}} dt + \int_0^t \langle \tilde{\tau}^s_{xz}, \mathcal{O}_5\rangle_{\mathbf{x}} dt \end{aligned} \tag{A3}$$

where,

$$\mathbf{U} = \left(v_x, v_z, P, \tau^s_{xx}, \tau^s_{xz}\right) \tag{A4}$$

$$\tilde{\mathbf{U}} = \left(\tilde{v}_x, \tilde{v}_z, \tilde{P}, \tilde{\tau}^s_{xx}, \tilde{\tau}^s_{xz}\right) \tag{A5}$$

The vector $\tilde{\mathbf{U}}$ represents adjoint-wavefield. The new objective function J calculates the first derivative of each parameter and equals zero:

$$\frac{\partial O}{\partial m} = 0 \tag{A6}$$

$$\frac{\partial O}{\partial U_i} = 0 \tag{A7}$$

$$\frac{\partial O}{\partial \tilde{U}_i} = 0 \tag{A8}$$

Finally, we can obtain the adjoint equations:

$$\begin{cases} \rho\dfrac{\partial \tilde{v}_x}{\partial t} = \mu\dfrac{\partial \tilde{\tau}^s_{xx}}{\partial x} - (\lambda+\mu)\dfrac{\partial \tilde{P}}{\partial x} + \mu\dfrac{\partial \tilde{\tau}^s_{xz}}{\partial z} + \alpha\left(v^{sim}_{xo} - v^{obs}_{xo}\right) \\ \rho\dfrac{\partial \tilde{v}_z}{\partial t} = -\mu\dfrac{\partial \tilde{\tau}^s_{xx}}{\partial z} - (\lambda+\mu)\dfrac{\partial \tilde{P}}{\partial z} + \mu\dfrac{\partial \tilde{\tau}^s_{xz}}{\partial x} + \beta\left(v^{sim}_{zo} - v^{obs}_{zo}\right) \\ \dfrac{\partial \tilde{P}}{\partial t} = -\left(\dfrac{\partial \tilde{v}_x}{\partial x} + \dfrac{\partial \tilde{v}_z}{\partial z}\right) + \left(P_{pre} - P_{obs}\right) + \gamma^*\varphi\left(P^{sim}_{ts} - P^{obs}_{ts}\right) \\ \dfrac{\partial \tilde{\tau}^s_{xx}}{\partial t} = \left(\dfrac{\partial \tilde{v}_x}{\partial x} - \dfrac{\partial \tilde{v}_z}{\partial z}\right) \\ \dfrac{\partial \tilde{\tau}^s_{xz}}{\partial t} = \left(\dfrac{\partial \tilde{v}_x}{\partial z} + \dfrac{\partial \tilde{v}_z}{\partial x}\right) \end{cases} \tag{A9}$$

and gradients:

$$\nabla_\lambda E = \int_0^t \left(\frac{\partial v_x}{\partial x} + \frac{\partial v_z}{\partial z}\right)\tilde{P} dt \tag{A10}$$

$$\nabla_\mu E = \int_0^t \left(\frac{\partial v_x}{\partial x} + \frac{\partial v_z}{\partial z}\right)\tilde{P} - \left(\frac{\partial v_x}{\partial x} - \frac{\partial v_z}{\partial z}\right)\tilde{\tau}^s_{xx} - \left(\frac{\partial v_x}{\partial z} + \frac{\partial v_z}{\partial x}\right)\tilde{\tau}^s_{xz} dt \tag{A11}$$

The expressions of P- and S-wave velocity can be obtained by using the chain rule.

frontiers | Frontiers in Earth Science

TYPE Original Research
PUBLISHED 16 January 2023
DOI 10.3389/feart.2022.1044072

OPEN ACCESS

EDITED BY
Qizhen Du,
China University of Petroleum,
Huadong, China

REVIEWED BY
Hanming Chen,
University of Petroleum, China
Hemin Yuan,
China University of Geosciences, China

*CORRESPONDENCE
Jianping Huang,
jphuang@upc.edu.cn
Liang Chen,
seismicwave@foxmail.com

SPECIALTY SECTION
This article was submitted to Solid Earth Geophysics,
a section of the journal
Frontiers in Earth Science

RECEIVED 14 September 2022
ACCEPTED 31 October 2022
PUBLISHED 16 January 2023

CITATION
Huang J, Chen L, Wang Z, Song C and Han J (2023), Adaptive variable-grid least-squares reverse-time migration. *Front. Earth Sci.* 10:1044072. doi: 10.3389/feart.2022.1044072

Adaptive variable-grid least-squares reverse-time migration

Jianping Huang[1,2]*, Liang Chen[1,2]*, Ziying Wang[1,2], Cheng Song[1,2] and Jiale Han[1,2]

[1]Key Laboratory of Deep Oil and Gas, China University of Petroleum (East China), Qingdao, China, [2]Pilot National Laboratory for Marine Science and Technology, Qingdao, Shandong, China

Variable-grid methods have the potential to save computing costs and memory requirements in forward modeling and least-squares reverse-time migration (LSRTM). However, due to the inherent difficulty of automatic grid discretization, conventional variable-grid methods have not been widely used in industrial production. We propose a variable-grid LSRTM (VG-LSRTM) method based on an adaptive sampling strategy to improve computing efficiency and reduce memory requirements. Based on the mapping relation of two coordinate systems, we derive variable-grid acoustic wave equation and its corresponding Born forward modeling equation. On this basis, we develop a complete VG-LSRTM framework. Numerical experiments on a layered model validate the feasibility of the proposed VG-LSRTM algorithm. LSRTM tests on a modified Marmousi model demonstrate that our method can save computational costs and memory requirements with little accuracy loss.

KEYWORDS

variable-grid method, LSRTM, adaptive sampling, imaging resolution, computing efficiency

Introduction

Migration technologies play an increasingly significant role in seismic data processing (Yilmaz, 2001). Reverse time migration (RTM) (Baysal et al., 1983; Whitmore, 1983), which uses two-way wave equations for wavefield propagation, is regarded as the most effective method for imaging steep dip and complex structures. Compared with one-way wave-equation migration (Claerbout, 1971; Xie and Wu, 2005) and ray-based migration methods (Schneider, 1978; Hill, 1990), RTM has no dip limitation and can correctly image prism and overturned waves. RTM has been widely studied and developed by many scholars because of its advantage in providing high-accuracy subsurface images (Sun and McMechan, 2001; Rocha et al., 2016; Du et al., 2017). However, RTM images usually suffer from artifacts (Zhang and Sun, 2009), incomplete illumination (Buur and Kühnel, 2008) and low-frequency noise (Díaz and Sava, 2016) because conventional RTM algorithm uses the adjoint of the linearized wave equation rather than its inverse (Nemeth et al., 1999).

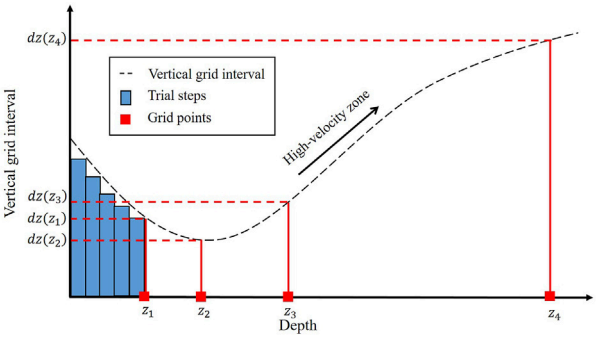

FIGURE 1
Principle of the adaptive sampling.

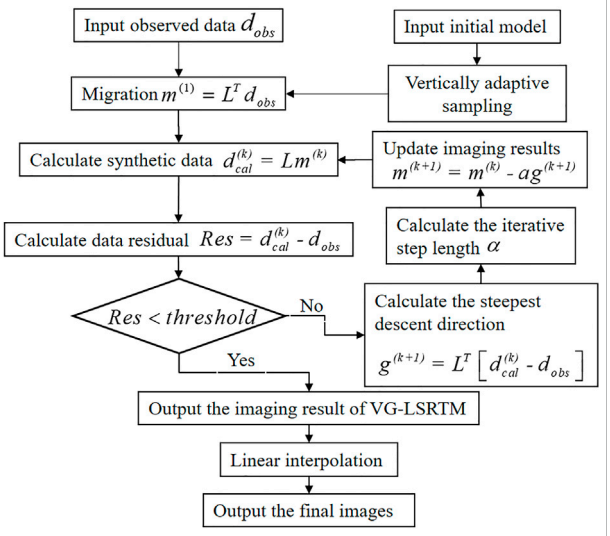

FIGURE 2
Flowchart of the proposed VG-LSRTM.

Inverse theory-based least-squares migration (LSM) (Lailly and Bednar, 1983) aims to obtain images with fewer artifacts and acquisition marks by approximating the exact inverse of the wave equation modeling operator (Lambaré et al., 1992; Kühl and Sacchi, 2003; Hu et al., 2016). Using the RTM operator to perform migration procedure under the framework of LSM leads to least-squares reverse-time migration (LSRTM) (Dai et al., 2012; Dong et al., 2012). The data-domain LSRTM method seeks to iteratively update the subsurface reflectivity by minimizing the residual between the simulated data and observed data (Dai and Schuster, 2013; Zhang et al., 2015; Wang et al., 2017). It has been extended to elastic (Feng and Schuster, 2017; Ren et al., 2017; Gu et al., 2018), viscoacoustic (Dutta and Schuster, 2014; Sun et al., 2016; Chen et al., 2017; Yang and Zhu, 2019) and anisotropic cases (Qu et al., 2017; Yang et al., 2019; Mu et al., 2020) due to its superiority in balancing amplitude, suppressing artifacts, and improving image resolution. However, limited by large computing costs (Dai and Schuster, 2013), the sensitivity to migration velocity (Tan and Huang, 2014; Li et al., 2017), and the mismatch of amplitudes (Zhang et al., 2015), conventional LSRTM is not extensively used in large-scale field data processing.

Many researchers have done valuable work to accelerate LSRTM. Dai et al. (2012) used multi-source strategy to improve the computing efficiency of LSRTM. After that, Dai and Schuster (2013), Li et al. (2018), Liu and Liu (2018), Zhao and Sen (2019), and Li et al. (2020) successively applied plane-wave theory and encoding technologies to LSRTM to reduce the computational costs. However, the crosstalk noise often occurs in LSRTM images when using the multi-source encoding algorithms, which seriously degrades the inversion quality. Speeding up the convergence rate of LSRTM is another way to save production costs. Duprat and Baina (2016) introduced a preconditioning factor into LSRTM and achieved fast convergence results. Rocha et al. (2018) developed an energy-based LSRTM algorithm to speed up the convergence of LSRTM. Thanks to the development of high-performance computer, the GPU/CPU parallel LSRTM algorithm has been developed to improve the efficiency (Xue and Liu, 2017; Zhang et al., 2018). In recent reports, some deep-learning frameworks have been used to alleviate the computing burden (Vamaraju et al., 2021) and reduce the number of iterations (Kristian and Mauricio, 2022) of conventional LSRTM.

Another promising application to speed up LSRTM is using the model-driven variable-grid methods. The use of irregular spatial grid interval can be traced back to Moczo's (1989) finite-difference modeling for SH-waves. Jastram and Behle (1992) proposed variable-grid spacing algorithm in depth domain and applied it to solve two-dimensional acoustic wave equation. Then, Jastram and Tessmer (1994) developed this method into elastic cases. Falk et al. (1996) used varying grid spacing to simulate the tube wavefield successfully. The variable-grid algorithms mentioned above usually use different finite-difference coefficients in the transition region between coarse and fine grids. Wang and Schuster (1996) proposed an interpolation-based variable-grid method for elastic and acoustic wave equation modeling. Wang (2001) further developed interpolation strategy into viscoelastic wave simulation. The variable-grid strategy has been successfully applied to waveform inversion and RTM. Ha and Shin (2012) developed an axis transformation method to speed up Laplace-domain full-waveform inversion (FWI). Li et al. (2014) proposed an efficient dual-variable algorithm and applied it to RTM. Sun et al. (2017) introduced the variable-grid technique into cross-well seismic data imaging. Wang et al. (2017) developed an adaptive FWI algorithm based on the variable-grid strategy to reduce the computational costs.

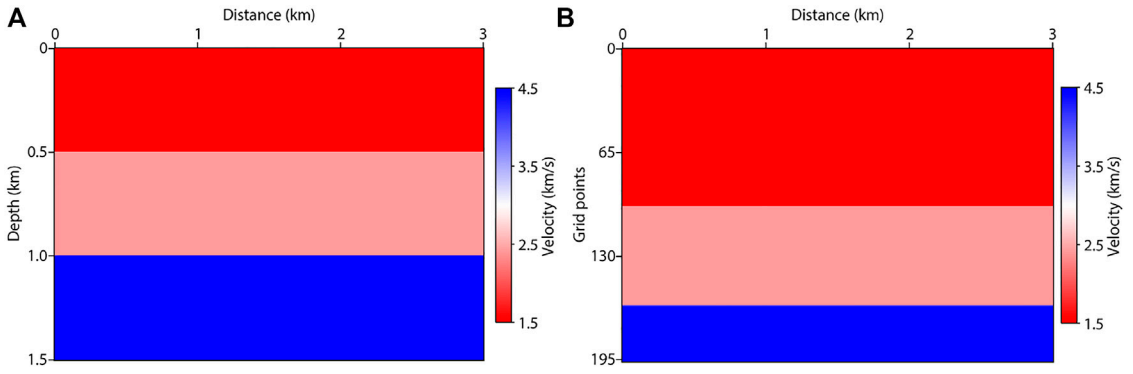

FIGURE 3
Layered model: **(A)** regular-grid model and **(B)** variable-grid model.

TABLE 1 Modeling parameters of FG-LSRTM, CG-LSRTM and VG-LSRTM tests.

Tests	Methods	Nx	Nz	dx (m)	dz
1	FG-LSRTM	601	301	5	5 m
2	CG-LSRTM	601	201	5	7.5 m
3	VG-LSRTM	601	197	5	Variable

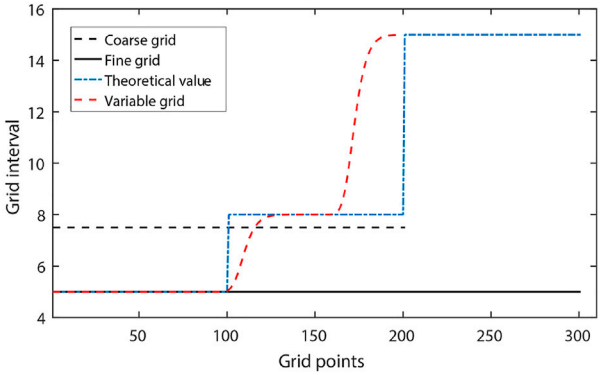

FIGURE 4
Comparison of vertical grid interval.

Since wavefield simulation and RTM are the basic units of LSRTM, these variable-grid methods mentioned above have the potential to accelerate LSRTM. However, there are many difficulties in applying them to LSRTM. First, conventional variable-grid algorithms always sample a specified area, the edge of which generates strong spurious reflections because the grid size in this area is much smaller than that in other areas. Such spurious reflections are hard to eliminate in seismic wave propagation, and is likely to reduce the quality of LSRTM images. Second, it is necessary to change the finite-difference scheme or coefficients of the transition regions between spatial grids of different sizes to achieve successful wavefield extrapolation, which poses challenges of accuracy and stability for the implementation of variable-grid LSRTM (VG-LSRTM). Finally, due to the difficulty inherent in automatically gridding complex velocity model, conventional variable-grid methods are not so practical and they are hardly applied to LSRTM. The pseudo-time domain method (Alkhalifah, 2003; Ma and Alkhalifah, 2013) provides a global grid discretization strategy to overcome these problems, which can be considered as a special variable-grid method. Li et al. (2017) developed a cross-correlation LSRTM algorithm in pseudo-time domain (PT-LSRTM) to improve the computing efficiency and reduce the sensitivity of velocity errors to imaging results. However, the demigration operator in pseudo-time domain is more complicated than that in depth domain. Therefore, PT-LSRTM cannot significantly reduce the computational costs.

To improve the computing efficiency of LSRTM without precision loss, we propose an adaptive VG-LSRTM algorithm based on a global sampling strategy in this paper. Our variable-grid approach is efficient and convenient, which does not require changing the finite-difference scheme and its coefficients, adding the transition region between grids of different sizes, and manually gridding the velocity model. We first derive a variable-grid first-order acoustic wave equation and the corresponding demigration equation based on a mapping relationship. Then, two numerical tests on synthetic data demonstrate the advantages of our method. After that, we discuss the possible risks of the proposed method in terms of stability and accuracy. Finally, we summarize the paper in the conclusion section.

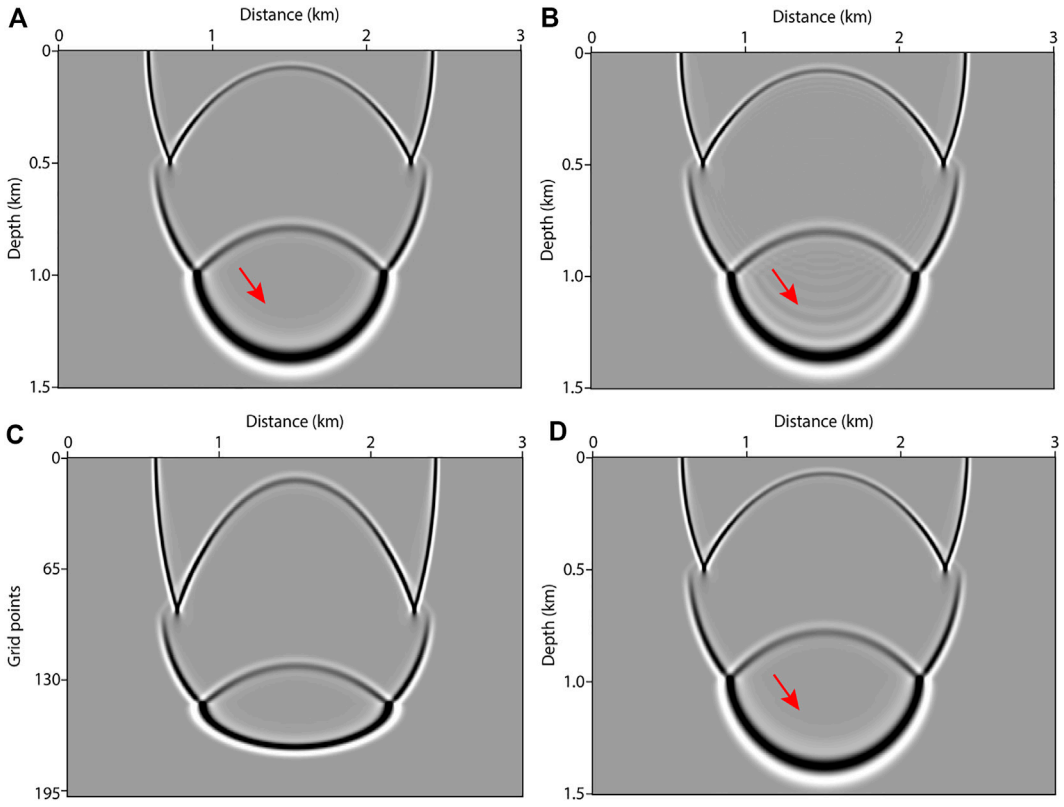

FIGURE 5
Wavefield snapshots computed by: **(A)** fine-grid method, **(B)** coarse-grid method, **(C)** variable-grid method, and **(D)** variable-grid method with linear interpolation.

Methodology

Adaptive sampling method and variable-grid acoustic wave equation

The 2D first-order velocity-stress acoustic wave equation in an inhomogeneous isotropic media is written as:

$$\begin{aligned} \rho \frac{\partial u}{\partial t} &= \frac{\partial p}{\partial x} \\ \rho \frac{\partial w}{\partial t} &= \frac{\partial p}{\partial z} \\ \frac{1}{\rho v^2} \frac{\partial p}{\partial t} &= \frac{\partial u}{\partial x} + \frac{\partial w}{\partial z} + S(t) \end{aligned} \tag{1}$$

where u and w are the particle velocity, p is acoustic pressure field, ρ is medium density, v is acoustic velocity, and $S(t)$ is the source term.

Eq. 1 has been widely used in forward modeling and LSRTM (Virieux, 1986; Li et al., 2017). It is easier to obtain better results by using finer spatial grid than coarser one when applying the finite-difference technique to solve Eq. 1. However, for those high-velocity zones, the use of fine grid leads to a waste of computing resources. In this section, we introduce an adaptive sampling method to solve the above problem based on the assumption that the formation velocity varies with depth and properties of the underground media.

Given an initial velocity model whose number of grid points and spatial grid spacing are already known. We use Eq. 2 to calculate its optimal vertical grid spacing along the depth direction:

$$dz(z) = \frac{v_{\min}(z)}{f_d k} \tag{2}$$

where $dz(z)$ denotes the optimal vertical grid spacing in depth z, $v_{\min}(z)$ is the minimum velocity of each layer along z-axis, k denotes the number of vertical grid points per wavelength, and f_d denotes the maximum frequency of the source. Obviously, $dz(z)$ decreases as k and f_d increase. To ensure that the grid dispersion never occur, k is set to ten in this paper.

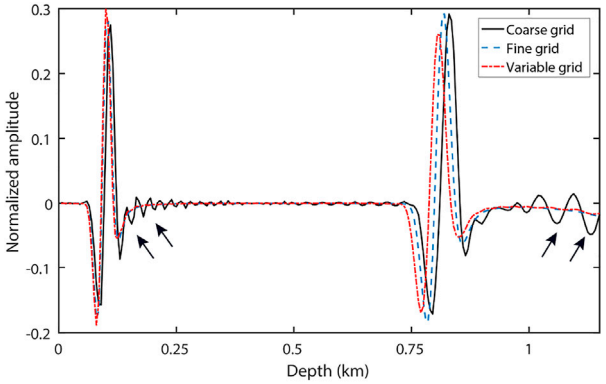

FIGURE 6
Comparison of the snapshots at a distance of 1.3 km for different forward modeling methods.

In order to keep the total depth of the initial model constant, we resample it using an adaptive sampling method. The process is illustrated in Figure 1. The horizontal axis in Figure 1 denotes depth of the initial model and the black dashed line in Figure 1 denotes the optimal vertical grid spacing. First, we take a small trial step from the surface of the model and gradually increase it to obtain the first grid point z_1, where $z_1 = dz(z_1)$. Then we use the same way to get the next grid point z_2, where $z_2 - z_1 = dz(z_2)$. Next, we repeat this process to the maximum depth of the model and get all of the grid points. In high-velocity zone, the grid interval is larger than that in low-velocity zone, and the grid points are sparser, which makes grid discretization more reasonable compared with regular-grid implementation. Now we obtain a new model, which has variable vertical grid interval. We keep the horizontal grid interval constant because the formation velocity varies mainly along the depth direction and our adaptive sampling method is not applicable to areas where the medium velocity changes slowly.

The initial model is located in Cartesian coordinate system $M(x, z)$ while the new model is located in a new rectangular coordinate system $N(\xi, \eta)$. There is a mapping relationship between the coordinate variables of the two coordinate systems. We use Eq. 3 to express this relation:

$$\begin{aligned} \xi &= x \\ \frac{\partial \eta}{\partial z} &= \varphi(z) \end{aligned} \tag{3}$$

where the ξ and η are the coordinate variables in $N(\xi, \eta)$, x and z are the coordinate variables in $M(x, z)$, and $\varphi(z)$ denotes the mapping relationship. It is important to note that the based on the adaptive sampling shown in Figure 1, η does not depend on x.

Thus, Eq. 1 can be rewritten as:

$$\begin{aligned} \rho\frac{\partial u}{\partial t} &= \frac{\partial p}{\partial \xi} = \frac{\partial p}{\partial x} \\ \rho\frac{\partial w}{\partial t} &= \frac{\partial p}{\partial \eta} = \frac{\partial p}{\partial z}\frac{\partial z}{\partial \eta} = \frac{\partial p}{\partial z}\frac{1}{\varphi(z)} \\ \frac{1}{\rho v^2}\frac{\partial p}{\partial t} &= \frac{\partial u}{\partial \xi} + \frac{\partial w}{\partial \eta} + S(t) \\ &= \frac{\partial u}{\partial x} + \frac{\partial w}{\partial z}\frac{\partial z}{\partial \eta} + S(t) \\ &= \frac{\partial u}{\partial x} + \frac{\partial w}{\partial z}\frac{1}{\varphi(z)} + S(t) \end{aligned} \tag{4}$$

Eq. 4 is the variable-grid acoustic wave equation, which can be solved in $M(x, z)$ by means of the mapping relation. Its computational complexity is not much different from that of Eq. 1. $\varphi(z)$ in Eq. 4 is obtained when resampling the initial model and it can be solved by the finite-difference method.

The principle of variable-grid LSRTM

Based on the superposition principle of the wavefield, the velocity model can be expressed as:

$$s^2 = s_0^2 + \Delta s^2 \tag{5}$$

where s denotes slowness, which is the reverse of velocity. s_0 denotes the background slowness fields and Δs is the perturbation. Similarly, the seismic wavefield can be separated into the background wavefield p_0 and the perturbation wavefield p_s:

$$p = p_0 + p_s \tag{6}$$

The background wavefield p_0 obeys Eq. 4:

$$\begin{aligned} \rho\frac{\partial u_0}{\partial t} &= \frac{\partial p_0}{\partial x} \\ \rho\frac{\partial w_0}{\partial t} &= \frac{\partial p_0}{\partial z}\frac{1}{\varphi(z)} \\ \frac{1}{\rho v^2}\frac{\partial p_0}{\partial t} &= \frac{\partial u_0}{\partial x} + \frac{\partial w_0}{\partial z}\frac{1}{\varphi(z)} + S(t) \end{aligned} \tag{7}$$

Substitute Eq. 5 and Eq. 6 into Eq. 4, subtract Eq. 7, and perform Born approximation (Dai et al., 2012), we get the control equation of p_s:

$$\begin{aligned} \rho\frac{\partial u_s}{\partial t} &= \frac{\partial p_s}{\partial x} \\ \rho\frac{\partial w_s}{\partial t} &= \frac{\partial p_s}{\partial z}\frac{1}{\varphi(z)} \\ s^2\frac{\partial p_s}{\partial t} &= \rho\left(\frac{\partial u_s}{\partial x} + \frac{\partial w_s}{\partial z}\frac{1}{\varphi(z)}\right) - \Delta s^2\frac{\partial p_0}{\partial t} \end{aligned} \tag{8}$$

Eq. 8 is the Born forwarding modeling equation, which can be rewritten as a matrix:

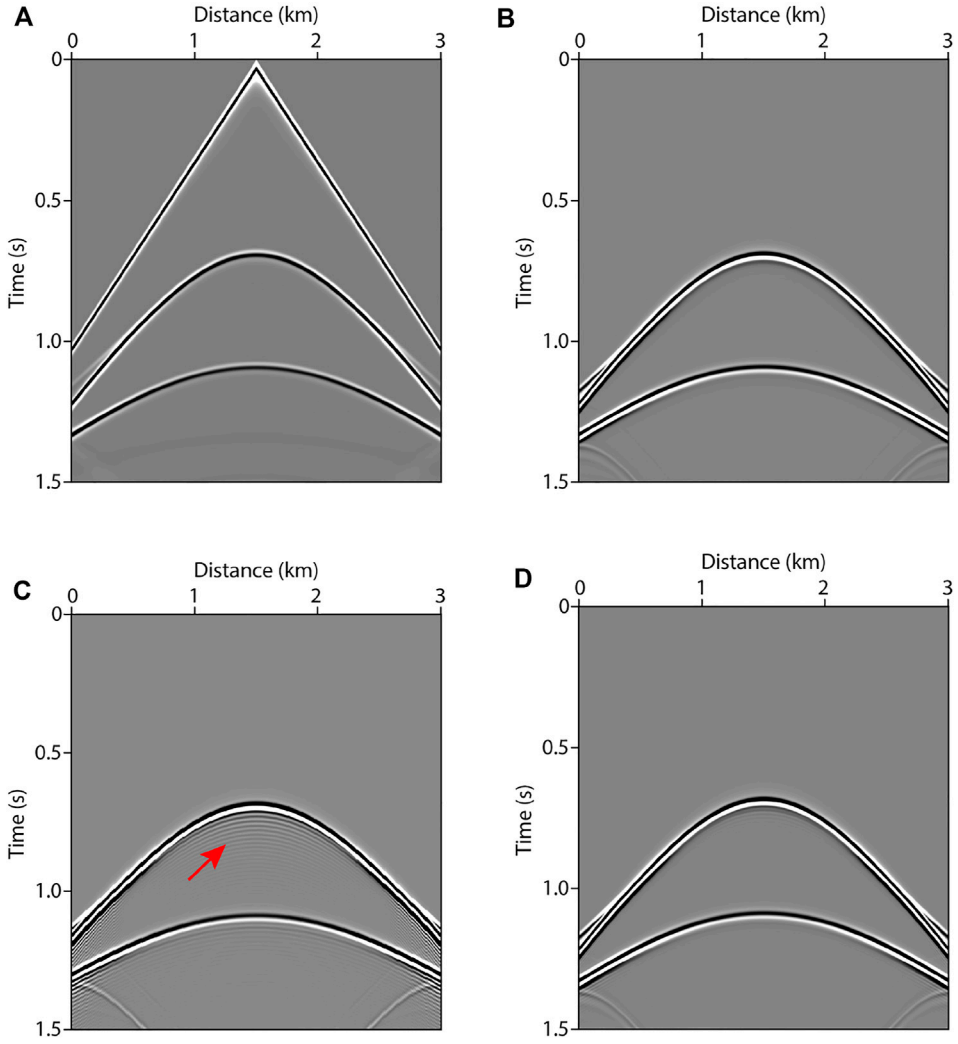

FIGURE 7
Single shot record: **(A)** observed data, **(B)** Born-modeled data at the first iteration of the fine-grid test, **(C)** Born-modeled data at the first iteration of the coarse-grid test, and **(D)** Born-modeled data at the first iteration of the variable-grid test.

$$p_s = Lm \tag{9}$$

where L denotes the Born (linearized) forwarding modeling operator, and $m = s^2$ is model parameter. The goal of LSRTM is to reconstruct the optimal reflectivity image of the earth (Dutta and Schuster, 2014). The objective function J is defined as:

$$J = \frac{1}{2}\|Lm - d_{obs}\|_2^2 \tag{10}$$

where $\|\cdot\|_2^2$ is the L2-norm of a vector and d_{obs} is the observed data. We use a gradient-based algorithm (Dai et al., 2011) to solve Eq. 10 as follows:

$$g = L^*(Lm - d_{obs}) \tag{11}$$

where g is the gradient and * denotes the conjugate transpose of a matrix. The process of the steepest descent method to solve the objective function can be expressed as:

$$\begin{aligned} m^{k+1} &= m^k - \alpha^k g^k \\ g^k &= L^*\left(Lm^k - d_{obs}\right) \\ \alpha^k &= \frac{(g^k)^* g^k}{(Lg^k)^* Lg^k} \end{aligned} \tag{12}$$

where k denotes the iteration index and α^k denotes the step length.

We summarize complete VG-LSRTM workflow in Figure 2. When "Yes" is output in the diamond box, we obtain the VG-LSRTM imaging result with irregular vertical grid interval. Then

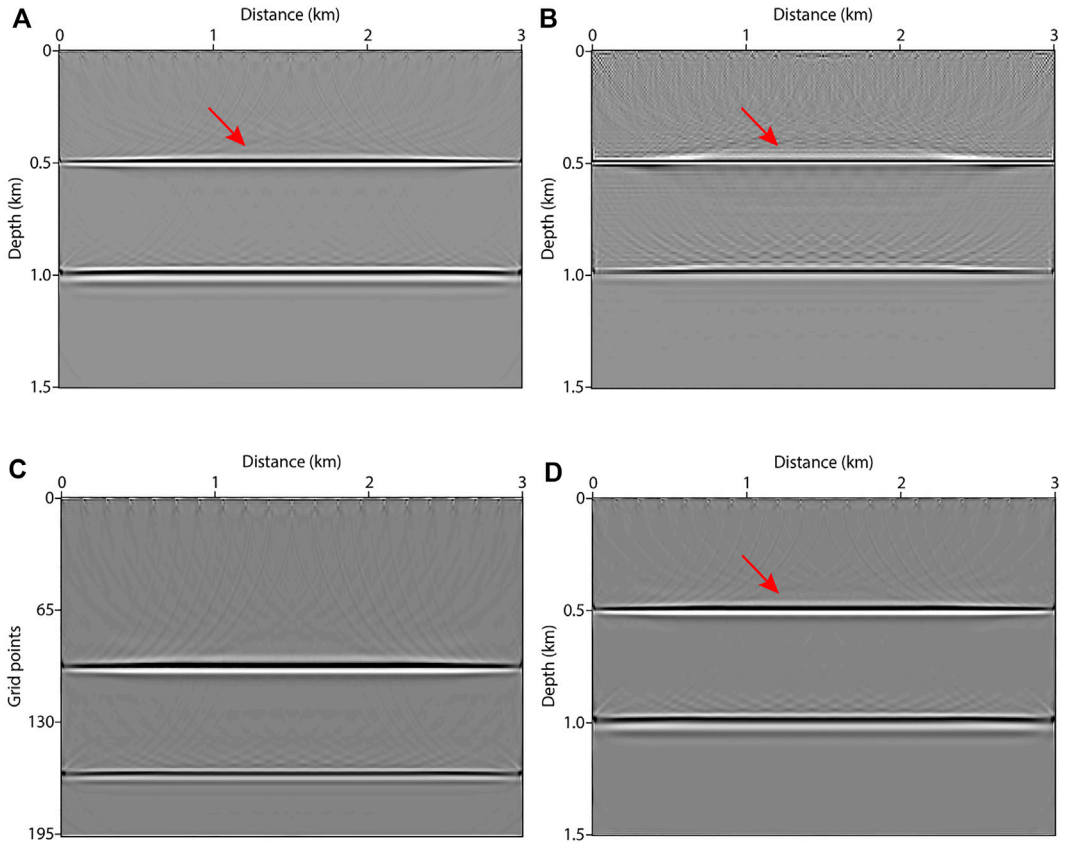

FIGURE 8
LSRTM images after 20 iterations: **(A)** FG-LSRTM image, **(B)** CG-LSRTM image, **(C)** VG-LSRTM image, and **(D)** VG-LSRTM image after linear interpolation.

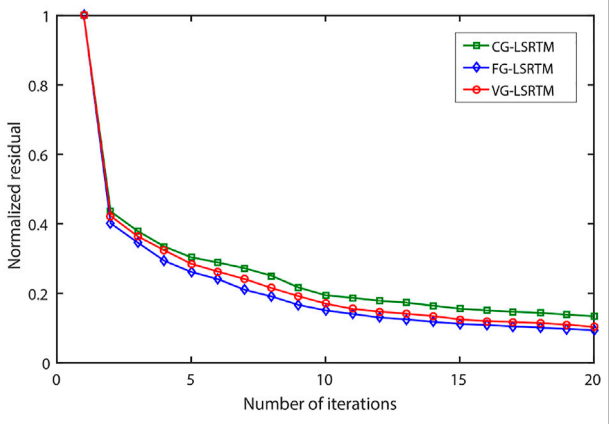

FIGURE 9
Normalized data residual convergence curves of the three LSRTM tests.

TABLE 2 Model parameters of FG-LSRTM, CG-LSRTM and VG-LSRTM tests.

Tests	Methods	Nx	Nz	dx (m)	dz
1	FG-LSRTM	681	701	10	5 m
2	CG-LSRTM	681	351	10	10 m
3	VG-LSRTM	681	360	10	Variable

we use linear interpolation technique to transform the variable-grid image into a regular-grid one based on the mapping relation.

Numerical examples

In this section, we demonstrate the feasibility and advantages of the proposed method with synthetic data. The numerical tests

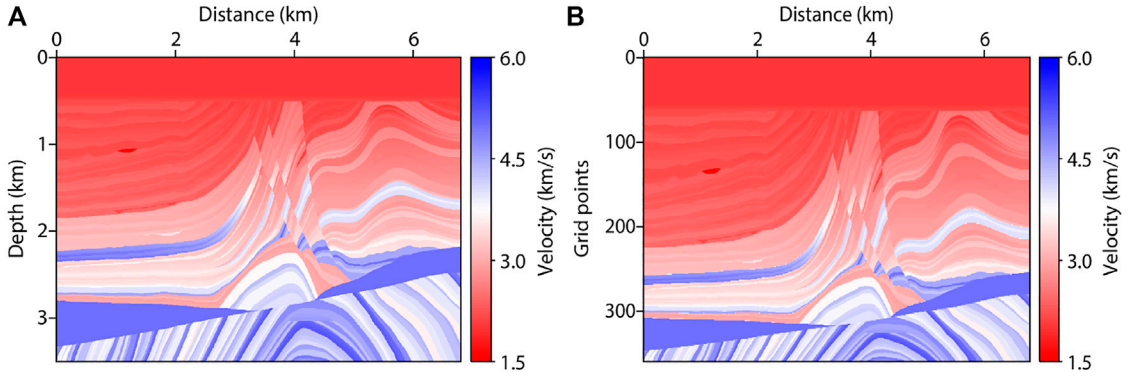

FIGURE 10
Modified Marmousi model: **(A)** regular-grid model, and **(B)** variable-grid model.

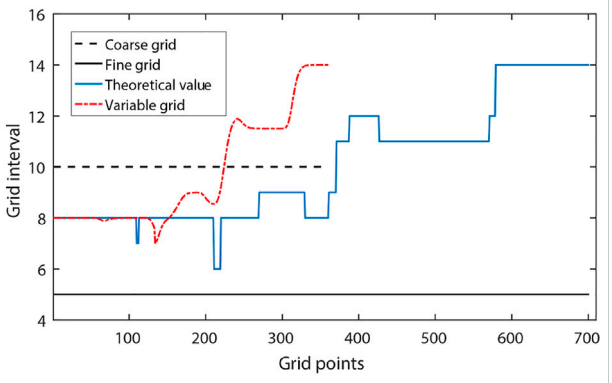

FIGURE 11
Comparison of vertical grid interval.

are for two models: 1) a layered model and 2) a modified Marmousi model.

Layered model

First, we use a layered model shown in Figure 3A to illustrate the implementation process of VG-LSRTM in detail. The model is 3 km wide and 1.5 km deep, which has three horizontal layers with velocity of 1,500 m/s, 2,500 m/s and 4,500 m/s, respectively. Three comparative tests shown Table 1 are designed to demonstrate the effectiveness of our method. In Test 1, the size of the fine-grid model grids is 601 × 301 with a 5 m grid spacing. 601 × 201 grid points are used in coarse-grid model (Test 2), with grid interval of dx = 5 m and dz = 7.5 m. The variable-grid model is displayed in Figure 3B, which is resampled from the fine-grid model. Compared with the fine-grid model, the number of vertical grid points of the variable-grid model is reduced by 34.6%.

Figure 4 shows the vertical grid spacing of these models. The blue dashed line denotes the theoretical optimal value of the fine-grid model, which is calculated by Eq. 2. The red dashed line displays the vertical grid spacing of the variable-gird model. It varies more smoothly between two layers than the blue line. For conventional variable-grid methods (Jastram and Tessmer, 1994; Wang and Schuster, 1996; Ha and Shin, 2012; Fan et al., 2015), it is inevitable to add a transition area between two layers with different velocity, change the finite-difference scheme of the seismic wave equation, or modify the finite-difference coefficients. When the modeling parameters are not reasonable, strong spurious reflections will occur in the transition area. Our adaptive variable-grid method is much easier to implement and can effectively avoid the spurious reflections.

Next, we test our method using forward modeling. A Ricker wavelet source with dominant frequency of 30 Hz is used. The time step is 0.5 ms. Figures 5A–C show the wavefield snapshots at 0.65 s, which are computed by the fine-grid, coarse-grid and variable-grid methods, respectively. The variable-grid snapshot (Figure 5C) is irregular in depth direction. For comparison purposes, we apply linear interpolation to it to get a regular-grid one, as shown in Figure 5D. As indicated by the red arrows, numerical dispersion in Figure 5B is stronger than that in Figures 5A,D. As shown in Figure 6, we extract a single trace from these snapshots at a distance of 1.3 km for further comparison. The black arrows indicate the dispersion. From Figure 6, we find that the blue line and the red line almost coincide but they are different from the black line.

In LSRTM tests, the recording time is 1.5 s. In total, 21 shots are evenly distributed on the surface and the shot interval is 150 m. Each shot has 601 receivers and the receiver interval is

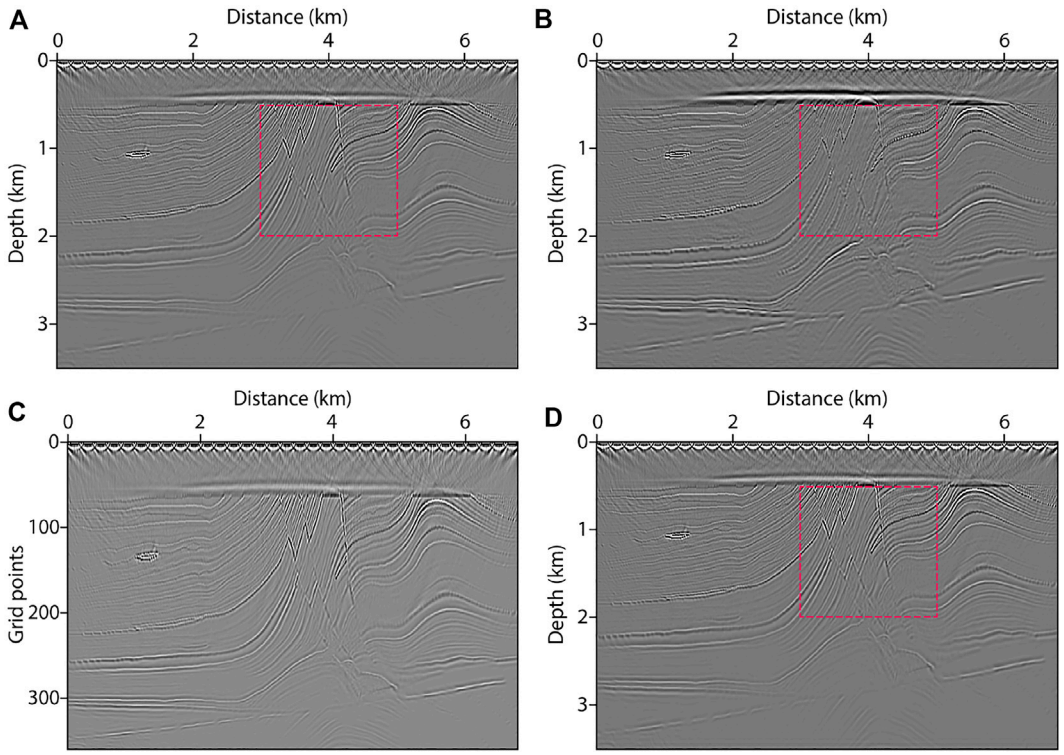

FIGURE 12
LSRTM images using different migration velocity model after 30 iterations: **(A)** FG-LSRTM image, **(B)** CG-LSRTM image, **(C)** VG-LSRTM image, and **(D)** VG-LSRTM image after linear interpolation.

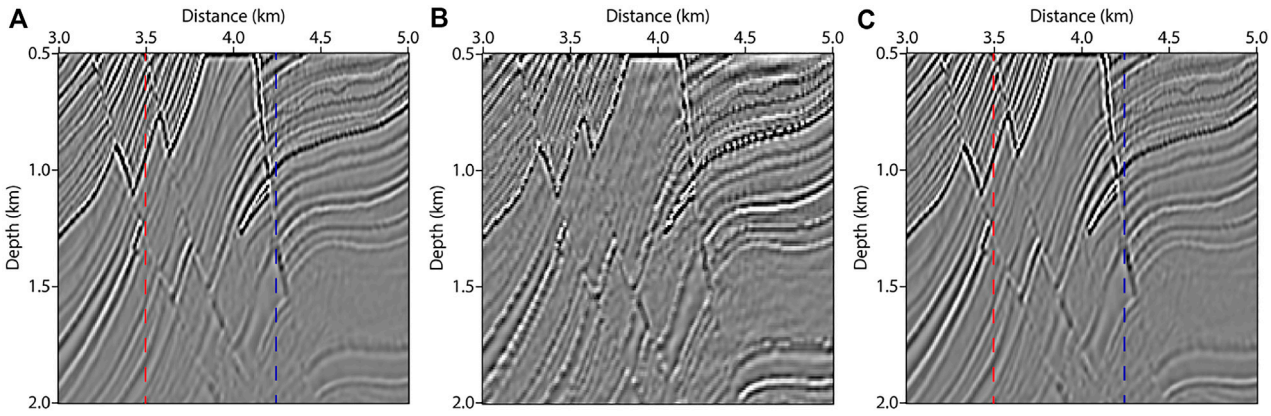

FIGURE 13
Magnified views of the dashed red boxes shown in Figure 12: **(A)** FG-LSRTM image, **(B)** CG-LSRTM image, and **(C)** VG-LSRTM image after linear interpolation.

5 m. Figure 7A shows the synthetic single shot record using the fine-grid model, which is regarded as the observed data. Figures 7B–D show the Born-modeled data at the first iteration of the fine-grid method, coarse-grid method and variable-grid method, respectively. Obviously, the numerical dispersion in Figure 7C is strong (see the red arrow). Figures 8A–C show the FG-LSRTM, CG-LSRTM and VG-LSRTM images after 20 iterations, respectively. Figure 8D shows the linear interpolation profile of the image in Figure 8C. As indicated by the red arrows in Figure 8, the FG-LSRTM and VG-LSRTM images show fewer

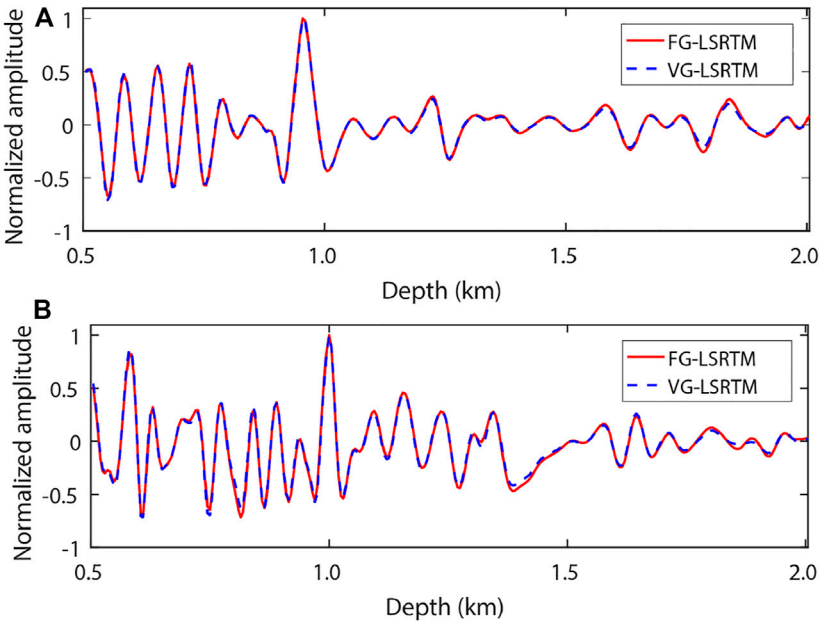

FIGURE 14
Vertical slices of Figure 13 at: **(A)** 3.5 km and **(B)** 4.25 km.

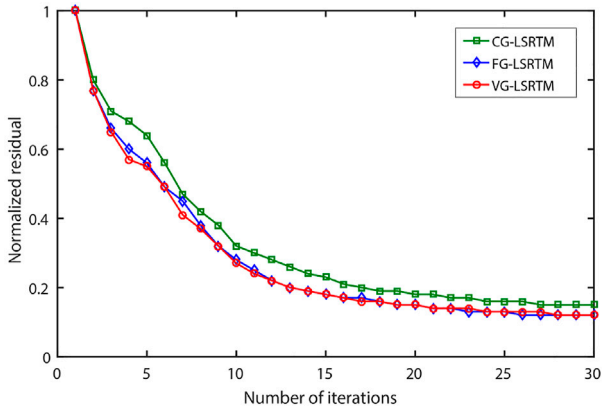

FIGURE 15
Normalized data residual convergence curves of CG-LSRTM, FG-LSRTM and VG-LRSRTM methods.

imaging artifacts, higher resolution, and better balance of reflector amplitudes compared with the CG-LSRTM image. Figure 9 shows the convergence curves of the normalized data residual. The convergence curves of FG-LSRTM method and the VG-LSRTM method almost coincide after 15 iterations, which means that the proposed algorithm converges as fast as conventional LSRTM.

These LSRTM tests are performed on a cluster using twenty-one server nodes. The CPU is a 2.20 GHz Intel Xeon Silver 4,214, which has forty-five compute nodes. The computing time of FG-LSRTM, CG-LSRTM and VG-LSRTM is 93 min, 62 min and 64 min, respectively. The VG-LSRTM method saves about 34.6% of memory compared to the FG-LSRTM method because the number of vertical grid of the variable-grid model is 34.6% of that of the fine-grid model. From the layered model tests, we conclude that the VG-LSRTM method can improve computing efficiency, reduce memory consumption, and provide high-resolution image with little accuracy loss.

Modified Marmousi model

Similar to the previous section, we use the coarse-grid, fine-grid, and variable-grid Marmousi models to further verify the advantages of the proposed method. The model parameters are shown in Table 2. Figure 10A shows the regular-grid model. Figure 10B displays the variable-grid model, which is resampled from the fine-grid model. From Table 2, the number of vertical grid points of the variable-grid model is 360, decreasing by 48.6%. The comparison of vertical grid interval is presented in Figure 11. We can see that the variable-grid grid interval (the red line) varies smoothly with model velocity.

In imaging tests, the time interval is 0.3 ms, and the recording time is 3 s. In total, 35 sources are distributed laterally from 0 to 6.65 km, and the shot interval is 200 m. Each shot has 681 receivers, and the receiver interval is 10 m. The dominant frequency of the Ricker wavelet source is 30 Hz. Figure 12 shows the images after

30 iterations. Figure 12A displays the FG-LSRTM image, Figure 12B shows the CG-LSRTM image, Figure 12C shows the VG-LSRTM image, and Figure 12D shows the VG-LSRTM image after linear interpolation. Figure 13 shows the magnified views of the dashed red boxes shown in Figure 12. Obviously, the images in Figures 13A,C show better imaging resolution than that in Figure 13B. To demonstrate that the VG-LSRTM method has high accuracy and low errors, we extract two traces from the images in Figures 13A,C (see the red and blue lines). Figures 14A,B show the single trace comparison at the distance of 3.5 km and 4.25 km, respectively. We can see that there is almost no amplitude and phase error between the FG-LSRTM and the VG-LSRTM image.

Figure 15 shows the normalized data residual convergence curves of these tests. We can see that the curves of the FG-LSRTM method and the VG-LSRTM method almost coincide, and they converge faster than that of the CG-LSRTM method. Each LSRTM test uses thirty-five nodes on a 2.20 GHz Intel Xeon Silver 4214 CPU. The computing time of FG-LSRTM, CG-LSRTM and VG-LSRTM is 25.6 h, 13.1 h and 13.8 h, respectively. Compared with the FG-LSRTM method, our VG-LSRTM method can save 46% of the computation time. From the numerical example of the modified Marmousi model, we conclude that the proposed VG-LSRTM method can greatly improve computing efficiency.

Discussion

Numerical tests on the layered model and the modified Marmousi model have shown that the proposed method is efficient and accurate. Nevertheless, the final effect that our method can achieve depends on initial spatial grid interval, the velocity structure of the model, and the maximum frequency of the source. Severe vertical velocity variation, small spatial grid interval, and the use of low-frequency source are favorable factors for the proposed VG-LSRTM algorithm. In addition, the accuracy loss of VG-LSRTM images mainly originates from the sampling process shown in Figure 1 because model velocity varies continuously while the grid points are obtained by discrete sampling. Other factors that may reduce the accuracy of the imaging results, such as the use of linear interpolation technology and the order of the finite-difference scheme for approximating $\varphi(z)$, have negligible effects on the final results. The stability condition of Eq. 4 is worth discussing. By analyzing the results of a large number of numerical tests, we find that the stability condition of Eq. 4 is slightly more stringent than that of Eq. 1.

Conclusion

Conventional variable-grid methods are difficult to implement and apply to LSRTM. We presented a VG-LSRTM algorithm based on an adaptive sampling strategy to accelerate LSRTM in this paper. We derived a variable-grid first-order stress-velocity acoustic wave equation and its corresponding Born forward modeling operator based on a mapping relationship between two coordinate systems. We developed a complete VG-LSRTM workflow and proved its feasibility using two numerical examples. Forward modeling tests for a layered model demonstrated that the proposed variable-grid method has high wavefield simulation accuracy. LSRTM tests for the layered model and a modified Marmousi model validated that our VG-LSRTM can save large computing costs and provide high-resolution imaging results as well as FG-LSRTM.

Data availability statement

The original contributions presented in the study are included in the article/Supplementary Material, further inquiries can be directed to the corresponding authors.

Author contributions

LC and JH contributed to the conception and design of the study. CS and JH organized the database and performed the statistical analysis. ZW modified the manuscript. All authors contributed to manuscript revision and read and approved the submitted version.

Funding

This research is supported by the Marine S&T Fund of Shandong Province for Pilot National Laboratory for Marine Science and Technology (Qingdao) (Grant No. 2021QNLM020001), the National Key R&D Program of China (Grant No. 2019YFC0605503C), and the National Outstanding Youth Science Foundation (Grant No. 41922028).

The authors declare that this study received funding from the Major Scientific and Technological Projects of China National Petroleum Corporation (CNPC) (grant no. ZD2019-183-003). The funder was not involved in the study design, collection, analysis, interpretation of data, the writing of this article, or the decision to submit it for publication.

Acknowledgments

We are grateful to the editor and the reviewers for reviewing this manuscript.

Conflict of interest

The authors declare that the research was conducted in the absence of any commercial or financial relationships that could be construed as a potential conflict of interest.

Publisher's note

References

Alkhalifah, T. (2003). Tau migration and velocity analysis: Theory and synthetic examples. *Geophysics* 68 (4), 1331–1339. doi:10.1190/1.1598126

Baysal, E., Kosloff, D. D., and Sherwood, J. W. C. (1983). Reverse time migration. *Geophysics* 48 (11), 1514–1524. doi:10.1190/1.1441434

Buur, J., and Kühnel, T. (2008). Salt interpretation enabled by reverse-time migration. *Geophysics* 73 (5), VE211–VE216. doi:10.1190/1.2968690

Chen, Y., Dutta, G., Dai, W., and Schuster, G. T. (2017). Q-least-squares reverse time migration with viscoacoustic deblurring filters. *Geophysics* 82 (6), S425–S438. doi:10.1190/geo2016-0585.1

Claerbout, J. F. (1971). Toward a unified theory of reflector mapping. *Geophysics* 36, 467–481. doi:10.1190/1.1440185

Dai, W., Fowler, P., and Schuster, G. T. (2012). Multi-source least-squares reverse time migration. *Geophys. Prospect.* 60 (4), 681–695. doi:10.1111/j.1365-2478.2012.01092.x

Dai, W., and Schuster, G. T. (2013). Plane-wave least-squares reverse-time migration. *Geophysics* 78 (4), S165–S177. doi:10.1190/geo2012-0377.1

Dai, W., Wang, X., and Schuster, G. T. (2011). Least-squares migration of multisource data with a deblurring filter. *Geophysics* 76 (5), R135–R146. doi:10.1190/geo2010-0159.1

Díaz, E., and Sava, P. (2016). Understanding the reverse time migration backscattering: Noise or signal? *Geophys. Prospect.* 64, 581–594. doi:10.1111/1365-2478.12232

Dong, S., Cai, J., Guo, M., Suh, S., Zhang, Z., Wang, B., et al. (2012). Least squares reverse time migration towards true amplitude imaging and improving the resolution. *82nd Annu. Int. Meet. Seg. Expand*, 1–5. doi:10.1190/segam2012-1488.1

Du, Q. Z., Guo, C. F., Zhao, Q., Gong, X. F., Wang, C. X., and Li, X. Y. (2017). Vector-based elastic reverse time migration based on scalar imaging condition. *Geophysics* 82 (2), S111–S127. doi:10.1190/geo2016-0146.1

Duprat, V., and Baina, R. (2016). An efficient least-squares reverse-time migration using true-amplitude imaging condition as an optimal preconditioner. *78th Annu. Int. Conf. Exhib. EAGE, Ext. Abstr*, 1–5. doi:10.3997/2214-4609.201601199

Dutta, G., and Schuster, G. T. (2014). Attenuation compensation for least-squares reverse time migration using the viscoacoustic-wave equation. *Geophysics* 79 (6), S251–S262. doi:10.1190/geo2013-0414.1

Falk, J., Tessmer, E., and Gajewski, D. (1996). Tube wave modeling by the finite-difference method with varying grid spacing. *PAGEOPH* 148, 77–93. doi:10.1007/BF00882055

Fan, N., Zhao, L. F., Gao, Y. J., and Yao, Z. X. (2015). A discontinuous collocated-grid implementation for high-order finite-difference modeling. *Geophysics* 80 (4), T175–T181. doi:10.1190/geo2015-0001.1

Feng, Z. C., and Schuster, G. T. (2017). Elastic least-squares reverse time migration. *Geophysics* 82 (2), S143–S157. doi:10.1190/geo2016-0254

Gu, B., Li, Z., and Han, J. (2018). A wavefield-separation-based elastic least-squares reverse time migration. *Geophysics* 83 (3), S279–S297. doi:10.1190/geo2017-0131.1

Ha, W., and Shin, C. (2012). Efficient Laplace-domain modeling and inversion using an axis transformation technique. *Geophysics* 77 (4), R141–R148. doi:10.1190/geo2011-0424.1

Hill, N. R. (1990). Gaussian beam migration. *Geophysics* 55, 1416–1428. doi:10.1190/1.1442788

Hu, H., Liu, Y., Zheng, Y., Liu, X., and Lu, H. (2016). Least-squares Gaussian beam migration. *Geophysics* 81 (3), S87–S100. doi:10.1190/geo2015-0328/1

Jastram, C., and Behle, A. (1992). Acoustic modelling on a grid of vertically varying Spacing1. *Geophys. Prospect.* 40 (2), 157–169. doi:10.1111/j.1365-2478.1992.tb00369.x

Jastram, C., and Tessmer, E. (1994). Elastic modelling on a grid with vertically varying spacing1. *Geophys. Prospect.* 42 (4), 357–370. doi:10.1111/j.1365-2478.1994.tb00215.x

Kristian, T., and Mauricio, S. (2022). Least-squares reverse time migration via deep learning-based updating operators. *Geophysics* 87 (6), S315–S333. doi:10.1190/geo2021-0491.1

Kühl, H., and Sacchi, M. D. (2003). Least-squares wave-equation migration for AVP/AVA inversion. *Geophysics* 68, 262–273. doi:10.1190/1/1543212

Lailly, P., and Bednar, J. (1983). The seismic inverse problem as a sequence of before stack migrations. *Conf. Inverse Scatt. Theory Appl.*, 206–220.

Lambaré, G., Virieux, J., Madariaga, R., and Jin, S. (1992). Iterative asymptotic inversion in the acoustic approximation. *Geophysics* 57, 1138–1154. doi:10.1190/1.1443328

Li, C., Gao, J. H., Gao, Z. Q., Wang, R. R., and Yang, T. (2020). Periodic plane-wave least-squares reverse time migration for diffractions. *Geophysics* 85 (4), S185–S198. doi:10.1190/geo2019-0211.1

Li, C., Huang, J., Li, Z., and Wang, R. (2018). Plane-wave least-squares reverse time migration with a preconditioned stochastic conjugate gradient method. *Geophysics* 83, S33–S46. doi:10.1190/geo2017-0339.1

Li, Q., Huang, J., and Li, Z. (2017). Cross-correlation least-squares reverse time migration in the pseudo-time domain. *J. Geophys. Eng.* 14 (4), 841–851. doi:10.1088/1742-2140/aa6B33

Li, Z., Li, Q., Huang, J., Na, L., and Kun, T. (2014). A stable and high-precision dual-variable grid forward modeling and reverse time migration method. *Geophys Prospect Pet.* 53 (2), 127–136. doi:10.3969/j.issn.1000-1441.2014.02.001

Liu, X., and Liu, Y. (2018). Plane-wave domain least-squares reverse time migration with free-surface multiples. *Geophysics* 83 (6), S477–S487. doi:10.1190/geo2017-0570.1

Ma, X., and Alkhalifah, T. (2013). Wavefield extrapolation in pseudodepth domain. *Geophysics* 78 (2), S81–S91. doi:10.1190/geo2012-0237.1

Moczo, P. (1989). Finite-difference technique for SH-waves in 2-D media using irregular grids-application to the seismic response problem. *Geophys. J. Int.* 99 (2), 321–329. doi:10.1111/j.1365-246X.1989.tb01691.x

Mu, X., Huang, J. P., Yang, J. D., Guo, X., and Guo, Y. D. (2020). Least-squares reverse time migration in TTI media using a pure qP-wave equation. *Geophysics* 85 (4), S199–S216. doi:10.1190/geo2019-0320.1

Nemeth, T., Wu, C., and Schuster, G. T. (1999). Least-squares migration of incomplete reflection data. *Geophysics* 64 (1), 208–221. doi:10.1190/1.1444517

Qu, Y., Huang, J. P., Li, Z. C., Guan, Z., and Li, J. L. (2017). Attenuation compensation in anisotropic least-squares reverse time migration. *Geophysics* 82 (6), S411–S423. doi:10.1190/geo2016-0677.1

Ren, Z., Liu, Y., and Sen, M. K. (2017). Least-squares reverse time migration in elastic media. *Geophys. J. Int.* 208, 1103–1125. doi:10.1093/gji/ggw443

Rocha, D., Sava, P., and Guitton, A. (2018). 3D acoustic least-squares reverse time migration using the energy norm. *Geophysics* 83 (3), S261–S270. doi:10.1190/geo2017-0466.1

Rocha, D., Tanushev, N., and Sava, P. (2016). Acoustic wavefield imaging using the energy norm. *Geophysics* 81 (4), S151–S163. doi:10.1190/geo2015-0486.1

Schneider, W. A. (1978). Integral formulation for migration in two and three dimensions. *Geophysics* 43, 49–76. doi:10.1190/1.1440828

Sun, J., Fomel, S., Zhu, T., and Hu, J. (2016). Q-compensated least-squares reverse time migration using low-rank one-step wave extrapolation. *Geophysics* 81 (4), S271–S279. doi:10.1190/geo2015-0520.1

Sun, R., and McMechan, G. A. (2001). Scalar reverse-time depth migration of prestack elastic seismic data. *Geophysics* 66, 1519–1527. doi:10.1190/1/1487098

Sun, X. D., Li, Z. C., and Jia, Y. R. (2017). Variable-grid reverse-time migration of different seismic survey data. *Appl. Geophys.* 14 (4), 517–522. doi:10.1007/s11770-017-0652-7

Tan, S., and Huang, L. J. (2014). Least-squares reverse-time migration with a wavefield separation imaging condition and updated source wavefields. *Geophysics* 79 (5), S195–S205. doi:10.1/1190/geo2014/0020/1

Vamaraju, J., Vila, J., Araya-Polo, M., Datta, D., Sidahmed, M., and Sen, M. K. (2021). Minibatch least-squares reverse time migration in a deep-learning framework. *Geophysics* 86 (2), S125–S142. doi:10.1190/geo2019-0707/1

Virieux, J. (1986). P-SV wave propagation in heterogeneous media: Velocity-stress finite-difference method. *Geophysics* 51, 889–901. doi:10.1190/1.1442147

Wang, P., Huang, S., and Wang, M. (2017). Improved subsalt images with least-squares reverse time migration. *Interpretation* 5 (3), SN25–SN32. doi:10.1190/INT-2016-0203.1

Wang, Y., and Schuster, G. T. (1996). Finite-difference variable grid scheme for acoustic and elastic wave equation modeling. *Seg. Tech. Program Expand. Abstr.* 15, 674–677. doi:10.1190/11826737

Wang, Y. (2001). Viscoelastic wave simulation in basins by a variable grid finite difference method. *Bull. Seismol. Soc. Am.* 91 (6), 1741–1749. doi:10.1785/0120000236

Whitmore, N. D. (1983). Iterative depth migration by backward time propagation. In 53rd Annual International Meeting, SEG, Expanded Abstracts, 382–385. doi:10.1190/1.1893867

Xie, X. B., and Wu, R. S. (2005). Multicomponent prestack depth migration using the elastic screen method. *Geophysics* 70 (1), S30–S37. doi:10.1190/1/1852787

Xue, H., and Liu, Y. (2017). Multi-source least-square reverse time migration based on MPI and CUDA hybrid accelerating algorithm. In 79th EAGE Conference and Exhibition. Paris, France, 1–5. doi:10.3997/2214-4609.201701126

Yang, J., Zhu, H., McMechan, G., Zhang, H. Z., and Zhao, Y. (2019). Elastic least-squares reverse time migration in vertical transverse isotropic media. *Geophysics* 84 (6), S539–S553. doi:10.1190/geo2018-0887.1

Yang, J., and Zhu, H. (2019). Viscoacoustic least-squares reverse-time migration using a time-domain complex-valued wave equation. *Geophysics* 84 (5), S479–S499. doi:10.1190/geo2018-0804.1

Yilmaz, O. (2001). *Seismic data analysis: Processing, inversion, and interpretation of seismic*. Tulsa, Oklahoma, USA: Society of Exploration Geophysicists, doi:10.1190/1.9781560801580

Zhang, Q., Mao, W., and Chen, Y. (2018). Attenuating crosstalk noise of simultaneous-source least-squares reverse time migration with gpu-based excitation amplitude imaging condition. *IEEE Trans. Geosci. Remote Sens.* 57, 587–597. doi:10.1109/TGRS.2018.2858850

Zhang, Y., Duan, L., and Yi, X. (2015). A stable and practical implementation of least-squares reverse time migration. *Geophysics* 80 (1), V23–V31. doi:10.1190/segam2013-0577.1

Zhang, Y., and Sun, J. (2009). Practical issues of reverse time migration: True amplitude gathers, noise removal and harmonic-source encoding. Proceedings of the Beijing International Geophysical Conference and Exposition, Beijing, China, 204.

Zhao, Z., and Sen, M. K. (2019). Frequency-domain double-plane-wave least-squares reverse time migration. *Geophys. Prospect.* 67, 2061–2084. doi:10.1111/1365-2478.12803

frontiers | Frontiers in Earth Science

TYPE Brief Research Report
PUBLISHED 18 January 2023
DOI 10.3389/feart.2022.1039300

OPEN ACCESS

EDITED BY
Lidong Dai,
Institute of geochemistry (CAS), China

REVIEWED BY
Shaoping Lu,
Sun Yat-sen University, China
Shoudong Huo,
Institute of Geology and Geophysics (CAS), China

*CORRESPONDENCE
Jianzhong Zhang,
zhangjz@ouc.edu.cn

SPECIALTY SECTION
This article was submitted to Solid Earth Geophysics,
a section of the journal
Frontiers in Earth Science

RECEIVED 08 September 2022
ACCEPTED 20 October 2022
PUBLISHED 18 January 2023

CITATION
Ma F, Hou F, Li T, Wu Z and Zhang J (2023), Crustal velocity structure in the South Yellow Sea revealed by the joint tomographic inversion of reflected and refracted seismic waves.
Front. Earth Sci. 10:1039300.
doi: 10.3389/feart.2022.1039300

Crustal velocity structure in the South Yellow Sea revealed by the joint tomographic inversion of reflected and refracted seismic waves

Fei Ma[1], Fanghui Hou[2,3], Tongyu Li[1], Zhiqiang Wu[2,3] and Jianzhong Zhang[1,2]*

[1]Key Laboratory of Submarine Geosciences and Prospecting Techniques, Ministry of Education of China, College of Marine Geosciences, Ocean University of China, Qingdao, Shandong, China, [2]Laboratory of Marine Mineral Resources, Qingdao National Laboratory for Marine Science and Technology, Qingdao, Shandong, China, [3]Qingdao Institute of Marine Geology, China Geological Survey, Qingdao, Shandong, China

The crustal velocity structure in the South Yellow Sea (SYS) Basin is crucial for understanding the basin's geological structure and evolution. OBS (ocean-bottom station) data from the OBS2013 line have been used to determine the crustal velocity structure in the SYS. The velocity model of the upper crust in the northern SYS was determined using first-arrival traveltime tomography. The model showed a higher resolution shallow crustal velocity structure but a lower resolution middle-lower crustal velocity structure. The crustal velocity structure, together with the Moho discontinuity in the SYS Basin, was also constructed using a human–computer interactive traveltime simulation, and the result was highly dependent on the prior knowledge of the operator. In this study, we reconstructed a crustal velocity model in the SYS Basin using a joint tomographic inversion of the traveltime and its gradient data of the reflected and refracted waves picked from the OBS data. The resolution of the inverted velocity structure from shallow-to-deep crust was improved. The results revealed that the massive high-velocity body below the Haiyang Sag of the Jiaolai Basin extends to the Qianliyan Uplift in the SYS; the low-velocity Cretaceous strata directly cover the pre-Sinitic metamorphic rock basement of the Sulu orogenic belt; and the thick Meso-Paleozoic marine strata are retained beneath the Meso–Cenozoic continental strata in the northern depression. The Moho depth in the SYS Basin ranges from 28 to 32 km.

KEYWORDS

South Yellow Sea Basin, crustal velocity, Moho discontinuity, OBS, reflection, refraction, joint inversion

Introduction

The South Yellow Sea (SYS) Basin, the main part of the Lower Yangtze region, is located in the continental shelf area between the Chinese Continent and the Korean Peninsula. With a total area of approximately 280,000 km^2 and a sea-bottom depth of less than 80 m, oil and gas exploration in the SYS Basin has never made a breakthrough. In 2013, the Qingdao Institute of Marine Geology of the China Geological Survey, in conjunction with the First Institute of Oceanography of the Ministry of Natural Resources and the Institute of Geology and Geophysics, Chinese Academy of Sciences, implemented the joint land–sea deep seismic exploration line OBS2013 (Figure 1, blue dotted line) (Liu et al., 2015) in the Jiaodong, Bohai, and SYS regions, which aimed to study the structure of oil- and gas-bearing basins accompanied by the morphology of Moho discontinuity and deep structures in the exploration area. With the OBS2013 line data, Zou et al. (2016) generated a velocity structure model of the upper crust in the northern part of the SYS using first-arrival traveltime tomography. Zhao et al. (2019a) obtained a continuous 2-D velocity and interface model by using a human–computer interaction simulation of refraction and reflection traveltime data picked from OBS2013. Zhang et al. (2021) processed and analyzed the converted shear wave of the OBS data by forward simulation of the shear wave data. Liu et al. (2021) constructed the crustal velocity structure in the SYS Basin by using a human–computer interaction simulation of the refraction and reflection traveltime picked from OBS data combined with gravity data and obtained the approximate shape of the Moho discontinuity. Among the aforementioned studies, the resolution of velocity in the shallow layer inverted using first-arrival traveltime tomography is high, but that in the middle-to-lower layer is low. The velocity structures and the Moho morphology obtained by employing the human–computer interaction simulation are heavily dependent on operator expertise.

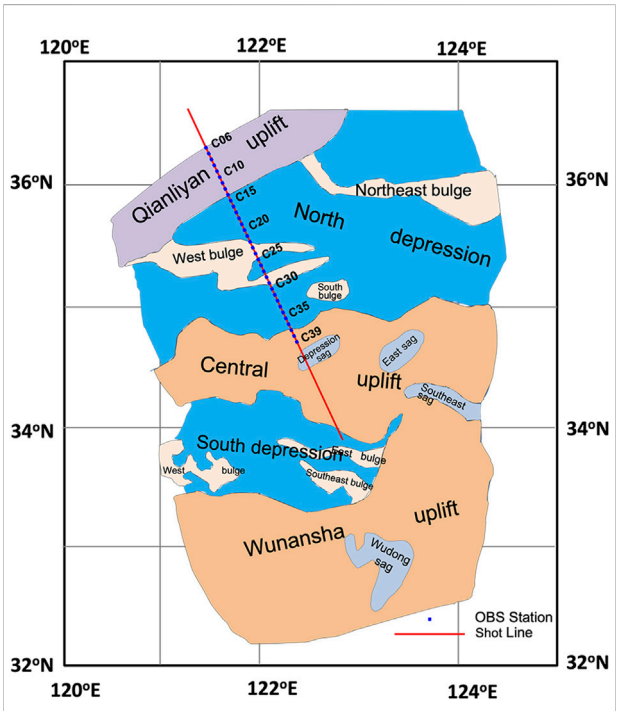

FIGURE 1
Tectonic regionalization of the SYS Basin and the position of survey line OBS2013.

To obtain a more precise velocity model and reduce the impact of human factors, this article proposes a joint tomographic inversion which can simultaneously use the traveltime and its gradient data of the reflected and refracted waves to invert the underground velocity model without determining the corresponding relationship between the seismic events and the reflection interfaces beforehand (Billette and Lambar, 1998). Moreover, the traveltime gradient can reflect the direction of ray propagation at the shot point and receiver point to solve the multipath problem of reflected rays, strengthen the constraint on the model space, and improve the inversion effect (Jin and Zhang, 2018). However, this requires picking the gradients in common-source gathers and in common-receiver ones, respectively. In data from survey line OBS2013, the OBS distance is large (6 km); in this case, the gradients cannot be picked in common-source gathers. To address this issue, we used a phase-shift wave-field extrapolation and the principle of reciprocity between a source and a receiver to pick the gradients in common-source gathers so that it becomes possible to use the joint tomography method (Alerini et al., 2009). Through this method, the crustal velocity structure and the undulating shape of the Moho discontinuity along this line are obtained. The related scientific problems are discussed, and some new understandings are attained.

Geological structure of the South Yellow Sea Basin and OBS2013 data

Tectonic division of the South Yellow Sea Basin

The SYS Basin is located to the east of the Tanlu Fault Zone and south of the Sulu Orogenic Belt. Its northern and southern edges are adjacent to the Sino-Korean block and South China block, with the Sulu Orogenic Belt and the Jiangshao Fault Belt as the boundaries, respectively. Moreover, the basin connects to the Lower Yangtze Subei Basin in the west. Overall, it is a superimposed basin on the Meso-Paleozoic marine strata which have been significantly transformed by Meso-Cenozoic tectonic plate movements (Wan, 2012; Li et al., 2017). The current SYS Basin is delimited in conformity with the stratigraphic

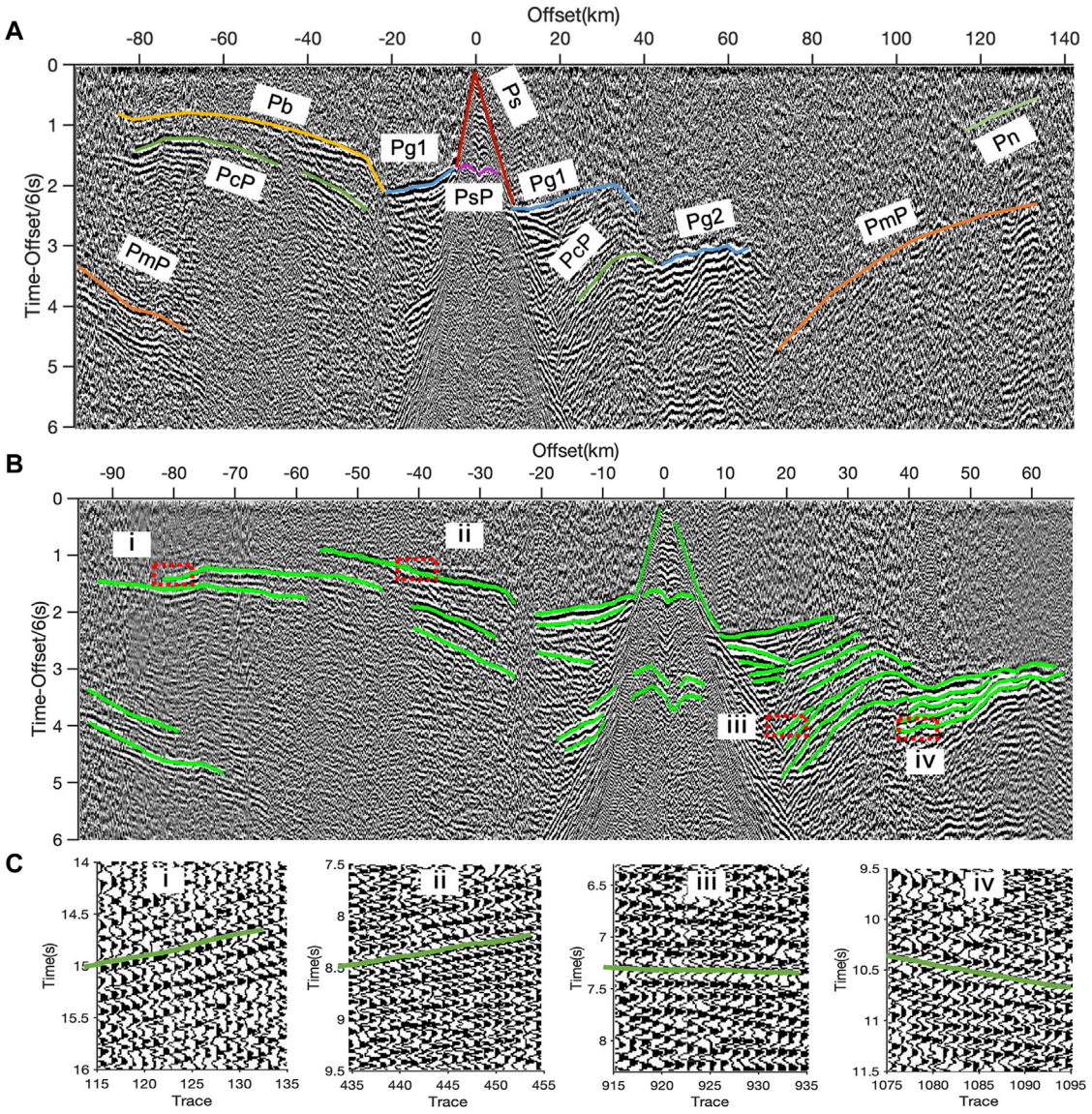

FIGURE 2
Seismic phase and event-picking of OBS19: **(A)** seismic phase identification of OBS19 seismic records, **(B)** seismic event-picking position of OBS19 seismic records, **(C)** the close-up of the pickup effect of the red dashed rectangles (i, ii, iii, and iv) in **(B)**.

distribution range since the Cretaceous–Paleogene extinction. From north to south, the basin can be categorized into five secondary structural units, namely, the Qianliyan Uplift, Northern depression, Central Uplift, Southern depression, and Wunansha Uplift (Figure 1). A series of faulted depressions, grabens, and other structures have also developed in the basin. The faulted depressions are primarily distributed to the west of 123°E and are characterized as northern faults in addition to the southern stratigraphic overlap, and the faulted depressions are steep in the north, and gentle in the south. Most of the structural lines are NNE and NE, controlling the basin's formation and development. The Mesozoic strata in the Northern depression, together with the Paleozoic strata in the Central Uplift and the Wunansha Uplift, have feasible hydrocarbon potential. Moreover, the OBSs of the OBS2013 survey line are essentially arranged in the south of the Qianliyan Uplift and the whole Northern depression.

OBS2013 data

OBS2013 survey line, with a length of 223 km, is the first deep seismic survey line deployed in the SYS area. A total of 39 OBSs

(C06–C39 in Figure 1) are deployed, including 17 short periodic MicroOBSs and 22 short periodic GeoprosOBSs. The distance between the OBSs is 6 km, and the sampling interval of the seismic wave is 4 ms. Additionally, the 2,501 shots are fired at a spacing of 125 m. The initial shot point is located at OBS03, and the termination shot point is 106 km away from OBS39 (red line in Figure 1).

It is necessary to note that we have denoised the OBS data to improve the signal-to-noise ratio (SNR). Due to the shallow-water depth and large wind waves in the area where the OBSs were located, a substantial amount of noise is found in the seismic records. Among the noise, random noise can be practically divided into low-frequency surge noise with a frequency of 0–3 Hz, high-frequency wind–wave noise with a frequency above 30 Hz, and ship-dynamic noise and coastal–industrial noise with a frequency of 20–200 Hz. Moreover, coherent noise can be generally classified into surface waves, shallow-reflection multiples, and water waves that are mainly concentrated in the direct-wave region, as well as wide-angle virtual reflection and deep refraction multiples positioned outside the direct-wave region (Zhao et al., 2020). According to the distribution characteristics of noise, data preprocessing comprises automatic gain control, bandpass filtering, and predictive deconvolution (Peacock and Treitel, 1969; Garret et al., 2012; Zhao et al., 2020).

Figure 2A illustrates the seismic phase identification of the post-noise reduction OBS19 seismic records (converted speed of 6 km/s), in which the Ps seismic phase is the inflected seismic phase in the sedimentary layer appearing on both sides of the station as the first arrival, and its apparent velocity is low. Pg1 is the refracted phase in the upper crust, followed by the Ps phase in the form of the first arrival. Simultaneously, the reflected seismic phase PsP at the bottom interface of the sedimentary layer can be identified near the converted traveltime of 1.5 s, exhibiting a significant hyperbolic symmetry. The Pb seismic phase of the left branch (the refraction seismic phase under the basement of the SYS's continental basin) is reduced from 2 s to 1.2 s at the 20-km offset due to the Qianliyan Fault, and then the seismic phase can be continuously traced to the 90-km offset. The PcP seismic phase (the reflected wave seismic phase at the upper and lower crust interfaces) appears at 20–80 km, and the converted traveltime ranges from 1.5 s to 2.5 s. The PmP phase (Moho reflection phase) appears at an offset of 90 km and a traveltime of 3.5 s. The reflected seismic facies PcP in the high-velocity marine sedimentary layer are recorded at 20 km of the right branch and extend to approximately 45 km. The Pg2 seismic phase (refracted phase in the mid-crust) occurs at 45–65 km, and the equivalent traveltime ranges from 3 to 4 s. In addition, the PmP phase appears at 70–135 km, with weak phase energy. At 120 km, the Pn seismic phase (upper mantle refraction seismic phase) appears at the conversion time of 1 s with weak energy (Liu et al., 2021; Zhang et al., 2021).

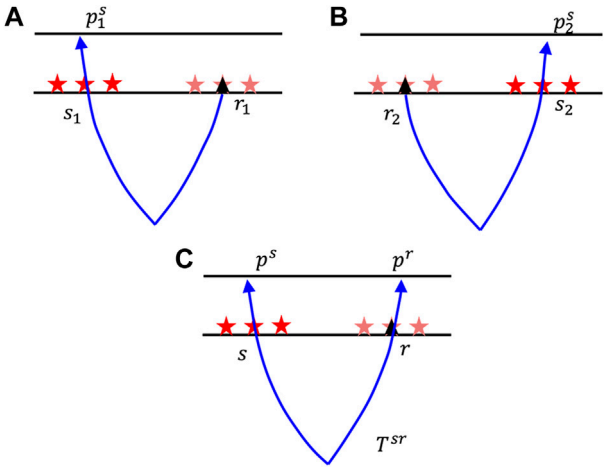

FIGURE 3
Schematic diagram of the principle of reciprocity: **(A)** Picking of data on common-receiver gathers at source s_1, **(B)** picking of data on common-receiver gathers at source s_2, and **(C)** use of the reciprocity to obtain the two gradients. The stars represent the sources and the triangles the receivers.

Methodology

For the tomographic inversion, the traveltimes and their gradients must be picked from the reflected and refracted phases in common-source and common-receiver gathers, respectively. Given the large OBS distance, we picked the traveltimes and their gradients of the same phase in the common-source gathers based on the principle of reciprocity. Since the sources are close to the sea surface and the OBS is located on the sea bottom, the sources are corrected to be located at the sea bottom by using a wave-field extrapolation technique to meet the principle of reciprocity.

Wave-field extrapolation

At present, the common wave equation datum correction methods can be divided into three categories: Kirchhoff integration method, finite difference method, and phase-shift method. The two previous methods are approximate solutions, while the wave equation transformed in the phase-shift will not distort the waveform and has high accuracy. Therefore, this study used the phase-shift method in the frequency–wavenumber domain to implement wave-field extrapolation (Gazdag, 1978; Cui et al., 2007; Alerini et al., 2009), redatuming and interpolation of the sources at receiver positions. First, the seismic records were transformed from the time–space domain to the frequency domain by using the Fourier transform. Afterward, wave-field extrapolation was performed using the "step-by-step accumulation" and "step-by-step parking" methods (Yang et al., 2007).

Picking traveltimes and their gradients at common-receiver gathers

The traveltime gradient refers to the tangent slope of the local correlation event in the seismic record at the center trace. It is the ratio of the traveltime difference △t between the two ends of the local coherent-phase axis centered on the track and the distance Δx between them. Because the source spacing is small, the traveltime and its gradient at each source can be picked in the common-receiver gather by using the slant stack method (Schleicher, et al., 2008).

Picking traveltimes and their gradients at common-shot gathers

Since the number of OBSs was small and the interval was large, the number of seismic records in a common source was insignificant, making the tracking of seismic events even more challenging. The aforementioned slant-stacking method was unsuitable for picking the seismic event traveltimes and the gradient data at each receiver point in the common-source gather. This study applied the principle of reciprocity between a source and a receiver to the traveltime and gradient pickup of the sparse OBS observation system (Alerini et al., 2009). Figure 3 presents the details of its principle. For the seismic records T1 with the receiver at r_1 and the source at s_1, the traveltime gradient p_1^s at source s_1 in the common-receiver gathers is picked, as exemplified in Figure 3A. As shown later, we circumvent the problem of picking slopes in common-source gathers by applying reciprocity of Green's functions and using information from common-receiver gathers. Concerning the seismic records T2 with the receiver point at r_2 and the source at s_2, the traveltime gradient p_2^s at point s_2 is picked in the common-receiver gathers, as illustrated in Figure 3B. In this way, we obtained the two gradients (Figure 3C).

Joint tomographic inversion of reflected and first-arrival waves

The first arrival includes direct and refraction waves, and its event traveltime and gradient data are straightforward to pick. The first arrival of small and medium offsets can describe a shallow seabed's characteristics, and the first arrival of large offsets can also reflect the deep strata information. In contrast, the observation angle of the reflected wave is limited, but the reflected wave contains a considerable amount of mid-deep information, which is more beneficial in the inversion of mid-deep crustal velocity. The joint tomographic inversion using first-arrival and reflected wave data can increase the coverage angle of the rays and their coverage times (Prieux et al., 2013; Liu and Zhang, 2022). Compared with a single first-arrival or reflected wave, joint inversion has a higher accuracy.

Following stereo-tomography (Billette et al., 2003; Lambare et al., 2004), the smooth velocity model was estimated from the traveltime and its gradient data of the local coherent events of both first-arrival and reflection waves. By modifying the velocity model and the location of the reflection points, the calculated and picked traveltimes and their gradients of the first-arrival and reflected waves are made consistent, thereby obtaining the underground velocity model (Li et al., 2019).

In joint tomography, the data space d of traveltime and its gradient tomography can be expressed as:

$$\mathrm{d} = \left[\left(\mathrm{x_s}, \mathrm{z_s}, \mathrm{px_s}, \mathrm{x_r}, \mathrm{z_r}, \mathrm{px_r}, \mathrm{t_{sr}} \right)_\mathrm{n} \right]_{\mathrm{n=1}}^{\mathrm{N}}, \tag{1}$$

where (x_s, z_s) is the coordinate of the source s; (x_r, z_r) is the coordinate of the receiver r; px_s and px_r are the traveltime gradients at the source and receiver points, respectively; and t_{sr} is the two-way traveltime. The subscript n represents the *n*th ray pair, and N represents the number of ray pairs.

The model space m is composed of discrete velocity parameters m_v, first-break wave section parameters $m_{fst_{ray}}$, and reflection wave section parameters $m_{ref_{ray}}$, which can be expressed as:

$$\mathrm{m} = \left(\mathrm{m_v}, \mathrm{m_{fst_{ray}}}, \mathrm{m_{ref_{ray}}} \right)^{\mathrm{T}}. \tag{2}$$

The objective function of joint tomographic inversion is:

$$\begin{aligned} O\left(m_{fst_{ray}}, m_{ref_{ray}}, m_v\right) &= \frac{1}{2}\varphi\left[d_{fst_{cal}}\left(m_{fst_{ray}}, m_v\right) - d_{fst_{obs}}\right]^T C_d^{-1}\left[d_{fst_{cal}}\left(m_{fst_{ray}}, m_v\right) - d_{fst_{obs}}\right] \\ &+\frac{1}{2}(1-\varphi)\left[d_{ref_{cal}}\left(m_{ref_{ray}}, m_v\right) - d_{ref_{obs}}\right]^T C_d^{-1}\left[d_{ref_{cal}}\left(m_{ref_{ray}}, m_v\right) - d_{ref_{obs}}\right] \\ &+\frac{1}{2}\lambda\left(m_v - m_{v_{prior}}\right)^T C_m^{-1} L^T L\left(m_v - m_{v_{prior}}\right), \end{aligned} \tag{3}$$

where the first two items are the data residuals, and the third item is the model constraint. Additionally, φ is the first-arrival inversion weight; λ is the damping coefficient that adjusts the relative size of the model constraint item role; $d_{fst_{obs}}$ and $d_{fst_{cal}}$ are the first-arrival observation data and calculation data, respectively; and $d_{ref_{obs}}$ and $d_{ref_{cal}}$ are the reflected-wave observation data and calculation data, respectively. m_v is the model, $m_{v_{prior}}$ is the *a priori* model; L represents the Laplace operator which carries on the smooth constraint to the model; T superscript is the matrix transpose, and C_d and C_m are the covariance matrices of the data and the model, respectively. The data items and model parameter items are weighted, and the observation data with different magnitudes, such as the traveltime and gradient, and the model parameters with different magnitudes, such as the velocity and reflection point position, are normalized.$d_{cal}(m)$ is a nonlinear function. At the initial model $m_{v_{prior}}$, the function is expanded by using Taylor series, and the linear term is obtained:

$$d_{cal}(m) = d_{cal}\left(m_{v_{prior}}\right) + G\left(m - m_{v_{proor}}\right), \tag{4}$$

where $G = (G_v, G_{ray})^T$, G_v is the kernel function matrix of the data about the node velocity of the discrete model, and G_{ray} is the kernel function matrix of the data about the ray parameters (reflection point coordinates, ray exit angle, and ray traveltime) (Billette and Lambar, 1998).

In order to obtain the minimum solution of objective function (3), after substituting Eq. 4 into Eq. 3, making the derivative of objective function model space parameter equal to 0, then the following linear inversion equation is obtained:

$$\begin{pmatrix} G_v^T C_d^{-1} G_v & G_{ray}^T C_d^{-1} G_{ray} \\ \lambda C_m^{-1} L & 0 \end{pmatrix} \begin{pmatrix} \Delta m_v \\ \Delta m_{ray} \end{pmatrix} = \begin{pmatrix} G_v^T C_d^{-1} \Delta d \\ 0 \end{pmatrix}, \quad (5)$$

where Δd represents the data residual vector, its element is the difference between the observed data and the data calculated by the current inversion model, and Δm_v and Δm_{ray} are the corrections of the ray segment parameters and discrete velocity values, respectively. In this way, it will continue iteratively until the mean square error between

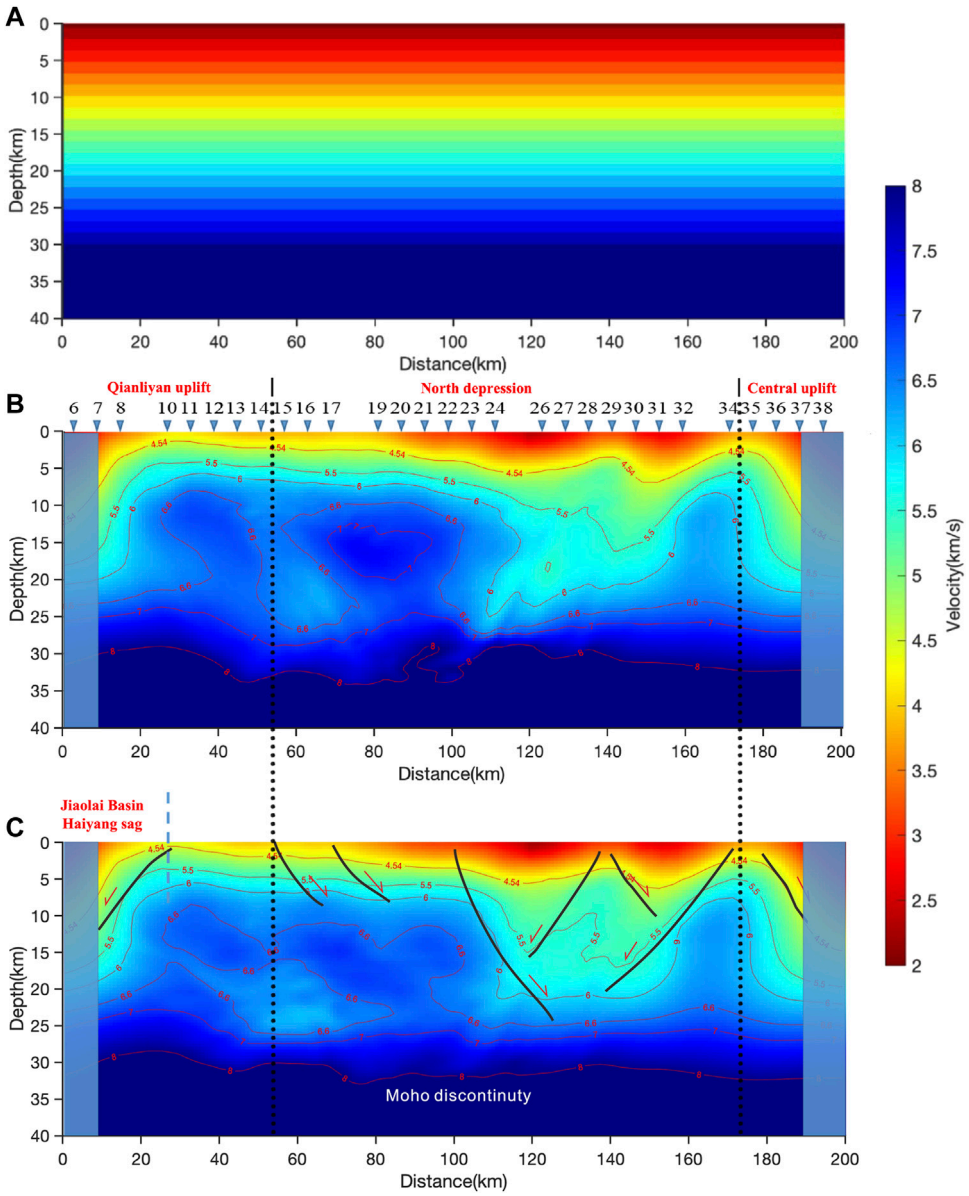

FIGURE 4
(A) Initial velocity model, **(B)** tomographic inversion results of first-arrival traveltimes and their gradients, and **(C)** tomographic inversion results of traveltimes and their gradients of first-arrival wave joint-reflected waves.

the inversion model calculation data and the observation data meets the given error limit.

Results

Picking traveltimes and their gradients

In total, 39 OBSs were encoded into the OBS2013 survey line in the SYS, of which 29 OBSs collected valid data. After preprocessing the robust OBS data, consistent with the OBS water-depth data, we extended the shot point from the sea surface to the seabed where the OBS was located using the phase-shifting wave-field extrapolation method from Chapter 3. Additionally, the local event traveltime and its gradient of the common source were picked through the principle of the reciprocity method. Figures 2B, C illustrate the result of the traveltimes and their gradients picked at the common receiver (OBS19). Then, Figure 2B portrays the pickup effect of the traveltime position at OBS19. The first-arrival seismic phases (Ps, Pb, Pg1, and Pg2) and reflected-wave seismic phases (PcP, PsP, and PmP) are picked. Moreover, Figure 2C displays the close-up of the picked effect of the red dashed rectangles (i, ii, iii, and iv). For all the valid OBS data, 284 groups of the first-arrival traveltimes and their gradients, along with 395 groups of reflection traveltimes and their gradients, were picked.

Joint tomographic inversion of traveltimes and their gradients

The crustal velocity distribution is inverted by the tomography using 284 groups of first-arrival traveltimes and their gradients, as well as 395 groups of reflection traveltimes and their gradients. According to the previous information on surface velocity in the study area and the velocity model constructed by the predecessors, the initial velocity model in Figure 4A is established. The model's length in the x direction is 200 km, the depth in the z direction is 40 km, the velocity increases linearly with depth, v= (2 + 0.2z) km/s, and the size of the initial discrete unit of the model is 4 km × 1.5 km.

First, 284 groups of first-arrival traveltimes and their gradients were employed for tomographic inversion. In the inversion process, the multiscale strategy was utilized to continuously subdivide the grid. Subsequently, the grid was divided every 20 iterations. After 60 iterations, we derived the inversion result with a grid size of 1 × 0.375 km (Figure 4B). Then, 395 groups of the reflection traveltimes and their gradients were added for joint tomographic inversion. The weight coefficient of the first-arrival data item is 0.4, and the reflection data item is 0.6. Using the same initial model and iteration parameters as the first-arrival inversion, the final inversion result of the reflection data is presented in Figure 4C. By tracking the RMSE (root mean square error) of position, slope, and traveltime of the source and receiver pairs in the iterative process, it is found that the inversion process is convergent. Comparing Figure 4B with Figure 4C, the tomographic inversion results using only the first-arrival data are fundamentally consistent with the joint inversion results above 15 km. However, the two inversion results for the mid-deep velocity below 15 km differ. The joint tomographic inversion result is of higher quality than the tomographic inversion result of the first-arrival data.

Based on the joint tomographic inversion results in Figure 4C, the shallow velocity of the model between OBS14 and OBS36 is low, and the velocity on both sides is higher than that in the middle. The tectonic boundary between the Qianliyan Uplift, Northern depression, and Central Uplift is clearly given, which is consistent with the tectonic boundary's location distribution in Figure 1. Moreover, the velocity model above a depth of 5 km (e.g., the velocity contour of 4.54 km/s) also reflects the distribution of secondary structures. OBS22, OBS23, and OBS24 are located on the North Branch of the Northern depression's Western bulge, and OBS29 is on the South Branch of the Northern depression's Western bulge.

The basement of the Jiaolai Basin comprises Late Archean–Late Proterozoic metamorphic rocks, which extensively crop out on the basin's northern and southern sides. Primarily, the sedimentary rock series is composed of the Lower Cretaceous Laiyang Group and Qingshan Group, as well as the Upper Cretaceous Wangshi Group. In particular, the Laiyang Group is primarily deposited by river lake facies clastic sediments, which are intercalated with dolomitic shale and a small number of pyroclastic rocks. In addition, the Qingshan Group is an intricate series of volcanic, pyroclastic, and typical sedimentary rocks. Finally, the Wangshi Group is made of river lake facies clastic rocks mixed with mudstone and pyroclastic rocks. For each set of strata, the thickness can reach several thousand meters, which are either in parallel unconformity or angular unconformity. A small amount of the Paleogene strata is present in numerous regions, such as in the Pingdu Sag, and a small number of Quaternary deposits are distributed in the basin's northwestern area (Qiu et al., 2011). Based on the joint inversion results itemized in Figure 4C in the Qianliyan Uplift area, because the high-velocity body below the Haiyang Sag of the Jiaolai Basin has a large-scale extension to the Qianliyan Uplift, the low-velocity Cretaceous strata directly cover the Sulu Orogenic Belt's pre-Sinian metamorphic rock basement.

As the central body of the lower Yangtze paraplatform, the SYS Basin is a multicycle superimposed basin of Meso-Paleozoic marine basins and Meso-Cenozoic continental basins based on the pre-Nanhua fold metamorphic crystalline basement. More specifically, the SYS Basin can be categorized into three structural layers from the bottom to the top: the Nanhua Early Middle Triassic marine strata as the lower structural layer, a late Cretaceous Paleogene half-graben

lacustrine deposit in the middle, and Neogene–Quaternary depression-type fluvial facies and marine continental facies clastic sediment as the upper layer (Zhang et al., 2014; Zhao et al., 2019b). The inversion results in Figure 4C show that in the Central Uplift area, due to the strong erosion since the Indo-China movement, the low-velocity Neogene–Quaternary strata in the upper structural layer are directly overlaid by the Mesozoic and Paleozoic carbonate formations in the lower structural layer. As a result, a strong difference in the formation velocity in the shallow part of the two regions exists. At depths of 5 km–20 km in the model, a large area of a relatively low-velocity anomaly from OBS22 to OBS32 in the Northern depression is observed. This indicates that under the Meso-Cenozoic continental strata of the middle and upper structural layers of the Northern depression, the geological situation of an exceedingly thick lower structural layer can be found in the Meso-Paleozoic marine strata.

The Moho discontinuity in Figure 4C is approximately determined according to the 8 km/s velocity contour. Its depth in the study area ranges from 28 km to 32 km. In the Qianliyan Uplift, affected by the strong subduction collision orogeny between the Yangtze block and the North China block during the Indosinian period, the Moho discontinuity fluctuates to a great extent, but in other regions, it fluctuates only at a very low level.

Conclusion

With the OBS2013 line in the SYS, this study combines the phase-shift wave-field extrapolation and the principle of reciprocity, and the traveltimes and their gradient picking of the local coherent events of sparse OBS data are realized. Simultaneously, the crustal velocity structure and the undulating shape of the Moho discontinuity in the SYS are revealed by joint tomographic inversion of reflected and refracted seismic waves. Accordingly, the crustal velocity structure substantiated that the high-velocity body in the deep Haiyang Sag of the onshore Jiaolai Basin extends to the SYS's Qianliyan Uplift area at a large scale. It is also worth noting that the low-velocity Cretaceous strata directly cover the pre-Sinian metamorphic rock basement of the Sulu Orogenic Belt, and the thick Meso-Paleozoic marine strata are preserved under the Meso-Cenozoic continental strata in the Northern depression. Finally, the fluctuation characteristics of the Moho discontinuity in a depth range of 28–32 km in the study area are further characterized.

Data availability statement

The raw data supporting the conclusion of this article will be made available by the authors, without undue reservation.

Author contributions

FM adapted the algorithm, analyzed the data, and wrote the manuscript; FH provided fruitful discussions on the tomographic results. TL provided fruitful discussions on the algorithm; ZW provided the original OBS2013 data and technical guidance. JZ conceived and revised the manuscript. All authors listed have made a substantial, direct, and intellectual contribution to the work, and approved it for publication.

Funding

This work was supported by the Shandong Provincial Natural Science Foundation (China) (Grant No. ZR2019MD001).

Conflict of interest

The authors declare that the research was conducted in the absence of any commercial or financial relationships that could be construed as a potential conflict of interest.

Publisher's note

All claims expressed in this article are solely those of the authors and do not necessarily represent those of their affiliated organizations, or those of the publisher, the editors, and the reviewers. Any product that may be evaluated in this article, or claim that may be made by its manufacturer, is not guaranteed or endorsed by the publisher.

References

Alerini, M., Traub, B., Ravaut, C., and Duveneck, E. (2009). Prestack depth imaging of ocean-bottom node data. *Geophysics* 74 (6), WCA57–63. doi:10.1190/1.3204767

Billette, F., Bégat, S., Podvin, P., and Lambaré, G. (2003). Practical aspects and applications of 2d stereotomography. *Geophysics* 68 (3), 1008–1021. doi:10.1190/1.1581072

Billette, F., and Lambar, G. (1998). Velocity macro-model estimation from seismic reflection data by stereotomography. *Geophys. J. Int.* 135 (2), 671–690. doi:10.1046/j.1365-246X.1998.00632.x

Cui, X., Li, H., Hu, Y., Hong, L., and Li, Q. (2007). Wavefield continuation datuming using a near surface model. *Appl. Geophys.* 4 (2), 94–100. doi:10.1007/s11770-007-0014-y

Garret, M., Rebecca, L., and Jan, S. (2012). Imaging the shallow crust with teleseismic receiver functions. *Geophys. J. Int.* 191, 627–636. doi:10.1111/j.1365-246X.2012.05615.x

Gazdag, J. (1978). Wave equation migration with the phase-shift method. *Geophysics* 43, 1342–1351. doi:10.1190/1.1440899

Jin, C., and Zhang, J. (2018). Stereotomography of seismic data acquired on undulant topography. *Geophysics* 83 (4), U35–U41. doi:10.1190/geo2017-0411.1

Lambare, G., Alerini, M., Baina, R., and Podvin, P. (2004). Stereotomography: A semi-automatic approach for velocity macromodel estimation. *Geophys. Prospect.* 52 (6), 671–681. doi:10.1111/j.1365-2478.2004.00440.x

Li, T., Liu, J., and Zhang, J. (2019). A 3D reflection ray-tracing method based on linear traveltime perturbation interpolation. *Geophysics* 84 (4), T181–T191. doi:10.1190/geo2018-0119.1

Li, X., Li, S., Suo, Y., Somerville, I., Huang, F., Liu, X., et al. (2017). Early Cretaceous diabases, lamprophyres and andesites-dacites in Western Shandong, North China Craton: Implications for local delamination and Paleo-Pacific slab rollback. *J. Asian Earth Sci.* 160, 426–444. doi:10.1016/j.jseaes.2017.08.005

Liu, J., and Zhang, J. (2022). Joint inversion of seismic slopes, traveltimes and gravity anomaly data based on structural similarity. *Geophys. J. Int.* 229 (1), 390–407. doi:10.1093/gji/ggab478

Liu, L., Hao, T., Lu, C., Wu, Z., Zheng, Y., Wang, F., et al. (2021). Crustal deformation and detachment in the Sulu Orogenic Belt: New constraints from onshore-offshore wide-angle seismic data. *Geophys. Res. Lett.* 48, e2021GL095248. doi:10.1029/2021GL095248

Liu, L., Hao, T., Lue, C., You, Q., Pan, J., Wang, F., et al. (2015). Crustal structure of bohai sea and adjacent area (north China) from two onshore–offshore wide-angle seismic survey lines. *J. Asian Earth Sci.* 98, 457–469. doi:10.1016/j.jseaes.2014.11.034

Peacock, K., and Treitel, S. (1969). Predictive deconvolution: Theory and practice. *Geophysics* 34 (2), 155–169. doi:10.1190/1.1440003

Prieux, V., Lambaré, G., Operto, S., and Virieux, J. (2013). Building starting models for full waveform inversion from wide-aperture data by stereotomography. *Geophys. Prospect.* 61, 109–137. doi:10.1111/j.1365-2478.2012.01099.x

Qiu, X., Zhao, M., Ao, W., Lu, C., Hao, T., You, Q., et al. (2011). OBS survey and crustal structure of the southwest sub-Basin and nansha block, south China sea. *Chin. J. Geophys.-CH.* 54 (12), 3117–3128. doi:10.3969/j.issn.0001-5733.2011.12.012

Schleicher, J., Costa, J., Santos, L., Novais, A., and Tygel, M. (2008). On the estimation of local slopes. *Geophysics* 74 (4), 25–33. doi:10.1190/1.3063968

Wan, T. (2012). *The tectonics of China: Data, maps and evolution*. Berlin, Heidelberg: Springer-Verlag. ISBN: 978-3-642-11866-1, 978-3-642-11868-5.

Yang, K., Fan, J., Cheng, J., Ma, Z., and Wang, L. (2007). An integrated wave equation datuming scheme for the overthrust data based on the one-way extrapolator. *Seg. Tech. Program Expand. Abstr.* 26 (1), 3124. doi:10.1190/1.2792938

Zhang, H., Qiu, X., Wang, Q., Huang, H., and Zhao, M. (2021). Data processing and seismic phase identification of OBS converted shear wave in the Xisha Block. *Chin. J. Geophys.-CH.* 64 (11), 4090–4104. doi:10.6038/cjg2021O0293

Zhang, X., Yang, J., Li, G., and Yang, Y. (2014). Basement structure and distribution of Mesozoic-Paleozoic marine strata in the South Yellow Sea basin. *Chin. J. Geophys.-CH.* 57 (12), 4041–4051. doi:10.6038/cjg20141216

Zhao, W., Wang, H., Shi, H., Xie, H., Zheng, Y., Chen, S., et al. (2019a). Crustal structure from onshore-offshore wide-angle seismic data: Application to northern sulu orogen and its adjacent area. *Tectonophysics* 770, 228220. doi:10.1016/j.tecto.2019.228220

Zhao, W., Zhang, X., Wang, H., Chen, S., Wu, Z., Hao, T., et al. (2020). Characteristics and noise combination suppression of wide-angle ocean bottom seismography (OBS) data in shallow water: A case study of profile OBS2016 in the south Yellow Sea. *Chin. J. Geophys.-CH.* 63 (6), 2415–2433. doi:10.6038/cjg2020N0360

Zhao, W., Zhang, X., Zou, Z., Wu, Z., Hao, T., Zhang, Y., et al. (2019b). Velocity structure of sedimentary formation in the South Yellow Sea Basin based on OBS data. *Chin. J. Geophys.-CH.* 62 (1), 183–196. doi:10.6038/cjg2018L0623

Zou, Z., Liu, K., Zhao, W., Liu, H., Zhou, H., Meng, X., et al. (2016). Upper crustal structure beneath the northern south yellow sea revealed by wide-angle seismic tomography and joint interpretation of geophysical data. *Geol. J.* 51 (S1), 108–122. doi:10.1002/gj.2847

frontiers | Frontiers in Earth Science

TYPE Original Research
PUBLISHED 20 January 2023
DOI 10.3389/feart.2022.1043790

OPEN ACCESS

EDITED BY
Qizhen Du,
China University of Petroleum, China

REVIEWED BY
Jianyong Xie,
Chengdu University of Technology, China
Roberto Scarpa,
University of Salerno, Italy
Yibo Wang,
Institute of Geology and Geophysics (CAS), China

*CORRESPONDENCE
Zhao Long,
zhaolong@lntu.edu.cn

SPECIALTY SECTION
This article was submitted to Solid Earth Geophysics, a section of the journal Frontiers in Earth Science

RECEIVED 14 September 2022
ACCEPTED 10 November 2022
PUBLISHED 20 January 2023

CITATION
Long Z (2023), Microseismic positioning of an isolated working face under complex geological conditions and its engineering application.
Front. Earth Sci. 10:1043790.
doi: 10.3389/feart.2022.1043790

Microseismic positioning of an isolated working face under complex geological conditions and its engineering application

Zhao Long*

School of Science, Liaoning Technical University, Fuxin, China

In view of the inability to accurately locate vibrations in isolated workings under complex geological conditions, an adaptive rotational categorization method, a downhill comparison method based on time-frequency analysis (TFA-DC method), a variable-step acceleration search method, and a dual-phase seismic source location method (TD-DL method) are proposed. A set of integrated software with features of "visualization", "interactive" and "one-click" was developed for microseismic data processing. Results show that compared with the improved STA/LTA method, the recognition accuracy of the island working face microseismic signal by the adaptive wheel classification method is increased by 4.8%. Compared with the improved STA/LTA method, the TFA-DC method has the advantage that it can simultaneously pick up the exact *p* wave and the peak S wave, and the failure ratio is 0. Compared with simulated annealing algorithm and genetic algorithm, stepwise accelerated search method has better results. The standard deviation of objective function value, location error and wave velocity error are all 0. Method improves the positioning of the TD - DL detector coordinates, dual phase and coherence of known information, such as the positioning result positioning error is only the *p* wave and S wave ChanZhen phase positioning method of 9.5% and 14.5%, to a certain extent offset the *p* wave and S wave ChanZhen phase calculation of the positioning error, so as to improve the effect of source localization precision of the inversion.

KEYWORDS

microseismic monitoring, adaptive wheel classification method, TFA -DC method, step-size accelerated search method, dual seismic source location

1 Introduction

With increase in mining depth and scale, the uncertainty of the underground environment in which it takes place gradually increases, which is manifested by the fact that the primary geological structure of the strata in which it is located is susceptible to extensive disturbance or even destruction. This may imply that the mining of mineral resources may also be accompanied by a number of environmental and safety hazards such as impact pressure, collapse of the mining area, rock explosion, and roofing of the tunnel flake (Pan et al., 2007; Cui et al., 2019; Li et al., 2019).

In order to monitor and prevent these safety hazards, microseismic monitoring technology is now commonly used in the mining process to monitor and locate disaster sources (Gong et al., 2010; Gong et al., 2012). This predicting is necessary as part of monitoring the rock interface damage, matrix or inclusions fracture during the mining process to ensure the safety of construction and reduce economic losses (Li and Xu, 2020). The core elements of microseismic monitoring are phase identification, arrival time pickup, algorithm optimization, and source localization.

For seismic phase recognition, Zhao et al. (2015) used microseismic waveform repetition, tail-wave drop, signal principal frequency, and occurrence time that fall under Fisher classification method parameters to construct a seismic phase recognition model. Dong et al. (2016) selected microseismic occurrence time, seismic moment, total radiated energy, P- and S-wave energy ratio, corner frequency, and static stress drop as feature parameters for microseismic recognition. Used Fisher classification method, and Plain Bayes method and logistic regression were used for classification. Jiang et al. (2021) proposed an earthquake phase identification method based on random forest classifier after reducing the data volume by singular value decomposition and used the time-frequency characteristics of microseismic signals. Wu et al. (2016) proposed an earthquake phase identification method based on S-transform, and the similarity of phase and frequency and random combination analysis of P-wave waveform.

In arrival pickup, Ross et al. (2018) proposed a method for the P-wave arrival pickup and the initial motion polarity determination using deep learning. Perol et al. (2018) proposed a method for seismic phase identification and arrival pickup based on U-shaped neural networks. Lee et al. (2017) proposed a modified energy ratio (MER) method for arrival pickup. Diehl et al. (2009) proposed a method for the P-wave arrival pickup based on a hybrid STA/LTA-Polarization-AIC algorithm. for P-wave arrival pickup is proposed based on the short time-window average/long time-window average (STA/LTA), polarization and AIC criteria.

In terms of optimization of algorithms, Li et al. (2014) proposed a simplex shape localization method based on L1 parametric statistics, which had high immunity to outliers with large deviations. Jia et al. (2017) analyzed the relationship between localization error and the number and location of sensors using high-density table-array and particle swarm algorithms. In the source location, the joint inversion localization method is more common (Li et al., 2013; Zheng et al., 2016; Xue et al., 2018), and there are many other methods, Wang et al. (2019) proposed a differential evolutionary microseismic localization method with improved localization objective function for traditional localization method which relied heavily on the walking time accuracy. Wang et al. (2020) proposed a hybrid microseismic source localization algorithm based on simplex-shortest path ray tracing.

The above research results have improved the accuracy of earthquake source localization to a certain extent, but there are some shortcomings. For the seismic phase identification, the commonly used STA/LTA method calculates the ratio of the long- and short-time windows of the whole signal, and the invalid background noise in the whole signal accounts for most of it, resulting in lot of arithmetic power and time; for the arrival pickup, with the increase of the geophone arrangement density (Jia et al., 2017; Zhao et al., 2019), the quality of the waveforms collected by each geophone is increasingly different for poor quality signals. Therefore, for some of the poor quality signals, even if the high-precision pickup method is used, the pickup results will have large errors, leading to an increase in the source inversion error. For optimization algorithms, traditional algorithms such as genetic algorithms and simulated annealing algorithms usually rely on the selection of iterative initial parameters, which may lead to distorted or scattered localization calculation results if they are not selected properly (Tian and Chen, 2002). Due to their fixed search step, these may also lead to poor accuracy or convergence of localization results. For different objective functions, and initial data (including geophone coordinates, P-wave initial value arrival time, etc.), the localization effect may occur for source localization, and hence it may be difficult to recognize the accurate initial arrival time of the single phase of the S-wave due to interference with other phases. On this basis, the current utilization of the S-wave single-phase relative to source localization is not high. The difference and connection between P-wave single-phase and S-wave single-phase in source localization are not clarified; the effect of source localization using S-wave arrival time alone is unknown.

Aiming at the above existing problems, by means of theoretical analysis, algorithm programming, numerical calculation and engineering verification, the adaptive wheel classification seismic phase identification method and time-frequency analysis-downhill comparison method (TFA-DC Method) are put forward respectively. The phases location method for the double seismic phase is TFA-DC-double Seismic Phases (TD-DL method), and the optimization algorithm of accelerated search with variable step size. And integrated into interactive microseismic signal processing software, the source inversion and location results can be obtained by one-click through the original signal, which provides a new feasible scheme for real-time microseismic monitoring.

2 Project overview

2.1 Geological conditions of the 8204–2 working face of Tashan Mine

Tashan Mine is a model mine in Datong area, and is a mega mine with the largest design capacity, with an annual production

TABLE 1 Coordinates of mining area of station.

Detector serial number	Coordinate/m		
	X	Y	Z
Station 1	1987.23	22567.34	60.41
Station 2	2,291.32	22618.45	46.54
Station 3	1,689.46	22383.53	61.27
Station 4	2016.45	23034.54	63.83
Station 5	918.66	22763.34	44.34
Station 6	1940.56	22400.87	62.64
Station 7	1,587.54	22614.56	54.82

of 15 million tons of coal in China. The project team conducted several field surveys of the Tashan Mine and finally selected the 8204–2 working face in the second pan area as the basis for the study. The mine conditions of 8204–2 working face of Tashan Mine are as follows:

Tashan mine 8204–2 working face is an isolated island working face, coal seam mining depth is about 500 m, coal seam thickness is 12–20 m averaging about 15 m, coal seam dip angle is 2–5°, uses comprehensive mining, the working face length is about 150 m, advances 10 cuts per day of about 8 m, and has no underground monitoring system.

Therefore, in view of the geological conditions at Datong Tashan Mine, the microseismic monitoring system was placed at the 8204–2 working face in the second pan area.

2.2 Tower hill mine introduction to microseismic monitoring

The initial selection of the site of the stations was based on the above-ground and below-ground comparison map of the 8204–2 working face of the Tashan Mine, which required each station to cover the 8204–2 working face as much as possible, and there should be no "three points and one line" between each ground station, which is conducive to observation and data processing (Jia et al., 2017). It was planned to set up 11 alternative ground monitoring stations in the mine. Initially, seven stations were set up for observations, and later, if necessary, 1–2 stations were set up according to the results from the observations, and key monitoring areas. After repeated surveys of the pre-selected locations, the specific locations of the seven ground monitoring stations were finally determined. The precise mine coordinates of the ground monitoring stations were measured on site by GPS positioning equipment at the mine site, as shown in Table 1.

As shown in Table 1, the distribution map of the ground monitoring stations in the mining area with seven stations is drawn, as shown in Figure 1, where the red mark is the location of the selected ground monitoring stations.

2.2.1 High-frequency microseismic collector architecture

The high-frequency microseismic signal collector consisted of a data collector, a three-component vibration velocity sensor, a GPS timing system, and a Wi-Fi transmission module.

The data collector consists of a first- and second preamplifier, an analog-to-digital conversion unit, a data storage unit, a control unit, a display, a hard disk, a USB module, a Wi-Fi interface, and a power supply module. The data collector adopted high-frequency data acquisition and synchronous segment index compression technology to achieve high-speed retrieval, high-precision data segmentation and rapid upload, and high efficiency in post-processing to browse data, count overall parameters, and sieve valid data.

Three-component high-frequency vibration velocity sensor was used to have complete, continuous signal acquisition, three-component vibration velocity sensors were assembled from one vertical and two horizontal sensors, which monitored the vibration signal in three directions: east-west, north-south, and vertical velocity, Each sensor was such that it covered a circular area of 1–2 km of monitoring, with the frequency of vibration velocity signal within 10–1,400 kHz flat response, high signal-to-noise ratio, small phase difference, high dynamic resolution, and strong temperature adaptability.

The collector equipment was IP68 rated for water and dust resistance and is equipped with 4 TB of space for binary stream data storage. Each collector is designed with eight sampling channels, which had a sampling channel sampling frequency of up to 10 kHz with a sensitivity of 100 ± 5% (V/m/s). A three-component vibration velocity sensor has six channels, GPS timing system occupies one channel, and the remaining one channel can be connected to other sensors. The design of the high-frequency micro-vibration collector is shown in Figure 2.

The GPS timing system determines the ground station data sampling time with the Earth coordinates of the ground station, occupying one acquisition channel of the data collector. The data collector uses its external port to read the PPS (Pulse Per Second) signal of the GPS timing system to synchronize with the vibration signal with a timing accuracy of 10 μs,, to ensure the sampling accuracy of 10 kHz of the data collector.

The Wi-Fi transmission module has the wireless transmission support of the data collector and the speed-sensor sensing data, which are, in turn, connected to the bridge data transmitter.

3 Details on the microseismic phase identification and the seismic source localization methods

3.1 Adaptive rotation categorization method fundamentals

The adaptive rotational categorization method consists of four main steps which are as follows::

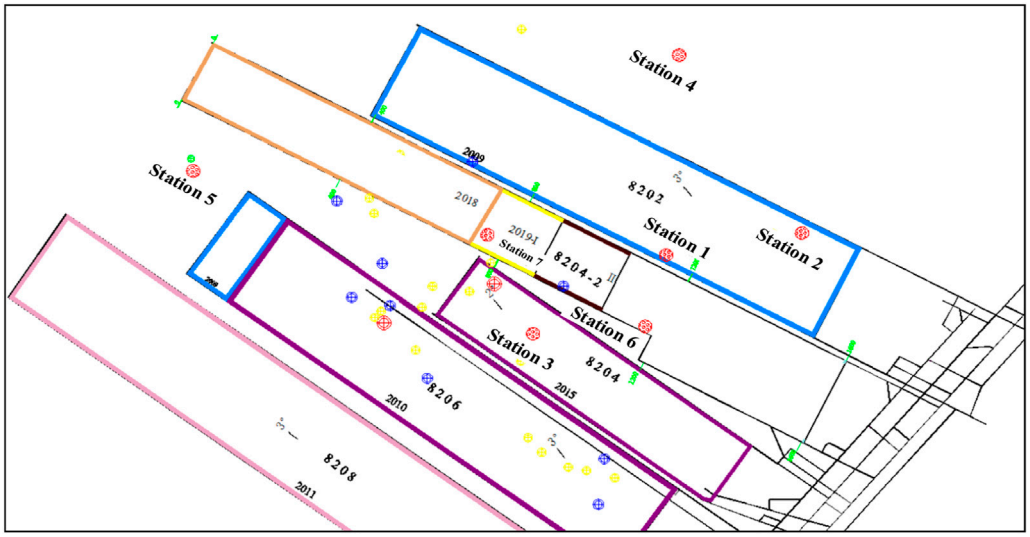

FIGURE 1
Distribution of ground monitoring stations in mining area.

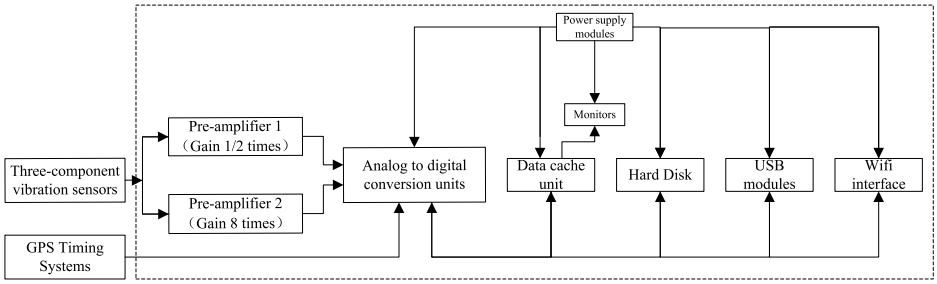

FIGURE 2
Structure of the high frequency microseismic collector.

1) Adaptive high-pass filtering

In order to reduce the interference of the background noise on the microseismic response and to improve the recognition accuracy and algorithm stability of the adaptive rotational categorization method, high-pass filtering of the original signal was required, and the lower high-pass filtering limit required for high-pass filtering needed to be entered manually. Therefore, in order to realize automatic process operation of the whole method, an adaptive high-pass filtering processing method that can process various forms of microseismic signals is needed.

For the automated operation of high-pass filtering, here a base over-zero rate was used, which used the period function to discriminate the period (the number of times it crosses the *X-axis* from bottom up per unit time) to estimate the frequency of the main trend waveform with higher energy and stable frequency in the intercepted signal. The number of times the signal crosses the *X-axis* from bottom up in 10 s is 9, so the base rate was 0.9 Hz. The number of segments of the intercepted signal calculated is shown in Figure 3.

2) Calculation of the upper and lower bounds of the background noise amplitude

In order to further bring out the microseismic response signal, and determine the basis for taking the radius of rotation circle R_w (mm/s) after the original signal had undergone the adaptive high-pass filtering to improve the signal-to-noise ratio, the 95% probability of the falling point in the horizontal axis interval (μ-2σ,μ+2σ) of the normal

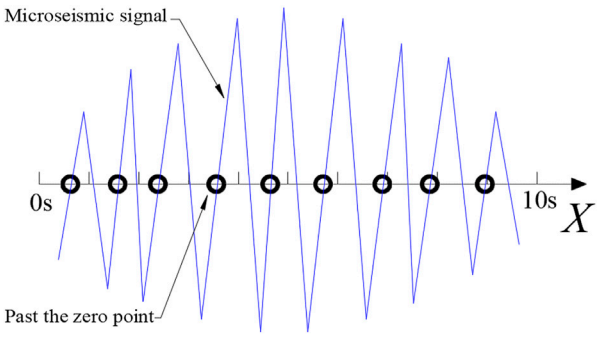

FIGURE 3
Calculation diagram of basic zero-crossing rate.

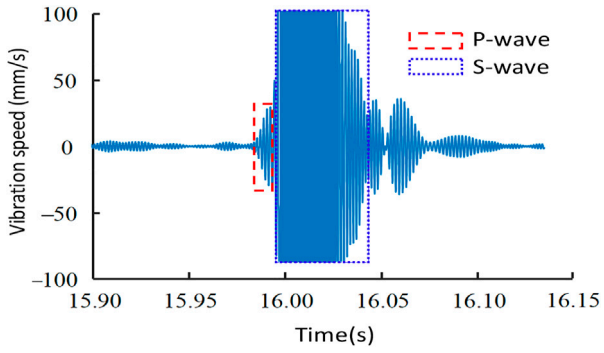

FIGURE 4
Overlap of P-wave and S-wave.

distribution was introduced as the confidence interval of the signal. This, method gradually used increasing the coverage from Y=0, and judging whether the whole signal was included. The method of 95% of data points was used to iteratively compare the upper and lower bounds of the background noise amplitude that satisfied the above conditions to ensure that the obtained results covered most of the background noise, invalid responses, and filtered out the microseismic response signals.

3) Rotation circle radius calculation and rotation iteration

A small number of higher amplitude data points were selected from a single microseismic response that provided the base data for the next step of grouping the exceedance points into categories. The center of the rotating circle was located on the *X*-axis, and its radius was taken as the range expansion factor, *Q*, times the distance between the upper bound D_u (mm/s) and the lower bound D_d (mm/s) of the background noise amplitude. By traversing all data points of the whole signal and comparing them, the data points larger than the radius R_w of the rotating circle were filtered out to obtain all the exceedance points needed for the next step. The iterative screening used the average of the absolute values of the two elements before and after in the whole segment signal to represent the amplitude of the signal here. This, increased the applicable range of the iterative comparison, and avoided the identification error caused by the radical change of a single data point.

4) Clustering of exceedance points

In order to finally obtain the influence region of the microseismic response in the microseismic signal, i.e., to identify the seismic phase of the whole microseismic signal, the overruns selected by the rotation circle needed to be grouped into the same group to represent a single seismic phase identification result, and into multiple groups to represent multiple seismic phase identification results. If the time difference between the two was greater than the grouping interval, F_{int}, the points were grouped into one category, after which the points were grouped into the next category.

3.2 TFA-DC method determine the pickup time

Speech and power density spectrograms were used to obtain the location and regularity of the background noise and the change of frequency, amplitude and energy of the microseismic signal before and after the initial arrival of P-wave and the S-waves. On this basis, the FIR band-pass filtering was carried out twice continuously with the main frequency of the S-wave as the circle point, and the specified filtering range in radius was used to filter out the high and low frequency background noise with regularity and power greater than that of P-wave and S-wave signals. This made the power density spectrogram of the S-wave of the main frequencies clearly appear, and also made the signal image smoother and more suitable for iterative comparison. Based on the above theoretical results, the TFA-DC method for the joint pickup of the P-wave and S-wave dual-oscillation phase arrivals was used by setting the mathematical expression of the full-subwave amplitude as a threshold, and followed three major relationships between the P-wave and the S-wave power magnitude, the arrival sequence, and the waveform overlap.

3.2.1 Connection between P wave and S wave

After analyzing the original signal by speech spectrogram and power density spectrogram and using two consecutive FIR bandpass filtering, the three relations between *p* wave and S wave are as follows: power magnitude relationship, arrival sequence relationship, waveform overlap relationship.

1) Power relationship

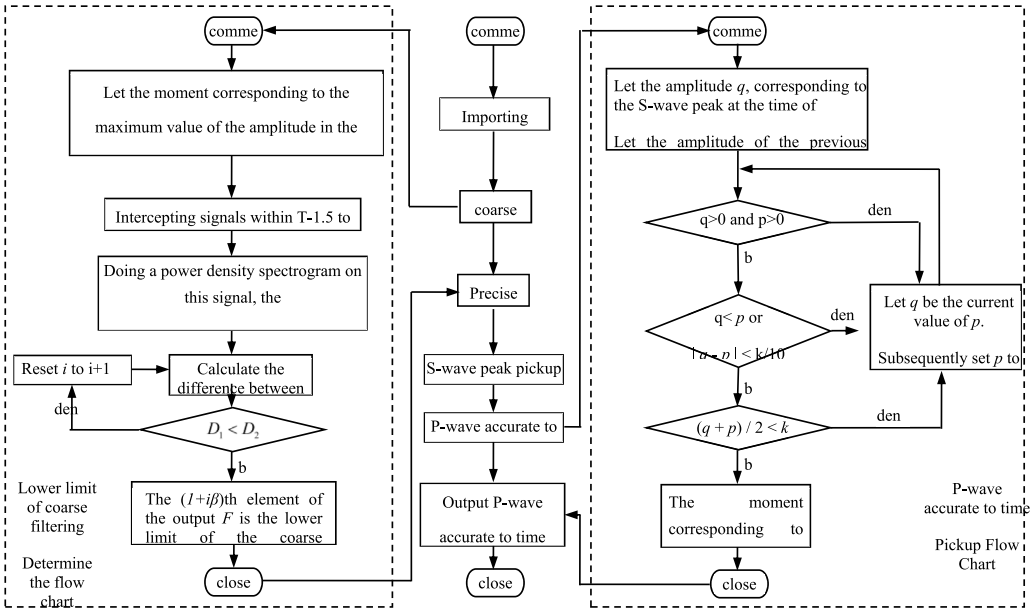

FIGURE 5
Flow chart of the TFA-DC method procedure.

The power and amplitude of S wave in the microseismic signal are larger than that of *p* wave, so the amplitude surge caused by the initial arrival of the microseismic signal is mainly caused by the arrival of S wave, so the seismic pickup by S wave is more concise than that by *p* wave.

2) The relationship of arrival sequence

In most cases, *p* wave velocity is greater than S wave velocity, so *p* wave should arrive at the detector first than S wave. That is, from the perspective of microseismic signal waveform, the shock change of microseismic signal waveform caused by the arrival of *p* wave should be on the left side of the shock change of microseismic signal waveform caused by the arrival of S wave.

3) Waveform overlap relationship

Usually, the distance between the seismogenic position and the detector is relatively small, so it is difficult to completely calm the mechanical vibration caused by the initial arrival of *p* wave before the arrival of S wave. Therefore, the *p* wave shape should overlap with the S wave shape, and the overlap is shown in Figure 4.

To sum up, to pick up the precise arrival time of *p* wave, the peak arrival time of S wave must be found first, and the precise arrival time information of S wave is often covered by the tail of *p* wave and background noise. Therefore, in order to improve the adaptability of the algorithm and the calculation speed of the algorithm, the peak arrival time of S wave must be extracted first.

3.2.2 When S wave peak value is collected

S there should be a *p* wave crest value after know signal with wavelet amplitude of the first great point, and according to the law of conservation of energy, mechanical vibration amplitude detector should be gradually decreases, and the S wave reaches the since the arrival, or S wave signal wavelet amplitude should gradually decreases, and there will be no signal wavelet amplitude repeated shocks, Therefore, the peak arrival time of S wave should be the time corresponding to the maximum amplitude of the signal wavelet after the precise arrival time of *p* wave, and the amplitude of the signal wavelet itself is the maximum value of the current wavelet. Therefore, the peak arrival time of S wave can be obtained by sorting all the sampled values of the signal according to the size.

3.2.3 P wave accurate time pickup

In order to obtain the precise time limit of *p* wave, the corresponding amplitude of the peak value of S wave and the amplitude of the left signal wavelet are successively compared by iterative comparison method. The program flow is shown in Figure 5, and the steps of the method are described as follows.

3.3 The variable-step accelerated search methods for microseismic optimization calculations

The variable-step acceleration search method (Jia et al., 2022) was divided into three major modules, namely, the continuous

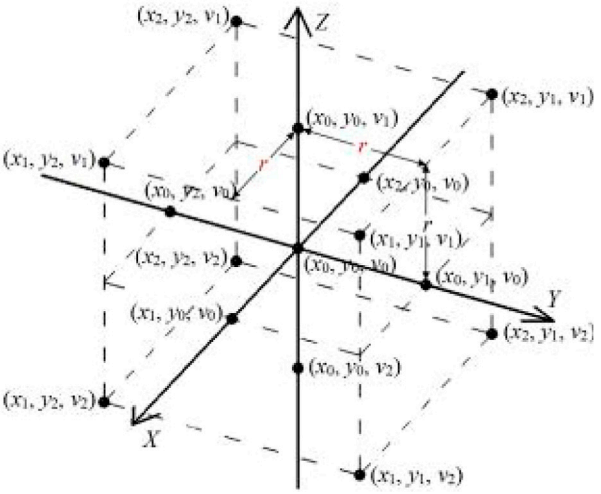

FIGURE 6
Diagram of specified points of three-dimensional polyhedron.

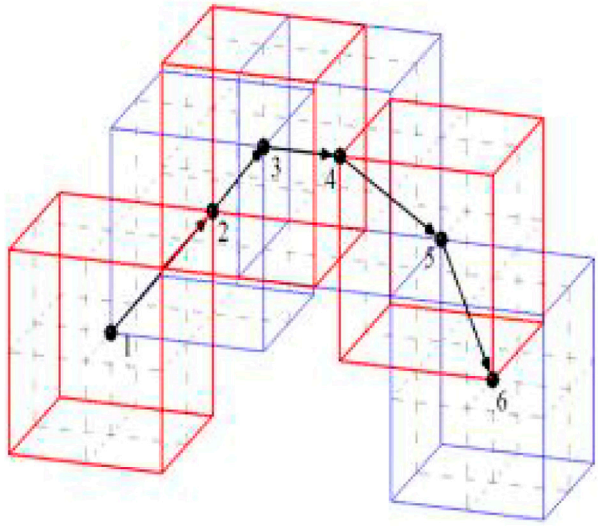

FIGURE 7
Schematic diagram of three-dimensional iterative process.

comparison module, the variable-step module, and the acceleration module, where the continuous comparison module was the main line process, and the variable-step module and the acceleration module were adjust the search step for the main line journey.

1) Continuous comparison module

The module essentially took the advantage of the uniqueness of the minimal value of the objective function by taking any starting point from which the objective function values of the adjacent specified points were calculated successively and compared numerically.

The objective function unknowns were three, and the positions of each prescribed point of the three-dimensional polyhedron are shown in Figure 6, and the three-dimensional iterative process is shown in Figure 7. When the unknown quantity of the objective function was four or more, it was reduced to a four-dimensional space or a multi-dimensional space above four dimensions according to mathematical induction.

Usually, the closer the value of the objective function was to zero, the more accurate was its corresponding source localization. When the value of the objective function failed to converge or had a large value, it indicated that the source could not be localized, or had a large error. The minimum point was found using the optimization algorithm, and the spatial location corresponding to this minimum point was the location of the source. Therefore, the microseismic source localization problem could be transformed into finding the value of the respective variable corresponding to its minimum value in the case of convergence of the multivariate objective function.

2) Variable step-size module

If the objective function value of each specified point was smaller than the objective function value of the starting point, then the coordinate value of the specified point with the smallest objective function was assigned to the starting point. Further, if no specified point with a smaller objective function value was found, then the distance from this point to each specified point (search step) was reduced to one-half of the original, and the cycle was iterated until the search step was smaller than the lower limit of the search step, and the current value of the desired variable was the final output.

3) Acceleration module

The essence of the acceleration module is to record the position number of the geometric center point of the polyhedron to each specified point of the polyhedron twice in succession, and if the position number is the same twice, the search step will be expanded to Q (the acceleration factor) times of the original one, so that the single-variable convergence process can be accelerated, thus speeding up the computation. In practical engineering problems, due to the increase in the anisotropy of the spatial distribution of the

objective function, a smaller acceleration factor can effectively improve the error tolerance rate in the face of the computational errors caused by the increase in the search step. Hence, the acceleration factor in the range of 1.0–1.5 can be better adapted to the convergence of different objective functions. In summary, the recommended value of the acceleration factor is 1.5, and the specific value can be adjusted according to the actual working conditions.

In the actual operation, the range of values of the four variables and the convergence range were usually different, and if a uniformly varying search step was applied to them, the individual variables converged while the rest continued to iterate gradually. This resulted in a lot of waste of arithmetic power as well as computation time. Therefore, the acceleration module was used whereby most of the variables converged while a single variable is calculated separately.

3.4 The TD-DL method study for microseismic source localization

The TFA-DC method was used to process the microseismic event signal by substituting the exact P-wave arrival time and the peak S-wave arrival time into the dual-phase objective function, and integrating the dual-phase wave velocity as the phase propagation speed., The variable-step acceleration search method was performed to search for the minimum value of the objective function, and a dual-phase source location method used both the exact P-wave arrival time and the peak S-wave arrival time.

A single microseismic event usually contained multiple seismic phase information such as the P-wave, the S-wave, the surface wave, and the reflection wave at the same time. Except for the P-wave, the rest were not used for localization calculation due to overlapping and interference problems. Therefore, the dual-earthquake phase objective function (Li et al., 2017), which used both the P-wave single-earthquake phase and the S-wave single-earthquake phase, was introduced, and the wave velocity of the dual-earthquake phase was integrated in it as follows (Eq. 1):

$$R(x_0, y_0, z_0, v_m) = \sqrt{\frac{\gamma}{N}\sum_{i=1}^{N}\left[\left(T_P^i - t_P^i - T_{P0}\right)^2 + \left(T_S^i - t_S^i - T_{S0}\right)^2\right] \Big/ 2 + \frac{(1-\gamma)}{N}\sum_{i=1}^{N}\left[\left(T_P^i - T_S^i\right) - \left(t_P^i - t_S^i\right)\right]^2} \quad (1)$$

where: $R\ (x_0, y_0, z_0, v_m)$ is the travel time residual of the double shock phase; v_m is the shock phase propagation velocity (m/s); γ is the equilibrium coefficient, taking values from 0 to 1.

It was because the P- and S-wave velocities were unknown and changed continuously, and the magnitude of this change varied during propagation, the algorithm failed to converge when the two wave velocities were substituted into the calculation independently. Therefore, due to the uncertainty of the wave velocity structure, the simultaneous substitution of the average wave velocities of the two single seismic phases for the localization inversion calculation lead to a decrease in the localization accuracy.

In view of the above unknowns and uncertainties, the average wave velocities of the P-wave and S-wave were set to the same value, and were thus calculated by substituting them into the variable-step acceleration search method together with the required spatial coordinates of the seismic source x_0, y_0, z_0. Firstly, this method avoided the pre-velocity measurements, and achieved real-time monitoring. Secondly, this method reduced the influence of the wave velocity structure on the localization accuracy, and made the objective function converge to the minimum value as much as possible. Finally, this method improved the convergence of the objective function because the degree of the geotechnical rupture was different under different seismic conditions. Due to this, the wave velocities of the P-waves generated by extrusion and the S-waves generated by shear were not constant. Under small-scale microseismic monitoring here, the propagation distance between P-wave and S waves had short propagation distances and their velocity variations were small. Hence, the ratio of the wave velocities of the P- and S waves in a single microseismic event were considered as constant. the seismic phase propagation velocity (v_m) was characterized as the uniform propagation velocity of the two.

The improved dual-phase objective function worked by forming an equation with four independent variables based on the existing geophone coordinates and the dual-phase arrival time. The minimum value of the objective function was searched in the definition domain using an optimization algorithm, and the values of the four independent variables corresponding to the minimum value were the required source inversion coordinates and their corresponding seismic phase propagation velocities.

TFA-DC method is an arrival picking method that can simultaneously obtain the P-wave accurate arrival time and the S-wave peak arrival time of microseismic signals. Firstly, by analyzing the speech spectra and power density spectra of the original signal, the position and rule of the background noise and the frequency, amplitude and energy changes of the microseismic signal before and after the initial arrival of *p* wave and S wave were obtained. The first band-pass filtering was carried out according to the algorithm to filter out the background noise of high and low frequencies with regular power greater than *p* wave and S wave signals, so that the main frequency of S wave in the power density spectrum was clearly displayed.

Then, the main frequency of S wave is taken as the dot, and the filtering range is specified as the radius to carry out the second bandpass filtering, which makes the signal image smoother and suitable for iterative comparison. Due to the radius of the choice of *p* wave and S wave frequency range, and the *p* wave velocity than the S wave, so the filtered waveform of *p* wave precisely

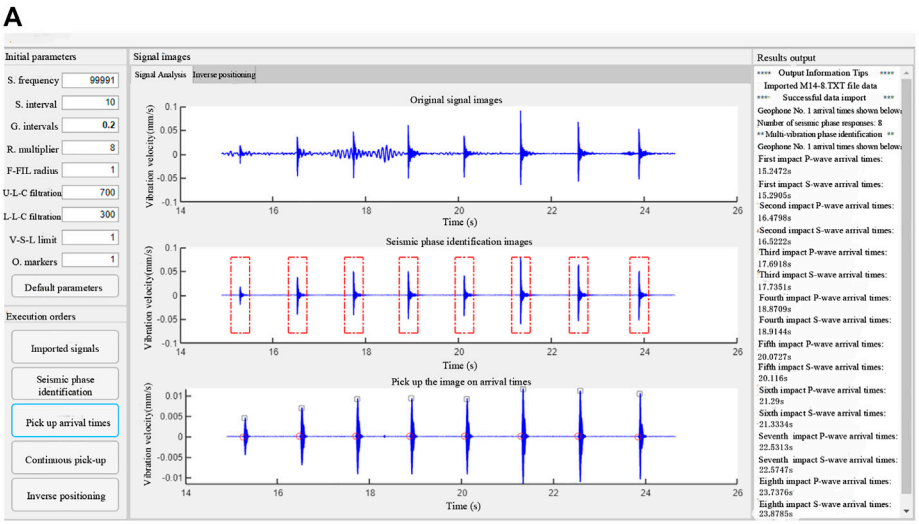

Signal analysis operator interface .

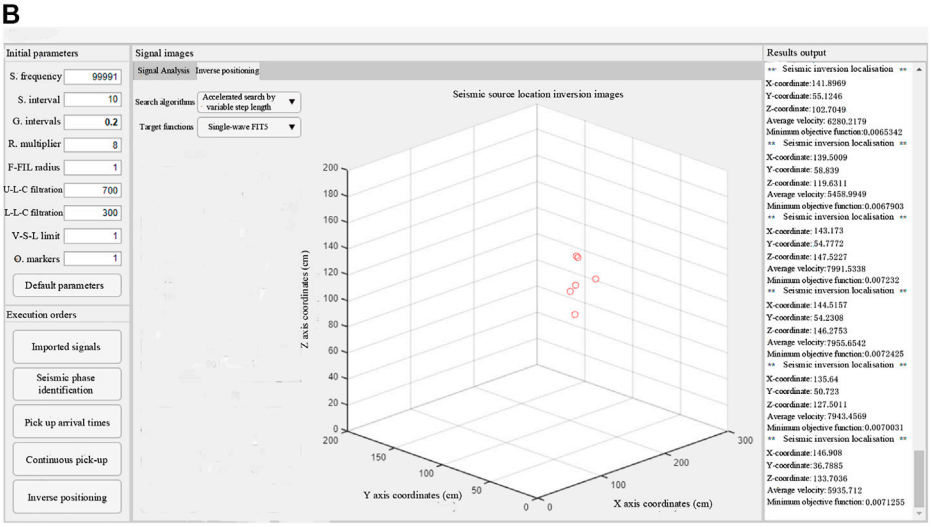

The operational interface for inversion positioning

FIGURE 8
Integrated software graphical user interface.

when the *p* wave to wave and S wave crest value that corresponds to the full signal waveform amplitude can be clearly revealed, and in most cases will not produce interference or covering.

Finally, the mathematical expectation of the full wavelet amplitude is set as a threshold, and the filtered signals are compared down hill according to the three relations of P-wave and S-wave power, arrival sequence and waveform overlap, so as to obtain the precise P-wave arrival time and the S-wave peak value represented by the first peak on the right side of the P-wave seismic phase.

Due to the smoothing effect of bandpass filtering on the abrupt signal, the smooth transition phenomenon of increasing or decreasing wavelet amplitude will occur at the abrupt signal, which leads to the fact that the P-wave accurate arrival time pickup in TFA-DC method is earlier than the actual arrival time. Since the S wave signal collected by the geophone needs a certain time course from its arrival to its peak value, and sometimes other seismic phases are superimposed on it, the peak value of S wave is actually later than its real arrival time. Therefore, the inversion and location of the source using the above *p* wave or S

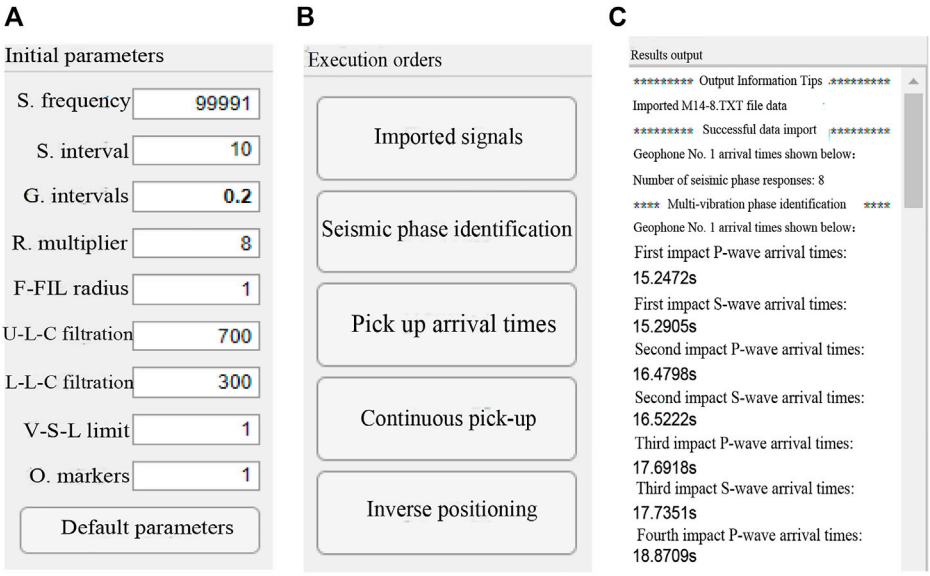

FIGURE 9
Basic function graphical user interface.

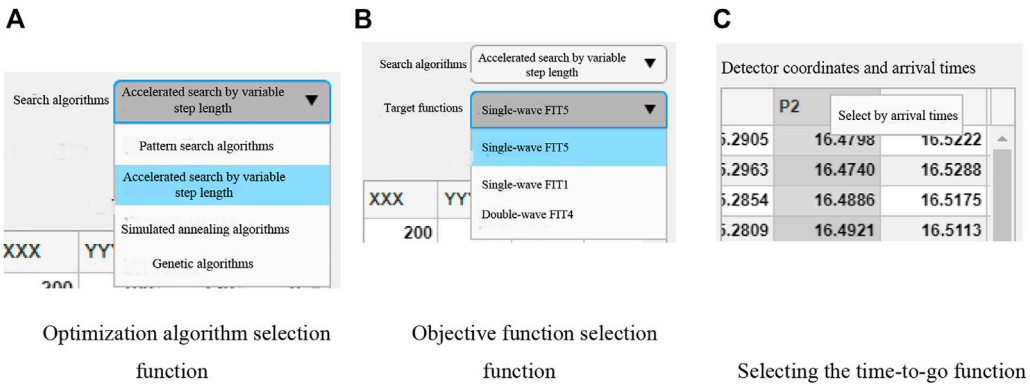

FIGURE 10
Display of some other functions.

wave single seismic phase time data alone may cause a certain deviation of the location results compared with the real source.

After selecting the objective function and importing the relevant time and geophone space coordinate information, the variable step acceleration search method is used to search the minimum value of the objective function. The value of the independent variable corresponding to the minimum value of the objective function obtained by iterative search is the spatial coordinate of the source.

The proposed TD-DL method is a new localization method including a complete set of microseismic localization solutions, which includes a joint TFA-DC dual-phase arrival pickup method that can pick up both the P-wave accurate arrivals and S-wave peak arrivals, a dual-phase objective function that

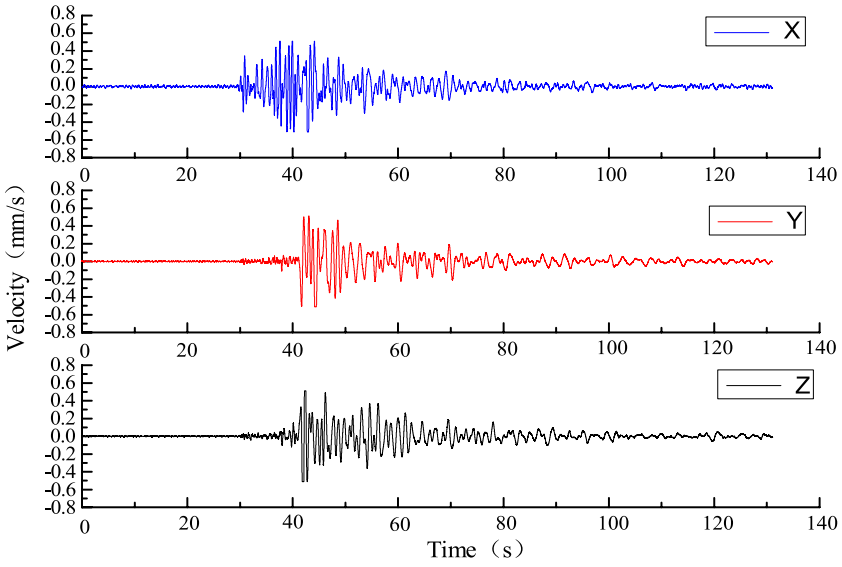

FIGURE 11
Schematic diagram of microseismic signal in microseismic monitoring project.

integrates wave velocities, and a variable-step acceleration search method, which combine to form the TD-DL method that can automatically pick up arrivals and calculate localization.

3.5 Integrated software development

All the microseismic signal processing methods proposed in this paper were integrated, and the graphical user interface of the integrated software was designed using Matlab programming language for the development of a full-process processing software for microseismic signals. As a microseismic signal processing software with the features of “visualization”, “interactive” and “one-click”, the software has the functions of signal playback, seismic phase identification, on-time pickup, and inversion. The integrated software has a graphical user interface as shown in Figure 7. The graphical user interface of the integrated software is shown in Figure 7.

3.5.1 Basic functions

The initial parameters required by the software were nine, namely sampling frequency, sampling interval, grouping interval, reduction multiplier, fine-filter radius, coarse-filter upper limit, coarse-filter lower limit, variable-step lower limit, and check mark. The sampling frequency, sampling interval, and grouping interval were required for echo identification, the reduction multiplier and fine filter radius were required for on-time pickup, the coarse-filter upper limit and coarse-filter lower limit were required for all functions, the variable-step lower limit was required for inversion positioning, and the check mark was required to limit the playback data. The abbreviations in Figures 8A, B are represented in detail as follows, details are: sample frequency (S. frequency)、sample interval (S. interval)、group intervals (G. interval)、reduced multiplier (R. multiplier)、fine filtration radius (F-FIL radius)、upper limit of coarse filtration (U-L-C filtration)、lower limit of coarse filtration (L-L-C filtration)、variable-step lower limit (V-S-L limit)、oscilloscope markers (O. markers).

The commands were import signal, phase identification, pickup time, continuous pickup and inversion positioning. The single pickup time function picks up the precise P-wave arrival time and the S-wave peak time of a single microseismic signal of the corresponding geophone, while the continuous pickup function picks up the P-wave precise time and S-wave peak time of multiple geophones corresponding to multiple microseismic signals in a single test. All the results of the above operations were obtained. The results of all the above operations are displayed in the result output panel for specific extraction of the valid information. The graphical user interface for the basic functions of the integrated software is shown in Figure 9.

3.5.2 Signal analysis functions

The soft-signal analysis interface was mainly divided into three image areas, namely the original signal image area, the seismic phase recognition image area, and the arrival pickup image area. The original signal image area shows the waveform of the original signal obtained from the import data function, the seismic phase recognition image area is the seismic phase recognition result obtained from the seismic recognition function through the red

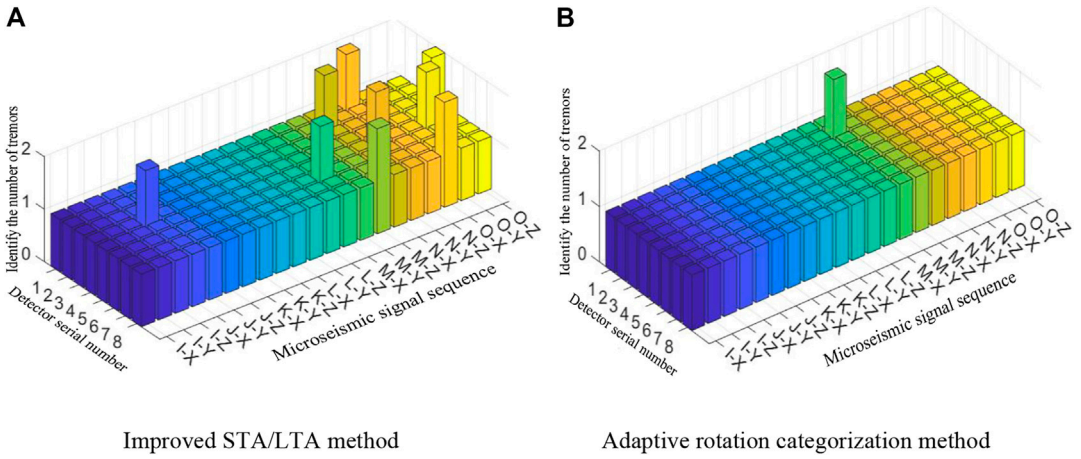

FIGURE 12
Microseismic phase identification results of the two methods.

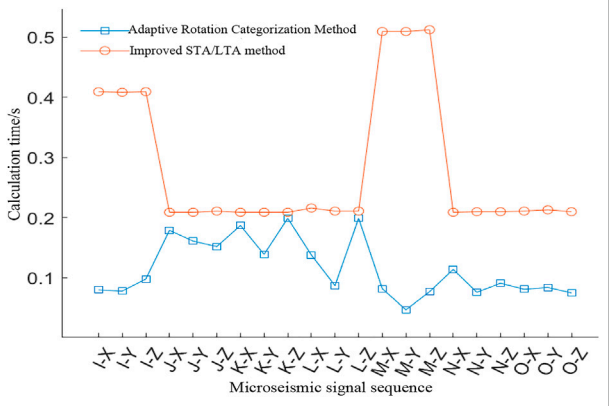

FIGURE 13
Calculation time for the two methods

dotted rectangular box, and the arrival pickup image area is the exact arrival time of the P-wave and the peak arrival time of the S-wave obtained from the pickup arrival function through the circle and the square, respectively.

3.5.3 Inverse positioning function

The inverse positioning interface was divided into four main functional areas, namely the optimization algorithm and objective function adjustment control, the geophone coordinates and the arrival time display and modification control, the initial parameters display and adjustment control, and the source inversion positioning image display and adjustment control. By entering the initial parameters such as the geophone coordinates, dual-phase arrival time, and the search starting point of the optimization algorithm, the inverse positioning function was used to locate the microseismic source inversion.

3.5.4 Other functions

To facilitate further analysis of the microseismic signals and a comparative analysis between different methods, the following functions are provided:

1) Optimization algorithms are available as pattern search algorithm, variable step accelerated search method, simulated annealing algorithm, and genetic algorithm.

TABLE 2 Comparison of the microseismic phase identification effects for the two methods.

Comparative indicators	Seismic phase identification method	
	Improving the STA/LTA methodology	Adaptive rotation categorization method
Number of successful identifications	159	167
Recognition accuracy	94.6%	99.4%
Standard deviation of identification deviation	0.225	0.077
Calculation time average/s	0.281	0.115
Calculation time standard deviation/s	0.127	0.071

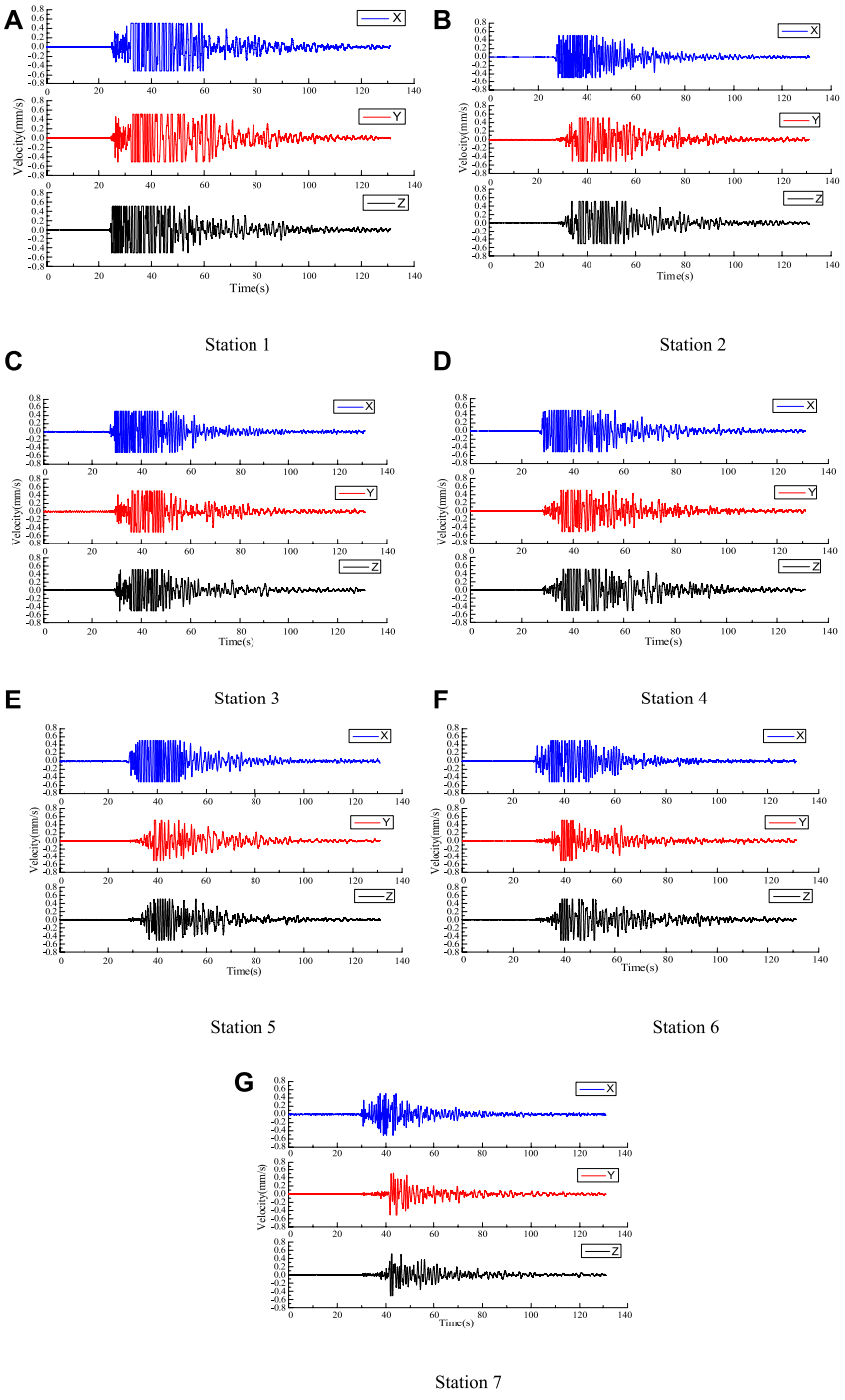

FIGURE 14
Three-component velocity profiles for each station for microseismic events.

2) The objective function could be selected as either single-phase or dual-phase, with two single-phase objective functions available under the single-phase option, and one dual-phase objective function corresponding to the dual-phase option.
3) The initial parameters and the geophone coordinates and the arrival support the function of modifying and restoring the default parameters.
4) The 3D plot window and the result output panel support clearing function.

TABLE 3 Analysis of arrival-time picking results of data from the practical engineering by TFA-DC.

Data serial number	1st microseismic signal arrival					2nd microseismic signal arrival					3rd microseismic signal arrives			
	When the P-wave arrives/s	Time lag/s	When the S-wave arrives/s	Time difference/s	Calculate run time/s	When the P-wave arrives/s	Time lag/s	When the S-wave arrives/s	Time lag/s	Computational runtimeTime/s	When the P-wave arrives/s	Time lag/s	When the S-wave arrives/s	Time lag/s	Calculate run time/s
Station 1	33.3444 53	0.011,880	35.305 053	0	1.992 557	33.950 253	0.012,670	35.246 253	0	1.897 983	33.568 053	0.016,910	35.190 653	0	1.618 210
Station 2	34.224 327	0.000,000	35.732 327	0	2.156 874	34.226 727	0.010,190	35.623 527	0	1.777 926	33.824 927	0.000,000	35.014 727	0	1.418 231
Station 3	34.632 081	-0.006 050	36.495 281	0	1.985 086	34.550 881	-0.004 420	35.877 881	0	2.125 512	34.053 081	0.004,350	35.347 081	0	1.906 152
Station 4	34.237 030	0.009,470	36.076 430	0	1.852 137	34.488 830	0.006,880	35.431 230	0	1.622 768	33.906 830	0.000,000	35.519 830	0	2.188 781
Station 5	34.584 766	0.008,400	36.029 166	0	1.663 114	34.266 566	0.011,120	35.855 966	0	1.914 234	34.128 766	0.008,280	35.199 966	0	2.220 169
Station 6	34.172 283	0.010,840	35.612 083	0	1.895 993	34.271 683	0.025,380	35.688 083	0	1.598 075	33.776 083	0.000,000	35.781 683	0	1.770 299
Station 7	34.378 501	-0.003 870	35.673 901	0	1.550 382	34.256 101	-0.004 150	35.360 701	0	1.836 228	34.097 501	-0.009 470	36.260 301	0	1.938 548

5) The initial arrival time could be selected according to the single or double oscillation phase with only the P-wave precise arrival time or only the S-wave peak arrival time, or a corresponding group of the precise P-wave arrival time and the peak arrival time of the S-wave could be selected at the same time.

Some of the other features are shown in Figure 10.

4 Engineering example validation

4.1 Engineering validation of the seismic phase identification

According to the monitoring results of the ground monitoring station of the Tashan mine, the microseismic signals generated from seven microseismic events with different periods and different seismic locations were classified, and the sources were named as "Source *I*" to "Source *O*", in which each event contained seven three-directional microseismic signals. Each event contained seven microseismic signals in the X-, Y-, and *Z*-axes, and each microseismic signal contained one microseismic response, and the signal form is shown in Figure 11.

4.1.1 Comparison of the effect of seismic phase recognition

The initial parameters used for the adaptive rotational categorization method in the following analysis were: sampling frequency, F_s =5000 Hz, sampling interval, C_{int} =10, grouping interval, F_{int} =10 s, and range expansion factor, Q = 2.

1) Analysis of identification results

Through daily monitoring of the microseismic events in the mine area, a total of 168 microseismic signals were collected from seven sources, seven geophones, and three sub-directions, which were expressed in the form of "source - sub-direction". For e.g. "*I-X*" indicates the microseismic signals from source *I* and the *X*-axis sub-direction of the geophone. The microseismic signal was monitored under source *I* (Liu et al., 2017). The results are shown in Figure 12, where each rectangle represents a segment of a microseismic signal, and the true value of microseismic response count of each segment was 1. If the result is 1, the recognition was classed under successful, and if not, the recognition was classed under failed. The absolute value of the difference between the number of phases and the true value of the microseismic response is called the recognition deviation.

From Figure 12A it can be seen that the number of recognition failures of the improved STA/LTA method is 9 times, the maximum magnitude of recognition bias is one time, and the distribution of recognition failure results is not regular. From Figure 12B it can be seen that the number of recognition failures of the adaptive rotational categorization

TABLE 4 Geophone coordinates and first arrival-time of the P-waves.

Detector serial number	Coordinate/m			P-wave initial arrival time/ms
	X	Y	Z	
Station 1	1987.23	22567.34	60.41	34.9
Station 2	2,291.32	22618.45	46.54	36.6
Station 3	1,689.46	22383.53	61.27	39.3
Station 4	2016.45	23034.54	63.83	41.1
Station 5	918.66	22763.34	44.34	42.3
Station 6	1940.56	22400.87	62.64	44.5
Station 7	1,587.54	22614.56	54.82	47.8

method is one time, and the maximum magnitude of recognition deviation is one time.

2) Calculation time analysis

As shown in Figure 13, the calculation time of the improved STA/LTA method and the adaptive rotational categorization method was higher than that of the adaptive rotational categorization method for the above 168 segments of microseismic signals with a mean value of 0.281 s and a wide range of variation of 0.303 s. The calculation time of the adaptive rotational categorization method is shorter than that of the improved STA/LTA method, with a mean value of 0.115 s and a small range of variation of 0.152 s. The calculation time of the adaptive rotational categorization method is shorter than that of the improved STA/LTA method. and the range of computation time variation is also smaller, with a polar difference of 0.152 s.

3) Comparison of the recognition effect of the two methods

By collating and analyzing the identification results with the computation time, the results are shown in Table 2.

As can be seen from Table 2, compared with the improved STA/LTA method, the recognition accuracy of the adaptive rotational categorization method is improved by 4.8%, the standard deviation of recognition deviation is 34.2% of the former, the mean value of computation time is 40.9% of the former, and the standard deviation of computation time is 55.9% of the former. This shows that the method has advantages over the improved STA/LTA method in terms of seismic phase recognition accuracy, stability, and computation speed and stability, and thus has advantages over the improved STA/LTA method.

4.2 Engineering validation of the TFA-DC method

To further verify the reliability of the TFA-DC method for microseismic signal arrival pickup, the microseismic signal data from the microseismic monitoring project at the Tashan Mine were selected for verification, as shown in Figure 14, and the pickup results are shown in Table 3.

According to Table 3, the following conclusions can be drawn:

1) The maximum time difference, the minimum time difference, the mean time difference and the standard deviation of the time difference at the peak of the S-wave to time are all 0 s.
2) The maximum time difference when the P-wave is accurate is 0.025380 s, the minimum time difference is 0 s, the average time difference is 0.007825 s, and the standard deviation of the time difference is 0.006180 s.
3) The maximum calculated run time is 2.220,169 s, the minimum calculated run time is 1.418,231 s, the average calculated run time is 1.853,774 s, and the standard deviation of the calculated run time is 0.220,383 s.
4) There is no pickup failure due to low signal-to-noise ratio in the above pickup results.

It can be seen that the TFA-DC method has certain advantages in terms of the types of the pickup waves, the average time difference, the standard deviation of time difference, the average computation time required for a single pickup, the standard deviation of time, and the success rate of pickup. This indicates that it is an effective method for picking up microseismic signals in time, and can thus meet the needs of engineering sites.

4.3 Engineering example validation of the variable-step accelerated search method

In order to further demonstrate the advantages of the variable-step acceleration search method for seismic source localization, the localization effects of the three algorithms, the simulated annealing algorithm, the genetic algorithm, and the variable-step acceleration search method, were compared using the P-wave initial arrival time and the spatial coordinates of the geophone from engineering field data under the simplified velocity model using the average wave velocity.

TABLE 5 The location results of the three algorithms.

Algorithm name	Ordinal number	Calculation result					
		Value of the objective function	Epicenter of earthquake X-axis coordinate/m	Y-axis of the source of the earthquake coordinate/m	Z-axis of the source of the earthquake coordinate/m	Average wave speed/(m-ms−1)	Computational runtime Time/s
simulated annealing algorithm	1	5.0535	4962.9986	22512.2460	33.1711	19.6681	0.3242
	2	5.0924	4984.5465	22503.3729	30.3694	19.4404	0.3240
	3	4.9254	4762.5225	22541.7894	17.3283	19.6651	0.6734
	4	4.9173	4429.1774	22536.9012	5.4555	19.6698	0.5431
	5	4.8792	4721.3913	22554.0068	64.2862	19.6877	0.5784
	6	4.9490	5806.3029	22551.1332	31.4845	19.6696	0.7054
	7	5.0316	4873.5630	22499.9251	33.4910	19.6696	0.3794
	8	4.8242	4612.7009	22571.8290	31.9297	19.6692	0.7131
	9	5.0530	4942.6721	22505.0755	21.8559	19.6627	0.3298
	10	4.7808	4755.8970	22608.0432	33.0843	19.6636	1.2724
genetic algorithm	1	3.0755	3190.5302	22715.0156	21.7622	19.5669	0.1839
	2	2.0944	2,828.6849	22663.0269	35.8069	11.4750	0.1831
	3	2.7797	2,659.0983	22661.0881	36.4068	12.3687	0.1807
	4	4.0425	1774.8754	22910.0040	16.9286	20.3000	0.1895
	5	4.0857	1704.4062	22908.3217	27.6348	19.4979	0.1801
	6	3.2071	2,600.7883	22702.3587	11.5437	19.5901	0.1843
	7	4.0667	1,197.1550	22777.5673	22.5223	19.5981	0.1946
	8	2.4051	2,978.3973	22665.7056	36.1533	11.2296	0.1827
	9	3.2700	3901.6363	22712.1750	36.5710	19.5314	0.1848
	10	2.5399	3152.5621	22675.4920	12.5687	11.5724	0.1844
Accelerated search method with variable step length	1	0.8149	2,731.3624	22651.4978	51.8261	6.5672	0.1211
	2	0.8149	2,731.3624	22651.4978	51.8261	6.5672	0.1291
	3	0.8149	2,731.3624	22651.4978	51.8261	6.5672	0.1276
	4	0.8149	2,731.3624	22651.4978	51.8261	6.5672	0.1289
	5	0.8149	2,731.3624	22651.4978	51.8261	6.5672	0.1265
	6	0.8149	2,731.3624	22651.4978	51.8261	6.5672	0.1432
	7	0.8149	2,731.3624	22651.4978	51.8261	6.5672	0.1450
	8	0.8149	2,731.3624	22651.4978	51.8261	6.5672	0.1204
	9	0.8149	2,731.3624	22651.4978	51.8261	6.5672	0.1369
	10	0.8149	2,731.3624	22651.4978	51.8261	6.5672	0.1266

4.3.1 Geophone coordinates and observation arrival times

The data obtained from blasting at the Tashan mine were used as an example to compare and analyze the positioning effects of the three algorithms. The first arrivals of the P-waves were picked up by the seven geophones after the blast, and the blast coordinates, i.e., the true values of the source, were determined at the site (2,732.7 m, 226,57.6 m, 56.3 m). The spatial coordinates of each geophone and the arrival times of the P-wave first arrivals picked up by them are shown in Table 4.

4.3.2 Analysis of the variable-step acceleration search method

To this end, the initial coordinates of the starting point were: X_0 = 1,000 m, one Y_0 = 20000 m, Z_0 = 30 m; the initial value of the

TABLE 6 Comparison of location effect of three algorithms.

Calculation result		Algorithm name		
		Simulated annealing algorithm	Genetic algorithm	Accelerated search method with variable step length
Value of the objective function	average value	4.9506	3.1567	0.8149
	(statistics) standard deviation	0.105 1	0.723 7	0
Positioning error/m	average value	2,156.2724	621.3889	7.6839
	(statistics) standard deviation	366.1830	524.5183	0
Calculation time/s	average value	0.584 3	0.184 8	0.130 5
	(statistics) standard deviation	0.2899	0.0043	0.0085

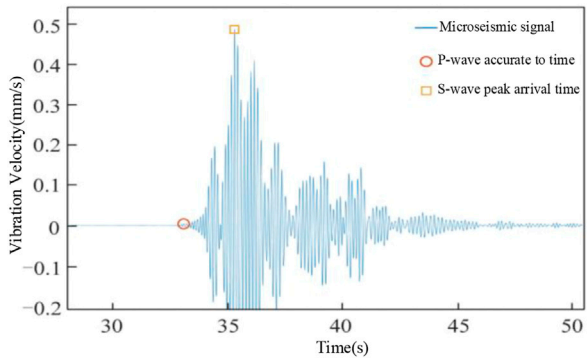

FIGURE 15
Schematic diagram of picking up mine seismic signal at arrival-time.

average wave velocity of the P-wave, $V_0 = 5$ m/ms: the upper limit of the model size, $X_u = 5000$ m: $Y_u = 30000$ m: $Z_u = 100$ m: the lower limit of the model size, $X_d = 0$ m, $Y_d = 0$ m, $Z_d = 0$ m; the upper limit of the velocity, $V_u = 20$ m/s: the lower limit of the velocity, $V_d = 0$ m/s: the search step for the lower limit, $J = 0.001$ m: and the initial value of search step, $r = 2000$ m. The results of the 10 calculations using the variable-step acceleration search method are shown in Table 5.

Data shown in Tables 5 and 6 imply that the mean and standard deviation of the objective function value, and the mean and standard deviation of the localization error of the variable step acceleration search method are smaller than the remaining two algorithms. This indicates that the accuracy and convergence stability of the results of this algorithm were better than the remaining two algorithms, and the mean value of the computation time was smaller than the remaining two algorithms.

TABLE 7 Arrival-time data of P-wave and S-wave of mine seismic signal.

Detector serial number	KZXH-1		KZXH-2		KZXH-3	
	P-wave arrival time/s	S Wave arrival time/s	P-wave arrival time/s	S Wave arrival time/s	P-wave arrival time/s	S Wave arrival time/s
Station 1	34.184	35.425	25.423	27.089	18.563	19.487
Station 2	34.394	35.912	25.404	26.776	18.364	19.861
Station 3	34.582	36.495	26.281	27.179	18.972	20.357
Station 4	34.237	36.013	26.411	27.508	18.662	20.222
Station 5	35.109	36.789	25.981	27.454	18.844	20.950
Station 6	34.072	35.512	25.015	26.909	18.864	19.064
Station 7	34.318	35.673	26.138	28.220	18.657	19.723

TABLE 8 Three-dimensional coordinates of the geophones at the

Detector Serial Number	Coordinate/m		
	X	Y	Z
Station 1	1987.23	22567.34	60.41
Station 2	2291.32	22618.45	46.54
Station 3	1689.46	22383.53	61.27
Station 4	2016.45	23034.54	63.83
Station 5	918.66	22763.34	44.34
Station 6	1940.56	22400.87	62.64
Station 7	1587.54	22614.56	54.82

Hence, the variable-step acceleration search method could find the optimal convergence point precisely and quickly with the specified P-wave arrival time, the target function model, and the coordinates of the geophones. and the results are guaranteed to be the same every time. The optimization algorithm had no substantial impact on the localization accuracy, which was mainly due to other factors such as P-wave arrival time, objective function model, geophone position coordinates, and wave speed model.

4.4 Engineering validation of the TD-DL methods

In order to further confirm the superiority and practicality of the TD-DL method in seismic-source inversion localization, the seismic signals from the microseismic monitoring project of the Tashan mine were selected for the on-time pickup and inversion localization calculation, and the results were compared with the localization calculation results of P-wave and S-wave single seismic phases. These signals were named as, "KZXH-1", "KZXH-2", and "KZXH-3". The time pickups of the above three groups of microseismic signals were performed using the TFA-DC method, and the time pickups obtained after the filtering process are shown in Figure 15, and the obtained P-wave precise time pickups and S-wave peak time pickups are shown in Table 7.

TABLE 9 Location results of each seismic phase in mine seismic signal.

Microseismic signal serial number	Positioning method	Seismic source inversion coordinates/m		True coordinates of earthquake source/m		Positioning error/m
		X	Y	X	Y	
KZXH-1	P-wave monooseismic phase	4517.149	20364.137	4543.334	20322.445	49.233
	S-wave monooseismic phase	4530.174	20364.112			43.696
	TD-DL methodology	4540.003	20 316.041			7.218
KZXH-2	P-wave monooseismic phase	4271.073	20488.176	4352.556	20443.235	93.054
	S-wave monooseismic phase	4351.157	20520.015			76.792
	TD-DL methodology	4345.139	20440.165			8.027
KZXH-3	P-wave monooseismic phase	4232.197	20590.101	4145.768	20578.202	87.226
	S-wave monooseismic phase	4170.037	20590.146			27.033
	TD-DL methodology	4144.161	20574.059			4.450

TABLE 10 Integrated software inversion of Tashan mine positioning data on April 10.

Number of seismic phase responses	Pickup on time (s)		Positioning coordinates (m)		
	P-wave	S-wave	X	Y	Z
1	26.9216	27.0223	2,546.2354	22713.2231	41.2253
2	32.5781	32.6974	2,784.5421	22756.2854	56.4235
3	37.2538	37.3569	2,897.6874	22743.5861	58.7456
4	44.3678	44.4567	2,987.2569	22684.5436	60.2468

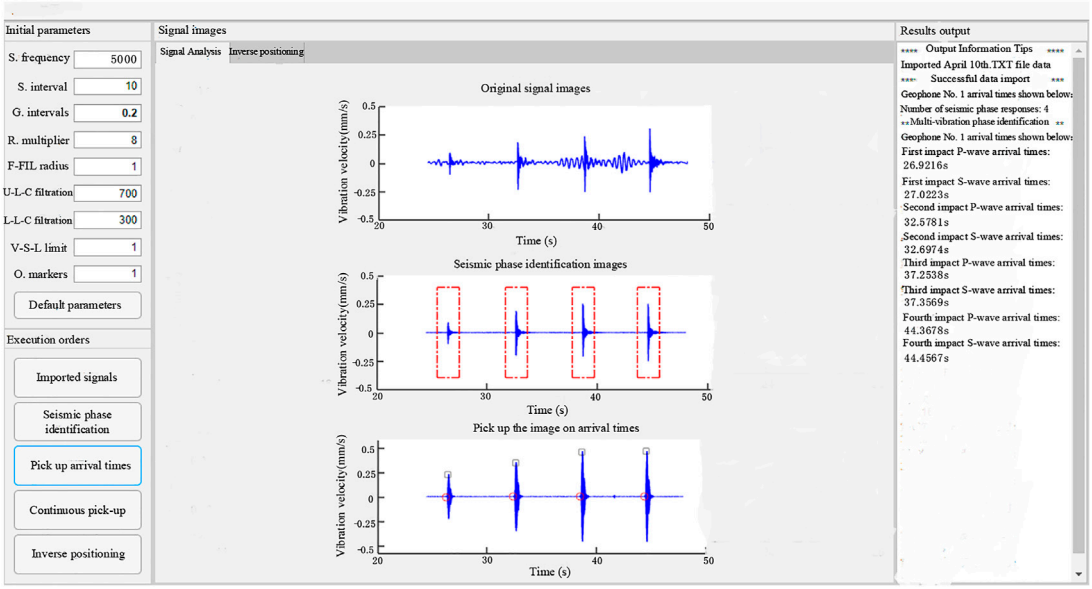

FIGURE 16
Software calculation of the April 10 microseismic arrival pickup event.

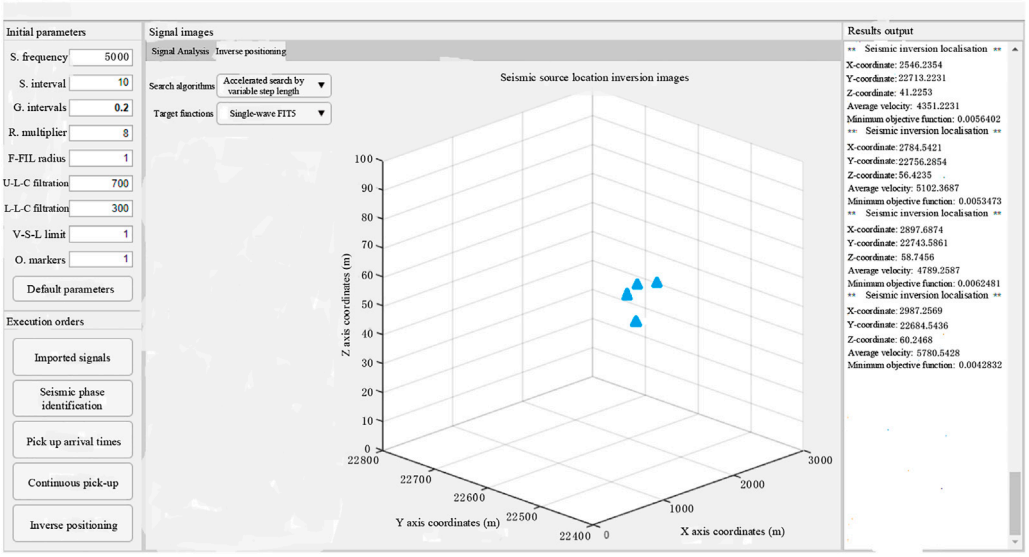

FIGURE 17
Software calculation of the microseismic localization results for the April 10 event.

4.4.1 Geophone arrangement

The geophones of the mine microseismic monitoring project were arranged at a depth of 2 m below the surface, and were only used for two-dimensional monitoring, i.e., monitoring the *X-axis* and *Y*-axis coordinates of the source location, so the coordinate variation range of the geophones are mainly distributed in the *X*-axis and *Y*-axis, and its coordinates are shown in Table 8.

4.4.2 Analysis of positioning results

In order to increase the constraint information at the arrival of the double-shock phase and improve the convergence and positioning accuracy of the localization algorithm, the *Z-axis* coordinates were imported at the same time in addition to the geophone *X-axis* and *Y-axis* coordinates for cooperative localization during the calculation., and only the *X*-axis and *Y*-axis coordinates are used for the localization results. Although the variation range of the *Z*-axis coordinates of the geophones was much smaller than that of the *X-axis* and *Y*-axis, the addition of the *Z-axis coordinates* increased the convergence error tolerance and reduced the converged objective function value. This indicated that the addition of the *Z-axis* coordinates improved the positioning accuracy. After importing the geophone coordinates and arrival data, the inverse localization calculations were performed using the variable-step accelerated search method, and the results were compared with the true coordinates of each source and the localization errors are shown in Table 9, where the true coordinates of the source were obtained from the reported seismic location of the mine.

From Table 9, it can be seen that under the source KZXH-1, the TD-DL method localization error is 14.7% and 16.5% of the P-wave and the S-wave single seismic phases, respectively; under the source KZXH-2, the TD-DL method localization error is 8.6% and 10.5% of the P-wave and the S-wave single seismic phases, respectively; under the source KZXH-3, the TD-DL method localization error is 5.1% and 16.5% of the P-wave and the S-wave single seismic phases, respectively.

4.5 Engineering applications of integration software

In January 2019, the high-frequency microseismic wireless ground monitoring system of Tashan coal mine was officially put into operation, and the monitoring was carried out during the operation of Tashan coal mine 8204–2 working face, which is an isolated island working face with the risk of power disaster. In April, the working face was advanced 120 m, and a total of 41 microseismic events were monitored, with a total release energy of 24,300 J, including 15 events below 102 J, 15 events between 102 J and 103 J, 12 events between 103 J and 104 J, and no events larger than 104 J. At this stage, the working face was widened, the advance speed was reduced, and the number of microseismic events and the energy of microseismic events were low.

The microseismic signal microseismic arrival time pickup and its localization were performed using the integrated software for microseismic events received at station one from 12:00 to 14:00 on April 10. From the integrated software, the microseismic arrival time and source location of the microseismic events in the mine was easily obtained. It was easy to operate and did not require complicated calculations. The process merely imported the measured microseismic waveform data by clicking on the arrival time pickup from the software, and the source inversion positioning to get the desired results. The obtained positioning data are shown in Table 10, and the positioning effect is shown in Figures 16, 17.

5 Conclusion

Combining simulated algorithms, geophone coordinates, initial arrival times, and microseismic signals obtained from actual projects. The main conclusions that can be drawn are as follows:

1) Analysis of microseismic signals based on monitoring of isolated working face at Tashan mine, the recognition accuracy of the adaptive rotation categorization method improved by 4.8%, the standard deviation of recognition deviation was 34.2% of the former, and the mean and standard deviation of calculation time were 40.9% and 55.9% of the former, respectively.
2) The TFA-DC method compares with the improved STA/LTA method, the average time difference and the standard deviation of the former P-wave were 6.18‰ and 3.98‰ of the latter, the average computation time and standard deviation required for a single pickup of the former were 43.99% and 10.54% of the latter, and the former arrival time pickup failure ratio was 0, while for the latter was 15.63%.
3) Under the simulated cases, when simulated annealing algorithm and the genetic algorithm were compared, the standard deviation of the objective function value, the standard deviation of the localization error, and the standard deviation of the wave velocity error of the variable-step acceleration search method were all 0; the average value of the localization error of this algorithm was 0.7% and 1.9% of the remaining two.
4) The TD-DL method offset the positioning errors obtained from the P-wave and S-wave single-phase calculations to a certain extent, thus improving the inversion positioning accuracy of the source; the average value of the positioning errors of the TD-DL method under the engineering data was 9.5% and 14.5% of the P-wave and S-wave single-phase positioning, respectively.
5) The software was integrated with “visual”, “interactive” and “one-click” features for microseismic data processing, and the analysis of the April data from the Tashan mine enables faster and more direct access to the location of the source of microseismic events.

Data availability statement

The original contributions presented in the study are included in the article/supplementary material, further inquiries can be directed to the corresponding author.

Author contributions

The author confirms being the sole contributor of this work and has approved it for publication.

Funding

2020 Liaoning Provincial Education Department Scientific Research Funding Project (LJ2020JCL022).

Conflict of interest

The author declares that the research was conducted in the absence of any commercial or financial relationships that could be construed as a potential conflict of interest.

Publisher's note

All claims expressed in this article are solely those of the authors and do not necessarily represent those of their affiliated organizations, or those of the publisher, the editors and the reviewers. Any product that may be evaluated in this article, or claim that may be made by its manufacturer, is not guaranteed or endorsed by the publisher.

References

Cui, F., Yang, Y. B., Lai, X. P., and Cao, J. T. (2019). Experimental study of physical similar materials based on microseismic monitoring key strata fracture induced rock burst. *Chin. J. Rock Mech. Eng.* 38 (4), 803–814. doi:10.13722/j.cnki.jrme.2018.1423

Diehl, T., Deichmann, N., Kissling, E., and Husen, S. (2009). Automatic S-wave picker for local earthquake tomography. *Bull. Seismol. Soc. Am.* 99 (3), 1906–1920. doi:10.1785/0120080019

Dong, L. J., Wesseloo, J., Potvin, Y., and Li, X. B. (2016). Discrimination of mine seismic events and blasts using the Fisher Classifier, Naive Bayesian Classifier and logistic regression. *Rock Mech. Rock Eng.* 49 (1), 183–211. doi:10.1007/s00603-015-0733-y

Gong, S., Dou, L., Ma, X., Mu, Z. L., and Lu, C. P. (2012). Optimization of network layout algorithm for improving microseismic positioning accuracy in coal mine. *Chin. J. Rock Mech. Eng.* 31 (1), 8–17. https://kns.cnki.net/kcms/detail/detail.aspx?FileName=YSLX201201004andDbName=CJFQ2012

Gong, S., Dou, L., Ma, X., and Liu, J. (2010). Selection of optimal number of channels to improve microseismic positioning accuracy in coal mine. *J. China Coal Soc.* 35 (12), 2017–2021. doi:10.13225/j.cnki.jccs.2010.12.014

Jia, B., Jia, Z., Zhao, P., and Chen, Y. (2017). Microseismic localization in small scale region based on high-density array. *Chin. J. Geotechnical Eng.* 39 (4), 705–712. https://kns.cnki.net/kcms/detail/32.1124.tu.20160918.1242.004.html

Jia, B., Li, F., Pan, Y., and Zhou, L. L. (2022). Microseismic source location method based on variable stepsize accelerated search. *Rock Soil Mech.* 43 (3), 843–856. doi:10.16285/j.rsm.2021.0872

Jiang, R. C., Dai, F., Liu, Y., and Li, A. (2021). A novel method for automatic identification of rock fracture signals in microseismic monitoring. *Measurement* 175, 109129. doi:10.1016/j.measurement.2021.109129

Lee, M., Byun, J., Kim, D., Choi, J., and Kim, M. (2017). Improved modified energy ratio method using a multi-window approach for accurate arrival picking. *J. Appl. Geophys.* 139 (1), 117–130. doi:10.1016/j.jappgeo.2017.02.019

Li, J., Lei, W., Zhao, H., Wang, T., Liu, Y. H., and Zhang, H. (2019). Microseismic response characteristics of coal and rock impact failure under repeated blasting. *J. China Univ. Min. Technol.* 48 (5), 966–974. doi:10.13247/j.cnki.jcumt.001053

Li, J., Zhang, H., Rodi, W. L., and Toksoz, M. N. (2013). Joint microseismic location and anisotropic tomography using differential arrival times and differential backazimuths. *Geophys. J. Int.* 195 (3), 1917–1931. doi:10.1093/gji/ggt358

Li, L., He, C., and Tan, Y. (2017). Research on microseismic observation system and source location objective function. *Acta Sci. Nat. Univ. Peking.* 53 (2), 329–343. doi:10.13209/j.0479-8023.2016.091

Li, N., Wang, E., Sun, Z., and Li, B. L. (2014). Source location method of simplex microseismic based on L1 norm statistics. *J. China Coal Soc.* 39 (12), 2431–2438. doi:10.13225/j.cnki.jccs.2013.1855

Li, X., and Xu, N. (2020). Research status and prospect of microseismic source location. *Prog. Geophys.* 35 (2), 598–607. https://kns.cnki.net/kcms/detail/11.2982.P.20190624.1628.197.html

Liu, X., Zhao, J., Wang, Y., and Peng, P. A. (2017). Microseismic P-wave automatic picking technology based on improved STA/LTA method. *J. Northeast. Univ. Nat. Sci. Ed.* 38 (5), 740–745. https://kns.cnki.net/kcms/detail/detail.aspx?FileName=DBDX201705028andDbName=CJFQ2017

Pan, Y., Zhao, Y., Guan, F., Li, G. Z., and Ma, Z. S. (2007). Research and application of seismic monitoring and positioning system. *Chin. J. Rock Mech. Eng.* 26 (5), 1002–1011. https://kns.cnki.net/kcms/detail/detail.aspx?FileName=YSLX200705020andDbName=CJFQ2007

Perol, T., Gharbi, M., and Denolle, M. (2018). Convolutional neural network for earthquake detection and location. *Sci. Adv.* 4 (2), e1700578. doi:10.1126/sciadv.1700578

Ross, Z. E., Meier, M. A., and Hauksson, E. (2018). P-wave arrival picking and first-motion polarity determination with deep learning. *J. Geophys. Res. Solid Earth* 123 (6), 5120–5129. doi:10.1029/2017jb015251

Tian, Y., and Chen, X. (2002). Review on seismic location. *Prog. Geophys.* 17 (1), 147–155. https://kns.cnki.net/kcms/detail/detail.aspx?FileName=DQWJ200201023andDbName=CJFQ2002

Wang, H., Liang, M., and Zhu, M. (2020). Hybrid localization algorithm of microseismic source based on simplex and shortest path ray tracing. *China Min. Ind.* 29 (10), 110121–111115. https://kns.cnki.net/kcms/detail/detail.aspx?FileName=ZGKA202010019andDbName=CJFQ2020

Wang, Y-H., Wang, B-l., and Duan, J-H. (2019). Microseismic location based on differential evolution algorithm. *Coal Geol. Explor.* 47 (1), 168–173. https://kns.cnki.net/kcms/detail/detail.aspx?FileName=MDKT201901026andDbName=CJFQ2019

Wu, S. J., Wang, Y. B., Zhan, Y., and Chang, X. (2016). Automatic microseismic event detection by band-limited phase-only correlation. *Phys. Earth Planet. Interiors* 261, 3–16. doi:10.1016/j.pepi.2016.09.005

Xue, Q., Wang, Y., and Chang, X. (2018). Joint inversion of location, excitation time and amplitude of microseismic sources. *Bull. Seismol. Soc. Am.* 108 (3A), 1071–1079. doi:10.1785/0120170240

Zhao, C., Tang, S., Qin, M., Guo, X. Q., Jiao, W. Y., and Liu, C. (2019). Experimental study on positioning accuracy of microseismic monitoring system. *Min. Technol.* 19 (2), 46–49. doi:10.13828/j.cnki.ckjs.2019.02.015

Zhao, G. Y., Ju, M. A., Dong, L. J., Li, X. b., Chen, G. h., and Zhang, C. x. (2015). Classification of mine blasts and microseismic events using starting-up features in seismograms. *Trans. Nonferrous Metals Soc. China* 25 (10), 3410–3420. doi:10.1016/s1003-6326(15)63976-0

Zheng, Y., Wang, Y., and Chang, X. (2016). Wave equation based microseismic source location and velocity inversion. *Phys. Earth Planet. Interiors* 261, 46–53. doi:10.1016/j.pepi.2016.07.003

frontiers | Frontiers in Earth Science

TYPE Methods
PUBLISHED 02 March 2023
DOI 10.3389/feart.2023.1128217

OPEN ACCESS

EDITED BY
Qizhen Du,
China University of Petroleum, China

REVIEWED BY
Weijia Sun,
Institute of Geology and Geophysics (CAS), China
Yike Liu,
Institute of Geology and Geophysics (CAS), China
Jianping Huang,
China University of Petroleum, China

*CORRESPONDENCE
Shaoping Lu,
lushaoping@mail.sysu.edu.cn

†These authors contributed equally to this work and share first authorship

SPECIALTY SECTION
This article was submitted to Solid Earth Geophysics, a section of the journal Frontiers in Earth Science

RECEIVED 20 December 2022
ACCEPTED 13 February 2023
PUBLISHED 02 March 2023

CITATION
Gao Z, Zhang S, Wu H, Ren K and Lu S (2023), Crosstalk attenuation for imaging of multiples based on angle gather residual moveout analysis. *Front. Earth Sci.* 11:1128217. doi: 10.3389/feart.2023.1128217

Crosstalk attenuation for imaging of multiples based on angle gather residual moveout analysis

Zihao Gao[1,2†], Shukui Zhang[1,2†], Han Wu[1,2], Kai Ren[1,2] and Shaoping Lu[1,2*]

[1]School of Earth Sciences and Engineering, Sun Yat-Sen University, Guangzhou, Guangdong, China, [2]Southern Marine Science and Engineering Guangdong Laboratory (Zhuhai), Zhuhai, Guangdong, China

Imaging of multiples, as a supplement to imaging of primaries, can provide a wider range of subsurface illumination. Therefore, it can provide more detailed information on subsurface structures. However, imaging of multiples suffers from crosstalk issues generated by unrelated events. Many strategies have been proposed to attenuate crosstalk, among which the angle domain Radon crosstalk attenuation algorithm achieves good application effect. In the angle domain, the true imaging is flat, while the crosstalk events have moveouts. Therefore, it is convenient to identify the crosstalk in angle gathers using the Radon transform. However, the conventional Radon transform lacks a quantitative description for crosstalk in angle gathers, which would affect the accuracy of crosstalk attenuation. In this paper, residual moveout kernels are derived with a Radon transform to attenuate crosstalk in angle gathers for imaging of multiples. First, two types of residual moveout (RMO) equations are derived based on the causality of crosstalk. A three-layer model is used to verify the correctness of the analytical solutions. Then, based on the derived equations, the two types of crosstalk can be attenuated respectively in the Radon domain. Synthetic experiments demonstrate that the derived RMO equations can effectively attenuate the crosstalk events in imaging of multiples.

KEYWORDS

imaging of multiples, radon transform, residual moveout, crosstalk attenuation, angle-domain common-image gather

1 Introduction

Unlike the conventional approach treats surface-related multiples as noises, imaging of multiples uses them as effective signals to image subsurface structures. Since the multiples have more propagation paths, imaging of multiples can provide more detailed information on subsurface structures (Berkhout and Verschuur, 2003). There are three main approaches for implementing imaging of multiples (Lu et al., 2021). The up-down wavefield imaging method (Berkhout and Verschuur, 1994; Liu et al., 2011) replaced the source wavelet with primary and multiples and used multiples as receivers for migration. The seismic interferometry proposed by Schuster and Rickett (2000) transformed multiples into primary and imaged them. In addition, the Marchenko imaging proposed by Wapenaar et al. (2014) used surface-related multiples and internal multiples for migration (Singh et al., 2017; Gu and Wu, 2022).

Although imaging of multiples has been implemented through different approaches, there still remains many undesired crosstalk issues in imaging result. Crosstalk is generated

due to the correlation of unrelated events (Liu et al., 2016; Lu et al., 2016; Lu et al., 2021). These crosstalk issues introduce difficulties in the interpretation of the imaging results. Therefore, it is crucial to attenuate them. Many methods have been proposed to attenuate crosstalk for imaging of multiples. One category is to remove crosstalk during the migration, such as the least-squares migration (LSM) (Berkhout, 2014; Ordoñez et al., 2014; Zhang and Schuster, 2014; Tu and Herrmann, 2015; Wong et al., 2015; Lu et al., 2018; Lu et al., 2021) and imaging using controlled-order multiples (Liu et al., 2016). However, such methods usually require a huge amount of computation or complete separation of different orders multiples. The other category is to deal with the crosstalk after migration, such as the angle domain Radon crosstalk suppression (Wang et al., 2014; Wong et al., 2015). In the angle domain, the moveouts of imaging are flat when imaging of multiples using the correct velocity, whereas the moveouts of crosstalk are curved. The Radon transform can attenuate curved events in angle gathers, and then the crosstalk issues can be addressed without increasing the calculation cost and separation of different orders multiples. However, this strategy using the tangent-squared approximation as the kernel function of the Radon transform lacks a quantitative explanation of the theoretical mechanism of crosstalk and therefore affects the accuracy of crosstalk attenuation.

To enhance the effectiveness of the Radon transform to attenuate the crosstalk in angle gathers, a better understanding of the crosstalk generation mechanism is needed. Mathematically, the crosstalk in angle gathers can be calculated and attenuated based on the causality (Lu et al., 2016; Lu et al., 2021). Here, we propose a method to attenuate crosstalk by applying the residual moveouts of crosstalk as kernel functions in the Radon transform. Imaging results with an improved signal-to-noise ratio can then be produced.

In this paper, for the purpose of convenience in analyzing the residual moveouts for crosstalk, we first review the principle of classifying crosstalk according to the causality. Next, we derive the RMO equations for two types of crosstalk in angle gathers based on the classification principle and verify the correctness of the equations in angle gathers using a three-layer model. Then, we compare the derived RMO equations with the tangent square approximation equation as kernel functions for the Radon transform and demonstrate the effectiveness of our method. Finally, we perform a numerical experiment with a subset of the Sigsbee2b model, which proves that our proposed method can attenuate most of the crosstalk and improve the signal-to-noise ratio of the imaging results.

2 Methodology

2.1 The classification of crosstalk

In this section, we explain the generation and classification of crosstalk in the imaging of multiples. We assume that the sea surface is a fully reflective interface. Therefore, in the imaging of multiples, the free-surface seismic data are multiplied by −1, loaded at the sea surface, and propagated forward as virtual sources to composite the subsurface source wavefields. Then, the images using cross-correlation imaging conditions in the frequency domain can be computed as:

$$I_m(\mathbf{x}) = \sum_{\omega}\left[\sum_{j} S_j(\mathbf{x};\omega)\sum_{l} R_l(\mathbf{x};\omega)\right] \tag{1}$$

where I_m represents the imaging results of multiples; $\mathbf{x}$ represents the vector coordinates of the imaging point; ω is the frequency; S_j and R_l respectively represent the forward-propagated source wavefields and the backward-propagated receiver wavefields; j and l respectively represent primary and the order of multiples for the source wavefields and receiver wavefields. When j equals 1, S_j represents the forward-propagated source wavefield of the primaries, and when j equals n (n≠1), S_j represents the forward-propagated source wavefield of the (n-1) thorder multiples. Similarly, when l equals 1, R_l represents the backward-propagated source wavefield of the primaries, and when l equals n, R_l represent the backward-propagated source wavefield of the (n-1) th-order multiples.

Eq 1 donates not only the correct imaging results of multiples, but also the crosstalk. To have a more intuitive understanding of the formation for crosstalk, we rewrite Eq 1 as:

$$\begin{aligned} I_m(\mathrm{x}) = &\sum_{\omega}[S_1(\mathrm{x};\omega)R_2(\mathrm{x};\omega) + S_2(\mathrm{x};\omega)R_3(\mathrm{x};\omega) + S_3(\mathrm{x};\omega)R_4(\mathrm{x};\omega) + \cdots] \\ &+ \sum_{\omega}[S_1(\mathrm{x};\omega)R_3(\mathrm{x};\omega) + S_2(\mathrm{x};\omega)R_4(\mathrm{x};\omega) + S_3(\mathrm{x};\omega)R_5(\mathrm{x};\omega) + \cdots], \\ &+ \sum_{\omega}[S_1(\mathrm{x};\omega)R_1(\mathrm{x};\omega) + S_2(\mathrm{x};\omega)R_1(\mathrm{x};\omega) + S_2(\mathrm{x};\omega)R_2(\mathrm{x};\omega) + \ldots] \end{aligned} \tag{2}$$

In Eq 2, the images can be divided into three parts. The first part corresponds to the correct imaging results of multiples, for example,

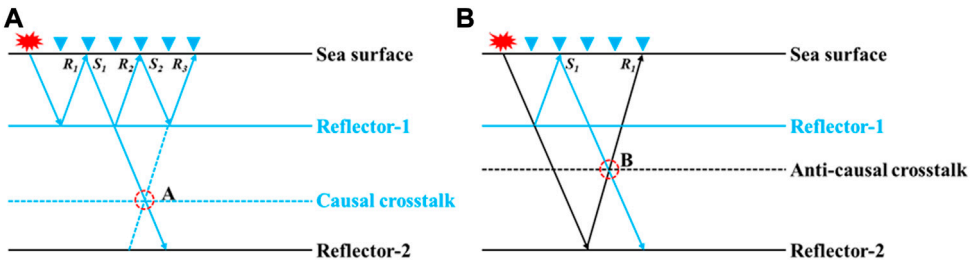

FIGURE 1
The ray paths diagrams for the two types of crosstalk. **(A)** The diagram of trajectories for causal crosstalk, **(B)** the diagram of trajectories for anti-causal crosstalk. In **(A)**, The virtual source S_1 (recorded primary reflections carried with information of reflector-1 as the source wavefield) and receiver wavefield R_3 (second order multiple) can generate causal crosstalk at position **(A)**. In **(B)**, the virtual source S_1 and receiver wavefield R_3 (recorded primary reflections carried with information of reflector-2 as the receiver wavefield) can generate anti-causal crosstalk at position **(B)**.

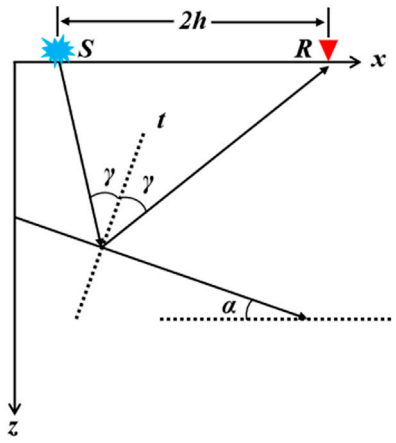

FIGURE 2
Reflection ray paths in a normal velocity medium. *a* is the inclination of the reflector and γ is the angle of the ray normal to the reflector. *S* and *R* are the position of the wavefield continued to the local source and receiver points in the subsurface respectively. *h* is the local subsurface half offset after the downward continuation. *z* and *x* are the depth and vertical position of the reflection point, respectively.

S_1 and R_2 constitute effective imaging according to the ray travel time and the cross-correlation imaging conditions (Clarebout, 1978). The second part and the third part are corresponding to the crosstalk generated by uncorrelated events. (Lu et al., 2021). classify the above crosstalk into two types based on causality, which are causal crosstalk and anti-causal crosstalk. To better understand the generation formation of crosstalk, we display the ray path diagrams for the two types of crosstalk (Figure 1).

We illustrate the diagram of trajectories for two types of crosstalk based on the cross-correlation imaging conditions from the second part and the third part in Eq 2 (Figure 1). In Figure 1A, the recorded primary reflection carried with information of reflector-1 at the sea surface forward propagated as the source wavefield S_1 (dashed blue arrow), and it cross-correlates with the receiver wavefield R_3 backward propagated (dashed blue arrow), which generates the crosstalk at position A. These crosstalk events are related to the wavefields after reflection with the reflector-1 and are deeper than the actual depth of reflector-1. Therefore, these events are called "causal crosstalk". Similarly, in Figure 1B, the recorded primary reflection carried with information of reflector-2 backward propagated as the source wavefield R_1 (black arrow), and it interacts with the virtual source S_1 (dashed blue arrow), which generates the crosstalk at location B. These events carried the information of reflector-2 are shallower than the real location, and actually contrary to the actual causality. Therefore, they are called "anti-causal crosstalk" (Lu et al., 2021).

The two types of crosstalk events are easily identified in simple models by their causality. However, the propagation paths of the wavefields are hard to judge and identify when there are many subsurface reflectors and complex structures. With the understanding of the classification mechanism of crosstalk, we can calculate the residual moveouts of the two types of crosstalk independently in angle gathers. And then, based on the derived equations, we can address the crosstalk issues under complex scenarios.

2.2 The calculation for the residual moveouts of crosstalk in the angle domain

Due to the arrival-time differences, the imaging events and crosstalk components have different moveouts in the angle

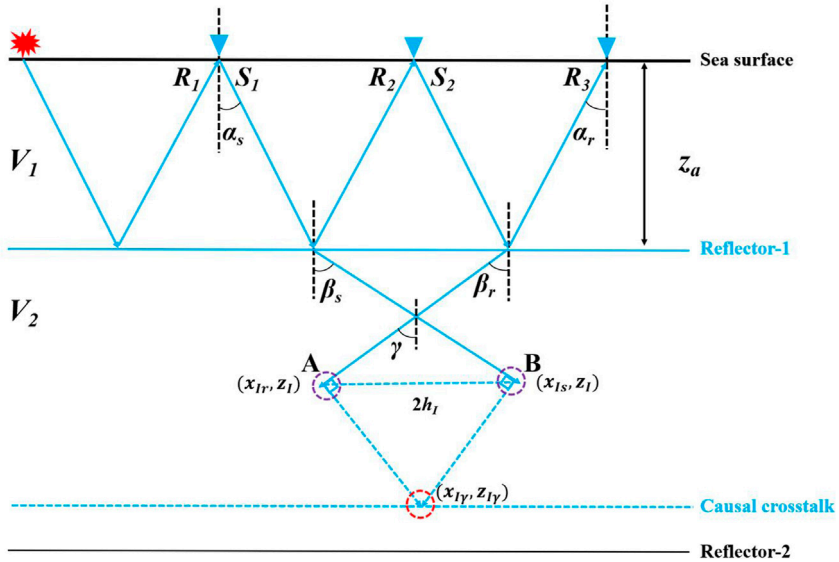

FIGURE 3
Ray paths for generating causal crosstalk. V_1 and V_2 are the velocity of the first and second layers, respectively. z_a is the depth of the reflector-1. α_s and α_r are the incident and emergent angles of the source and receiver rays with respect to the vertical direction. β_s and β_r are the angles of the source and the receiver rays with respect to the vertical direction after refraction by the reflector-1. γ is the half-aperture angle, which is equal to $(\beta_s+\beta_r)/2$.

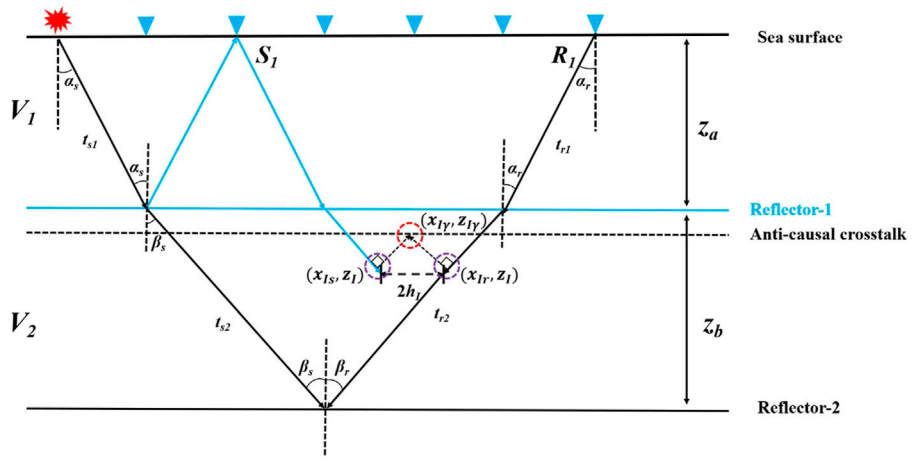

FIGURE 4
Ray paths for generating anti-causal crosstalk. V_1 and V_2 are the velocity of the first and second layers, respectively. z_a and z_b are the depth of the reflector-1 and reflector-2. α_s and α_r are the incident and emergent angles of the source and receiver rays with respect to the vertical direction. β_s and β_r are the angles of the source and the receiver rays with respect to the vertical direction after refraction by the reflector-1. γ is the half-aperture angle, which is equal to $(\beta_s+\beta_r)/2$. h_I is the subsurface half-offset, which is equal to $(x_{Ir}-x_{Is})/2$.

domain. Based on the differences in moveouts, we can attenuate crosstalk in angle gathers using the Radon transform. To quantitatively characterize the moveouts in the angle domain for crosstalk and attenuate them, in this section, we first derive the residual moveout equations for two types of crosstalk.

There are many methods for generating angle gathers, such as subsurface offset-to-angle conversion (Sava and Fomel, 2003; Biondi and Symes, 2004) and directional vector (Yoon and Marfurt, 2006; Xu et al., 2011). In this paper, we use the subsurface offset-to-angle algorithm to calculate the imaging angles. Based on the slant stack principle proposed by Sava and Fomel (2003), the subsurface offset gathers generated after the migration can be converted into angle gathers. The subsurface offset-angle conversion can be expressed as:

$$\tan\gamma = -\frac{\partial z}{\partial h}\Big|_{t,x}. \tag{3}$$

In Eq 3, t is the travel time, z and x are the depth and vertical position of the reflection point, respectively, and h is the local subsurface half-offset after downward continuation (Figure 2). The crosstalk events can be converted from the subsurface offset domain to the angle domain based on Eq 3. Meanwhile, using this conversion approach, we can derive the RMO equations for two types of crosstalk in angle gathers.

2.2.1 Calculation of the residual moveout for causal crosstalk

There are two types of crosstalk, which are causal crosstalk and anti-causal crosstalk. In this section, we derive the RMO equation for causal crosstalk. First, we can obtain the relationship between depth and subsurface offset based on the results after migration and then use the subsurface offset-to-angle conversion relationship to calculate the RMO equation for causal crosstalk.

Alvarez et al. (2007) gives the RMO equation for multiples in angle gathers for imaging of primaries. The causal crosstalk events in

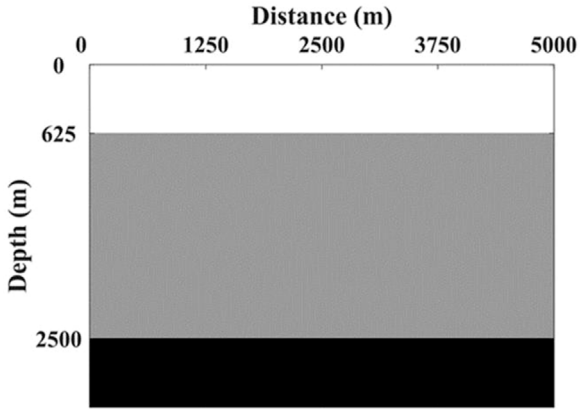

FIGURE 5
A three-layer velocity model with two flat reflectors.

imaging of multiples have similar kinematic characteristics as the previous ones in angle gathers. Thus, we use the approach of Alvarez et al. (2007) to obtain the RMO equation for causal crosstalk.

In Figure 3, based on the travel time and the trigonometric relationship, the forward-propagated virtual source wavefield S_1 ends up at a specific location (x_{Is}, z_I) in the subsurface (as purple dashed circles indicate) after migration. Similarly, the backward-propagated receiver wavefield R_3 ends up at (x_{Ir}, z_I). The causal crosstalk can be generated by cross-correlating the source and receiver wavefield propagated into the subsurface. Combining the above principles and the derivation of Alvarez et al. (2007), the depth z_I of the imaged causal crosstalk and the subsurface half-offset h_I can be displayed as:

$$z_I = z_a + \rho\sqrt{z_a^2 + \frac{h_I^2}{1-\rho^2}} \quad (\rho \neq 1), \tag{4}$$

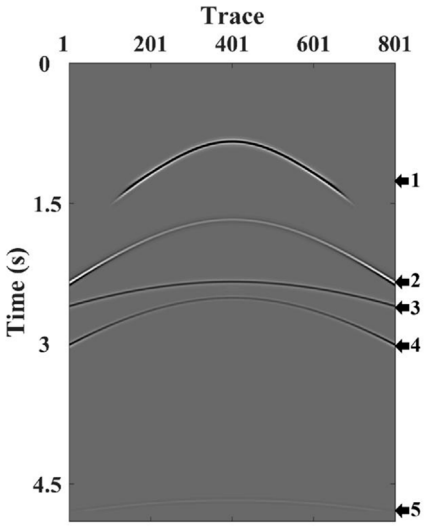

FIGURE 6
The simulated common shot gather. Arrows 1,2,4 represent the primary, first-order multiple and second-order multiple associated with the first layer. Arrows 3,5 represent the primary and first-order multiple waves associated with the second layer.

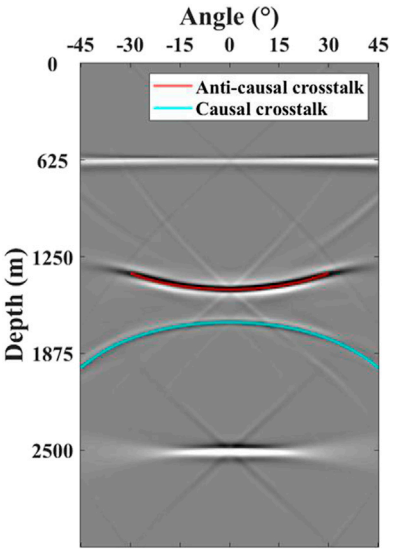

FIGURE 8
Two types of crosstalk in angle gathers. The red solid and the light blue line represent the calculated anti-causal crosstalk and causal crosstalk, respectively.

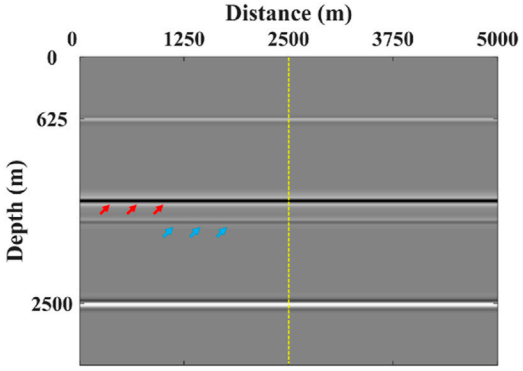

FIGURE 7
The migration result using primaries and multiples. The light blue arrows and the red arrows indicate causal crosstalk and anti-causal crosstalk, respectively.

where ρ is equal to V_2/V_1; V_1 and V_2 are the velocity of the first and second layers, respectively; z_a is the depth of the reflector-1.

Based on Eqs 3, 4, we can obtain the relationship between the depth $z_{I\gamma}$ and the half-aperture angle γ in the angle domain as:

$$z_{I\gamma} = z_a\left\{1 + \frac{\cos\gamma[\rho^2 - \tan^2\gamma(1-\rho^2)]}{\sqrt{\rho^2 - \sin^2\gamma}}\right\}. \quad (5)$$

Eq. 5 is the moveout equation for causal crosstalk in angle gathers. In Eq. 5, when reflector-2 has the same velocity as reflector-1 (ρ=1), the imaging depth for causal crosstalk in angle gathers is $z_{I\gamma}(0)=2z_a$. This indicates that when multiples are used for migration at a constant velocity, the causal crosstalk is a flat moveout in angle gathers. That is, the imaging depth does not vary with the change of angle. By subtracting the flat moveout from Eq. 4, the RMO for causal crosstalk in angle gathers can be followed as:

$$\Delta n_{RMO} = z_{I\gamma}(0) - z_{I\gamma} = z_a\left\{\rho - \frac{\cos\gamma[\rho^2 - \tan^2\gamma(1-\rho^2)]}{\sqrt{\rho^2 - \sin^2\gamma}}\right\}, \quad (6)$$

where $z_{I\gamma}(0)$ denotes the depth of causal crosstalk when the velocity of reflector-1 (ρ=1) is used for the migration. Eq. 6 shows the relationship between the RMO of the causal crosstalk in angle gathers and the half-aperture angle γ and it qualitatively characterizes the kinematics mechanisms of the causal crosstalk when the multiples are migrated with the correct velocity.

2.2.2 Calculation of the residual moveout for anti-causal crosstalk

Similar to the calculation of the RMO equation for causal crosstalk, we first obtain the relationship between imaging depth and subsurface offset for anti-causal crosstalk based on travel time and Snell's law. Then, we calculate the RMO equation for anti-causal crosstalk in terms of the subsurface offset-to-angle conversion relationship proposed by Sava and Fomel (2003). However, when anti-causal crosstalk events are imaged, they involve information from two different reflectors and therefore have different kinematic mechanisms compared to causal crosstalk events. In the following, we give a detailed derivation of the RMO equation for anti-causal crosstalk in angle gathers.

The RMO equation for anti-causal crosstalk can actually be calculated based on the travel time of the CMP gathers and Snell's law. In Figure 4, the forward-propagated virtual source wavefield S_1 with information of reflector-1, and the backward-propagated receiver wavefield R_3 with information of reflector-2, end up at a

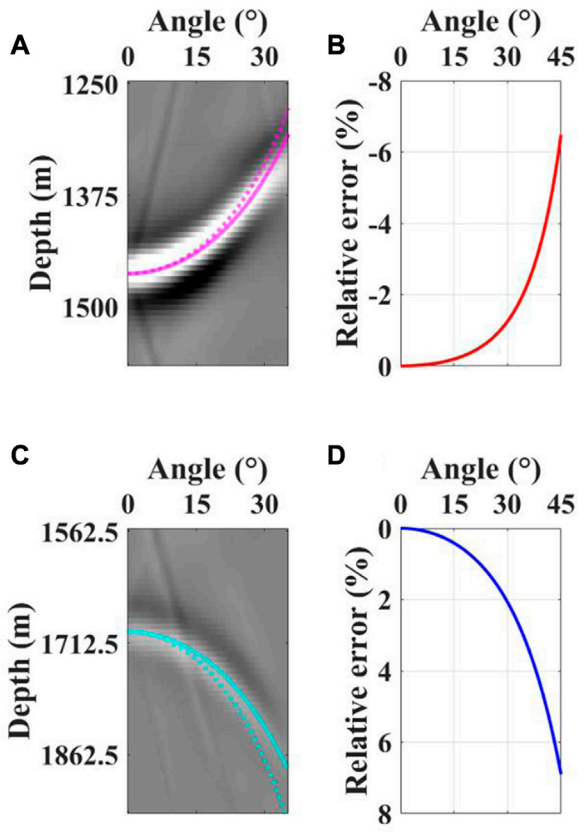

FIGURE 9
Comparison of the tangent-squared approximation equation and two RMO equations in the angle domain. **(A)** and **(C)** are the curves corresponding to the tangent-squared approximation equation and RMO equation for anti-causal and causal crosstalk in angle gathers, respectively. **(B,D)** are the relative error of the tangent-squared approximation to the more accurate RMO equation for anti-causal and causal crosstalk, respectively. The solid pink line and the pink dashed line represent the results of the derived RMO equation for anti-causal crosstalk and the tangent-squared approximation equation in angle gathers. The light blue solid line and the light blue dashed line represent the results of the derived RMO equation for causal crosstalk and the tangent-squared approximation equation in angle gathers.

particular location (x_{Is}, z_I) and (x_{Ir}, z_I) in the subsurface (as purple dashed circles indicate) after migration, respectively. By correlating the two wavefields, the anti-causal crosstalk will be generated.

Based on the cross-correlation imaging conditions, the anti-causal crosstalk follows the same travel time in imaging as the primary from the second layer. As shown in Figure 4, the total travel time in the second layer contains four main components, which can be described as:

$$T = t_{s1} + t_{s2} + t_{r2} + t_{r1}, \tag{7}$$

where the subscript s refers to the source-side rays and the subscript r refers to the receiver-side rays; t_{s1} and t_{s2} represent the time of forward-propagating rays from virtual source to reflector-1, from reflector-1 to reflector-2; t_{r1} and t_{r2} represent the time of backward-propagating rays from receiver side to reflector-1, from reflector-1 to reflector-2.

Based on Equation 7 and the geometry relationship shown in Figure 4, we can calculate the depth z_I of the crosstalk event and the half-offset h_I as:

$$\begin{cases} z_I = z_a + z_b - V_2 t_{s1} \cos\beta_s \\ h_I = (\rho^2 - 1) V_1 t_{s1} \sin\alpha_s \end{cases}, \tag{8}$$

where z_I represents the depth of the anti-causal crosstalk events.

Combining Eq 8 and the travel time relationship, the relationship between the depth z_I of causal crosstalk and the subsurface half-offset h_I can be computed as:

$$z_I = z_a + z_b - \rho\sqrt{z_a^2 - \frac{h_I^2}{\rho^2 - 1}}. \tag{9}$$

According to the principle of slant stack (Eq. 3), we can turn Eq 9 into the relationship between the depth of anti-causal crosstalk in angle gathers and half-aperture angle. As shown in Figure 4, the depth of anti-causal crosstalk in angle gathers can be expressed based on the principle of Eq 3 as:

$$z_{I\gamma} = z_I - h_I \tan\gamma. \tag{10}$$

Substitute Eqs 9, 10 and combining Snell's law, the relationship between the depth $z_{I\gamma}$ and the half-aperture angle γ can be calculated as:

$$z_{I\gamma} = z_a + z_b - z_a \frac{(\rho^2 - 1)\sin\gamma\tan\gamma + \rho^2\cos\gamma}{\sqrt{\rho^2 - \sin^2\gamma}}. \tag{11}$$

Therefore, the residual moveout equations for anti-causal crosstalk can be expressed in angle gathers as:

$$\Delta n_{RMO} = z_{I\gamma}(0) - z_{I\gamma} = z_a\left[-\rho + \frac{(\rho^2 - 1)\sin\gamma\tan\gamma - \rho^2\cos\gamma}{\sqrt{\rho^2 - \sin^2\gamma}}\right], \tag{12}$$

where $z_{I\gamma}(0)$ is the depth of anti-causal crosstalk in angle gathers when migrated at a constant velocity (ρ=1). Eq. 12 shows the relationship between the RMO of anti-causal crosstalk and the half-aperture angle γ.

To test our derived equations of crosstalk in angle gathers, we use a three-layer flat model as shown in Figure 5. In this model, we set the P-wave velocities of each layer to 1,500 m/s, 2,500 m/s, and 4,000 m/s. The model contains 800 points in the horizontal direction and 400 points in the vertical direction with a grid size of 6.25 m. The acquisition geometry with fixed distribution is used for numerical simulations. We use 500 shots to simulate shot gathers with each shot interval of 6.25 m, and each shot gather has eight hundred traces. For one shot gather, we deploy both the sources and receivers at the surface with minimum and maximum offsets of 0 km and 2.5 km. The synthetic data is produced by the constant density acoustic wave equation. We use an impulse wavelet with a peak frequency of 25 Hz to mimic a P-wave source. The simulated shot gather is shown in Figure 6. The total record time is 4.9 s, and the sampling rate is 0.5 ms. To clearly show the crosstalk events in the imaging results, the direct arrivals, internal multiples, and multiples beyond the second order associated with the first layer have been removed.

We use the cross-correlation imaging conditions to image primaries and multiples from seismic records (as shown in Figure 6). The corresponding stacked migration results are

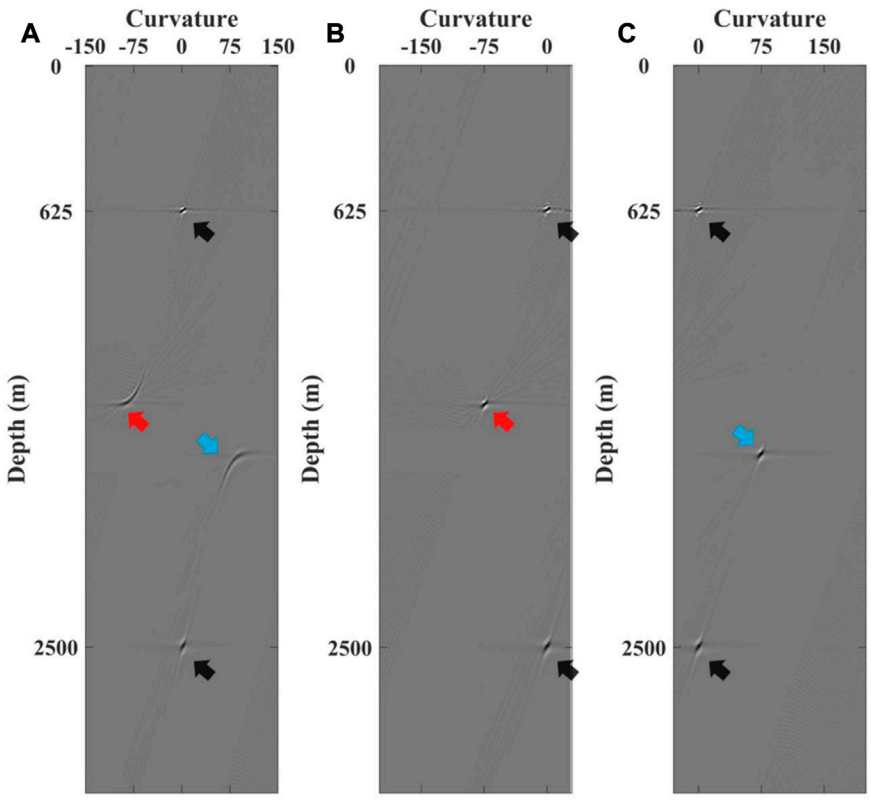

FIGURE 10
Comparison of Radon transform for angle gathers using tangent square approximation and two RMO equations. **(A)** Results of Radon transform for two types of crosstalk using tangent square approximation equation as kernel function, **(B)** Results of Radon transform for anti-causal crosstalk using derived RMO equation of anti-causal crosstalk as kernel function, **(C)** Results of Radon transform for causal crosstalk using derived RMO equation of causal crosstalk as the kernel function. The black arrows indicate the location of the actual imaging in the Radon domain. The red arrows indicate the location of anti-causal crosstalk in the Radon domain. The blue arrows indicate the location of causal crosstalk in the Radon domain.

shown in Figure 7, which can not only have correct imaging at a depth of the reflectors but also produce two types of crosstalk at the wrong locations.

In Figures 6, 7, the actual image of the first layer is generated by the primary and multiples of adjacent orders (arrows 1 and 2, arrows 2 and 3) reflected from the first layer based on the cross-correlation conditions. Similarly, the actual image of the second layer is generated by the primary and multiples of adjacent orders (arrows 3 and 5) reflected from the second layer based on the cross-correlation conditions. For the two types of crosstalk, arrows 1 and 4 are respectively used as virtual source wavefield and receiver wavefield to generate causal crosstalk (as light blue arrows indicate); arrows 1 and 3 are respectively used as virtual source wavefield and receiver wavefield to generate anti-causal crosstalk (as red arrows indicate).

To verify our derived equations, we extracted the angle gathers at 2.5 km (yellow dotted line in Figure 7) and stacked the analytic solutions of the derived equations onto the angle gathers obtained after migration. Figure 8 shows the angle gathers, which are extracted from the stacked imaging results after migration.

In Figure 8, we notice that the actual imaging events are horizontal in the angle domain, while the crosstalk events are curved. Moreover, the derived analytical solutions (as red and light blue curves indicate) and the actual curves of the crosstalk can be fitted well, which proves the correctness of our method. We use the subsurface offset-to-angle algorithm to obtain angle gathers; thus, the half-aperture angle γ for crosstalk is related to the offset. In this model, the maximum offset at the surface is 2.5 km, and it can be calculated that the maximum value of the analytical solution curve for causal crosstalk (as the light blue curve indicates) corresponding to the angle gathers is 45°, while the maximum value of the analytical solution curve for anti-causal crosstalk (as red curve indicates) corresponds to only 30°.

2.2 The attenuation of crosstalk in the radon domain

In the Radon domain, the imaging events and crosstalk in angle gathers can be effectively distinguished. This is because the imaging events in angle gathers are well-focused in the Radon domain, which makes it easy to separate the crosstalk in angle gathers. To separate imaging events and crosstalk more accurately in the Radon domain, we apply the two types of RMO equations derived above as new kernel functions to the Radon transform. Finally, we proved the accuracy of our derived RMO equations using model simulations.

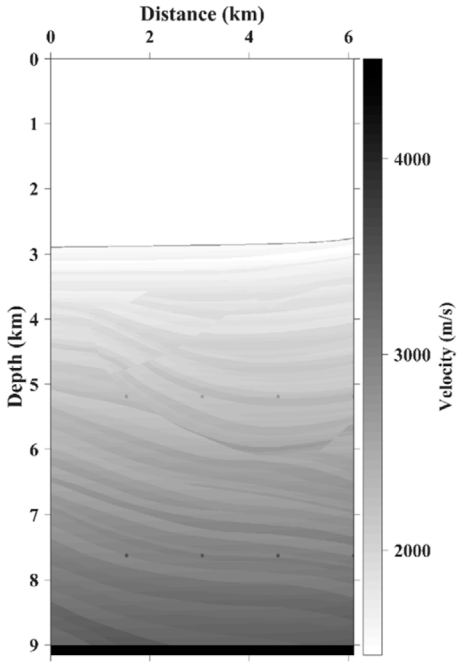

FIGURE 11
The Sigsbee2b velocity model.

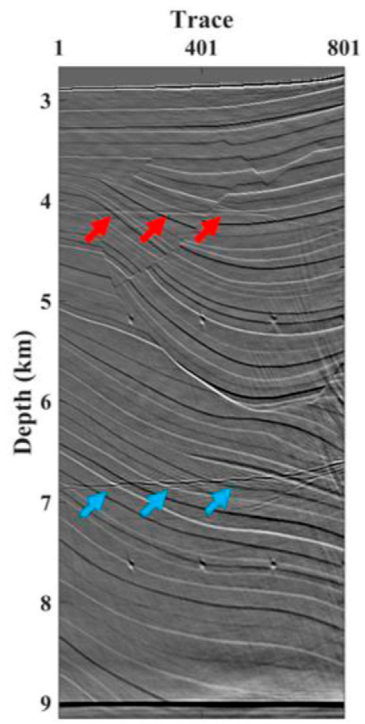

FIGURE 12
The imaging results of migration. The red arrows and light blue arrows mark the locations of anti-causal crosstalk and causal crosstalk, respectively.

The generic expression for the Radon transform in the angle domain (Sava and Guitton, 2005) can be expressed as:

$$z(q,\gamma) = z_0 + qg(\gamma), \tag{13}$$

where γ is the half-aperture angle, z_0 is the depth when γ is zero, q is a curvature parameter, and g(γ) is a function that approximates the residual moveout of the crosstalk in angle gathers.

Wang et al. (2014) performed the Radon transform on angle gathers by applying the principle of Eq 13 and used the tangent square approximation equation as the kernel function, which can be expressed as (Biondi and Symes, 2004; Sava and Guitton, 2005; Alvarez et al., 2007)

$$g(\gamma) = \tan^2\gamma. \tag{14}$$

This approach using Eq 14 as the kernel function can separate the imaging events from the crosstalk by focusing on different curvature portions in the Radon domain. By removing the curvature portion associated with the crosstalk and stacking the results in angle gathers after the inverse Radon transform, the final imaging results can be recovered. However, Eq 14 is not derived based on the generation mechanism of crosstalk, which may influence the capability of focusing crosstalk in the Radon domain. Therefore, we use two more approximate RMO equations as new kernel functions based on Eqs 6–12, which can be expressed as:

$$g_{anti-causal}(\gamma) = -\rho + \frac{(\rho^2-1)\sin\gamma\tan\gamma - \rho^2\cos\gamma}{\sqrt{\rho^2-\sin^2\gamma}}, \tag{15}$$

$$g_{causal}(\gamma) = \frac{\cos\gamma(\rho^2 - \tan^2\gamma(1-\rho^2))}{\sqrt{\rho 2-\sin^2\gamma}} - \rho, \tag{16}$$

where Eqs 15, 16 are the RMO equation for anti-causal crosstalk and causal crosstalk, respectively.

Figure 9 displays the comparison of the tangent-squared approximation equation and two RMO equations in the angle domain. Compared to the tangent-square approximation, Eqs 15, 16 provide a more accurate description of the kinematic shape for crosstalk in angle gathers (Figures 9A, C). To show this difference, we make the relative error of the two derived RMO equations with the tangent square approximation with increasing angle (Figures 9B, D), respectively. Note that when the aperture angle is small, both derived RMO equations and the tangent-squared approximation can fit the actual curves. However, as the aperture angle increases, the derived RMO equations can better fit the actual curves as shown in Figures 9A, C. We use the two RMO equations and tangent square approximation equation as kernel functions to apply the Radon transform for angle gathers, and the results are shown in Figure 10.

In Figure 10, the actual imaging results of multiples in the Radon domain are focused at zero curvature (as black arrows indicate), while the crosstalk events are focused at non-zero curvature (as light blue arrows and red arrows indicate). In addition, the results of the Radon transform for angle gathers using these two equations as kernel functions are more focused in the Radon domain (Figures 10B, D). Based on the focused capabilities, our method can separate the correct imaging and crosstalk in the Radon domain, thus recovering high signal-to-noise imaging results.

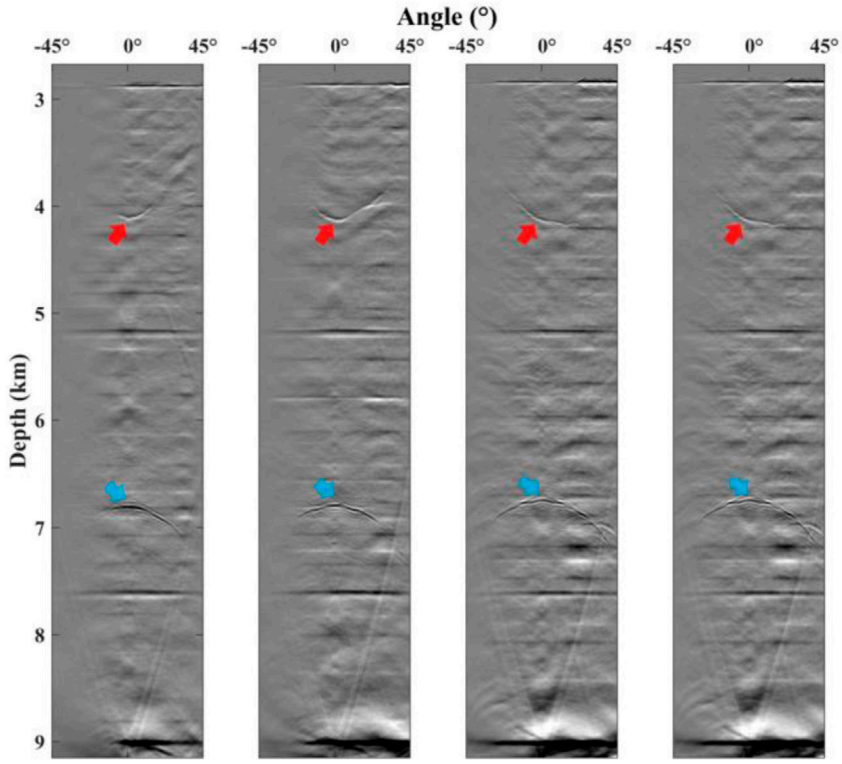

FIGURE 13
Angle gathers after migration. The red arrows and light blue arrows mark the locations where the anti-causal crosstalk and the causal crosstalk are located, respectively.

3 Numerical examples

We apply the proposed method to numerical examples. A subset of the Sigsbee2b model, as shown in Figure 11, is used to test the feasibility and robustness of our method.

The subset of the Sigsbee2b model has 801 grid points in the horizontal direction and 1,201 grid points in the vertical direction, and the grid size is 7.62 m. The velocity model used for producing seismic records is shown in Figure 11, which contains the faults portion of the Sigsbee2b model. A Ricker wavelet with a dominant frequency of 25 Hz and a maximum frequency of 45 Hz is employed to mimic a P-wave source. The number of shots is 125, with a shot interval of 48.72 m and a receiver interval of 22.86 m. For one shot gather, we deploy both the sources and receivers at the surface with minimum and maximum offsets of 0 m and 6,096 m. Split-spread acquisition geometry is used for numerical simulation. The length of the data record is 20 s, and the time sample interval is 0.8 ms. The seismic records with direct waves and ghost waves are removed for imaging of multiples.

The Sisgbee2b model has a high-velocity reflector at the bottom, which can produce multiples with strong amplitudes. We use the one-way wave-equation migration algorithm for the imaging of multiples. Figure 12 shows the imaging result for the subset of the Sigsbee2b model. From the comparison of the imaging result (Figure 12) with the actual Sigsbee2b velocity model (Figure 11), it can be seen that not only the correct imaging events are generated, but also events are generated at the wrong locations. Similar to the model in Figure 1, these wrong events, i.e., crosstalk, are generated by primaries and multiples related to the water bottom and the bottom reflector of the Sigsbee2b model based on the cross-correlation imaging conditions. In Figure 12, the red arrows indicate the anti-causal crosstalk event, which is related to the bottom of the Sigsbee2b model, and the light blue arrows indicate the causal crosstalk event, which is related to the water bottom. Note that these two types of crosstalk are not much different from the actual imaging events in terms of characteristics, which can be challenging to attenuate crosstalk in the imaging results. Moreover, the two above have different moveouts in the angle domain, and the crosstalk events are more separable. Therefore, to show the difference between crosstalk events and effective imaging, we apply the subsurface offset-angle conversion algorithm to compute the angle gathers after migration.

Figure 13 shows the angle gathers of the 201st, 401st, 601st, and 801st seismic traces. The imaging angle range in each angle gather is from −45° to 45° with a sampling of 0.5°. In Figure 13, the crosstalk events are curved in the angle domain, while the actual imaging is flat. In addition, the crosstalk events display different bending patterns due to their kinematic mechanisms. Among them, the curve that bends upward is anti-causal crosstalk (as red arrows indicate), and the curve that bends downward is causal crosstalk (as light blue arrows indicate). As discussed in the preceding section, the Radon transform can separate these two crosstalk events from the effective imaging and thus achieve the purpose of attenuating the crosstalk. By using the RMO equations for two types of crosstalk

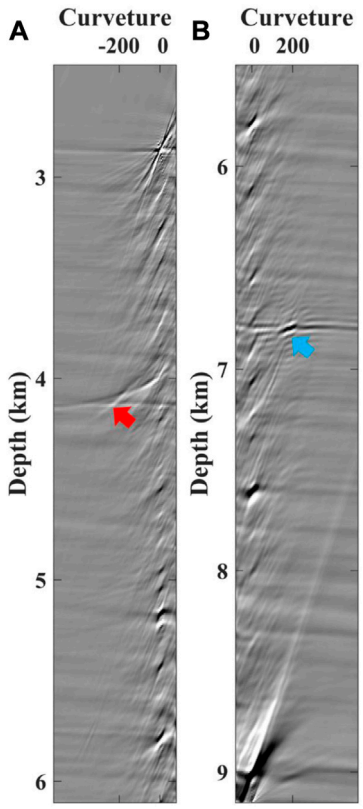

FIGURE 14
Results in radon domain after radon transform with two kernel functions. **(A)** The Radon transform using the RMO equation of anti-causal crosstalk as the kernel function, **(B)** the Radon transform using the RMO equation of causal crosstalk as the kernel function. The red arrows and light blue arrows mark the locations where the anti-causal crosstalk and the causal crosstalk are located, respectively.

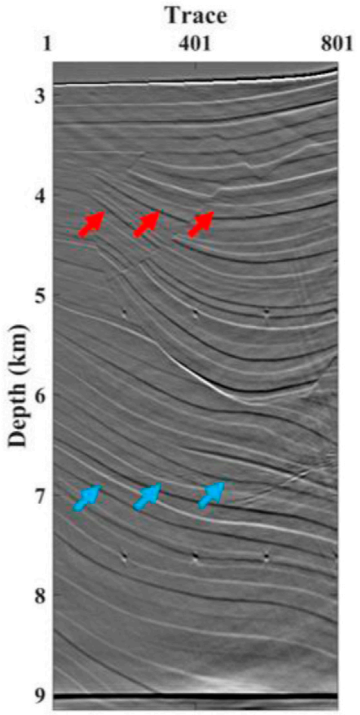

FIGURE 15
Denoised migration result. The red and light blue arrows mark the positions of the two types of crosstalk before being denoised.

previously obtained as the kernel functions for the Radon transform and by performing the Radon transform on the obtained angle gathers, we can separate the crosstalk and the actual imaging in the Radon domain.

Figure 14 shows the results of the Radon transform using two kernel functions for trace 401 of ADCIGs**.** In Figure 14, the actual imaging is focused on the zero-curvature portion, while the anti-causal crosstalk and the causal crosstalk are respectively distributed on the left (as the red arrow indicates in Figure 14A) and right sides (as the light blue arrow indicates in Figure 14B) of the zero-curvature portions in the Radon domain. In this domain, the two types of crosstalk and effective imaging correspond to three different curvature components, respectively. The results of the radon transform in Figure 14 show that our method can significantly separate crosstalk and the correct imaging in the Radon domain when facing complex reflectors. Therefore, the effective imaging results in the Radon domain can be obtained by removing the non-zero curvature components in Figures 14A, B with a suitable function. Next, we transfer the effective images in the Radon domain to the angle domain by inverse Radon transform and stack the angle gathers of 801 traces to obtain the imaging results with crosstalk attenuated.

Figure 15 shows the imaging result after attenuating crosstalk events. Compared with the imaging results without crosstalk attenuation (Figure 12), the imaging results in Figure 15 have better resolution with two types of crosstalk attenuated. In addition, some of the less obvious crosstalk events are also attenuated to some extent. In summary, the proposed method to attenuate crosstalk for imaging of multiples can be used for complex models, which demonstrates the feasibility and robustness of our proposed method.

4 Conclusion

To solve the problem of unphysical kernel functions when applying the Radon transform to remove crosstalk in the angle domain, we derive two RMO equations for crosstalk based on the causality and apply them to attenuate crosstalk in the Radon domain. The RMO equations can accurately describe the kinematic mechanism of the crosstalk in the angle domain. A simple model verifies the accuracy of the RMO equations. Compared with the Radon transform using the conventional tangent-squared approximation, our equations can make the crosstalk more focused in the Radon domain and can better separate the crosstalk from the actual imaging. A subset of the Sigsbee2b model is used for the numerical test, and it has validated the feasibility and robustness of our method. The crosstalk attenuated using our method has recovered high signal-to-noise imaging results, which benefits the subsequent geological interpretation. In our paper, we use the subsurface offset-to-angle algorithm to obtain ADCIGs, therefore, for 3D seismic data, we need to face the challenge of extracting ADCIGs more efficiently to

address a large number of calculations. In addition, our approach assumes that the source ghost and receiver ghost do not exist. Therefore, in practical seismic data processing, this situation may have an influence on the accuracy of crosstalk attenuation.

Data availability statement

The raw data supporting the conclusion of this article will be made available by the authors, without undue reservation.

Author contributions

ZG and SZ contributed to the methodology and wrote the original draft of the paper. SL contributed to the conceptualization and supervision. Data analysis was conducted by HW and KR. All authors reviewed the final submitted version of the manuscript.

Funding

This study is partially funded by the National Natural Science Foundation of China (grant no. 42074123), National Natural Science Foundation of China (grant no. 42230805) and the Pearl River Talent Program of Guangdong, China (grant no. 2017ZT07Z066).

Acknowledgments

Our great gratitude goes to the reviewers Yike Liu, Jianping Huang, Weijia Sun and the editor Qizhen Du. Their careful work and thoughtful suggestions helped greatly improve this paper.

Conflict of Interest

The authors declare that the research was conducted in the absence of any commercial or financial relationships that could be construed as a potential conflict of interest.

Publisher's note

References

Alvarez, G., Biondi, B., and Guitton, A. (2007). Attenuation of specular and diffracted 2D multiples in image space. *GEOPHYSICS* 72, V97–V109. doi:10.1190/1.2759439

Berkhout, A. J. G. (2014). Review paper: An outlook on the future of seismic imaging, Part I: Forward and reverse modelling. *Geophys. Prospect.* 62, 911–930. doi:10.1111/1365-2478.12161

Berkhout, A. J., and Verschuur, D. J. (2003). "Transformation of multiples into primary reflections," in *SEG technical Program expanded abstracts 2003* (Tulsa: Society of Exploration Geophysicists), 1925–1928. doi:10.1190/1.1817697

Berkhout, A. J., and Vershuur, D. J. (1994). "Multiple technology: Part 2, migration of multiple reflections," in *SEG technical Program expanded abstracts 1994* (Tulsa: Society of Exploration Geophysicists), 1497–1500. doi:10.1190/1.1822821

Biondi, B., and Symes, W. W. (2004). Angle-domain common-image gathers for migration velocity analysis by wavefield-continuation imaging. *GEOPHYSICS* 69, 1283–1298. doi:10.1190/1.1801945

Gu, Z., and Wu, R.-S. (2022). Internal multiple removal and illumination correction for seismic imaging. *IEEE Trans. Geosci. Remote Sens.* 60, 1–11. doi:10.1109/TGRS.2021.3080210

Liu, Y., Chang, X., Jin, D., He, R., Sun, H., and Zheng, Y. (2011). Reverse time migration of multiples for subsalt imaging. *Geophysics* 76 (5), WB209–WB216. doi:10.1190/geo2010-0312.1

Liu, Y., Liu, X., Osen, A., Shao, Y., Hu, H., and Zheng, Y. (2016). Least-squares reverse time migration using controlled-order multiple reflections. *GEOPHYSICS* 81, S347–S357. doi:10.1190/geo2015-0479.1

Lu, S., Liu, F., Chemingui, N., Valenciano, A., and Long, A. (2018). Least-squares full-wavefield migration. *Lead. Edge* 37, 46–51. doi:10.1190/tle37010046.1

Lu, S., Qiu, L., and Li, X. (2021). Addressing the crosstalk issue in imaging using seismic multiple wavefields. *GEOPHYSICS* 86, S235–S245. doi:10.1190/geo2020-0364.1

Lu, S., Whitmore, N., Valenciano, A., Chemingui, N., and Ronholt, G. (2016). "A practical crosstalk attenuation method for separated wavefield imaging," in *SEG technical Program expanded abstracts 2016* (Dallas, Texas: Society of Exploration Geophysicists), 4235–4239. doi:10.1190/segam2016-13849878.1

Ordoñez, A., Söllner, W., Klüver, T., and Gelius, L. J. (2014). Migration of primaries and multiples using an imaging condition for amplitude-normalized separated wavefields. *GEOPHYSICS* 79, S217–S230. doi:10.1190/geo2013-0346.1

Sava, P. C., and Fomel, S. (2003). Angle-domain common-image gathers by wavefield continuation methods. *GEOPHYSICS* 68, 1065–1074. doi:10.1190/1.1581078

Sava, P., and Guitton, A. (2005). Multiple attenuation in the image space. *GEOPHYSICS* 70, V10–V20. doi:10.1190/1.1852789

Schuster, G. T., and Rickett, J. (2000). *Daylight imaging in V(x, y, z) media*. Utah tomography and modeling-migration: Project midyear report, 55–66.

Singh, S., Snieder, R., van der Neut, J., Thorbecke, J., Slob, E., and Wapenaar, K. (2017). Accounting for free-surface multiples in Marchenko imaging. *GEOPHYSICS* 82, R19–R30. doi:10.1190/geo2015-0646.1

Tu, N., and Herrmann, F. J. (2015). Fast imaging with surface-related multiples by sparse inversion. *Geophys. J. Int.* 201, 304–317. doi:10.1093/gji/ggv020

Wang, Y., Zheng, Y., Zhang, L., Chang, X., and Yao, Z. (2014). Reverse time migration of multiples: Eliminating migration artifacts in angle domain common image gathers. *GEOPHYSICS* 79, S263–S270. doi:10.1190/geo2013-0441.1

Wapenaar, K., Thorbecke, J., van der Neut, J., Broggini, F., Slob, E., and Snieder, R. (2014). Marchenko imaging. *GEOPHYSICS* 79, WA39–WA57. doi:10.1190/geo2013-0302.1

Wong, M., Biondi, B. L., and Ronen, S. (2015). Imaging with primaries and free-surface multiples by joint least-squares reverse time migration. *GEOPHYSICS* 80, S223–S235. doi:10.1190/geo2015-0093.1

Xu, S., Zhang, Y., and Tang, B. (2011). 3D angle gathers from reverse time migration. *GEOPHYSICS* 76, S77–S92. doi:10.1190/1.3536527

Yoon, K., and Marfurt, K. J. (2006). Reverse-time migration using the poynting vector. *Explor. Geophys.* 37, 102–107. doi:10.1071/EG06102

Zhang, D., and Schuster, G. T. (2014). Least-squares reverse time migration of multiples. *GEOPHYSICS* 79, S11–S21. doi:10.1190/geo2013-0156.1

frontiers | Frontiers in Earth Science

TYPE Original Research
PUBLISHED 06 July 2023
DOI 10.3389/feart.2023.1136423

OPEN ACCESS

EDITED BY
Jian Sun,
Ocean University of China, China

REVIEWED BY
Ying Hu,
Chengdu University of Technology, China
Qiang Guo,
China University of Mining and Technology, China

*CORRESPONDENCE
Yiqiong Zhang,
cugbzyq@163.com

RECEIVED 03 January 2023
ACCEPTED 21 June 2023
PUBLISHED 06 July 2023

CITATION
Wang Z, Zhang Y, Ji Z, Jin S, Jiang R, Wang X, Wang Y, Sheng S and Lin Y (2023), Application of a new hydrocarbon detection technique with phase decomposition in carbonate reservoir of the Pre-Caspian Basin.
Front. Earth Sci. 11:1136423.
doi: 10.3389/feart.2023.1136423

Application of a new hydrocarbon detection technique with phase decomposition in carbonate reservoir of the Pre-Caspian Basin

Zhen Wang[1], Yiqiong Zhang[1]*, Zhifeng Ji[1], Shutang Jin[2], Ren Jiang[1], Xueke Wang[1], Yankun Wang[1], Shanbo Sheng[2] and Yaping Lin[1]

[1]Research Institute of Petroleum Exploration and Development, China National Petroleum Corporation (CNPC), Beijing, China, [2]China National Oil and Gas Exploration and Development Co., Ltd. (CNODC), Nursultan, Kazakhstan

Due to the low porosity and thin thickness of the Carboniferous carbonate reservoir in the Pre-Caspian Basin, the impedance difference between the reservoir and the surrounding rock is not obvious, and the seismic response characteristics are weak. It is ambiguous to detect oil and gas based on the convention attribute amplitude and frequency information. According to the geological characteristics of the Carboniferous Reservoir in the Pre-Caspian Basin, we proposed a new hydrocarbon detection method from the phase decomposition of sensitive frequency in post-stack seismic data, which improves the accuracy of hydrocarbon detection. The forward model that is a method of numerical analysis is utilized to testify the feasibility of hydrocarbon detection with phase decomposition, which showed that the amplitude of oil and gas layers in −90° phase components is stronger than that of water layer. The special frequency band seismic data sensitive to oil and gas is decomposed into 10 Hz, 20 Hz, 30 Hz, 40 Hz, 50 Hz, and 60 Hz single frequency energy body, and then hydrocarbon is detected according to the amplitude anomaly in specific frequency energy body. The application of forward model and filed example demonstrates that the fluid type in the reservoir can be directly identified by the phase decomposition technique, which has higher accuracy than the conventional hydrocarbon detection technology with post-stack data. After the application of this technology, the coincidence between hydrocarbon results and oil test results in the block was increased from 60% to 80%, and the coincidence rate is much higher than the detection results using conventional attributes, more than 90%. All the two exploration wells deployed according to the detection results have obtained higher oil production, new discovered oil geologic reserves have been increased to 5.54 million tons.

KEYWORDS

Pre-Caspian Basin, phase decomposition, hydrocarbon seismic direct detection, frequency, seismic signals analysis, fluids detection, forward modeling analysis

1 Introduction

Carbonate reservoirs in the eastern margin of Pre-Caspian Basin are characterized by strong vertical and horizontal heterogeneity, larger differences in the type, scale and hydrocarbon-bearing property of the reservoir space. Multiple oil-water systems are developed in the Carboniferous system, with smaller oil layer thickness (single layer thickness of about 2 m), and limited distribution range. The updip direction is shielded by lithological and physical changes, resulting in great uncertainty for quantitative analysis. Therefore, it is necessary to predict the reservoir distribution and fluid properties, so as to improve the drilling success rate. Many theoretical researches and new technologies had been used in the carbonate reservoirs' exploration (e.g., Zhao W et al., 2014), such as forward and inversion modeling of complex wave field of fracture-porous media petrophysical model, identification of structural tensor small fault from seismic gradient, quantitative prediction of fracture-cavity reservoir by cloud transform stochastic simulation, and gas reservoir detection based on pre-stack elastic parameter inversion and frequency division attribute. But there are some issues in the corresponding seismic prediction technologies, such as weak theoretical methods and low prediction accuracy. At present, reservoir fluid detection by seismic data includes pre-stack detection and post-stack detection. Pre-stack fluid detection is mainly based on AVO theory for pre-stack fluid parameter inversion. Post-stack fluid detection is chiefly based on the "bright spot" of amplitude attribute, seismic wave absorption attenuation theory and 90° phase shift technique (Cao et al., 2010; Qiao et al., 2018; Zheng et al., 2019; Guo et al., 2022). The seismic wave absorption attenuation theory uses seismic amplitude changing with frequency to detect fluids. The 90° phase shift technique only makes 90° phase rotation to zero-phase seismic data to better depict formation lithology (Chen et al., 2012). Due to complex underground geological conditions, reservoir seismic response is not only affected by non-fluid factors such as reservoir type, physical properties, thickness and interference, but also by fluid properties in the reservoir (Yang et al., 2010; Chen X et al., 2020; Chen et al., 2022), so conventional fluid detection techniques have ambiguity in practical application.

Phase decomposition was originally proposed by Castagna et al. (2016). This technique has been applied in sandstone reservoirs (Barbato et al., 2017; Castagna et al., 2019; Selmara et al., 2019; Zhou et al., 2019), and achieved remarkable results. All the applications conducted phase decomposition in full-band seismic data, and the application of phase decomposition to carbonate reservoirs is very limited.

In view of the shortcomings of conventional post-stack hydrocarbon detection methods, this paper applies phase decomposition technique to directly detect hydrocarbons based on in seismic data volume of sensitive frequency under the premise of only post-stack seismic data. First, establish a forward model based on the statistics of reservoir parameters in the study area, decompose the frequency and phase of forward modeling results and actual seismic data, and find out the frequency and phase components that are sensitive to oil layers. Finally, the method is applied to predict lithologic reservoirs in the slope area of the Central Block in the eastern margin of the Pre-Caspian Basin to verify the effectiveness of the method.

2 Regional geology

The Pre-Caspian Basin is one of the world's largest petroliferous basins, with an area of about 585,000 km^2, most of which is located in the west of Kazakhstan, and the maximum thickness of sedimentary rocks is 21 km. Tectonically, it belongs to the foreland basin in the southeast of the Eastern European Craton. The basin widely develops the Permian Kungurian gypsum-salt layer, which is vertically divided into two major structural strata (pre-salt and post-salt) (Zhao et al., 2010; Zheng et al., 2011; Zhao et al., 2016). Several world-class giant oil and gas fields have been proved in the basin, but the exploration degree

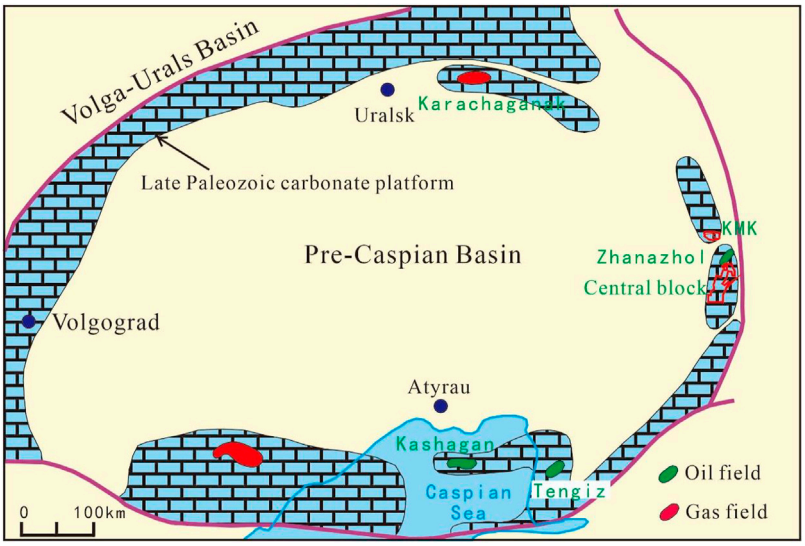

FIGURE 1
Location of the Central Block in the eastern Pre-Caspian Basin.

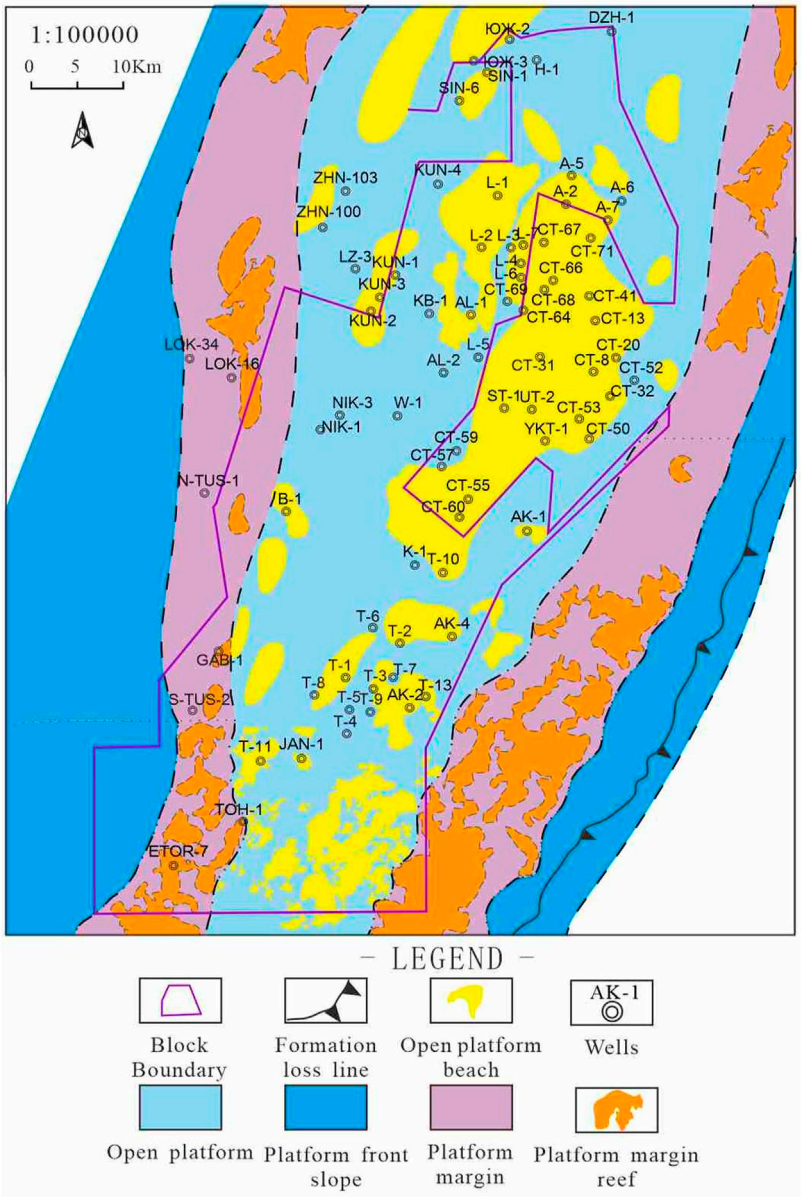

FIGURE 2
Carboniferous sedimentary facies distribution of the Study area.

of the basin is uneven. The exploration degree of the post-salt layers is relatively high, while the exploration of the pre-salt Paleozoic strata is mainly concentrated at the basin margin (Xu et al., 2009), and the remaining exploration area is large. However, the drilled wells show that the relationship between oil and water is complex and the drilling success rate is low, leading to low exploration effect at present. The Central Block of the Kazakhstan Pre-Caspian Basin is the first risk exploration block of PetroChina (Jin et al., 2015), which is located in the uplift zone of the eastern margin of the basin with higher exploration degree, covering an area of 3,262.3 km^2 (Figure 1). The main exploration target layer is the pre-salt Carboniferous KT-I and KT-II layers (Fang et al., 2008; Xu, 2011; Liang et al., 2013; He et al., 2014). In the Central Block, North Truva Oilfield and Takyr hydrocarbon-bearing structure have been discovered successively. Since 2012, large pre-salt structural traps have been drilled, and exploration in this area has shifted from structural traps to lithological traps. The study area is located in the northern part of the Central Block, covering an area of 450 km^2 (Figure 2). The study area is mainly developed in the Carboniferous carbonate reef reservoirs developed in the open platform, with one shoal being one reservoir. There is no unified oil-water interface, and the oil-water relationship is complicated. At present, 24 Wells have been drilled and 3D seismic data of "two widths and one height" have been collected, which is conducive to oil and gas detection and research.

According to the drilling, well logging, lithology, and paleontology data of the exploration block and its surrounding oil and gas fields, the strata are vertically divided into three sets of main stratigraphic combinations (Figure 3), which are in order

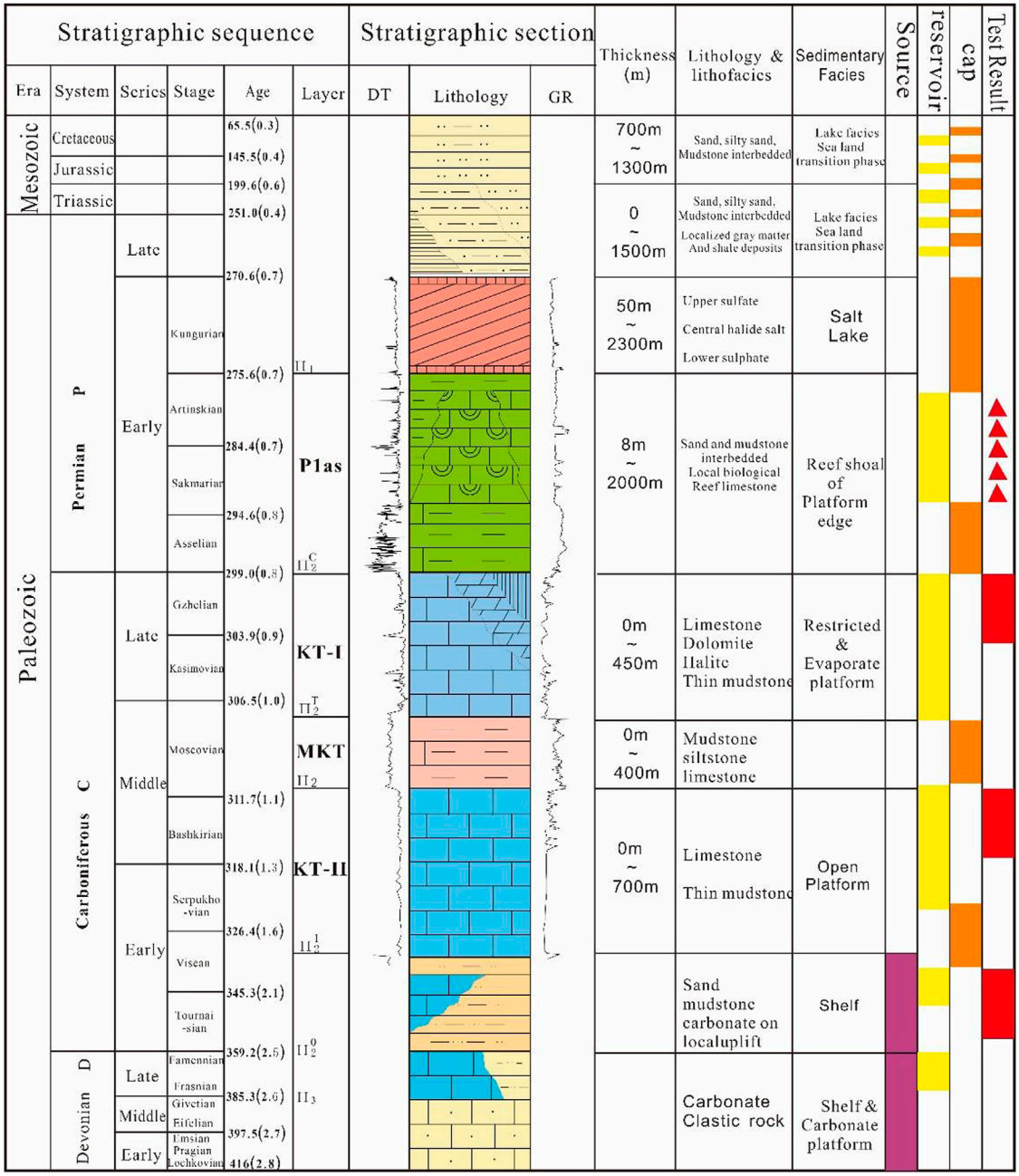

FIGURE 3
Composite stratigraphic column of the Central Block.

from bottom to top: the pre-salt Paleozoic carbonate and clastic combination, the lower Permian Kungurian Formation salt stratum, and the post-salt Permian-Quaternary clastic combination.

3 Principle of phase decomposition

Phase decomposition is a new and unique application. It is different from the 90° phase-shifting technique of seismic sedimentary facies (Pan et al., 2013). It is significantly different from the traditional phase rotation. It does not rotate the seismic trace with a simple phase angle, but decomposes the seismic trace into various phase components.

In the past, seismic attribute research was mainly conducted in amplitude domain and frequency domain, but rarely in phase domain, due to the lack of effective algorithm to decompose the phase domain. In 2015, John Castagna invented the least square method (CLSSA) frequency and phase decomposition algorithm (Castagna et al., 2016; Castagna et al., 2019), which achieved a fundamental breakthrough in this domain. The phase decomposition technique is to transform the seismic wave in the phase domain. On this basis, the corresponding components of different phases can be extracted, and specific

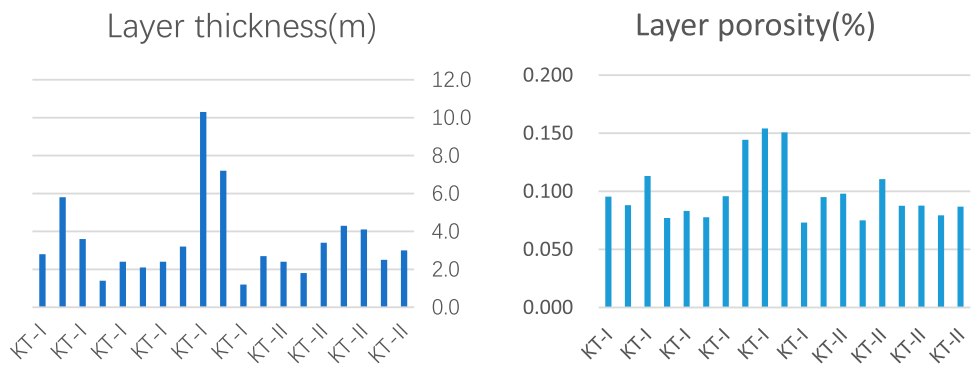

FIGURE 4
Statistics of KT-I and KT-II layer's thicknesses.

combinations of different phase profiles can be made to highlight the characteristics of formation fluids. The basic formula of time-frequency analysis commonly used in seismic signal processing is shown in Formula (1).

$$S(t) = \int S'(f,t)df \tag{1}$$

where, $S'(f,t)$ is the time-frequency analysis of seismic signals; f is frequency.

Formula 1 does not consider the phase change, but in fact, the seismic wave is a function of the three parameters (amplitude, frequency and phase). When considering the phase change, Formula 1 becomes Formula 2:

$$S'(\theta,t) = \int_{f1}^{f2} S'(f,\theta,t)df \tag{2}$$

where, $S(f,\theta,t) = A(f,t)\cos\theta(f,t)$, f_1 and f_2 are used to define the bandwidth of the target layer. If $S'(\theta,t)$ is defined as phase gather, which is used to characterize the relationship between amplitude versus frequency and time in seismic signals.

When the frequency is fixed, Formula 2 becomes Formula 3:

$$S'(t) = \int_{\theta1}^{\theta2} S'(\theta,t)d\theta \tag{3}$$

where, θ_1 and θ_2 are used to define the phase width of the target layer. Formula 3 is the basis of phase decomposition and reconstruction technique. When all phase and frequency variation ranges are considered, $S'(t) = S(t)$.

It is found that the zero-phase component of seismic signals often represents the information of stratum interface, and the change of pore fluids or lithology in the stratum will cause amplitude anomaly in the −90° phase component (Lin et al., 2007). According to this characteristic, the phase decomposition technique can be used to directly identify the fluid types in the reservoir.

4 Synthetic analysis of forward modelling

Seismic wave forward modeling is to obtain the propagation rule of seismic wave in the known underground geological model, including propagation time, path, energy, etc. (Zhao L et al., 2014; Chen Y et al., 2020). Forward modeling is the first step to understand the unknown problems in seismic research. The rules obtained from forward modeling in a given geological model can improve people's understanding of the unknown model, thus helping to solve the problem.

4.1 Statistics of well logging parameters

According to the well logging interpretation results, the thicknesses of various layers of Carboniferous KT-I and KT-II layers are counted (Figure 4). The well logging interpretation shows that the thin layers less than 5 m thick are the dominated, and the thicknesses of all oil layers of KT-II layer are less than 5 m. From the porosity statistics, the average porosity of the oil layers of KT-I and KT-II layers is about 10%.

According to the statistics of petrophysical analysis results of various lithofacies, the velocity and density values of each layer are given as follows: the velocity of caprock above layer KT-I is about 2,900 m/s, the density is about 1.9 g/cm^3; the velocity of layer KT-I is 5,950 m/s, the density is 2.68 g/cm^3; the velocity of mudstone interlayer is 2,800 m/s, and the density is 2.1 g/cm^3; The velocity of layer KT-II is 6,100 m/s, the density is 2.7 g/cm^3; the velocity of MKT mudstone is 3,050 m/s, and the density is 2.1 g/cm^3.

4.2 Analysis of forward model and its seismic response characteristics

According to the reservoir characteristics in well, considering reservoir thickness, the distance between reservoir and formation top, and the mudstone interlayer, a forward model of the target reservoir is established, and it is filled with physical parameters (such as velocity, density, porosity) from statistics of well-logging data.

As shown in Figures 5A, B, according to the actual formation development, layer KT-I is designed four reservoir groups: the first two groups are filled with oil and gas respectively, and the last two groups are filled with water. Two groups are 2 m from the top interface of layer KT-I, and another two groups are about 50 m from the top interface of layer KT-I. The mudstone interlayer with a thickness of about 2 m is

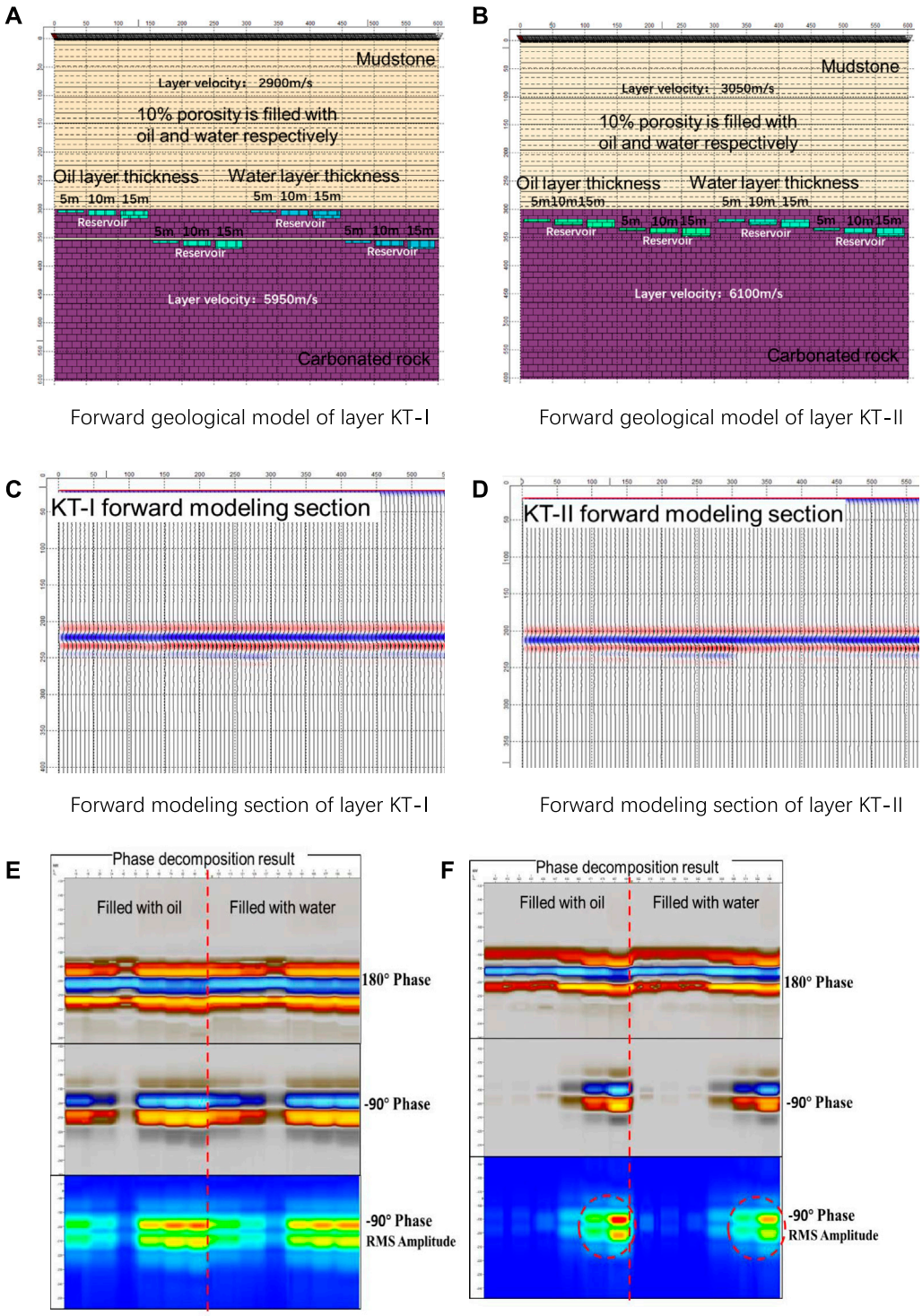

Forward geological model of layer KT-I

Forward geological model of layer KT-II

Forward modeling section of layer KT-I

Forward modeling section of layer KT-II

FIGURE 5
Geological model, forward modeling records and phase decomposition results.

embedded in layer KT-I. Four groups of reservoirs are also designed for layer KT-II: two groups are 20 m from the top interface of layer KT-II, and another two groups are 40 m from the top interface of layer KT-II.

The sections obtained by using 30 Hz dominant frequency, Ricker wavelet, surface shooting, single row receiving and wave equation forward modeling method are shown in Figures 5C, D.

When the reservoir of layer KT-I is close to the top interface (2 m): 10–15 m thick oil layer will significantly weaken the reflection intensity of the overlying interface, but 15 m thick water layer will also significantly weaken the reflection intensity of the overlying interface. Then, the oil layer and water layer are difficult to identify. When the reservoir of layer KT-I is farer from the top interface

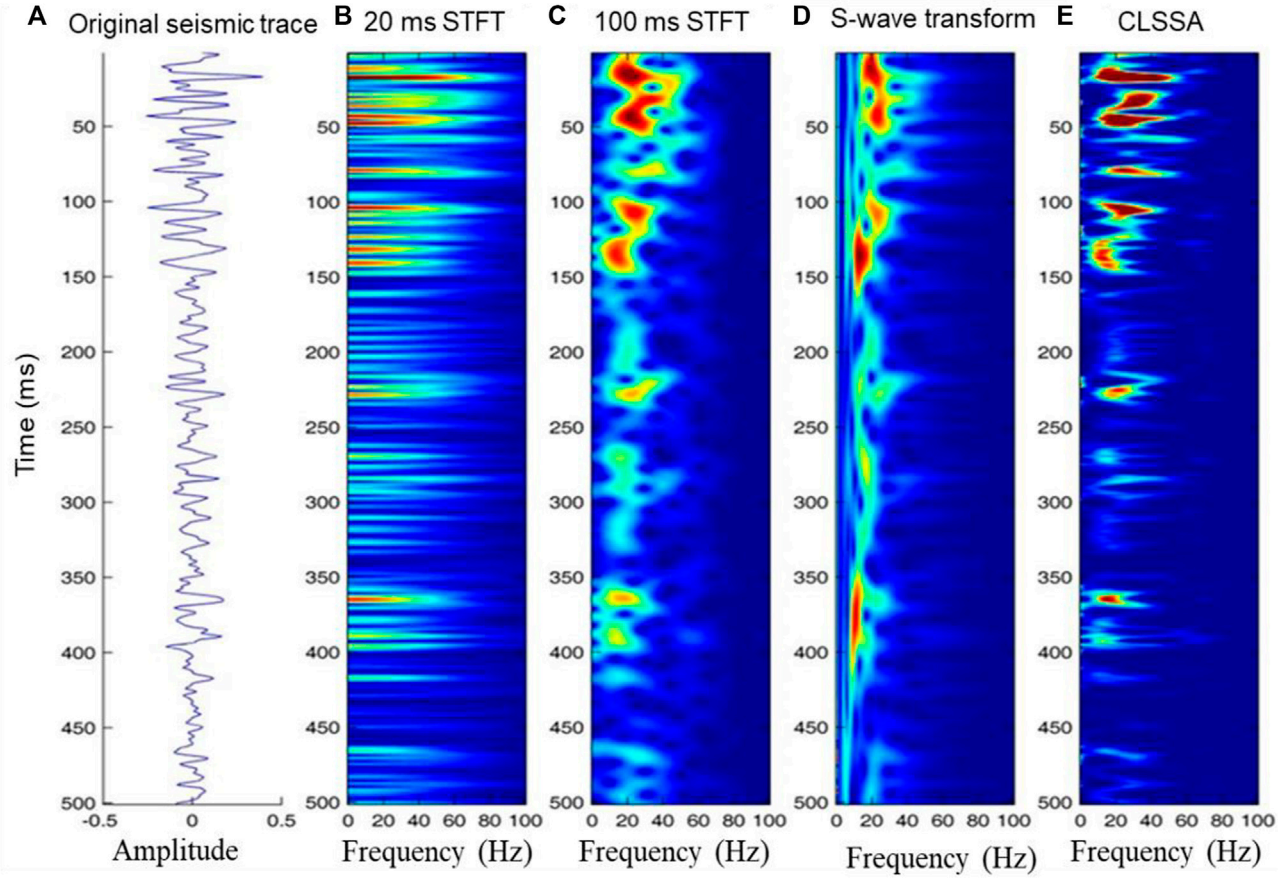

FIGURE 6
Comparison of spectrum decomposition results of different methods applied to actual seismic traces ((**A**) actual seismic records, **(B)** Fourier transform with 20 ms window, **(C)** Fourier transform with 100 ms window, **(D)** wavelet transform, **(E)** least squares spectrum decomposition).

(>50 m) and there is a mudstone interlayer: the reservoir has stronger reflection (relative to the surrounding rock and mudstone interlayer), thus the reservoir can be identified.

When the reservoir of layer KT-II is 20 m from the top interface: 10–15 m oil layer weakens the reflection intensity of the overlying interface, similar to that of layer KT-I, but the weakening degree is reduced. The 0–15 m thick water layer will also cause the above phenomenon. When the reservoir of layer KT-II is 40 m away from the top interface: the reservoir is characterized by stronger reflection (relative to the surrounding rock and mudstone interlayer), and the top and bottom of the reservoir with a certain thickness can be identified. Therefore, oil layer and water layer cannot be determined from the conventional seismic reflection amplitude alone.

4.3 Phase decomposition of forward modeling result

The forward modeling results of layer KT-I and layer KT-II are decomposed by phase decomposition technique (Figures 5E, F) to obtain 180° and −90° phase component sections. From the phase decomposition results of layers KT-I and KT-II, the 180° phase component section mainly reflects the characteristics of layer KT-I interface; On the −90° phase component section, the waveform is distributed in blocks, similar to the shape of the reservoir in the geological model; RMS amplitude is calculated in −90° phase component, and it can be seen that the reflection characteristics of the reservoir are more obvious. Moreover, the amplitude intensity of oil layer is greater than that of water layer. Therefore, the phase decomposition technique can be used to identify the existence of oil and gas reservoirs.

5 Applications

5.1 Spectrum decomposition of seismic data

The phase information of seismic data can be obtained by spectrum decomposition of seismic data, so the selection of spectrum decomposition algorithm is also crucial to the result of phase decomposition. Spectrum decomposition has been widely used in fine geological interpretation. Due to the sensitivity of frequency change, many subtle stratigraphic features have been more finely interpreted and identified in the frequency domain (Zhang et al., 2017; Chen Y et al., 2020). Affected by stratum absorption and other factors, seismic

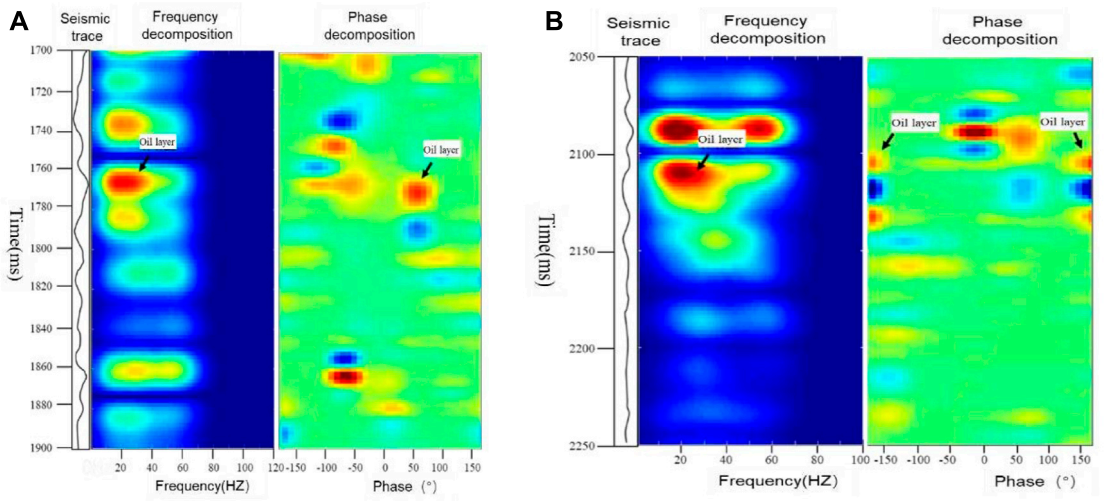

FIGURE 7
Analysis of sensitive frequency and phase of oil layers in different intervals.

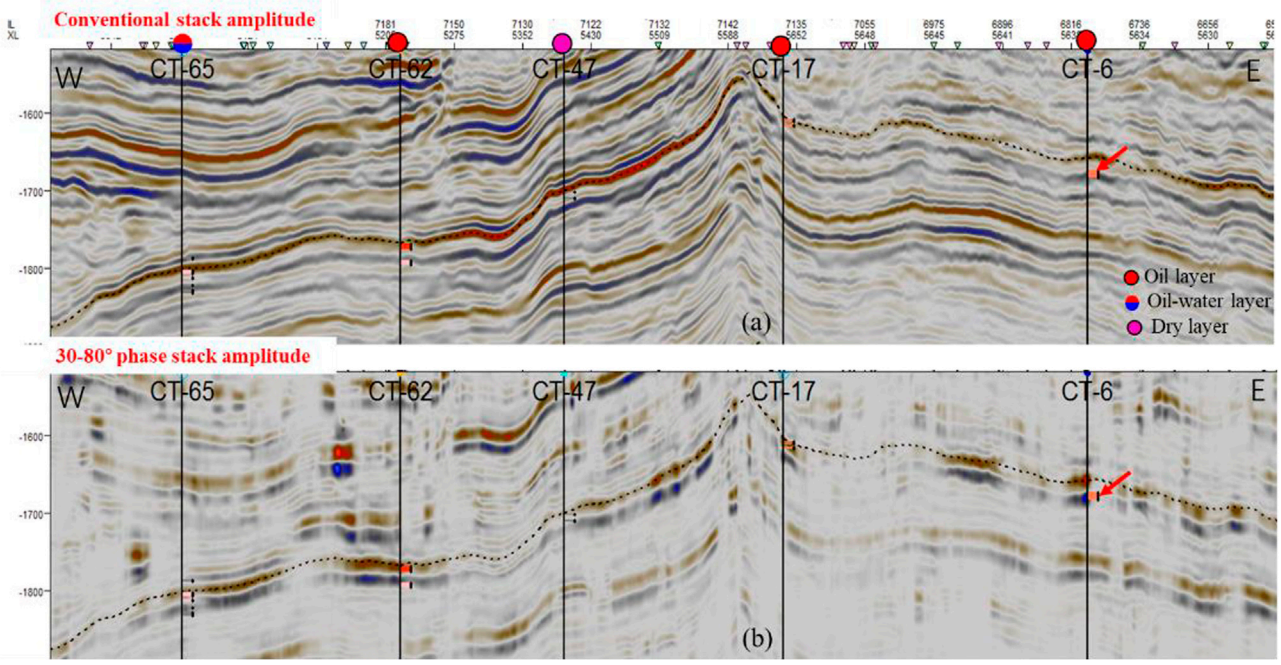

FIGURE 8
Seismic attribution comparison in the KT-I layer. **(A)** Conventional stack data volume and **(B)** Specified phase stack volume.

wavelet changes with time and space. In order to reflect the influence of stratum in the target layer on seismic wavelet, spectrum decomposition must be carried out in a small time window. There are several different implementation methods for spectrum decomposition. In the early stage, the short time Fourier transform (STFT), continuous wavelet transform (CWT), S-wave transform (ST) and other methods were used for spectrum decomposition. Affected by the time window tailing effect, these methods have low resolution in time and frequency.

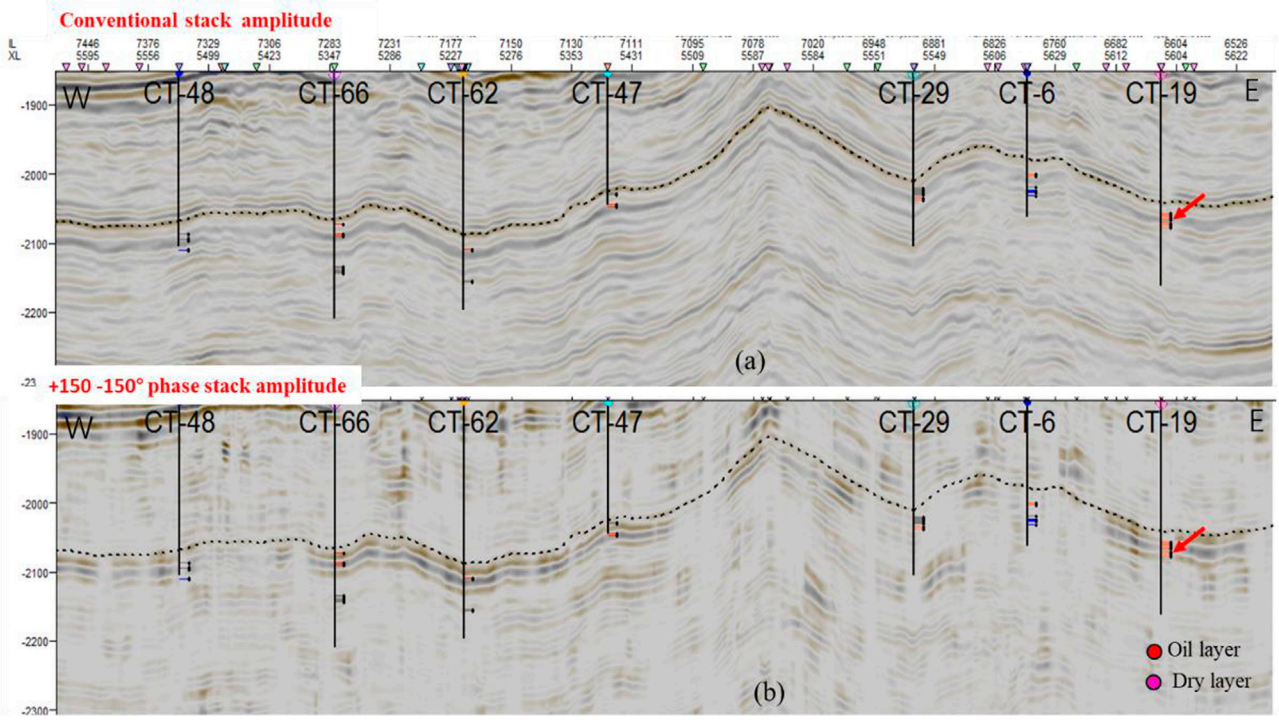

FIGURE 9
Comparison of conventional stack data volume **(A)** and specified phase stack volume **(B)** of KT-II.

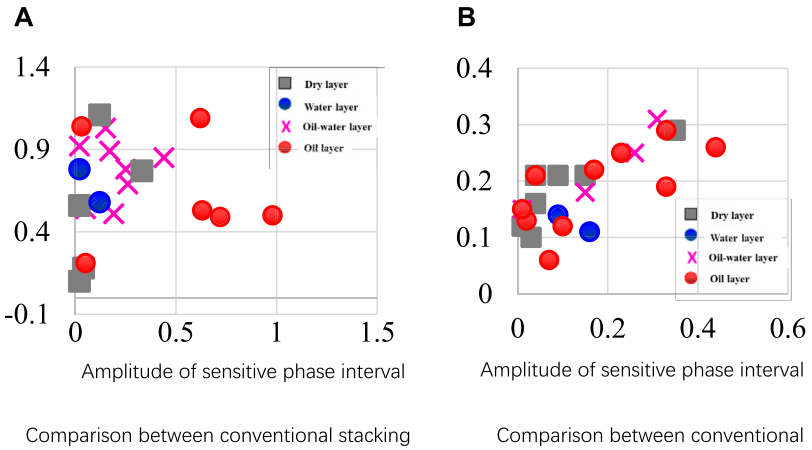

FIGURE 10
Cross plot of RMS amplitude of well point and RMS amplitude of phase decomposition reconstruction volume in different intervals.

In this paper, the constrained least squares spectrum analysis (CLSSA) is used for spectrum decomposition. Compared with other methods, the CLSSA method has higher resolution in time and frequency. Compared with the discrete Fourier transform, it reduces the tailing effect of the window and spectrum smoothing, which can ensure better maintenance of the reflection spectrum characteristics in the short window. Compared with short-time Fourier transform, the improvement of resolution by CLSSA method increases with the shortening of time window length. Therefore, the least square method is superior to short-time Fourier transform and continuous wavelet transform in spectrum decomposition.

The time-frequency spectrum obtained by applying different spectral decomposition methods to the actual seismic traces (Figure 6). It can be seen that the frequency spectrum of the 20 ms Fourier transform is artificially widened, and the truncation effect in the time domain is obvious. The time lag effect of 100 ms Fourier transform and wavelet transform is obvious, and the wavelet transform moves to

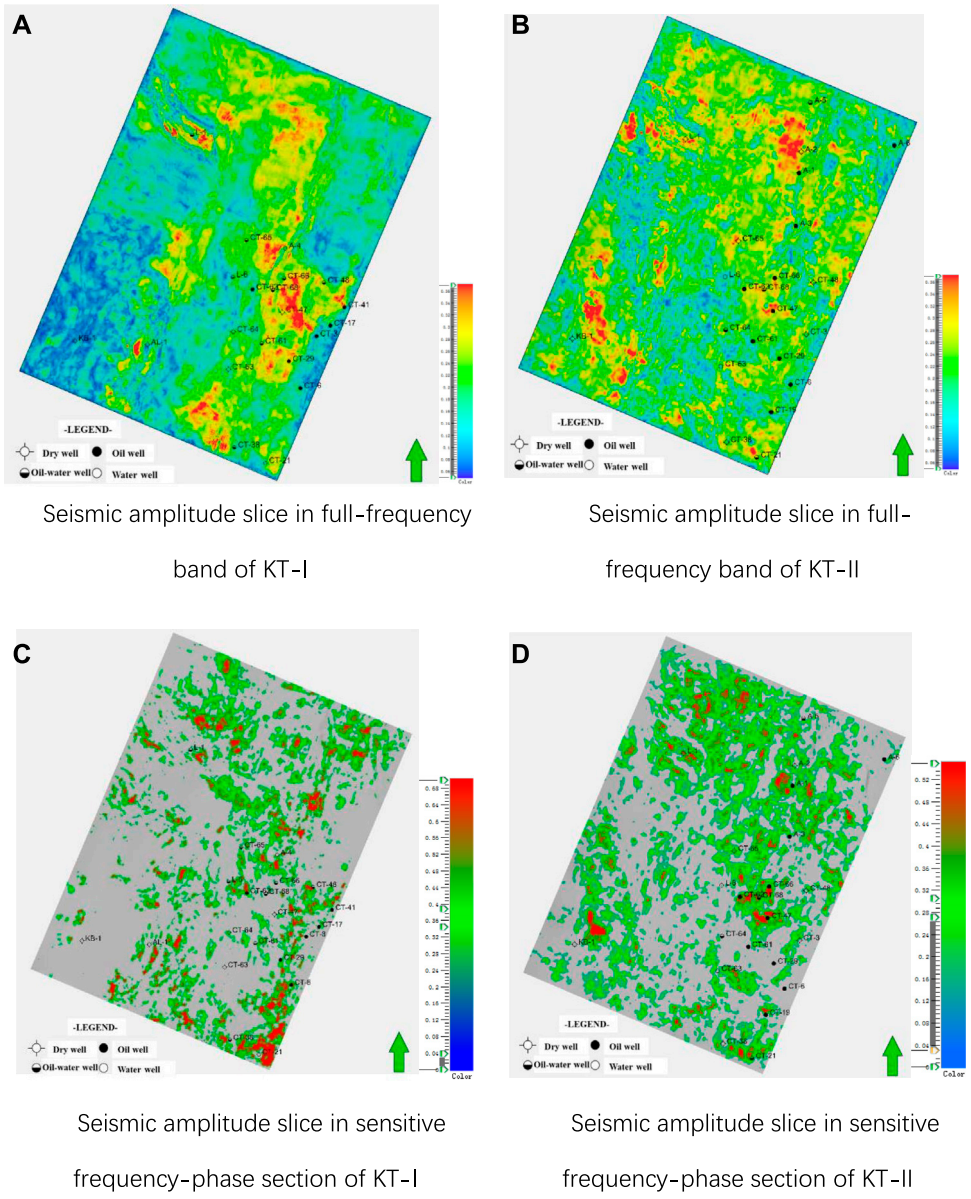

Seismic amplitude slice in full-frequency band of KT-I

Seismic amplitude slice in full-frequency band of KT-II

Seismic amplitude slice in sensitive frequency-phase section of KT-I

Seismic amplitude slice in sensitive frequency-phase section of KT-II

FIGURE 11
Comparison of oil and gas detection effects between conventional amplitude and amplitude after phase decomposition.

the low frequency end. The spectrum decomposition of the least squares method has high vertical resolution, and is closely related to the energy of the seismic traces. The tailing effect in frequency domain and time domain is small.

5.2 Frequency band sensitivity to hydrocarbons and phase optimization

A lot of attempts have been made on the input data of phase decomposition for oil and gas detection. The first attempt is to use the original full-frequency data for phase decomposition, and the effect of identifying oil-water layers is indistinct. Therefore, on the basis of least square spectrum decomposition processing, single frequency data was innovatively adopted for phase decomposition by 10 Hz, 20 Hz, and 30 Hz single frequency volumes. According to the characteristics of the spectrum gather of the well side traces, the oil and gas response energy is concentrated near 20 Hz, so the 20 Hz single frequency volume is finally used for phase decomposition.

As shown in Figure 7A, through fine reservoir calibration, it can be found that the amplitude energy group of KT-I oil layer is about 20 Hz on the frequency gather and 30°–80° on the phase gather. The sensitive frequency bands of layers KT-II and KT-I are close, as shown in Figure 7B, but the sensitive phases are different, and they are located between 150° and 180° and between −150° and −180°.

5.3 Analysis of detection effect

After the sensitive frequency and phase are determined, oil and gas can be detected according to the amplitude corresponding to the specified frequency and phase section. The detection effect of this method is illustrated from the two dimensions of section and plane.

It can be seen from the section (Figures 8, 9) that the amplitude difference between oil layer and dry layer is not obvious in the conventional section. After the phase decomposition and data reconstruction of seismic data in sensitive frequency band, the designated phase stacking section can better distinguish oil layer and dry layer. On the overall phase stacking section, the amplitude of oil layer is stronger than oil-water layer, and oil-water layer is stronger than dry layer.

In the phase interval stack volume, to extract the slice of RMS attribute of KT-I and KT-II respectively, and use the amplitude characteristics previously analyzed to detect fluids. Moreover, the RMS amplitude at the well point and the RMS amplitude of the phase decomposition are intersected, as shown in Figure 10. Compared with the amplitude detection results of conventional section, the phase decomposition results have a better distinction between the oil layer and oil-water layer of KT-I. The intersection results of KT-II are slightly worse than KT-I, but compared with the conventional seismic amplitude attributes, it has a better identification accuracy for oil layer.

According to the threshold value obtained from well intersection analysis, the fluid ranges of KT-I and KT-II can be carved. The left part in Figure 11C shows the fluid carving result of upper KT-I, and Figure 11D shows that of upper KT-II. Compared with conventional seismic amplitude attributes (Figures 11A, B), the fluid results identified by phase decomposition have a higher coincidence rate with the drilled wells. There are 6 industrial oil flow wells in layer KT-I, 6 wells are matched, thus the coincidence degree is 100%. There are 10 industrial oil flow wells in layer KT-II, 8 wells are matched, thus the coincidence degree is 80%. Moreover, according to the prediction results, the drilled wells L-4 and L-7 have both obtained industrial oil flow in the target formation. Hereinto, Well L-4 obtained daily oil production of 4.89 m^3 in Carboniferous KT-I in testing, and obtained maximum daily oil production of 24 m^3 in KT-II; Well L-7 obtained daily oil production of 12 m^3 in Carboniferous KT-II in testing after acid fracturing. It also verifies the accuracy of oil and gas detection results.

6 Conclusion

In the case that conventional amplitude and frequency cannot distinguish fluids clearly, this paper provides a new idea for oil and gas detection. Its core is to find the corresponding sensitive frequency and phase of oil and gas layers. In a specific study area, the sensitive frequency and phase are different, so it is necessary to analyze and optimize according to forward modeling and actual data. Therefore, in practical application, it is necessary to strengthen the combination of well and seismic analysis.

The phase range of oil layer energy concentration of KT-I layer in the Pre-Caspian Basin is 30°–80°, and the characteristics of oil layer, oil-water layer and dry layer on section are obvious, thus they can be effectively distinguished; The phase range of energy concentration of KT-II oil layer is between +150° and −150°.

Both forward modeling and practical application results show that the phase decomposition technique is highly reliable for fluid identification under the carbonate reef facies controlled constraint, and the identification results can be used for well location optimization, which is of great significance for improving the exploration efficiency of complex carbonate rocks. However, this method has some limitations. It requires drilling data to optimize the sensitive frequency and phase, thus it is difficult to apply in the area without wells.

Data availability statement

The original contributions presented in the study are included in the article/Supplementary material, further inquiries can be directed to the corresponding author.

Author contributions

ZW and SJ designed and directed the project; RJ, SS, and YZ performed the experiments; XW, YL, and YW contributed significantly to analysis and manuscript preparation; YZ, ZW, and RJ performed the data analyses and wrote the manuscript. All authors contributed to the article and approved the submitted version.

Funding

National Major Science and Technology Projects of China (Grant No. 2016ZX05029), and PetroChina Science and Technology Major Project (Grant Nos 2019D-4307; 2021DJ31). The authors declare that this study received funding from PetroChina Science and Technology Major Project. The funder was not involved in the study design, collection, analysis, interpretation of data, the writing of this article, or the decision to submit it for publication. The authors declare that PetroChina Science and Technology Major Project was not involved in the study design, collection, analysis, interpretation of data, the writing of this article, or the decision to submit it for publication.

Conflict of interest

This research was funded by the China National Petroleum Corporation Science and Technology Program (No. 2019D-4307; 2021DJ31) and National Major Science and Technology Projects of China (Grant No. 2016ZX05029).

Authors ZW, YZ, ZJ, RJ, XW, YW, and YL were employed by CNPC. Authors SJ and SS were employed by CNODC.

Publisher's note

References

Barbato, U., Portniaguine, O., Winkelman, B., and Castagna, J. (2017). Phase decomposition as a dhi in bright-spot regimes: A gulf of Mexico case study. *Soc. Explor. Geophys.* 2017, 3976–3980. SEG Technical Program Expanded Abstracts 2017. doi:10.1190/segam2017-17737608.1

Cao, X., Chang, X., Liu, Y., and Chunlei, Z. (2010). Seismic singularity attribute and its applications in hydrocarbon detection. *Petroleum Explor. Dev.* 37 (3), 325–329. doi:10.1016/s1876-3804(10)60036-5

Castagna, J., Chesnokov, E., Zheng, Y., and Oyem, A. (2019). *Reservoir delineation using bandwidth extension and phase decomposition*. Houston: University of HOUSTON.

Castagna, J., Oyem, A., Portniaguine, O., and Aikulola, U. (2016). Phase decomposition. *Interpretation* 4 (3), N1–N10. doi:10.1190/int-2015-0150.1

Chen, C., Feng, S., and Aling, M. (2012). Application of 90° phase data in lithologic interpretation. *Oil Geophys. Prospect.* 47 (1), 95–99.

Chen, H., Peng, L., Chen, X., Hu, Y., Li, R., and Fang, Y. (2022). A three-parameter W transform and its application to gas reservoir identification. *Geophysics* 87 (5), V521–V532. doi:10.1190/geo2021-0803.1

Chen, X., Chen, H., Fang, Y., and Hu, Y. (2020). High-order synchroextracting time-frequency analysis and its application in seismic hydrocarbon reservoir identification. *IEEE Geoscience Remote Sens. Lett.* 18 (11), 2011–2015. doi:10.1109/lgrs.2020.3009259

Chen, Y., Bi, J., Qiu, X., Yang, H., and Cao, J. (2020). A method of seismic meme inversion and its application. *Petroleum Explor. Dev.* 47 (06), 1235–1245. doi:10.1016/s1876-3804(20)60132-5

Fang, J., Wu, L., and Gao, G. (2008). Sedimentary facies and types of carbonate rock reservoir in caspian seashore basin: A case from carboniferous. *Petroleum Explor. Dev.* 35 (4), 498–508.

Guo, Q., Ba, J., and Luo, C. (2022). Nonlinear petrophysical amplitude variation with offset inversion with spatially variable pore aspect ratio. *GEOPHYSICS* 87 (4), M111–M125. doi:10.1190/geo2021-0583.1

He, L., Zhao, L., and Li, J. (2014). Complex relationship between porosity and permeability of carbonate reservoirs and its controlling factors: A case of platform facies in Pre-Caspian Basin. *Petroleum Explor. Dev.* 41 (2), 206–214. doi:10.1016/S1876-3804(14)60026-4

Jin, S., Zheng, J., and Yu, B. (2015). *Late Paleozoic sequence stratigraphy and sedimentary facies in the eastern margin of the PreCaspian basin*. Beijing: Petroleum Industry Press.

Liang, S., Wang, Y., and Jin, S. (2013). Controlling of tectonic evolution on hydrocarbon occurrence in PreCaspian Basin. *Petroleum Geol. Exp.* 35 (2), 174–178.

Lin, C., Zhang, X., and Dong, C. (2007). Hepatoprotective effects of Chai-Hu-Ching-Kan-Tang on acetaminophen-induced acute liver injury in rats. *Acta Pet. Sin.* 28 (2), 69–79. doi:10.1142/S0192415X07004631

Pan, W., Liu, H., and Zhang, L. (2013). Application of 90°-phase seismic data in prediction of sandstone. *J. Geomechanics* 19 (3), 304–314.

Qiao, Z., Han, Z., and Kong, S. (2018). Application of extremal amplitude and hydrocarbon detection technique to the oil and gas exploration in the Bohai Sea. *Oil Drill. Prod. Technol.* 40 (A01), 4. doi:10.13639/j.odpt.2018.S0.006

Selmara, D. A. E., Castagna, J. P., and Gil, G. (2019). Case study: Phase-component amplitude variation with angle. *GEOPHYSICS* 84 (4), B285–B297. doi:10.1190/geo2018-0762.1

Xu, C., Qian, G., and Zhang, J. (2009). *Geological characteristics and reservoir-forming assemblages*. BeiJing: Petroleum Industry Press.

Xu, K. (2011). *Hydrocarbon accumulation characteristics and exploration practice in the Middle Block of the eastern margin of the Precaspian Basin*. BeiJing: Petroleum Industry Press.

Yang, Z., Sha, X., and Li, Z. (2010). Hydrocarbon detection and application in lithologic resevoir exploration. *Nat. Gas. Geosci.* 21 (5), 822–827.

Yu, H., Zhang, Y., and Li, J. (2013). Identification of the carbonate reservoir based on spectral decomposition. *Prog. Geophys.* 28 (3), 1440–1446. doi:10.6038/pg20130338

Zhang, H., Ma, J., and Jiang, Z. (2017). Application of spectral decomposition technique in reservoir characterization and fluid identification. *Complex Hydrocarb. Reserv.* 10 (1), 31–33.

Zhao, L., Geng, J., Cheng, J., Han, D., and Guo, T. (2014). Probabilistic lithofacies prediction from prestack seismic data in a heterogeneous carbonate reservoir. *GEOPHYSICS* 79 (5), M25–M34. doi:10.1190/geo2013-0406.1

Zhao, L., Li, J., Li, K., Zifei, F., Heng, S., and Xubin, C. (2010). Development and genetic mechanism of complex carbonate reservoir fractures: A case from the zanarol Oilfield, Kazakhstan. *Kazakhstan. Petroleum Explor. Dev.* 37 (3), 304–309. doi:10.1016/s1876-3804(10)60034-1

Zhao, W., Yang, W., and Zhao, W. (2014). The review of technical progress in application of seismic reservoir and hydrocarbon prediction. *Prog. Geophys.* 29 (5), 2337–2346.

Zhao, W., Zhao, L., Wang, X., Wang, S., Sun, M., and Wang, C. (2016). Phase behavior characteristics and water-flooding development technical policy of weakly volatile oil in carbonate reservoirs. *Petroleum Explor. Dev.* 43 (2), 308–314. doi:10.1016/s1876-3804(16)30035-0

Zheng, J., Peng, G., and Sun, J. (2019). Fusing amplitude and frequency attributes for hydrocarbon detection using 90° phase shift data. *Geophys. Prospect. Petroleum* 58 (1), 130–138.

Zheng, J., Wang, Z., and Xue, L. (2011). *Petroleum Geology Theory and exploration practice in salt-bearing basins in central Asia*. Beijing: Petroleum Industry Press.

Zhou, J., Ba, J., Castagna, J., Guo, Q., Yu, C., and Jiang, R. (2019). Application of an STFT-based seismic even and odd decomposition method for thin-layer property estimation. *IEEE Geoscience Remote Sens. Lett.* 16 (9), 1348–1352. doi:10.1109/lgrs.2019.2901261

Frontiers in Earth Science

Investigates the processes operating within the major spheres of our planet

Advances our understanding across the earth sciences, providing a theoretical background for better use of our planet's resources and equipping us to face major environmental challenges.

Discover the latest Research Topics

See more →

Frontiers

Avenue du Tribunal-Fédéral 34
1005 Lausanne, Switzerland
frontiersin.org

Contact us

+41 (0)21 510 17 00
frontiersin.org/about/contact